AERODYNAMICALLY INDUCED MOTIONS OF BLUFF BODIES SUSPENDED BENEATH HELICOPTERS

D. Chan, et al

Bristol University

Prepared for:

Army Research and Development Group (Europe)

October 1975

Report No. AD

UNIVERSITY OF BRISTOL

DEPARTMENT OF AERONAUTICAL ENGINEERING

AERODYNAMICALLY INDUCED MOTIONS OF BLUFF BODIES SUSPENDED BENEATH HELICOPTERS

FINAL TECHNICAL REPORT

by

D. Chan, J. W. Flower and A. Simpson

October 1975

EUROPEAN RESEARCH OFFICE
United States Army
London N.W.1., England

Contract Number DAJA 37-73-C-0477

REPORT DOCUMENTATION PAGE

READ INSTRUCTIONS BEFORE COMPLETING FORM

1. REPORT NUMBER	2. GOVT ACCESSION NO. / 3. RECIPIENT'S CATALOG NUMBER
4. TITLE (and Subtitle): AERODYNAMICALLY INDUCED MOTIONS OF BLUFF BODIES SUSPENDED BENEATH HELICOPTERS	5. TYPE OF REPORT & PERIOD COVERED: FINAL TECHNICAL REPORT OCT 72 - OCT 75
	6. PERFORMING ORG. REPORT NUMBER
7. AUTHOR(s): D. Chan, J.W. Flower, A. Simpson	8. CONTRACT OR GRANT NUMBER(s): DAJA 37-73-C-0477
9. PERFORMING ORGANIZATION NAME AND ADDRESS: Department of Aeronautical Engineering, University of Bristol, Bristol U.K.	10. PROGRAM ELEMENT, PROJECT, TASK AREA & WORK UNIT NUMBERS: 6,11,02A-200611-2B 33H - 00 - 333
11. CONTROLLING OFFICE NAME AND ADDRESS: U.S. Army R&S Gp (EUR), Box 65, FPO NEW YORK 09510	12. REPORT DATE: OCT 75
	13. NUMBER OF PAGES: 271
14. MONITORING AGENCY NAME & ADDRESS (if different from Controlling Office)	15. SECURITY CLASS. (of this report): UNCLASSIFIED
	15a. DECLASSIFICATION/DOWNGRADING SCHEDULE

16. DISTRIBUTION STATEMENT (of this Report)

Distribution Unlimited

Approved for public release

17. DISTRIBUTION STATEMENT (of the abstract entered in Block 20, if different from Report)

18. SUPPLEMENTARY NOTES

19. KEY WORDS (Continue on reverse side if necessary and identify by block number)

Underslung Load, Instability, Aerodynamics, Cargo Containers, Heavy Lift Helicopters

20. ABSTRACT (Continue on reverse side if necessary and identify by block number)

SEE OVER

DD FORM 1 JAN 73 1473 EDITION OF 1 NOV 65 IS OBSOLETE

In this Report, which is concerned with an investigation into aerodynamic mechanisms supporting underslung load instability, the results of the three years' work are presented and discussed. Certain important dynamic features of the aerodynamic actions on rectangular cargo container shapes have now been identified, namely those arising from the existence of some appreciable phase lags in the growth and decay of separation bubbles. It is shown that some of the aerodynamic coefficients vary with frequency to such an extent that the use of quasi-steady aerodynamic theory may lead to meaningless results. A simple, quasi-empirical, mathematical model governing separation bubble growth has been devised, and this has been found to give adequate representation of the unstable aerodynamic pitching moments associated with pitching oscillations.

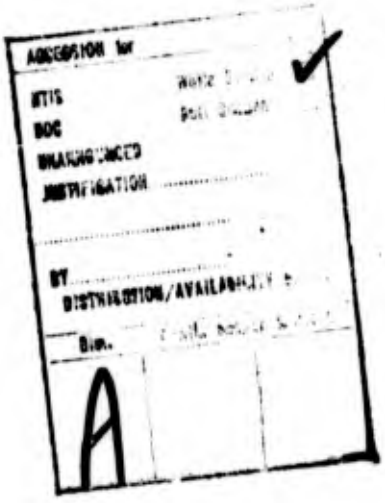

AERODYNAMICALLY INDUCED MOTIONS OF BLUFF BODIES SUSPENDED BENEATH HELICOPTERS

FINAL TECHNICAL REPORT

by

D. Chan, J.W. Flower and A. Simpson

SUMMARY

In this Report, which is concerned with an investigation into aerodynamic mechanisms supporting underslung load instability, the results of the three years' work are presented and discussed. Certain important dynamic features of the aerodynamic actions on rectangular cargo container shapes have now been identified, namely those arising from the existence of some appreciable phase lags in the growth and decay of separation bubbles. It is shown that some of the aerodynamic coefficients vary with frequency to such an extent that the use of quasi-steady aerodynamic theory may lead to meaningless results. Also, free stream turbulence is shown to exert a profound effect on container stability. A simple, quasi-empirical, mathematical model governing separation bubble growth has been devised, and this has been found to give adequate representation of the unstable aerodynamic pitching moments associated with pitching oscillations. In parallel with these aerodynamic investigations, the lateral dynamics of containers with parallel strops has been studied and means of obviating single-degree-of-freedom instabilities and flutter have been suggested.

CONTENTS

id.

1. INTRODUCTION

Over the past thirty years, a considerable number of philosophies on the air transport of freight has evolved. One of the most important of these philosophies concerns the use of helicopters to convey freight "externally" by suspending it directly, or within a container, beneath the helicopter fuselage by using strop and lifting hook configurations. In this way, loads whose bulk would preclude air transportation by any other means may be carried successfully. Furthermore, turn-round times are minimised by such procedures - an important advantage in many civil and military operations. Ordnance, strategic supplies (including food) and even troops may be transported efficiently by this means and recovery operations may be performed with optimum speed. On the civil side, crane helicopters have been used in the erection of bridges, towers and other buildings and structures, and even for the transport of mobile operating theatres.

However, inevitably, there are limitations of this simple "external" mode of freight transportation, these being associated with the aerodynamic forces which arise when there is motion of air relative to the suspended body. These forces can lead to static and dynamic states of instability of the suspended body or of the combined helicopter/freight system. In many instances, the severity of the dynamic instability has been such as to make it necessary to jettison the suspended freight. In many other instances, less severe dynamic instability states of the freight have created handling difficulties and have necessitated radical reduction of forward speed of the helicopter. These difficulties probably stem from the poor Dutch Roll damping characteristics of most helicopters - particularly at the higher forward speeds.

While it is not possible to rule out *a priori* the possibility of instability types requiring motion of *both* freight and helicopter, it is recognised generally that most of the troublesome motions are those which may be ascribed to freight oscillation *per se* with the helicopter fuselage assumed fixed in space and with the aerodynamic forces on the freight being assumed to be generated by a uniform airstream impinging on it. Assumptions of this type have been a common feature of the literature to date and, indeed, will be upheld by the authors of this Report. Even when such assumptions are made, the number of freightage shapes, lifting hook arrangements and strop configurations makes the task of *general* stabilisation an extremely difficult one. It is, in fact, desirable to sub-divide the class of suspended freight problems further if progress is to be made towards their understanding.

If the aerodynamic forces acting on a bluff body (the freight) and its supporting strops cause the body to oscillate unstably, two possibilities exist:-

(a) The body itself possesses the attribute of aerodynamic instability when suitably suspended.

(b) The strop system (usually cables) is aerodynamically unstable, in whole or in part.

These possibilities are, of course, not mutually exclusive and may interact. However, if the freight mass is large and one is primarily interested in the low-frequency or pendulum types of freight motion, the inherent dynamic instabilities of the strops (which are relatively high frequency vibrations generated by the shedding of vortices from the cables) will not, in general, interact with those of the freight mass; for while parametric interaction is possible[1], between high frequency forces and low frequency response motions, such may be ruled out in the present problem on purely physical grounds. It is for such reasons that the emphasis in the present research, and in many related studies, has been placed on the aerodynamics of the actual freight. A knowledge of the aerodynamic characteristics of the freight should enable most of the important instability modes of the freight/strop arrangement to be assessed and, hopefully, cured. The cure might involve aerodynamic devices attached to the freight and/or the specification of optional strop arrangements[2]. It might, however, involve the application of active control technology via the "active arm" concept[3] or automatic movement of the helicopter.[4] Whatever solution is adopted, a knowledge of the freight aerodynamics is an essential prerequisite.

Now in the early studies of plate-load instability, Sheldon[2] used aerodynamic information obtained from static tests to calculate the stability modes of flat plates suspended by strops beneath helicopters. In this way, Sheldon was able to suggest strop arrangements which would allow forward flight speeds up to the design envelope values without incurring unstable oscillation or static divergence of the suspended pallets. However, two salient points regarding Sheldon's work are frequently overlooked:-

(a) There was no way in which the <u>pitch damping</u> derivative could be calculated from static test data, and Sheldon measured this derivative dynamically over a wide range of incidences and windspeeds for his thick flat plates. These results showed a marked dependence on the frequency parameter.

(b) Many of the results in the aerodynamically unstable longitudinal "flutter" mode were calculated from derivatives obtained at much lower frequency parameters than those obtaining at the actual flutter conditions. One must therefore conclude that these latter calculations (and others such as those based on the equations developed in Reference 5) might not produce accurate predictions of stability boundaries. Some investigators[5] ignore completely the pitch and yaw damping derivatives and base their predictions totally on data obtained from static aerodynamic tests. Such omissions are certainly not justified, since Sheldon's measurements[2] show that these derivatives can become negative under certain conditions involving high values of frequency parameter.

Several authors have followed the small perturbation approach in the study of towed load stability - see, for example, References 2 - 7. Of these, only Sheldon[2] and Liu[4] mention sensitivity of the stability boundaries to parameter changes and, in particular[2], to changes in derivative values. By far the most important derivative from the viewpoint of the "flutter mode" stability of a flat plate load was found by Sheldon to be the pitch damping. Further, since Sheldon's plates were

'thick', one might expect that this derivative is also a most significant one for the various container box shapes. Again, this derivative is precisely the one which Liu's slender body/viscous cross-flow approach[4] cannot sensibly predict! In Liu's words:- "It appears that the axial and normal forces are predicted adequately but that the moment coefficient is not satisfactory" and "the viscous cross-flow term in the theoretical calculations accounts for the separation effects on the upper surface (no bubble) but does not account for separation on the lower surface (in the bubble)" for a container box at positive incidence. Indeed, it will be shown herein that bubbles exist on all surfaces of the 1:0.4:0.4 and 1:0.2:0.2 box containers over an appreciable range of incidences centred on zero and that, therefore, theories such as Liu's are highly suspect when estimating pitch and yaw damping in this range. The associated 'stiffness' derivatives would also be in error as would any predictions of steady moments.

From what has been said, it will be clear that there is a dearth of information on certain bluff-body aerodynamic derivatives, and particularly on the manner in which these are influenced by frequency parameter. Also, in instances where aerodynamic forces change rapidly with frequency parameter and at the same time exhibit strong amplitude-dependent nonlinearities, the value of the small perturbation (linear) approach may be questioned. Thus emerged the major objectives of this Contract Work:- Stated broadly these were to investigate the nature of the aerodynamic forces acting on the various freight-load shapes as these shapes were forced, inexorably, to execute motions typical of those observed in practice and in free-model tests, and to gain an understanding of the aerodynamic mechanisms involved in the production of unstable motions - ultimately with a view to suggesting cures. Furthermore, the various mechanisms were to be checked by inserting the measured aerodynamic force information into the equations of motion of the appropriate freight-strop configuration and observing the similarity, or otherwise, of the predicted and actual motions.

In view of the number of freight-load shapes, a decision had to be made at an early stage as to which 'shape' should be used in the lengthy developmental process from which the ultimate six-degrees-of-freedom test facility would eventually emerge. After much deliberation, the 1:0.4:0.4 container was chosen as being by far the most common freight conveying shape. Thus, as by-products of the developmental process, aerodynamic information on this important shape would become available for use by other workers[3] in the field of underslung load stability and control. A wide selection of these results is, in fact, presented herein. Another decision which had to be taken at an early stage in this research study was that of determining the most typical equilibrium orientation of the container. For single-strop configurations, the 'broadside-on' equilibrium position was inevitable and much time was devoted to free-body tests in such cases. However, it became clear, from the literature that the 'minimum drag' equilibrium position was favoured, supported by a twin-strop suspension system which gave the container a small nose-down attitude. It was decided, consequently, to develop the processing methods in relation to this 'minimum drag' equilibrium position and small angles of departure therefrom.

From the outset, it was decided that the measurement of surface pressures during oscillatory motion would be the major means by which the aerodynamic information would be gleaned. These pressure measurements would be supplemented by flow visualisation studies in order to obtain a fuller understanding of the aerodynamic mechanisms involved. From the pressures, forces would be obtained by numerical quadrature and all six components of force would be displayed as time histories juxtaposed against the time history of the input motions. Such information would enable the various aerodynamic derivatives to be obtained, if required, for various motion amplitudes, frequencies and windspeeds. At a relatively early stage it was recognised that free-stream turbulence could influence container stability in a dramatic way, and that the application of the aerodynamic information based on low-turbulence wind-tunnel results[8] could lead to the inaccurate prediction of stability boundaries in certain cases (see Reference 9). Thus, it was decided also to perform a limited investigation into the effects of level of turbulence.

With regard to the development of the test facility, effort has been concentrated into two main channels:- (a) The perfection of pressure scanning techniques and the allied computer processing. (b) The design and construction of the six-degree of freedom test rig. These activities will be described fully at a later stage in this Report. Considerable effort has also been expended in an attempt to gain understanding of the aerodynamics of box shapes by recourse to numerical solutions of the two-dimensional Navier-Stokes equations.[10] Again, in an attempt to model the aerodynamic characteristics of a container in the neighbourhood of the minimum drag position, mathematical expressions have been obtained which appear to explain all the major features of the lift and moment curves and dynamic effects thereon.

Owing to the growth of methods for processing equations of motion elsewhere[3,4], this aspect of the work has been 'played down' in relation to what is, perhaps, the more immediate and fundamental problem - namely that of determining the aerodynamic forces. Indeed, it seems now that to spend time on routine methods of equation-solving would detract from the volume of aerodynamic information supplied and would simply duplicate work elsewhere[3,4]. This view is supported by the extremely complex aerodynamic picture which has evolved from the results to date - particularly with regard to the aerodynamic pitching and yawing moment characteristics. Much effort will need to be expended in the understanding of these results, and the authors believe that this constitutes aerodynamic research of an extremely fundamental nature.

Finally, it is hoped that the results and ideas presented herein will prove invaluable to those engaged in the process of load stabilization and that, in particular, the derivative information will be of immediate and direct relevance to the active-control studies being undertaken elsewhere.

2. PRELIMINARY STUDIES

2.1 Free Oscillation Tests

The problem of oscillatory loads suspended beneath helicopters is that these loads execute motions which are undesirable because they limit

controllability and forward speed. The conditions under which these oscillations become unacceptable depend on a number of aerodynamic and geometric parameters. It is necessary that these parameters which lead to the unstable motions be defined in the first instance, so that a more definite attack on the problem can be formulated.

In order to define those aerodynamic and geometric parameters which contribute most to the dynamic behaviour of the container loads, it is necessary to observe visually the modes of oscillation of a freely suspended container. For reasons given in Section 1 of this report, the 20' x 8' x 8' container was chosen as the most typical container to model and to observe visually in the free oscillation studies, although some attention has been given to the 40' x 8' x 8' container.

It was decided to construct 1/20th scale balsa models and to conduct a series of free oscillation tests. These tests involved the variation of the stropping configuration, weight, moment of inertia and wind speed.

The stropping consisted of cotton cords from each corner joined above the load centre to a single cord as shown in Figure 2.1. The single cord was then attached to the superstructure of the 3'6" open-jet wind tunnel.

In the flow it was observed that the model aligned itself so that its major axis was perpendicular to the wind vector. This was the case, even when the model's major axis was initially aligned parallel with the free stream flow. Subsequent observations of the model showed that its mode of oscillation at low velocities (1-15 ft/sec.) was a steady oscillation in yaw about a mean position (with major axis perpendicular to the flow). At medium wind speeds (15-20 ft/sec.) a lateral oscillation with coupled sideslip and yaw, in phase, was observed. At higher wind speeds (21-30 ft/sec.) the model inclined itself at up to 20° to the vertical with steady yaw oscillations about these positions.

It was found possible to measure the frequency at which the model oscillated in a particular mode with a stop watch. By varying the windspeed it was possible to obtain a relationship between the oscillation frequency of the freely oscillating model and the free stream velocity. These results were then verified in another of the Department's wind tunnels. This wind tunnel was of the recirculatory closed section type with a working section dimension 18' x 8'6". Only a few cases were studied in order to verify the consistency of results in the tunnels.

The relative lengths of the strop were altered and the effects on the oscillations were observed. The results of these tests are shown in Figures 2.2, 2.3, 2.4. The stropping configuration was then altered to a bifilar or twin strop arrangement as shown in Figure 2.1, and the tests repeated. These results showed that the model was unstable at medium and higher windspeeds, usually with a steady oscillation in yaw, although at higher windspeeds it sometimes broke out into erratic elliptic oscillations involving some longitudinal motion.

It was also possible to demonstrate the importance of yaw inertia effects on the oscillations. With the total weight of the model held constant, the yaw inertia could be changed by altering the positions of the masses within the container. Results for the single strop configuration (Figure 2.3) showed that the yaw frequency of the container with the maximum yaw inertia was approximately half the value of that obtained with the minimum yaw inertia. The bifilar stropping configuration led to a distinct change in the mode of oscillation of the container for the same windspeeds as the yaw inertia was changed. It was observed that the model exhibited a large amplitude sideslip/yaw coupled oscillation when the yaw inertia was a maximum, and a steady yaw oscillation when the masses were moved close to the centre of gravity. This change in the mode of oscillation was perhaps the most significant result obtained from these tests. The results are shown in Figure 2.5.

It was noted that when the model oscillated in its yawing modes about its preferred equilibrium position (that is, with its major axis perpendicular to the wind), the oscillation frequency was relatively easy to measure. However, where the model executed a pure sideslip motion, it was not possible to gain accurate estimates of the frequency, because the motion could be of small amplitude and difficult to follow. Therefore, the yaw frequency was measured whenever possible even though the motion may have contained a sideslip as a constituent. In these cases a qualitative picture only was obtained regarding the modes of oscillation.

A 1/20th scaled model of a 40' x 8' x 8' container was also constructed. The tests performed on this model only included the variation of the stropping configuration, that is, the parameters a,b shown in Figure 2.1. It was found that the model executed relatively unsteady motions. Moreover, the oscillations were found not to be repeatable at low wind speeds, (i.e. less than 7 ft/sec.). Figure 2.6 shows the yaw frequency plotted against windspeed, the graph showing that the model executes a steady yaw oscillation of almost constant frequency over a range of wind speeds.

From the range of tests conducted, it was noted that there were two predominate modes of oscillation of the model. The first was an oscillation motion about the preferred orientation axis of the model. The second, a sideslip and yaw oscillation combined, also about the preferred orientation axis of the model. However, since the preferred orientation is not the orientation at which container loads are now slung beneath helicopters (as this incurs a substantial drag penalty) free oscillation tests were also conducted on a 1:0.4:0.4 model which was constrained, by strops, to oscillate with its major axis parallel to the flow.

In the preferred orientation case, the model showed itself to be statically stable. That is, the model returned to its equilibrium position when moved up to about $\pm$ 80° from that position. However, the model showed itself to be dynamically unstable in its preferred orientation, the motion in yaw building up to limit cycles as implied earlier.

When the model's orientation was such that the major axis was parallel to the wind flow, it again showed itself to be statically stable and

dynamically unstable. However, in this case, the limit cycle amplitude is such that an incursion into the bounding statically unstable regions is implied and this means that a restraint in yaw is essential if the equilibrium condition is to be maintained. Hence the need for the twin strop configuration in this case.

In summary, steady oscillations in yaw were frequently in evidence with more complex motions involving several degrees of freedom being observed at the higher speeds. Negative damping was apparent at certain attitudes, leading sometimes to the limit cycle oscillations and sometimes to divergence.

2.2 Mathematical Representation of the Yawing Motion

One of the motions of a freely suspended 1:0.4:0.4 container model was an oscillation (limit cycle type) in yaw with little or no coupling with other motions. This motion took place about the preferred (broadside-on) equilibrium configuration of a container suspended by a single strop. For such a system, the mechanical stiffness in yaw is invariably small and will be ignored in what follows. The equation of motion here is:

$$I_{zz}\ddot{\psi} = N(\psi, \dot{\psi}) \qquad \ldots\ldots\ldots\ldots\ldots\ldots\ldots\ldots\ldots\ldots \quad (2.1)$$

where $N(\psi, \dot{\psi})$ is the aerodynamic yawing moment, I_{zz} the yawing moment of inertia and ψ the yaw angle. In order to represent the broad characteristics of the yawing oscillation, one might write

$$N(\psi, \dot{\psi}) = -C_{m1} qSc \sin 2n\psi + C_{m2} \frac{qSc^2}{V} \cos 2m\psi \cdot \dot{\psi} \qquad (2.2)$$

where q is the dynamic pressure, S the reference area and c the reference chord. The trigonometric terms are introduced to conform with the obvious requirements of rotational symmetry of the yawing moment. However, this representation is approximate only, and one should view the trigonometric terms as typical components of a Fourier series for $N(\psi, \dot{\psi})$, the parameters C_{m1} and C_{m2} being analgous to dimensionless Fourier coefficients.

With the above expression for N substituted, the equation of motion may be readily reduced to the dimensionless form

$$\frac{d^2\bar{\psi}}{d\tau^2} - C\frac{d\bar{\psi}}{d\tau}\cos v\bar{\psi} + \sin\bar{\psi} = 0 \qquad \ldots\ldots\ldots\ldots\ldots \quad (2.3)$$

wherein $\bar{\psi} = 2n\psi$, $\nu = m/n$, $\tau = \alpha t$, $\alpha^2 = 2nA$, $A = \frac{qSc\,C_{m1}}{I_{zz}}$,

$C = B/\alpha$, $B = \frac{qSc^2 C_{m2}}{VI_{zz}}$. This form has just two free parameters, namely the damping C and the periodic ratio, ν. The former determines the rate at which motion will build up from rest while the latter determines the existence, or otherwise, of limit cycles or autorotation. Three phase planes are shown in Figures 2.7 to 2.9, these being achieved with C = 0.1 and ν = 1, 2 and 3 respectively. It is observed that when ν = 1, the system autorotates and when $\nu > 1$ the system has one or more limit cycles in the range $-\pi \leq \bar{\psi} \leq \pi$.

The static test results of Laub and Kodani[8] suggest that n should be given unit value. Unfortunately, this value cannot represent the yawing moment characteristic near $\psi = \pm 90^\circ$ in view of the existence of higher harmonic dependence of N on $\bar{\psi}$ in that region due to actions within the separation bubbles. However, n = 1 gives a good shape representation for most other regions provided the yaw axis remains normal to the flow. In order to obtain the coefficient m, and hence ν, and the damping factor C, etc., the case where the motion, ψ, is forced inexorably was studied. For this case, with n = 1 and $\psi = \psi_o + a\sin\omega t$, one obtains

$$N/q = -C_{m1} Sc \sin 2\psi + C_{m2} \frac{Sc^2}{V} \dot{\psi} \cos 2m\psi \qquad \ldots\ldots\ldots \quad (2.4)$$

By using the results of a very preliminary oscillatory test in which pressures on an inexorably oscillating container (0.4' x 0.4' x 1') were measured and integrated to produce the yawing moment for $\psi_o = 0$ (see Figure 2.10), the aerodynamic parameter C_{m2} was estimated to be 2. The details of this testing procedure are given fully in Section 3. From a similar static test (see Figure 2.11), the coefficient C_{m1} was estimated to be 0.15. Also, on the basis of dynamic tests performed at $\psi_o = 0$ and -45°, and subsequent comparison with the appropriate representations of N (equation 2.4), a typical value m = 4 was suggested.

With the coefficients thus assigned in equation (2.4), and with S = 0.4 ft^2, c = 0.4 ft (0.4' x 0.4' x 1' container), a = 21.5°, ω = 5.71/sec and V $\approx$ 50 f/s, the equation (2.4) becomes

$$N/q = -0.024 \sin 2(\psi_o + 0.375 \sin 5.71t)$$

$$+ 0.00549 \cos 5.71t \cos 8(\psi_o + 0.375 \sin 5.71t) \qquad \ldots\ldots \quad (2.5)$$

and this is plotted for $\psi_o = 0, -45^\circ$ and -90° in Figures 2.12 to 2.14 respectively and compared with corresponding measured values. The correspondence is seen to be good for $\psi_o = 0$ and -45°, but not for $\psi_o = -90^\circ$, as expected. Furthermore, the model at $\psi_o = 0$ is found to represent the system well for a wide range of windspeeds, but the case where $\psi_o = -45^\circ$ is modelled well only at the higher speeds.

Referring back to the equation of free motion, it is noted that $\nu = 4$ and $C > 0$, implies limit cycle behaviour typified by the phase plane diagram of Figure 2.9. This model accords broadly with observations of the freely suspended container.

In this simple manner, the major features of the yawing oscillation about the 'broadside-on' equilibrium configuration of box-like container cargo loads can be modelled with a good degree of success. Progress on this type of representation, however, was prevented by absence of accurate aerodynamic data beyond the few instances referred to herein. Also, it seemed that the twin-strop configuration, imposing the 'minimum drag' equilibrium position (major-axis windward $\psi_o = -90^\circ$). was more typical of future applications than the $\psi_o = 0$ case studied here, where this orientation is the one in which the representation via equation (2.5) works least well. It was therefore decided to channel effort into the quest for aerodynamic data (Sections 3 and 4) and, ultimately, into better means of representing aerodynamic characteristics in the neighbourhood of $\psi_o = -90^\circ$ (Section 7).

3. DETERMINATION OF DYNAMIC FORCES AND MOMENTS FROM WIND TUNNEL TESTS

The aerodynamic forces acting on a load in unsteady motion depend, in principle, upon the whole past history of the motion. A comprehensive coverage of all possible conditions would therefore depend not only on the instantaneous orientation of the load and its velocity in all six degrees of freedom, but the way in which the velocities had been varying prior to that point. An experimental investigation involving systematic variation of <u>all</u> associated parameters would be prohibitive, and could not be contemplated. It was decided to concentrate attention on steady oscillations of simple harmonic type, where even this could involve all combinations of initial setting of orientation, amplitude of oscillation in each degree of freedom, phase relationships between the various degrees of freedom, and frequency of oscillation compared with wind velocity. This latter parameter is best expressed as

$$\text{frequency parameter} = \frac{2\pi \text{ frequency (c/s)} \times \text{model length (ft)}}{\text{Wind speed (ft/s)}}$$

At model scale the higher representative frequency parameters demand either high frequency for moderate wind speeds, or modest frequencies at low wind speed. The first would be difficult to engineer, and the second makes direct measurement of forces and moment difficult, with the aerodynamic forces being probably two orders of magnitude down on inertia forces. It was, therefore, decided to extract the force and moment information from pressure measurements, as for a bluff shape with sharp edges, friction forces are negligible and separations from the sharp edges lead to comparatively smooth pressure distributions.

Development of a rig allowing movement in up to six degrees of freedom would obviously take time, and it was decided to start testing by using models with one degree of freedom only. Study of free oscillations had shown the almost overriding importance of knowing the yawing characteristics, and this motion was therefore chosen as the subject of the first tests.

3.1 Single Degree of Freedom Models

3.1.1 Models

Two 1/20th scale models were constructed from perspex. The system of axes chosen to define model position and movement and the associated forces and moments are shown in Figure 3.1. The y coordinate runs along the major chord and the x coordinate along a minor chord of the model. The z coordinate is along the second minor chord. For the preferred orientation for the container with single strop, the x-axis would face upstream, the y axis sideways, and a yawing motion would be about the z axis. It should be noted that for the 1:0.4:0.4 container shape there would be no difference in form for aerodynamic forces generated by pitch or by yaw. For convenience in testing, the model was usually mounted in the wind tunnel with z axis horizontal, a pitching motion then corresponding to the yaw observed with the freely suspended models.

The first model was arranged to be pitched (or yawed) about a minor (z) axis and a second model about the major (y) axis. Thirty-nine pressure points were incorporated into the first model, the distribution being on the faces normal to the x and y axes, as shown in Figure 3.2. With a limitation of 48 tabulations on the scanivalve, a distribution of pressure points was chosen such that the matrix of points was different on each side of the model in an attempt to give a better overall coverage.

Each pressure point is assumed to give an average pressure over some area, and this area to have some moment arm about the axis of the model. These areas and moment arms represent 'weightings' to be applied to each pressure reading when integrating to give total force and moment components. These weightings are given in Appendix 1.

3.1.2 Model support and actuation

The model support and associated apparatus is shown schematically in Figure 3.3. The model is shown to be supported by a stand, the axis of rotation being the z-axis. The axis of the model also contains a position recorder to register angular position at any instant of time.

The forcing mechanism of the rig consisted of a 'four-bar linkage' driven by an induction motor with a reduction gear drive. A microswitch, positioned on one link of the mechanism, provided a pulse to an Analogue Digital Converter for initiation of the scanning procedure. The relative ratios of the links in the 'four-bar linkage' were chosen such that the model motion was close to simple harmonic motion. The length of one

link could be set to give any amplitude from $\pm 10^{\circ}$ to $\pm 29.5^{\circ}$ in steps of about 5°. The analysis of this mechanism is given in Appendix 2, with a comparison of experimental and theoretical position traces.

3.1.3 Instrumentation

The instrumentation and associated apparatus is best introduced by describing the process by which the final results were obtained.

The pressure points on the model were connected by tubes to the tabulations of a scani-valve, and sampled in turn while the model was oscillating. The scani-valve contains a reluctance type transducer which converts an unsteady pressure into an electrical signal directly proportional to and in phase with it. This is done by means of a carrier frequency of 3 KHz, which is amplitude modulated by the unsteady pressure. The electrical signal is detected in an amplitude demodulator to give the required output to a D.C. Amplifier. The signal is then fed into an Analogue to Digital Converter (A.D.C.) which effectively 'chops' the continuous signal into discrete parts for processing by a Hewlett Packard 2100A computer (of which the A.D.C. is a piece of peripheral equipment). This equipment is illustrated in Figure 3.4. The unsteady pressure signal is fed to channel 1 of the A.D.C. whilst the pulse obtained from the microswitch of the 'four-bar' linkage is fed to channel 0.

The 'trigger' pulse remains at -0.65 volts when the contacts of the microswitch are not made. When the contacts are made the pulse signal rises to about -0.1 volt. As soon as the pulse signal rises to -0.35 volts (a preset value designated in a computer program), the A.D.C. commences to 'scan' the unsteady pressure signal at a preset rate. The computer was loaded with a program at the beginning of a test; the program contains a numerical averaging process which is described in Appendix 3. The computer outputs the pressures as a function of time on to a data tape. This tape is then fed into a second bank of programs for the evaluation of the aerodynamic forces on the model.

3.1.4 Wind Tunnels

Most of the testing was with the first model (rotating about a minor axis) and was almost entirely in the Department's 3'6" diameter. open jet wind tunnel, with speeds in the range 44 ft/s - 66 ft/s. A few check tests were however made in the lower working section (18' x 8'6") of the Department's large wind tunnel.

3.1.5 Test Technique

Static Tests

To obtain steady aerodynamic forces and moments from the rig, the model was set at incidence and the steady pressures recorded.

Each pressure point was selected in turn on the scani-valve and two seconds of signal recorded on the data tape. After all the relevant pressure points had been covered the model was set at a new incidence and the procedure repeated.

Dynamic Tests

The test procedure for these cases was first to oscillate the model about a mean datum position and record the deviation angle by means of the position recorder. A calibration of the recorder showed the signal to be linear with angle. With constant amplitude and frequency the individual pressure points were then selected in turn and the pressure signals processed and recorded. The parameters selected for the averaging process were such that 31 sample values were taken for each signal trace, at a time interval of 0.05 seconds; i.e. a total length of signal of 1.5 seconds. The voltage traces of the unsteady signals were averaged over four signals. When all pressure points had been covered the next test case - involving a change of windspeed, datum position, or amplitude - was selected and the procedure repeated.

Processing of Results

The data tapes produced from the static and dynamic tests were fed into the second computer program for the evaluation of the aerodynamic forces and moments. This program accepts the box data of area, moment arm and weightings. The data tapes were then fed in and the integrated results were then immediately available via the teleprinter.

3.2 Multi-degree of Freedom Models

3.2.1 Six Degree of Freedom Rig

Consideration of the free model tests suggested that

(a) comprehensive dynamic model tests with prescribed motion would need to cater for more than one degree of freedom, probably three, possibly four,

(b) the particular degrees of freedom needed with their associated amplitudes and phase relationships would be difficult to anticipate.

It was therefore decided to attempt to design a rig with six degrees of freedom, where any combination of freedoms could be used, with selected amplitudes and phase lags. One type of rig might have involved three degree of freedom angular movement of a model about a universal joint, mounted on sets of rails giving, respectively, vertical, fore and aft, and sideways movement. Such a complex rig would, however, seem extremely difficult to engineer and would be unduly costly. The design chosen moves the complexity from inside the model and tunnel by using wire supports, and concentrates it in the actuating mechanism outside of the tunnel.

The tunnel used for the six-degree of freedom rig, is the 8'6" x 18' low speed working section of the Department's large wind tunnel.

The wire supports are in the form of eight wire circuits, as illustrated in Figure 3.5, with one additional wire with spring to take the dead weight of the model. The eight circuits are two more than necessary to define six degrees of freedom, but were deemed desirable as being more versatile and better able to cater for a range of model shapes. The over-constraint implied is taken out by suitable springs. Each circuit passes from the model over four pulleys back to the model, incorporating a spring tensioning device which ensures that any extension of a circuit - say in a vertical circuit when the model is moved horizontally - is split equally between the two halves of the circuit. Four circuits are vertical defining vertical, pitch and roll motions, and four circuits horizontal defining fore and aft, side and yaw motions. The tensioning device for each circuit is on a vertical lever, pivoted about the upper end, with the circuit wires passing over pulleys at the lower end, and with attachment for actuation also near the lower end (See Figure 3.6).

Actuation for each circuit is from outside of the tunnel and operates below the glass walls of the tunnel. For the first phase of testing, the circuits were connected to a simple lever arrangement driven through a gearbox by a $3/4$ HP induction 1500 rpm motor. The final design for the actuation, catering for all degrees of freedom is illustrated for one vertical circuit in Figure 3.7. The motor is a $3\frac{1}{2}$ HP, 1440 rpm Crompton-Parkinson 230 V D.C. machine (controlled to $\pm$ 1% on speed by an air cooled Thyristor unit), driving two pulleys with 90 degree phase difference; these pulleys incorporate tensioning devices and are attached to a pyramid of pulleys, with diameter ratios of 2:1 between consecutive pulleys. Six pulleys defining movement in the six degrees of freedom are driven by the pyramid pulleys at a chosen amplitude and with phase relationships of 0, 90, 180 or 270 degrees. Individual circuits are connected to three of these pulleys in a way that compounds the individual movements into the single appropriate movement for the circuit.

All pulleys are mounted on ball bearings, but the size of the pulley chosen has led to some problems with wires breaking periodically. Replacement of individual wire segments is made with simple brass connectors.

3.2.2 Models

Two $1/10$th scale models (2' x 0.8' x 0.8') of the 1:0.4:0.4 container were made for the six-degree of freedom rig. The first model was of simple construction, was painted black, and was for use in flow visualisation studies.

The second model was pressure tapped and is illustrated in Figure 3.8. The system of axes and the sign convention for the aerodynamic

forces are the same as for the smaller boxes, and are shown in Figure 3.1. In all, there were 78 standard pressure tappings, 15 on each of the major faces and 9 on each minor face. Additionally 10 tappings were provided on each major face and 4 on each minor face for the purpose of obtaining more detailed pressure distributions when desired. For the most part, the 78 standard pressure tappings were used to assess the overall forces.

It was decided that the basic arrangement of the pressure points should be entirely regular and symmetrical, contrary to that used on the smaller models. The reasons for adopting the regular pattern were:

(i) It makes for simpler numerical integration procedures.

(ii) In general multi-degree of freedom tests, it is difficult to be certain where separated regions will end, or indeed whether a face will necessarily be leeward or windward. Throughout the range of testing the various faces will, in general, play varying roles, and it would not appear to be possible to devise an irregular system of holes (as with the smaller models) to optimise the accuracy of the overall force output. A regular pattern, under such circumstances, seems the logical choice.

(iii) A symmetric distribution can be used to minimise errors associated with signal drift (see Section 3.4.3).

Based on flow visualisation observations (Section 5 and Reference 9) it was felt that the 'mesh' of pressure points would be of sufficient fineness to guarantee reasonable integrated results, even in situations where the separation bubble is, say, fairly small with separation and reattachment lines in close proximity. The distribution of points is shown in Figure 3.9.

3.2.3 Instrumentation and Test Technique

The model was provided with instrumentation to measure the unsteady pressures, in a manner similar to that described for the small models. A schematic layout of the apparatus is shown in Figure 3.10. It will be appreciated that the instrumentation is slightly different from that used for the small models. The reason for this difference was that the maximum wind speed in the 10' x 8' 6" working section was about 45 ft/s, posing a major problem of measuring small pressures. To overcome this it was necessary to use more sensitive scanivalve transducers requiring separate auxiliary equipment. These transducers work on the principle of the condenser microphone. When sensing unsteady pressures, a diaphragm, two microns thick, moves and in so doing varies the frequency of the 5.5 MHz carrier wave. The carrier wave is, therefore, frequency modulated to give an unsteady signal, in phase and directly proportioned to the unsteady pressure.

This type of transducer requires an oscillator to be mounted in the vicinity of the transducer itself. It was therefore necessary to mount two oscillators inside the model as shown in Figure 3.10 so that the system could function efficiently. The output from these oscillators was fed to two converters which effectively detect the carrier wave and produce the unsteady pressure signal. This signal is then fed to the A.D.C. where the process for recording is the same as that outlined in Section 3.2.1.

The method outlined in Section 3.1 for triggering the A.D.C. had an error associated with it. This error arose due to the rise time of the pulse compared with the length of pressure signal. This can be seen from an observation of the pulse (Figure 3.4). It will be observed that the pulse remains at - 0.35 volt for 0.2 secs. This results in an average error of up to 4 - 5% in phase, with up to more than 10% for some individual pressure readings. It was decided to improve the triggering pulse to the A.D.C. in order to reduce this error, and this was achieved by reducing the rise time of the pulse and improving the manner by which the computer programme triggers the instant the pulse rises. The average error was then reduced to about 3% with a maximum of around 6% for a few individual pressure readings.

The tunnel (working section 18' x 8' 6") is, of course, recirculatory and when run at high speed for any length of time, the air temperature is raised appreciably. With the air in the laboratory at 70°F, tunnel air can achieve 95° after about two hours running at 40 f/s in the lower duct. Regrettably, most proprietary pressure transducers are not temperature-compensated and a substantial drift may occur due to a temperature change of the magnitude alluded to above. The integration procedure used on the 1' x 0.4' x 0.4' models involved a point-by-point march around the box and an ultimate summation. If such a procedure were adopted on the large model, the results (forces and moments) would be unintelligible due to the temperature drift effect over the extremely lengthy test period.

Fortunately, it was possible to overcome the temperature problem without having to expend heavily on temperature control within the tunnel, provided only <u>overall</u> forces/moments were required. The solution consisted of adopting an order of marching through the mesh of points which involved, alternately, reading points on <u>opposite sides</u> of the box. The <u>time between</u> readings for these points is thus optimally short and the temperature effect minimised. These "opposite" pressures are then subtracted algebraically, multiplied by their collocation area and ultimately summed and/or weighted to give the overall forces. Finally, at every tenth tabulation on the Scanivalve, the static pressure is measured so that the temperature drift can be subtracted from pressure readings, again minimising temperature effects.

The actual test procedure was virtually the same as that described for the smaller models in Section 3.1.5.

4. RESULTS FROM THE PRESSURE DISTRIBUTION TESTS

In this section, the results forming the main stream output of this research project are presented. The section is subdivided into two major subsections concerned with results from the single degree of freedom models and those from the six degree of freedom rig. All results presented here relate to the 1:0.4:0.4 container geometry albeit that the model scale for the six degree of freedom rig is twice that used for the single degree of freedom models.

4.1 Single Degree of Freedom Models

The tests were performed on the 1' x 0.4' x 0.4' perspex pressure-tapped model with pitching about a minor axis of the model, the axis being normal to the airstream. The other model of the same dimensions, pitching about the major axis of the model, has yet to be tested. The earliest tests involved a shorter support sting (pitching axis) than the one employed currently, but this led to an aerodynamic interference effect between the support stand and the model (Figure 4.1) which led in turn to erroneous results for aerodynamic pitching moment. This effect is shown in Figure 4.2 where the $C_{mz} \sim \psi$ curves obtained from static tests are compared with the results from direct force measurement by Laub and Kodani[8]. The X and Y force coefficients were not noticeably affected by this interference phenomenon.

Initially, it was thought that the $C_{mz} \sim \psi$ discrepancy (Fig. 4.2) in the neighbourhood of $\psi_o = 90^o$ could be due to tunnel turbulence and, indeed, the report on turbulence effects[9] arose because of this phenomenon. It is shown in Section 6 that free stream turbulence could, in fact, have led to the type of discrepancy evidenced in Figure 4.2. However, the intensity of turbulence in the 3' 6" open-jet tunnel is by no means high enough to produce the discrepancy which was, in the event, attributable completely to the interference effect. All subsequent tests were thus performed with the longer sting.

4.1.1 The Static Results

Results for the stationary model are presented in Figure 4.3 and it is seen that there is good agreement between the $C_{mz} \sim \psi$ results obtained by integration of pressure forces and those obtained directly by Laub and Kodani[8]. These results indicate that the model is statically stable in the regions $90^o \geq \psi_o \geq 83^o$, $35^o \geq \psi_o \geq 0$ and in corresponding regions implied by the cyclic symmetry of the $C_{mz} \sim \psi$ curve. Elsewhere, of course, $\partial C_{mz}/\partial \psi$ is positive indicating static instability.

4.1.2 The Dynamic Results

All the dynamic test data presented here were obtained for an impressed pitching oscillation of amplitude 29.5^o (approximately simple harmonic) about equilibrium positions defined by $\psi_o = 90^o$, 45^o and zero. Detailed pressure distributions are included for the $\psi_o = 90^o$ case only, and these are presented in Figures 4.4, 4.5 and 4.6 which

relate to tests at V = 48, 55 and 66 f/s respectively. The frequency of the impressed motion was about 0.9 Hz throughout so that the test velocities imply frequency parameters (based on 1' chord) from about 0.11 to 0.08. The upper graph in each figure shows the position of the model at any time while the lower ones show the pressure traces. Pressure points 10 - 14 are on the upper surface while points 25 - 28 are on the lower surface. (Figure 3.2 refers)

The pressure traces for the points 10 - 14 show that as the box pitches downwards, the pressures increase on the upper surface achieving a maximum at $\psi - \psi_0 = 29.5^\circ$. As the negative pitch angle develops, the separated region on the upper surface shrinks - the reattachment line moving forward until at $\psi - \psi_0 = 29.5^\circ$, the separated region (bubble) has virtually disappeared and the flow is attached across the entire surface. Meanwhile on the lower surface, the pressure traces from points 25 - 28 indicate decreasing pressures as the separated region grows with the separation line moving rearwards as the negative pitch develops.

The position of the reattachment line can be related to the discontinuity in the pressure curves. This is shown very clearly by reference to Figure 4.6:- In the case of pressure point 10 reattachment occurs at about t = 0.3 sec where $\psi - \psi_0 = 15^\circ$ (approximately). At pressure points 11, 12, 13 and 14 it occurs at 0.35, 0.4, 0.45 and 0.47 sec respectively, where $\psi_0 - \psi = 0$, 10, 15 and 16 degrees respectively.

The above behaviour accords closely with that observed during smoke visualisation tests [9] in the 18' x 8' 6" section of the large wind tunnel. For 'clean' flow, the tests of Reference 9 show that the reattachment line on the upper surface moves rearwards as incidence increases and that reattachment does not occur for incidence angles greater than 10°, or thereabouts.

Forces and Moments

Typical unsteady aerodynamic forces and moments generated by the prescribed motion of the model are shown in Figures 4.7 and 4.8 which relate to the cases where $\psi_0 = 90^\circ$ and 45° respectively for a test velocity of 48 f/s. These Figures show that the X force is in phase with the motion of the container model whilst an almost constant drag force is recorded in the y direction. The pitching moment curves are seen to follow closely the static moment characteristic (Figure 4.3) as the box pitches upwards through the zero ($\psi_0 = 90^\circ$) position. However, there are phase lags between the motion of the model and the quasi-static pitching moment, and it is therefore instructive to present the information in terms of moment/incidence "loop" diagrams. A selection of these is shown in Figures 4.9 to 4.16.

The interpretation of these loop diagrams is as follows:-

(a) If there is no separation (loop) between the moment loci for increasing and decreasing values of ψ, then there is no dynamic effect and the system can be said to be dynamically neutrally stable.

(b) If the points associated with increasing ψ lie above those for decreasing ψ (clockwise loops), then there is positive work done by the incident wind tending to overdrive the motion. In this situation the box is dynamically unstable.

(c) Anticlockwise loops indicate aerodynamically damped situations.

(d) When coupled loops appear, then over the cycle, the system is aerodynamically damped (driven) if the area enclosed by the anticlockwise loops is greater (less) than those enclosed by the clockwise loops.

(e) When these areas (energy inputs) balance, then over a cycle there is no net input of energy to the box system.

(f) Stable limit cycles occur when there is no net energy exchange over the cycle and there is a destabilising (clockwise) loop in the vicinity of the mean position of the box.

Figures 4.9, 4.10 and 4.11 show that there is an unstable loop in the region of zero incidence for $\psi_o = 90^o$. The two outer loops tend to stabilise the motion by virtue of being anticlockwise in direction. These loops signify that the motion is stable in that outer region since the work is negative. However, the motion with the major axis initially parallel to the wind is dynamically unstable. With the datum position at 45° (Figs. 4.12 and 4.13) and the box pitching about this position, the loop figure shows the box to be dynamically stable since negative work is being done. With the major axis perpendicular to the wind vector (Figs. 4.14 to 4.16) the loop plots show two small stable loops at the extremities. The motion here is unstable and will ultimately build up to a limit cycle. This, of course, accords with the free model test results of Section 2 where a yaw limit cycle was observed.

It must be borne in mind that the motions of the box are being prescribed so that a loop figure from a free oscillation of the box would predict more accurately the stability of the motion. However, prescribing motions of the box enables information about the nature of the motion and its stability to be collected and built-up in a regular and controllable manner.

4.2 Results from the Multi-Degree-of-Freedom Model

The tests leading to the results presented here were performed in

one or two degrees-of-freedom only, the tests being designed so that certain important features of the aerodynamic forces could be brought to the fore. As with the smaller model the information is initially in the form of pressure traces against time, these being integrated to give (for the large model) up to six components of force or moment as traces against time. Results as graphs of pressure or force against time and as loop plots are presented in detail for two cases only, representing basic in line and broadside on conditions. In other cases loop plots are included, and derivatives have been computed and are presented in tabulated form. The range of conditions covered, and indication of which results are presented is given in Table 1.

4.2.1 Cases Investigated - Major Axis Near Stream Direction

(a) $\psi_o = +90^\circ$, $\theta_o = 0^\circ$, $d\psi = \pm 10^\circ$

In the first set of results presented (Fig. 4.17), a selection of pressure distributions is shown for prescribed pitching motions of 10° amplitude for the 2' x 0.8' x 0.8' container model about the datum position $\psi_o = 90^\circ$ at a windspeed of 24 f/s, i.e. with the major (y) axis in the stream direction. Three frequency values were employed giving the frequency parameter $w_d = \omega d/V = 0.321$, 0.360 and 0.455, the pressure results for these being shown respectively in Figures 4.17(a), (b) and (c). These pressure distributions are, of course, similar to those obtained for the small model in the previous section. Pressure points 12, 14, 16, 18 and 21 are situated on the top surface of the container while points 13, 15, 17, 19 and 22 are on the lower surface. The largest pressure variations are seen to occur at points 14 and 15, presumably due to the passage of the reattachment lines at distances not too far removed from the separation lines (front edges) implying less decay of turbulence in the shear layers and greater pressure differences within and without the bubble than those achieved further rearwards. The strongest suctions in fact occur at points 12 and 13 which are even closer to the separation lines, but the pressure variation is less than that at points 14 and 15 simply because the 10° amplitude of container motion is not sufficient to allow the reattachment line to cross points 12 and 13. The variation of pressure at these points thus represents the effects of bubble growth and decay. It is seen clearly, for example, that as the bubble on the upper surface shrinks (maximum down incidence) the suction increases, while as it grows the suction decreases.

While the pressure discontinuities which signify reattachment are absent from the pressure traces for points 12 and 13, they are apparent at all other points indicating that the reattachment lines travel about $3/4$ of the length of the box as the box executes motion in pitch of amplitude 10°. This observation accords with those of the flow visualisation tests (Reference 9 and Section 5) which show this order of magnitude of reattachment line movement.

It should, perhaps, be noted that there is no obvious effect of frequency parameter on the shapes of the pressure/time curves though there is, apparently, a bulk movement of the traces towards the positive pressure side as w_d is increased.

The pressure distributions were integrated to give aerodynamic forces and moments as a function of time. These are shown in Figures 4.18(a) to 4.18(c); these corresponding to the pressure distributions presented in Figures 4.17(a) to 4.17(c) respectively. Only F_x, F_y and M (pitching moment) are shown. In character, these graphs are similar to those obtained from the smaller model (Figures 4.7 and 4.8). The X force is observed to be in-phase with the model displacement whilst a virtually constant drag force is recorded in the y direction. Note that if the unit area is taken as 0.64 ft^2, i.e. the area of the box face normal to the flow at equilibrium, the drag coefficient approximates to 1.1 which again accords with established results for a rectangular bluff shape with its major dimension parallel to the wind.

The shapes and phasing of the F_x and F_y graphs appear not to be affected by the changes in wd as one progresses from Figure 4.18(a) to (c), but the phase of the moment curve changes significantly with w_d. The higher harmonic content of the moment curve could be due to the fact that the imposed motion swings over the peaks of the $C_{mz} \sim \psi$ curve presented in Figure 4.3.

As in the case of the small model, it was found instructive to plot the moment curves against model position to provide loop diagrams. Figures 4.19(a), (b) and (c) are the loop diagrams appropriate to the moment curves of Figures 4.18(a), (b) and (c) respectively. The loop diagrams are interpreted as explained in Section 4.1.2 and in all three cases here it is seen that the loop is described in the clockwise sense implying dynamic instability, as for the small model. This also accords with the results of the free oscillation tests described in Section 2.

(b) $\psi_o = 80^\circ$, $\theta = 0^\circ$, $d\psi = \pm 10^\circ$

Another test was conducted wherein $\psi_o = 80^\circ$ with the pitching amplitude maintained at 10° and the windspeed at 29 f/s. Frequency parameters w_d = 0.321 and 0.455 only were considered and the results are presented in loop diagram form in Figure 4.20. For both frequency parameter values, the diagrams are seen to have two loops - a stable one in the region $0 \leq d\psi \leq 10^\circ$ and the expected unstable one in the region $-10 \leq d\psi \leq 0$. This latter (unstable) region is, indeed, the one revealed in Figures 4.19(a) to (c) whilst the stable region corresponds with that experienced at the extremities of the 29.5° amplitude swing on the small model (Figures 4.9 to 4.11). It should be noted that the slope of the major axis of the unstable loop is negative (implying static stability) while that of the stable loop is positive (implying static instability. The effect of frequency parameter increase here has been to increase the areas of both the stable and unstable loops by a small amount.

A summary of some of the loop plots from this section and section 4.1 is shown in Figure 4.21. It is shown that where several loops are present in the same diagram, some stable and some otherwise, then the individual regions when studied separately via tests at the appropriate setting, ψ_o, and at a reduced amplitude, will exhibit similar stability characteristics to those deduced from the original, large amplitude, multiloop diagram. It seems, therefore, that a qualitative picture of likely unstable regions might be deduced from a single set of large amplitude tests. For detail, however, one must test within the sub-loops and that contention is reflected in the remainder of the results to be presented here.

(c) $\psi_o = 90^\circ$, $\theta_o = 5^\circ$, $d\psi = 5.5^\circ$

This is the situation in which the major axis is 5° from the stream direction, and where a 5.5° oscillation is imposed in the perpendicular direction; e.g. 5° yaw with 5.5° oscillation in pitch.

Results for this case are presented in some detail in Figures 4.22 and 4.23. Figure 4.22 relates to a frequency parameter, w_d, of 0.842 and Figure 4.23 to w_d = 0.344. In Figures 4.22(a) and 4.23(a) the force coefficients C_x, C_y and C_z are shown plotted against time over $1\frac{1}{4}$ cycles of container pitch oscillation. The coefficient C_y is seen to be substantially constant with a value of - 1.02 at the higher and - 1.10 at the lower frequency parameter. There is a slight fluctuation in C_y at about twice the impressed frequency, as expected. The sideforce coefficient, C_z, is also seen to be virtually constant at a value of - 0.08 at both values of w_d. This represents a sideforce in the usual sense of positive aerofoil lift. In common with C_y, there is a slight fluctuation in C_z at twice the impressed frequency. The coefficient C_x is seen to be in phase with the impressed motion which again accords with the usual definition of aerofoil lift. The amplitude of C_x is seen to be slightly larger at the lower frequency parameter than at the higher.

In Figures 4.22(b) and 4.23(b) the moment coefficients C_{mx}, C_{my} and C_{mz} are shown plotted against time. C_{mx} is seen to fluctuate at twice the imposed frequency and its mean value is negative implying static stability in yaw for a yaw angle of $\theta_o = 5^\circ$. This static stability is uninfluenced by pitch frequency parameter (cf. Figures 4.25(a) and (b) which show that pitch static stability is radically affected by pitch frequency parameter over the same frequency parameter range). This conclusion is, of course, not unexpected. What is perhaps more unexpected is the appearance of a significant rolling moment coefficient C_{my}. This is seen to fluctuate at the impressed frequency and its direction is such as to produce positive roll for positive $d\psi$. Frequency parameter has little effect on $|C_{my}|$, but the variations of this derivative are somewhat smoother at the lower frequency parameter value.

The coefficient C_{mz} is seen to change markedly with frequency parameter. At the higher value of w_d, the maximum and minimum values are about 0.05 and - 0.04 while at the lower w_d these values are respectively 0.02 and - 0.04. For this latter frequency parameter, there appears to be a sizeable fourth harmonic component present in the $C_{mz} \sim t$ trace. Also, a significant shift of phase appears to take place as w_d increases. This dramatic effect of frequency parameter on the pitching moment derivative might surprise anyone with a strictly aeronautical background, but such variations are well known in suspension bridge theory - even at low values of frequency parameter. These effects are probably associated with the pockets of separated flow ("bubbles") which exist on many sharp-edged bodies. The reason for the strong fourth harmonic dependency of C_{mz} has yet to be found and indeed this is one of the subjects on which attention will be focussed in the near future.

In view of the obvious difficulty in interpreting the time histories of the coefficients, they may be presented as loop diagrams. This is done in Figures 4.22(c) and 4.23(c) for the moments C_{mx} and C_{my} and in Figures 4.22(d) and 4.23(d) for C_{mz}. Note that only the loop diagram for force/moment associated with the displacement/rotation in its own direction can be interpreted in the manner described previously, (e.g. $C_{mz} \sim \psi$ in the present case). Nevertheless the "cross" or "indirect" loop diagrams provide a compact means of presenting aerodynamic force information. Thus, for example, Figure 4.22(c) shows rolling moment varying almost linearly with pitch.

Figure 4.22(d) shows the "direct" loop diagram at the higher frequency parameter and this indicates dynamic instability. The inclination of the loop is positive indicating static instability also, that is in so far as static instability is meaningful in a dynamic experiment of this kind. On the other hand, Figure 4.23(d) indicates dynamic instability, but here the inclination is negative implying static stability. It can be deduced, therefore, that in this case one effect of frequency parameter increase is to change the sign of the part of the pitching moment which is in-phase with the impressed motion.

The higher harmonic content of the various time histories of aerodynamic forces and moments often make it difficult to interpret even the loop diagrams. A numerical procedure has been utilised (see Appendix 4) which fits a Fourier series to the time histories, evaluating the coefficients of the various harmonics. The procedure also operates upon the displacement histories and by comparing coefficients of like harmonics of force/moment and displacement/rotation, aerodynamic derivatives are obtained. These derivatives are more general than the accepted small-amplitude derivatives of aeronautics in that they are meaningful for large amplitude motion also. In large amplitude applications, the derivatives obtained by this process are really overall indicators of stability; i.e. "describing functions".

A set of derivatives obtained by the procedure of Appendix 4 is given in Table II which will be discussed at a later stage.

(d) $\psi_o = 90^\circ$, $\theta_o = -5^\circ$, $d\psi = 5.5^\circ$

This case should be a mirror image of the previous case and was performed to check the symmetry of flow.

For this case the "direct" loop diagrams only are presented for $w_d = 0.842$ and 0.374. These are shown in Figures 4.24(a) and 4.24(b) respectively. In common with the previous case, both diagrams indicate dynamic instability, but paradoxically the inclination of the loops is positive at both frequency parameter values implying static instability, although the extent of this instability is less at the lower w_d value, which is constant with the positive yaw case. A full set of derivatives for this case is given in Table II: the important derivatives can be seen to be in fair agreement with the previous case.

(e) $\psi_o = 90^\circ$, $\theta_o = 0$, $d\psi = 5.5^\circ$

The "direct" loop diagrams for this case are given in Figures 4.25(a) and 4.25(b). Here, both loops imply dynamic instability, but the 'static stability' varies, being positive at low frequency parameter and negative at high frequency parameter.

Complete derivative information is given in Table II.

(f) $\psi_o = 90^\circ$, $\theta_o = 0$, $d\psi = 13.5^\circ$

Direct loops for $w_d = 0.957$, 0.719 and 0.478 are given in Figures 4.26(a), (b) and (c) respectively. Again it is seen that all loops indicate dynamic instability, but that there is a variation of static stability as frequency parameter changes, i.e. as before, the container is statically stable at lower w_d values and statically unstable for higher w_d values.

(g) $\psi_o = 90^\circ$, $\theta_o = 0^\circ$ and 5°: Heave Motions Imposed

In Figures 4.27(a) to (d) the results from tests in pure heave are presented for two values of w_d, viz 0.32 and 0.84 for the case $\psi_o = 90^\circ$, $\theta_o = 0^\circ$ where $|dx| = 1.9"$. It will be observed that the C_x force is approximately symmetric about the abscissa for the two wind speeds. Nearly constant forces C_y and C_z are recorded in the y and z directions respectively (see Figure 4.27(a)), but there were small fluctuations in these forces at twice the impressed frequency.

The aerodynamic moments are shown in Figure 4.27(b), and it will be observed that by far the larger moment is C_{mz}, which is non-harmonic when compared with the position trace of the model. It is interesting to note that C_{mz} and C_z both decrease in magnitude with decreasing w_d.

In Figures 4.28(a) to (d), the aerodynamic forces are shown for the case $\psi_o = 90^o$, $\theta_o = 5^o$ when $w_d = 0.34$ and 1.02 and $|dx| = 1.9"$. It is interesting to note that the results are much the same as in the $\theta_o = 0^o$ case except where the 5° yaw on the model produces an expected mean side force C_z (as shown in Figure 4.28(a)).

In the case where a pure heave motion is prescribed, no work is done throughout the prescribed motion except by forces in the direction in which the motion takes place. Thus it was found instructive to plot C_x with the appropriate position trace dx and also for comparison the "cross loop" $C_{mz} \sim x$. The two cases for $\theta_o = 0^o$, $\theta_o = 5^o$ are shown in Figures 4.27 and 4.28(c and d).

In Figures 4.27(c and d) C_x and C_{mz} are shown plotted against dx for $\theta_o = 0^o$ (zero yaw) for the above mentioned w_d values. Figures 4.28 (c and d) show the corresponding cases for $\theta_o = + 5^o$. It is evident from the $C_x \sim x$ loop that the heave motion is dynamically stable. This is also borne out in Table II, where the derivatives are given. It will be observed from Table II that it is only C_{xx} and C_{yx} derivatives which show any tendency to increase positively with increasing frequency parameters. At zero frequency parameter, these derivatives will be zero. The remaining static derivatives are much smaller in magnitude and therefore play a smaller role in the stability of the model in this motion. (Again, these would be zero at $w_d = 0$.) The damping derivatives are also small in magnitude in all cases except for C_{xx} which becomes proportionately negative with increasing frequency parameter. The C_x force vector has the effect of negative damping on the model and must therefore stabilize the motion. The evidence of large damping derivatives indicates the importance of the damping forces in the x direction (see Table II).

(h) $\psi_o = 90^o$, $\theta_o = 0$: Combined Pitch and Heave Motions Imposed in Phase

Results shown in Figures 4.29(a) to (d) indicate the effect of a combined heave and pitch oscillation. Here $|d\psi| = 3\frac{1}{2}^o$ and $|dx| = 1.9"$. Figure 4.29(a) shows the forces C_x, C_y, C_z for $w_d = 0.39$ and 1.02. A symmetric C_x force is recorded and it is greater in magnitude than that recorded in zero pitch cases. Nearly constant forces C_y and C_z are recorded in their respective directions which are similar to those obtained in the previous subsection.

The aerodynamic moments for the two w_d values are presented in Figures 4.29(b). It is again noticeable that C_{mz} is by far the largest moment recorded for the $w_d = 0.39$ case, whilst C_{mx} and C_{my} are of smaller magnitude. It is also observed in this case that there is a change in continuity of the C_{mx} factor, i.e. peaks occur at the extremities of the prescribed motion, $d\psi = - 3.5^o$, $dx = - 1.9"$, but not at the other extremity, $d\psi = + 3.5^o$. The effect of increasing frequency parameters can be clearly seen to reduce the overall aerodynamic force magnitudes.

The corresponding loop plots are shown in Figures 4.29(c) and (d) for the combined pitch and heave motion. Once again C_x has been plotted against dx, and C_{mz} has been plotted against $d\psi$. The $C_{mz} \sim \psi$ loop is shown to be dynamically unstable whilst the $C_x \sim x$ loop is dynamically stable.

(i) $\psi_o = 90^\circ$, $\theta_o = 5^\circ$, Combined Pitch and Heave Motions

Loop plots are shown in Figure 4.30 for $|d\psi| = 3\frac{1}{2}^\circ$ and $|dx| = 1.9"$, and derivatives in Table II. These should be compared with the previous case to see the affect a change in datum attitude makes. The important derivatives (C_x, C_{mz}) are in fact very similar, showing little sensitivity to θ_o. These tests were performed for $w_d = 0.39$ and 0.97.

Note that with a combined motions the use of 'derivatives' in this form is open to question, and should only be used in conjunction with those for the individual motions.

(j) Case $\psi_o = 90^\circ$, $\theta_o = 0$: Combined Heave and Roll in Phase

The aerodynamic forces associated with a combined heave and roll motion with $|dx| = 1.9"$ and $|d\phi| = 10.7^\circ$, are shown in Figures 4.31(a) to (d) for two w_d values, namely 0.41 and 1.02. Again, the stability of the combined motion can be deduced from the total area of the $C_x \sim x$ and $C_{mz} \sim \phi$ diagrams, but detailed discussion will be deferred until a later stage.

(k) $\psi_o = 90^\circ$, $\theta_o = 0^\circ$, $d\psi = \pm 11.5^\circ$

This case virtually repeats case (a) but with a closer coverage of w_d, eight values in all being taken (from 0.151 to 1.075). Graphical results are not given but the full set of derivatives is given in Table II. Note particularly the small values of $C_{y\psi}$ and $C_{z\psi}$ compared with $C_{x\psi}$ (as is to be expected), the variation in $C_{x\psi}$ with w_d, (an acceleration effect) and irregular variation of $C_{x\dot{\psi}}$ with w_d. $C_{mz\psi}$ and $C_{mz\dot{\psi}}$ also show interesting variations with w_d.

(l) $\psi_o = 90^\circ$, $\theta_o = 0^\circ$, $dy = 3.5"$

With major axis along the stream direction this case has imposed fore-and-aft motion for two values of w_d. Loop plots given in Figure 4.32 for the C_y force component only, as this should be the only significant force due to symmetry. The full derivatives are given in Table II, and these confirm that C_y dominates. The C_{yy} derivative increases rapidly with w_d indicating a strong acceleration effect. The $C_{y\dot{y}}$ is relatively constant and shows dynamic stability.

(m) $\psi_o = 95^o$, $\theta_o = 0^o$, $d_y = \pm$ 3.5"

This case is similar to (1) but with the major axis inclined at 10° to the stream direction. There is no significant differences between the two cases and derivatives only are presented (Table II).

4.2.2 Broadside on position

$\psi_o = 90^o, \theta_o = -90^o, d\psi = \pm 10^o$

Pressure distributions are given for the case where the box is oscillated about a datum position broadside on to the stream, i.e. the orientation likely to be adopted by a container on a single strop. This case has proved to be of considerable interest, partly because it relates to an observed oscillation of a freely suspended container and partly because the dynamic stability is shown to change sign with frequency parameter. In order to assess this change more frequency parameters than usual were taken for this case. Pressure results are presented for selected points at three values of frequency parameter (w_d = 0.44, 0.57, 0.88) and force components for eight values (0.28, 0.38, 0.42, 0.51, 0.53, 0.69, 0.72, 1.08).

Pressure traces are presented in Figures 4.33 to 4.35. Typical pressure traces from points on top and bottom surfaces are shown in Figure 4.33, on the small end faces in Figure 4.34, and on front and rear surfaces in Figure 4.35. For points on top and bottom surfaces it is apparent that the variation of pressure during one cycle increases as frequency parameter increases, and also that the pressure lags the motion by an increasing amount. Similar conclusions can be made for points on the end faces, although here, in addition, it is very noticeable that as frequency parameter increases so the pressure differences between points on the same face tend to decrease and the variation takes on a more definite pattern. This pattern seems closely related to that for nearby points on top and bottom surface. Forward surfaces exhibit pressure variations that can be related to movement of the forward stagnation point. Rearward facing surfaces near end faces show pressure similar to those on the end faces but with less suction and some phase lag.

Some of the implications of these pressures are discussed further in the section on flow visualisation.

Force coefficients for the three axis are shown in Figure 4.36, moment coefficients in Figure 4.37 and some loop plots in Figure 4.38. Note the drag force dominates, with a small variation at twice the frequency of oscillation of the model. The force along the major axis (C_y) increases in magnitude and has increasing phase lag as frequency parameter increases.

The moment coefficients about y and z axes would be zero in a truly symmetric flow. In this case, noticeable moments were found, although with little consistency over the range of frequency parameter. The largest component was C_x, initially in antiphase with the motion, almost disappearing for $w_d = 0.69$ and then increasing rapidly in magnitude with further increase in w_d, and tending to be more in phase.

The loop plots for C_{mx} (Figure 4.38) show clearly the change from negative to positive dynamic stability with increase of w_d.

Derivatives are shown in Table II.

4.2.3 The Effects of Free-Stream Turbulence

An experiment was performed in order to investigate the effects of free-stream turbulence on the aerodynamic actions on an oscillating 1:0.4:0.4 container model in the standard orientation: $\psi_o = +90^o$, $\theta_o = 0$. The likely role of turbulence had been recognised earlier[9], and the subject is discussed further in Sections 5 and 6 herein. The present experiment involved two pitching tests ($|d\psi| = 10^o$) - one in the 'clean' tunnel and the other with a 10% turbulence grid suspended 4' 6" upstream of the model. The frequency parameter of the tests was $w_d = 0.41$.

In the interests of economy of space, only the "direct" loop diagrams, $C_{mz} \sim \psi$, are shown (Figure 4.39). Figure 4.39(a) refers to the 'clean' free stream, while Figure 4.39(b) relates to the 10% grid turbulence case. It will be seen that the sense of rotation around the loop is clockwise (dynamically unstable) for the 'clean' case and anticlockwise (dynamically stable) for the 10% grid turbulence case. Also, the inclination of the loop in the former case indicates static stability and in the latter, static instability. Thus, the effect of free stream turbulence has been to reverse the aerodynamic stability attributes of the container in this orientation.

5. FLOW VISUALIZATION STUDIES

The flow visualization work undertaken during the contract period has been central to the entire research effort - not surprisingly since a principal objective was to develop a thorough understanding of the complex aerodynamic phenomena responsible for underslung load oscillations. The visualization studies fall into two categories:-

(i) Studies involving a stationary model in "clean" and turbulent airstreams.

(ii) Studies involving an oscillating model executing pitching, heaving and fore-and-aft motions in a "clean" airstream.

The visualization methods first used were surface etching, in which a mixture of "dayglo" pigment and kerosene was employed, smoke visualization and more recently the helium bubble technique. The "dayglo"

etchings involved relatively high speed flow and were recorded photographically in ultra-violet light. On the other hand, the smoke visualization results were obtained at very low windspeeds and recorded either by high speed "still" or cine photography. In many respects, the smoke technique was found to give unsatisfactory definition, but some of the flow features revealed by this method were so interesting that a helium bubble visualization apparatus was obtained in order to study them further and in more detail.

The results from surface flow and smoke tests are presented first, with results from the helium bubble tests following.

5.1 Flow Around a Stationary Model of a 1:0.4:0.4 Container in "Clean" and Turbulent Airstreams

The object of this work was primarily to obtain information as to the effects of free-stream turbulence on the flow around the 1:0.4:0.4 container model with a major axis near the stream direction. The 2' x 0.8' x 0.8' visualization model was used in these tests, being supported by the six-degree-of-freedom suspension rig in the centre of the 8' 6" x 18' working section of the Department's large wind tunnel. The six-degree-of-freedom facility was, of course, used only in its static mode - namely to set incidence for the various static cases to be considered. Two sets of tests were performed; (i) using "dayglo" and kerosene on the upper surface of the model, and (ii), using smoke. From (i), the 'plan' shape of the separated region was given while (ii) provided some indication of the 'elevational' shape. Additionally, the use of smoke enabled the various side flows and entrainment regions to be assessed. In the tests, the incidence angle was varied in steps of 5° from - 15° to + 15° relative to the broadside on reference position.

5.1.1 Surface Visualization Tests

The test procedure was straightforward:- Incidence was set by using a clinometer and a mixture of "dayglo" and kerosene was sprayed on to the upper surface of the model. Windspeed was raised to 30 f/s and held at this speed until the kerosene had dried-out, leaving a "dayglo" etching of the surface flow pattern. The etching was then photographed in ultraviolet light. A 10% turbulence grid was then introduced some 4 ft upstream of the model and the tests repeated. Due to the considerable evaporation time of kerosene, these simple tests extended over three complete working days.

5.1.2 Smoke Visualization Tests

These tests were performed over the same range of incidence angles as the surface visualization tests, but the flow speed was necessarily much lower, i.e. 5 f/s approximately. Tests were again performed with and without the turbulence-producing grid. For each case, the single smoke probe was positioned in such a manner that the optimal definition of bubble elevational shape above the model centre line resulted. By using a thin plastic ruler, the maximum height of the shear layer

enclosing the separated region (bubble) above the model was measured as closely as possible. The probe was then positioned on the surface in such a way as to reveal the maximum distance from the leading edge of the model to the reattachment line. This afforded a check on the surface etching procedure above. An assessment of the flows on the sides of the container was made, briefly, for each incidence. Entrainment into the separated region on the upper surface from these side flows was also studied, again briefly.

5.1.3 Results of the Visualization Studies

The flow visualization tests with model stationary were conducted principally in order to assess the effect of stream turbulence. It is thought worthwhile to use the observations first to describe the main features of the flow at zero incidence and at incidence, and then to present the results and discuss the effect of stream turbulence.

(a) General Description of Flow Around Container Model

(i) Zero Incidence

At zero incidence the flow divides equally about the four long faces. The flow separates at the leading edge of the faces, and tends to reattach perhaps one third of the way towards the rear. The reattachment point is not, however, at the same distance from the leading edge across the whole face - the distance is greater towards the centre, smaller towards the edge of the face. There was in addition some small indication that the mainstream fluid was entrained towards the edge of the face, leaving the separation 'bubble' towards the centre. This means that the region of separation includes the point of reattachment towards the centre, and excludes it towards the edge.

The flow within the 'bubble' is forward on the centre line, outwards near the leading edge, and rearwards near the side edges of the upper face. A more detailed investigation of the flow was made using the Helium Bubble Apparatus, and this is discussed in Section 5.3.

(ii) Container at Incidence

The pattern of flow with small incidence relates closely to that at zero incidence. For positive incidence, i.e. with the front of the container rising, the top surface becomes the leeward surface with the separation "bubble" becoming larger, while on the lower surface the "bubble" becomes smaller. On the side faces the separated regions link into those on the upper and lower surfaces, being longer towards the top of the face and shorter towards the bottom. A feature of some importance as incidence increases is that the flow up from the side faces creates vortices of considerable strength along the side edges of the upper surface. At incidences of around 15° these vortices effectively meet, and the outflow from the separation above the upper surface passes above them. The 're-attachment' line is contained by the vortices, although the region of separation extends past the rear of the box and contains the 'bubble', the vortices along the side edges, and the outflow from the bubble.

(b) Results with Low and High Intensity Free Stream Turbulence

The flow patterns obtained from the tests are summarised in Figure 5.1 which illustrates at a glance the effects of turbulence. The most obvious of these effects is the shortening and deepening of the 'bubble' as turbulence intensity is increased. The variations of 'bubble' height and length with incidence for clean and turbulent flows are shown in Figure 5.2. It can be seen that in spite of being shorter the 'bubble' with free stream turbulence is usually deeper - i.e. the proportions of bubble are very dependent on turbulence, and this seems to indicate a difference of flow within the bubble. Another significant effect is the shortening of the distance between a secondary vortex (parallel to the leading edge) and the leading edge. A particularly dramatic instance is that of $\alpha = 10^{\circ}$ where a 'bubble' exists for the turbulence case and does not for the 'clean' case. Likewise, the secondary vortex exists for the $\alpha = -10^{\circ}$ case in the clean configuration but vanishes at this incidence when grid turbulence is present. Again, the clean configuration gives rise to a parallel streamwise vortex pair at $\alpha = 5^{\circ}$ and above, but this pair is not evident in the grid turbulence configuration until $\alpha = 15^{\circ}$.

The clarity of the 'dayglo' etchings was greater in the clean configuration at all incidences tested suggesting, as expected, more regular flow conditions. This was particularly noticeable beneath the 'bubble' where the strong vorticity within the 'bubble', inducing flow forward along the centre line, was evidenced in most cases. While smoke introduced at the leading edge was entrained into the bubble at a surprisingly low rate, that introduced on the sides of the box near to the leading edge filled the bubble rapidly. The secondary vortex parallel with the leading edge is clearly a stable arrangement relative to the major vortex 'pair'. The direction of flow in this vortex will thus be such as to carry fluid windward along the surface and thence upwards and forwards towards the shear layer and the leading edge.

The above effects are also present in the grid turbulence configuration, and judging from the rate at which smoke was entrained into the bubbles from the side faces, this effect was more marked. However, despite this entrainment, the bubble is smaller in length, though slightly thicker. With regard to why the bubble should be shorter, the "turbulence energy in the shear layers" argument can not be used since these layers are very thin and the turbulence scales contained within them are of an order smaller than those generated by the grid. There does, however, seem to be some connection between the proportions of a 'bubble' and the 'vigour' of its internal flow. A completely stagnant flow would have a dividing streamline of constant pressure, whilst a contained flow, with a dynamic pressure approaching that of the main stream, would have large pressure variations. The pressure near the front of the bubble might approach free stream stagnation pressure (deflecting the main stream and deepening the bubble) while further back the pressure might be less than ambient, drawing the main stream towards the surface. The proportions of a separation bubble would therefore be affected by the vigour of the internal flow. Now in the present studies it is evident that the flow within the bubbles is being 'energised' by the continual entrainment from the free stream. This continuing exchange

process would, however, be supplemented by turbulence in the main stream, plausibly leading to the observed shorter and deeper bubbles. This is, however, only surmise and could well be investigated further.

5.2 Flow Around an Oscillating Model of a 1:0.4:0.4 Container in a 'Clean' Airstream - Smoke Visualization

Following the static tests some short tests were performed with an oscillating model in the six-degree-of-freedom rig. Smoke was introduced by using the smoke probe, sometimes with the probe attached to the model and sometimes with probe fixed ahead of the model. The model was oscillated in pitch and in heave at various frequencies, and the resulting smoke patterns filmed using a 16 mm cinecamera.

Study of the film sequences revealed a pronounced effect of motion by ever increasing amounts as frequency increased. In an extreme case, corresponding to unrealistically high frequencies, the bubble size appeared to be 180° out of phase with the motion, with minimum bubble size occurring on the upper surface at maximum positive incidence. An interesting feature was the way in which the excess air leaving a decaying bubble at high frequency, could travel along the model surface as a distinct vortex.

Detailed analysis of these films was made difficult by certain shortcomings of the smoke technique:- Smoke effectively makes visible a volume of air, but while to the eye some of the flow detail can be seen, this is difficult to record on film. Also the eye can be easily misled as evidenced with tests where the probe was fixed ahead of the model. The changing position of probe relative to model gave an impression of movement which proved most confusing. The films gave no indication as to where across the model the smoke was present - in most cases the profile related to the bubble at the centreline of the model, but in others this was hidden by smoke in the vortex regions along the edges of the upper face, shown in plan in Figure 5.1 at 15°. The smoke when injected directly into the bubble made visible any air that at some stage passed close to the point of injection. Where the bubble was entraining air the smoke filled region excluded the reattachment line. Where the bubble was decreasing in size reattachment was within the smoke filled region - the smoke region then including the bubble and a volume of air downstream that had passed through the bubble. The dynamic motion leads to greater interchange of air between the free stream and the bubble, and hence problems of interpretation become greater. Other features of the flow past the oscillating model have been revealed by use of the Helium Bubble Technique (Section 5.4).

5.3 Flow Visualisation by using the Helium Bubble Technique - Static Model

The shortcomings of the smoke technique when applied to flow around the container model led to interest in, and purchase of, an AEL Helium Bubble Generator (Model 3). This unit blows large quantities of bubbles with helium, the bubbles being passed into the airstream by a supply of compressed air. Within limits the buoyancy and size of the bubbles can be adjusted by suitable manipulation of the control valves. The bubbles become clearly visible when lit by a spotlight at around 90°

from the viewing position, and viewed against a dark background.

Some encouraging preliminary tests had been made with a static model, where details of the three-dimensional flow could be clearly seen. To record the detail of 3-d flow for analysis on film requires, however, that the flow at different positions across the model be separately identified. Experiments were carried out with lighting arrangements illuminating sections of the flow. The light source used for most of the tests was a 250 watt Halogen lamp slide projector.

The results presented here are for a beam of light 1.6" wide illuminating in turn six sections across the model. The model attitudes are ψ_o = 78°, 80°, 83°, 85°, 87°, 90° and 100°, corresponding to the long (y) axis being near stream direction with pitch (in tunnel axes) of +12°, +10°, +7°, +5°, +3°, 0°, and - 10° respectively. In all cases photographs for all six sections are presented, the first 1.6" section, (a), being that closest to the viewing position and extending from the near edge in 1.6"; the second section, (b), extends from 1.6" to 3.2", and so on. The tunnel velocity was constant at 3.2 ft/sec for each case.

$\psi_o = 100°$

This case is presented in Figure 5.3. The air can be seen to separate at the front edge of the model (i.e. on the left), forming a separation bubble some 30% of model length in the edge sections, rising to approximately 50% at the centre. This is a fairly straightforward pattern, as were those obtained for larger values of ψ_o, not reproduced here.

$\psi_o = 90°$

This is the datum case with major axis along the stream direction, and results are presented in Figure 5.4. The air separating from the front now forms a bubble extending on average half way down the model. (Note: the near vertical lines are the four support wires at the corners of the box, and the centre counterbalancing wire. When in the illuminating beam they show as white lines, when on the camera side of the illuminating beam they show as black lines.) The edge sections (a) show a clearly defined bubble region with smooth flow above and behind. Sections (b) to (e) by comparison show traces crossing the main flow at a large angle. These traces are consistent, are not due to turbulence, and indicate vorticity in those regions.

$\psi_o = 87°$

This case is shown in Figure 5.5. The pattern is similar to that for 90°, but with vorticity now being evident behind the separation bubble in all six sections. Note that the regions with vorticity are

often very distinct and can well be followed by smoother flow, e.g. (e) where towards the trailing edge the flow is almost completely streamwise.

$\psi_o = 85^\circ$

Presented in Figure 5.6, this case introduces a new pattern. Figure 5.6(b) shows flow within the separation bubble apparently radiating in all directions from a point on the surface, with no circulating flow evident. This corresponds to an accelerating or decelerating cross flow. In Figures 5.6(c) and (d), near the model centreline vorticity is evident above the forward part of the separation bubble.

$\psi_o = 83^\circ$

The same features are evident in Figure 5.7 as in 5.6, but with the separated region being again larger, apparently extending to the rear of the model on the centreline.

$\psi_o = 80^\circ$ and 78°

The cases are shown in Figures 5.8 and 5.9 respectively. The separated region again increases in extent as ψ_o decreases, more cross flow inside the separated regions is evident (e.g. Figure 5.9(f), in part at least inflow from the side faces of the model), and vorticity can be seen outside of the separated region.

A 'summary' of Figures 5.3 - 5.9 are given in 5.10. The pictures in these cases are with the whole flow field above the model illuminated, i.e. they correspond to a superpositioning of each group of six photographs.

An attempt to illustrate the main features of the flow around the model is given in Figure 5.11. Features include:

(i) A separation bubble with flow into the bubble near the edges and outflow at the centre.

(ii) Flows around the top and side faces interfering and forming minor vortices.

(iii) Upflow from the side, when the model is at incidence generating vortices initially near the edge, but increasing in strength and moving in as incidence increases. These vortices will also take inwards the minor vortices of (ii).

(iv) The inflow towards the centre line from opposite sides interfering as incidence increases to the extent that a plume or almost two-dimensional jet is formed near the centre line that lifts up through the top of the separation bubble and forms further vortices.

5.4 Flow Visualisation by Using the Helium Bubble Technique - Oscillating Model

To distinguish the significant differences between the steady and unsteady flows over a container model it is necessary to capture the history of the flow whilst the model is oscillating. Some cine film records were taken, but in order to obtain good quality still photographs at representative positions during an oscillation a switching technique was evolved. A Pentax camera was arranged to be operated by a solenoid. The solenoid was energised by first closing a switch in a circuit after the model had reached a steady oscillating condition, with final closing of the circuit coming from a micro-switch attached to the driving motor structure. The position of the micro-switch was varied to provide eight photographs at equi-spaced time intervals during the oscillation.

The probe head of the Helium Bubble Apparatus was positioned 4 ft upstream of the model, and illumination was by the 250 watt Halogen projector positioned downstream of the model.

Pitch Oscillation

Figures 5.12 - 5.14 show the flow patterns for a pitch oscillation (in tunnel axes) of $\pm$ 11.5° from a datum position with major axis along wind direction. The three figures are for frequency parameters of 0.97, 1.94 and 2.31 respectively. The flow is from left to right, with the sequence starting with maximum incidence, (a), incidence then decreasing to minimum, (d) and (e), then increasing again.

At the lowest frequency parameter (Figure 5.12) the pictures resemble those for a steady model, but with some phase lag evident. The separated region is smallest in (e) and (f), largest in (a) and (b), i.e. the bubble size lags the motion by perhaps 45°. For w_d = 1.94 (Figure 5.13) the leading edge bubble is smallest in (f) and (g), and the shedding of the separated flow can be clearly seen. Starting with (g) and following through (h) and (a) the bubble can be seen to be somewhat over half the model length in (b). In (c) and (d) the separated flow can be seen to be extending towards the back edge of the model and in (e) no longer separating from the leading edge. In (f) and (g) the mass of fluid once in the bubble approaches the back edge, passing that edge in (h) while another separated region is growing at the front. The quality of the photographs in Figure 5.14 is perhaps not as good as the others, but it can be clearly seen that the smallest leading edge separations are now in the region (g) and (h) with largest near (d), i.e. bubble size is now almost completely out of phase with the motion.

This observed lag in bubble size, together with the results of earlier sections has led to the mathematical model proposed in Section 7.2.

A more detailed study of the unsteady flow was made by illuminating in three strips across the width of the model. Results are shown in Figure 5.15 where the 3.2 section refers to the nearer part of the flow from the edge of the model in 3.2"; the 6.4 section refers to the centre section - from 3.2" to 6.4" from the edge; the 9.6" section refers to the far side - from 6.4" to 9.6" from the near edge. This should be compared with Figure 5.15, the main point of interest being the variation in size of the separation bubble across the model.

The unsteady flow visualization was at higher values of frequency parameter than the pressure and force results because of difficulties in obtaining good pictures at higher wind velocities. Dynamic (or acceleration) effects are therefore more obvious, but are still representative of certain real situations.

Fore-and-Aft Oscillations

Similar results were obtained with fore-and-aft movement of the model. Figures 5.16 to 5.18 give results for frequency parameters of 1.94, 3.22 and 5.54 respectively. The flow is again left to right with the first photograph, (a), being taken near the maximum forward position.

As the model moves rearwards in Figure 5.16 the separated flow collects and thickens near the front until the rearward position is reached, (d); in (e) the separated flow is shed with a new bubble growing from the leading edge; in (f) this flow clears the rear of the model, with evidence of a smaller secondary vortex of opposite sense being shed later. For the very high frequency parameter represented in Figure 5.18 the same major features are evident, although in this case the rapid rearward movement can for a short time leave the separation bubble ahead of the model.

5.5 Flow Visualization for the Broadside On Position - $\psi_o = 0$

A very limited investigation with smoke was made for oscillations about the broadside on position. This followed the obtaining of the results presented in Section 4 where the damping derivative was found to change sign with change in magnitude of frequency parameter. For a static model the flow separates from all leading edges and contains the separated, rather dead air, region behind the model. The division between the two regions is essentially in line with the side face - as sketched in Figure 5.19(a). With change of attitude the side flow can reattach, with the division between the side flow and the base region still being in line with the side face. With oscillation at moderate to high frequency parameter there was evidence that

(i), the vorticity shed in the base region could "lock on" to the model oscillation, and

(ii), the line dividing the side and base flows changed for certain parts of the cycle to being in line with the base rather than the side, as indicated in Figure 5.19(c).

It seems probable that the change from dynamic instability to dynamic stability with increase in frequency parameter is associated with these two factors.

6. DIRECT ASSESSMENT OF PITCH AND YAW STABILITY OF RECTANGULAR CONTAINERS BY SINGLE-DEGREE-OF-FREEDOM FREE VIBRATION TESTS.

The impetus for this particular study came from the flow visualization tests (Section 5 and Reference 9) in which it was observed that free stream turbulence levels could influence radically the shape and size of the separated regions around a 1:0.4:0.4 container model. It was desired to produce quickly a confirmation of certain deductions, regarding container pitch stability, made on the basis of these visualization studies. It appeared that the most expedient way of providing such confirmation was by conducting free vibration tests in pure pitching motion. The preliminary results are described briefly in Reference 9, but at that stage the measurement media were simply a stop-watch and travelling microscope. Results from a more accurate and controlled set of tests are presented in this Section. First, however, the benefits of this type of testing will be defined:-

It is perhaps unfortunate that the most-used cargo container shape, viz. the 1:0.4:0.4 box, possesses the attribute of intrinsic single-degree-of-freedom aerodynamic instability, in pitch and yaw, when the major axis is either parallel or normal to the flow (see Section 2.1). While the pitch instability may be 'cancelled' by suitable stropping configurations (e.g. Sheldon[2]), there is little that can be done to counteract the lateral (yawing) instability, aside perhaps from the implementation of active control technology[3]. It is therefore highly desirable that this type of oscillatory instability be understood and that measures be taken, if possible, to eliminate it by aerodynamic means. This might lead to the addition of appendages (e.g. fins and guides), but the optimum positioning of such devices can be determined only when the underlying mechanisms are understood. One way in which an understanding may be gained is by building up a comprehensive picture of aerodynamic damping characteristics via free oscillation tests. Another is by the use of the pressure measurement method described in Sections 3 and 4. The two approaches are complementary, and one may be used to check the other. Of course, the pressure method has much greater generality and, furthermore, is more accurate in many instances owing to uncertainties regarding the type of mechanical damping present in free-oscillation rigs.

A major advantage of free oscillation testing is that the effect of modifications to the shape can be investigated rapidly. It is therefore easy to study possible "cures".

6.1 The Test Equipment

The container models were constructed from 5 mm plywood on softwood frames of section 1" x 1". The box dimensions were:-

Small box	12" x 4.8" x 4.8"
Large box	24" x 4.8" x 4.8"

Each box was provided with a pitch axis ball-bearing arrangement through the centres of area of two major faces, and a "wire attachment" protruding from the leeward minor face. The spindle diameter was 0.25", this being supported on 0.5" x 0.125" elliptic-section struts in the working section of the 3'6" open-jet tunnel. The struts themselves could be rotated in yaw up to $\pm$ 35° if necessary. In order to support the box under test, a spring was connected to the tunnel superstructure via a strain gauge arm and a thin wire was attached to the lower end of the spring, passing through the wire attachment on the box, and ultimately terminating in a scale pan to which masses could be added in order to vary suspension frequency. The whole arrangement is illustrated in Figure 6.1.

The strain gauges on the measuring arm were connected to a Tinsley dynamic strain gauge conditioning unit. Signals from the gauges, representing forces in the spring and hence displacement of the rear of the box, were amplified in the Tinsley unit and passed, via a Krohn-Hite filter, to a 12-channel S.E. direct writing oscillograph. Traces representing the pitching motion of the box could thus be readily obtained.

The pitch attitude of the box could be set by using a clinometer and then fixed by tightening a grub screw which secured the wire to the box via the wire attachment device. The whole set-up could be implemented in a few minutes.

6.2 The Test Procedure

With the container model supported as shown in Figure 6.1, the model was displaced from equilibrium and released. The resulting decaying motion was recorded on the U.V. paper thus giving a wind-off datum. This procedure was repeated for various starting amplitudes and it was possible in this way to build up a comprehensive "logarithmic decrement" (log.dec.)/amplitude picture. The slight amount of stiction in the bearings led to the usual linear (or approximately linear) decay envelope implying log.dec. decreasing with increasing amplitude. (Figure 6.2). This lengthy procedure was repeated for each and every initial setting of the box.

With the wind turned on, similar traces of free pitching motion were obtained for a range of windspeeds. This was done for three freestream conditions; (a) clean flow, (b) flow through a 0.030" mesh gauze and (c) flow through a grid generating a turbulence intensity of 10%. Both container models were tested in this way, but rather more emphasis was placed on the 1:0.4:0.4 model. The maximum starting amplitude in any of the tests was about 3°, and most results were extracted at amplitudes much smaller than this.

6.3 Theoretical Basis of the Method

Referring to Figure 6.1, the equation of pitching motion of the container is

$$I\ddot{\alpha} + b\dot{\alpha} + Kr^2\alpha = qSd\left(C_{mo} + C_{m\alpha}\alpha + \frac{\dot{\alpha}d}{V}C_{m\dot{\alpha}}\right) + \text{higher order terms} \quad \ldots\ldots (6.1)$$

where $I = \bar{I} + Mr^2 + \frac{1}{3}M_s r^2 + M_w r^2$, $\bar{I}$ is the moment of inertia of the container, M the total suspended mass, M_s the spring mass, M_w the wire mass, r the distance between the central axis and the wire, K the spring stiffness and b the structural damping coefficient. The steady aerodynamic moment $qSdC_{mo}$ is balanced at the equilibrium position, α_o, so that if θ is the deviation from this position, equation 6.1 reduces to

$$\ddot{\theta} + \left[\frac{b - \frac{1}{2}\rho VSd^2C_{m\dot{\alpha}}}{I}\right]\dot{\theta} + \left[\omega_o^2 - \frac{qSdC_{m\alpha}}{I}\right]\theta = 0 \quad \ldots\ldots (6.2)$$

where $\omega_o^2 = Kr^2/I$ defines the undamped natural frequency, $f_o = \omega_o/2\pi$ Hz, in vacuo. Equation (6.2) may be rewritten as

$$\ddot{\theta} + 2\Delta\dot{\theta} + \omega^2\theta = 0 \quad \ldots\ldots (6.3)$$

where $\Delta = \frac{b - \frac{1}{2}\rho VSd^2C_{m\dot{\alpha}}}{2I} \equiv \Delta(V) =$ total damping exponent $\ldots\ldots (6.4)$

and $\omega^2 = \omega_o^2 - \frac{\frac{1}{2}\rho V^2SdC_{m\alpha}}{I} \equiv \omega^2(V^2) \equiv 4\pi^2f^2 \quad \ldots\ldots (6.5)$

where f is the aeroelastic frequency.

The solution of equation (6.3) is

$$\theta = A \exp(-\Delta t) \sin(\nu t + \phi) \qquad \ldots\ldots\ldots\ldots\ldots\ldots\ldots\ldots \quad (6.6)$$

where $\nu^2 = \omega^2 - \Delta^2 \equiv 4\pi^2 f_D^2$ (f_D being the damped aeroelastic frequency) while A and ϕ are arbitrary. If p complete cycles of the motion described by equation (6.6) are observed, and the natural logarithm of the terminal amplitudes is taken, one obtains

$$\Delta/f_D = \frac{1}{p} \operatorname{Ln}\left[|\theta_1|/|\theta_p|\right] \equiv \delta = \text{"wind-on" log.dec.} \ldots\ldots\ldots \quad (6.7)$$

Thus $$\Delta = f_D \, \delta \qquad \ldots\ldots\ldots\ldots\ldots\ldots\ldots\ldots\ldots\ldots \quad (6.8)$$

and since both f_D and δ can be measured directly from $\theta \sim t$ traces, the damping exponent Δ can be calculated. When this has been done, the equation following (6.6) can be used to calculate $\omega^2 = 4\pi f_D^2 - \Delta^2$. If this procedure is also adopted at V = 0, then $\Delta \rightarrow \Delta_0 = b/2I$ and $f_D \rightarrow f = \frac{1}{2\pi}\sqrt{\omega_0^2 - \Delta_0^2}$, so that Δ_0 and ω_0^2 may be determined. Thus finally from equations (6.4) and (6.5) one obtains

$$C_{m\dot{\alpha}} = \frac{4I(\Delta_0 - \Delta)}{\rho V S d^2}, \quad C_{m\alpha} = \frac{2I(\omega_0^2 - \omega^2)}{\rho V^2 S d} \ldots$$
$$\ldots\ldots\ldots\ldots \quad (6.9)$$

The total moment of inertia is the only structural parameter required in the determination of the aerodynamic coefficients by the above method. To determine I, the following procedure was adopted during the tests:- First the natural circular frequency, wind-off, namely ω_0, was determined. Mass M was then increased in steps, leading at each step to an increase δI in I (see equation (1)). The change, $\delta\omega_0^2$, in ω_0^2 was recorded at each step. Thus, since

$$r^2 K = (\omega_0^2 + \delta\omega_0^2)(I + \delta I) \qquad \ldots\ldots\ldots\ldots\ldots\ldots\ldots \quad (6.10)$$

one obtains $$I = -\frac{\delta I}{\delta\omega_0^2}\omega_0^2 - \delta I$$

giving, in the limit, $$I = -\frac{dI}{d\omega_0^2}\omega_0^2 \qquad \ldots\ldots\ldots\ldots\ldots\ldots \quad (6.11)$$

Thus, the shape of the $\delta\omega_o^2 \sim \delta I$ graph at its origin can be used for $dI/d\omega_o^2$ in (6.11) and I determined. Stiffness K can then be found by using $K = \omega_o^2 I / r^2$.

6.4 Results for the 1 : 0.4 : 0.4 Container

For clarity in this Section, wind axes, in accordance with internationally accepted aeronautical definition will be used. The container has its major axis streamwise when pitch angle, α, and yaw angle, ψ, are zero. Figure 1 is sufficiently explicit as regards the required axis definitions.

For the 1 : 0.4 : 0.4 container model, the values of I and K were determined as 0.058 slug.ft^2 and 2 lb/in. respectively. The "wind-off" damping factor, Δ_o, for the model and its suspension system is shown plotted against $|\theta|$ in Figure 6.2. (This is a typical plot: several, in fact, were obtained - all showing small departures from Figure 6.2 as attitude changed. This dependence on attitude reflected the change in stiction force with angular position of the container model on its spindle). The derivatives, $C_{m\alpha}$ and $C_{m\dot{\alpha}}$, were then obtained by using equations (6.9) in which the $|\theta|$ - dependent values of ω^2 and Δ were obtained from the U.V. traces of $\theta \sim t$ as V was varied. Note that the conditioning of the method based on equations (6.9) for low density fluids, such as air, at low speeds favours accurate determinations of $C_{m\dot{\alpha}}$, while $C_{m\alpha}$ is obtained only approximately owing to the high degree of frequency resolution required to separate "wind-on" and "wind-off" ω^2 values. Some doubt is also cast upon the accuracy of the $C_{m\alpha}$ values obtained here owing to the possibility of a significant $C_{m\ddot{\alpha}}$ effect.

Figure 6.3 shows the variation of $C_{m\dot{\alpha}}$ versus reduced velocity, $V/\omega d$ as α_o and ψ_o are varied. From the viewpoint of severity of onset of dynamic instability, the $\alpha_o = 0, \psi_o = 0$ configuration is the most troublesome, the instability diminishing as α_o is increased. The container is seen to be dynamically stable when $\alpha_o = 10^o$ and more stable when $\alpha_o = 15^o$ when $\psi_o = 0$. Provision of yaw relative to the (0, 0) position is also seen to be stabilizing, but less powerfully so than provision of incidence. However, provision of yaw relative to the $(10^o, 0)$ position is seen to be <u>destabilizing</u>. Indeed, the orientation $(10^o, 10^o)$ is almost as unstable as the (0, 0) case. All cases show a very marked dependence of $C_{m\dot{\alpha}}$ on reduced velocity (and hence on its reciprocal, viz. frequency parameter $w_d = \omega d/V$). The reasons underlying these variations are as yet not understood, but are not entirely unexpected in view of the critical dependence of $C_{m\dot{\alpha}}$ on the dynamics of the separation bubbles. The pressure studies and the theoretical model of Section 7 will throw light onto this point.

Figure 6.4 shows the variation of C_{m_α} and $C_{m_{\dot{\alpha}}}$ with $V/\omega d$ for the (0, 0) position as $V/\omega d$ achieves higher values. Note that $C_{m_{\dot{\alpha}}}$ levels off beyond $V/\omega d$ of 5. In the range $6 \leq V/\omega d \leq 10$, C_{m_α} is seen to be constant and negative implying <u>static stability</u> at the (0, 0) position. The rise in $|C_{m_\alpha}|$ as $V/\omega d$ falls below 6 is thought to be a spurious effect associated with lack of frequency resolution power. Indeed, any point on the $C \sim V/\omega d$ curve for $V/\omega d < 6.5$ is highly suspect.

In view of the strong evidence pointing towards the major influence of the separation bubble dynamics on the pitching moment derivatives, it was thought that a device which enabled pressures to be communicated rapidly between the bubbles on the lower and upper faces of the oscillating container would lead to a lessening of the dynamic instability phenomenon. This was checked by providing the container model with a "stand-off plate" (4.8" x 4.8" x 5 mm ply) mounted $\frac{1}{4}$" forward of the leading face (Figure 6.5). Figure 6.4 shows that the "stand-off plate" fomented dynamic stability whilst reducing static stability. However, the reduction of dynamic instability was not as dramatic as had been expected and the device was therefore not tested in other orientations. The partial success of this device does, nevertheless, point the way towards an ultimate 'cure' based on "separation bubble control".

The effect of free stream turbulence on container stability had been highlighted in Reference 9, and the general conclusions of that study were confirmed dramatically by the present tests. Four orientations of the container were reconsidered for free stream turbulence of intensity 10%; the results for $C_{m_{\dot{\alpha}}}$ being presented in Figure 6.6. By juxtaposition of Figures 6.3 and 6.6, the magnitude of the turbulence effect can be at once appreciated. The (0, 0) position which was most unstable for the clean free stream is stable for the turbulent free stream. (This result agrees with that of the turbulence study of Section 4). The (10°, 10°) position is also stabilized by turbulence. However, the (10°, 0) case suffers a slight destabilizing effect when turbulence is introduced. Again, the effect of the "stand-off plate" is seen to be stabilizing - though less so here than in the clean free stream case.

Figure 6.7 illustrates the variation of C_{m_α} with α_o assessed by free vibration tests with and without free stream turbulence at a reduced velocity of 0.216. In the clean flow, static stability obtains for the region $-8° \leq \alpha_o \leq 8°$ with $\psi_o = 0$. The extent of the stable region is seen to be decreased by yawing the container. Provision of free stream turbulence via a 10% turbulence grid <u>destabilizes</u> the system in the static sense - again dramatically. The "stand-off plate" magnifies this destabilizing effect.

6.5 Results for the 1 : 0.2 : 0.2 Container

For the 1 : 0.2 : 0.2 container model, the values of I and K were determined as 0.306 slug ft^2 and 2 lb/in. respectively. The "wind-off" damping factor, Δ_o, followed amplitude variations much the same as those typified in Figure 6.2.

Figure 6.8 shows the derivative $C_{m\dot{\alpha}}$ for the 1 : 0.2 : 0.2 model which, when compared with the 1 : 0.4 : 0.4 model (Figure 6.3) is seen to be intrinsically more stable in the dynamic sense. It is of interest to note that there is a similarity of shape in the $C_{m\dot{\alpha}} \sim V/\omega d$ curves for the two container models. Increase of $V/\omega d$ is seen to be destabilizing up to a certain value in all cases in Figure 6.8. For the (0, 0) orientation, the stability actually changes from positive to negative as $V/\omega d$ increases, the cross-over occurring at $\frac{V}{\omega d} = 3$. Again, incidence variations from the (0, 0) position are generally stabilizing as indeed are small variations in yaw as typified by the (0, 5°) curve. The case (10°, 10°) here is the most unstable of all - again parallelling the result from the 1 : 0.4 : 0.4 container model. The strong dependency of all curves on $V/\omega d$ should again be noted, and the studies of Section 7 will throw light on this dependency.

The (0, 0) orientation was studied for free-stream turbulence sensitivity, and, once more, the introduction of 10% grid turbulence was shown to exert a dynamically stabilizing influence, except in a small region close to $V/\omega d = 2.3$ where it was mildly destabilizing. Unlike the 1 : 0.4 : 0.4 case, however, the very marked dependence here of $C_{m\dot{\alpha}}$ on $V/\omega d$ when turbulence was present stands out.

Finally, Figure 6.9 shows the $C_{m\alpha} \sim \alpha_o$ characteristics inferred from the very small number of free vibration tests on the 1 : 0.2 : 0.2 container. The container is shown to be statically unstable in clean flow at $\alpha_o = 0$ and this effect is accentuated by grid turbulence. The effects of yaw on $C_{m\alpha}$ could not really be inferred owing to paucity of experimental points. However, at the frequency parameter appropriate to Figure 6.9 (viz. $\omega d = 0.22$), $C_{m\alpha}$ may safely be taken from static curves such as those of Laub and Kodani[8].

6.6 Attempted Stabilization of the 1 : 0.4 : 0.4 Container Load

This subject has been mentioned previously in Section 6.4 where the stabilizing influence of a stand-off plate was discussed. The effect of such a device was found to be only marginally beneficial - a small return for potentially high installation and operating costs. The stand-off plate concept is only one of a number of stabilization methods based on the philosophy of 'appendaging' the towed body; drogue chutes and inflatable leading surfaces being other examples. At face value, such ideas have many attractions provided suitable stabilizing appendages can be conceived, but there is an overriding consideration of time penalty on turnaround and a need for skilled personnel to effect the fixing. In an unloading operation where,

for example, a container is being removed from a ship's hold, the method might prove impracticable in view of space restriction and costly if staged lifting/appendage-fixing were envisaged.

In view of the difficulties mentioned above, it was considered desirable to examine the possibility of stabilizing appendages attached to the basic lifting strops rather than to the container itself. Provided the appendages are uncomplicated, the above difficulties are overcome. Furthermore, the possibility of designing strops and appendages which stabilize a large variety of freight loads is an attractive one from the viewpoint of cost-effectiveness. While such a goal might not be a generally attainable one, it is sufficiently attractive to warrant some effort here. Accordingly, the limited objective of stabilization of the 1:0.4:0.4 container, regardless of the magnitude and distribution of mass contained within it, will be aimed at here. If such can be achieved by purely passive means, a significant advance will have been made.

At the outset, it should be appreciated that a twin strop arrangement holding the container at or near its minimum drag position is viewed as axiomatic. The primary consideration must then be to obviate the dynamic instability modes (i.e. pitching and yawing freedoms, per se, negatively damped). The pitching instability is readily constrained-out by suitable kinematic design of the strops. This leaves the yawing instability, which might then be attacked by the addition of stabilizing appendages. However, even when all single-freedom instabilities have been removed, a larger problem still remains, namely flutter and divergence in combinations of the individual degrees of freedom. Even when the strop design obviates container pitch and roll, thus removing longitudinal instabilities and leaving only the sideslip and yaw freedoms, the likelihood of divergence in yaw and sideslip/yaw flutter is akin to that of day following night!!! This important subject will be discussed later in this Section, and for the moment attention will be focussed on the suppression of classical negative aerodynamic damping in pure yaw.

In the preliminary tests on yaw stabilization, the test facility shown in Figure 6.1 was employed - various 'fences' being attached to the major face of the container shown in that Figure. (It should now be imagined that the container is being viewed from above and that the pitching axis of Figure 6.1 is, in fact, the yawing axis with $\alpha \equiv \psi =$ yaw angle. The yaw device shown at the top of the Figure is now a pitch device on which nose-up or nose-down settings can be achieved). The following observations were made:-

(i) Solid fences, both straight and curved, attached near the leading edge were inevitably destabilizing, giving increased magnitudes of negative yaw damping.

(ii) In the range of pitch settings (-7°, 7°), it was not possible to stabilize yaw motions by means of sensibly small fences, the reference values of aerodynamic negative damping being too strong.

(iii) For pitch settings between $\alpha_o = -8^\circ$ and -15°, small fences attached near the trailing edge of the major surface (Figure 6.1) stabilized the yaw motion over a wide range of amplitudes and frequency parameters. The stabilizing influence of the fences was only marginal in the static sense.

(iv) Side fins of small height attached along the edges of the major surface of the container enhanced static stability and improved dynamic stability marginally in the above range of nose-down settings.

As a result of these preliminary tests, it was decided to concentrate upon the 10° nose-down orientation (a case previously considered by Boeings in their flight test work) as being the container configuration where aerodynamic yaw damping (positive or negative) is small. At this setting one may derive the maximum benefits from sensibly small trailing edge fences and other stabilizing appendages. Figures (6.10) relate to this case and are largely self-explanatory. Figure (6.10) itself shows the yaw velocity derivative, $C_{N\dot{\psi}}$, for the basic container as a function of yaw amplitude at various frequency parameters. Negative values of $C_{N\dot{\psi}}$ imply dynamic stability in yaw motion per se. It is seen that there is a deterioration of stability as frequency parameter and amplitude are increased. This behaviour with amplitude is entirely consistent with the results of Sections 2 and 4.

Figure (6.10a) illustrates the effects produced by side fins with a small gap. These are seen to improve the yaw dynamic stability at the large amplitude end, whilst producing only marginal improvements at low amplitude. Increasing the gap (Figure (6.10b) is seen to be detrimental, particularly at small amplitudes. There is an interesting change in shape of the curves due to the increased gap, and the sensitivity to frequency parameter is seen to be diminished.

Figure (6.10c) shows the effect on yaw dynamic stability of a low fence at the trailing edge. Comparing with Figure (6.10), the effect is seen to be stabilizing across the entire amplitude range for all frequency parameters studied. Increasing fence height improves stability still further, as is evident from Figure (6.10d). It should, however, be noted that the improvement in stability is at the expense of increased drag. When sidefins are provided in addition to this larger fence, yaw dynamic stability is again improved as shown in Figure (6.10e). The purpose of sidefin addition, however, is rather to enhance the static stability of the system

about the yaw axis. In order to appreciate this latter feature, Table 6.I (below) has been compiled. This Table presents the mean values of $C_{N\dot{\psi}}$ for a double amplitude in yaw of 4°. For clarity, the $C_{N\dot{\psi}}$ values have been related to the appropriate Figure numbers.

TABLE 6.I

$C_{N\dot{\psi}}$ FOR 1:0.4:0.4 CONTAINER, 10° NOSE DOWN, WITH APPENDAGES, AT $W_d = 0.1$

Figure Number	6.10	6.10(a)	6.10(b)	6.10(c)	6.10(d)	6.10(e)
$C_{N\dot{\psi}}$	0.90	-0.63	-1.56	0.90	0.86	0

It is seen that the side fins per se greatly improve static stability while the trailing edge fences have little or no influence. The combination of side fins and trailing edge fence yields neutral static stability in yaw along with the considerable dynamic stability benefits mentioned above.

The case of $\alpha_o = -5°$ orientation is introduced in Figure 6.11, which on direct comparison with Figure 6.10, is seen to exhibit a much greater degree of dynamic instability in yaw than the $\alpha_o = -10°$ case. Addition of the large trailing edge fence and two side fins (Figure 6.11(a)) exerts a stabilizing influence, particularly at low Wd values, but this is insufficient to provide positive yaw damping at any amplitude or frequency parameter value considered here. It should be noted, however, that the $\alpha_o = -5°$ case yields a high degree of static stability in yaw, the $C_{N\dot{\psi}}$ values being -3.6 and -5.3 for the clean and 'appendaged' containers respectively.

Figure (6.12) shows the $C_{N\dot{\psi}}$ derivatives for the $\alpha_o = -15°$ case, and these are seen to be negative for all amplitudes and frequency parameters considered here. The container in this orientation is thus thoroughly dynamically stable in yaw. However, the mean value of $C_{N\dot{\psi}}$ is 2.56 implying strong static instability. This is reduced to $C_{N\dot{\psi}} = 1.92$ by adding side fins and a rear fence. The dynamic stability is again improved (Figure (6.12a)) by the appendages.

Figure (6.13) relates to the $\alpha_o = -10°$ case, but here the motion is in pitch. The container is only just stable at low amplitudes, becoming dynamically unstable at larger amplitudes. The presence of side fins (Figure (6.13a)) does not influence this picture, as might have been expected. When a rear fence is added (Figure 6.13b), its effect is mildly destabilizing, but it is thought that such an instability might be cured by stropping.

Having shown how the yaw motion, per se, might be stabilized by the provision of appendages of a type which can be attached to the strops, the problem of combined mode instabilities must now be considered:-

6.6.1 Lateral Flutter and Divergence

From the viewpoint of the avoidance of single degree of freedom dynamic instability, it has been shown to be desirable for the container to adopt a 10° nose-down attitude (± 2° or so) at equilibrium. In this attitude, single freedom stability in yaw may be augmented by side fins and a trailing-edge fence attached to the strops. If, as wind speed relative to the container is increased, the container adopts nose-down attitudes of less than, say, 7°, the risk of single freedom yaw instability arises. On the other hand, if attitudes involving nose-down greater than, say, 12° develop, there will be excessive instability in yaw. It is thus important to use parallel strops of equal length as shown in Figure (6.14). Such stropping not only fulfills the yaw stability requirements, but also constrains-out any single freedom pitch instabilities which might be present.

Likewise, it is considered desirable to restrict possibilities of lateral interactions by constraining-out the roll motions. This may be achieved most simply by adopting a four strop, parallel, equal length support system (also shown in Figure (6.14)). If such is adopted and the helicopter is considered to be 'fixed', the container has just three degrees of freedom - one longitudinal and two lateral. It is easily shown that (for low Vd at least) that the longitudinal motion per se is stable; a feature that is evident in the freely suspended model tests of this configuration. The lateral motions involving container sideslip and yaw are, however, problematic, for while these motions per se might be stable (or rendered stable by appendages), the possibility of combined sideslip/yaw divergence and flutter is by no means remote: Indeed, it might even be regarded as inevitable.

In order to study sideslip/yaw flutter and divergence of a container suspended as in Figure (6.14), one might resort to undamped flutter theory. In this, only the inertia and total stiffness terms are retained in the equations of motion. The adoption of undamped theory does not usually lead to errors of significant magnitude, but it must be borne in mind that flutter due to damping coupling or damping/stiffness coupling cannot be predicted by this means. It is clear that the most significant damping terms will be the aerodynamic actions induced by sideslip; i.e. those involving the derivatives C_{Y_v} and C_{N_v} where, as usual, $v = \dot{y}$. Provided $C_{N_{\dot{\psi}}}$ is sufficiently negative, this derivative, along with $C_{Y_{\dot{\psi}}}$, is unlikely to play a vital role in the flutter phenomenon. Mechanical damping in this

class of problems is negligibly small and will be disregarded. In the following treatment, the full equations of motion will be stated and inferences drawn by means of undamped theory. The influence of the damping terms $C_{y\dot{v}}$ and $C_{N\dot{v}}$ will be discussed subsequently. Frequency parameter effects will be ignored throughout and small amplitude stability only will be considered.

The equations of motion in sideslip and yaw for the container-strop configuration shown in Figure (6.14) are

$$\underset{\sim}{A}\,\ddot{\underset{\sim}{q}} + \underset{\sim}{B}\,\dot{\underset{\sim}{q}} + (\underset{\sim}{E}+\underset{\sim}{C})\underset{\sim}{q} = \underset{\sim}{0} \qquad \ldots\ldots\ldots\ldots (6.12)$$

where $\underset{\sim}{A} = \begin{bmatrix} 1, & k^2 \end{bmatrix}$,

$$\underset{\sim}{B} = \frac{1}{2}\frac{\rho V d^2}{m}\begin{bmatrix} C_D + C_{y\psi}, & -C_{y\dot{\psi}} \\ C_{N\psi}, & -C_{N\dot{\psi}} \end{bmatrix}$$

$$\underset{\sim}{C} = \frac{1}{2}\frac{\rho V^2 d^2}{mc}\begin{bmatrix} 0, & -C_{y\psi} \\ 0, & -C_{N\psi} \end{bmatrix}$$

$$\underset{\sim}{E} = \frac{k_1}{m}\begin{bmatrix} 1+r^2, & \sigma_1 - r^2\sigma_2 \\ \sigma_1 - r^2\sigma_2, & \sigma_1^2 + r^2\sigma_2^2 \end{bmatrix}$$

$$\underset{\sim}{q} = \{ y/c, \psi \},$$

m = mass of container

$k = \bar{k}/c$ = radius of gyration of container/length of container

$r^2 = T_2/T_1$ (T_1, T_2 = forward, leeward strop tensions)

$c\sigma_1$ = distance (along central axis) of forward strop from container C.G.

$c\sigma_2$ = distance (along central axis) of leeward strop from container C.G.

$$T_1 + T_2 = \{ (mg-L)^2 + D^2 \}^{1/2}$$

$$T_1 - T_2 = \frac{\left\{1 + \frac{D^2}{(mg-L)^2}\right\}^{1/2}}{\left\{1 + \frac{D\tan\Theta}{mg-L}\right\} c(\sigma_1+\sigma_2)} \left[-2M\sec\Theta - (mg-L)\left\{(c_2-c_1)\left(1 + \frac{D\tan\Theta}{mg-L}\right) + d\tan\Theta - \frac{d\cdot D}{mg-L}\right\}\right]$$

D = drag force

L = lift force

M = pitching moment

d = container depth

Θ = nose down incidence angle

c_1 = distance from container leading edge to windward strop (along container)

c_2 = distance from container trailing edge to leeward strop (along container)

$k_1 = T_1/\ell$

$k_2 = T_2/\ell$

and ℓ = strop length.

A 'BASIC' program has been written to solve the above equations for flutter boundaries. This program has been used to determine the flutter boundaries for the case where the rate derivatives $C_{Y\dot{\psi}}$ and $C_{N\dot{\psi}}$ are ignored. ($C_{N\dot{\psi}}$ is assumed <u>negative</u> and small while $C_{Y\dot{\psi}}$ is negligibly small. The influence of <u>small</u> $C_{N\dot{\psi}}$ on the flutter boundaries will be negligible, the principal aerodynamic damping actions stemming from the first column of matrix $\underset{\sim}{B}$.) However, one can learn rather more from a purely analytic study of the undamped case ($\underset{\sim}{B} = \underset{\sim}{0}$) than from a whole set of numerical studies of the full equations. Writing $\underset{\sim}{B} = \underset{\sim}{0}$ in equation (6.12) and assuming a solution in the form $\underset{\sim}{q} = \underset{\sim}{q}\, e^{\exp(\tilde{\lambda} Vt/c)}$ one obtains the secular determinant

$$\begin{vmatrix} \lambda^2 + \chi(1+r^2), & \chi(\sigma_1 - r^2\sigma_2) - a C_{Y\psi} \\ \chi(\sigma_1 - r^2\sigma_2), & k^2\lambda^2 + \chi(\sigma_1^2 + r^2\sigma_2^2) - a C_{N\psi} \end{vmatrix} = 0 \cdots$$

..... (6.13)

where $\chi = k_1 c^2/mV^2$, $a = \rho d^2 c/2m$. This expands to

$$k^2\lambda^4 + \left[\chi\{\sigma_1^2 + r^2\sigma_2^2 + k^2(1+r^2)\} - a C_{N\psi}\right]\lambda^2$$

$$+ \chi^2 r^2(\sigma_1+\sigma_2)^2 + \chi a\{(\sigma_1 - r^2\sigma_2)C_{Y\psi} - (1+r^2)C_{N\psi}\} = 0 \cdots$$

..... (6.13A)

The undamped flutter requirement is synonymous with that of frequency coalescence - this being simply

$$\left[\chi\left\{\sigma_1^2+r^2\sigma_2^2+k^2(1+r^2)\right\}-aC_{N\psi}\right]^2$$
$$=4k^2\left[\chi^2r^2(\sigma_1+\sigma_2)^2+a\chi\left\{(\sigma_1-r^2\sigma_2)C_{\gamma\psi}-(1+r^2)C_{N\psi}\right\}\right]$$

or

$$\left[\chi\left\{\sigma_1^2+r^2\sigma_2^2-k^2(1+r^2)\right\}-aC_{N\psi}\right]^2$$
$$=4k^2(\sigma_1-r^2\sigma_2)\chi\left[aC_{\gamma\psi}-\chi(\sigma_1-r^2\sigma_2)\right] \quad \ldots . \qquad \ldots . \ (6.14)$$

Without need for further expansion, one can now make an important deduction regarding the occurrence of undamped flutter: The derivative $C_{\gamma\psi}$ is typically large and positive when α_o is near to -10°, and the final bracket in equation (6.14) is thus positive also. As χ is essentially positive, it is seen that flutter <u>cannot occur</u> when

$$\sigma_1-r^2\sigma_2<0$$

i.e. when $$\sigma_1 T_1 < \sigma_2 T_2 \qquad \ldots . \ (6.15)$$

<u>Thus, it would appear that by suitable arrangement of the tensions in the strops, the possibility of flutter is ruled out.</u>

Now the condition for divergence is the vanishing of the term independent of λ in equation (6.13A). The divergence speeds are thus given by

$$\frac{2k_1c}{\rho d^2V_D^2}=\frac{(1+r^2)C_{N\psi}-(\sigma_1-r^2\sigma_2)C_{\gamma\psi}}{r^2(\sigma_1+\sigma_2)^2} \qquad \ldots . \ (6.16)$$

At $\alpha_o = -10^\circ$, $C_{N\psi} < C_{\gamma\psi}$ both derivatives being positive. Therefore, divergence is <u>fomented</u> by condition (6.15) and it is seen that, in this respect, <u>the requirement of a divergence-free system conflicts with that of a flutter-free system.</u> If one designs a system such that condition (6.15) is met, one can then increase V_D by the following means:-

(i) Increasing the strop separation, $(\sigma_1 + \sigma_2)c$

(ii) Nosing down slightly in order to reduce $C_{N\psi}$

The provision of a fin, while reducing $C_{N\psi}$, increases $C_{Y\psi}$ and so this is unlikely to yield a solution. Also, the amount of nosing-down that can be done is very strictly limited by the increasing tendency for $C_{N\psi}$ to become positive. It should also be noted that the addition of appendages designed to stabilize yaw per se might prove ultimately deleterious since the increased drag of, say, a trailing edge fence could produce T_1 and T_2 which violate condition (6.15) at a lower windspeed than would the clean container.

In a preliminary numerical experiment in which undamped flutter theory was used, an actual container model (1' x 0.4' x 0.4', balsa, mg = 0.24 lb) formed the basis of the study. This model was stropped as in Figure (6.14), the reference strop length being ℓ = 2.25 ft. In these tests, the parameters of the problem were all varied and their effects on the divergence and flutter speeds tabulated. These results are given in Table IV. A notable feature of the results is the virtual independence of the flutter speed of the aerodynamic parameters $C_{Y\psi}$ and $C_{N\psi}$, even when departures of these parameters from their reference values are large. This insensitivity really reflects condition (6.15); flutter is much more sensitive to parameters which affect the tension difference (e.g. pitching moment). Thus, there would appear to be scope for ingenuity in devising strop systems which meet condition (6.15), but which are not divergence-prone.

Another important feature which is not directly evident from Table IV is that of the severity of flutter onset. The computer program showed that the onset of flutter could be, and indeed usually was, extremely hard. As soon as the container had achieved an attitude where condition (6.15) was violated, the excess of flight speed over critical speed was usually very considerable. At marginally smaller flight speeds, flutter was completely absent. This 'hard' flutter was experienced when seeking to substantiate computer results in the wind tunnel and, predictably, the model was destroyed. Associated with 'hard' flutter onset was usually a very 'soft' divergence onset. However, at a different incidence, the divergence onset might be 'hard' and the flutter onset 'soft'.

The above comments regarding the 'hardness' of onset of instability must be borne in mind by the active control arm designer. There are some flutter conditions which are so severe that any control action of sensible magnitude at the upper end of the strops would prove futile.

In order to check the validity of the undamped theory, the full flutter equations were solved for every case presented in Table IV. In no cases were the undamped results of Table IV more than 1 f/s in error in their prediction of the flutter speed. The damping terms were found to be inevitably destabilising and gave a harder flutter onset. It is significant that the full flutter theory predicts a flutter boundary only when the tension condition (6.15) is violated. Indeed, for every entry in Table IV, flutter occurred at windspeeds only 1-3% above those for which condition (6.15) was first violated.

The above calculations were supported by wind tunnel tests on a balsa scale model stropped as in Figure (6.14). In a large majority of the 25 cases studied (each case corresponding to an entry in Table IV), there was good agreement with the simple theory.

In summary, it would appear that the task of passive stabilisation is rendered difficult by the conflict between the 'no flutter' and 'no divergence' requirements when this type of stropping is employed. Divergence, however, might be deferred to a higher speed range by shortening the strops and increasing their separation. Flutter might then be prevented by attaching to the leeward strops (at their join with the upper surface of the container) a lift-producing surface yielding increased T_2 as V increases. From the standpoint of flutter as well as of freightage efficiency, container drag should be kept to a minimum consistent with $C_{N\dot{\psi}} < 0$. A nose-down attitude of between 8° and 12° would appear to be optimal in this respect. Fins are found to exert only a marginally stabilizing effect, while drogues are deleterious in view of their effect on drag. Increased freightage weight militates against flutter and divergence - as does reduction of container yaw moment of inertia.

6.6.2 The Tandem 'V' Strop Arrangement

The 'V' strop was originated by Dr. D.F. Sheldon (of R.M.C.S., Shrivenham, U.K.), its object being to provide a constraint against yaw motions. For the strop system of Figure (6.14), the major problem has been shown to be lateral flutter and divergence. Flutter is ruled-out if the total number of lateral degrees of freedom is reduced to one, and such is accomplished on a rigid container by a parallel suspension with 'V' strops (Figure 6.15). The only lateral mode is combined sideslip and roll and divergence is excluded since yaw cannot occur.

A series of wind tunnel tests was performed on 1' x 0.4' x 0.4' container models of various weights and moments of inertia, stropped as in Figure 6.15(a) with $\Theta \approx 10^\circ$. For a strop length of 2.25' and a minimum strop separation of 0.6' (the strops being symmetrically disposed), flutter and divergence were obviated at all practical windspeeds. It might be noted that V_{max} in these tests produced a blowback angle $\mu = 50^\circ$. At the higher velocities, the yawing constraint was jeopardised by leeward

cable slackness. This was remedied by a 0.1' deflector strip at 20° incidence relative to the container upper surface (Figure 6.15b) which produced larger T_2.

Regrettably, time did not permit an extensive study of the tandem 'V' strop, but the tests performed with this arrangement, with Ⓗ = 10° and leeward deflector plate fitted, showed great promise. However, an obvious danger in stropping with such a high degree of restraint is that helicopter motions could effectively relax the constraint and produce a helicopter/freight flutter mode. This subject is currently under investigation at R.M.C.S., Shrivenham, U.K.

7. MATHEMATICAL MODELS

Parallel to the main experimental work two mathematical approaches have been investigated. The first approach, started before wind tunnel results were obtained, attempts solution of the Navier-Stokes equations for two-dimensional flow past an oscillating rectangular box by a finite difference technique. The second approach, started after the wind tunnel results were available, attempts to represent the flow past the oscillating model by simple expressions in order to gain understanding of the flow mechanism, and as an aid to interpretation of the results.

7.1 Finite Difference Solutions

The modern computer has made practical the calculation of flows around a variety of shapes. Much work is being done in this field, with finite element and finite difference techniques fighting for pre-eminence. It was felt desirable to enter this field for the following reasons:-

(a) It might lead to information on separated flows around bluff bodies which experimental methods might not reveal.

(b) It might be possible to calculate forces/moments on an oscillating container, albeit in two dimensions.

(c) An efficient 'numerical wind tunnel' would be a valuable tool in this particular field.

Accordingly the compressible two-dimensional Navier Stokes Equations have been solved in the neighbourhood of a 1:0.4 rectangle by using two versions of the finite difference method. Details of the method have been presented in a report[10], and are only briefly summarised here.

Two finite difference models, one explicit and one implicit, were used to simulate the viscous compressible flow around an accelerating or pitching rectangular box. A grid system fixed relative to the box was chosen, although this required revision of the domain boundary conditions and of the fluid momentum equations.

The boundaries of a finite domain can create serious problems, with pressure waves emanating from the obstacle surface being reflected from the boundaries and creating instabilities (the organ pipe phenomenon). This was solved by a coordinate stretching technique, the effect of which was to reduce the local speed of sound and viscosity of the fluid as the domain boundaries were approached.

Finally in the construction of an implicit finite difference program, an algorithm for dealing with the nonlinear terms is suggested. These nonlinear terms have previously impeded the implicit solution of these equations. This also enables a satisfactory error analysis to be carried out on the derived linear equations.

Numerical solutions using this technique have been obtained for a few cases. Some problems still exist, leading at the moment to limitations on run time before instabilities arise. One computer output, extending over the starting process and one cycle of oscillation is presented as Figure 7.1. In conjunction with the explicit method a program has been formulated to derive force and moment characteristics. One result obtained is shown in Figure 7.2.

This work was started in the early days of the contract parallel to the wind tunnel work, and before wind tunnel results were forthcoming. With the flow of test results now established, and appreciating the limitations of the two-dimensional theoretical approach with regard to real containers, this work has been given a low priority. The potential of this approach is however not limited to the container problem, and it would seem well worthy of further investigation.

7.2 Mathematical Models Based on Simplified Flow Assumptions

The results from the pressure, free oscillation, and flow visualization tests show many interesting points that need to be explained and correlated in order that results can be presented in the most meaningful way. One approach to interpretation is by way of mathematical expressions for pitching moment, etc., based on simple physical ideas deriving from observation and measurement. Ideally, the physical ideas should be soundly based, and the derived expressions

explain as many features as possible of the results without anticipating these features. To this end the most interesting features that might be represented for a simple pitching (or yawing) motion are the varying static and dynamic stability characteristics that correspond to various attitudes, for smooth or turbulent flow.

Observation shows the separation bubbles varying in size with attitude, with bubble size lagging the motion. The pressure measurements show the highest suctions near the front of the models when the orientation is with major axis close to the stream direction, with pressures approaching ambient near the rear. In some ways this is similar to flow over thin wings or flat plates where separation bubbles form near the leading edge. Much work has been done on wings, with correlations and comparisons of results made, and some of the ideas arising from wing investigations would seem to have some relevance to the container model.

The potential flow solutions for flow past conventional aerofoils give reasonable agreement with experiment. With thin wings or flat plates pressure distributions are distorted near the leading edge by the leading edge separation bubble. A fair approximation to the actual pressure distribution has been obtained by assuming a constant level of pressure in the separated region, with pressures behind the separation reverting to the potential solution. The length of the bubble has been suggested as being twice the distance from leading edge to where the potential pressure equals that within the separation. This is illustrated in Figure 7.3(a). With the container shape the suctions near the front would seem more modest, but, ignoring the small contribution coming from the front and rear faces, similar assumptions lead to promising results.

A first approach, ignoring almost entirely the actual wind tunnel results, was to assume a basic pressure distribution that varied linearly from some value at the front edge to ambient at the rear, with a separation bubble defined as for thin wings, as shown in Figure 7.3(b). With a constant pressure assumed for the static model, pitching moment variations with incidence (from major axis in stream direction) can be deduced, and some of these are shown in Figure 7.4. This shows in one case a region of static stability about the major axis in stream direction position, with static instability for larger angles. It also shows that the static stability decreases and may disappear for shorter bubbles - this would appear consistent with the observed difference between stability characteristics in smooth and turbulent flow. If the effects of an oscillation are simulated by making the bubble size lag the motion, then curves such as those given in Figure 7.5 result. These are in the form of loops with a positive input of work, or 'negative damping'. A mean line through the loops shows a positive increase in slope with motion - or the increase in 'static stability' or acceleration effect noted in the wind tunnel results. The area of the loops also seems to vary with initial bubble length - as noted between results for the model in turbulent as against laminar flow - and the shape of the loops are very dependent on amplitude. For larger amplitudes the work input is concentrated

near the centre of the motion.

The main objections to the simple flow model assumed are that discontinuities occur in all the curves when the bubble length equals the full length of the model, and it seems difficult to choose the constants in the equations to give the right order of C_m and incidence. This was perhaps to be expected, and the next stage was to postulate a slightly different flow model that utilised rather more directly certain of the wind tunnel results.

It was noted that the sudden change in pressure assumed at the rear of the bubble was not apparent in the wind tunnel results - that the pressure tended to a much smoother variation. An alternative model was therefore proposed in which a basically linear variation of pressure was simply cut off near the front of the box. This illustrated in Figure 7.6(a). Results corresponding to a stationary model were first computed, with the values of the parameters illustrated in Figure 7.6(b) chosen to give moments of the correct order of magnitude. The results for pitching moment and lift are presented in Figure 7.7, comparing favourably with wind tunnel results. The level of pressure within the bubble was taken as $C_p = 1$, which is close to that found in experiment, for example in Figure 4.6. The variation of bubble length given in Figure 7.8 also compares favourably with the experimental results of Figure 5.2.

Detailed wind tunnel results with turbulence are not available, but indications are that bubble length would be shorter, depth larger and hence levels of suction greater. Computed moment curves for varying levels of suction within the bubble are shown in Figure 7.9. This shows the same trend as that inferred from experiment - a decrease in stability, near major axis in stream direction, for increase in bubble suction.

The modelling of unsteady flow required further assumptions to be made. It has been observed that bubble size lags the motion leading, with incidence increasing, to bubble lengths shorter than those for the same attitude when static. Now the smaller bubble implies a higher suction, partly to turn the flow around a smaller radius and partly to entrain more air. It was assumed that the effect of lag could be computed by applying a phase lag to incidence, computing bubble length for that incidence, and assuming that length to apply at the correct incidence with a corresponding change in bubble suction (Figure 7.10).

Results for oscillations of amplitude 15° and 30° and with phase lags of 0, 30, 60 and 90 degrees are shown in Figure 7.11. Points of interest, all in agreement with experiment, are:-

(a) a phase lag results in unstable loops,

(b) the energy input is more apparent for smaller angles,

(c) a mean line through the loop shows increasing slope (or decreasing 'static' stability) with increasing phase lag. This change in angle should really be attributed to an acceleration, or $C_{m\ddot{\alpha}}$ effect.

Note that phase lag (P) is simply related to frequency parameter w_d, by $w_d \approx \text{Tan } P$.

Now the loops formed are all destabilising, in no case having the stabilising subloops observed in the experimental results. It should be noted, however, that the only dynamic effect assumed can in no way represent the conventional damping that occurs, for example, with attached flow past streamlined shapes in pitching motion, or with completely detached flows past bluff shapes in fore and aft motion. If this type of damping is added loops such as those shown in Figure 7.12 are produced. With increase of conventional, or viscous type, damping the destabilising loop becomes progressively more stable with, for the amplitude of $\pm$ 30° illustrated, stabilising subloops appearing at the extremities of the motion. The effect of amplitude is shown in Figure 7.13. For one level of damping and one phase lag the loops are dynamically unstable for small amplitude, becoming more stable (per unit amplitude) as amplitude increases - indicating the approach to a limit cycle situation.

Figure 7.14 illsutrates the effect of datum error. This is of interest in comparison with the wind tunnel results of Section 4, indicating that certain asymmetries in the results may simply be due to comparatively small changes in flow direction.

The bubble lengths implied in these computations can be easily computed - one case is presented in Figure 7.15.

In summary, the simplified flow model seems to lead to lift, moment and bubble characteristics that follow fairly closely those obtained from experiment, in particular representing many of the static and dynamic stability and instability regions.

Extension to higher angles, and to cases involving other degrees of freedom, would seem possible and could well form part of further investigations.

The broadside on ($\psi_o = 0$) case has a flow pattern where the separated flows around the side faces do not re-attach. During oscillation the flow may re-attach, the variation in angle for re-attachment being very dependent on amplitude and frequency parameter (see Sections 4 and 5). It seems probable that a simplified flow pattern could be postulated that would lead to a mathematical model for this case as well, and again this could form a part of further investigations.

Such mathematical models would seem the most compact and meaningful way by which the very non-linear characteristics of the container model can be represented for use in analysis of container motion.

8. CONCLUSIONS AND SUGGESTIONS FOR FURTHER RESEARCH

The most important results stemming from this investigation are those presented in Section 4, i.e. results from pressure measurements in wind tunnels. Results from several other related investigations have been presented in Section 2 (Free Oscillation Tests), Section 5 (Flow Visualization Studies), Section 6 (Free Vibration Tests) and Section 7 (Mathematical Models). In all cases, appropriate discussion has been included in the Section, with some cross reference. Indications are that all investigations are in broad agreement.

The extensive pressure and flow visualisation tests have revealed extreme complexity in the flow situation around bluff container shapes, relating to separated flows. These flows may or may not reattach and will usually involve strong interaction between component flows on normal stream wise faces. The dynamic tests clearly showed the pronounced lag effects at moderate to high frequency. Attempts to model the flow with simple mathematical expressions show considerable promise, and it is felt that this will be the most suitable means of representing the complex, non-linear, aerodynamic characteristics for use in future stability investigations.

With particular regard to the stability characteristics, about a central minor axis, of a 1:0.4:0.4 cargo container, the following conclusions may be drawn:-

1. The container exhibits yaw static stability over a small angle range from major axis in stream direction and over a large angle range from major axis across stream direction for a 'clean' flow.

2. A small amount of yaw removes the 'in stream direction' stability.

3. Turbulence in the free stream can also remove the stability.

4. The container is dynamically unstable at virtually all orientations, although with major axis across the stream the resulting motion is in the form of a limit cycle.

5. The static stability characteristics are closely associated with the size of the separated regions, and the dynamic stability characteristics with the growth and decay of these regions.

6. Minor changes in flow appear to give rise to large changes in stability characteristics.

These conclusions relate to motion in pure yaw and the comments regarding static stability need to be modified in those cases where the axis of yaw rotation is not central to the container (as, for example, on twin strop suspensions).

While only one shape has been investigated in detail, the overriding impression is that any bluff shape which generates large separated flows will almost certainly exhibit similar troublesome characteristics at many attitudes. Because of the diversity of cargo shapes and of the lack of knowledge of aerodynamic actions, it is very unlikely that an assessment can be made, a priori, of the stability for a particular cargo. The best that can be done is, probably, to acquire experience of aerodynamic characteristics of bluff shapes so that maximum magnitudes of destabilising actions may be assessed.

An obvious suggestion for further research is the extension of the joint integrated-pressure/flow visualization techniques developed herein to other bluff shapes in order to assess the stability implications of changes in shape of underslung cargo loads. However, with the vast improvement in methods of direct force transduction over the past five years, an investigation into the possibility of direct dynamic force measurement as an alternative to the techniques used herein, might be undertaken. The above techniques might also be extended to investigate such related items as problems arising from flows around helicopter fuselages or, in an entirely different field, those stemming from unsteady flows over pitching aircraft carrier decks.

Problems involving appreciable aerodynamic hysteresis effects have been shown to abound on the simple container shapes studied herein, and it is felt that more effort should be expended in the investigation of the many aspects of what might be termed 'dynamic stall'. These studies have also highlighted the extremely complex structure of wakes behind simple bluff shapes and this could well be the subject of a research study in its own right. These are areas where there are very few academic guidelines.

Finally, the decaying oscillation technique used herein should be developed since it provides a method by which rapid assessments of overall stability may be made. This method is ideally suited to the problem of assessing the stability, in a single degree of freedom, of complex shapes, e.g. vehicles.

REFERENCES

1. BOLOTIN, V.V. "The dynamic stability of elastic systems" Holden-Day, San Francisco, 1964.

2. SHELDON, D.F. "A study of the stability of a plate-like load towed beneath a helicopter" Ph.D. Thesis, University of Bristol, Faculty of Engineering, June 1968.

3. KISIELOWSKI, E. et al. "Design optimisation study of the active arm external load stabilization system for helicopters" USAAMRDL Tech. Rep. 74, February 1974.

4. LIU, D.T. "In-flight stabilization of externally slung helicopter loads" USAAMRDL Tech. Report 73-5. Contract DAAJ02 - 70-C-0067, May 1973.

5. POLI, C. & CROMACK, D. "Dynamics of towed bodies using a single point suspension system" AIAA Paper No: 72-486.

6. REID, W.P. "Stability of a towed object" SIAM J. APPl. Math. Vol 15(1), Jan 1967, pp.1-12.

7. PINSKER, W.J.G. "A form of lateral instability of lifting free flight models towed by a helicopter" ARC R & M 3641, H.M.S.O. 1970.

8. LAUB, G.H. & KODANI, H.M. "Wind tunnel investigation of aerodynamic characteristics of scale models of three rectangular-shaped cargo containers" NASA TMX-62, 169 July 1972.

9. FLOWER, J.W. & SIMPSON, A. "Free stream turbulence on the aerodynamic characteristics of underslung bodies" University of Bristol Report No: SF/US/1, Contract No: DAJA 37-72-C-0447, 1974.

10. LEECH, C.M. & CHAN, D.C. "Finite difference solutions of compressible viscous fluid flow around pitching bluff bodies" Univ. of Bristol, Report No: SF/US/2, Contract No: DAJA 37-72-C-0447, 1974.

APPENDIX 1

DERIVATION OF AERODYNAMIC FORCES AND MOMENTS FROM THE MODELS

The pressure distributions obtained from the oscillatory models (Section 3) were used to obtain overall aerodynamic forces. Such forces were derived using areas and moment arms ascribed to each pressure point. These areas and moment arms are given in this Appendix, together with details of the integration process.

The pressure distributions derived in Section 3 were expressed as discrete voltages associated with a time from the being of the signal. The pressure at a typical point k may be taken as P_{kj} where j runs from 1 to some value (see Appendix 3) to give a number of discrete values to pressure throughout the oscillation. If A_k is the area associated with point k, then $A_k P_{kj}$ is a force associated with point k. For any one face of the model the elemental forces can be summed for the points on that face to give discrete values to the total force throughout the oscillation.

$$\{F_j\} = \left\{ \sum_{k=1}^{k=N} A_k P_{kj} \right\}$$

Small Model

With the small model the pressure points were not always at the centre of the area associated with them and weighting factors (W_k) were therefore associated with them, making the force associated with the point $W_k A_k P_{kj}$.

Each face only contributes to force in a direction normal to the face, or in general the force could be multiplied by direction cosines (always zero or $\pm$ unity) to give the contribution in any direction. The total force vector is therefore

$$\left[\{F_{j\phi}\}\right] = \left[\left\{ \sum_{k=1}^{k=N_{PTS}} L_{\phi k} W_k A_k P_{kj} \right\}\right]$$

where $L_{\phi k}$ is the vector of direction cosines for point k appropriate to the x and y directions, and F is a matrix having two components (ϕ = x and y in turn) for each value of j, corresponding to different times during the motion.

The aerodynamic moments are obtained in similar fashion, where the elemental forces are multiplied by an appropriate moment arm, equal to the distance of the centre of the element from each axis, (N_k).

The resulting moments can be expressed as a matrix having three components for each time during the motion.

$$\left[\left\{M_{\phi j}\right\}\right] = \left[\left\{\sum_{k=1}^{k=N_{PTS}} L_{\phi k}\ W_k\ A_k\ N_k\ P_{kj}\right\}\right]$$

Values of $L_{\phi k}$, $W_k A_k$ and N_k for the small model are given in Table III.

Large Model

The procedure for the large model is similar to that for the small, but without the weighting factors W_k, and allowing for all three directions (i.e. ϕ = x, y and z).

Expressed in coefficient form

$$\left[\left\{C_{\phi j}\right\}\right] = \left[\left\{\frac{1}{qA_\phi} \sum_{k=1}^{k=N_{PTS}} L_{\phi k}\ A_k\ P_{kj}\right\}\right]$$

where $q = \frac{1}{2}\rho V^2$, and A_ϕ is the appropriate reference area for the ϕ direction.

Similarly, the moment coefficients are expressed as

$$\left[\left\{C_{m_{\phi j}}\right\}\right] = \frac{1}{q\bar{V}}\left[\left\{\sum_{k=1}^{k=N_{PTS}} L_{\phi k}\ A_k\ N_{\phi k}\ P_{kj}\right\}\right]$$

where $\bar{V}$ is the volume of the model.

Values of $L_{\phi k}$, A_k and $N_{\phi k}$ for the large model are given in Table III.

APPENDIX 2

ANALYSIS OF THE OSCILLATORY MECHANISM FOR THE MODELS

In Section 3.1.2 it was stated that a mechanism was used to prescribe the motions of the 1:0.4:0.4 model. The mechanism consisted of a constant speed motor with a link arm connected via a rotor arm in such a way as to impart rotary motion about the z axis of the model. This mechanism is easily analysed and the analysis is given in Figure A2.1. A comparison of the theoretical and experimental position traces using equation 1 in Figure A2.2 shows good agreement.

APPENDIX 3

AVERAGING PROCEDURE FOR PRESSURE SIGNALS

In Section 3 a procedure was mentioned which averaged the unsteady pressure signals. This was necessary in order to ensure that the final digitised signals were sufficiently representative of the actual surface pressures. The basis of the procedure was an algorithm in which three basic parameters could be chosen to average the unsteady signals and hence optimise the integrity of the overall pressure distribution. These parameters were the number of signals N_{SIGS}, the number of sample values N_{SAM} (or ordinates) and the number IS of values spread between consecutive ordinates (i.e. between sample values). These parameters are shown in Figure A3.1.

The discrete values of the digitised voltage are represented by S_j. The parameter j also represents time along the abscissa and is indicative of the signal time depending upon the rate at which the signal is being scanned by the A.D.C. The spread values between ordinates are numerically averaged to give each S_j value.

The algorithm which carries out this process may be expressed as

$$\left[S_j \right]_{j=1,N_{SAM}} = \left[\sum_{i=1}^{i=N_{SIGS}} \sum_{k=1}^{k=IS} \frac{B_{kij}}{(N_{SIGS}.IS)} \right]_{j=1,N_{SAM}}$$

where B_{kij} is the discrete value of signal obtained at spread point k, for the sample point j, on signal trace i, (where IS spread values and N_{SIGS} signal traces have been used to produce each sample value S_j). In the case of the small model four signal traces were chosen as the optimum ($N_{SIGS} = 4$), with 10 spread values for 31 sample values in 1.5 seconds of signal trace.

APPENDIX 4

PROGRAMME FOR EVALUATION OF DERIVATIVES

The data available are values of θ and M over p time intervals, say, spanning a period of excitation; viz:-

t_o	t_1	t_2	.	.	.	.	t_p
θ_o	θ_1	θ_2	.	.	.	.	θ_p
M_o	M_1	M_2	.	.	.	.	M_p

where $t_p - t_o = \frac{2\pi}{\omega}$ = excitation period = T seconds.

If it is assumed that

$$\theta = a\cos\omega t + b\sin\omega t$$

$$M = A_o + \sum_{j=1}^{s} A_j \cos j\omega t + B_j \sin j\omega t$$

then, by Fourier Series theory,

$$a = \int_o^T \frac{\omega}{\pi} \theta(t) \cos\omega t dt ,$$

$$b = \int_o^T \frac{\omega}{\pi} \theta(t) \sin\omega t dt ,$$

$$A_o = \int_o^T \frac{\omega}{2\pi} M(t)\, dt ,$$

$$A_j = \int_o^T \frac{\omega}{\pi} M(t) \cos j\omega t dt ,$$

and

$$B_j = \int_o^T \frac{\omega}{\pi} M(t) \sin j\omega t dt .$$

As the time intervals, dt = T/p, are equal, Simpson's rule can be used to effect the above quadratures. If the vectors

$$\underset{\sim}{\theta} = \{\theta_0, \ldots, \theta_p\} \quad , \quad \underset{\sim}{M} = \{M_0, \ldots, M_p\}$$

$$\underset{\sim}{c}_j = \{\cos j\omega t_0, \ldots, \cos j\omega t_p\} \quad , \quad \underset{\sim}{s}_j = \{\sin j\omega t_0, \ldots, \sin j\omega t_p\}$$

are defined along with the weighting matrix

$$\underset{\sim}{W} = \text{Diag}\,[1, 4, 2, 4, 2, 4, \ldots, 1] \quad \text{(Simpson's rule)},$$

then

$$a = \frac{2}{3p}\ \underset{\sim}{\theta}^T\ \underset{\sim}{W}\ \underset{\sim}{c}_1 \ ,$$

$$b = \frac{2}{3p}\ \underset{\sim}{\theta}^T\ \underset{\sim}{W}\ \underset{\sim}{s}_1 \ ,$$

$$A_j = \frac{2}{3p}\ \underset{\sim}{M}^T\ \underset{\sim}{W}\ \underset{\sim}{c}_j \ , \quad j \neq 0$$

$$B_j = \frac{2}{3p}\ \underset{\sim}{M}^T\ \underset{\sim}{W}\ \underset{\sim}{s}_j \ , \quad j \neq 0$$

and

$$A_0 = \frac{1}{3p}\ \underset{\sim}{M}^T\ \underset{\sim}{W}\ \underset{\sim}{1} \ ,$$

where

$$\underset{\sim}{1} = \{1, 1, \ldots, 1\} \qquad \text{(order p + 1 x 1)}.$$

When assessing derivatives, one only has to consider the harmonic components of excitation and response. Hence, we shall be concerned only with the coefficients a, b, A_1, B_1 - taking careful note of the other A_j, B_j since these measure the departure from linear behaviour. From the definitions of ΔC_m and θ we have $\Delta C_m = (a\cos\omega t + b\sin\omega t)C_{m\alpha} + \omega(-a\sin\omega t + b\cos\omega t)C_{m\dot{\alpha}}$

$$\equiv \frac{A_1}{qSd}\cos\omega t + \frac{B_1}{qSd}\sin\omega t \ ,$$

whence, on comparing coefficients

$$C_{m\alpha} = \frac{aA_1 + bB_1}{qSd(a^2+b^2)}$$

$$C_{m\dot{\alpha}} = \frac{bA_1 - aB_1}{qSd\omega(a^2+b^2)}$$

This gives a rapid and systematic means for evaluating the derivatives from the traces or, rather, from the raw force data. The cross derivatives may be determined similarly by replacing A_1 and B_1 by the appropriate harmonic terms in the Fourier Series for the various forces.

Thus, if $F_x = E_o + \sum E_j \cos\omega jt + F_j \sin\omega jt$,

then $$C_{x\alpha} = \frac{aE_1 + bF_1}{qS(a^2 + b^2)}$$

and $$C_{x\dot{\alpha}} = \frac{bE_1 - aF_1}{qS\omega(a^2 + b^2)}$$

where $$E_j = \frac{2}{3p} \underset{\sim}{F}_x^T \underset{\sim}{W} \underset{\sim}{c}_j ,$$

$$F_j = \frac{2}{3p} \underset{\sim}{F}_x^T \underset{\sim}{W} \underset{\sim}{s}_j$$

and $$\underset{\sim}{F}_x \equiv \{F_{xo}, F_{x1}, \cdots, F_{xp}\} .$$

For convenience in computation, it is sometimes better to evaluate the dimensional derivatives

$$M_\alpha = qSd\, C_{m\alpha}, \quad F_{x\alpha} = q\, S\, C_{F_{x\alpha}}$$

TABLE I

SCOPE OF TESTS ON 1:0.4:0.4 CONTAINER TO DATE (18.12.75)

ψ_o (deg)	θ_o (deg)	w_d	$\lvert d\psi \rvert$ (deg)	$\lvert dx \rvert$ (in)	$\lvert dy \rvert$ (in)	$\lvert d\phi \rvert$ (deg)	P	F	L	D
90	0	.14	21.5				X	X	X	
90	0	.12	21.5				X✓	X✓	X✓	
90	0	.10	21.5				X	X	X	
45	0	.12	21.5				X	X	X	
45	0	.12	21.5				X✓	X✓	X✓	
45	0	.10	21.5				X	X	X	
0	0	.14	21.5				X	X	X	
0	0	.12	21.5				X✓	X✓	X✓	
0	0	.10	21.5				X	X	X	
90	0	.32	10				X✓	X✓	X✓	
90	0	.36	10				X✓	X✓	X✓	
90	0	.45	10				X✓	X✓	X✓	
90	0	.48	13.5				X	X	X✓	
90	0	.72	13.5				X	X	X✓	
90	0	.96	13.5				X	X	X✓	
90	0	.842	5.5					X	X✓	X✓
90	0	.56	5.5					X	X✓	X✓
90	0	.42	5.5					X	X✓	X✓
90	0	.37	5.5					X	X✓	X✓
90	5	.84	5.5					X✓	X✓	X✓
90	5	.540	5.5					X✓	X✓	X✓
90	5	.39	5.5					X✓	X✓	X✓
90	5	.34	5.5					X✓	X✓	X✓
90	-5	.841	5.5					X	X✓	X✓
90	-5	.56	5.5					X	X✓	X✓
90	-5	.42	5.5					X	X✓	X✓
90	-5	.37	5.5					X	X✓	X✓
90	0	1.02	10	Turbulence				X	X✓	X✓
90	0	.84		2.5				X✓	X✓	X✓
90	0	.56		2.5				X✓	X✓	X✓

Continued ....

TABLE I (Continued)

ψ_o (deg)	θ_o (deg)	w_d	$\lvert d\psi \rvert$ (deg)	$\lvert dx \rvert$ (in)	$\lvert dy \rvert$ (in)	$\lvert d\phi \rvert$ (deg)	P	F	L	D
90	0	.44		2.5				X✓	X✓	X✓
90	0	.32		2.5				X✓	X✓	X✓
90	5	.88		2.5				X✓	X✓	X✓
90	5	.56		2.5				X✓	X✓	X✓
90	5	.42		2.5				X✓	X✓	X✓
90	5	.34		2.5				X✓	X✓	X✓
90	0	1.02	3.5	1.9				X✓	X✓	X✓
90	0	.68	3.5	1.9				X	X	X✓
90	0	.48	3.5	1.9				X✓	X✓	X✓
90	0	.39	3.5	1.9				X	X	X✓
90	-5	.97	3.5	1.9				X	X✓	X✓
90	-5	.65	3.5	1.9				X	X	X✓
90	-5	.48	3.5	1.9				X	X	X✓
90	-5	.39	3.5	1.9				X	X✓	X✓
90	0	1.02		1.9		11		X✓	X✓	X✓
90	0	.65		1.9		11		X	X	X✓
90	0	.51		1.9		11		X	X	X✓
90	0	.41		1.9		11		X✓	X✓	X✓
90	0	.74			3.54			X	X✓	X✓
90	0	.50			3.54			X	X	X✓
90	0	.37			3.54			X	X	X✓
90	0	.34			3.54			X	X✓	X✓
95	0	.74			3.52			X	X	X✓
95	0	.50			-3.52			X	X	X✓
95	0	.40			3.52			X	X	X✓
90	0	.11	29.5				X✓	X✓	X✓	
90	0	.10	29.5				X✓	X✓	X✓	
90	0	.08	29.5				X✓	X✓	X✓	
80	0	.321	10					X	X✓	X✓
80	0	.455	10					X	X✓	X✓

Continued ....

TABLE I (Continued)

ψ_o (deg)	θ_o (deg)	w_d	$\lvert d\psi \rvert$ (deg)	$\lvert d\theta \rvert$ (deg)	$\lvert dy \rvert$ (in)	$\lvert d\phi \rvert$ (deg)	P	F	L	D
90	0	0.15	11.5					X	X	X✓
90	0	0.18	11.5					X	X	X✓
90	0	0.23	11.5					X	X	X✓
90	0	0.34	11.5					X	X	X✓
90	0	0.36	11.5					X	X	X✓
90	0	0.44	11.5					X	X	X✓
90	0	0.65	11.5					X	X	X✓
90	0	1.08	11.5					X	X	X✓
90	-90	0.28		10°				X✓	X✓	X✓
90	-90	0.38		10°				X✓	X✓	X✓
90	-90	0.42		10°				X✓	X✓	X✓
90	-90	0.51		10°			X✓	X✓	X✓	X✓
90	-90	0.53		10°				X✓	X✓	X✓
90	-90	0.69		10°			X✓	X✓	X✓	X✓
90	-90	0.72		10°				X✓	X✓	X✓
90	-90	1.08		10°			X✓	X✓	X✓	X✓

GLOSSARY FOR TABLE I

X	indicates that pitching moments only are evaluated.
X	indicates evaluation of all components of force.
P	indicates pressure distribution study.
F	indicates integrated force evaluation.
L	indicates loop diagram plot.
D	indicates derivatives obtained.
✓	indicates that the particular case is discussed in this Report.

TABLE II

AERODYNAMIC DERIVATIVES FOR 1:0.4:0.4 CONTAINER

(i) $\psi_o = 90^\circ$, $-\theta_o = 90^\circ$, $d\theta = \pm 10^\circ$

W_d	.2809	.3795	4176	.5121	.5259	.6938	.7169	1.0754
$C_{x\theta}$	.0674	.0186	-.1294	-.0666	-.1652	-.0318	.2352	.1009
$C_{y\theta}$	.7435	.3634	-.1843	-.0861	-.7925	-2.9043	-3.4900	-3.0443
$C_{z\theta}$	.0037	.1245	-.0166	-.2061	-.0923	-.1708	-.3557	-.6973
$C_{mx\theta}$	-.6279	-.5651	-.3906	-.2083	-.2090	.2501	.2972	-.7786
$C_{my\theta}$	-.0469	-.0521	.0905	-.0159	.0867	-.0278	.0043	.0294
$C_{mz\theta}$	.0485	.0850	.1509	.1459	.1347	.0485	.0753	-.0840
$C_{x\dot{\theta}}$	-.1831	.1320	-.1860	-.2886	.3391	.3512	-.0881	-.0904
$C_{y\dot{\theta}}$	-3.1131	-3.6412	-3.2447	-3.3970	-3.3400	-1.8473	-.8090	2.5476
$C_{z\dot{\theta}}$	.0155	-.1710	.0360	-.2608	.1136	-.0196	-.0635	.4850
$C_{mx\dot{\theta}}$	.7467	.7864	.7716	.6504	.8277	.1132	-.9130	-1.3648
$C_{my\dot{\theta}}$	.0043	.0289	.0813	.0401	.0678	.020	-.1072	.0442
$C_{mz\dot{\theta}}$	.2148	-.0575	-.0314	-.1128	-.0513	-.1178	.0362	-.0637

(ii) $\psi_o = +90^\circ$, $\theta_o = 0^\circ$, $d\psi = \pm 5.5^\circ$

W_d	.3740	.4208	.5611	.8416
$C_{x\psi}$	-.9406	-.9172	-.9994	-.6074
$C_{y\psi}$	-.1126	-.1059	-.2317	-.3408
$C_{z\psi}$	.1446	-.0152	.0477	.0269
$C_{mx\psi}$	.0491	-.0574	-.0543	-.0986
$C_{my\psi}$	-.0117	.0164	.0363	.0194
$C_{mz\psi}$	-.1780	-.0126	.1751	.3039
$C_{x\dot{\psi}}$	1.0182	1.4277	.5705	.3179
$C_{y\dot{\psi}}$	-.4202	-.2039	-.0606	-.1226
$C_{z\dot{\psi}}$	.1326	.0439	.1111	-.0207
$C_{mx\dot{\psi}}$	-.1338	.0522	-.0223	-.0317
$C_{my\dot{\psi}}$	-.0876	.0512	.0235	-.0162
$C_{mz\dot{\psi}}$	1.2346	.8605	.7822	.3462

TABLE II (CONTINUED)

(iii) $\psi_o = +90^\circ$, $\theta_o = +5^\circ$, $d\psi = \pm 5.5^\circ$

W_d	.3441	.3871	.5377	.8416
$C_{x\psi}$	-1.2937	-1.3096	-1.2558	-.9905
$C_{y\psi}$	-.1839	-.1234	.1052	-.2551
$C_{z\psi}$	-.0386	-.0556	-.2263	.1552
$C_{mx\psi}$	-.0169	-.0439	-.0868	.0348
$C_{my\psi}$	-.2182	-.1695	-.1854	-.1820
$C_{mz\psi}$	-.0133	.0452	.2302	.4008
$C_{x\dot{\psi}}$	1.2686	.7818	.6500	-.1182
$C_{y\dot{\psi}}$	-.3639	-.3016	-.2296	-.1765
$C_{z\dot{\psi}}$	.1804	-.0051	-.0016	.1144
$C_{mx\dot{\psi}}$	.0965	.1125	.1744	.0517
$C_{my\dot{\psi}}$	.2656	.2482	.2175	.0228
$C_{mz\dot{\psi}}$	.8076	.6459	.5439	.2843

(iv) $\psi_o = +90^\circ$, $\theta_o = -5^\circ$, $d\psi = \pm 5^\circ$

W_d	.3740	.4208	.5611	.8416
$C_{x\psi}$	-1.1179	-1.4019	-1.0957	-.7820
$C_{y\psi}$	-.2521	-.2178	-.2113	-.3602
$C_{z\psi}$	.0452	.0041	-.0566	-.0626
$C_{mx\psi}$	.0034	-.0797	-.0977	-.0893
$C_{my\psi}$	.160	.2035	.1685	.1494
$C_{mz\psi}$	.1013	.2607	.1730	.2361
$C_{x\dot{\psi}}$	1.2868	.9479	.7683	.2000
$C_{y\dot{\psi}}$	-.2799	-.2644	-.1884	-.0074
$C_{z\dot{\psi}}$	-.0022	-.0868	-.2180	-.0168
$C_{mx\dot{\psi}}$	-.3292	-.0651	-.2558	-.0490
$C_{my\dot{\psi}}$	-.2893	-.2435	-.1714	-.1306
$C_{mz\dot{\psi}}$	.6713	.7970	.4904	.2193

TABLE II (CONTINUED)

(v) $\psi_o = +90°$, $\theta_o = 0°$, $d\psi = \pm 9°$

10% Free Stream Turbulence

$\bar{W}_d$	.4075	1.0188
$C_{x\psi}$	-1.1053	-.3065
$C_{y\psi}$	-.1481	-.0090
$C_{z\psi}$	-.0328	.0267
$C_{mx\psi}$	-.0626	.0044
$C_{my\psi}$	.0475	.0029
$C_{mz\psi}$	.0661	.1479
$C_{x\dot{\psi}}$	1.4234	.0634
$C_{y\dot{\psi}}$	-.2407	-.1019
$C_{z\dot{\psi}}$	-.0010	-.0076
$C_{mx\dot{\psi}}$	.0217	-.0134
$C_{my\dot{\psi}}$	-.0309	.0117
$C_{mz\dot{\psi}}$	1.0973	-.1894

(vi) $\psi_o = 95°$, $\theta_o = 0°$, $dy = 3.52"$

W_d	.4033	.4963	.7445
C_{xy}	-.0568	-.0428	.0086
C_{yy}	.1481	.7588	1.2154
C_{zy}	-.0147	.0664	-.0428
C_{mxy}	.0175	.0544	.0038
C_{myy}	.0296	.0190	-.0062
C_{mzy}	.0115	-.0412	-.0428
$C_{x\dot{y}}$	.0941	-.5208	-.2039
$C_{y\dot{y}}$	-2.5058	-2.7113	-2.4787
$C_{z\dot{y}}$	-.0642	-.0648	.0277
$C_{mx\dot{y}}$	-.0847	.0528	-.0192
$C_{my\dot{y}}$	-.0351	-.0091	.0705
$C_{mz\dot{y}}$	-.1358	.1310	.0031

TABLE II (CONTINUED)

(vii) $\psi_o = +90^\circ$, $\theta_o = 0^\circ$, dy = 3.54"

W_d	.3366	.3722	.4963	.7445
C_{xy}	-.0454	.0346	.0223	.0203
C_{yy}	.1618	.1225	.7549	1.9647
C_{zy}	.0369	.0057	.0218	-.0022
C_{mxy}	.0035	-.0131	-.0605	.0348
C_{myy}	.0076	.0250	-.0082	-.0596
C_{mzy}	.0235	-.0024	.0064	.1053
$C_{x\dot{y}}$	.1772	-.0926	.2001	.0350
$C_{y\dot{y}}$	-2.2980	-2.1171	-2.2190	-2.6653
$C_{z\dot{y}}$	-.1002	-.1121	-.0883	-.0061
$C_{mx\dot{y}}$	-.0488	.0603	-.0318	-.0086
$C_{my\dot{y}}$	-.0670	.0355	-.0148	-.0236
$C_{mz\dot{y}}$	-.057	.1297	.0047	.0074

(viii) $\psi_o = +90^\circ$, $\theta_o = 0^\circ$, $d\psi = \pm 11.5^\circ$

W_d	.1509	.1783	.2268	.3441	.3562	.4424	.6452	1.07547
$C_{x\psi}$	-1.2419	-1.1723	-1.1589	-1.1779	-1.0738	-1.1085	-.9651	-.7853
$C_{y\psi}$	-.0427	.1595	-.0373	-.0622	.0478	-.0180	-.0065	.0068
$C_{z\psi}$	-.0144	-.0222	-.0063	.0484	-.0206	-.0018	-.0429	.0241
$C_{mx\psi}$	-.0223	-.0244	-.0349	.0240	-.0566	-.0092	-.0547	-.0388
$C_{my\psi}$	.0001	.0124	.0200	-.0052	.0164	-.0146	.0089	.0119
$C_{mz\psi}$	-.2040	-.1820	-.2201	-.0268	-.0944	-.0363	.1235	.3792
$C_{x\dot{\psi}}$	1.3986	1.1802	-.5212	1.0679	.4967	.2130	.4086	-.0827
$C_{y\dot{\psi}}$	-.2799	-.2294	.1190	-.0607	.0098	-.1730	-.1602	-.0283
$C_{z\dot{\psi}}$	.2884	-.1229	.2333	-.0123	-.0451	.0920	.0309	.0760
$C_{mx\dot{\psi}}$	.0632	-.0385	.0905	-.1060	-.0751	-.0454	.0551	.0289
$C_{my\dot{\psi}}$	.0228	.0674	-.1137	-.0029	.0074	.0376	.0090	.0244
$C_{mz\dot{\psi}}$	.8226	.7066	.7281	.7240	.6973	.7042	.3765	.1958

TABLE II (CONTINUED)

(ix) $\psi_o = +90^\circ$, $\theta_o = 5^\circ$, $d\psi = +3.5^\circ$, $dx = 1.91"$

W_d	(a)	.3871	(b)	.4839	(c)	.6452	(d)	.9679
C_{xx}	.9052	-1.1668	.9063	-1.1682	1.1415	-1.4714	2.0945	-2.6998
C_{yx}	.1060	-.1367	-.0623	.0803	.1043	-.1344	.2214	-.2854
C_{zx}	.0847	-.1092	.0867	-.1118	.0708	-.0913	.0073	-.0094
C_{mxx}	-.0006	.0007	.006	.0080	-.0107	.0138	-.0702	.0904
C_{myx}	.0774	-.0998	.1210	-.1560	-.0401	.0517	.0943	-.1216
C_{mzx}	-.3400	.4383	-.5249	.6767	-.7132	.9193	-1.2750	1.6434
$C_{x\dot{x}}$	-2.7616	3.5597	-2.8239	3.6400	-2.5125	3.2386	-2.6554	3.4228
$C_{y\dot{x}}$	.8985	-1.1581	.7009	-.9034	.4721	-.6086	.1344	-.1733
$C_{z\dot{x}}$	-.1295	.1670	-.1102	.1420	-.1628	.2098	.0362	-.0466
$C_{mx\dot{x}}$	-.3006	.3875	-.1390	.1792	-.2129	.2744	-.1398	.1802
$C_{my\dot{x}}$	-.3097	.3992	-.3267	.4212	-.3280	.4228	-.2711	.3495
$C_{mz\dot{x}}$	-.7974 x	1.0279 x x	-.3016 x	.3887 xx	.0099 x	-.0128 xx	.9035 x	-1.1647 xx

(x) $\psi_o = +90^\circ$, $\theta_o = 5^\circ$, $dx = 2.5"$

W_d	.3366	.4208	.5611	.8799
C_{xx}	-.0655	-.1826	.1436	1.0162
C_{yx}	.4183	.3462	.3467	.0195
C_{zx}	-.1373	-.1249	-.1717	-.0417
C_{mxx}	-.1079	-.0239	-.0079	-.1576
C_{myx}	-.0925	-.0730	-.1596	-.1350
C_{mzx}	-.201	-.1854	-.5155	-.6912
$C_{x\dot{x}}$	-1.9002	-2.0094	-2.0354	-2.0159
$C_{y\dot{x}}$	.2674	.3487	.2798	.3526
$C_{z\dot{x}}$	-.1807	-.3212	.1658	-.0150
$C_{mx\dot{x}}$	-.2073	-.1136	-.0576	-.2260
$C_{my\dot{x}}$	-.3224	-.0766	-.2171	-.1793
$C_{mz\dot{x}}$	.1365	.2554	.3363	.4940

TABLE II (CONTINUED)

(xi) $\psi_o = +90^\circ$, $\theta_o = 0^\circ$, $d\psi = 3.5^\circ$, $dx = 1.91"$

W_d		.3871		.4839		.6792		1.0188
$C_{x\beta}$	.7434	-.9662	.7508	-.9758	.7455	-.9689	1.5346	-1.9946
$C_{y\beta}$	.0715	-.0930	.1651	-.2146	.4576	-.5948	.9155	-1.1899
$C_{z\beta}$	.1266	-.1646	-.0584	.0759	.1264	-.1643	.0082	-.0107
$C_{mx\beta}$	.0971	-.1263	.1010	-.1313	.0937	-.1218	.1161	-.1509
$C_{my\beta}$	.0290	-.0377	.0058	-.0075	.0212	-.0275	-.0776	.1008
$C_{mz\beta}$	-.2601	.3380	-.1824	.6270	-.8160	1.0606	-1.2475	1.6214
$C_{x\dot{\beta}}$	-2.8679	3.7276	-2.7949	3.6327	-2.0041	2.6048	-2.4565	3.1928
$C_{y\dot{\beta}}$	1.1268	-1.4645	.8764	-1.1391	.1523	-.1979	.2475	-.3217
$C_{z\dot{\beta}}$	.2648	-.3442	.0922	-.1198	-.2548	.3312	-.0596	.0774
$C_{mx\dot{\beta}}$	.2505	-.3256	.0449	-.0583	-.3635	.4724	-.1540	.2001
$C_{my\dot{\beta}}$	.0239	-.0311	.0616	-.0801	.2584	-.3358	.0204	-.0266
$C_{mz\dot{\beta}}$	-.6027	.7833	-.3466	.4505	-.2185	.2840	.5825	-.7572
	*	**	*	**	*	**	*	**

* $\beta \equiv x$ ** $\beta \equiv \psi$

(xii) $\psi_o = 0^\circ$, $\theta_o = 0^\circ$, $dx = 2.5"$

W_d	.3226	.4399	.5611	.8416
C_{xx}	-.0517	-.0546	.2216	.7453
C_{yx}	.0366	.0574	.4061	.2536
C_{zx}	-.0398	.0359	-.0648	-.0048
C_{mxx}	.0654	.0703	-.0107	.0572
C_{mzx}	-.2111	-.2857	-.4517	-.6724
$C_{x\dot{x}}$	-1.4712	-1.8878	-1.5481	-2.1660
$C_{y\dot{x}}$	.2438	.1144	.0190	.2721
$C_{z\dot{x}}$	.0329	.0837	.1248	-.0522
$C_{mx\dot{x}}$	.0648	-.1418	-.0155	-.1859
$C_{my\dot{x}}$	.1320	.0623	.1030	.0032
$C_{mz\dot{x}}$	-.3940	-.0714	.1081	.6601

TABLE II (CONTINUED)

(xiii) $\psi_o = 90°$, $\theta_o = 0°$, $dx = 1.9"$, $d\phi = 10° - 40'$

W_d	(a)	.4075	(b)	.5094	(c)	.6452	(d)	1.0188
$C_{x\phi}$	-.2232	.0950	-.2173	.0925	-.2979	.1268	.7556	-.3216
$C_{y\phi}$	.7580	-.3226	.7300	-.3107	.1650	-.0702	.5008	-.2131
$C_{z\phi}$	.0469	-.0200	.1203	-.0512	-.2503	.1065	-.1445	.0615
$C_{mx\phi}$	.1123	-.0478	.0918	-.0391	.0622	-.0264	.0873	-.0371
$C_{my\phi}$	.0546	-.0232	.0307	-.0130	-.0292	.0124	.0926	-.0394
$C_{mz\phi}$	-.2267	.0965	-.2018	.0859	-.3563	.1516	-.8418	.3583
$C_{x\dot{\phi}}$	-1.9162	.8155	-1.5412	.6559	-1.8786	.7995	-2.4427	1.0396
$C_{y\dot{\phi}}$	.1665	-.0708	.0121	-.0051	-.1084	.0461	.0710	-.0302
$C_{z\dot{\phi}}$	.0409	-.0174	.1818	-.0774	-.0412	.0175	.1673	-.0712
$C_{mx\dot{\phi}}$	-.2894	.1231	.0492	-.0209	-.0914	.0389	-.0957	.0407
$C_{my\dot{\phi}}$	-.0232	.0099	.0315	-.0134	-.0613	.0261	.0362	-.0154
$C_{mz\dot{\phi}}$	.1275	-.0543	-.1641	.0698	.6002	-.2554	.9062	-.3857
	*	**	*	**	*	**	*	**

* Derivatives non-dimensionalised by displacement e.g. $dx = 1.9" \approx 0.154'$ for the value of W_d given.

** Derivatives non dimensionalised by angular displacement e.g. $d\phi = 10° - 40'$

For example the derivative $C_{x\phi}$ is -.2232 where the derivative has been non-dimensionalised by $dx = 1.9"$ and .0950 where the non-dimensional parameter is $d\phi = 10° - 40'$. This is also true of the other combined motions.

NOTES ON TABLE II

1. The derivatives with respect to a, x and y are really the <u>in-phase</u> component of the associated force coefficient and, as such, include all acceleration effects.

2. The existence of substantial C_{xx} and C_{yy} terms is indicative of acceleration effects. In general, these are seen to diminish as frequency is reduced - as expected.

TABLE III (A)

AREA AND MOMENT COEFFICIENTS AND AREA DIRECTION COSINES FOR 2'×8'×8' CONTAINER MODEL

k	$L_{\phi k}$	A_k	N_{zk}	N_{yk}
1	1	-0.106	0.8	-0.266
2	1	0.106	0.8	0.266
3	1	-0.106	0.4	-0.266
	1	0.106	0.4	-0.266
	1	-0.106	0.0	-0.266
	1	0.106	0.0	-0.266
	1	-0.106	-.4	-0.266
	1	0.106	-.4	-0.266
	1	-0.106	-.8	-0.266
	1	0.106	-.8	-0.266
	1	-0.106	0.8	0.000
	1	0.106	0.8	0.000
	1	- .106	0.4	0.000
	1	0.106	0.4	0.000
	1	-0.106	0.0	0.000
	1	0.106	0.0	0.000
	1	-0.106	-.4	0.000
	1	0.106	-.4	0.000
	1	-0.106	-.8	0.000
	1	0.106	-.8	0.000
	1	-0.106	0.8	0.266
	1	0.106	0.8	0.266
	1	-0.106	0.4	0.266
	1	0.106	0.4	0.266
	1	-0.106	0.0	0.266
	1	0.106	0.0	0.266
	1	-0.106	-.4	0.266
	1	0.106	-.4	0.266
	1	-0.106	-.8	0.266
	1	0.106	-.8	0.266
	-1	-0.071	0.266	-0.266
	-1	0.071	0.266	-0.266
	-1	-0.071	0.8	-0.266
	-1	0.071	0.0	-0.266
	-1	-0.071	-.266	-0.266
39	-1	0.071	-.266	-0.266
	-1	-0.071	0.266	0.000
	-1	0.071	0.266	0.000
	-1	-0.071	0.000	0.000

continued above

k	$L_{\phi k}$	A_k	N_{zk}	N_{yk}
40	-1	0.071	0.000	0.000
41	-1	-0.071	-.266	0.000
	-1	0.071	-.266	0.000
	-1	-0.071	0.266	0.266
	-1	0.071	0. 266	0.266
	-1	-0.071	0.000	0.266
	-1	0.071	0.000	0.266
	-1	-0.071	-.266	0.266
	-1	0.071	-.266	0.266
	0	-0.106	-.8	0.266
	0	0.106	-.8	0.266
	0	-0.106	-.4	0.266
	0	0.106	-.4	0.266
	0	-0.106	0.000	0.266
	0	0.106	0.000	0.266
	0	-0.106	0.4	0.266
	0	0.106	0.4	0.266
	0	-0.106	0.8	0.266
	0	0.106	0.8	0.266
	0	-0.106	-.8	0.000
	0	0.106	-.8	0.000
	0	-0.106	-.4	0.000
	0	0.106	-.4	0.000
	0	-0.106	0.0	0.000
	0	0.106	0.0	0.000
	0	-0.106	0.4	0.000
	0	0.106	0.4	0.000
	0	-0.106	0.8	0.000
	0	0.106	0.8	0.000
	0	-0.106	-.8	-0.266
	0	0.106	-.8	-0.266
78	0	-0.106	-.4	-0.266
	0	0.106	-.4	-0.266
	0	-0.106	0.0	-0.266
	0	0.106	0.0	-0.266
	0	-0.106	0.4	-0.266
	0	0.106	0.4	-0.266
86	0	-0.106	0.8	-0.266
	0	0.106	0.8	-0.266

TABLE III(B)

	$D_{\phi k}$	A_k	N_k
1	1	-0.04	0.4
2	1	-0.04	0.2
3	1	-0.04	0
4	1	-0.04	-0.2
5	1	-0.04	-0.4
6	1	-0.04	0.35
7	1	-0.0265	0.1
8	1	-0.0265	-0.1
9	1	-0.04	-0.35
10	1	-0.0134	0.4
11	1	-0.0134	0.2
12	1	-0.0134	0
13	1	-0.0134	-0.2
14	1	-0.0134	-0.4
15	0		
16	1	0.06	-0.35
17	1	0.04	-0.1
18	1	0.04	0.1
19	1	0.06	0.35
20	1	0.0266	-0.4
21	1	0.0266	-0.2
22	1	0.0266	0
23	1	0.0266	0.2
24	1	0.0266	0.4
25	1	0.02	-0.35
26	1	0.0135	-0.1
27	1	0.0135	0.1
28	1	0.02	0.35
29	0		
30	0		
31	-1	0.08	0
32	-1	0.02667	-0.1
33	-1	0.02667	0.1
34	-1	0.02667	0
35	-1	0.04	0.1
36	-1	-0.04	-0.1
37	-1	-0.05334	0
38	-1	-0.01333	0.1
39	-1	-0.01333	-0.1

TABLE IV

COMPUTED FLUTTER AND DIVERGENCE SPEEDS FOR 1'x0.4'x 0.4' CONTAINER SUPPORTED BY 4-STROP PARALLEL SUSPENSION ARRANGEMENT

θ°	m slug	$\bar{k}$ ft	ℓ ft	$(a+\sigma_2)c$ ft	c_1 ft	c_2 ft	$C_{N\psi}$ *	$C_{y\psi}$ *	C_D *	C_L *	C_M *	V_F † f/s	V_D f/s
12	.012	.4	2.25	1	0	0	146	273	80.5	23.4	69.1	22.5	-
"	"	.1	"	"	"	"	"	"	"	"	"	40.8	-
"	"	.4	"	"	"	"	73	"	"	"	"	22.6	-
"	"	"	"	"	"	"	146	137	"	"	"	22.6	-
"	"	"	"	"	"	"	"	273	40	"	"	39.7	-
"	"	"	"	"	"	"	"	"	80.5	50	"	23.5	-
"	"	"	"	"	"	"	"	"	"	23.4	0	19.8	-
"	"	.2	"	.6	0	.4	"	"	"	"	69.1	24.0	12.3
"	.0076	.4	"	"	"	"	"	"	"	"	"	22.0	9.8
"	.024	"	"	"	"	"	"	"	"	"	"	38.6	17.5
"	.012	"	1.5	"	"	"	"	"	"	"	"	27.7	-
"	"	"	2.25	"	"	"	73	"	"	"	"	25.5	-
"	"	"	"	"	"	"	146	137	"	"	"	30.9	16.6
"	"	"	"	"	"	"	"	273	161	"	"	17.8	-
"	"	"	"	"	"	"	"	"	80.5	50	"	29.6	12.7
"	"	"	"	"	"	"	"	"	"	23.4	0	23.9	-
"	"	"	"	.8	.1	.1	"	"	"	"	69.1	22.8	-
"	"	.1	"	"	"	"	"	"	"	"	"	29.9	-
"	.0076	.4	"	"	"	"	"	"	"	"	"	17.9	-
"	.012	"	5	"	"	"	"	"	"	"	"	23.7	-
"	"	"	10	"	"	"	"	"	"	"	"	-	11.8
"	"	"	1.5	"	"	"	"	"	"	"	"	-	22.6
"	"	"	2.25	"	"	"	73	"	"	"	"	22.2	-
"	"	"	"	"	"	"	292	"	"	"	"	25.8	-
"	"	"	"	"	"	"	-300	"	"	"	"	25.8	-
"	"	"	"	"	"	"	146	546	"	"	"	22.7	-
"	"	"	"	"	"	"	"	136	"	"	"	23.6	-
"	"	"	"	"	"	"	"	1	"	"	"	21.6	-
"	"	"	"	"	"	"	"	273	161	"	"	15.0	-
"	"	"	"	"	"	"	"	"	80.5	100	"	27.3	-
"	"	"	"	"	"	"	"	"	"	23.4	69.1	17.8	-
"	"	"	"	"	"	"	50	120	100	70	140	24.0	-
"	"	"	"	"	0	.2	146	273	80.5	23.4	69.1	23.0	-
"	"	.1	"	"	"	"	"	"	"	"	"	29.6	-
"	.0076	.4	"	"	"	"	"	"	"	"	"	18.5	-
"	.012	"	1.5	"	"	"	"	"	"	"	"	23.0	-
"	"	"	5	"	"	"	"	"	"	"	"	24.0	-
"	"	"	2.25	"	"	"	70	"	"	"	"	23.0	-
"	"	"	"	"	"	"	-70	"	"	"	"	22.0	-
"	"	"	"	"	"	"	2	"	"	"	"	22.0	-
"	"	"	"	"	"	"	146	400	"	"	"	22.7	-
"	"	"	"	"	"	"	"	137	"	"	"	23.8	-

* Nominal values from Ref. 8. These are suitably scaled in the program.

† Undamped lower critical speed.

TABLE IV CONTINUED

Θ°	m slug	$\bar{k}$ ft	ℓ ft	$(\sigma_1+\sigma_2)c$ ft	c_1 ft	c_2 ft	$C_{N\psi}$ *	$C_{y\psi}$ *	C_D *	C_L *	C_M *	V_F ≠ f/s	V_D f/s
12	.012	.4	2.25	.8	0	.2	146	273	161	234	69.1	14.7	-
"	"	"	"	"	"	"	"	"	30	"	"	-	23.8
"	"	"	"	"	"	"	"	"	80.5	50	"	24.5	-
"	"	"	"	"	"	"	"	"	"	23.4	1	19.9	-
"	"	"	"	"	"	"	"	"	"	"	200	36.6	-
"	"	"	"	"	"	"	50	300	120	80	0	16.7	-
"	"	"	"	.6	.2	.2	146	273	80.5	23.4	69.1	26.0	-
"	"	.1	"	"	"	"	"	"	"	"	"	23.5	-
"	.0076	.4	"	"	"	"	"	"	"	"	"	20.9	-
"	.012	"	1.5	"	"	"	"	"	"	"	"	26.0	-
"	"	"	6	"	"	"	"	"	"	"	"	-	11.5
13	"	"	2.25	"	"	"	"	"	"	"	"	26.8	-
12	"	"	"	"	"	"	-70	"	"	"	"	22.6	-
"	"	"	"	"	"	"	146	400	"	"	"	25.0	-
"	"	"	"	"	"	"	"	137	"	"	"	29.0	-
"	"	"	"	"	"	"	"	273	161	"	"	17.0	-
"	"	"	"	"	"	"	"	"	80.5	70	"	29.0	-
"	"	"	"	"	"	"	"	"	"	23.4	200	-	20.5
"	"	"	"	"	"	"	"	"	"	"	-100	19.2	-
8	"	"	"	1	0	0	122	238	72	18	100	26.0	-
"	"	.1	"	"	"	"	"	"	"	"	"	>41	-
"	.0076	.4	"	"	"	"	"	"	"	"	"	21.0	-
"	.012	"	6	"	"	"	"	"	"	"	"	26.0	-
"	"	"	2.25	"	"	"	-200	"	"	"	"	19.8	-
"	"	"	"	.6	.2	.2	-122	"	"	"	"	21.0	-
"	"	.1	"	"	"	"	"	"	"	"	"	>47	-
"	.0076	.4	"	"	"	"	"	"	"	"	"	16.6	-
"	.012	"	6	"	"	"	"	"	"	"	"	21.0	-
"	"	"	2.25	.5	.25	.25	"	"	"	"	"	21.4	-
"	"	.1	"	"	"	"	"	"	"	"	"	>43	-
"	.0076	.4	"	"	"	"	"	"	"	"	"	16.5	-
"	.012	"	6	"	"	"	"	"	"	"	"	21.0	-
16	"	"	2.25	.6	.2	.2	484	325	88.3	26.7	5.1	-	12.2
"	"	"	"	1	0	0	"	"	"	"	"	23.2	-

* Nominal values from Ref.8. These are suitably scaled in the program.
≠ Undamped lower critical speed.

CONTAINER STROPPING ARRANGEMENT

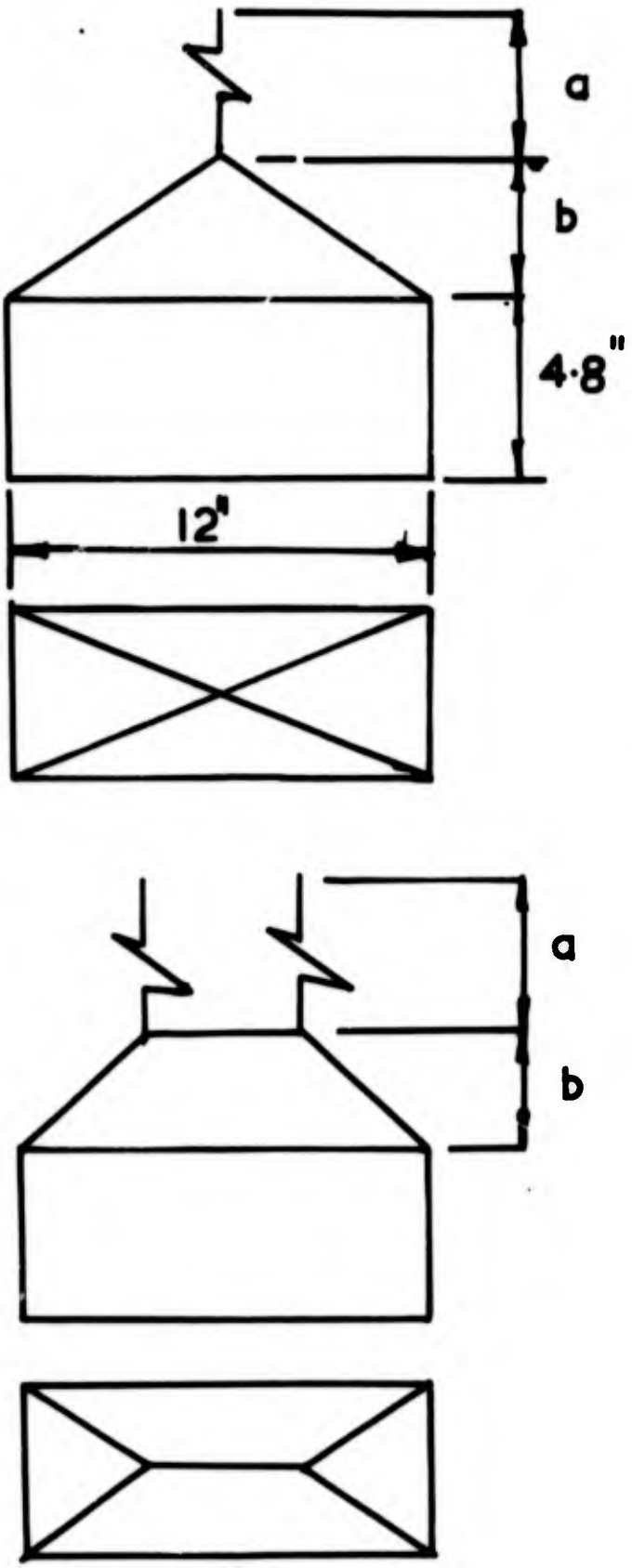

FIG 2.1

SMALL MODEL 1.0x.4x.4

CONTAINER SPECIFICATIONS

WEIGHT 1·09 LB a =3·6" b =1·4" (Δ)

WEIGHT 1·57 LB a =3·6" b =1·4" (o)

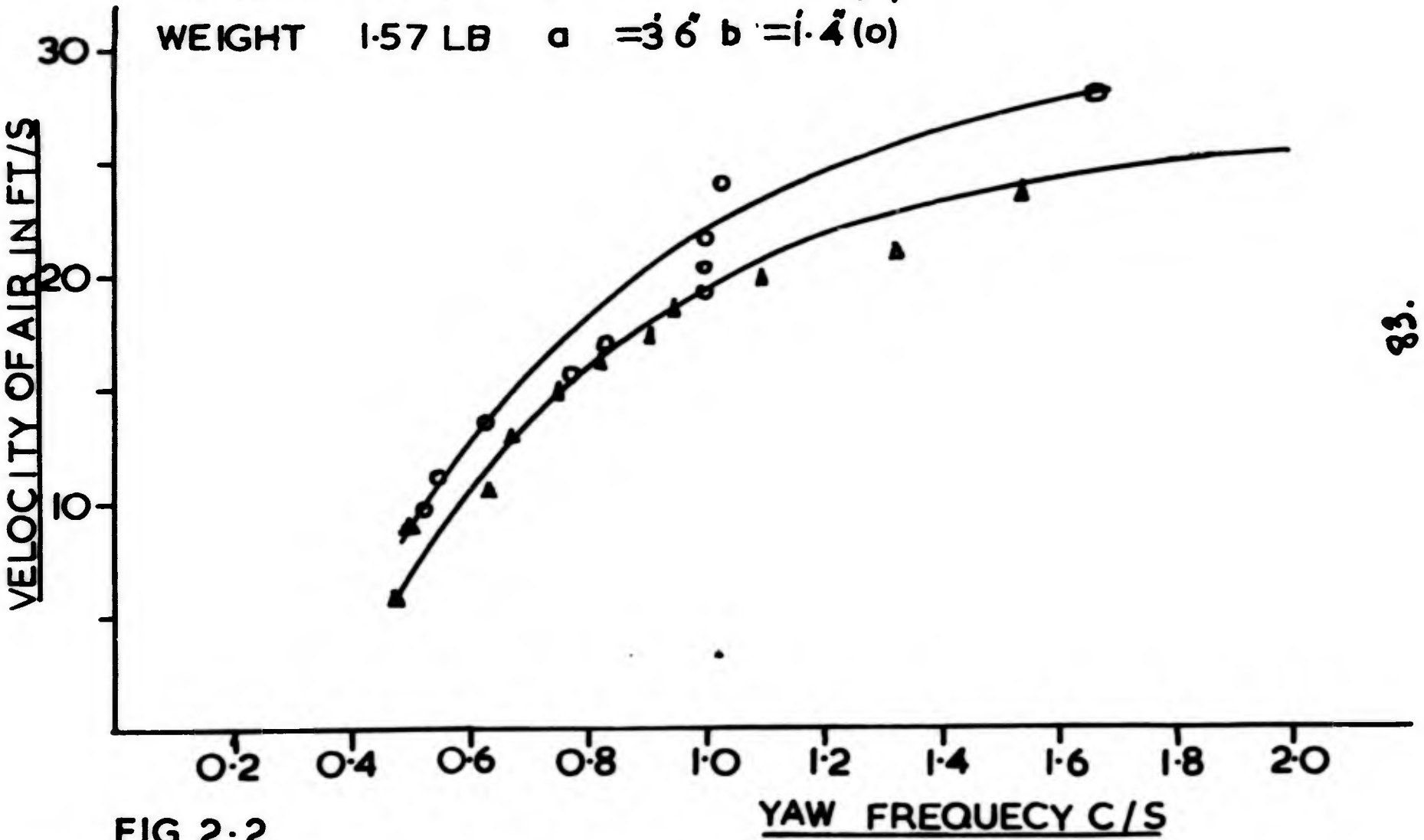

FIG 2·2

SMALL MODEL 1.0'x.4'x.4'

CONTAINER SPECIFICATIONS

WEIGHT 1·09 LB a=2·0" b=11·5" (a) , WEIGHT AT ENDS(----)

WEIGHT 1·57 a=2·0" b=11.5" (b)

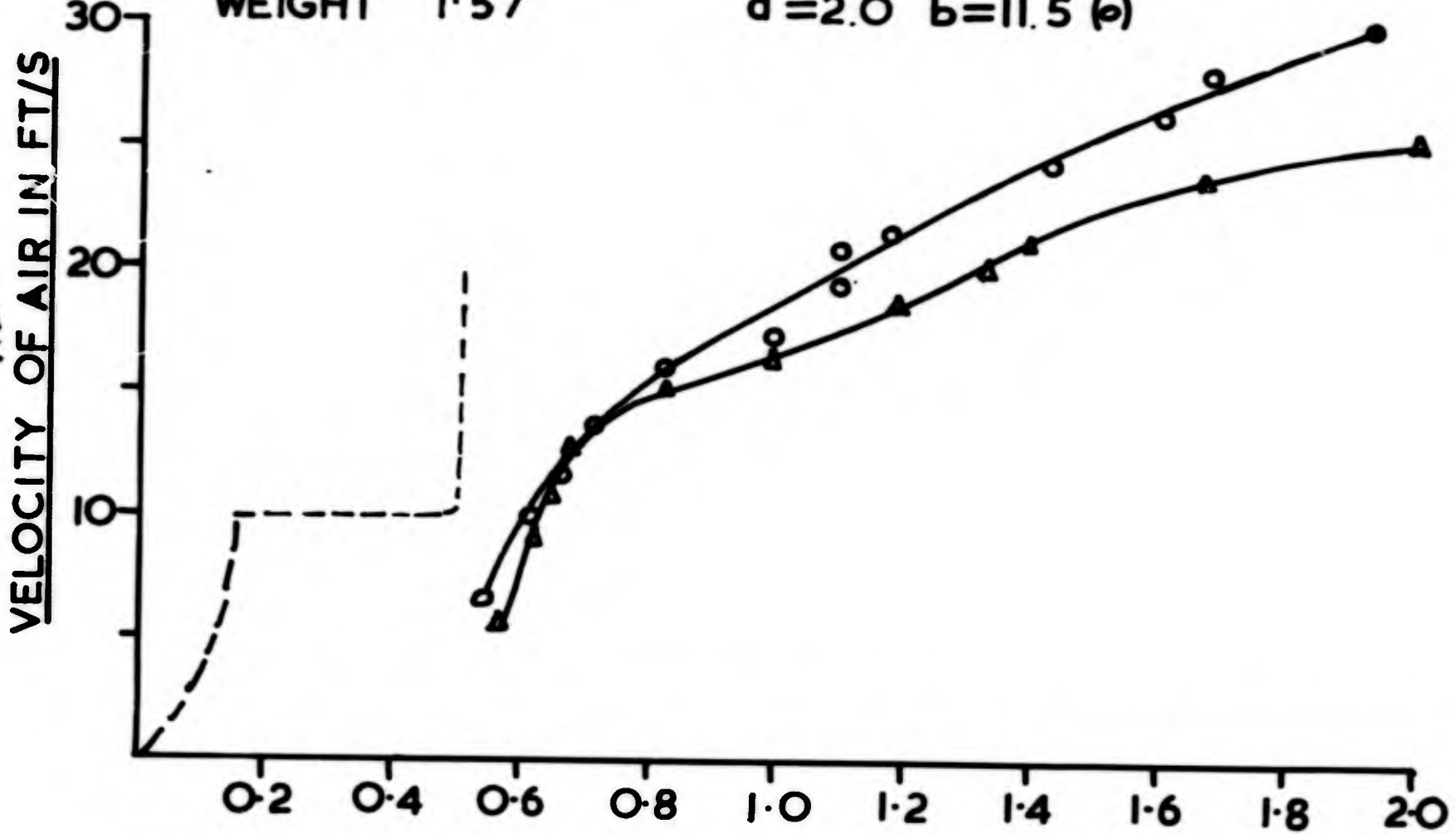

FIG 2.3

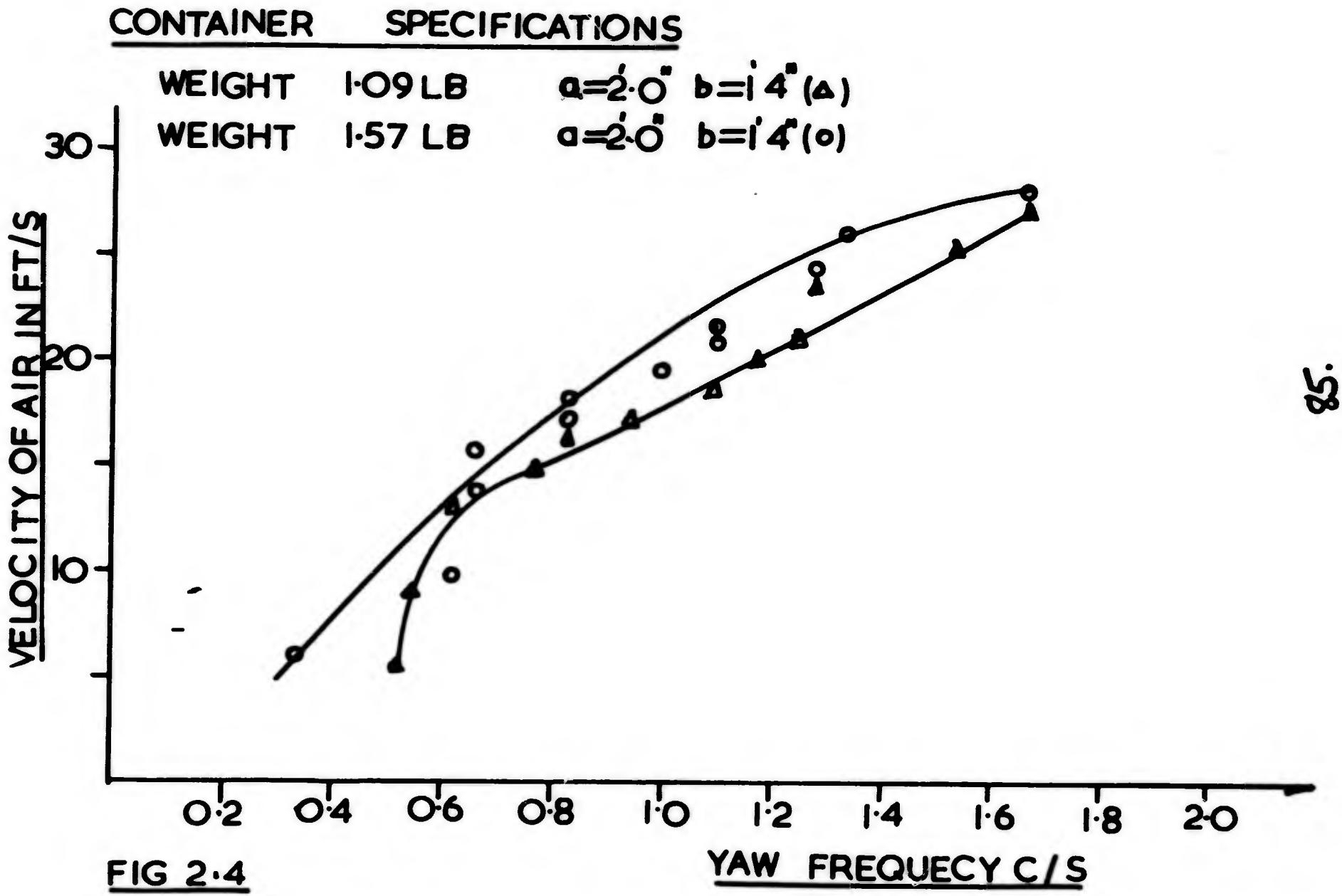
CONTAINER SPECIFICATIONS
WEIGHT 1·09 LB a=2'·0" b=1'4" (Δ)
WEIGHT 1·57 LB a=2'·0" b=1'4" (o)
VELOCITY OF AIR IN FT/S
30
20
10
0·2
0·4
0·6
0·8
1·0
1·2
1·4
1·6
1·8
2·0
YAW FREQUECY C/S

FIG 2·4

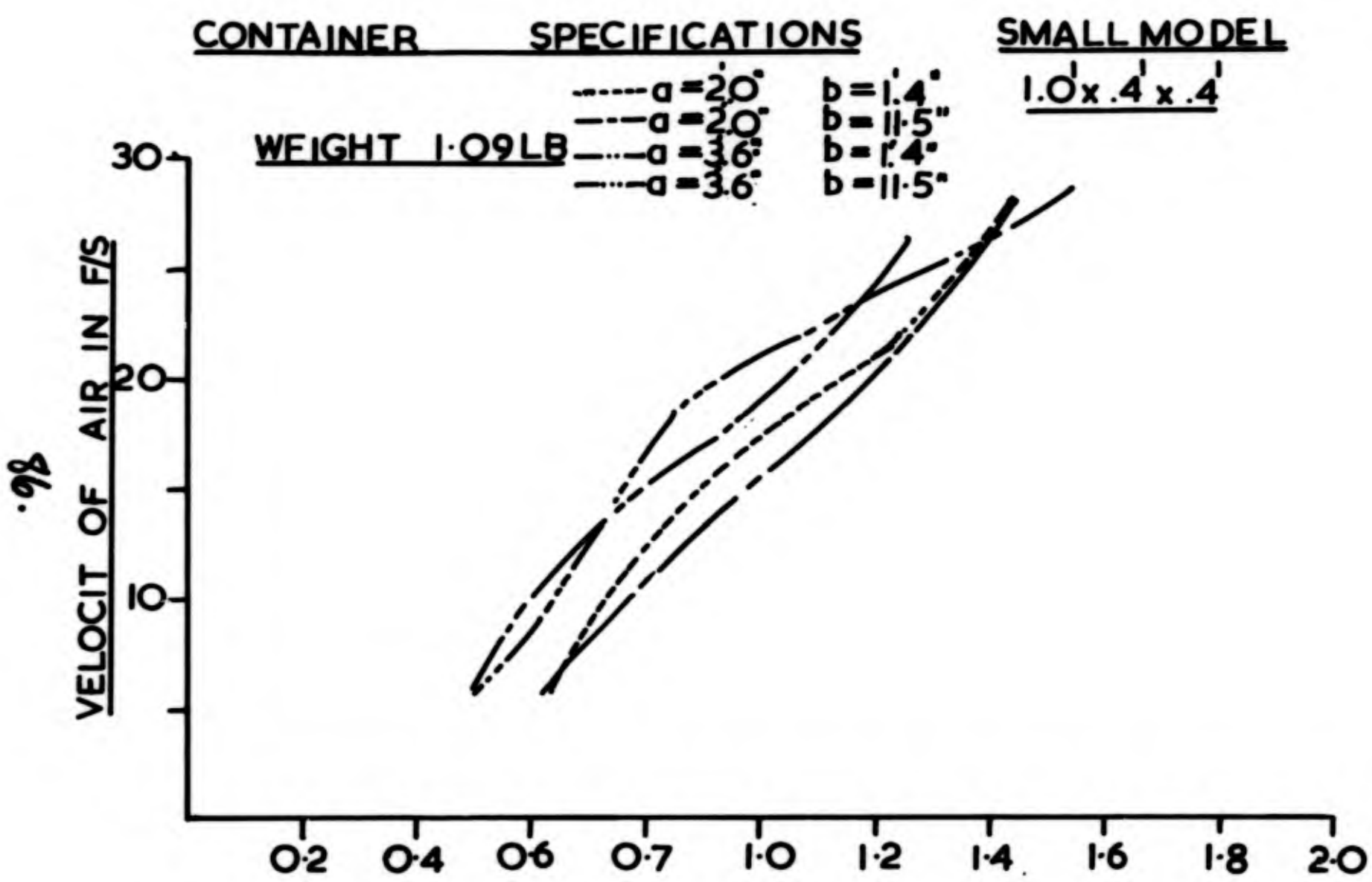
CONTAINER SPECIFICATIONS
SMALL MODEL
1.0' x .4' x .4'
a = 2.0° b = 1.4°
a = 2.0° b = 11.5"
a = 3.6° b = 1.4°
a = 3.6° b = 11.5"
WEIGHT 1·09 LB
VELOCIT OF AIR IN F/S
·98
30
20
10
0·2
0·4
0·6
0·7
1·0
1·2
1·4
1·6
1·8
2·0
YAW FREQUENCY IN C/S

FIG 2·5

LARGE MODEL 2.x.4 x .4

CONTAINER SPECIFICATIONS

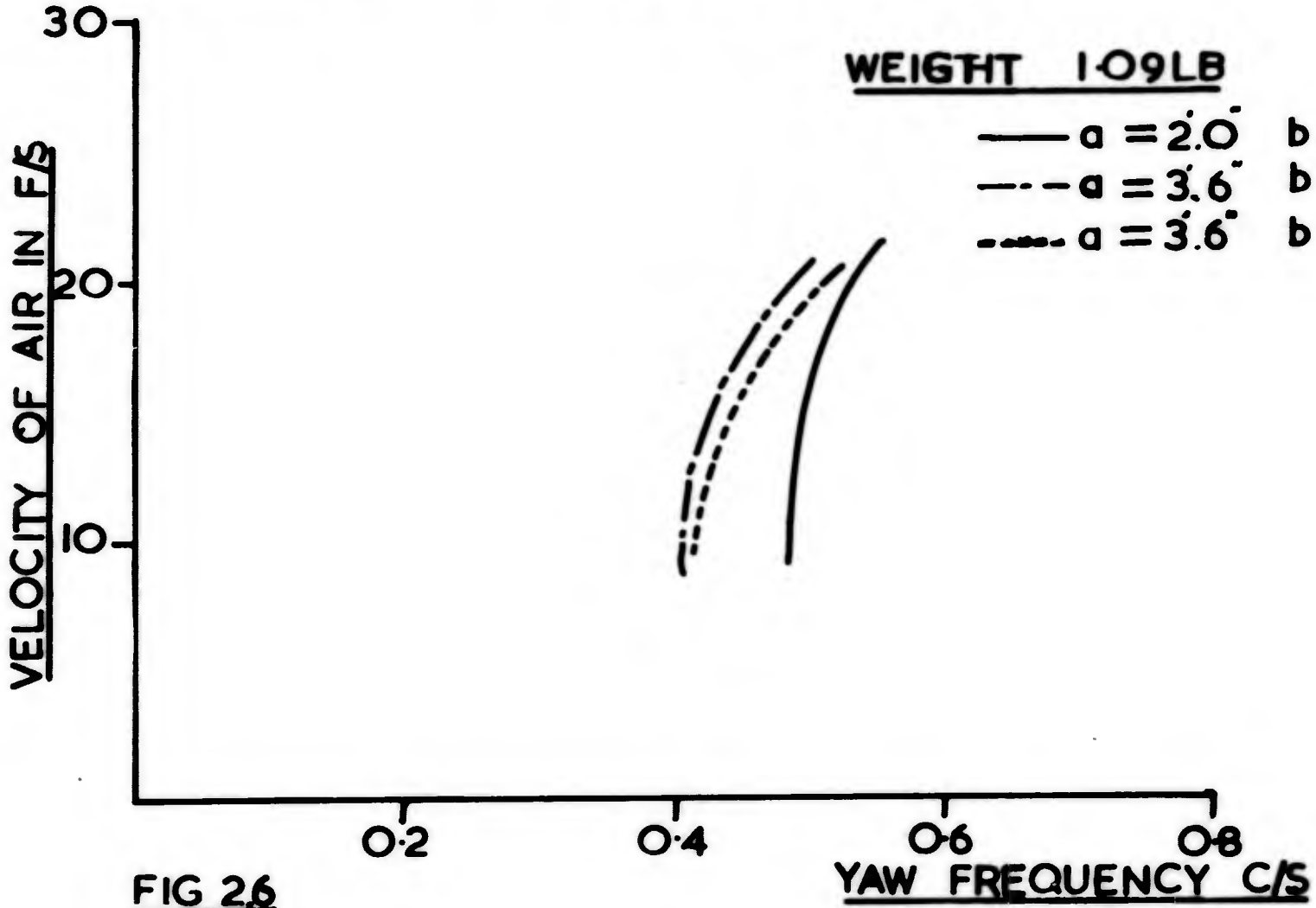

FIG 26

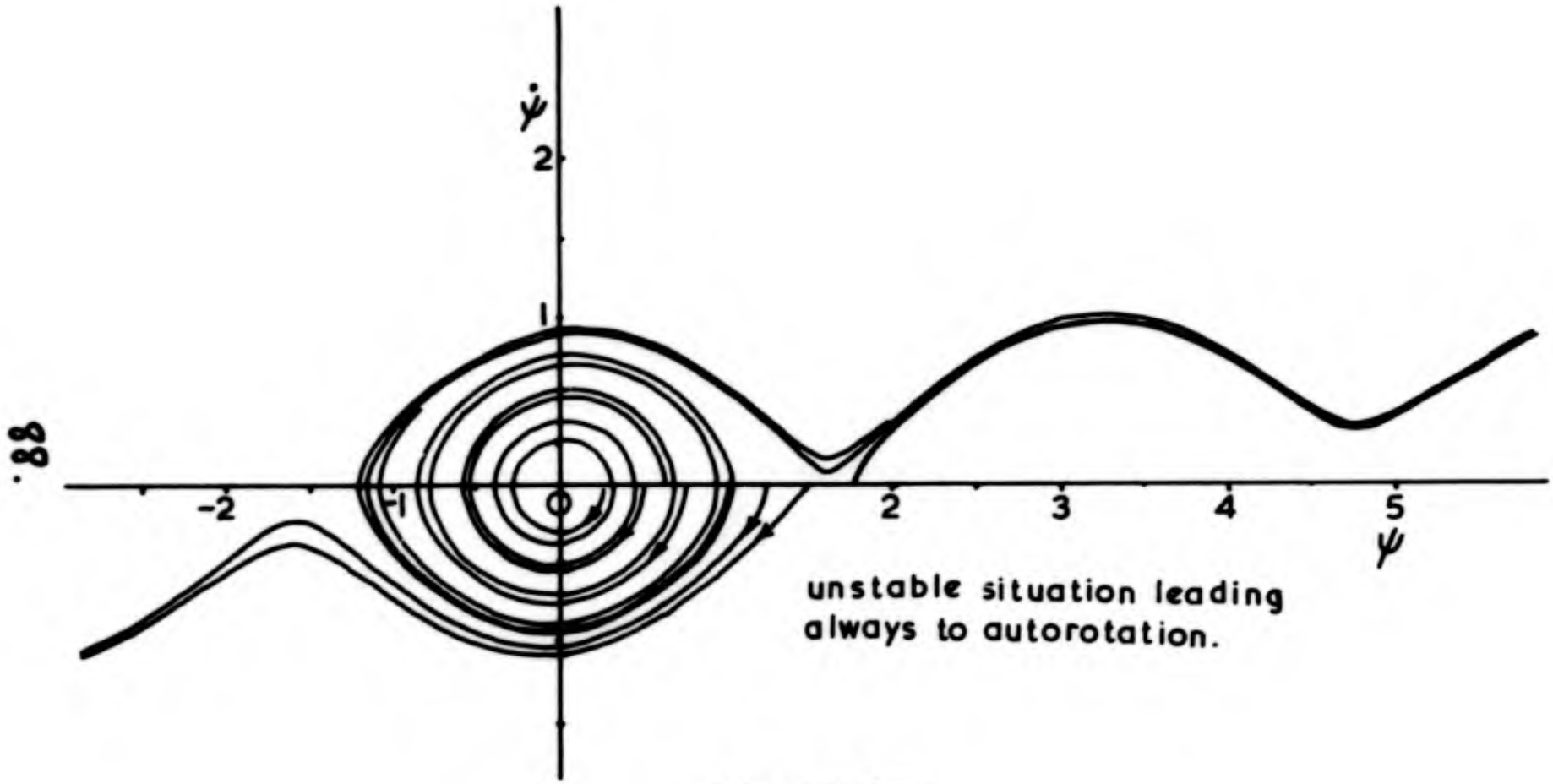

FIGURE 2·7

YAW MOTION MATHEMATICAL MODEL IN THE PHASE PLANE WITH c=0·1 AND ∂=1.

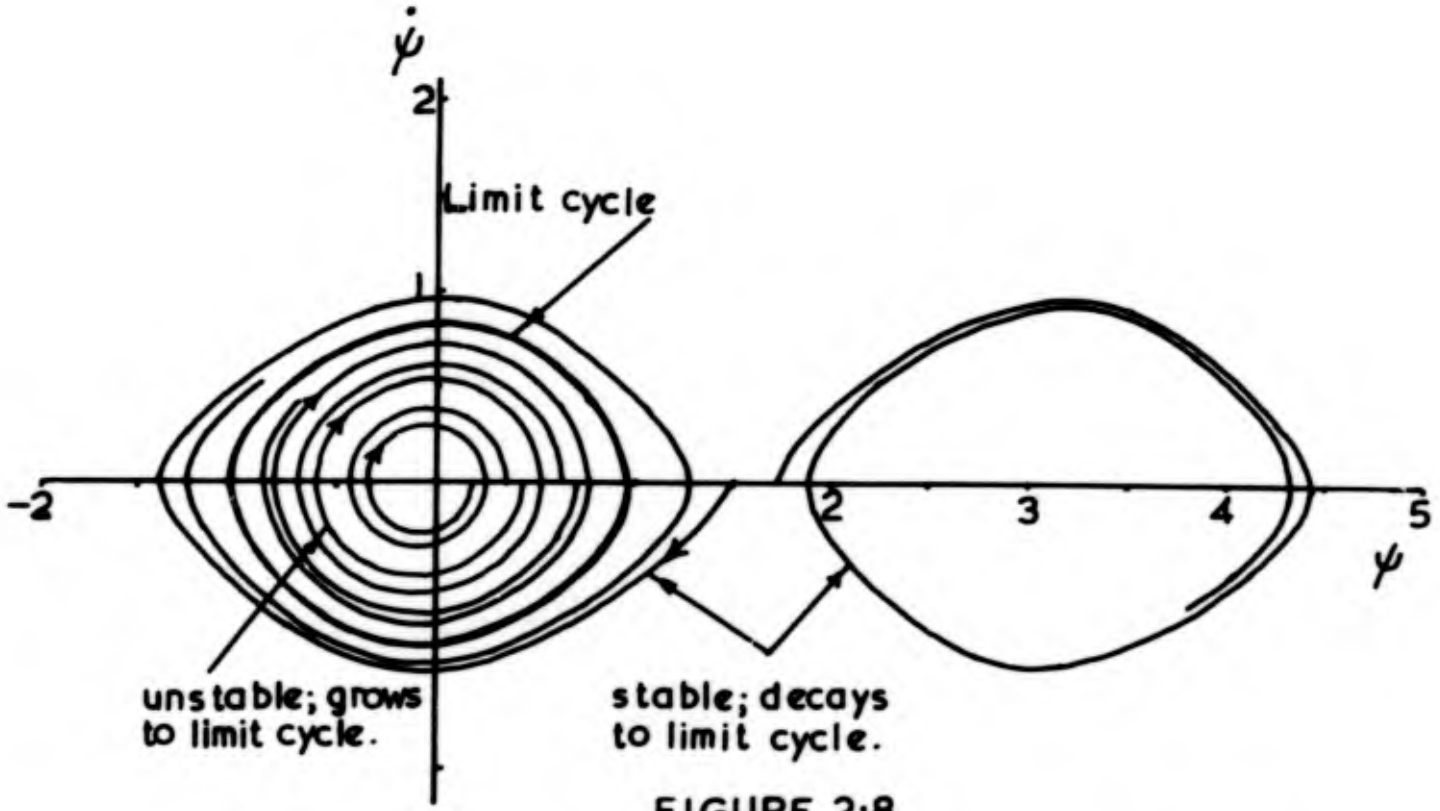

FIGURE 2·8

YAW MOTION MATHEMATICAL MODEL IN THE PHASE PLANE WITH c=0·1 AND δ=2.

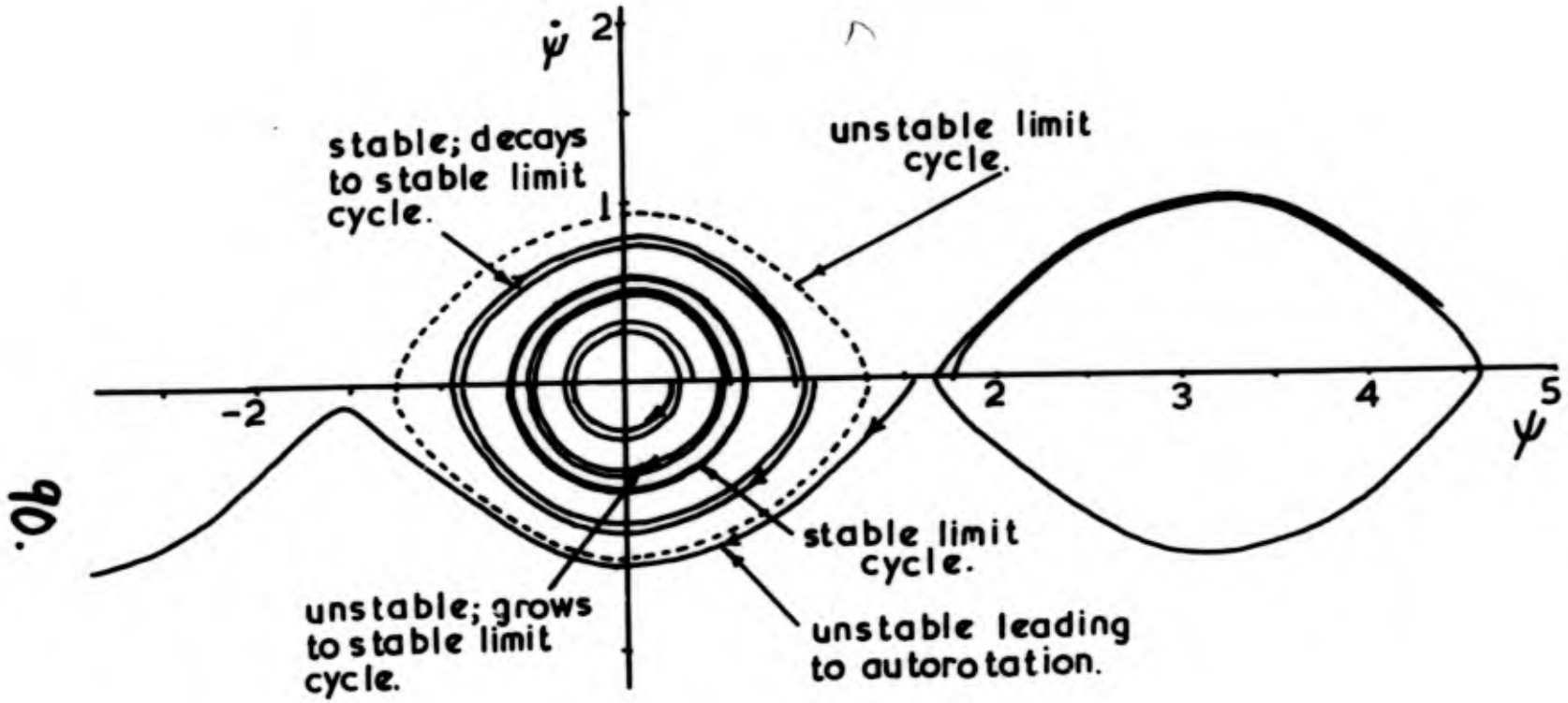

FIGURE 2·9

YAW MOTION MATHEMATICAL MODEL IN THE PHASE PLANE WITH $c=0{\cdot}1$ AND $\delta=3$

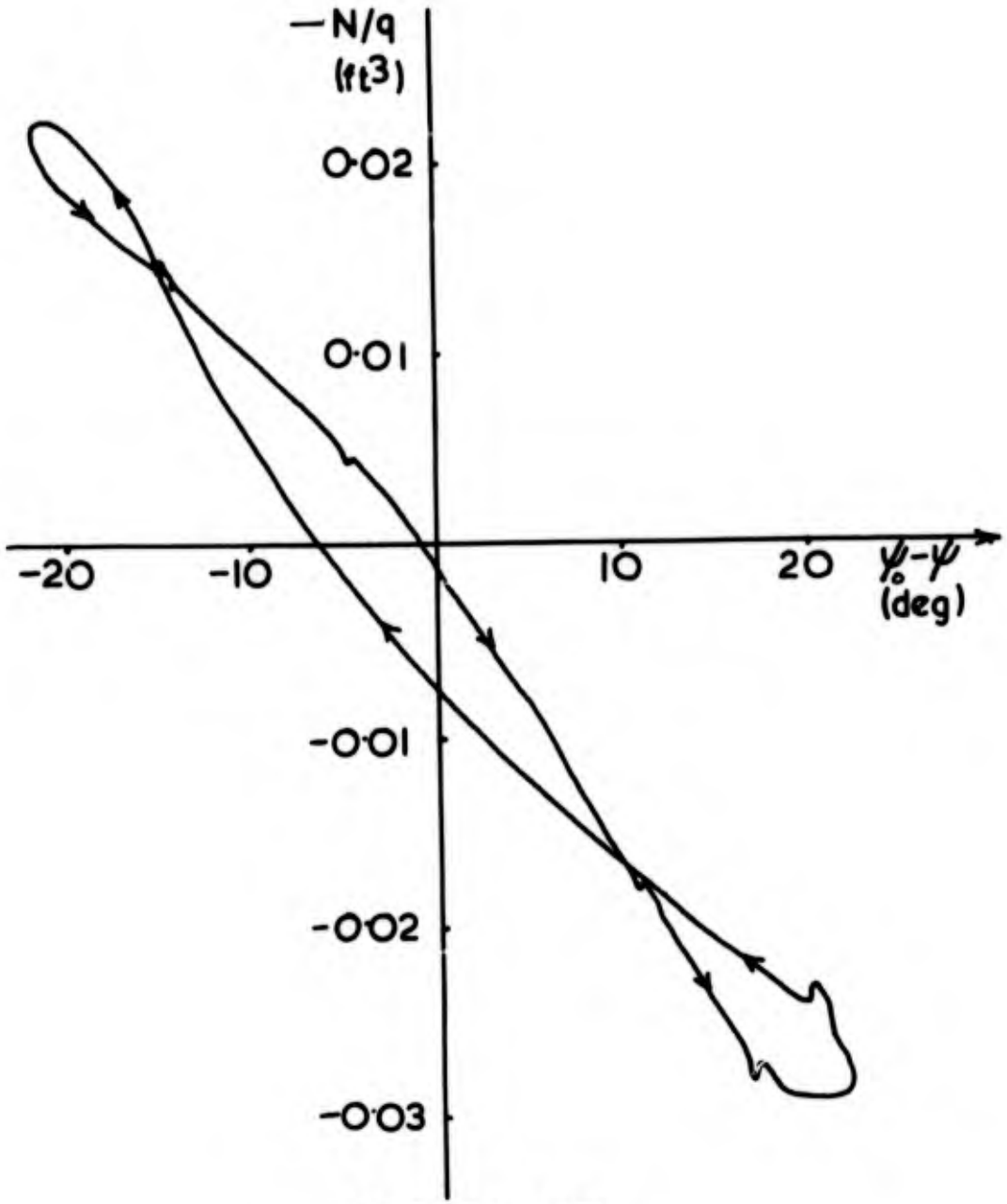

FIGURE 2·10

$-N/q \sim \psi_0 - \psi$ FOR $\psi_0 = 0$ AND V = 46 f/s FOR 1:0·4:0·4 PILOT MODEL

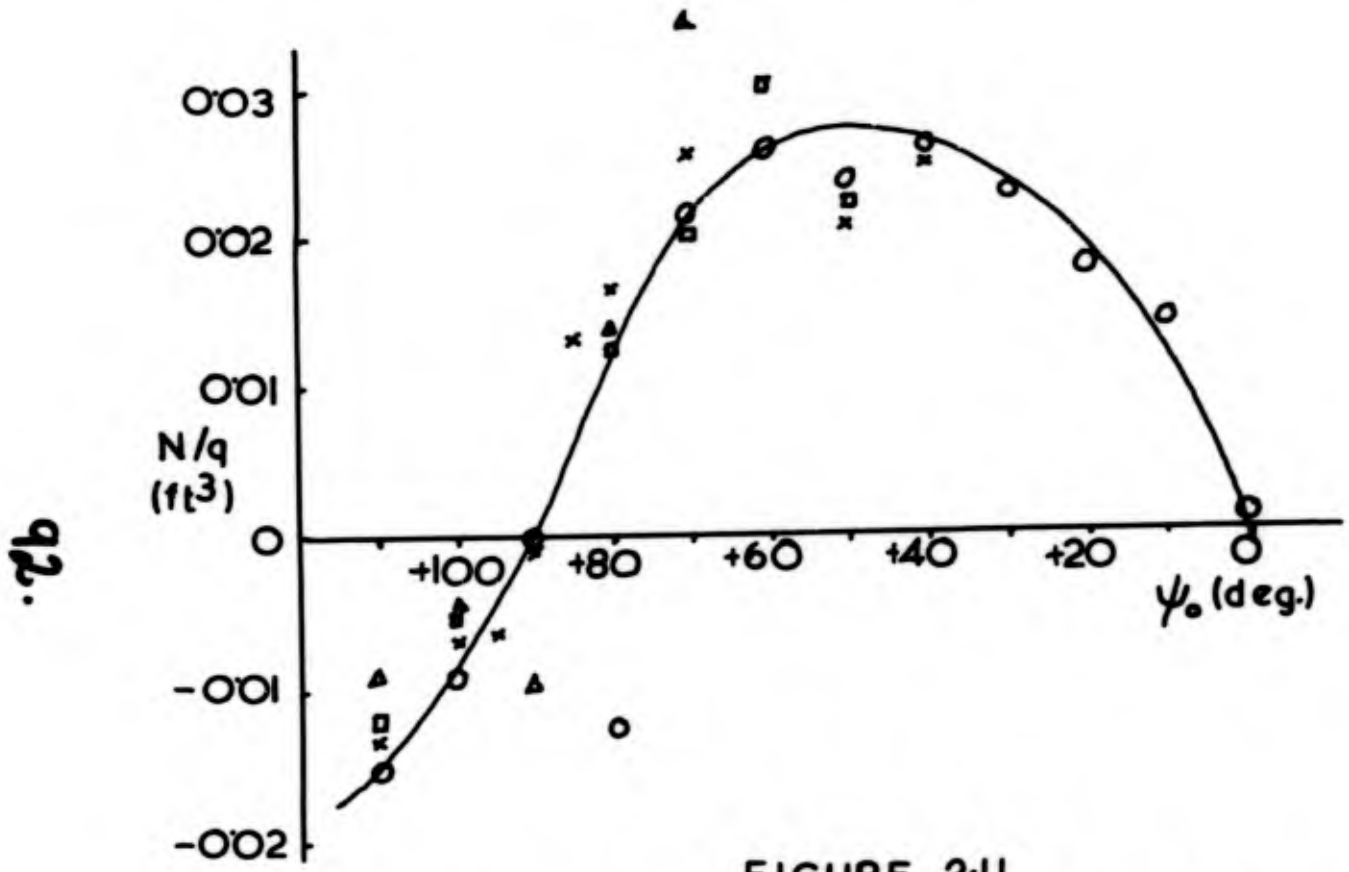

FIGURE 2·11

N/q ~ ψ₀ : RESULTS FROM EARLY STATIC TEST ON 1:0·4:0·4 PILOT MODEL

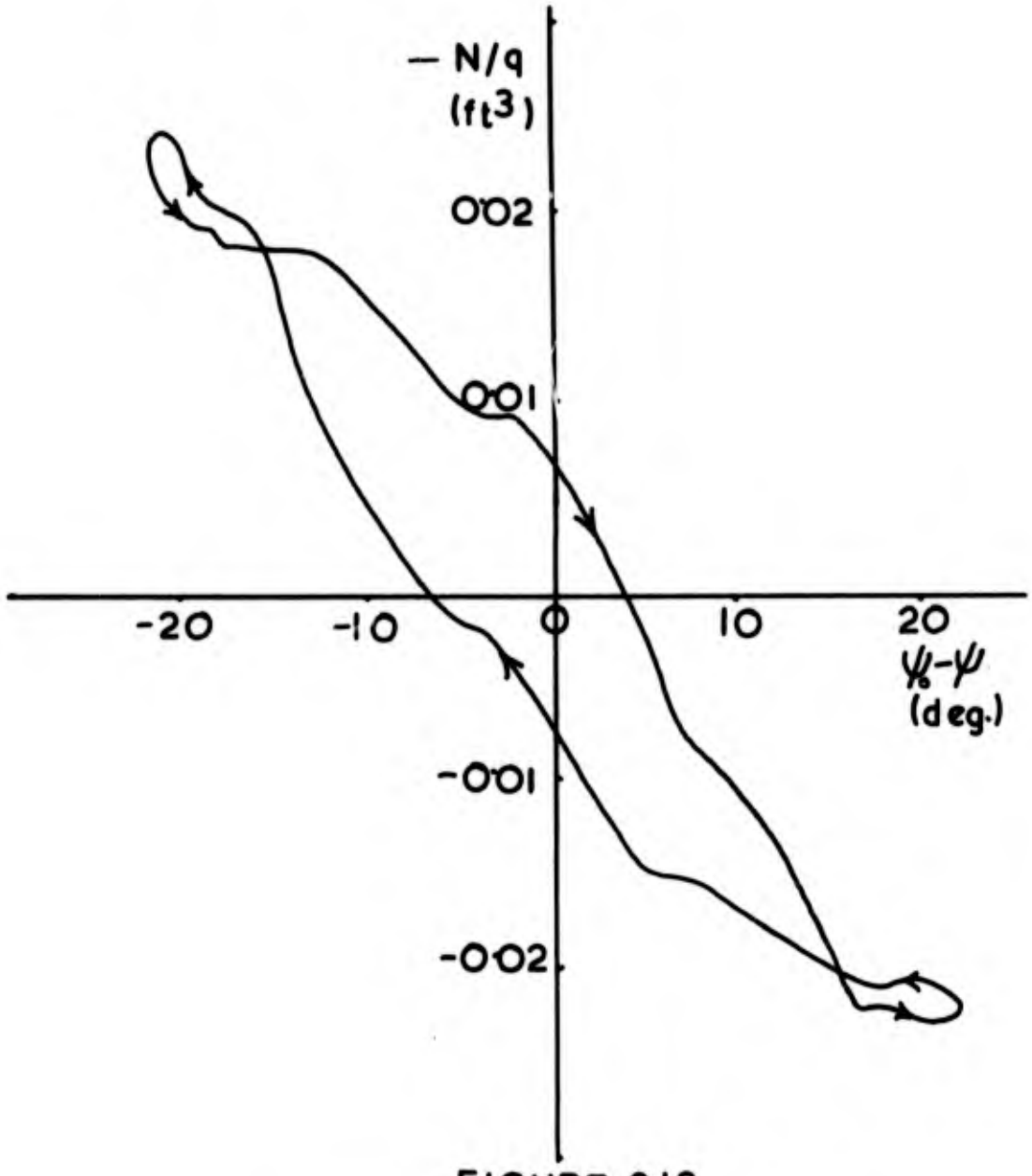

FIGURE 2·12

$-N/q \sim \psi_0 - \psi$ FOR $\psi_0 = 0$ AND V = 55 f/s FOR 1:0·4:0·4 PILOT MODEL.

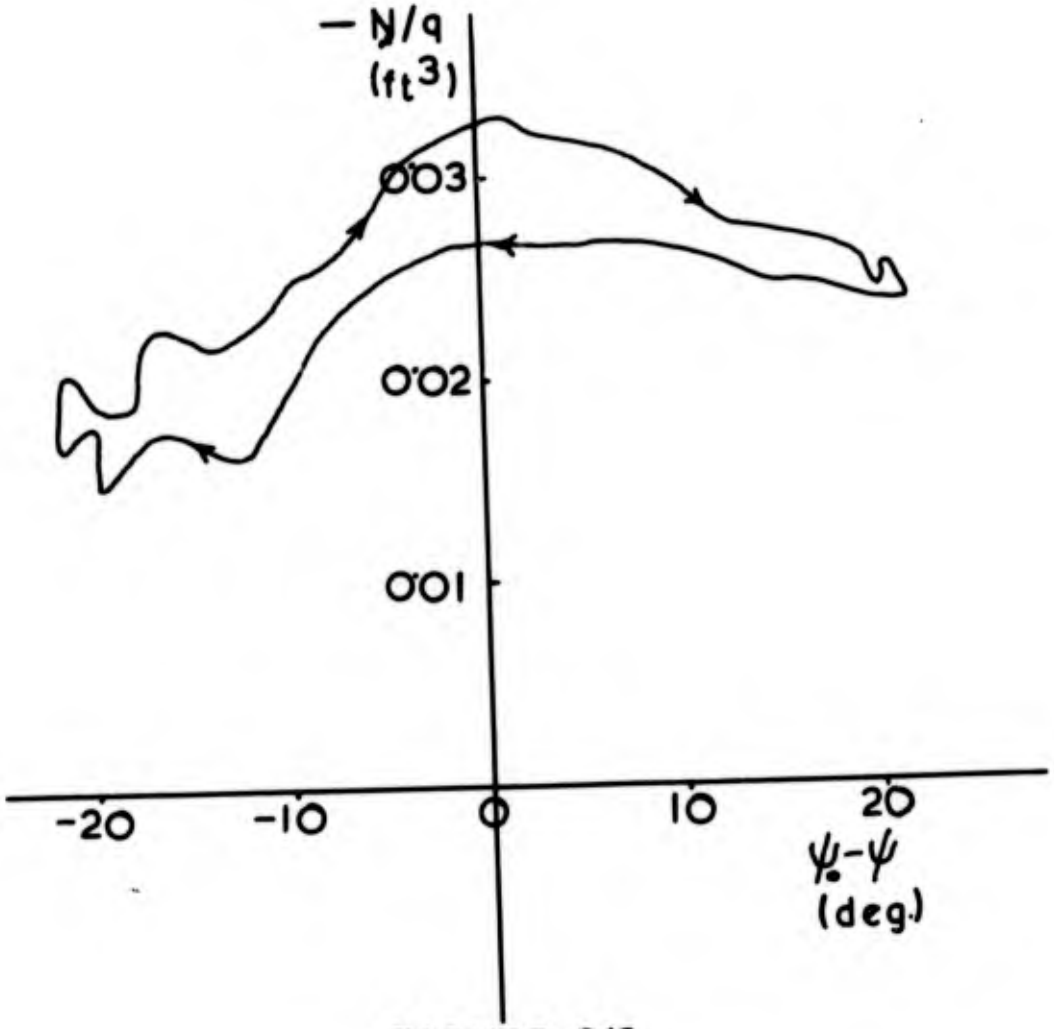

FIGURE 2·13

$-N/q \sim \psi_0 - \psi$ FOR $\psi_0 = +45°$ AND V = 55 f/s FOR 1:0·4:0·4 PILOT MODEL

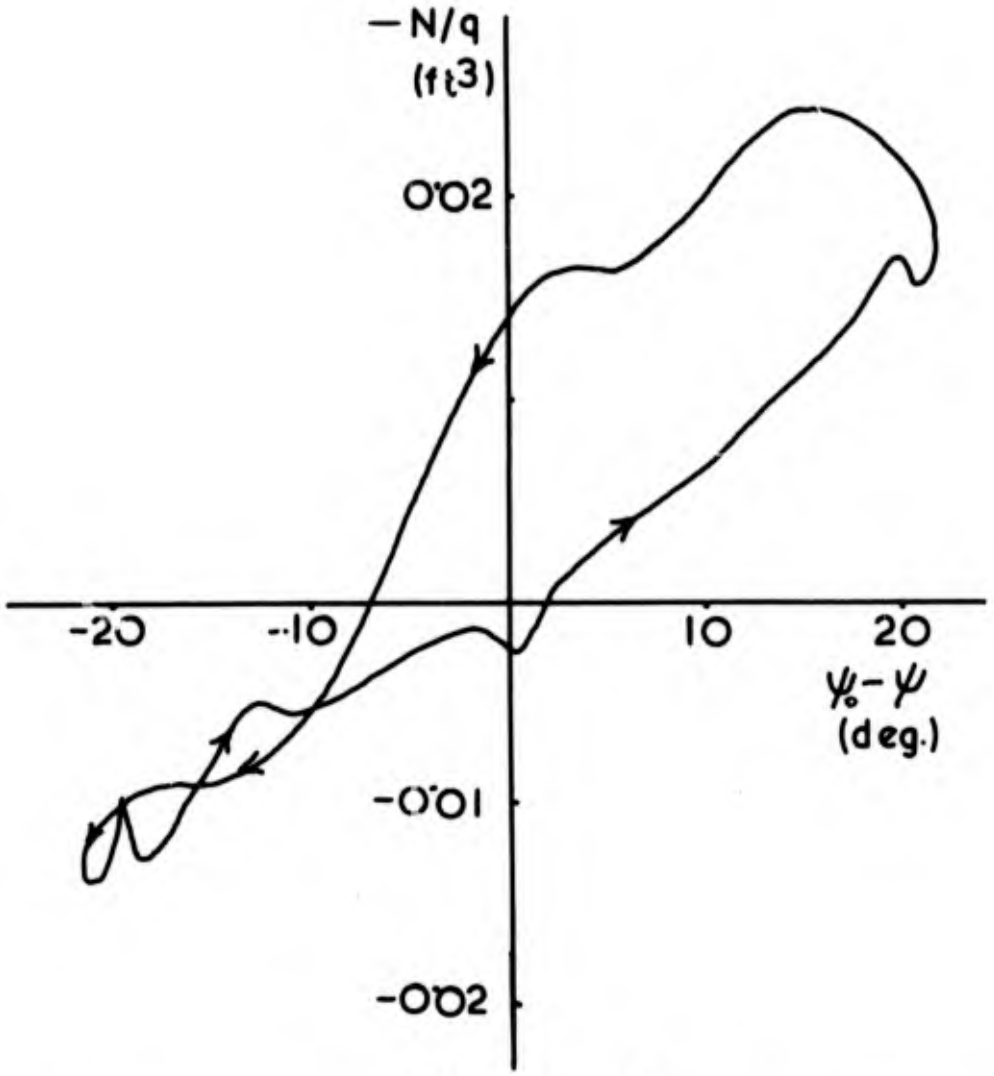

FIGURE 2·14

$-N/q \sim \psi_0 - \psi$ FOR $\psi_0 = +90°$ AND V=55 f/s FOR 1:0·4:0·4 PILOT MODEL

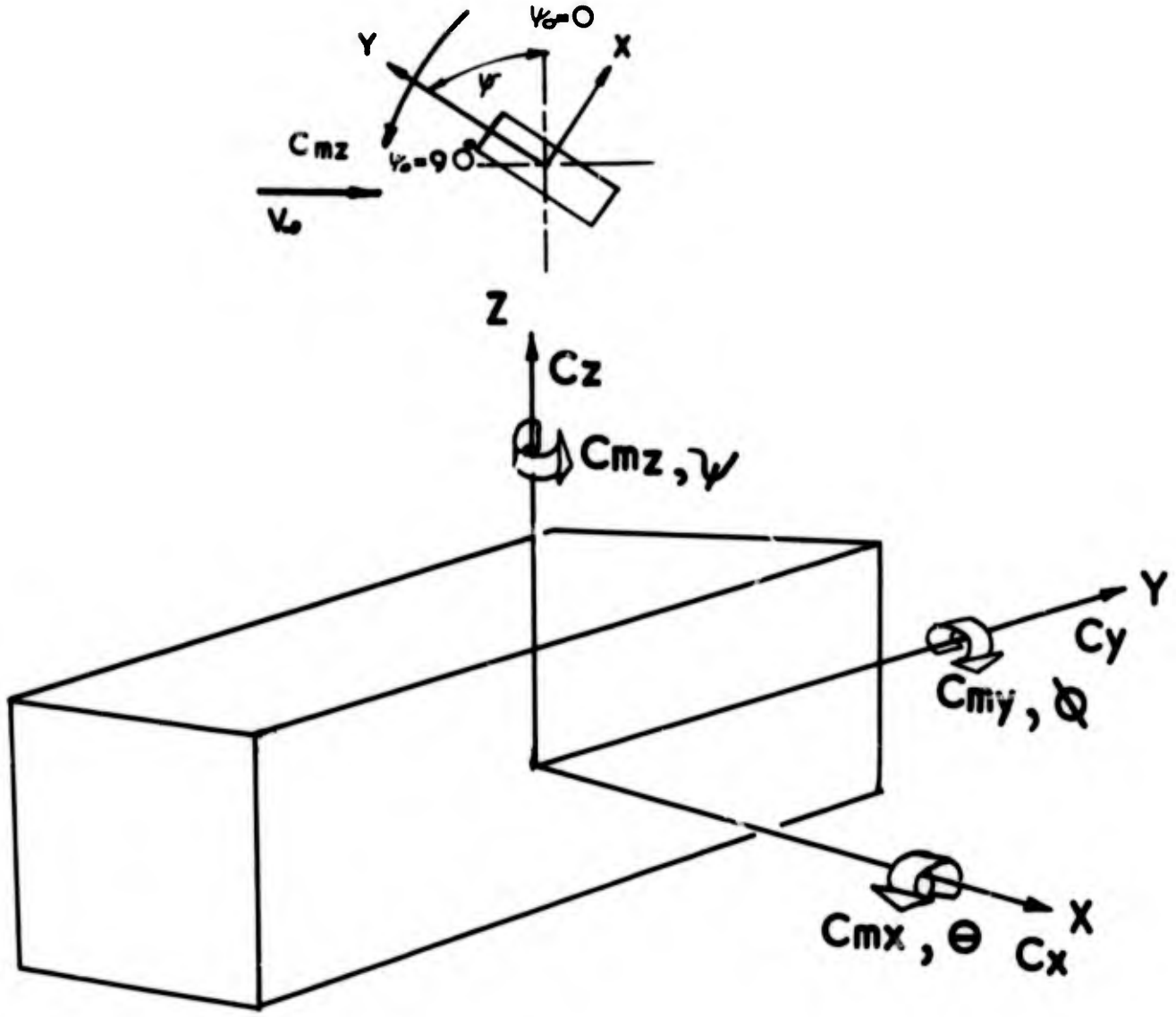

FIG 3.1 CO ORDINATE SYSTEM OF AXIS

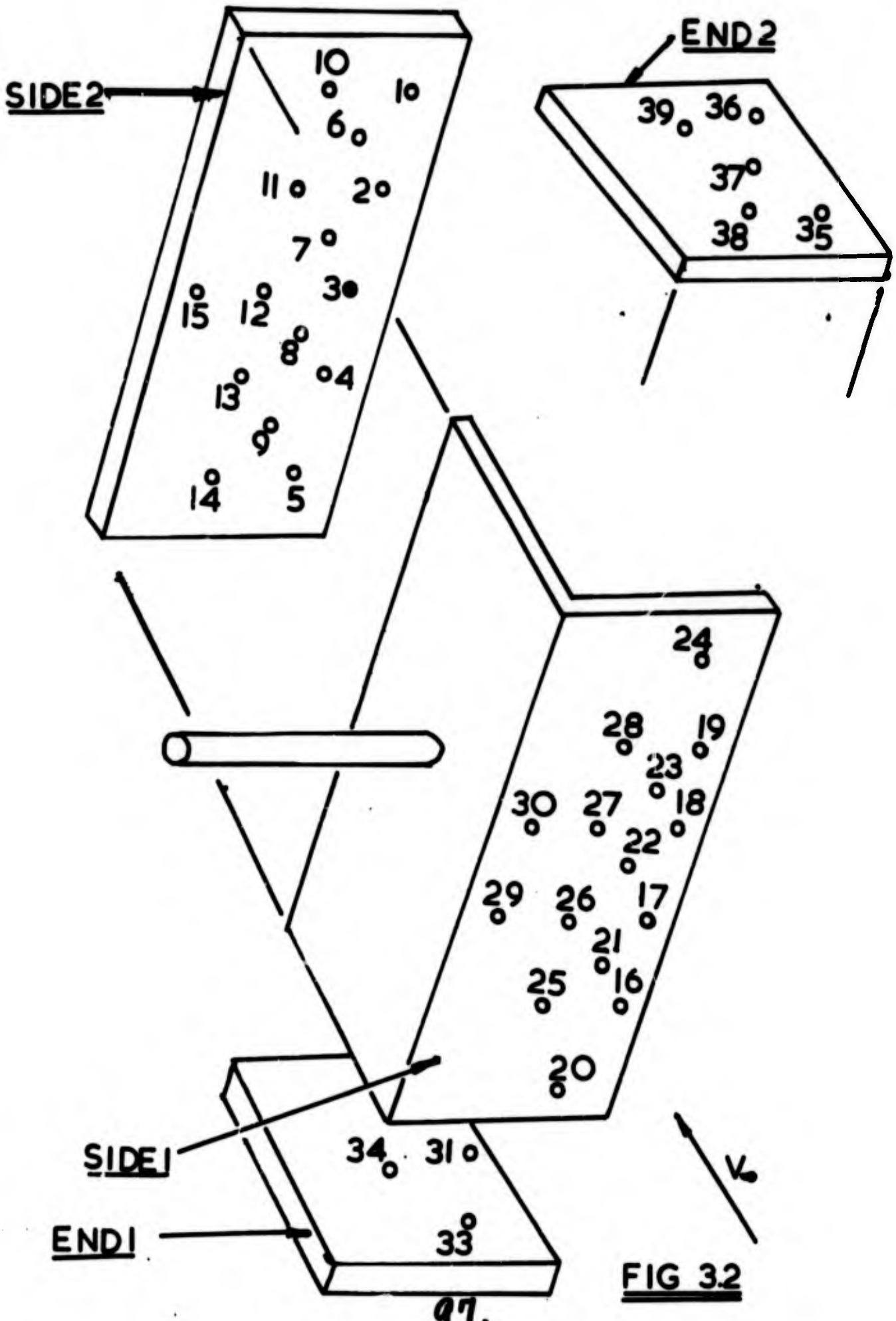
SIDE2
END2
SIDE1
END1
10
10
6
11
2
7
3
15
12
8
13
4
9
14
5
39
36
37
38
35
24
28
19
23
30
27
18
22
29
26
17
21
25
16
20
34
31
33
V

FIG 3.2

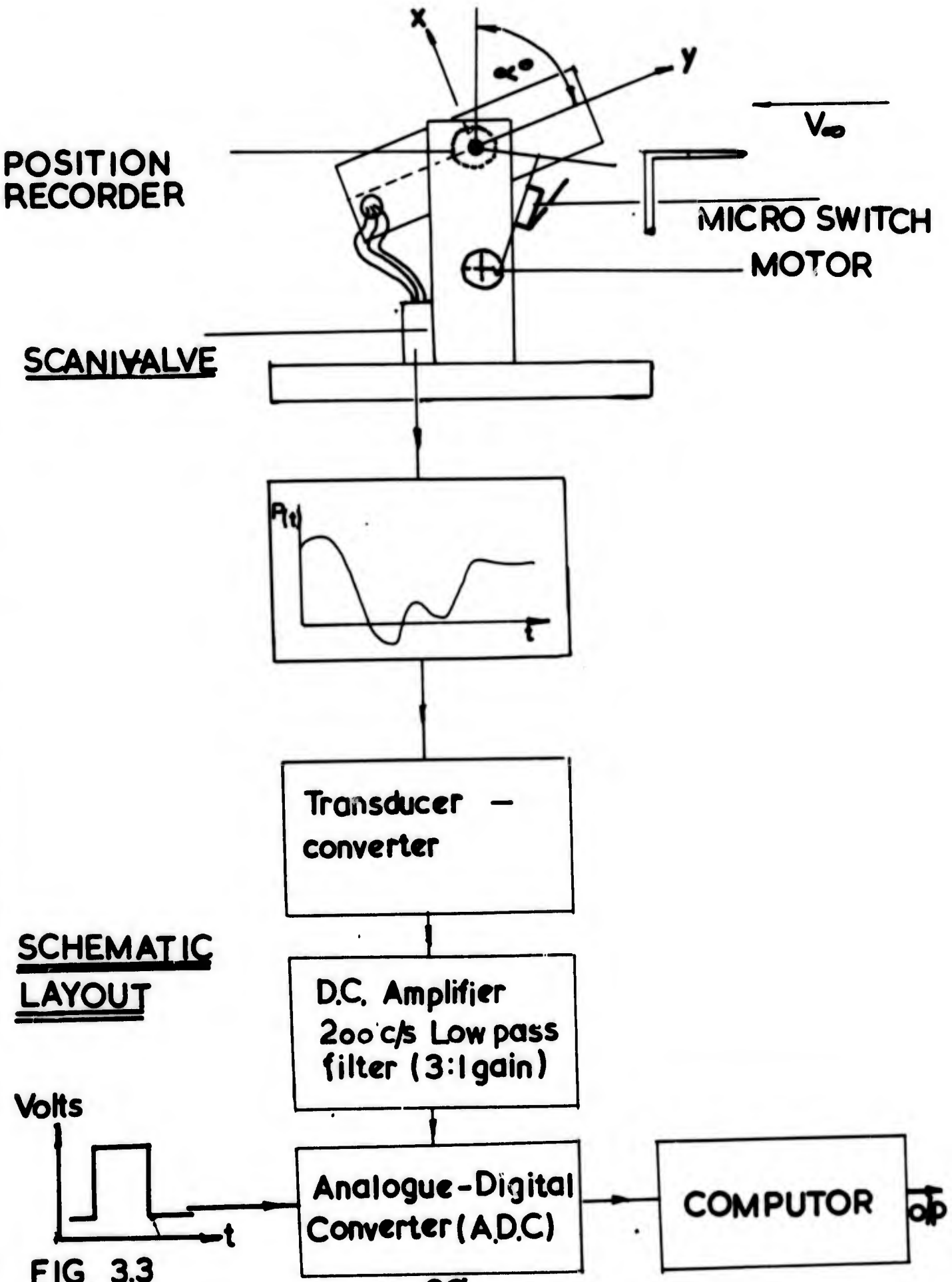

SCHEMATIC LAYOUT

FIG 3.3

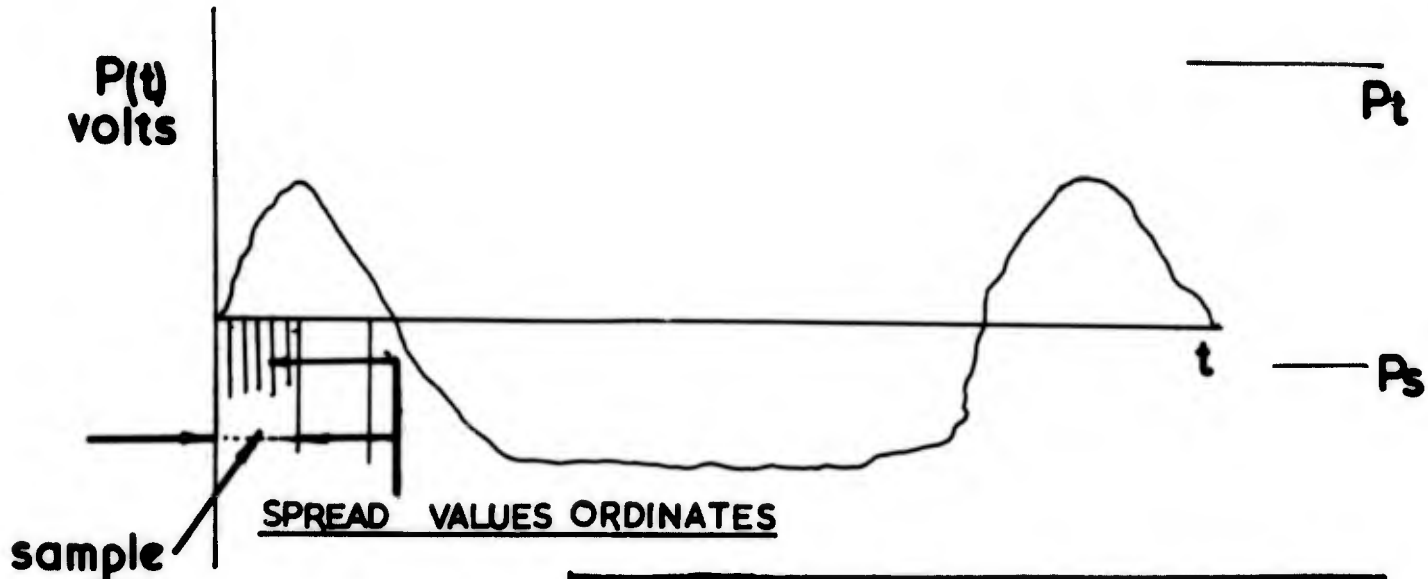

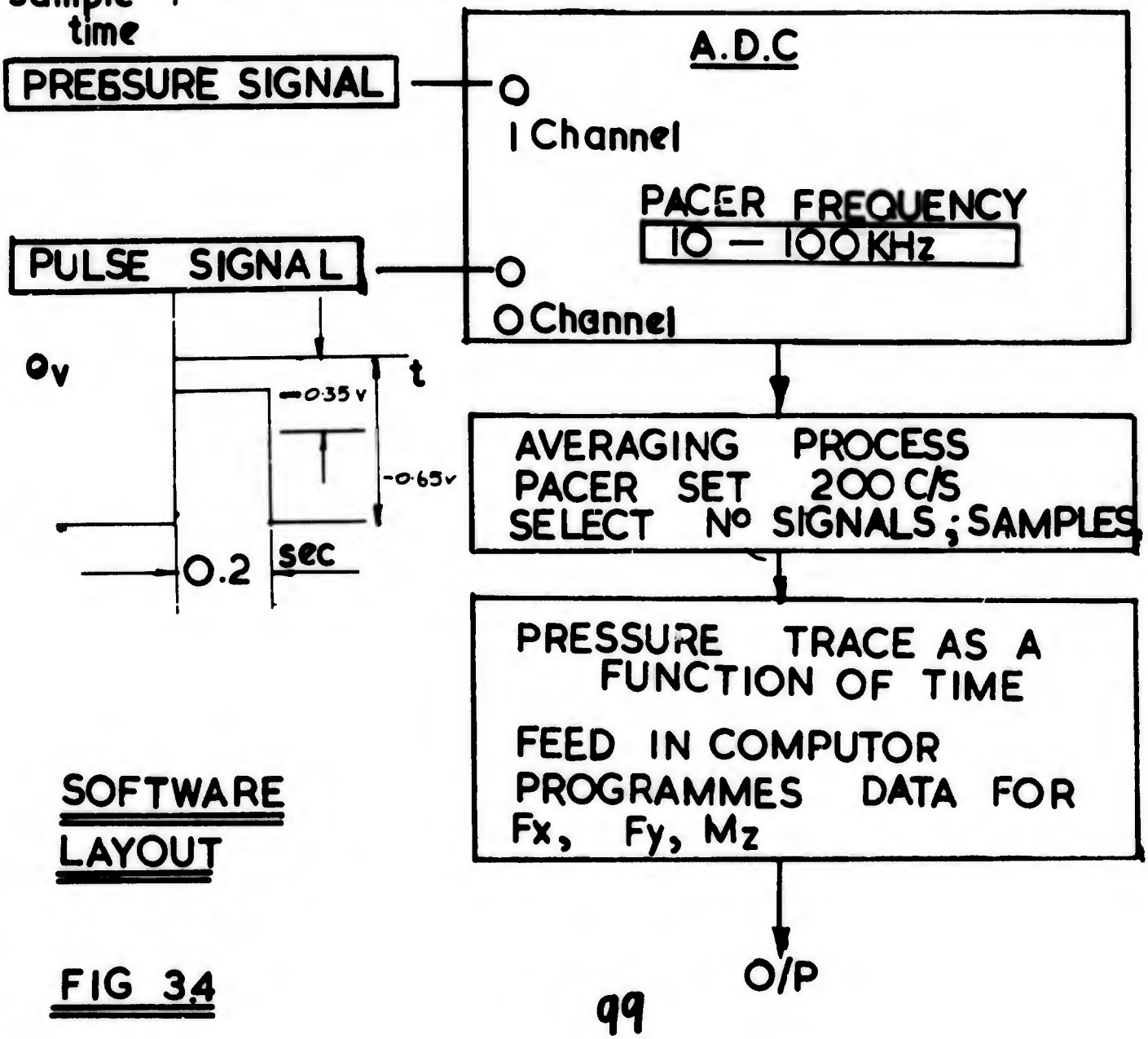

SOFTWARE LAYOUT

FIG 3.4

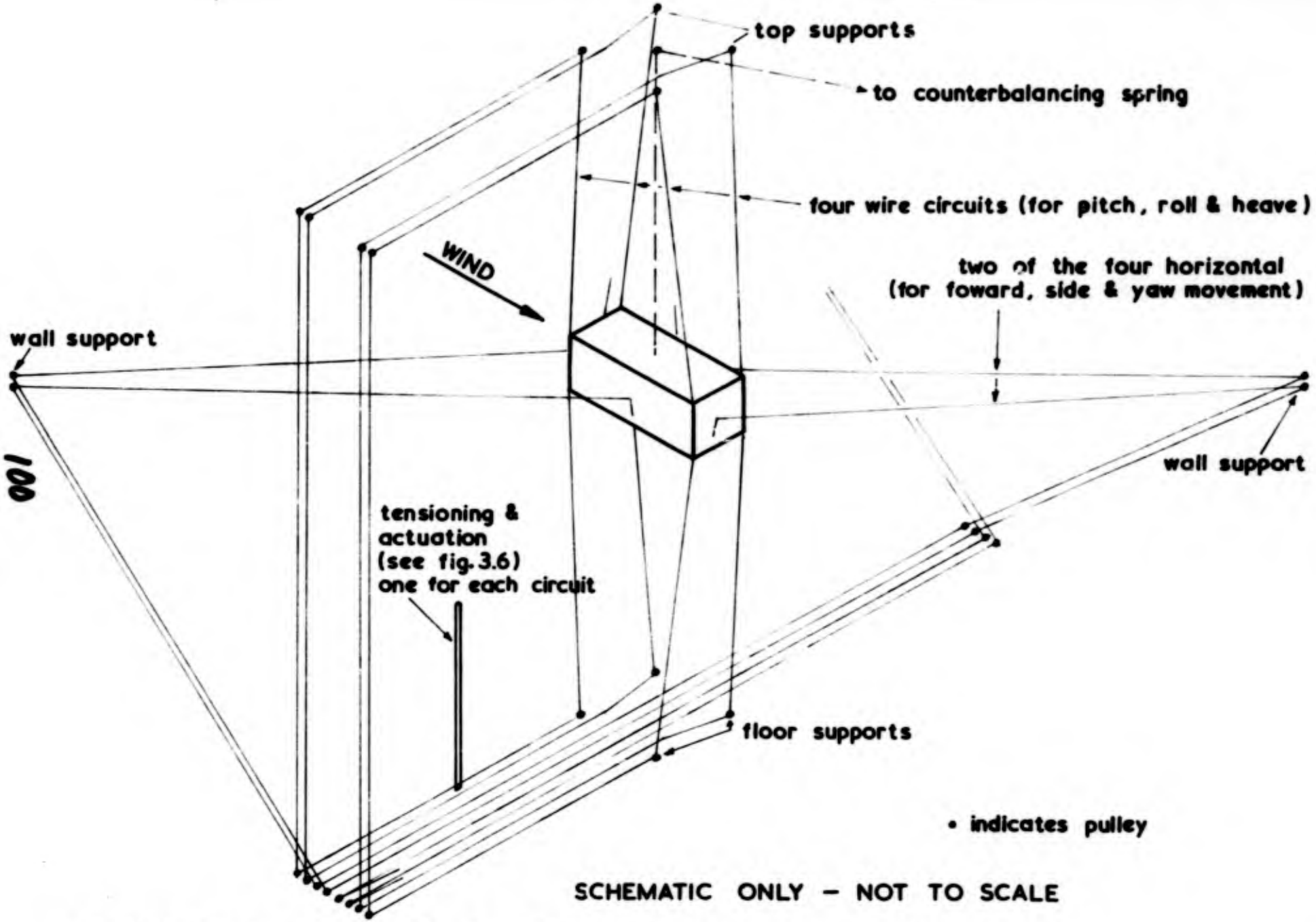

FIGURE 3.5 SIX DEGREE OF FREEDOM WIRE SUPPORT RIG

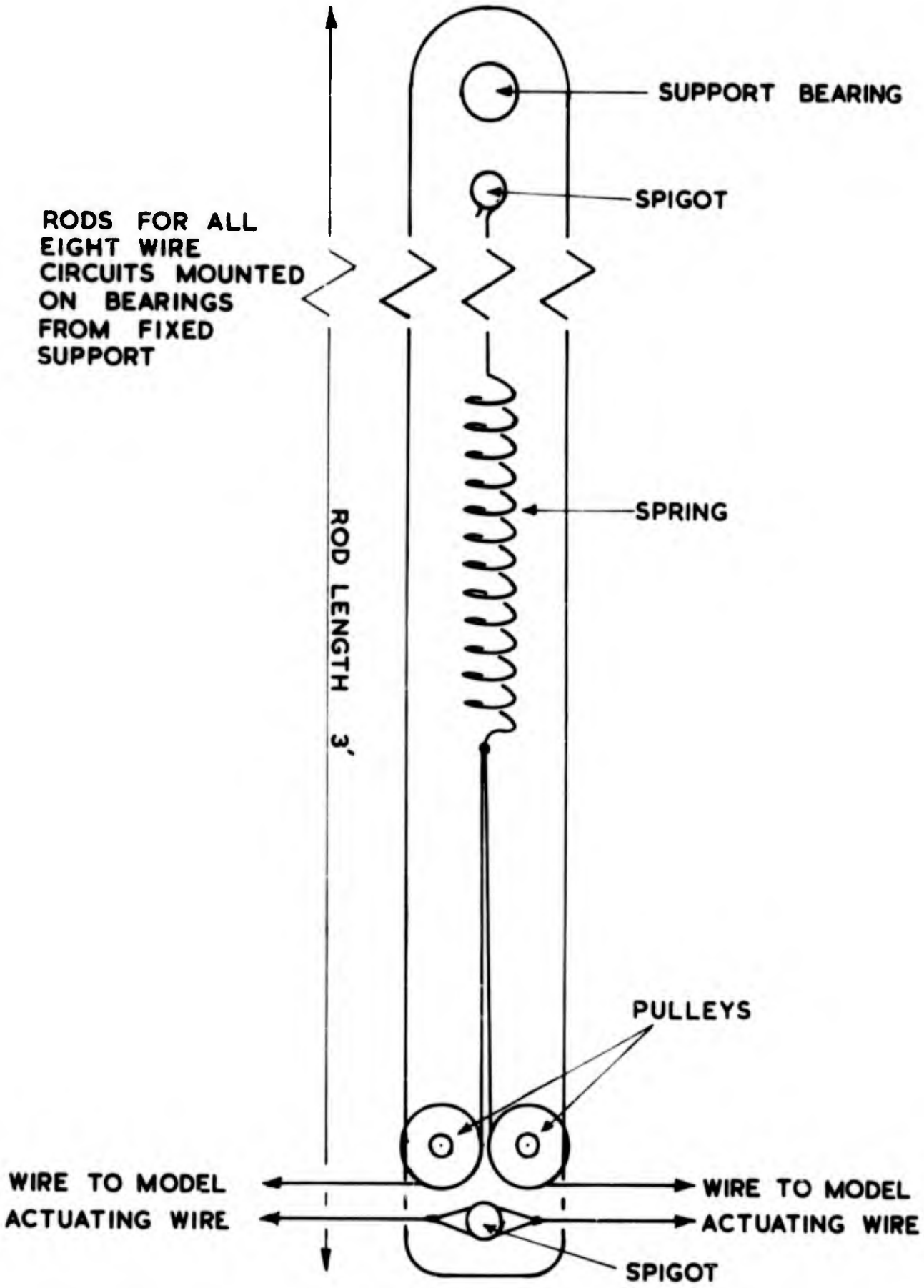

FIGURE 3.6 ARRANGEMENT OF TENSIONING DEVICES

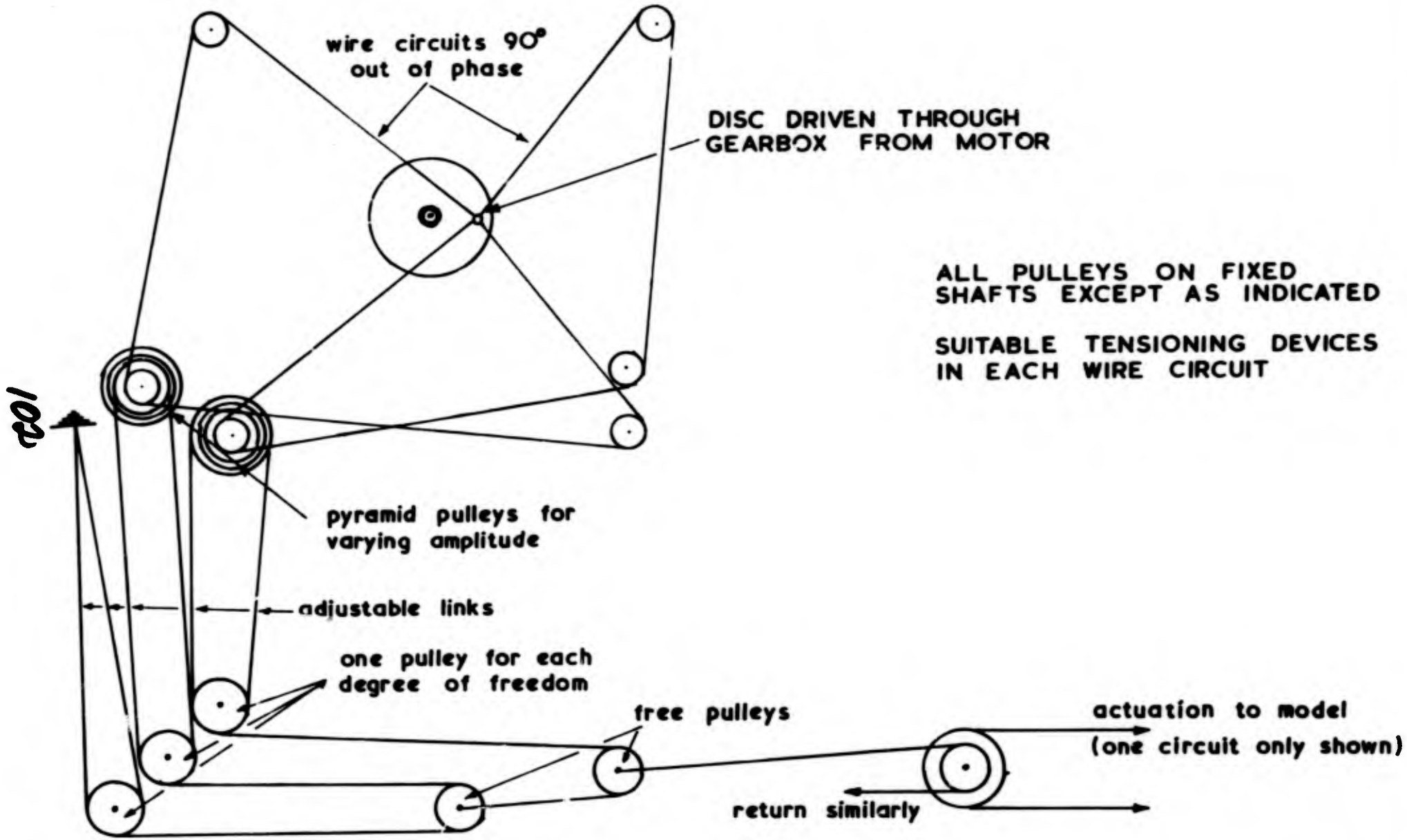

FIGURE 3.7 ACTUATION DESIGN – SCHEMATIC

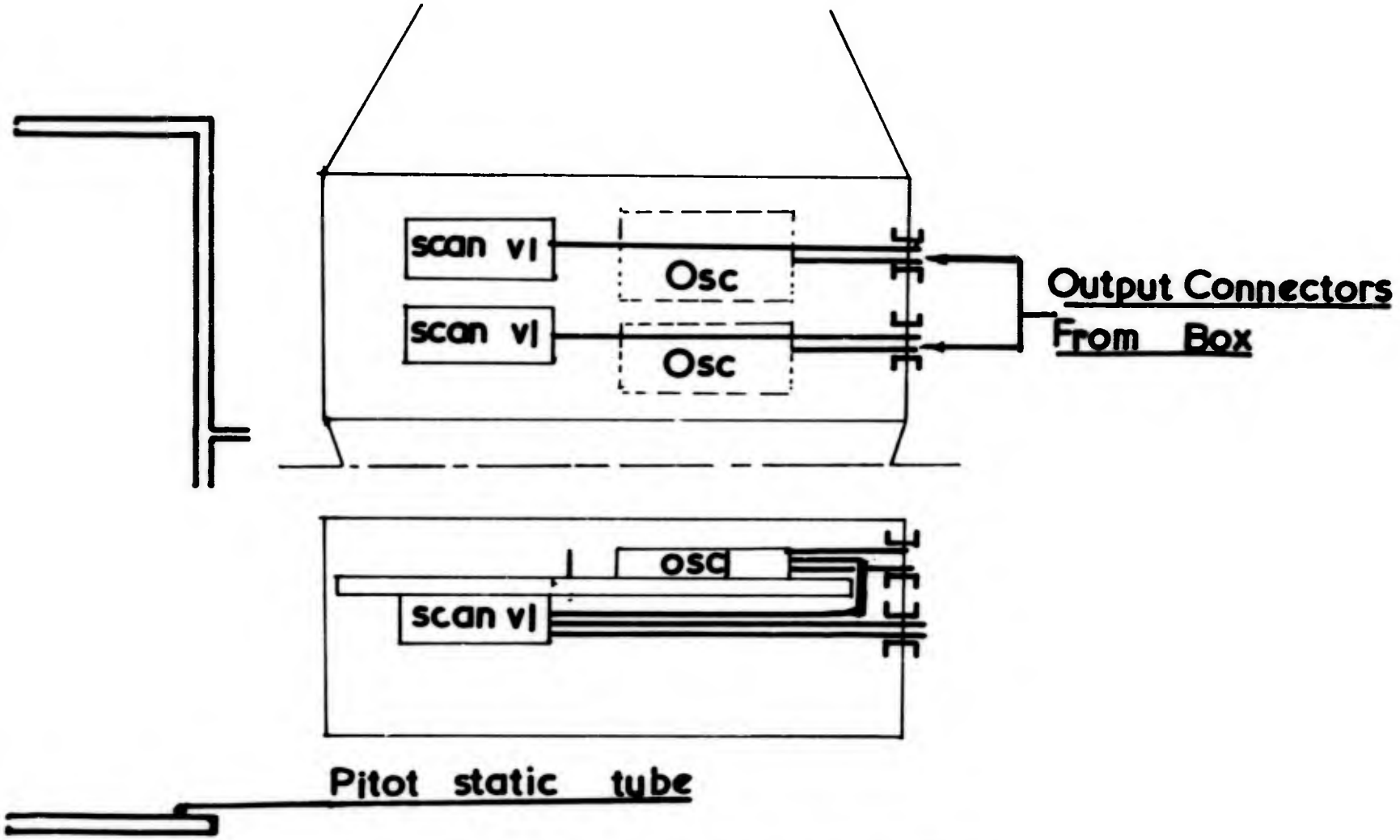

SCHEMATIC LAYOUT OF BOX

FIG 3.8

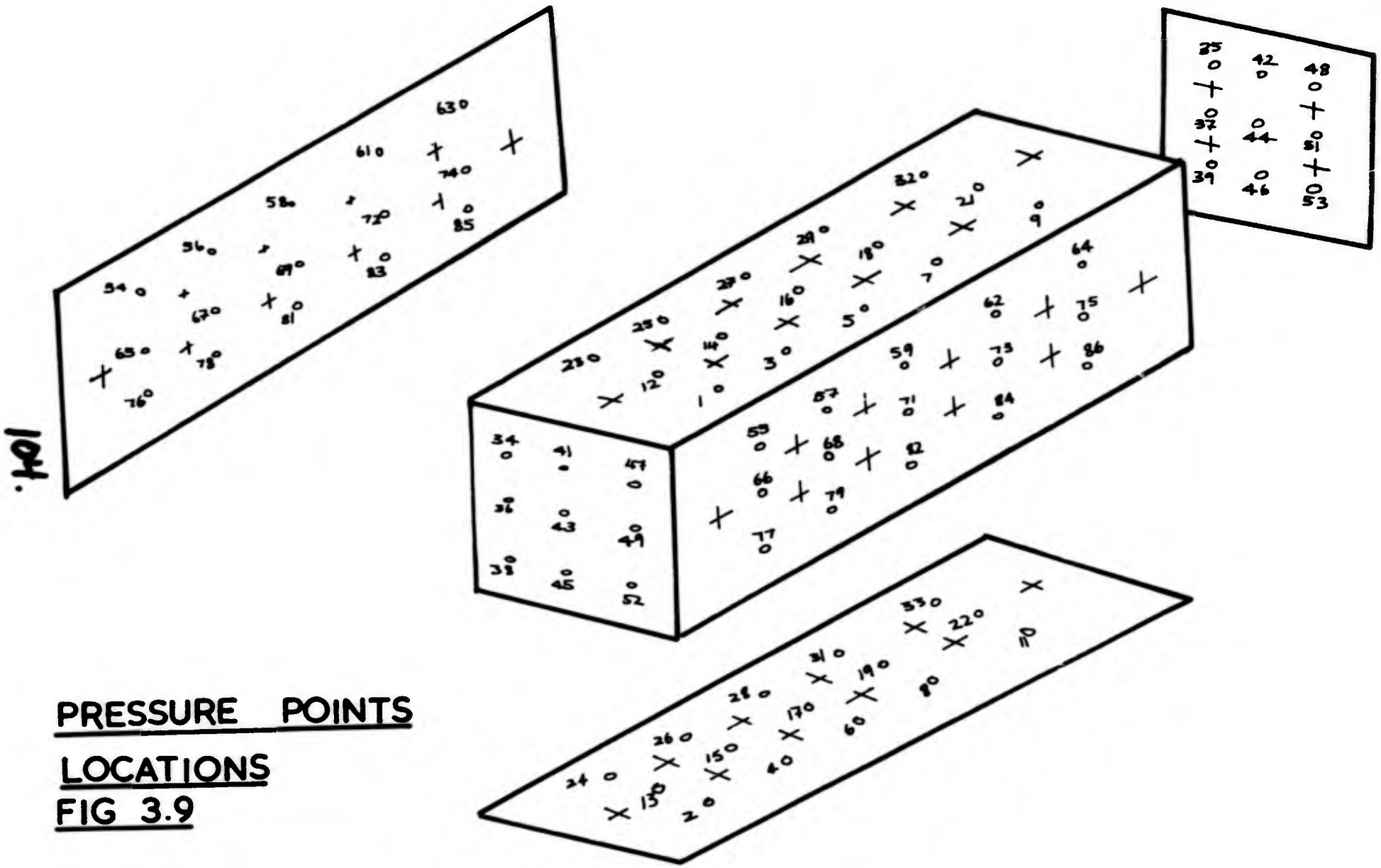

PRESSURE POINTS

LOCATIONS

FIG 3.9

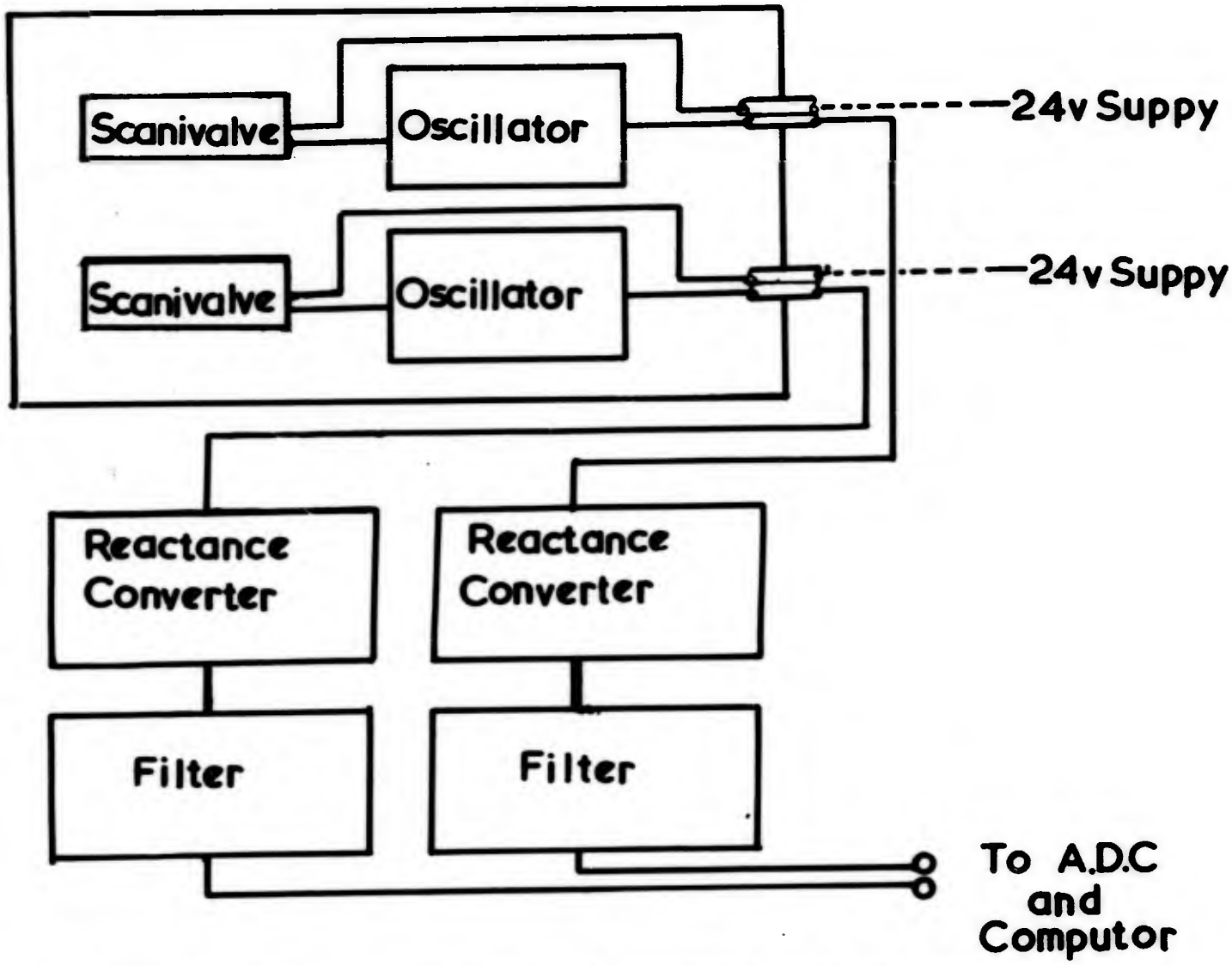

FIG 3.10 SCHEMATIC LAYOUT OF INSTRUMENTATION

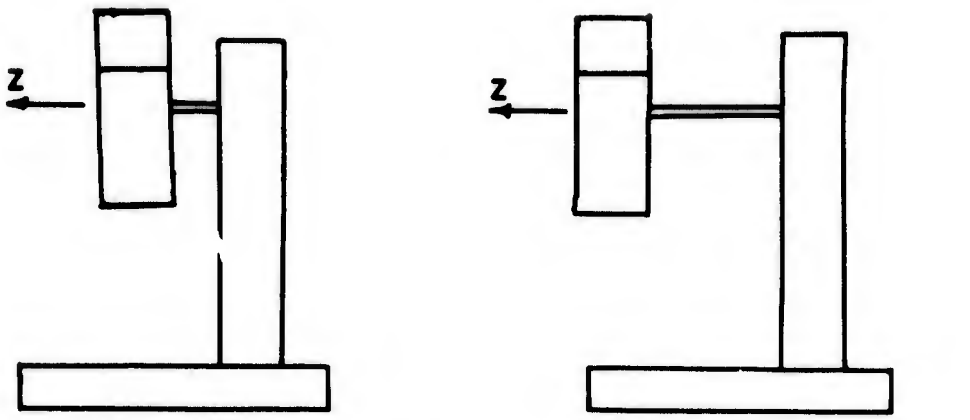

short sting (producing interference)

long sting (interference free)

(air flow out of plane of paper)

FIGURE 4·1

STING SUPPORT ARRANGEMENTS FOR 1:0·4:0·4 SMALL (PILOT) CONTAINER MODEL.

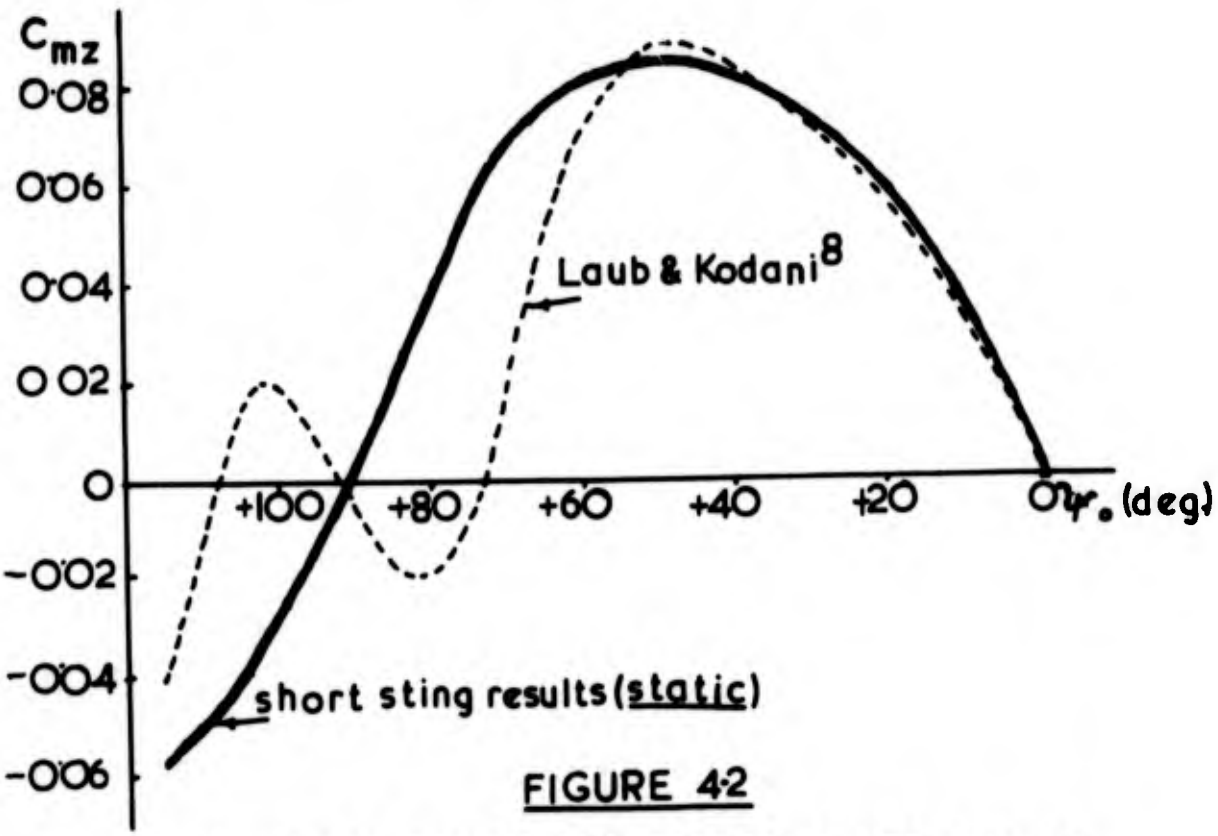

FIGURE 4·2

$C_{mz} \sim \gamma_{r_0}$ FOR SHORT-STING PILOT MODEL (C_{mz} BASED ON S=0·4 m², d=1')

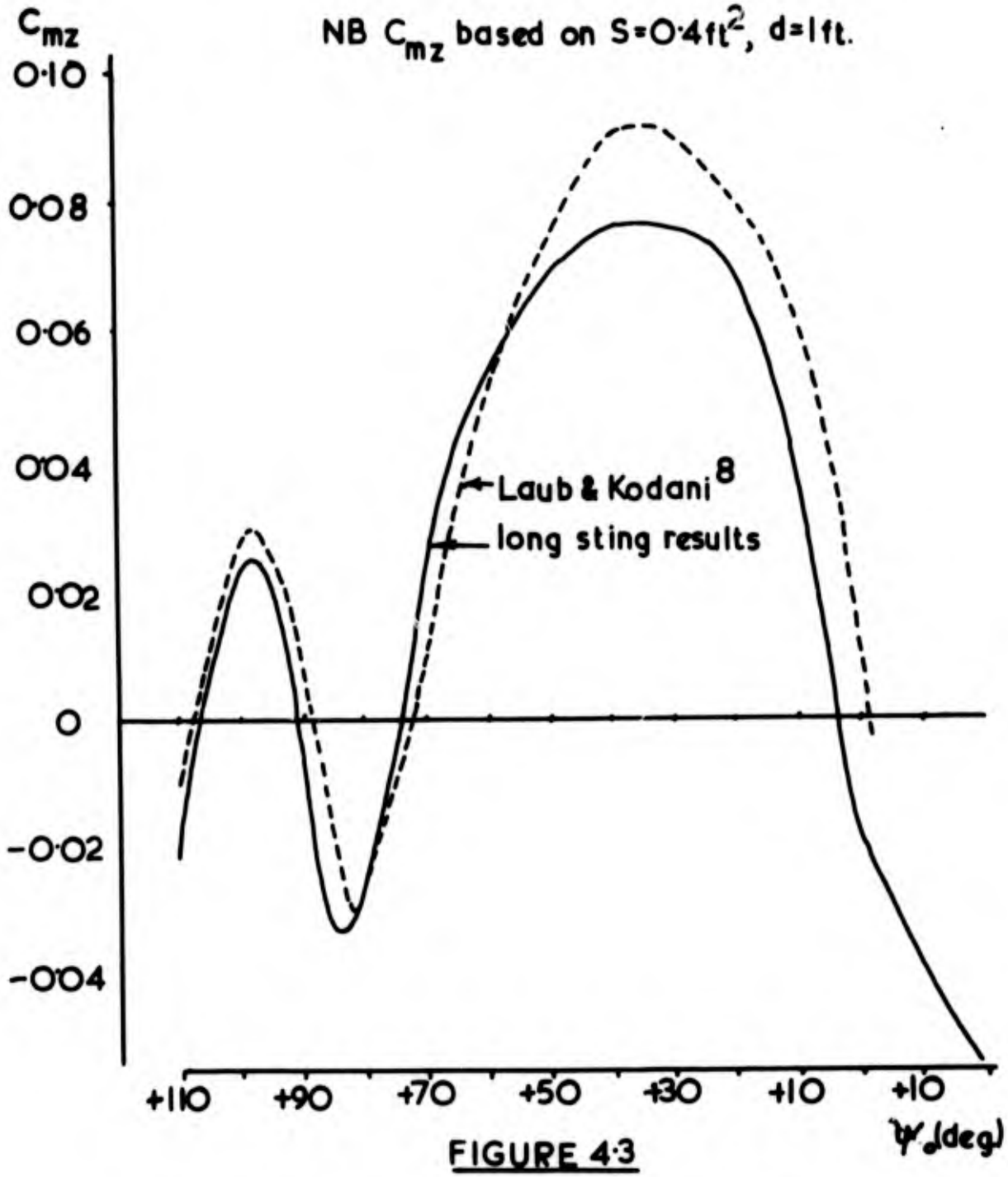

FIGURE 4·3

COMPARISON OF PRESSURE-INTEGRATED AND DIRECTLY-MEASURED PITCHING MOMENT RESULTS FOR 1:0·4:0·4 PILOT MODEL.

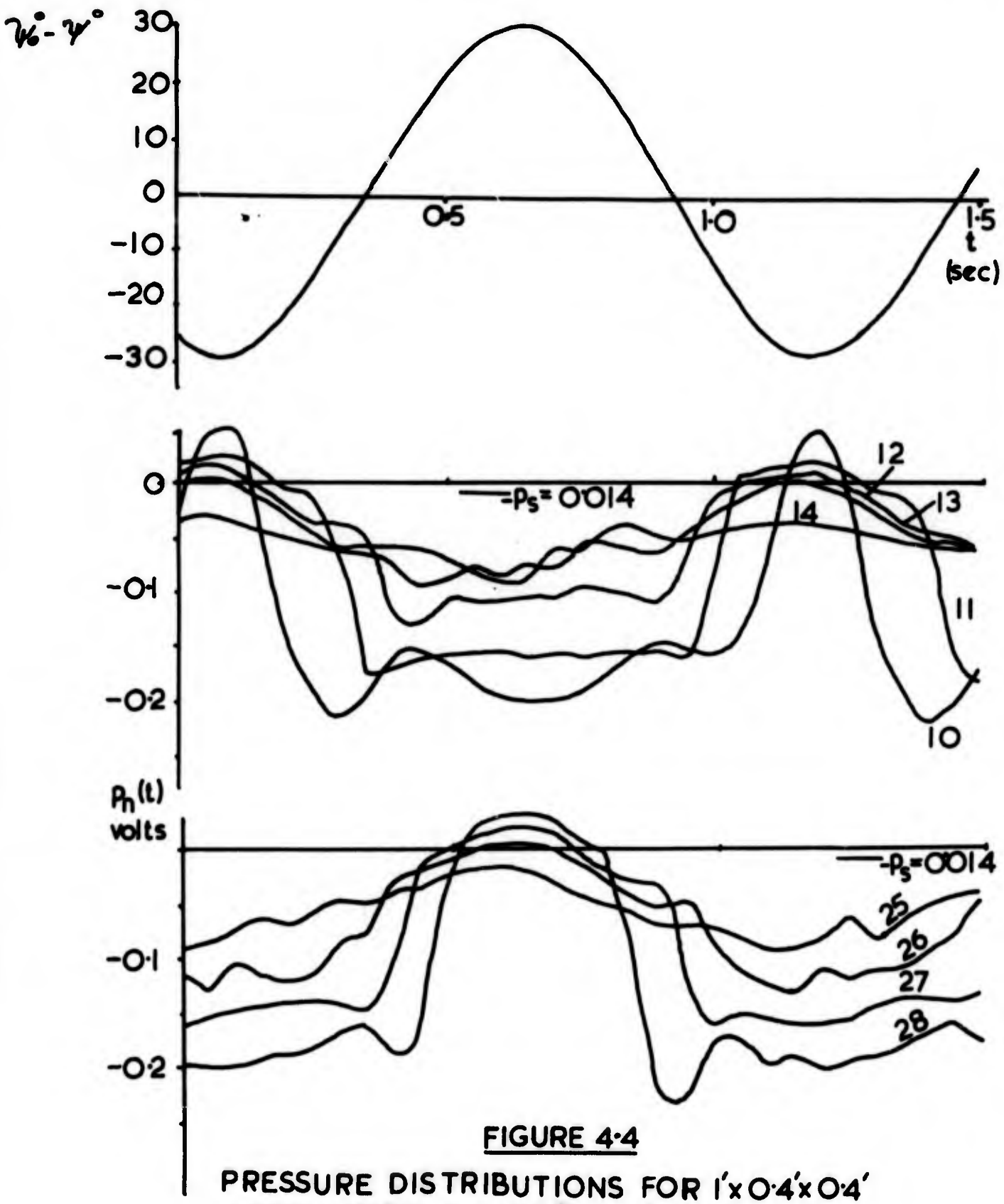

FIGURE 4·4

PRESSURE DISTRIBUTIONS FOR 1'x 0·4'x 0·4' MODEL WHEN $\psi_0 = +90°$, V=48 f/s.

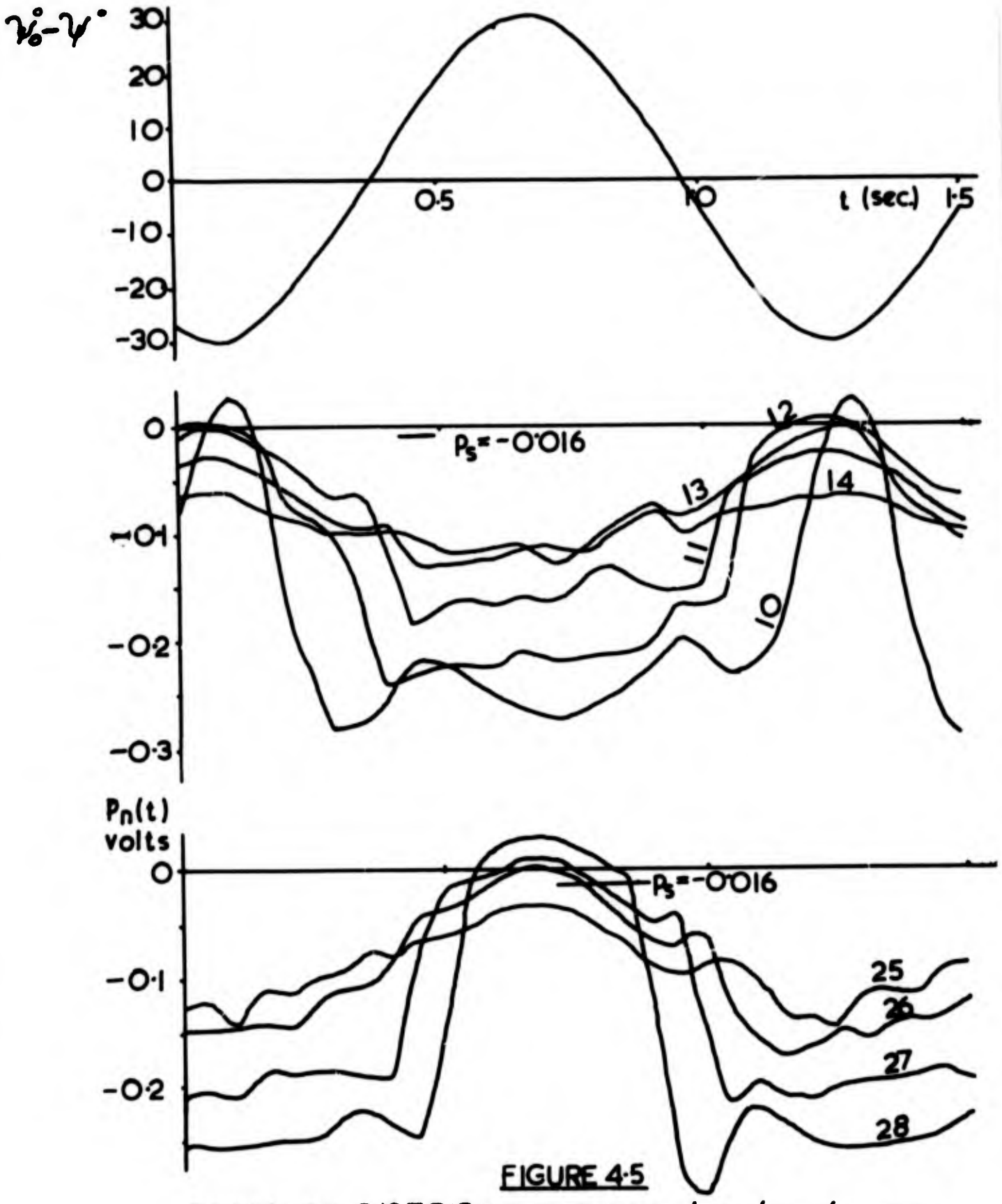

FIGURE 4·5

PRESSURE DISTRIBUTIONS FOR 1'×0·4'×0·4' MODEL WHEN $\psi_0 = +90°$, V=55 f/s.

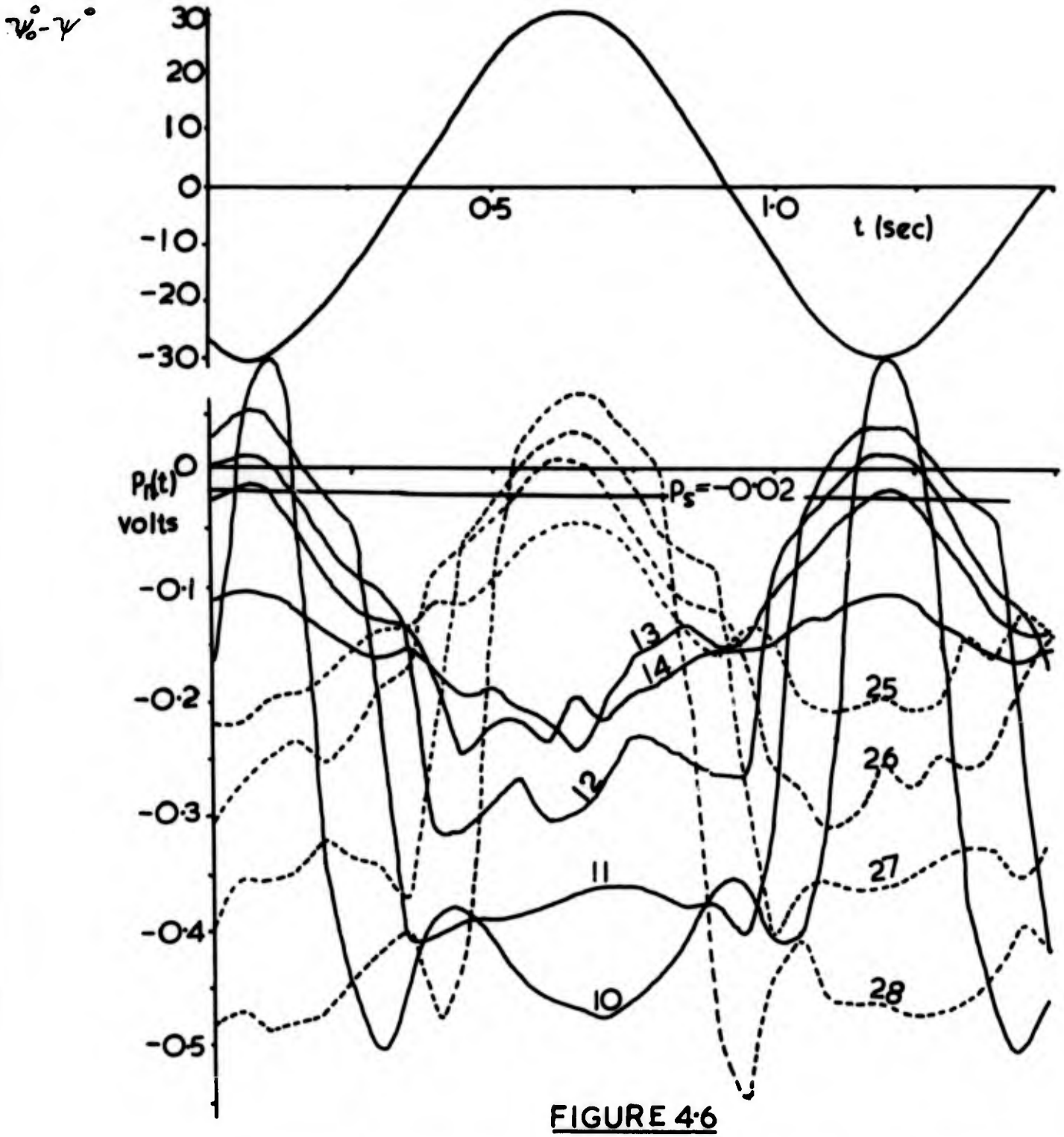

FIGURE 4·6

PRESSURE DISTRIBUTIONS FOR 1′ x 0·4′ x 0·4′ MODEL WHEN $\psi_0 = +90^\circ$, V = 66 f/s.

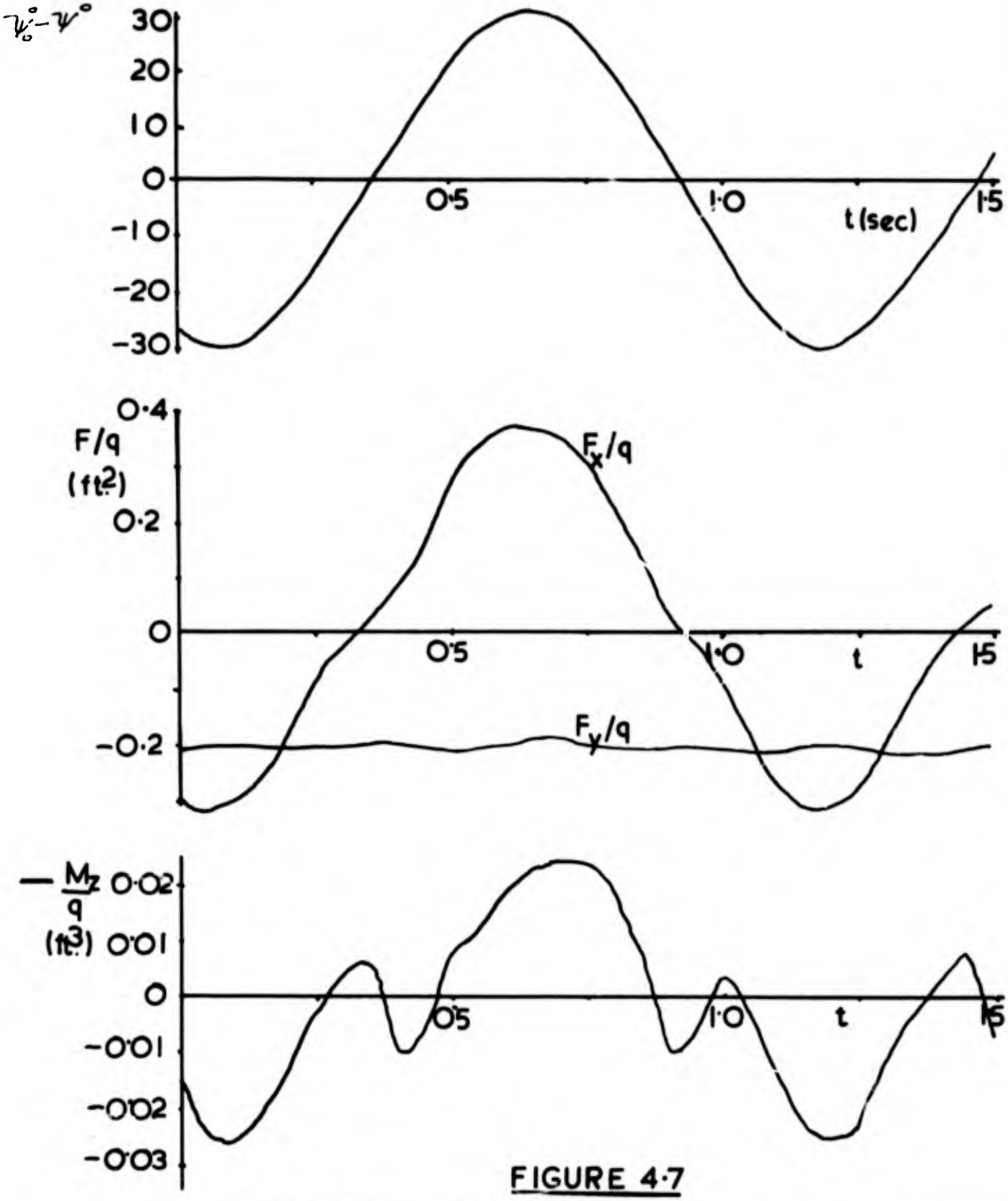

FIGURE 4·7

INTEGRATED FORCES AND MOMENT FOR 1'x0·4'x0·4' MODEL WITH $\psi_o = +90^\circ$, V=48 f/s.

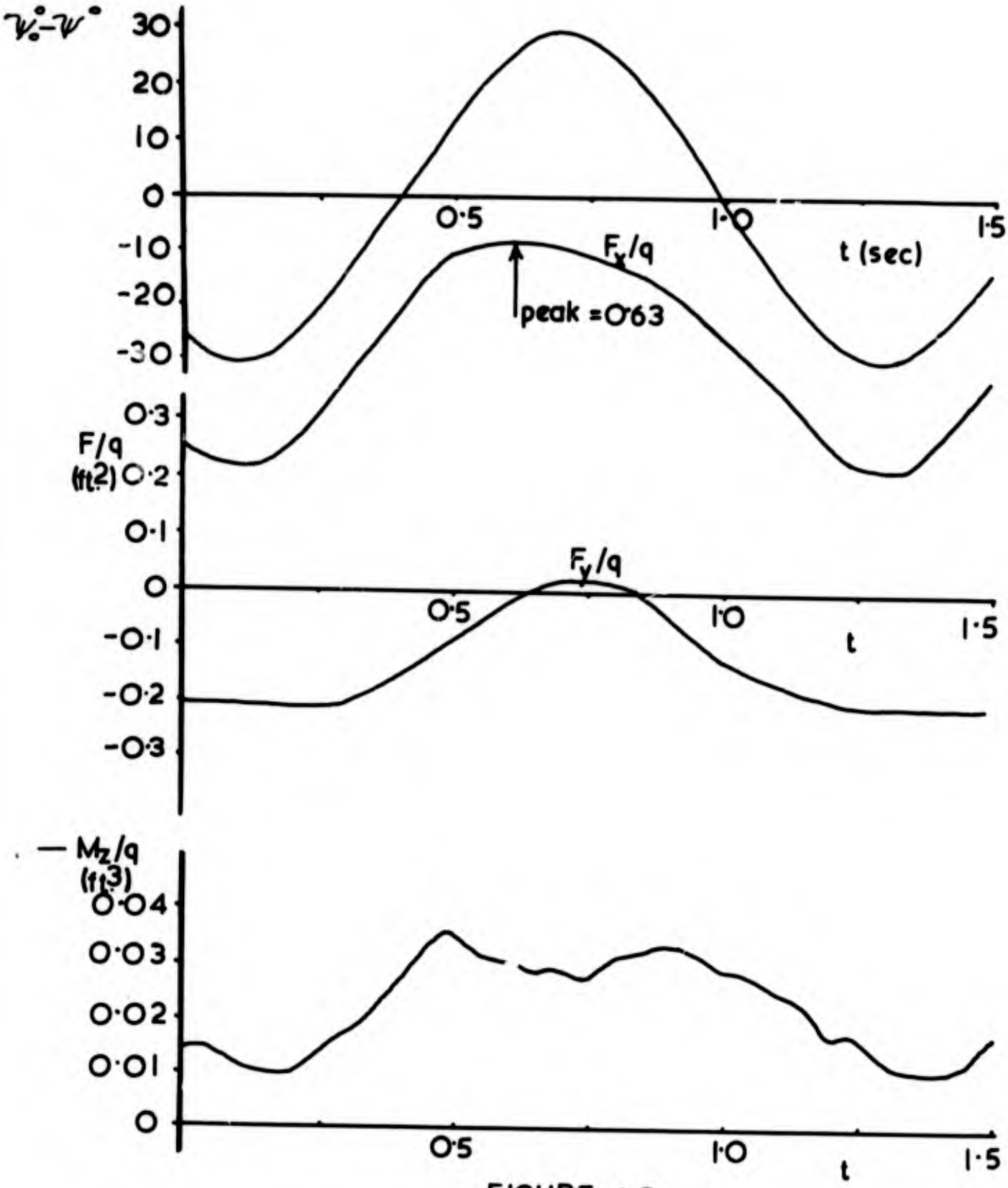

FIGURE 4·8

INTEGRATED FORCES AND MOMENT FOR 1'x0·4'x 0·4' MODEL WITH $\psi_o = +45°$, V=48 f/s.

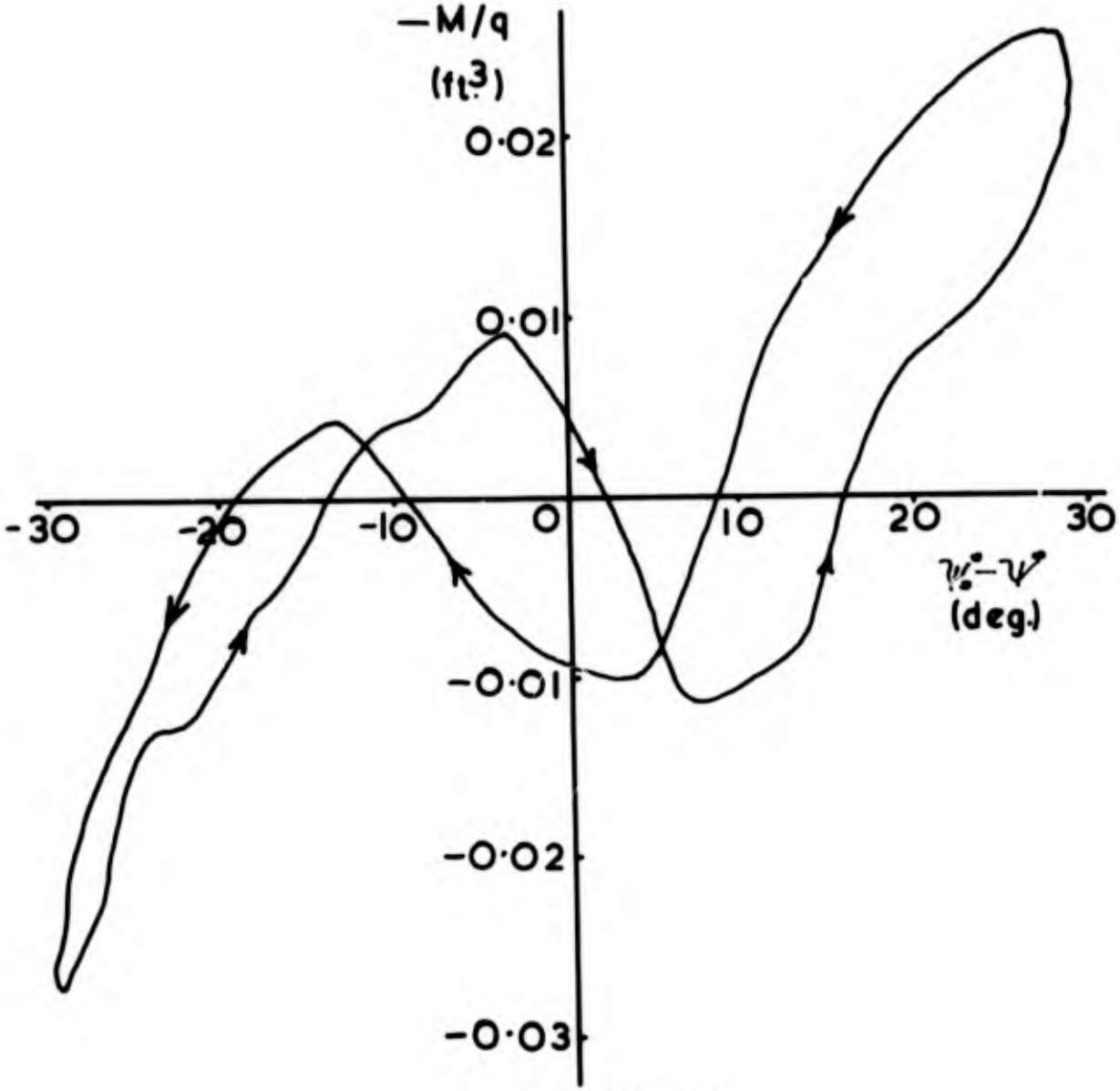

FIGURE 4·9

—M/q ~ $\psi_0 - \psi$, LOOP DIAGRAM FOR 1'x0·4'x 0·4' MODEL WITH $\psi_0 = +90^\circ$, V=48f/s.

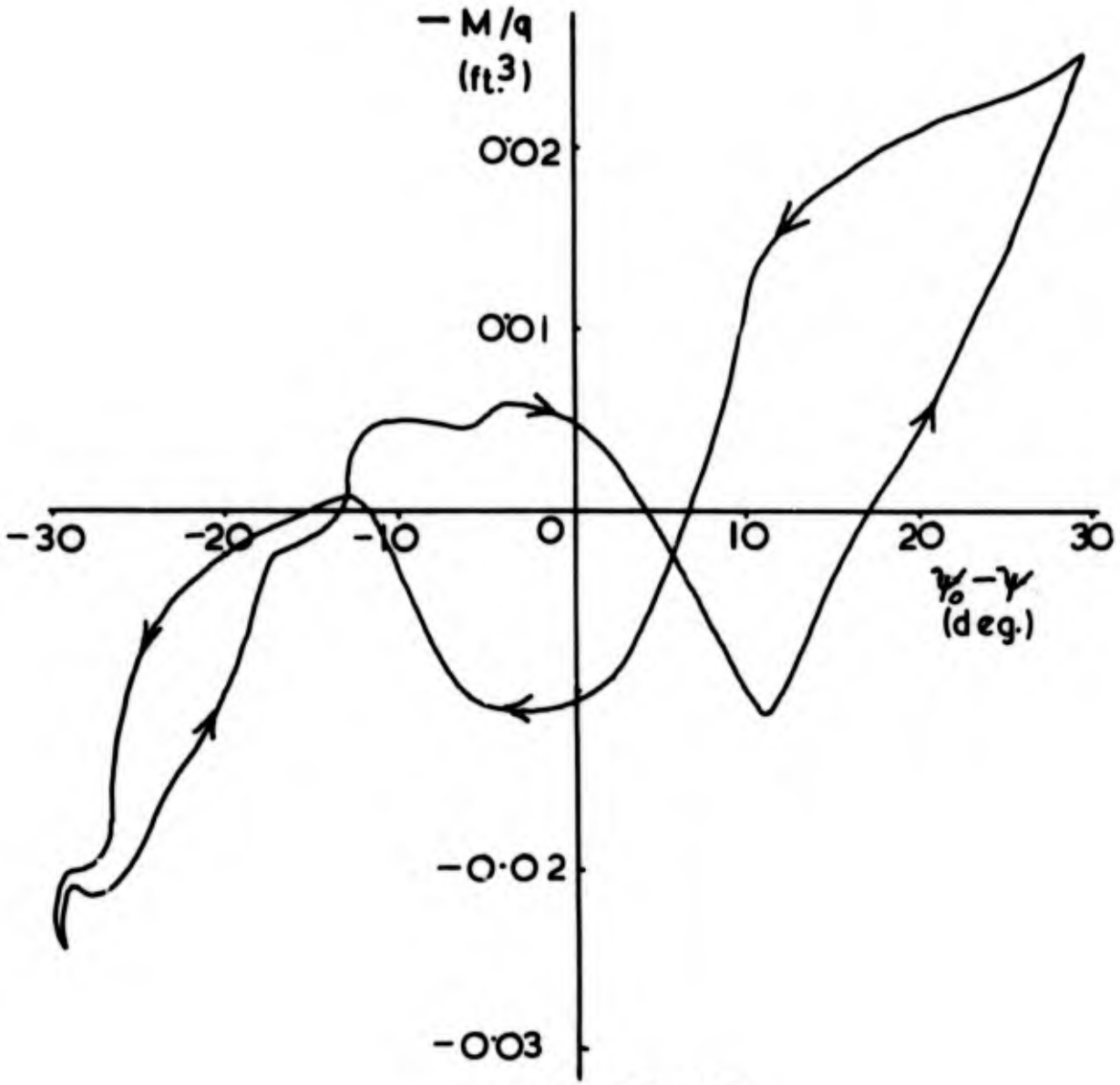

FIGURE 4·10

$-M/q \sim \psi_0 - \psi$ LOOP DIAGRAM FOR 1′ x 0·4′ x 0·4′ MODEL WITH $\psi_0 = +90^\circ$, V = 55 f/s.

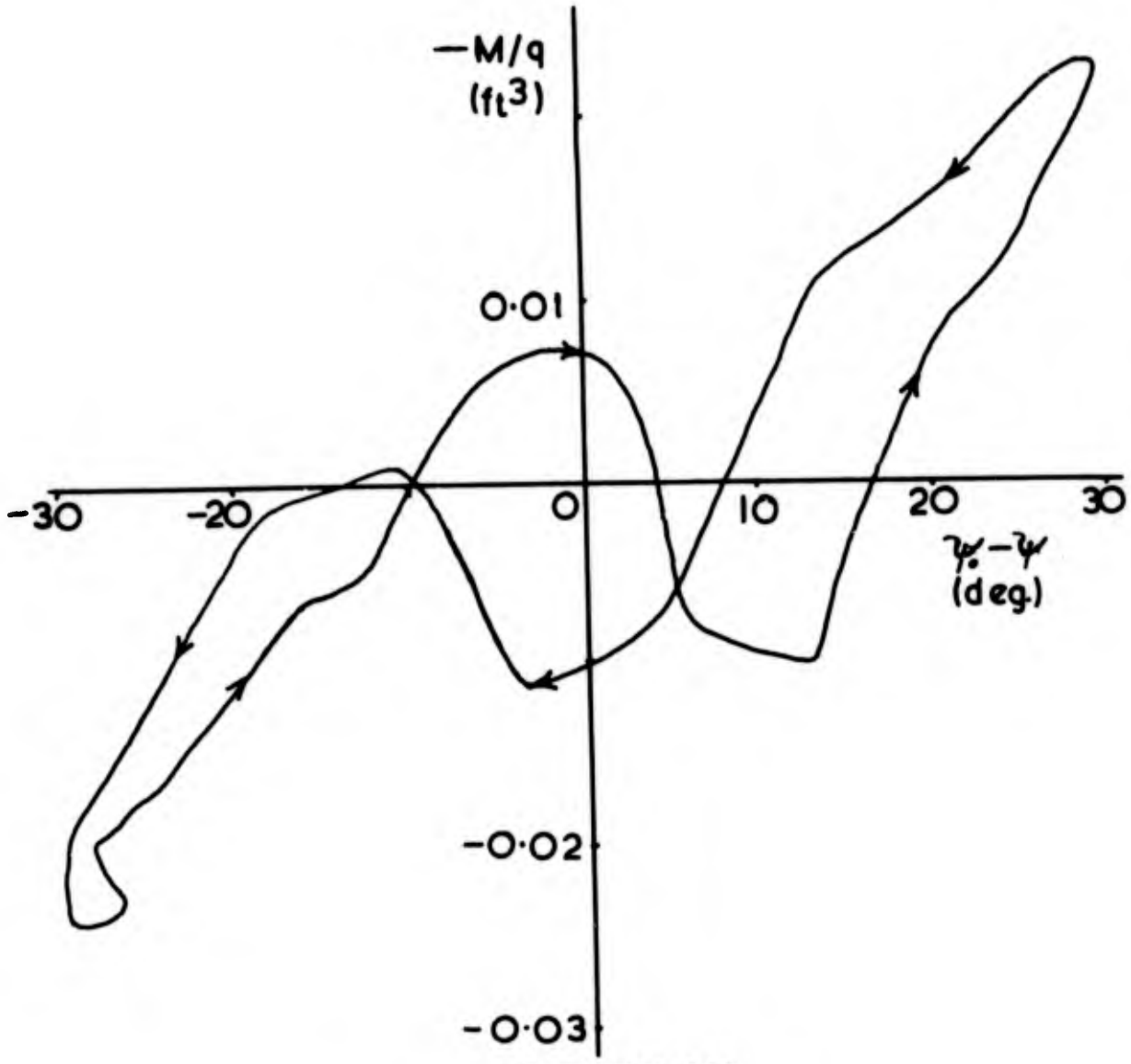

FIGURE 4·11

$-M/q \sim \psi_0 - \psi$ LOOP DIAGRAM FOR 1′×0·4′×0·4′ MODEL WITH $\psi_0 = +90^0$, V=66 f/s.

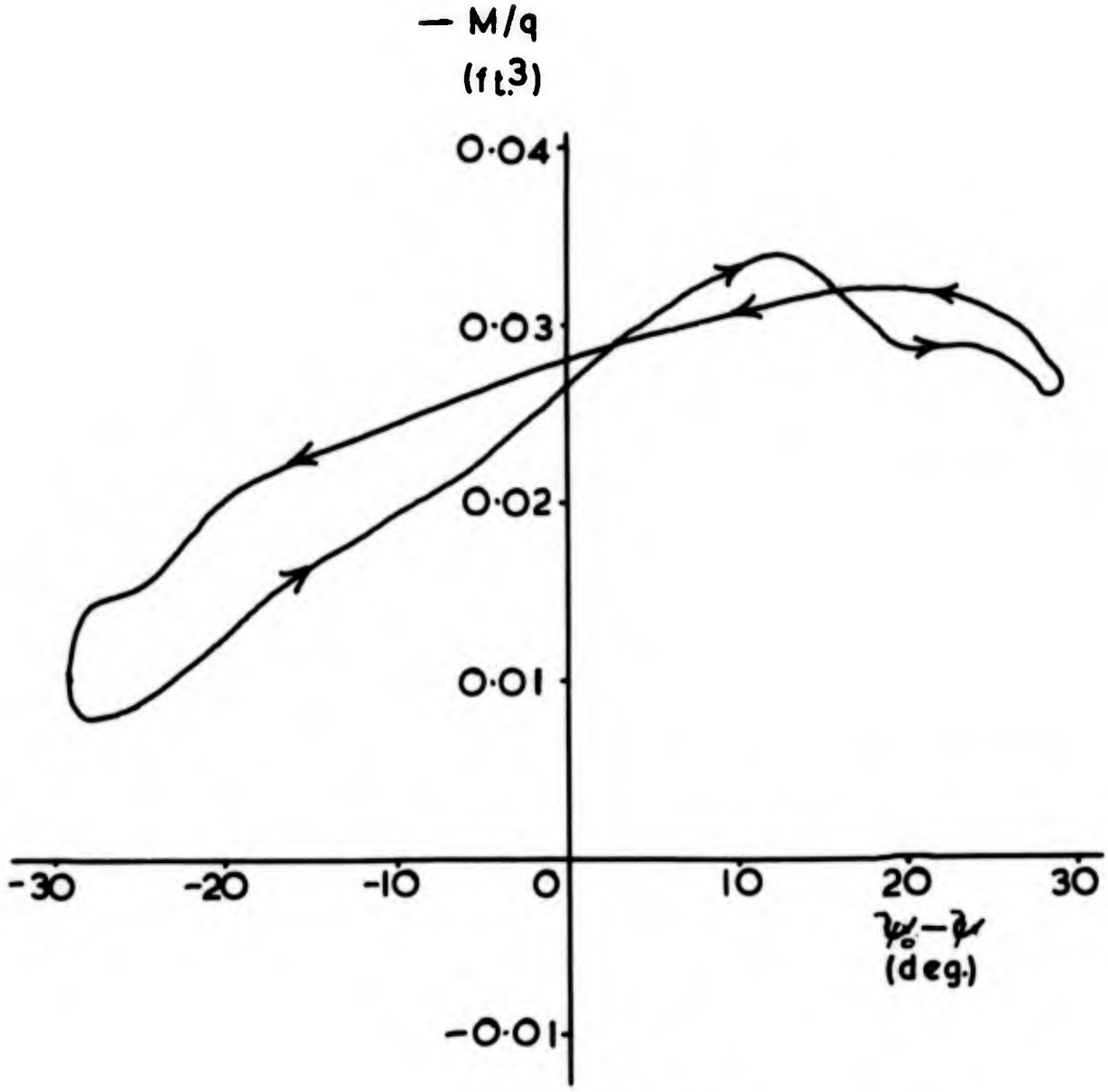

FIGURE 4·12

— M/q ~ $\psi_0 - \psi$ LOOP DIAGRAM FOR 1'x0·4'x0·4' MODEL WITH $\psi_0 = +45°$, V = 48 f/s.

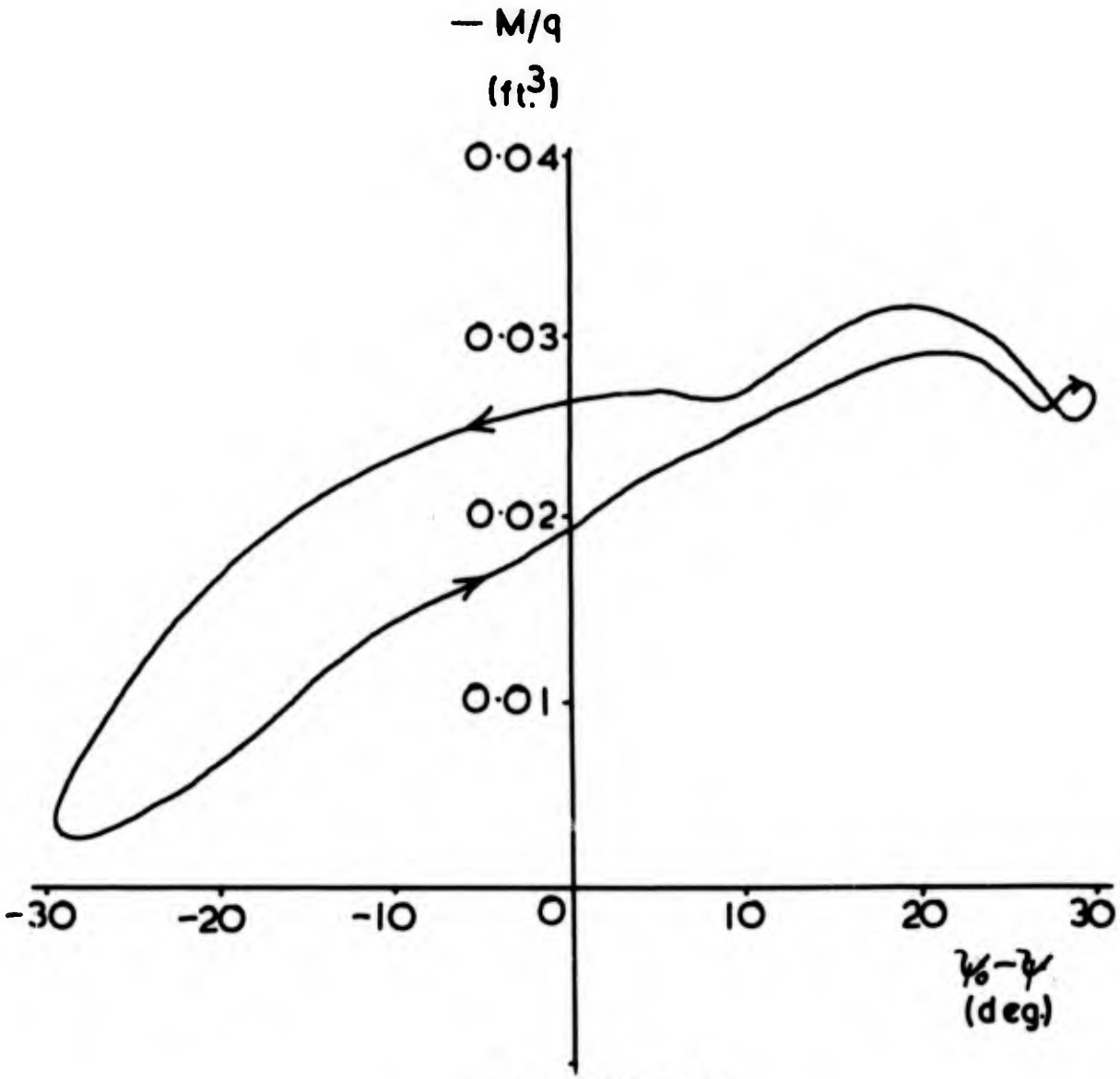

FIGURE 4·13

$-M/q \sim \psi_0 - \psi$ LOOP DIAGRAM FOR 1'x0·4'x0·4' MODEL WITH $\psi_0 = +45°$, V=66 f/s.

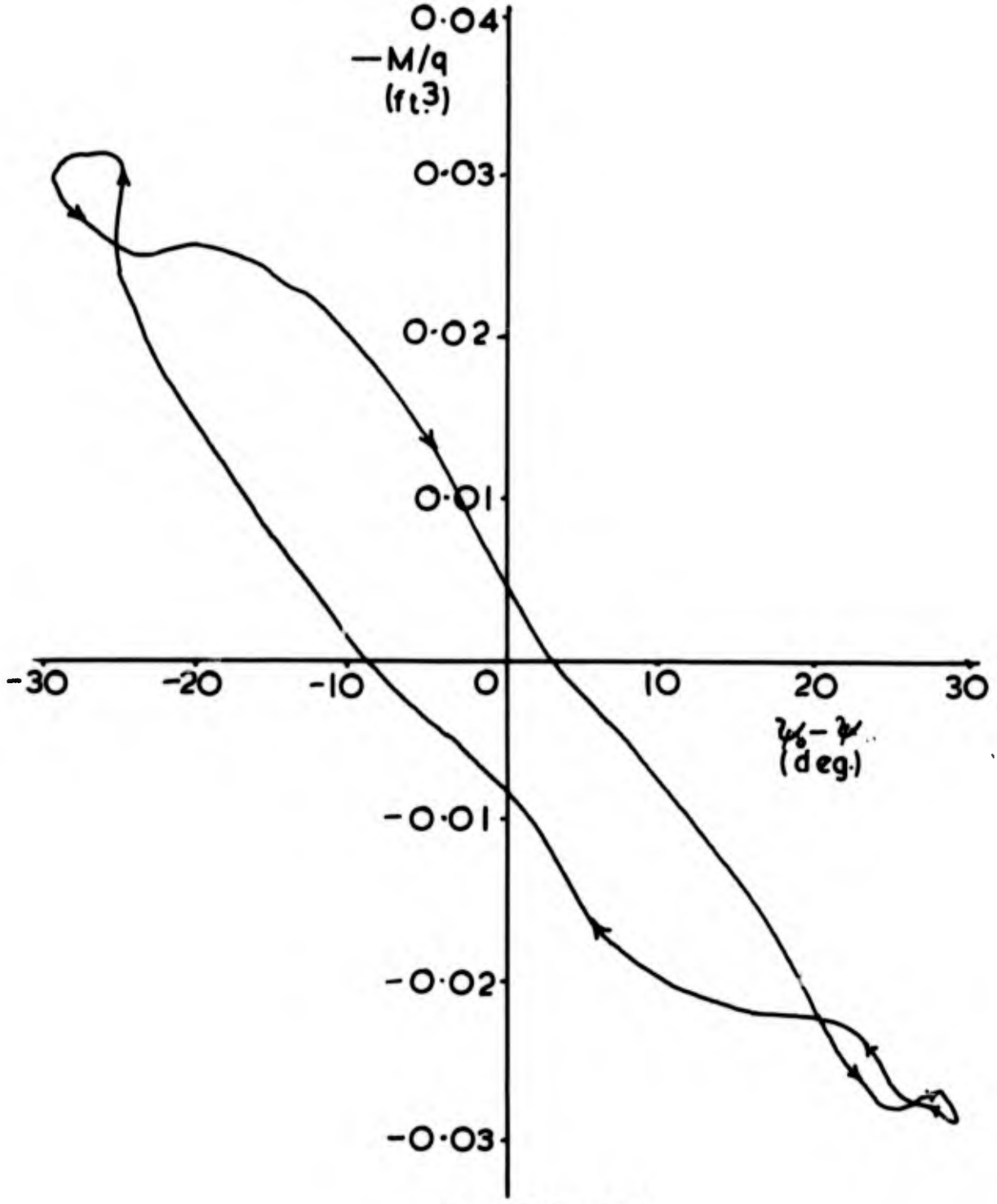

FIGURE 4·14

$-M/q \sim \psi - \psi_0$ LOOP DIAGRAM FOR 1′×0·4′×0·4′ MODEL WITH $\psi_0 = 0$, V=48 f/s.

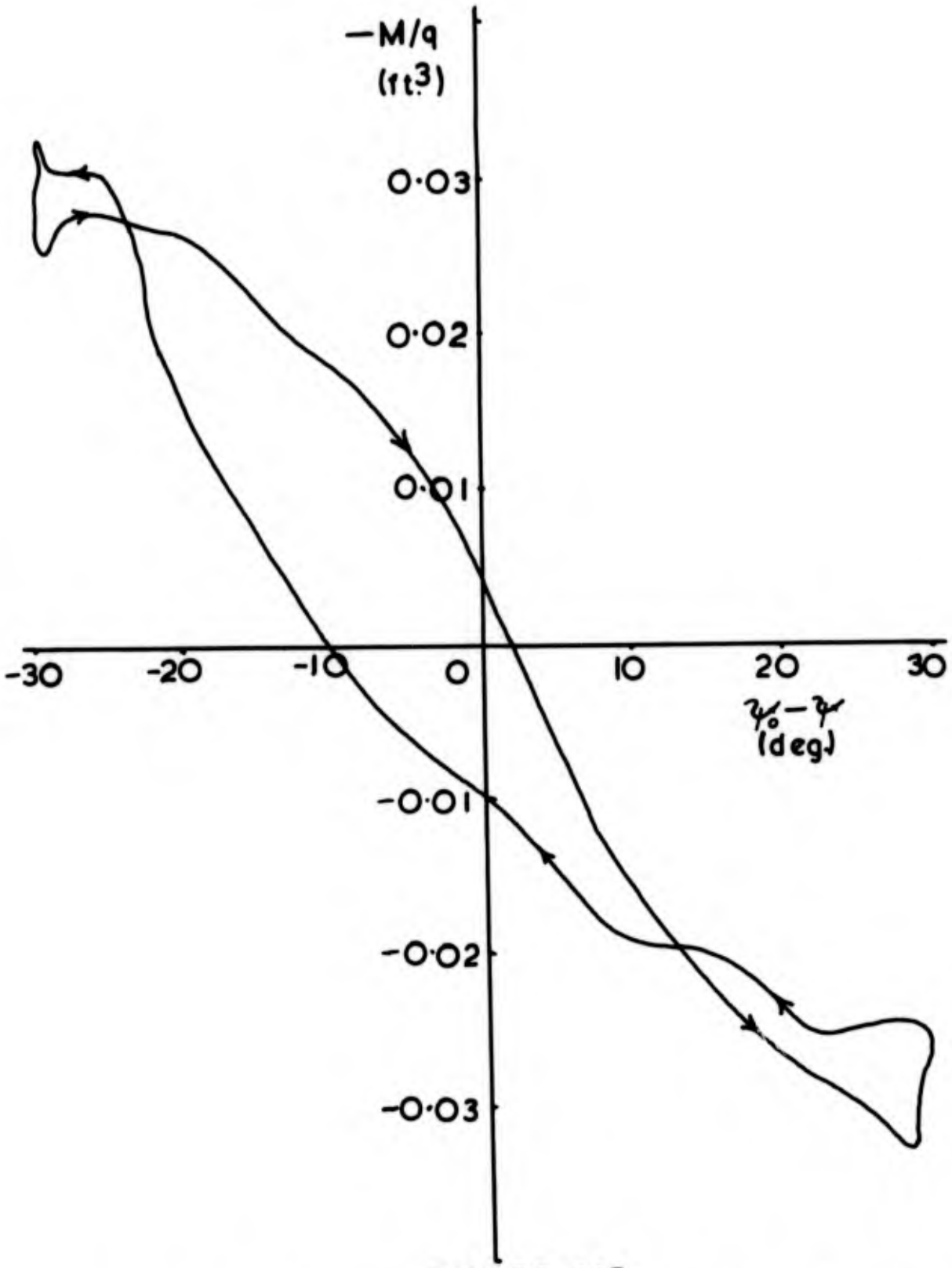

FIGURE 4·15

$-M/q \sim \gamma_0 - \gamma$ LOOP DIAGRAM FOR 1'x0·4'x 0·4' MODEL WITH $\gamma_0 = 0$, V = 55 f/s.

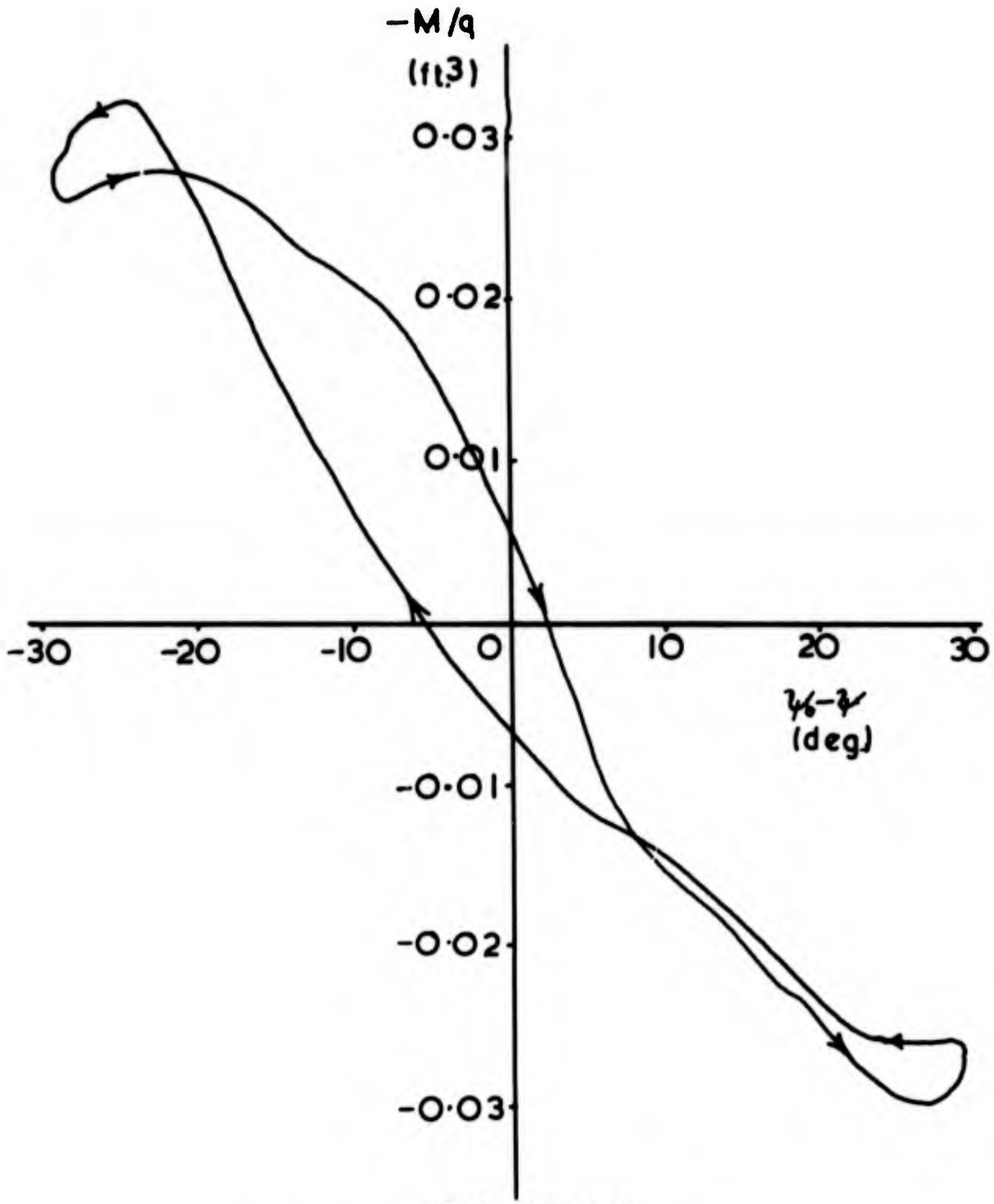

FIGURE 4·16

$-M/q \sim \psi_0 - \psi$ LOOP DIAGRAM FOR 1'x0·4'x0·4' MODEL WITH $\psi_0 = 0$, V= 66 f/s.

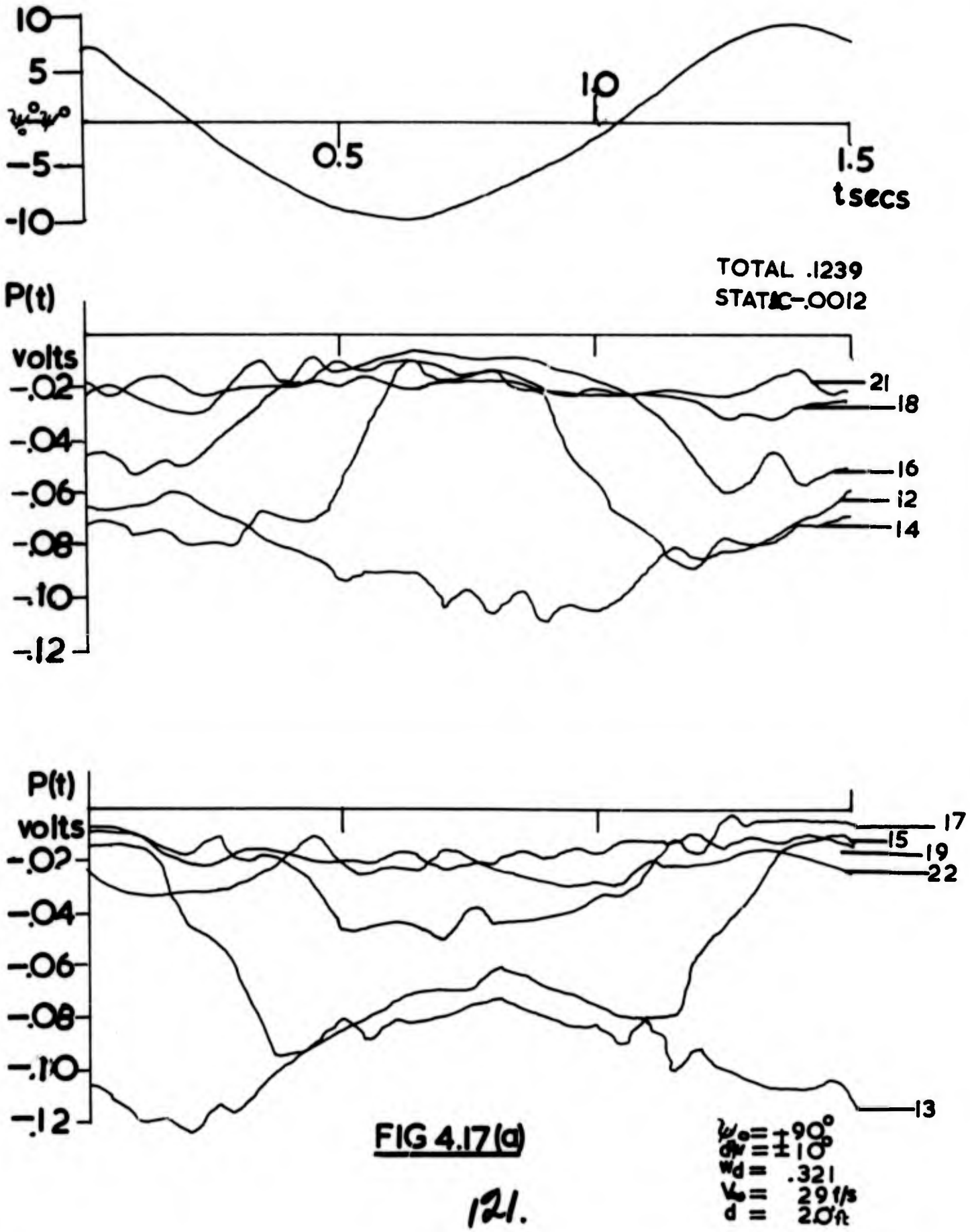

FIG 4.17(a)

$\psi_o = \pm 90°$
$\phi_w = \pm 10°$
$w_d = .321$
$V_\infty = 29$ f/s
$d = 2.0$ ft

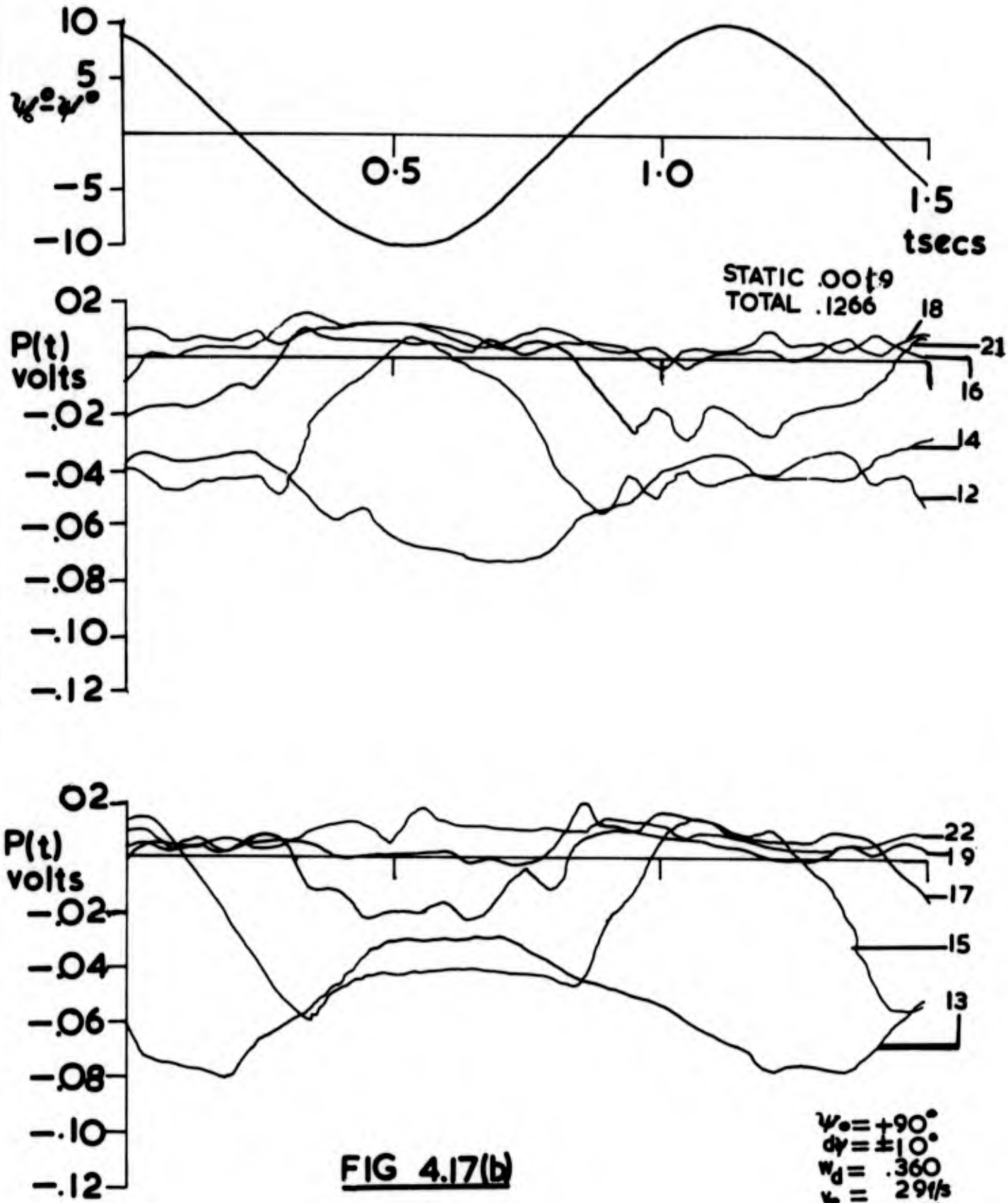
10
5
$\psi^\circ = \psi^\circ$
−5
−10
0·5
1·0
1·5
tsecs
STATIC .0019
TOTAL .1266
02
P(t)
volts
−.02
−.04
−.06
−.08
−.10
−.12
18
21
16
14
12
02
P(t)
volts
−.02
−.04
−.06
−.08
−.10
−.12
22
19
17
15
13
$\psi_\circ = \pm 90^\circ$
$d\psi = \pm 10^\circ$
$w_d = .360$
$v_a = 291/s$
$d = 2.0'$

FIG 4.17(b)

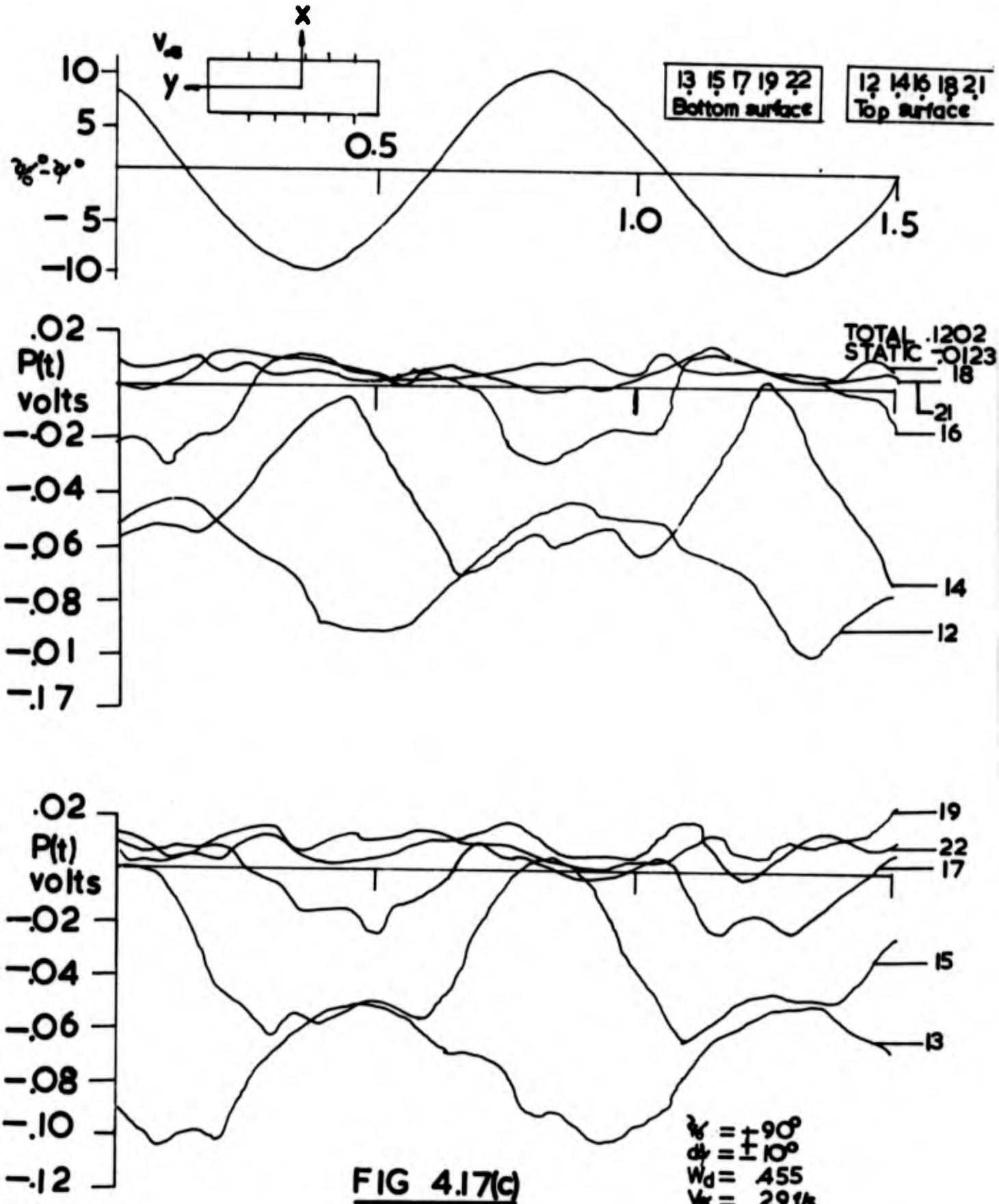
X
y
10
5
0.5
1.0
1.5
−5
−10
13 15 17 19 22
Bottom surface
12 14 16 18 21
Top surface
.02
P(t)
volts
−.02
−.04
−.06
−.08
−.01
−.17
TOTAL .1202
STATIC .0123
18
21
16
14
12
.02
P(t)
volts
−.02
−.04
−.06
−.08
−.10
−.12
19
22
17
15
13
$\psi = \pm 90°$
$d\psi = \pm 10°$
$W_d = .455$
$V_\infty = 29$ f/s
$d = 2.0$ ft

FIG 4.17(c)

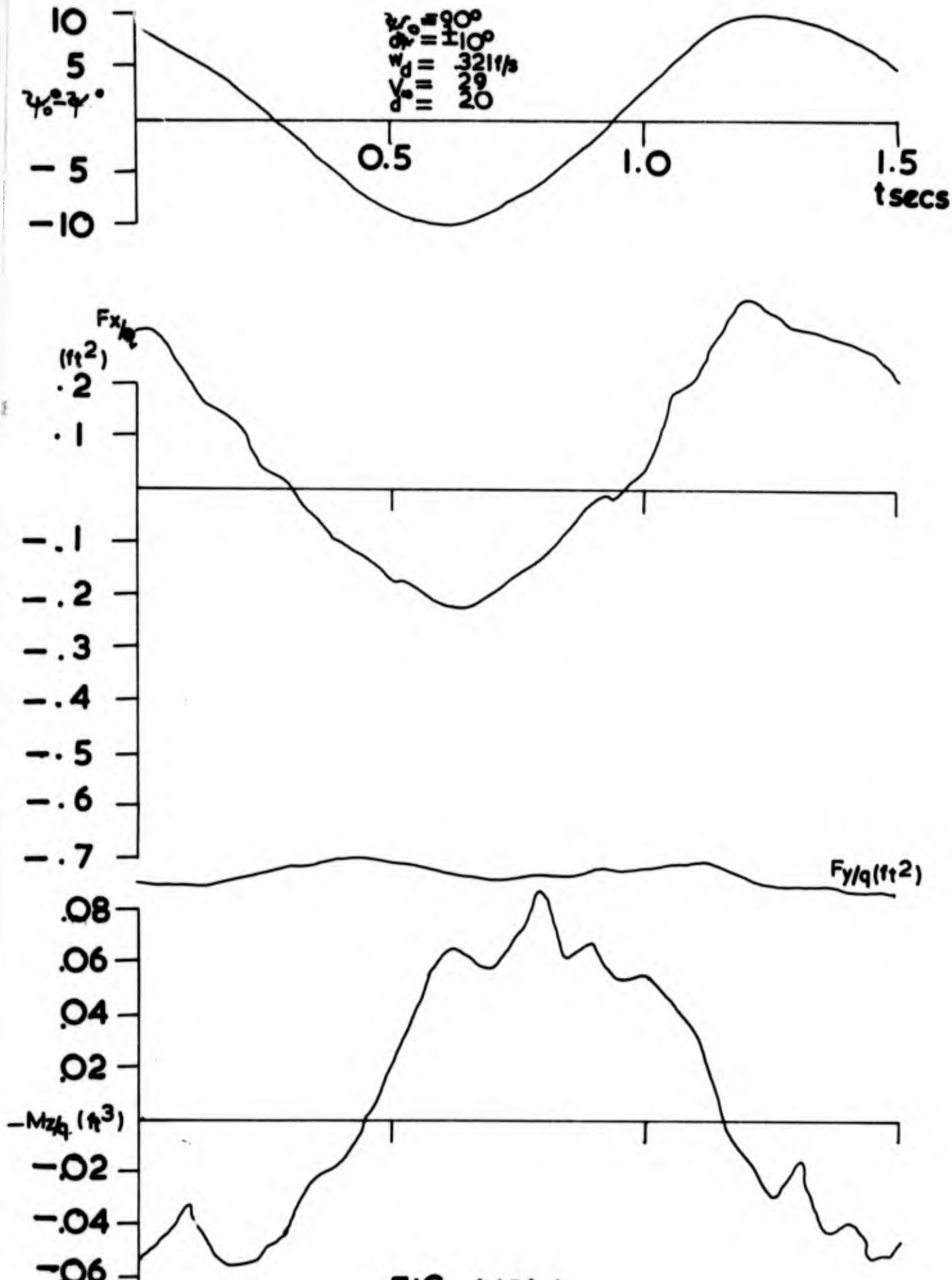
10
5
$\gamma_0 - \psi$°
−5
−10
$\gamma_0 = 90°$
$\phi_0 = \pm 10°$
$w_d = 32$ ft/s
$V_0 = 29$
$d = 20$
0.5
1.0
1.5
t secs
F_x/q (ft²)
.2
.1
−.1
−.2
−.3
−.4
−.5
−.6
−.7
F_y/q (ft²)
.08
.06
.04
.02
$-M_{z_q}$ (ft³)
−.02
−.04
−.06
−.08

FIG 4.18(a)

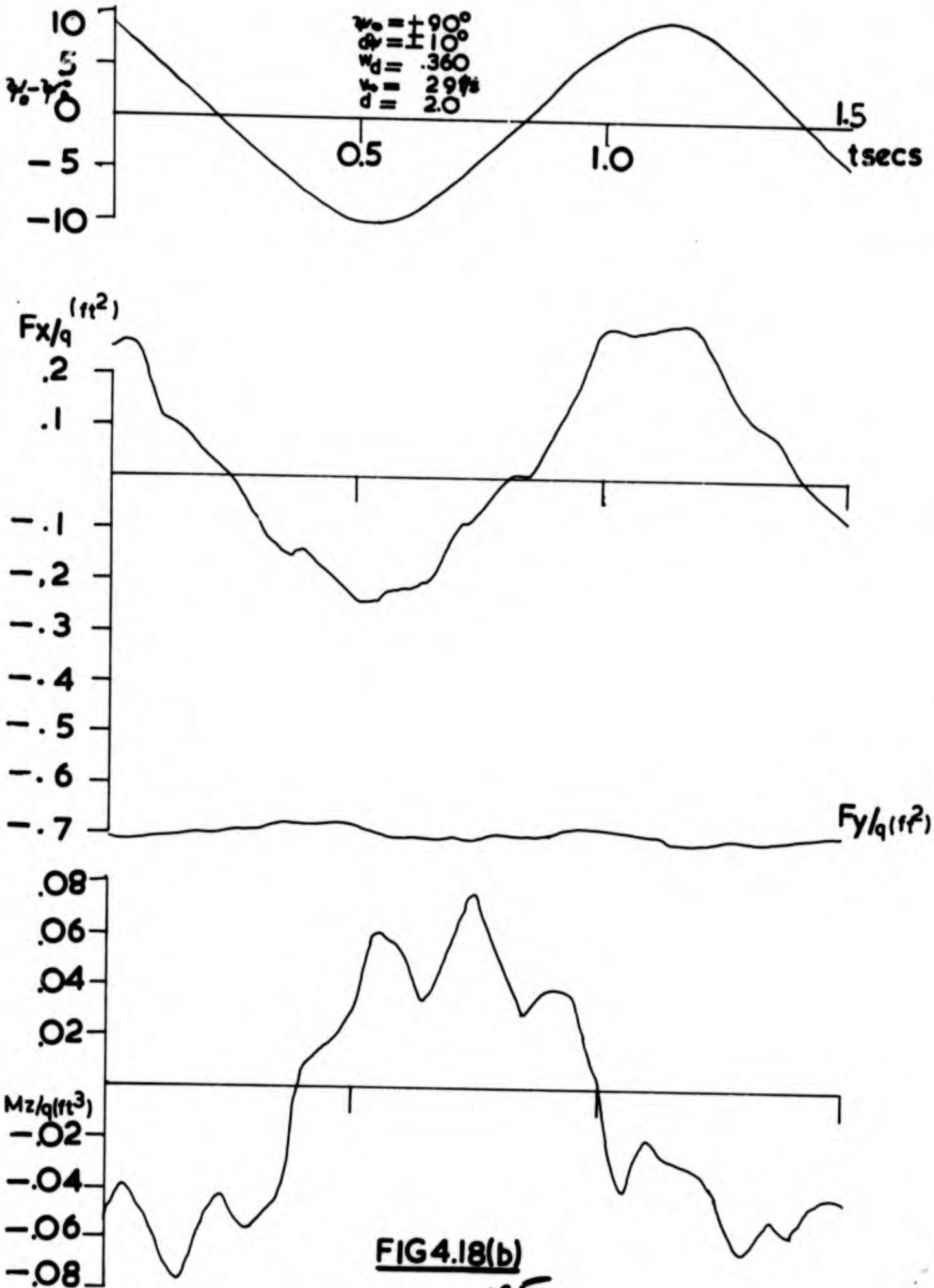
10
5
0
−5
−10
ψ-ψ₀
ψ₀ = ±90°
φ = ±10°
w_d = .360
w_h = 29 ft
d = 2.0
0.5
1.0
1.5
tsecs
Fx/q (ft²)
.2
.1
−.1
−.2
−.3
−.4
−.5
−.6
−.7
Fy/q (ft²)
.08
.06
.04
.02
Mz/q (ft³)
−.02
−.04
−.06
−.08

FIG 4.18(b)

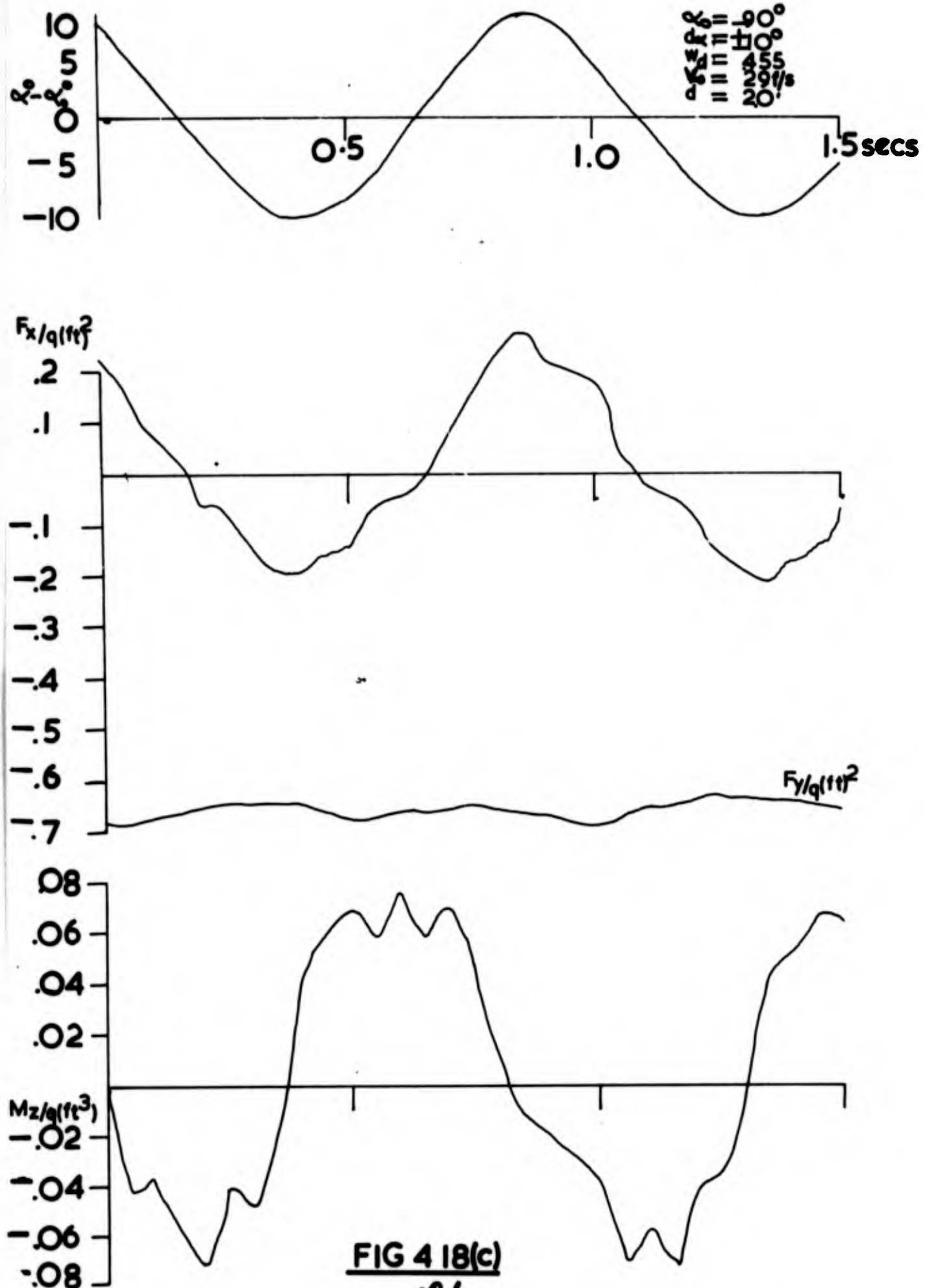
10
5
0
−5
−10
α − α₀
0·5
1.0
1.5 secs
α₀ = −90°
α = ±10°
= 455
= 29 f/s
= 20°
Fx/q(ft)²
.2
.1
−.1
−.2
−.3
−.4
−.5
−.6
−.7
Fy/q(ft)²
.08
.06
.04
.02
Mz/q(ft³)
−.02
−.04
−.06
−.08

FIG 4 18(c)

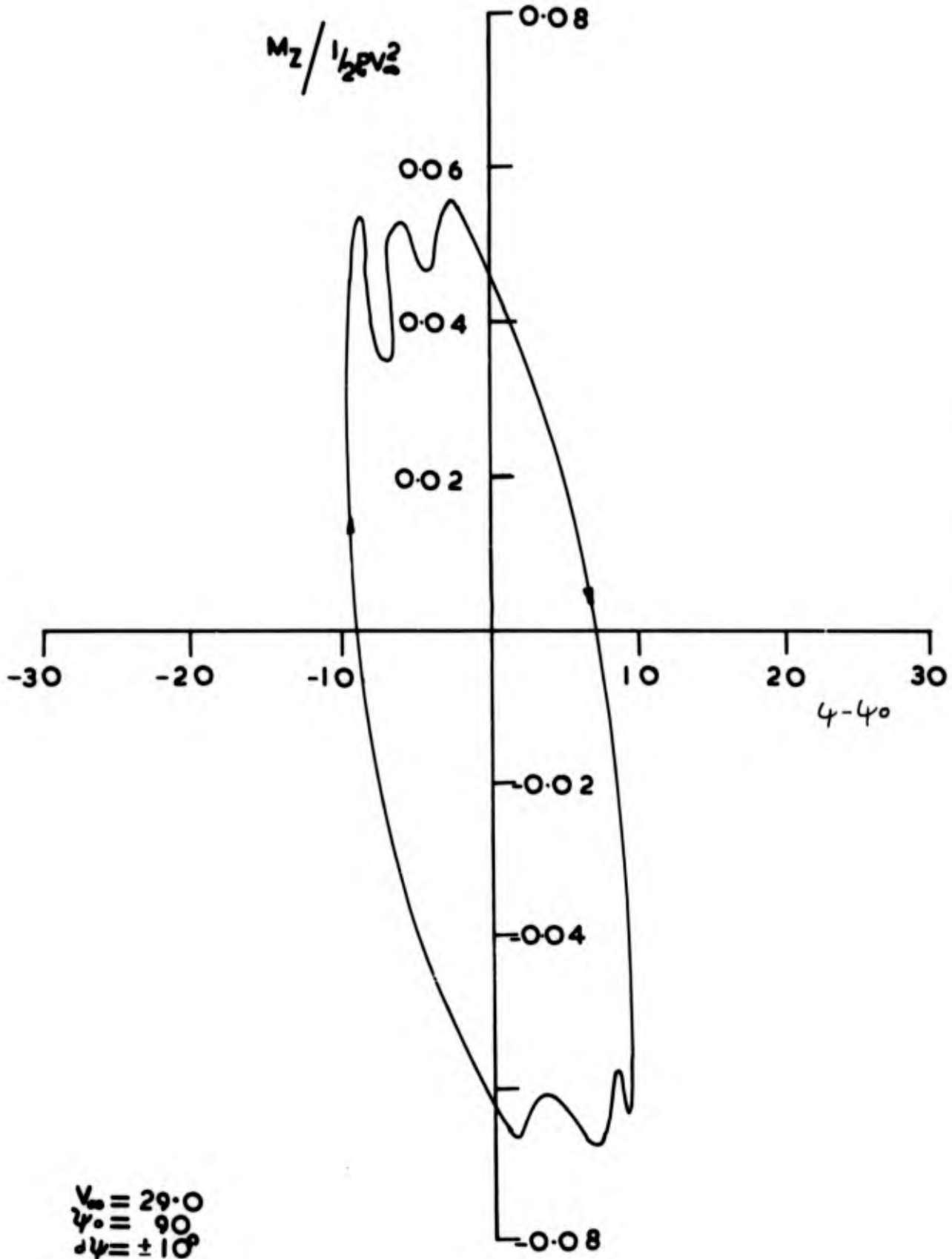

$V_\infty = 29{\cdot}0$
$\psi_0 = 90$
$\Delta\psi = \pm 10^\circ$
$T_p = 1{\cdot}35$
$W_d = {\cdot}32$

FIG 4.19 (a)

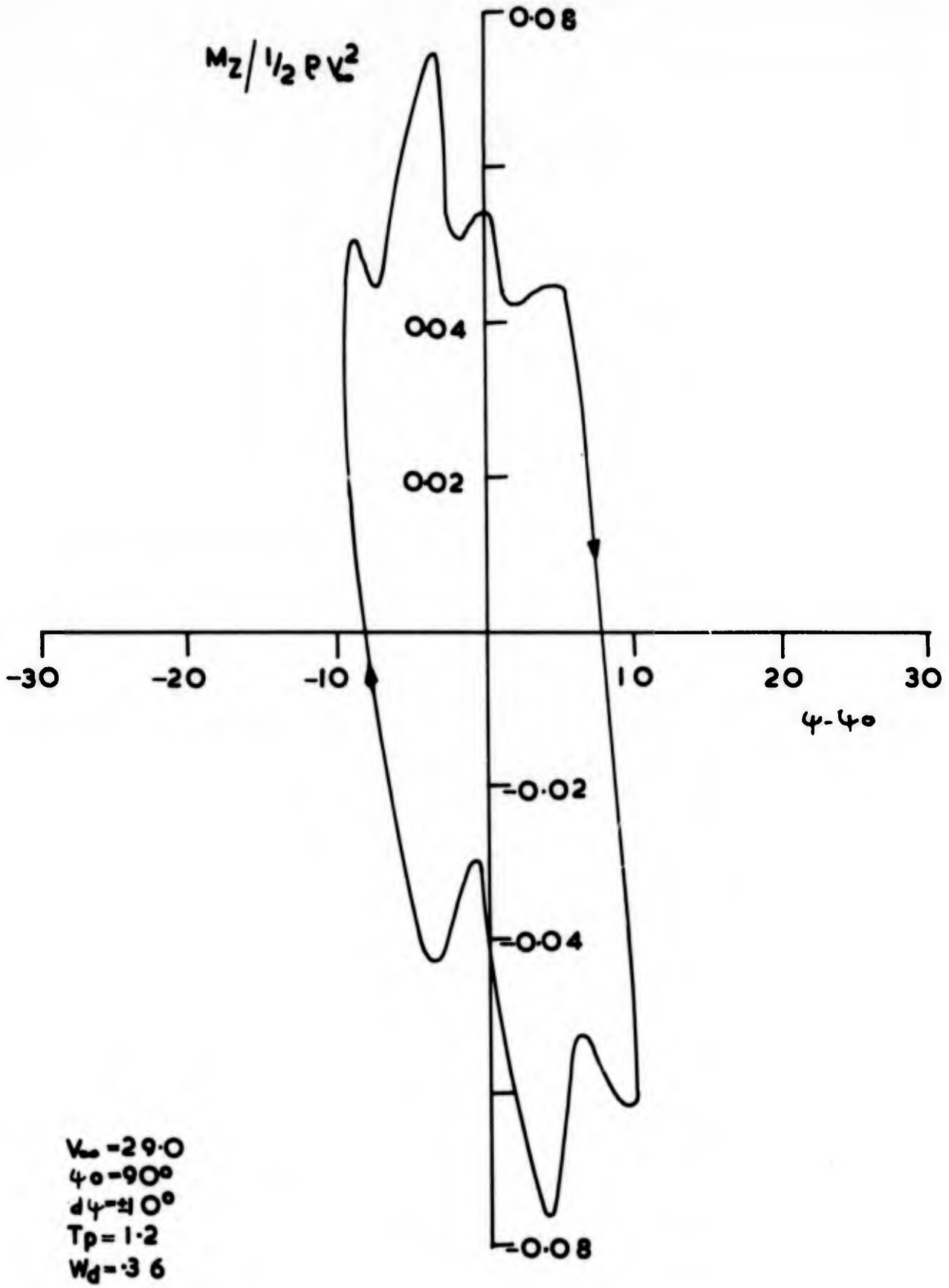
$M_Z / \frac{1}{2} \rho V_\infty^2$
0·08
004
002
-30
-20
-10
10
20
30
ψ-ψ₀
-0·02
-0·04
-0·08
V∞ =29·0
ψ₀=90°
dψ=±10°
Tp= 1·2
Wd=·3 6

FIG 4.19(b)

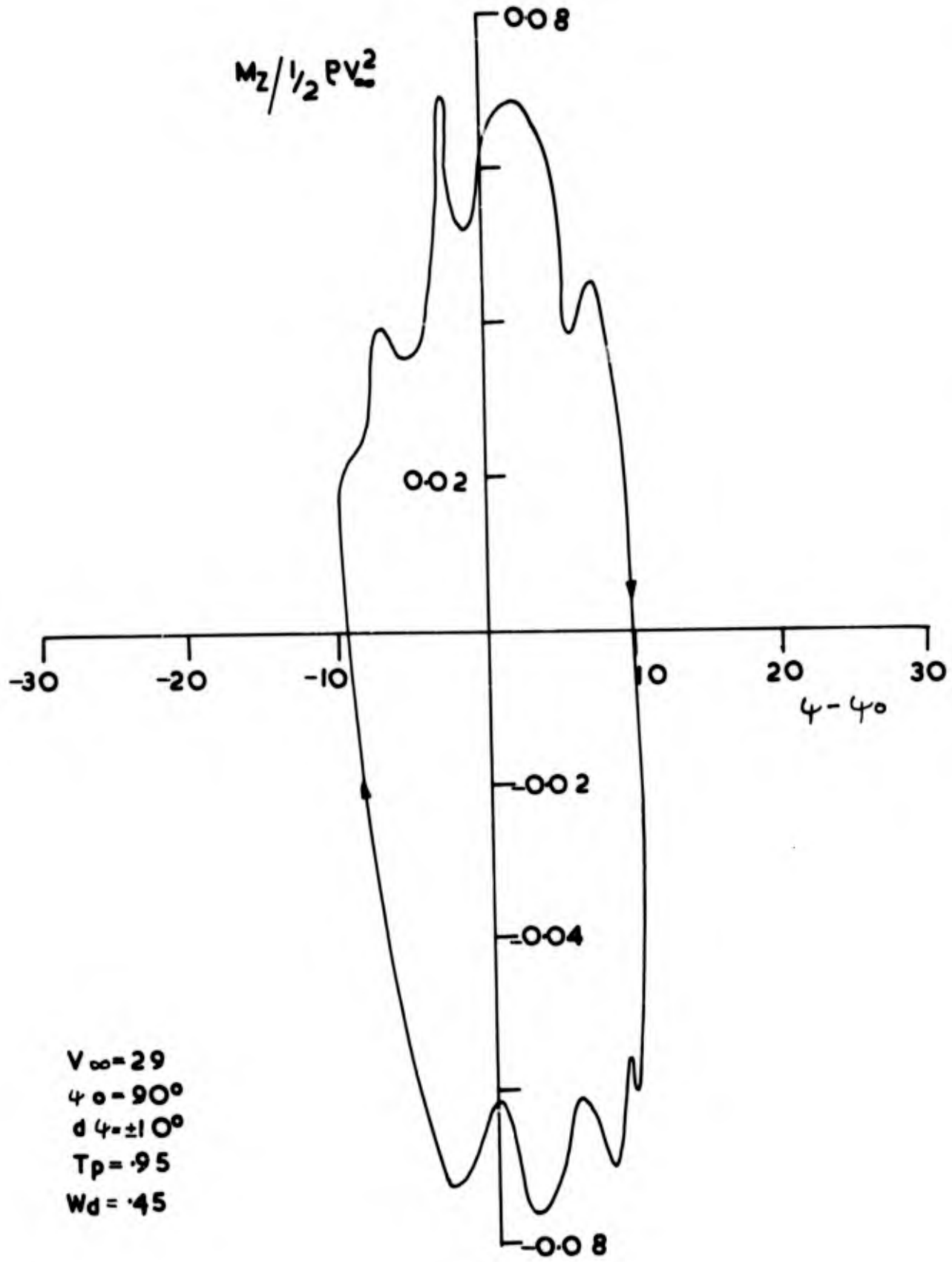
$M_z/\frac{1}{2}\rho V_\infty^2$
·008
·002
-·002
-·004
-·008
-30
-20
-10
10
20
30
$\psi - \psi_0$
$V_\infty = 29$
$\psi_0 = 90°$
$d\psi = \pm 10°$
$T_p = .95$
$W_d = .45$

FIG 4.19(c)

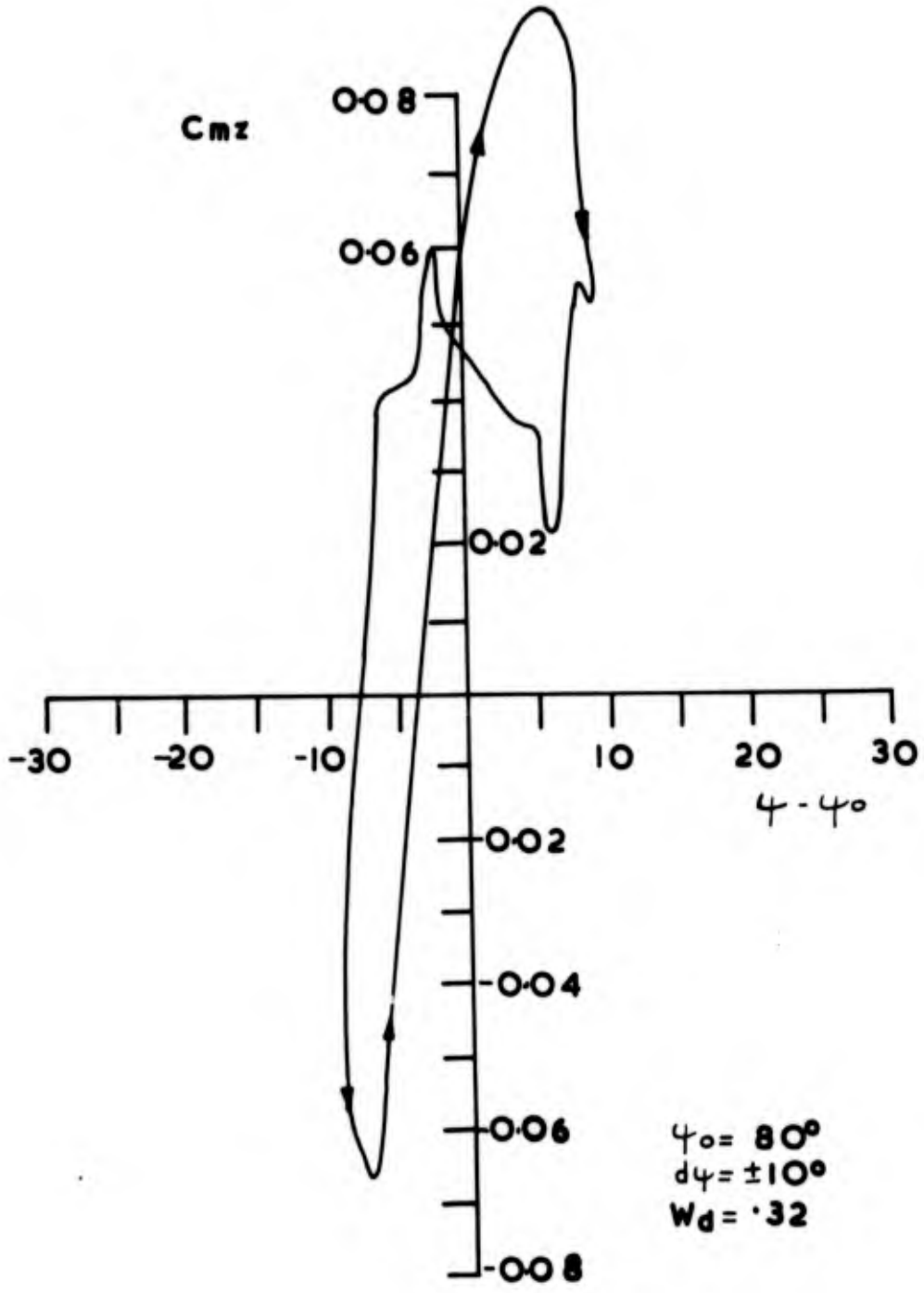
Cmz
0·08
0·06
0·02
-30
-20
-10
10
20
30
ψ - ψo
0·02
-0·04
-0·06
-0·08
ψo = 80°
dψ = ±10°
Wd = ·32

FIG 4.20(a)

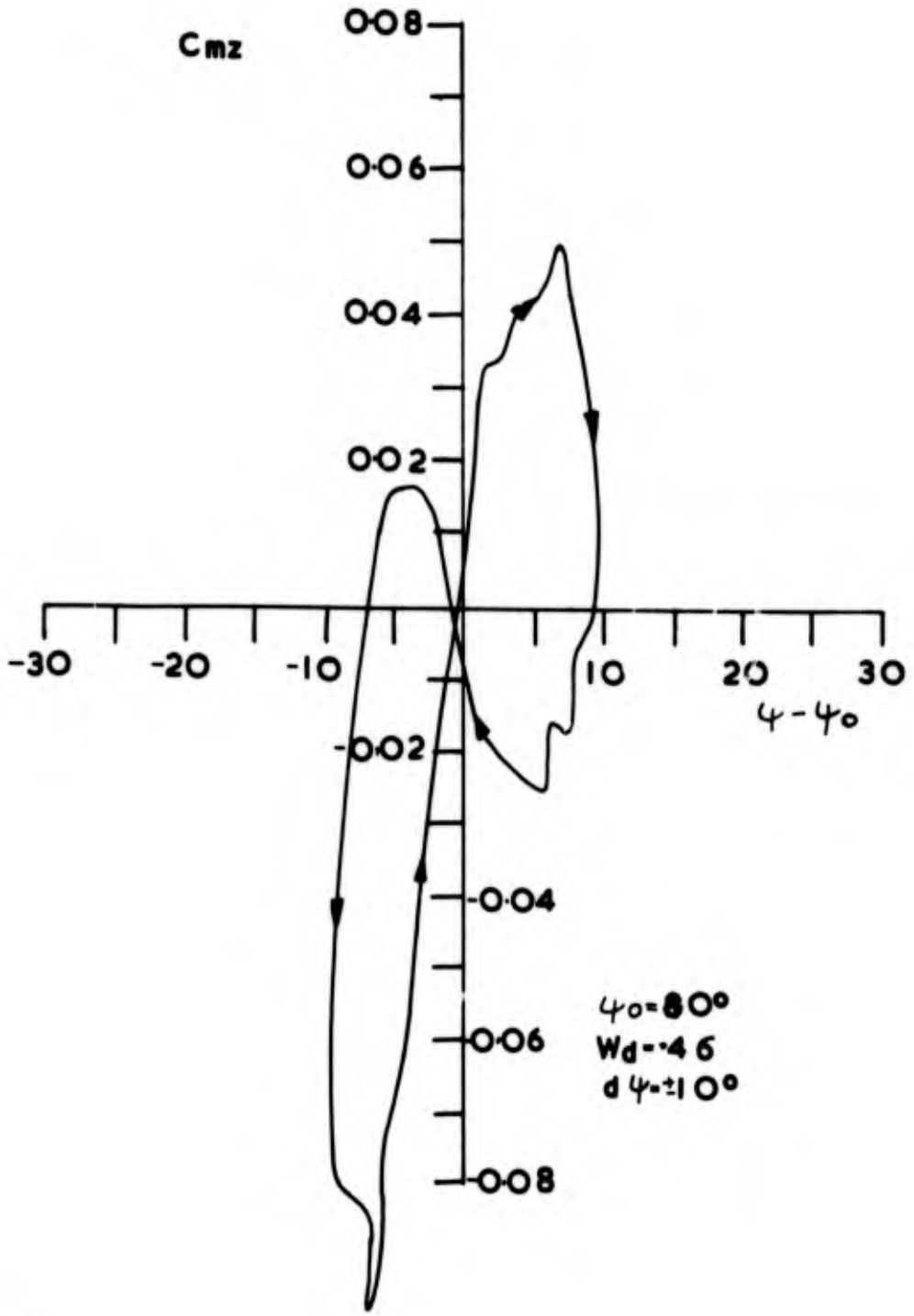
Cmz
0·08
0·06
0·04
0·02
-0·02
-0·04
-0·06
-0·08
-30
-20
-10
10
20
30
ψ-ψo
ψo=80°
Wd=·46
dψ=±10°

FIG 4.20(b)

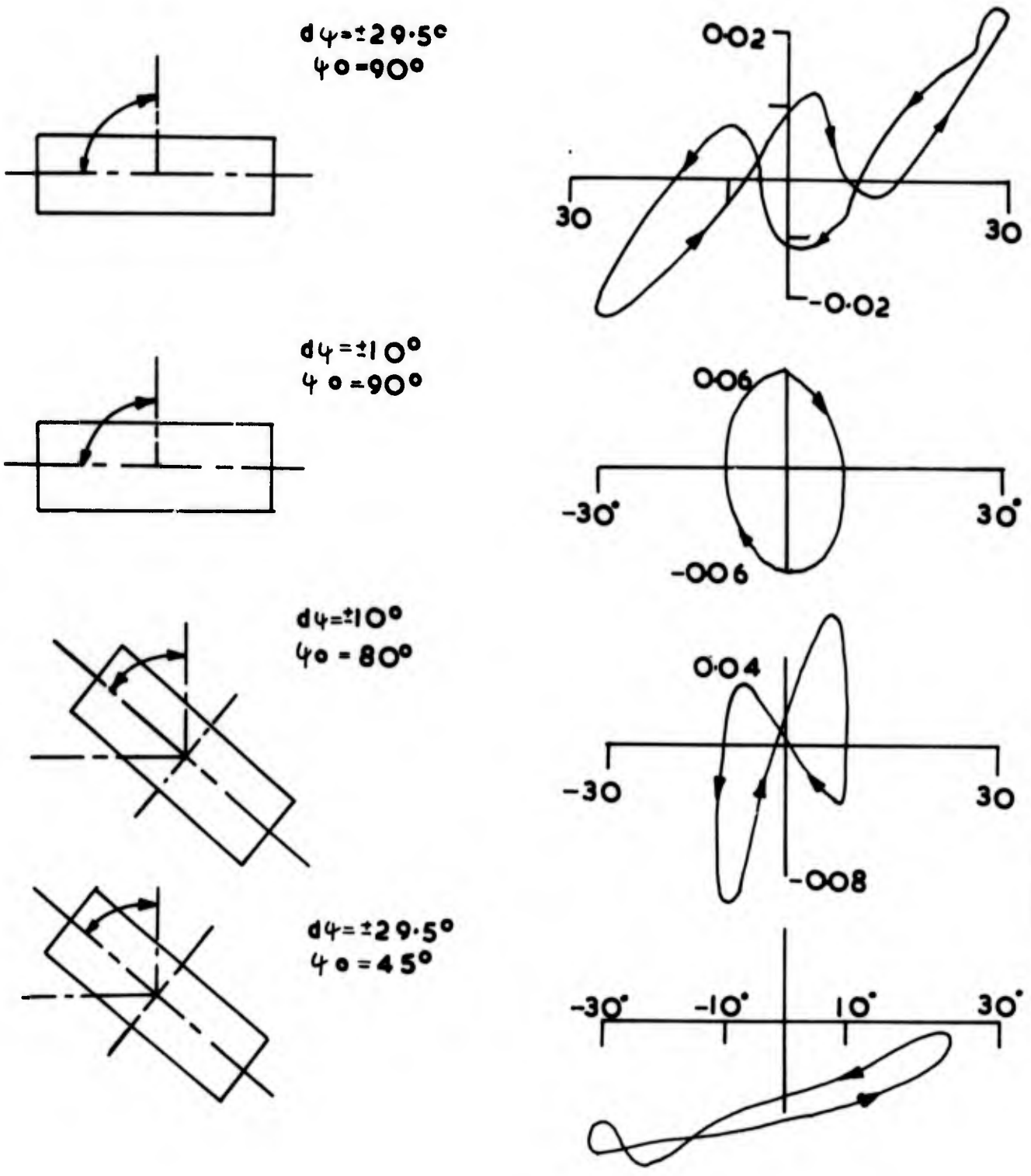

FIG. 421

SUMMARY OF LOOP DIAGRAM TYPES

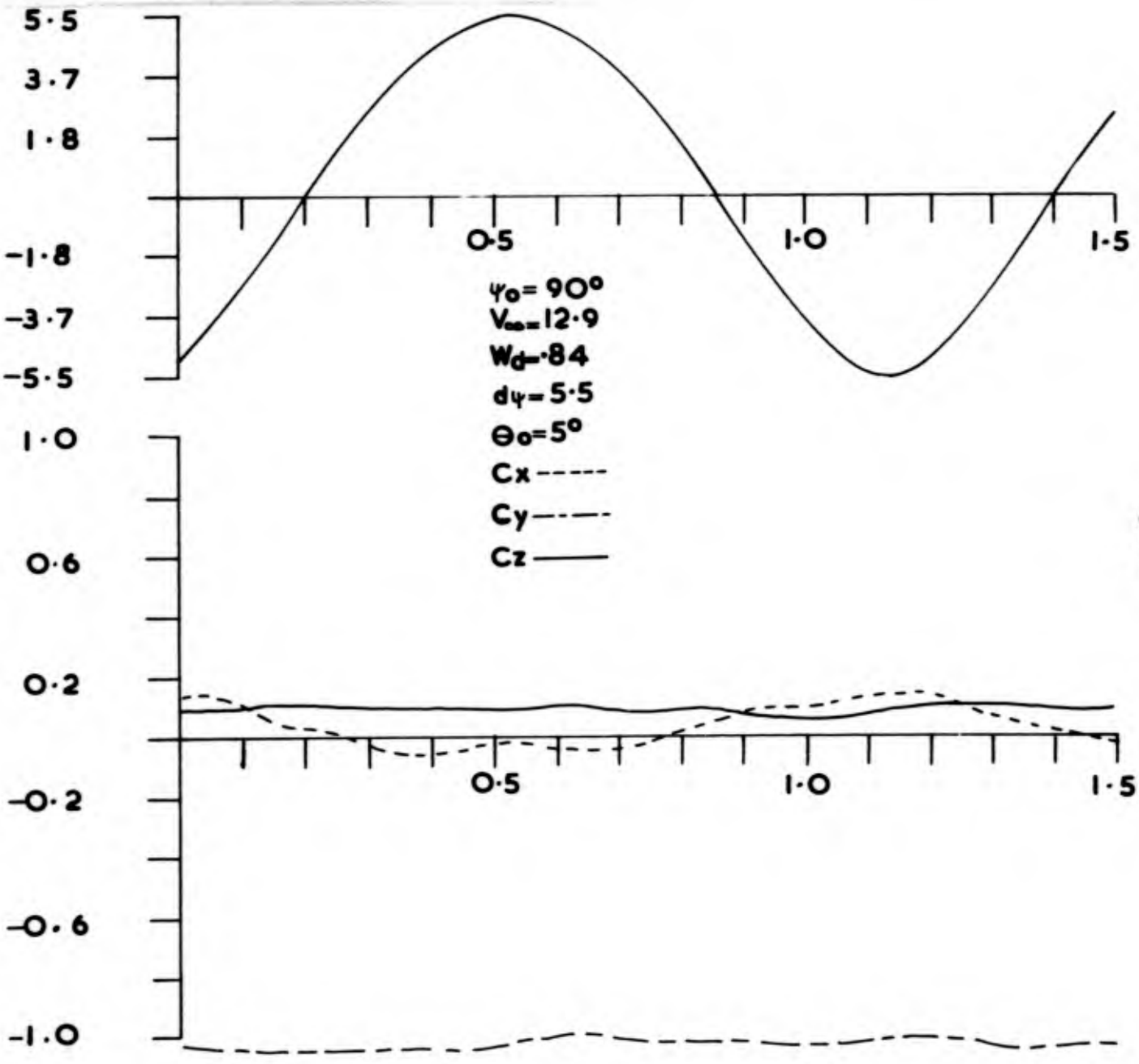
5·5
3·7
1·8
-1·8
-3·7
-5·5
0·5
1·0
1·5
ψo = 90°
V∞ = 12·9
Wd = ·84
dψ = 5·5
Θo = 5°
Cx
Cy
Cz
1·0
0·6
0·2
-0·2
-0·6
-1·0
0·5
1·0
1·5

FIG 4.22(a)

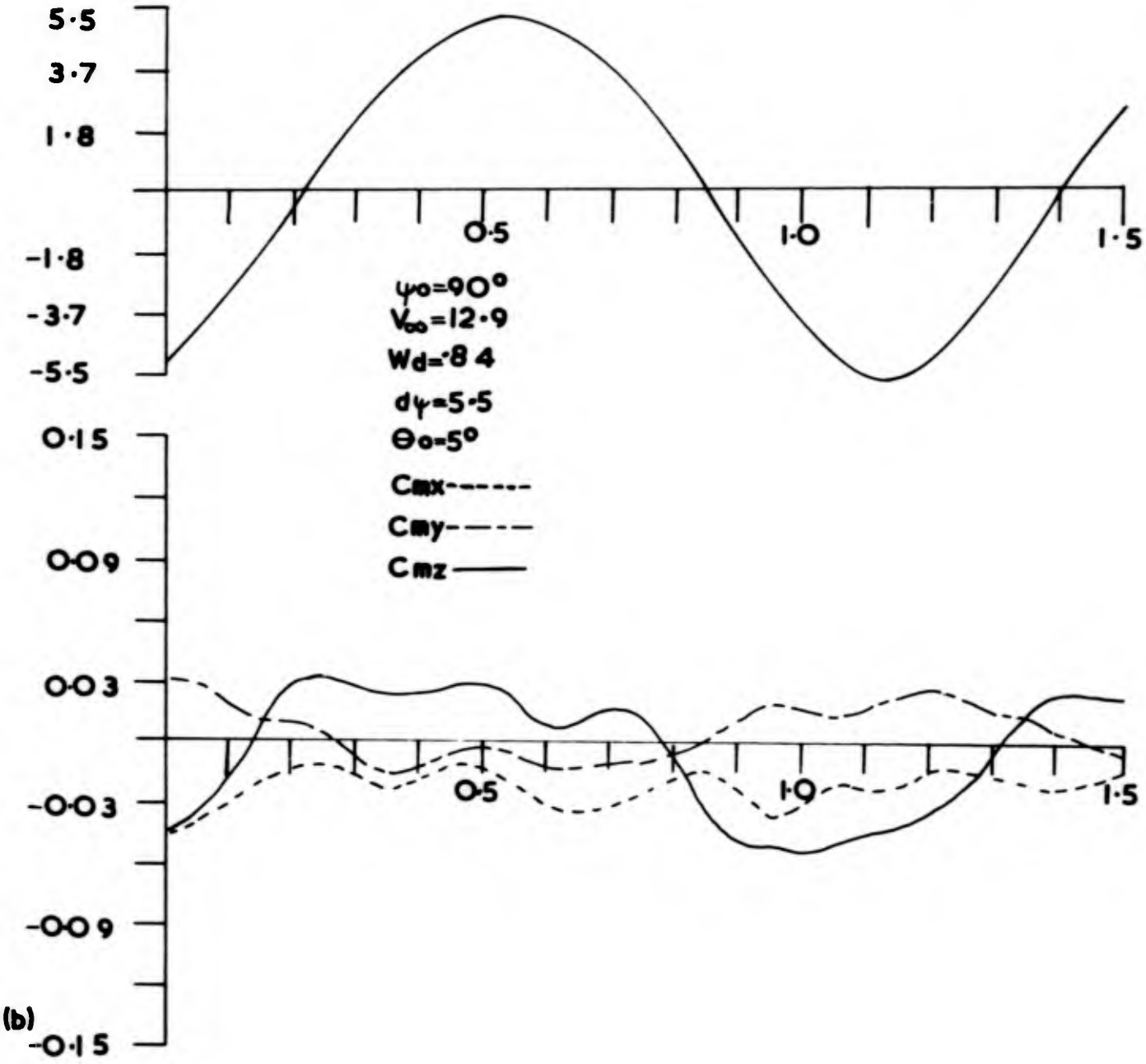
5·5
3·7
1·8
-1·8
-3·7
-5·5
0·5
1·0
1·5
ψo=90°
V∞=12·9
Wd=·84
dψ=5·5
Θo=5°
Cmx------
Cmy— — —
Cmz——
0·15
0·09
0·03
-0·03
-0·09
-0·15
0·5
1·0
1·5

FIG 4.22(b)

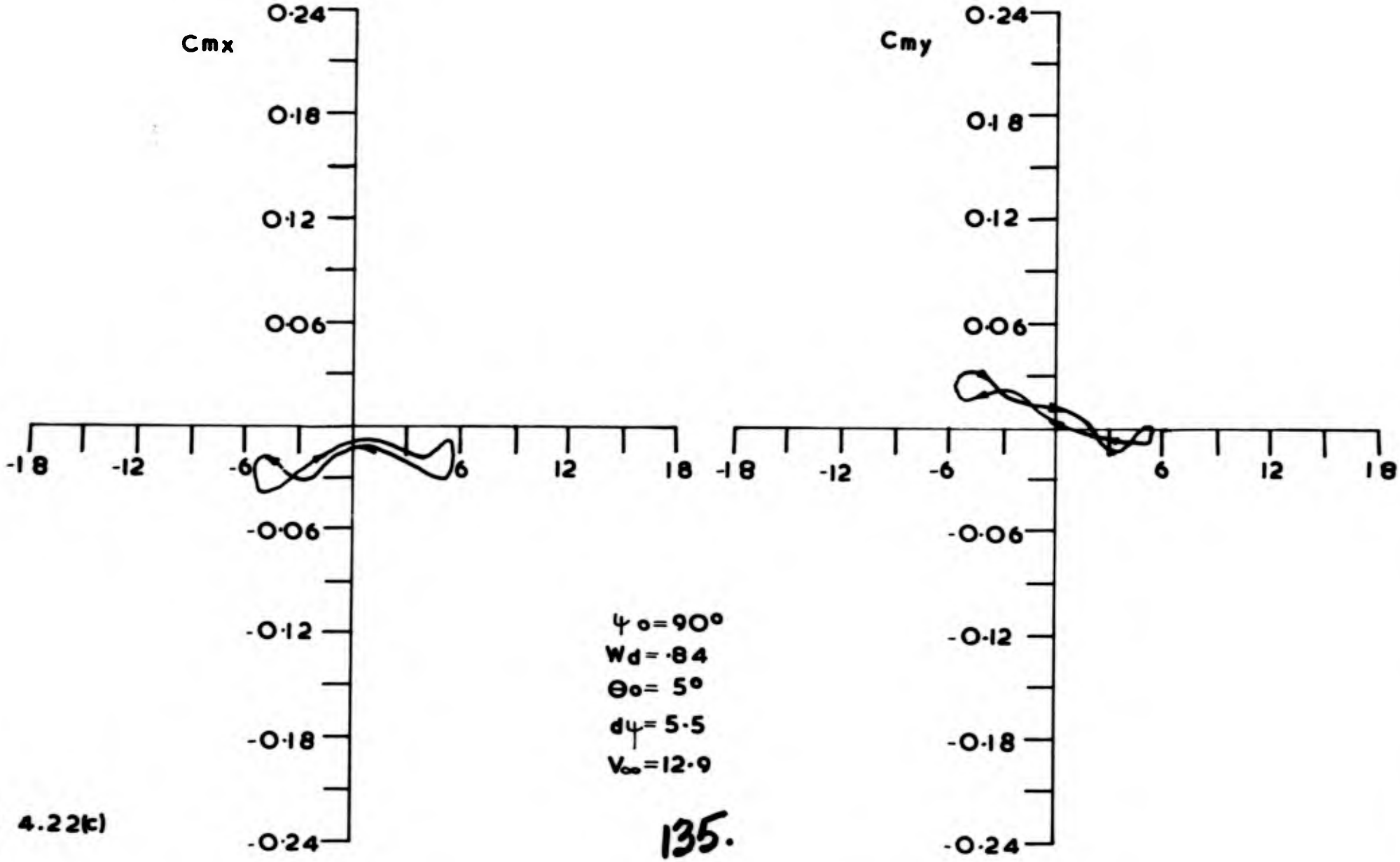
Cmx
0·24
0·18
0·12
0·06
-0·06
-0·12
-0·18
-0·24
-18
-12
-6
6
12
18
Cmy
0·24
0·18
0·12
0·06
-0·06
-0·12
-0·18
-0·24
-18
-12
-6
6
12
18
ψ o=90°
Wd=·84
θo= 5°
dψ= 5·5
V∞=12·9

FIG 4.22(c)

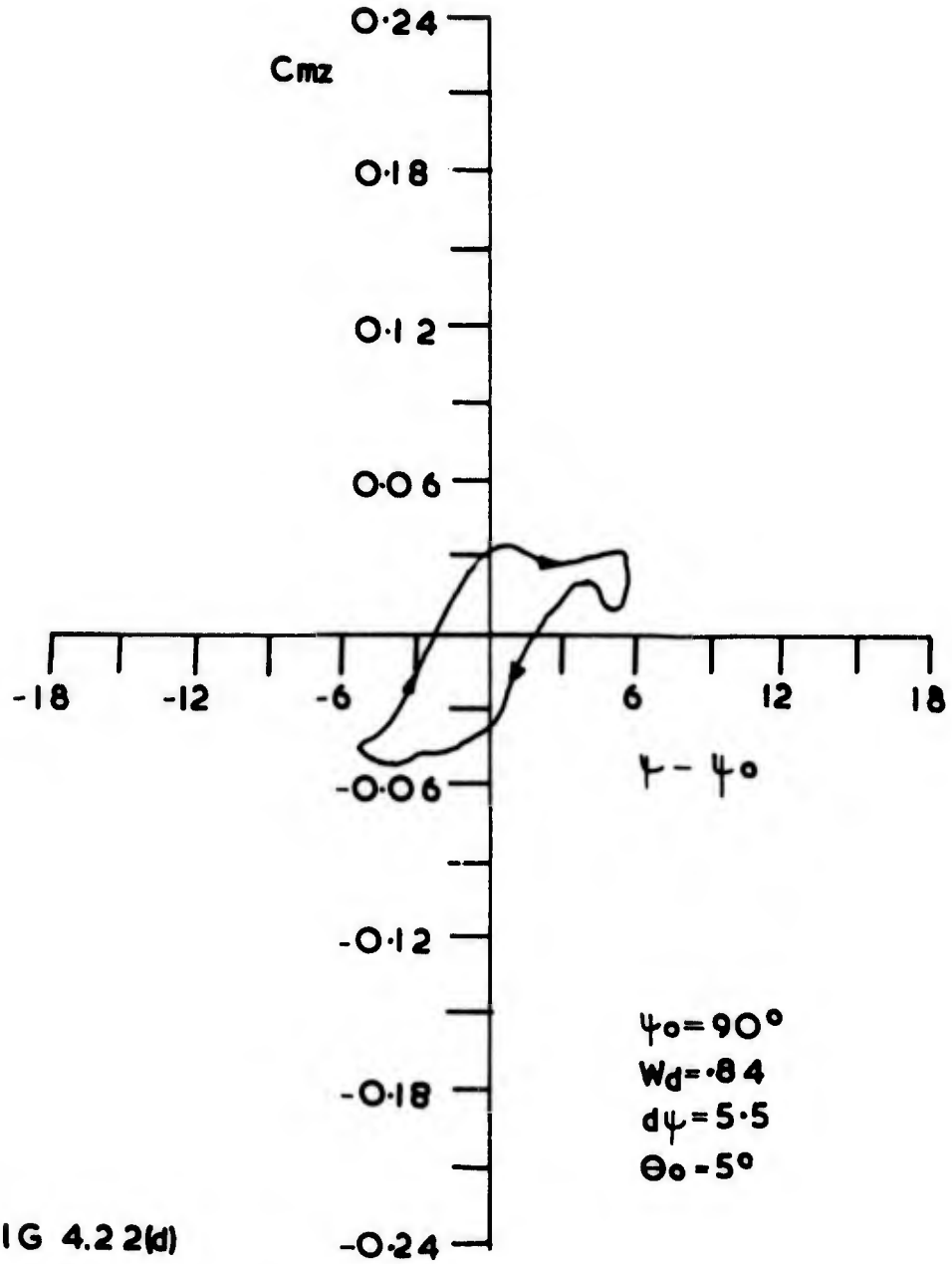
0·24
Cmz
0·18
0·12
0·06
-18
-12
-6
6
12
18
ψ - ψo
-0·06
-0·12
-0·18
-0·24
ψo = 90°
Wd = ·84
dψ = 5·5
Θo = 5°

FIG 4.2 2(d)

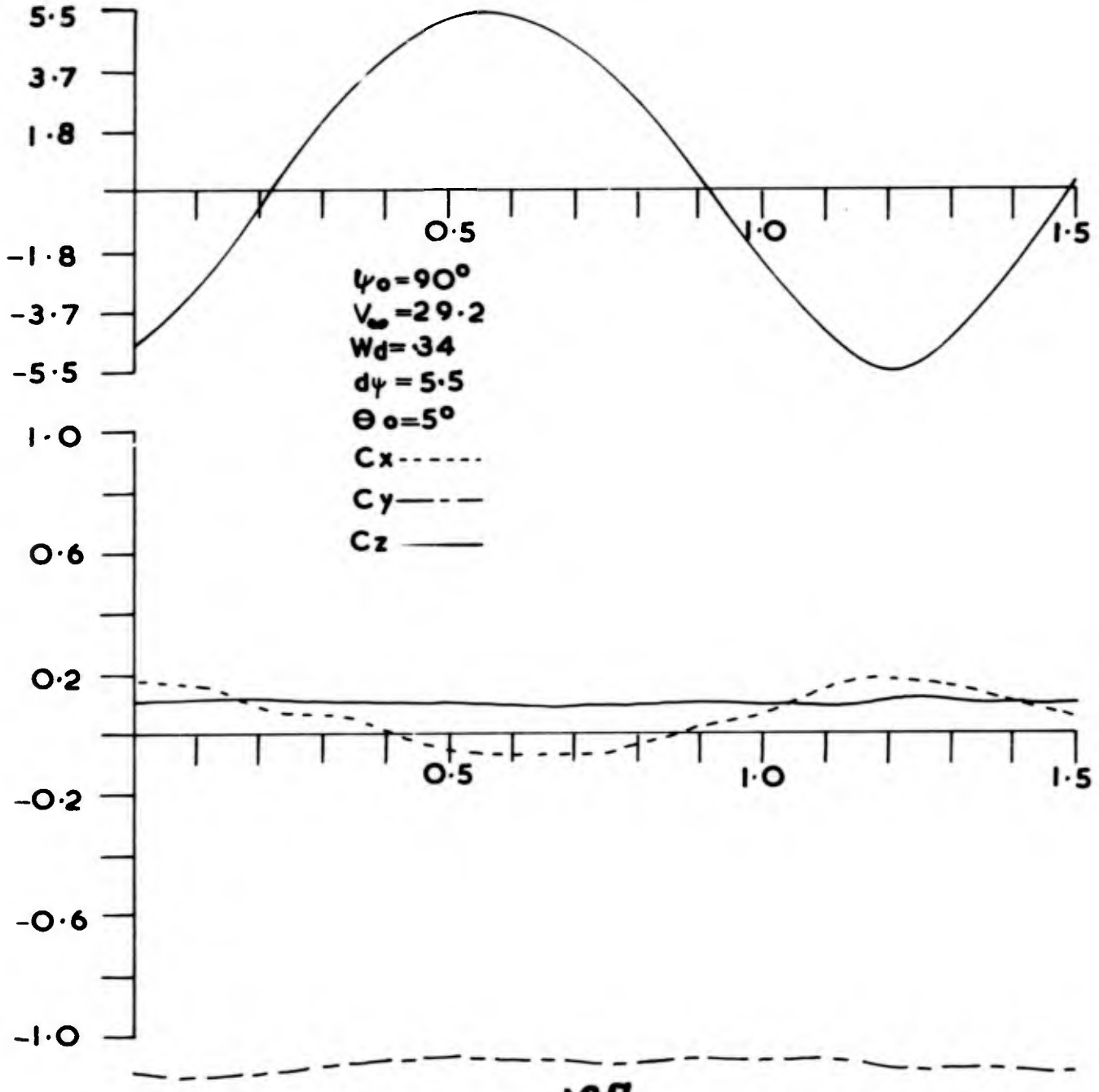
5·5
3·7
1·8
-1·8
-3·7
-5·5
0·5
1·0
1·5
ψo=90°
V∞=29·2
Wd=·34
dψ=5·5
Θo=5°
Cx
Cy
Cz
1·0
0·6
0·2
-0·2
-0·6
-1·0
0·5
1·0
1·5

FIG 4.23(a)

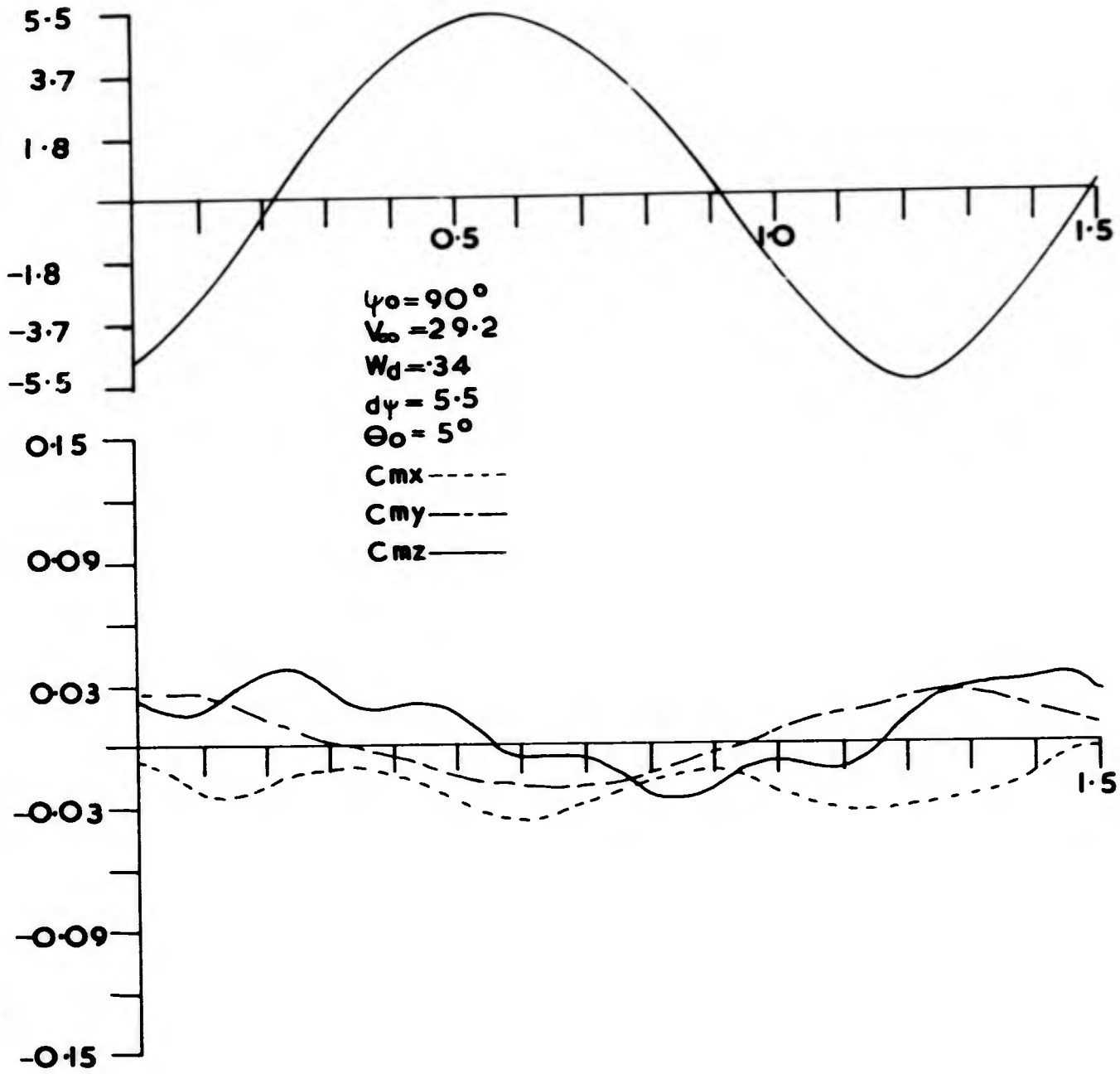
5·5
3·7
1·8
-1·8
-3·7
-5·5
0·5
1·0
1·5
ψo = 90°
V∞ = 29·2
Wd = ·34
dψ = 5·5
Θo = 5°
Cmx
Cmy
Cmz
0·15
0·09
0·03
-0·03
-0·09
-0·15
1·5

FIG 4.23(b)

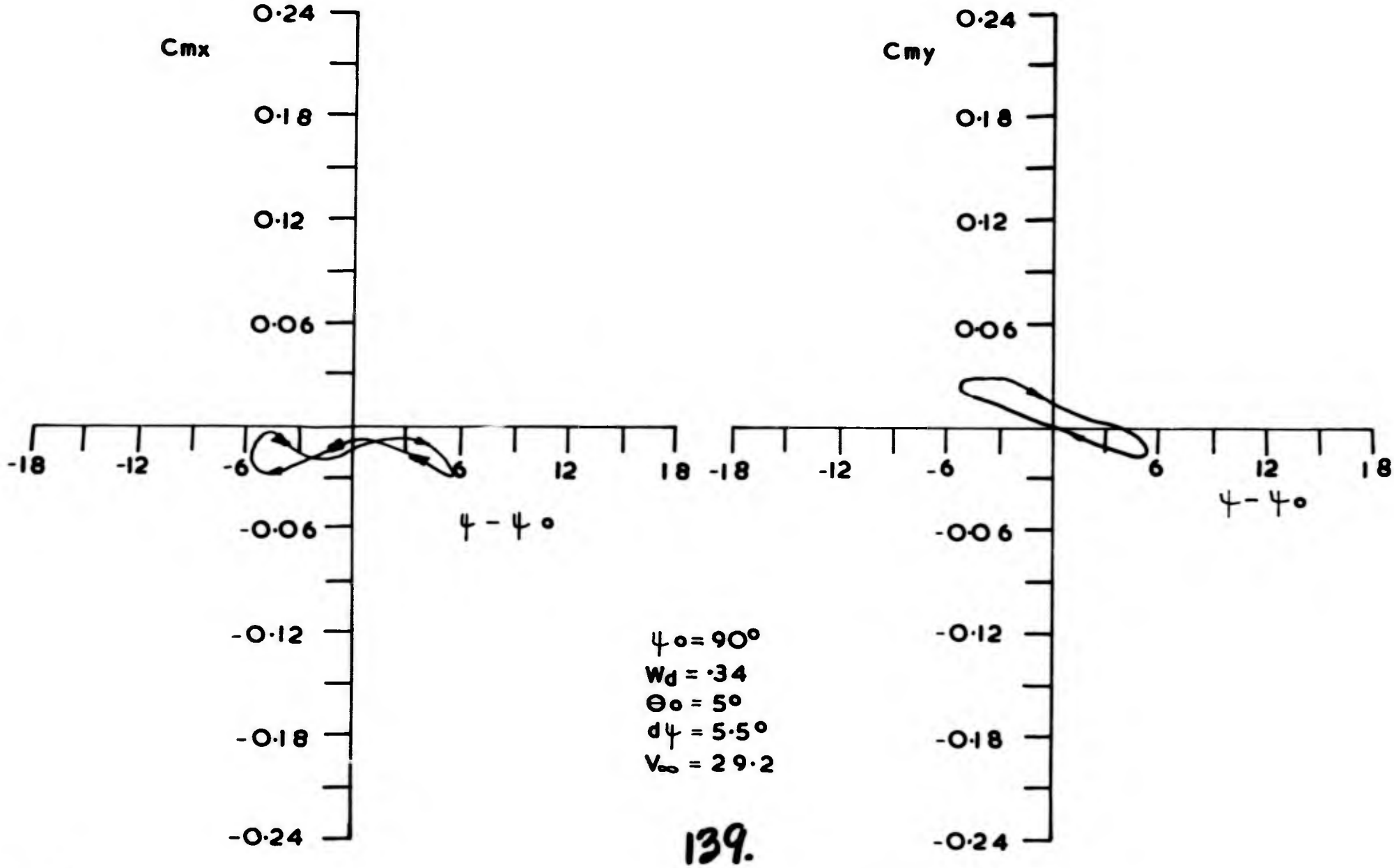
Cmx
0·24
0·18
0·12
0·06
-0·06
-0·12
-0·18
-0·24
-18
-12
-6
6
12
18
ψ - ψ₀
Cmy
0·24
0·18
0·12
0·06
-0·06
-0·12
-0·18
-0·24
-18
-12
-6
6
12
18
ψ - ψ₀
ψ₀ = 90°
Wd = ·34
Θ₀ = 5°
dψ = 5·5°
V∞ = 29·2

139.

FIG 4.23(c)

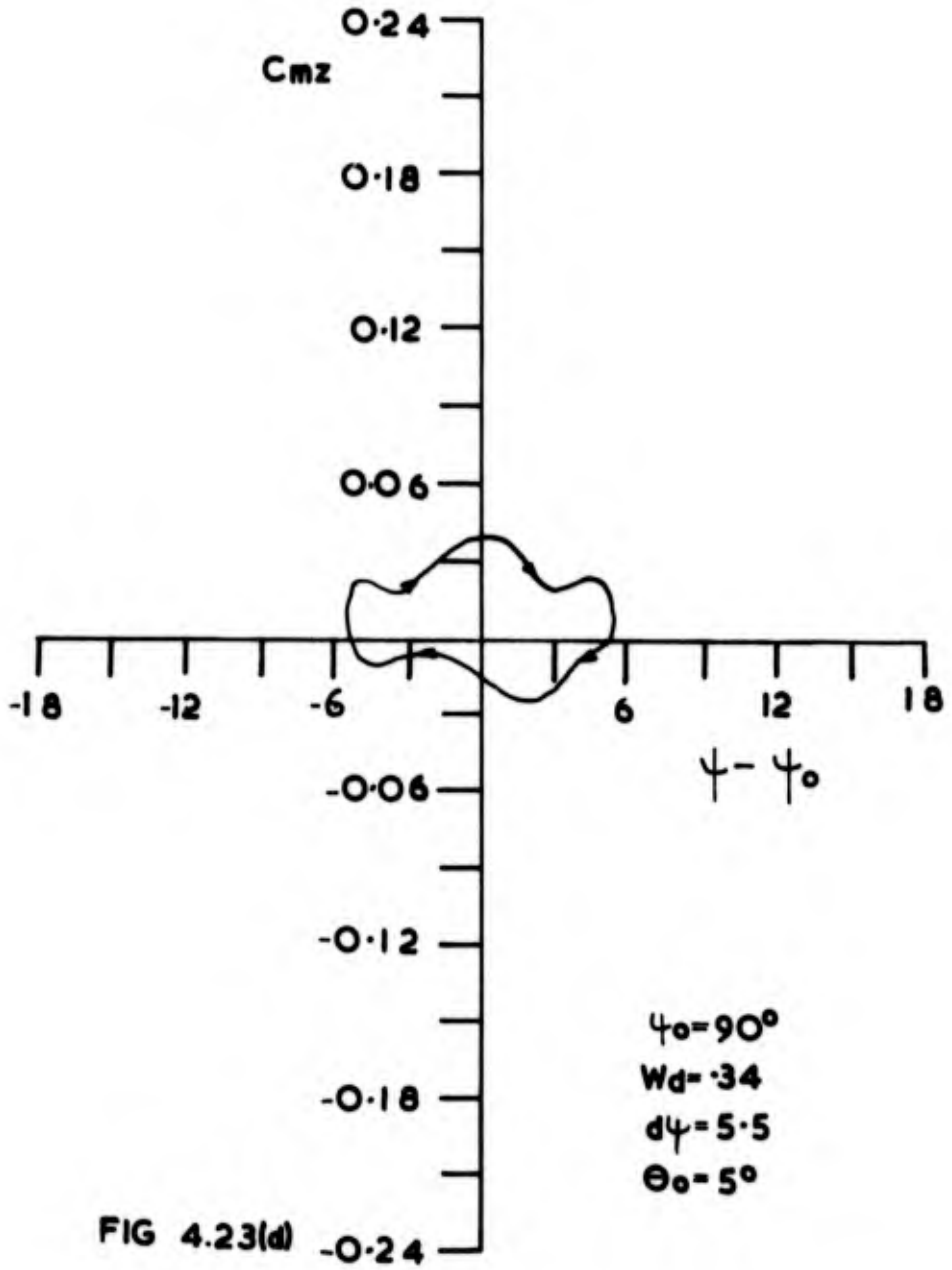
0·24
Cmz
0·18
0·12
0·06
-0·06
-0·12
-0·18
-0·24
-18
-12
-6
6
12
18
ψ - ψo
ψo = 90°
Wd = ·34
dψ = 5·5
Θo = 5°

FIG 4.23(d)

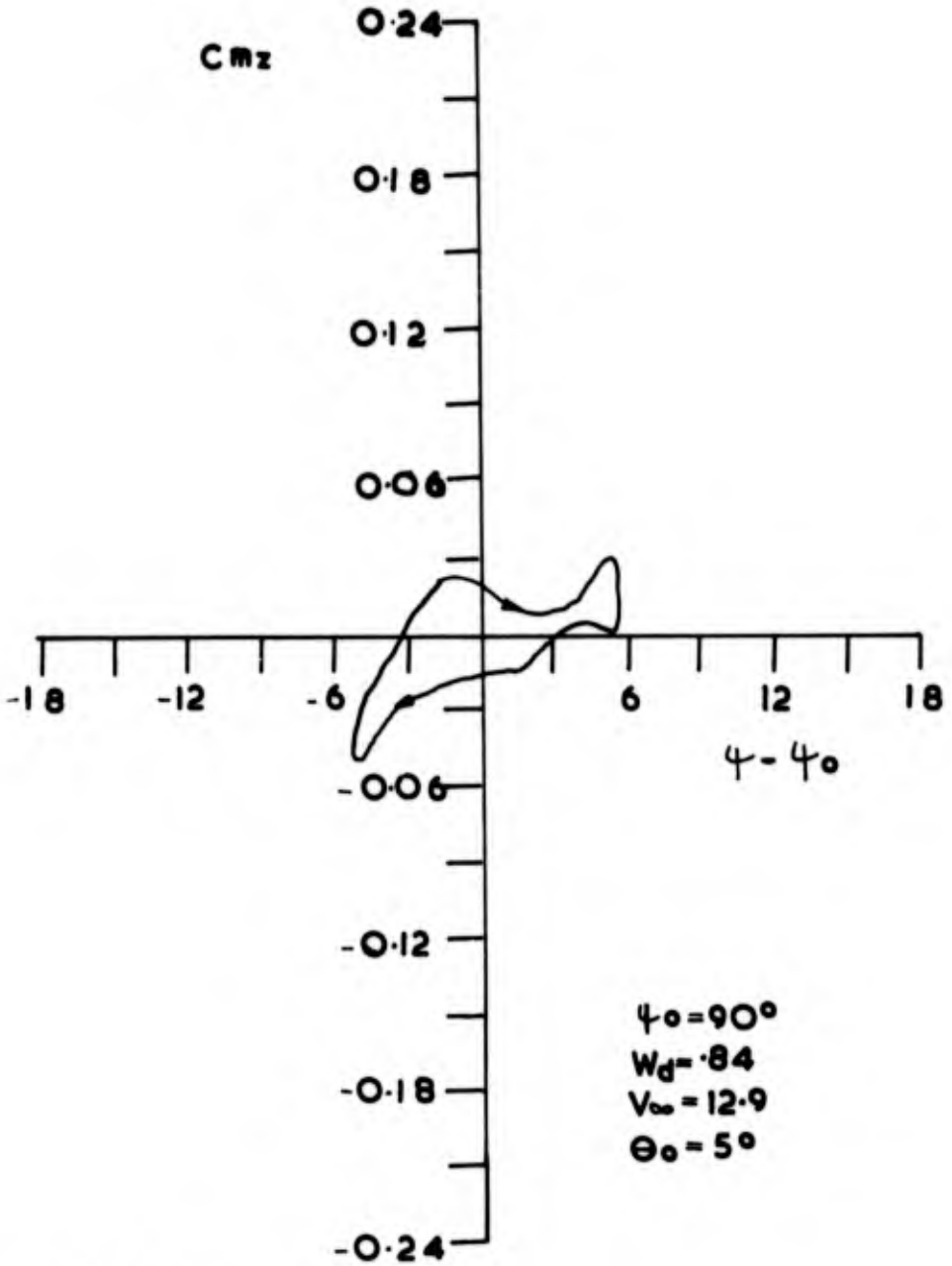
Cmz
0·24
0·18
0·12
0·06
-0·06
-0·12
-0·18
-0·24
-18
-12
-6
6
12
18
ψ - ψo
ψo = 90°
Wd = ·84
V∞ = 12·9
Θo = 5°

FIG 4.24(a)

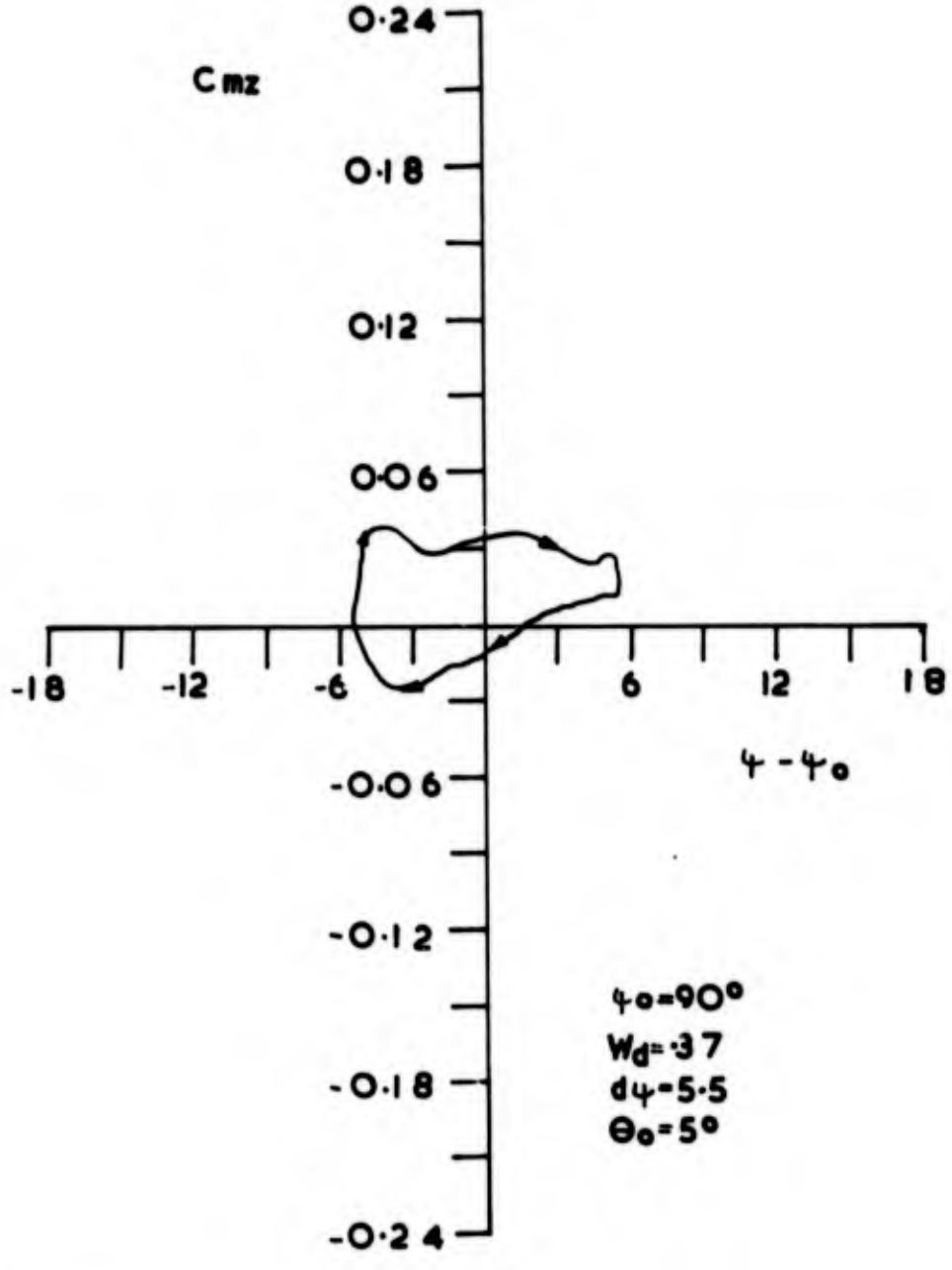
0·24
Cmz
0·18
0·12
0·06
-18
-12
-6
6
12
18
ψ - ψo
-0·06
-0·12
-0·18
-0·24
ψo=90°
Wd=·37
dψ=5·5
Θo=5°

FIG 4.24(b)

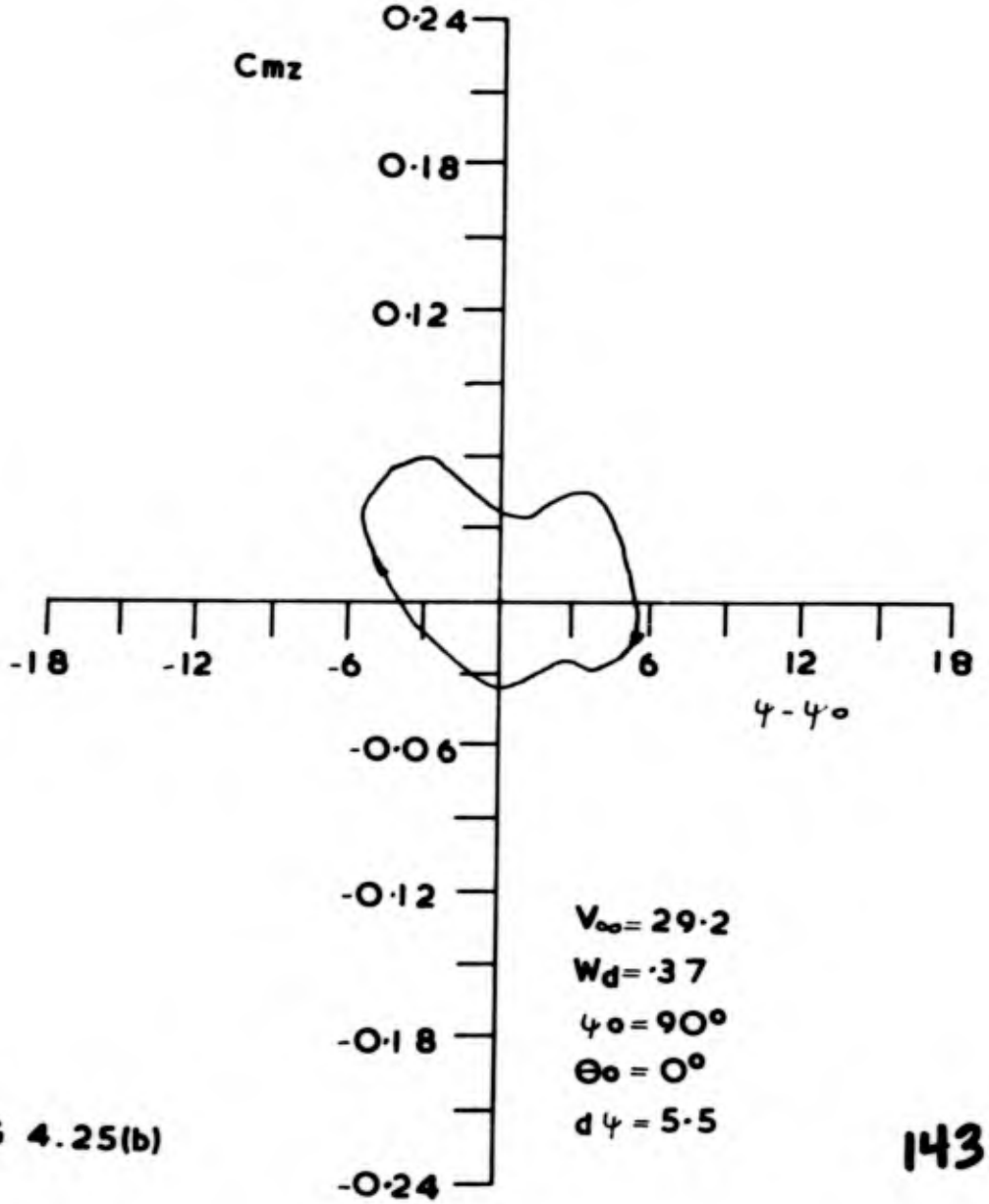

FIG 4.25(b)

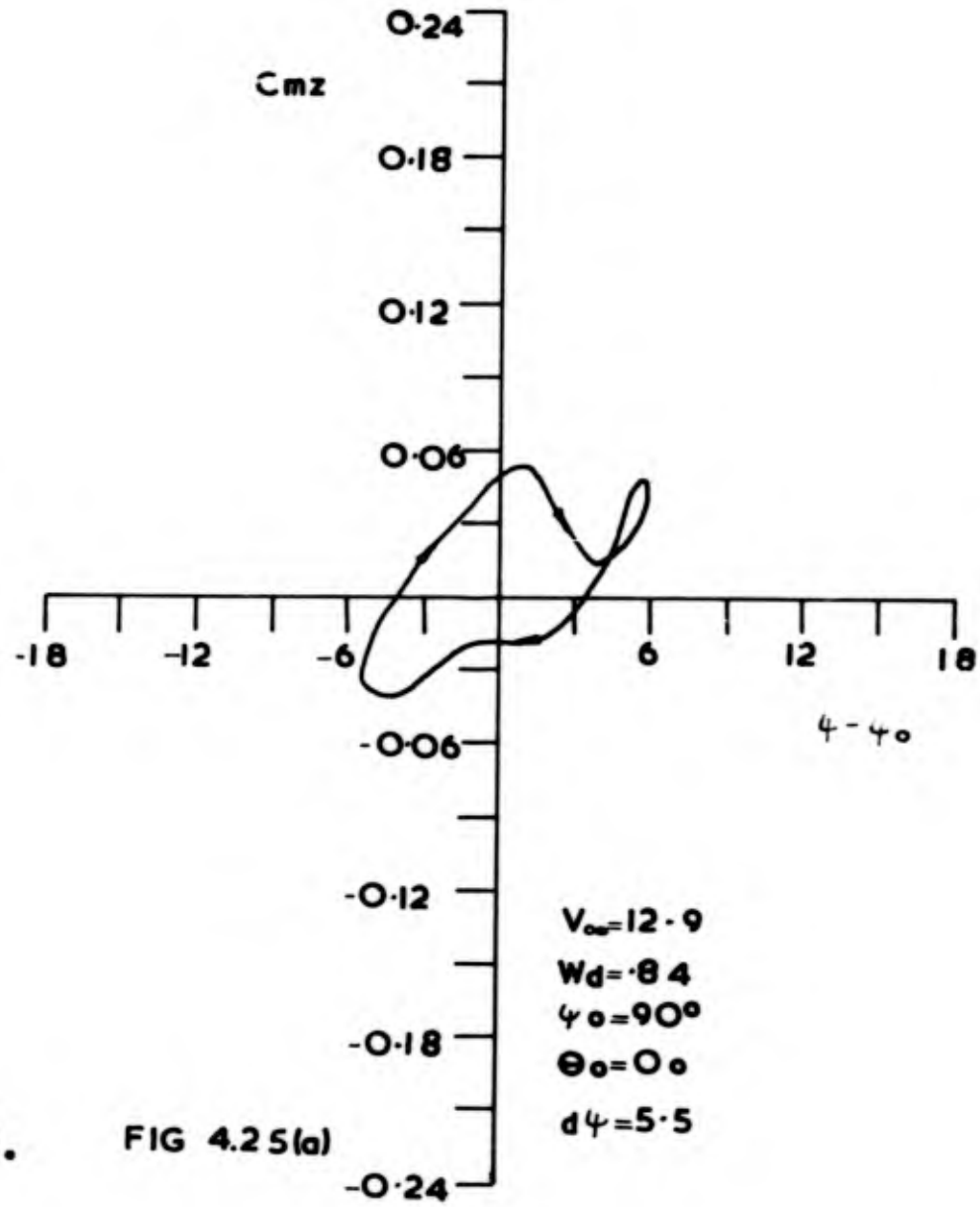

FIG 4.25(a)

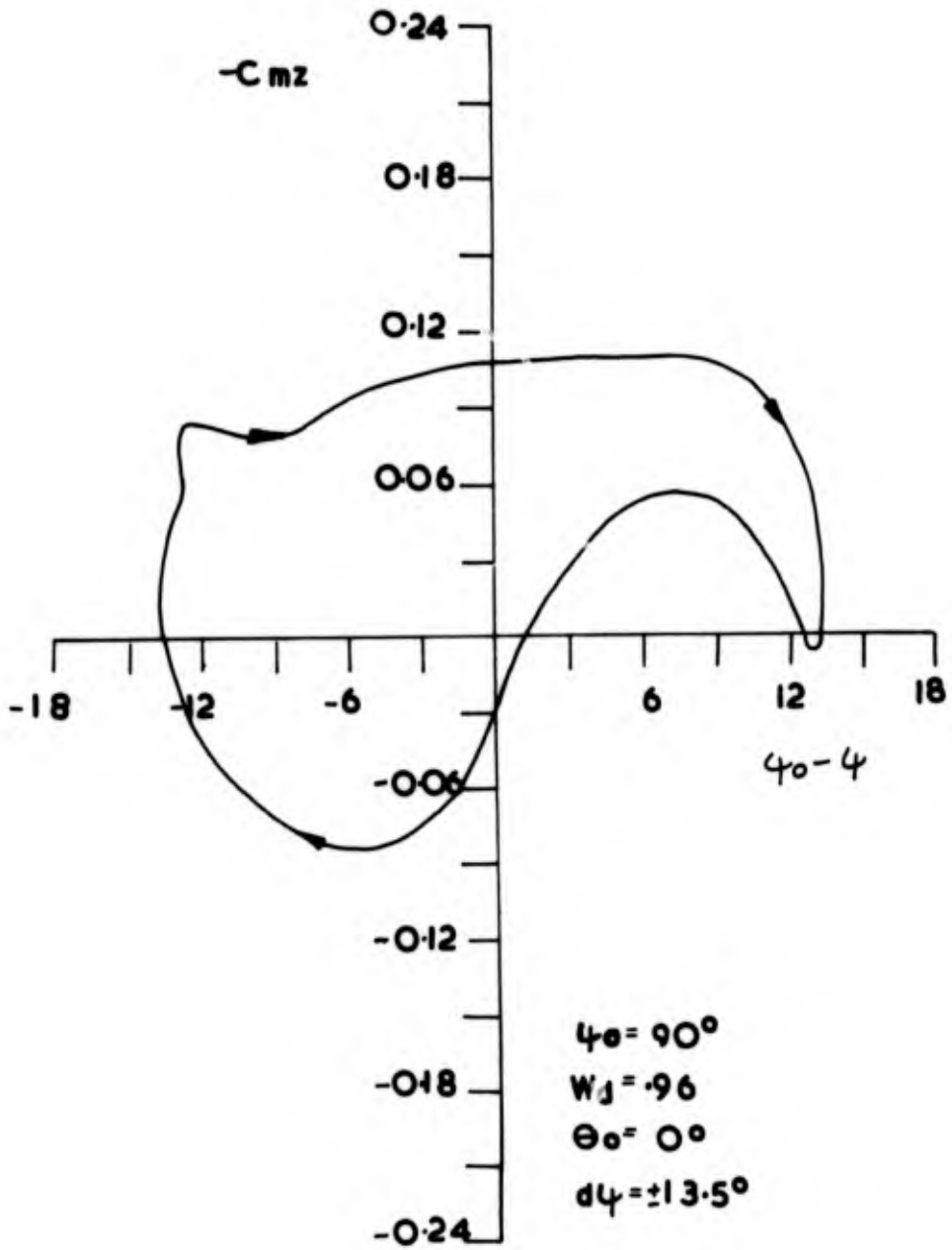
0·24
-Cmz
0·18
0·12
0·06
-0·06
-0·12
-0·18
-0·24
-18
-12
-6
6
12
18
40-4
40= 90°
W1 = ·96
Θo= 0°
d4 = ±13·5°

FIG 4.26(a)

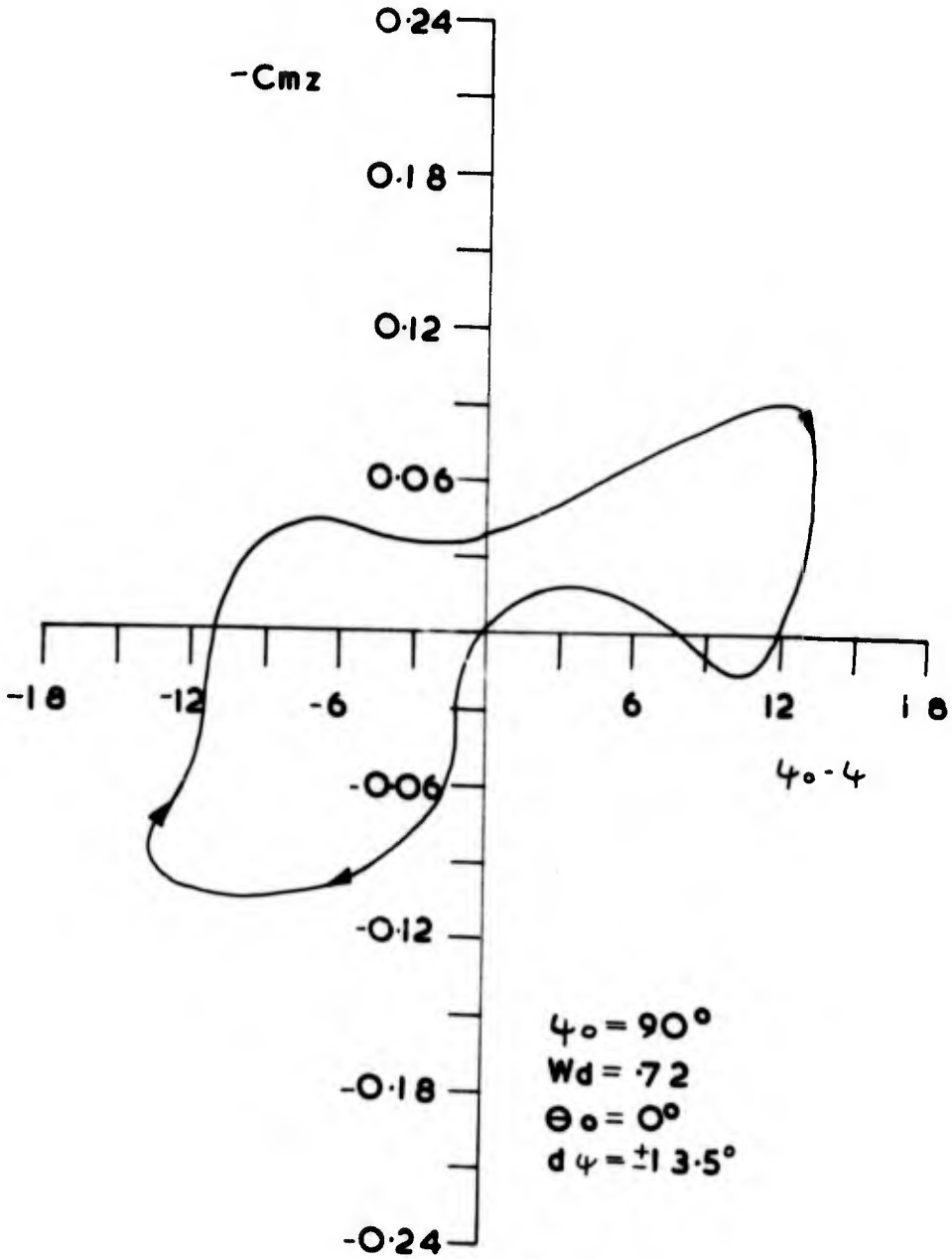
0·24
-Cmz
0·18
0·12
0·06
-18
-12
-6
6
12
18
φo-φ
-006
-0·12
-0·18
-0·24
φo = 90°
Wd = ·72
θo = 0°
dφ = ±13·5°

FIG 4.26(b)

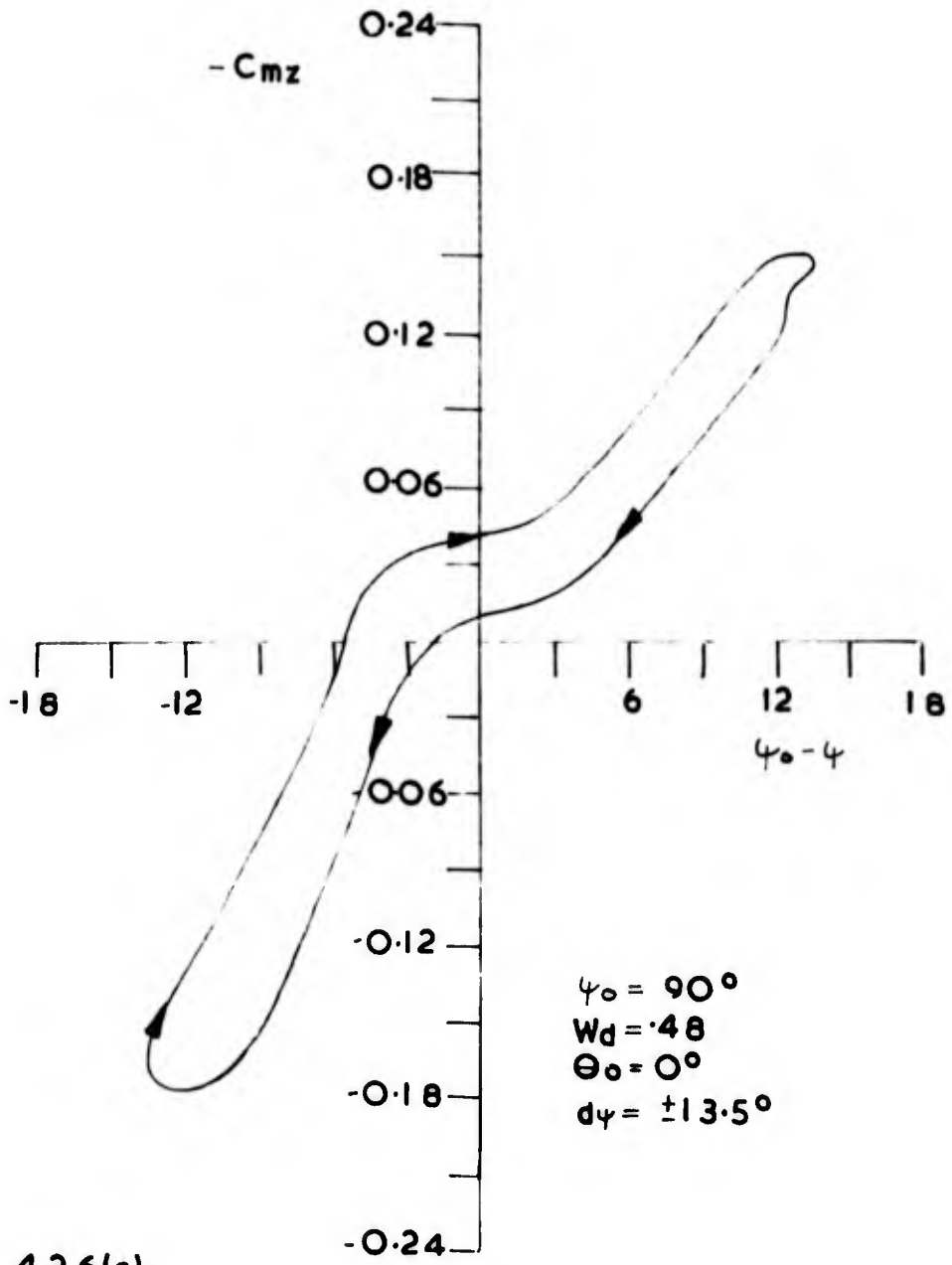
-Cmz
0·24
0·18
0·12
0·06
-0·06
-0·12
-0·18
-0·24
-18
-12
6
12
18
$\psi_o - \psi$
$\psi_o = 90°$
$W_d = \cdot 48$
$\Theta_o = 0°$
$d\psi = \pm 13·5°$

FIG 4.26(c)

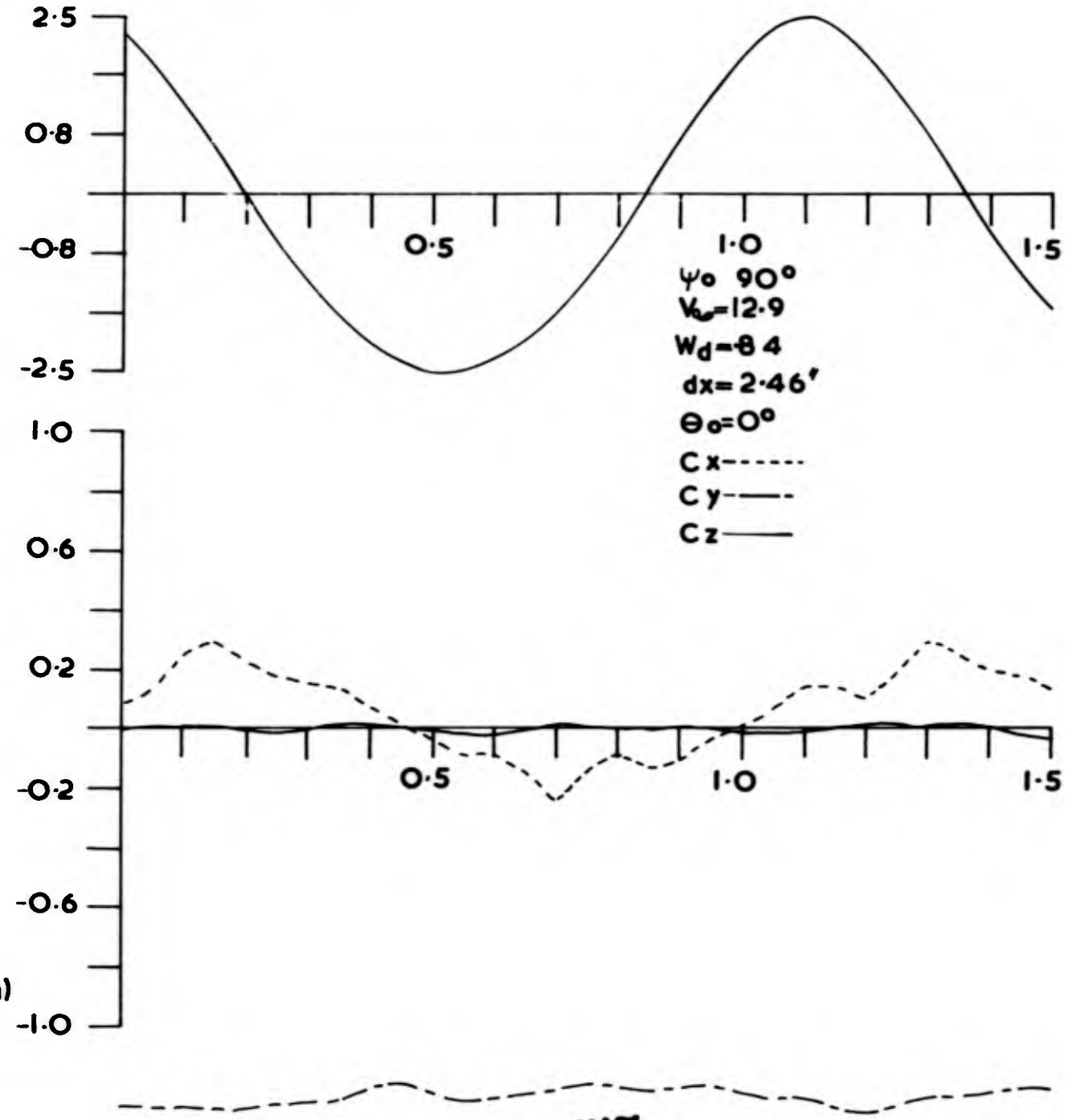
2·5
0·8
-0·8
-2·5
0·5
1·0
1·5
ψo 90°
V∞=12·9
Wd=8·4
dx=2·46'
Θo=0°
Cx
Cy
Cz
1·0
0·6
0·2
-0·2
-0·6
-1·0
0·5
1·0
1·5

FIG 4.27(a)

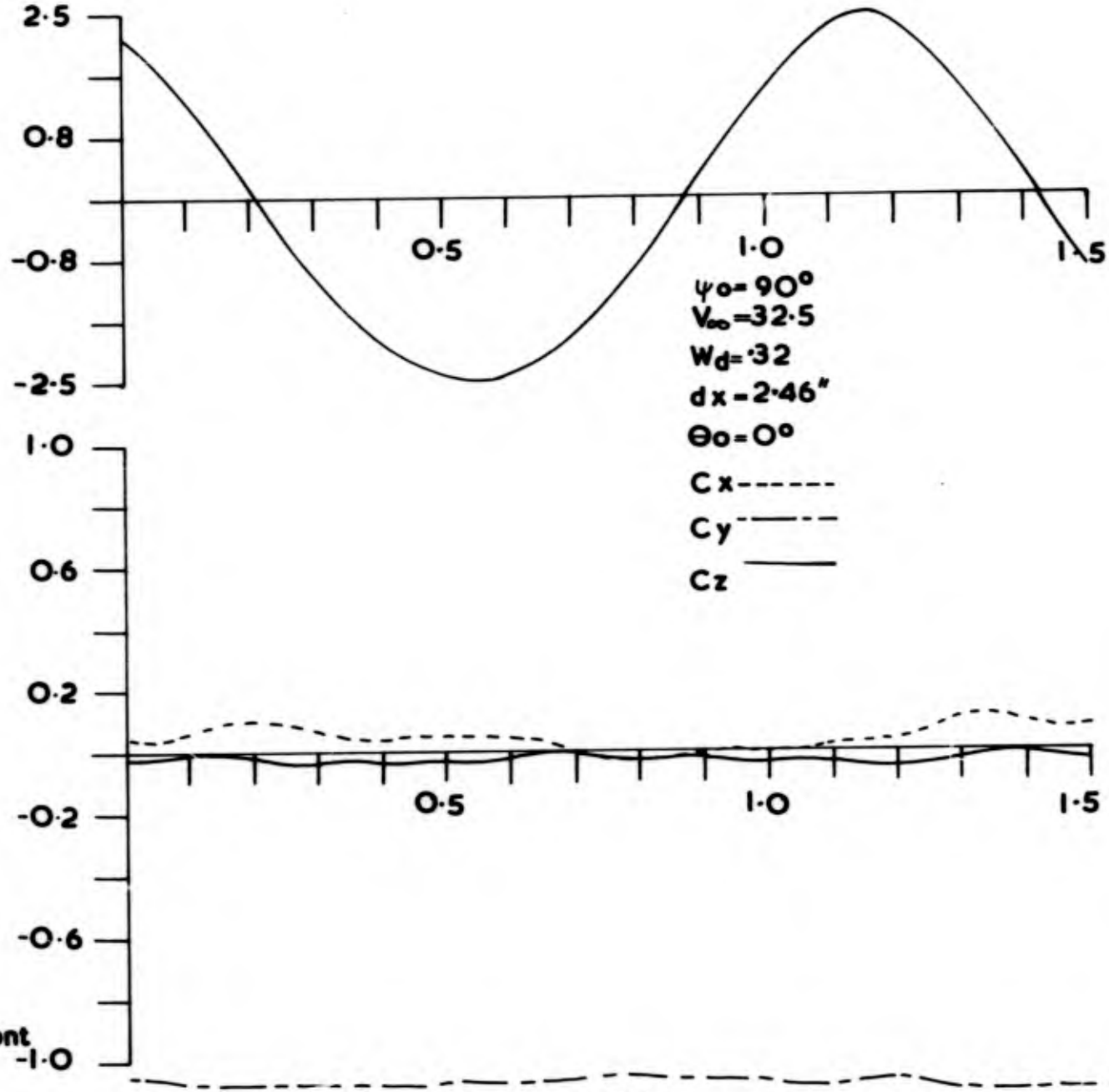

FIG 4.27(a)cont

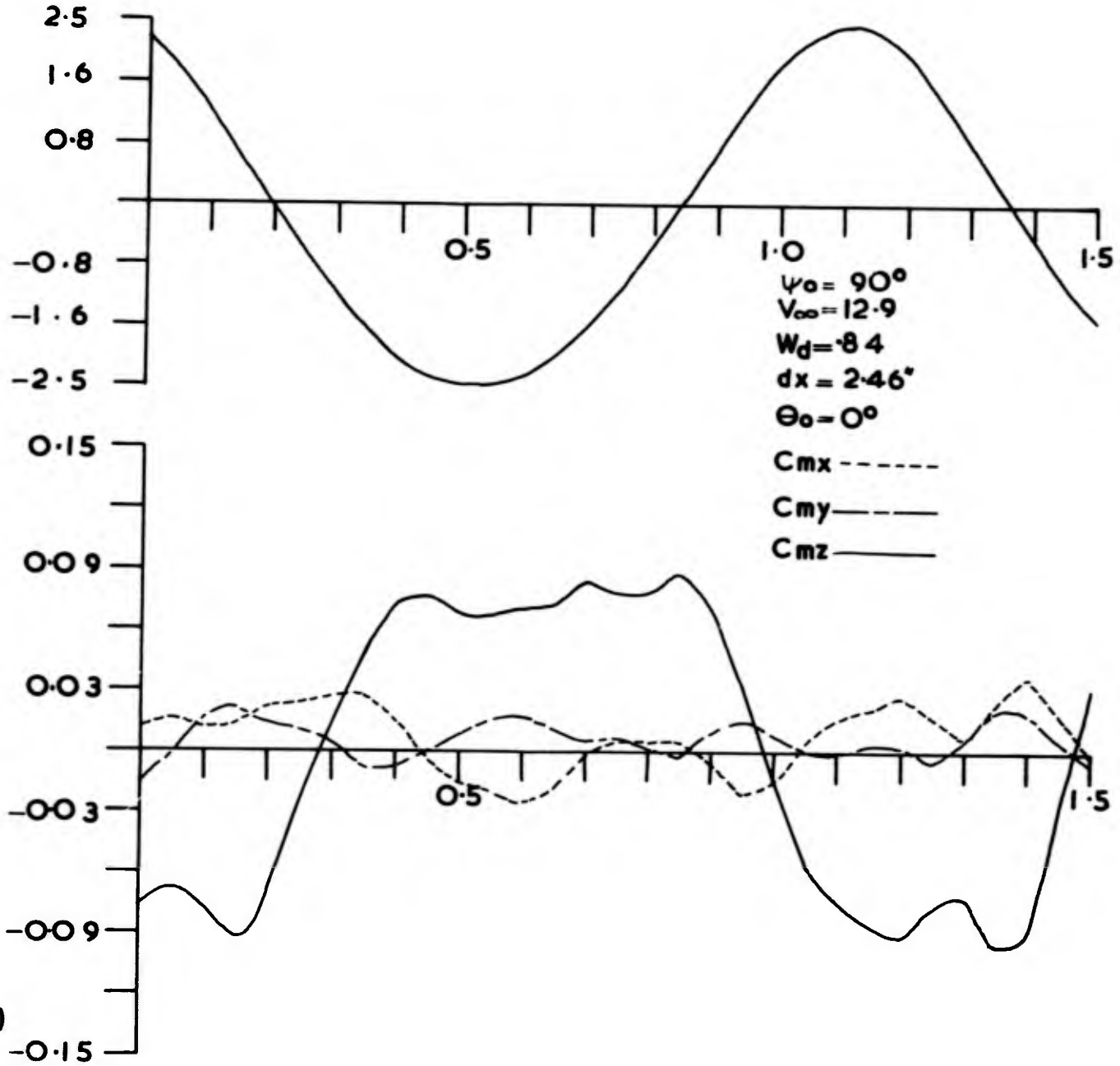
2·5
1·6
0·8
-0·8
-1·6
-2·5
0·5
1·0
1·5
ψo = 90°
V∞ = 12·9
Wd = ·84
dx = 2·46"
Θo = 0°
Cmx
Cmy
Cmz
0·15
0·09
0·03
-0·03
-0·09
-0·15
0·5
1·5

FIG 4.27(b)

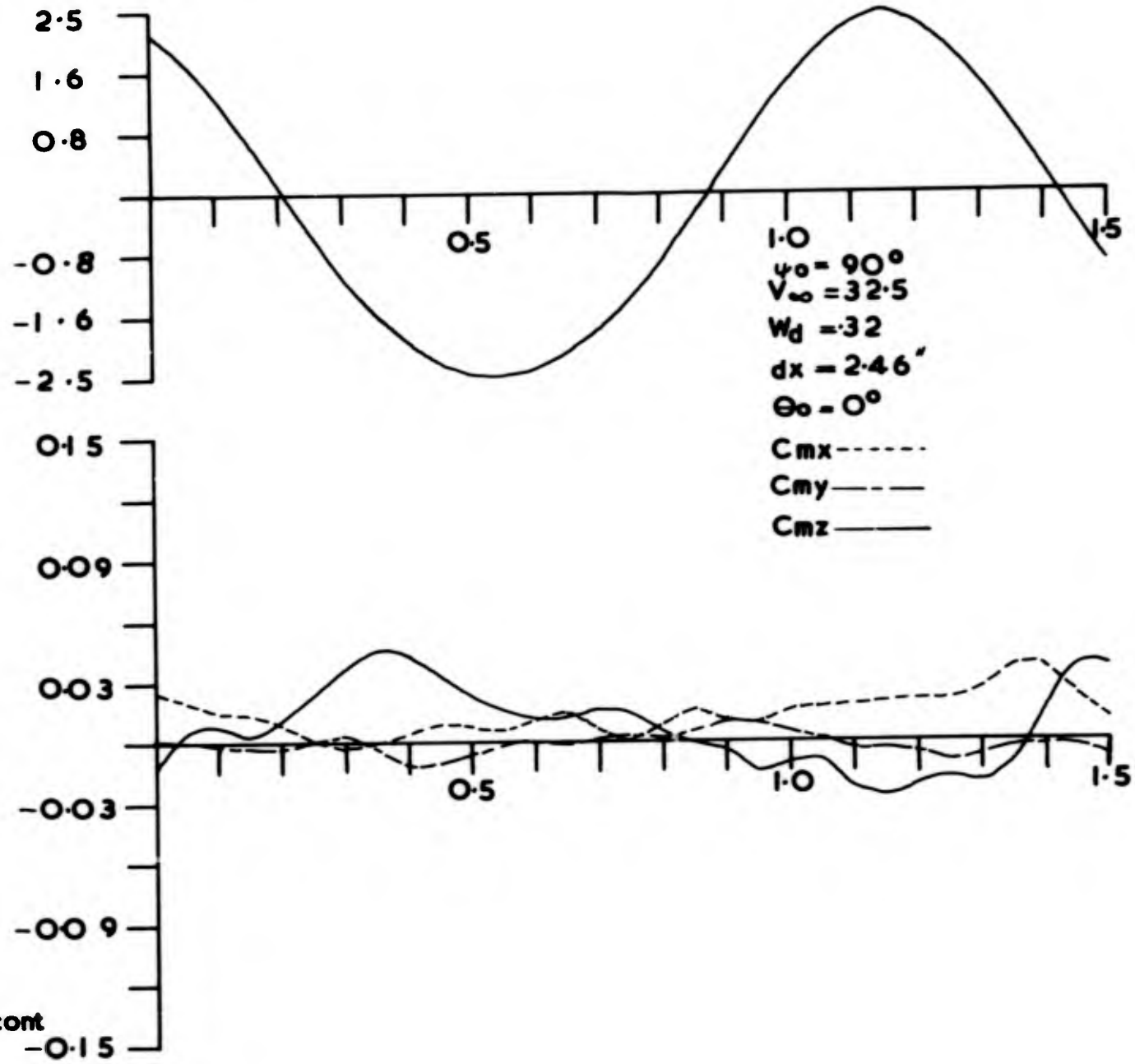

FIG 4.27(b)cont

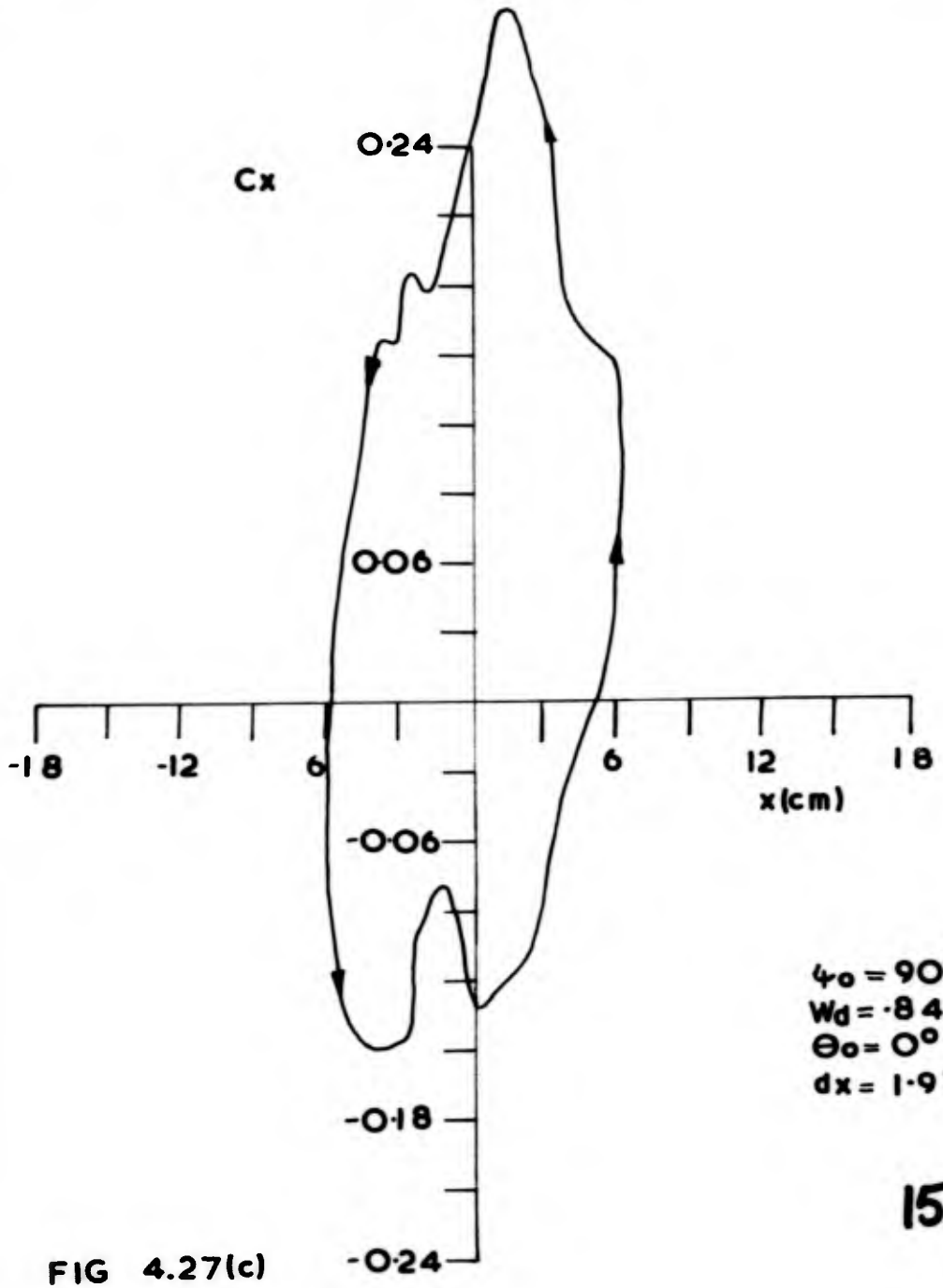

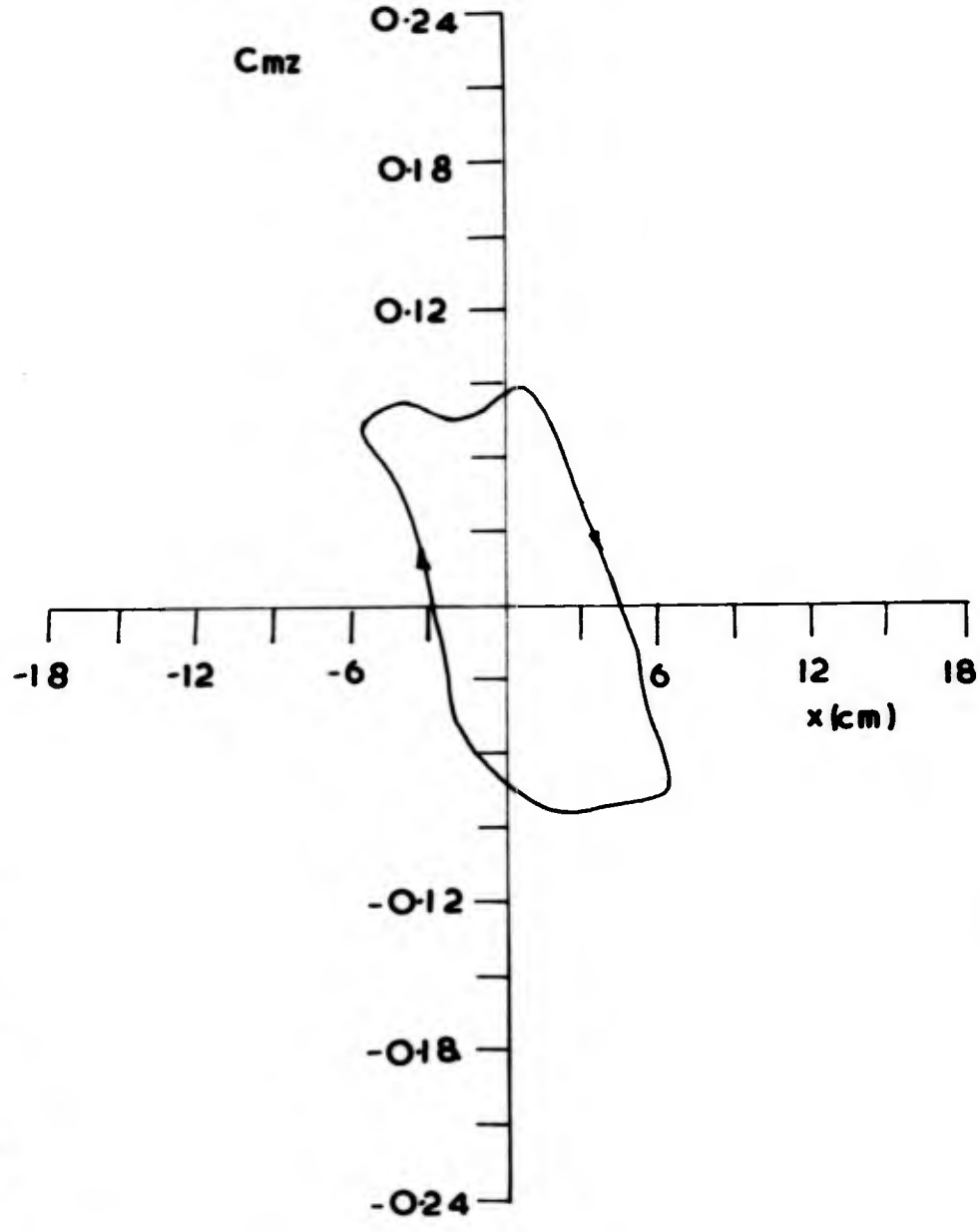

$\phi_0 = 90°$
$W_d = \cdot 84$
$\theta_0 = 0°$
$dx = 1 \cdot 9''$

151.

FIG 4.27(c)

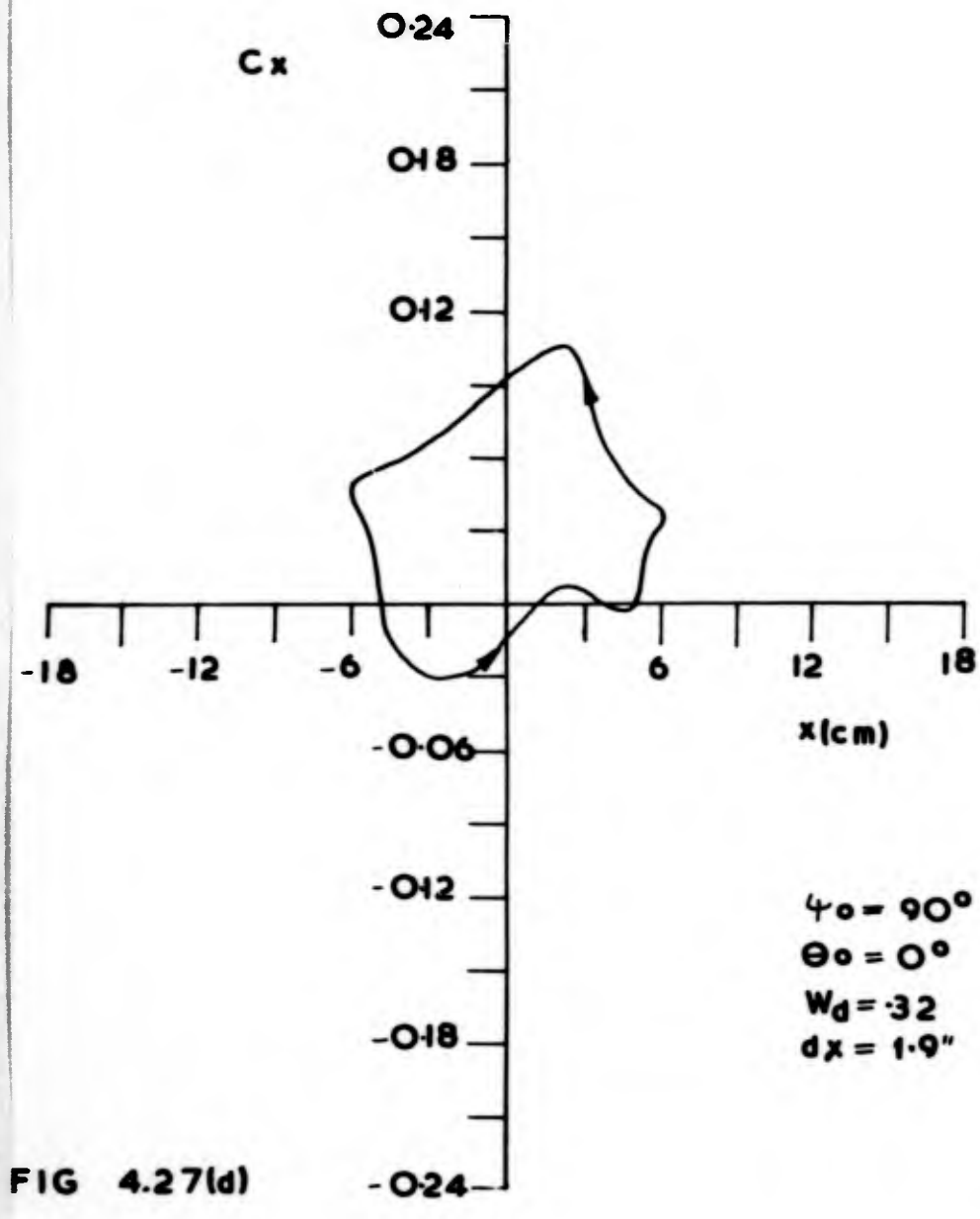
Cx
0·24
0·18
0·12
-0·06
-0·12
-0·18
-0·24
-18
-12
-6
6
12
18
x(cm)
φo = 90°
θo = 0°
Wd = ·32
dx = 1·9"

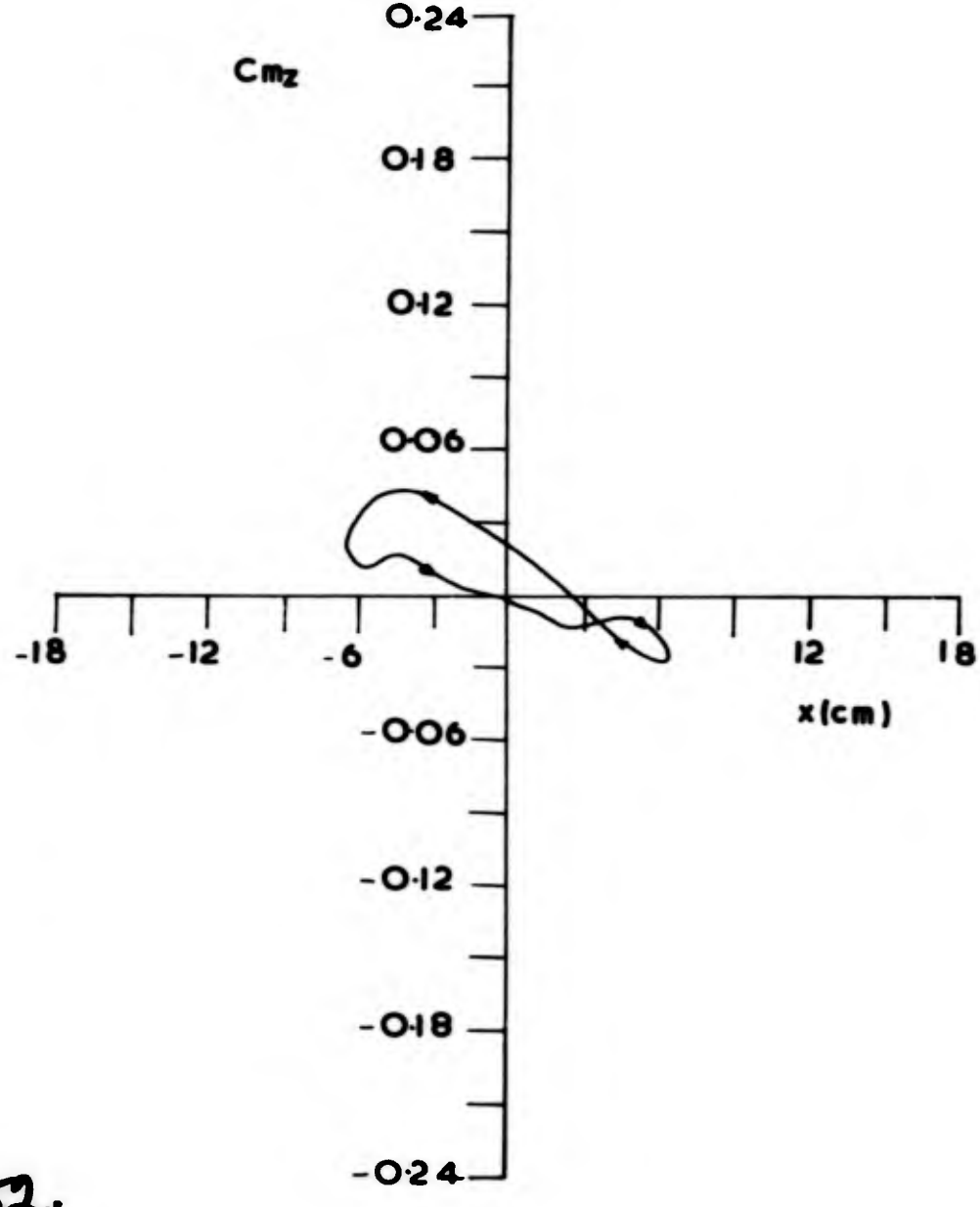
Cmz
0·24
0·18
0·12
0·06
-0·06
-0·12
-0·18
-0·24
-18
-12
-6
12
18
x(cm)

FIG 4.27(d)

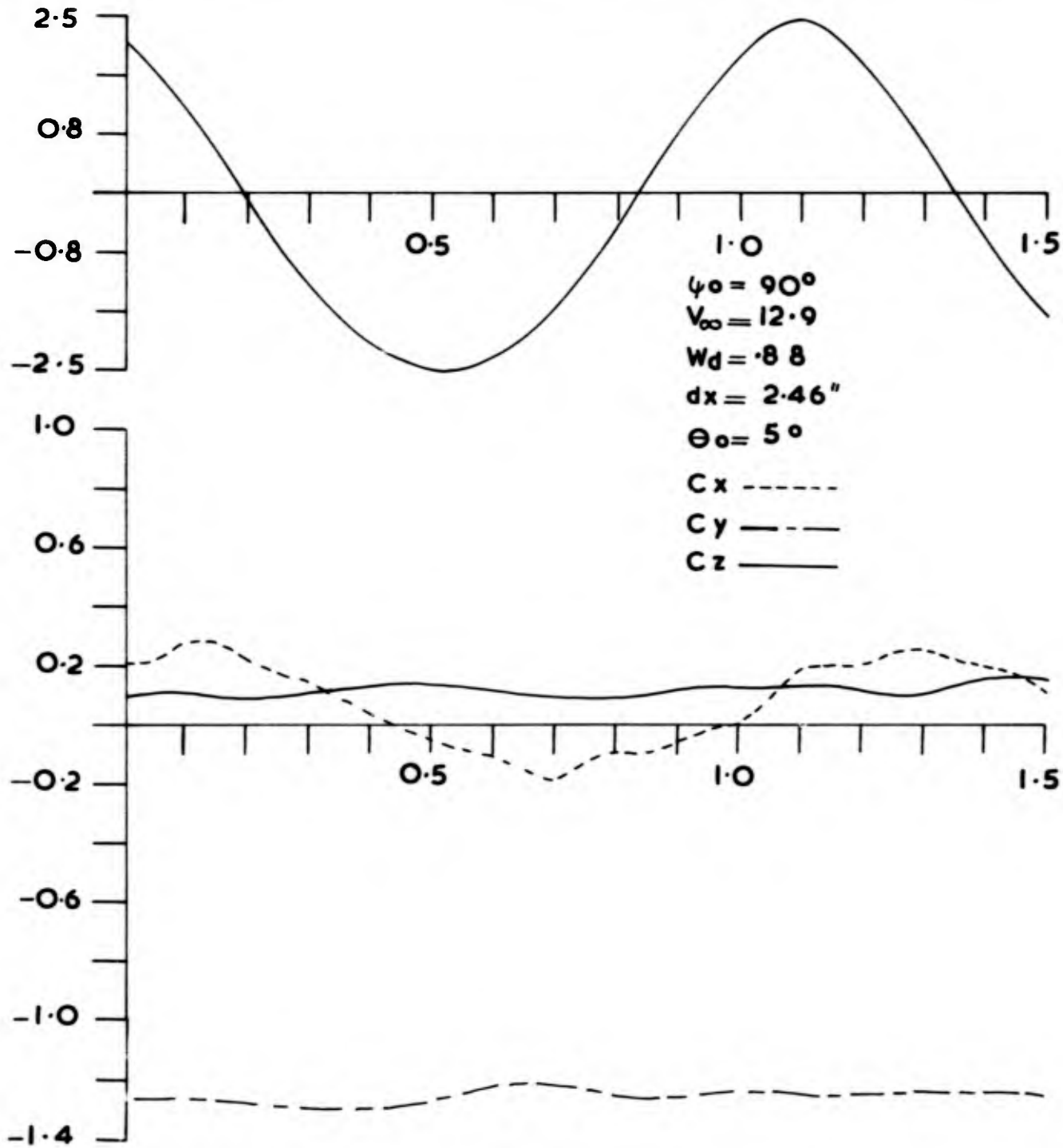
2·5
0·8
−0·8
−2·5
0·5
1·0
1·5
ψo = 90°
V∞ = 12·9
Wd = ·8 8
dx = 2·46"
Θo = 5°
Cx
Cy
Cz
1·0
0·6
0·2
−0·2
−0·6
−1·0
−1·4
0·5
1·0
1·5

FIG 4.28(a)

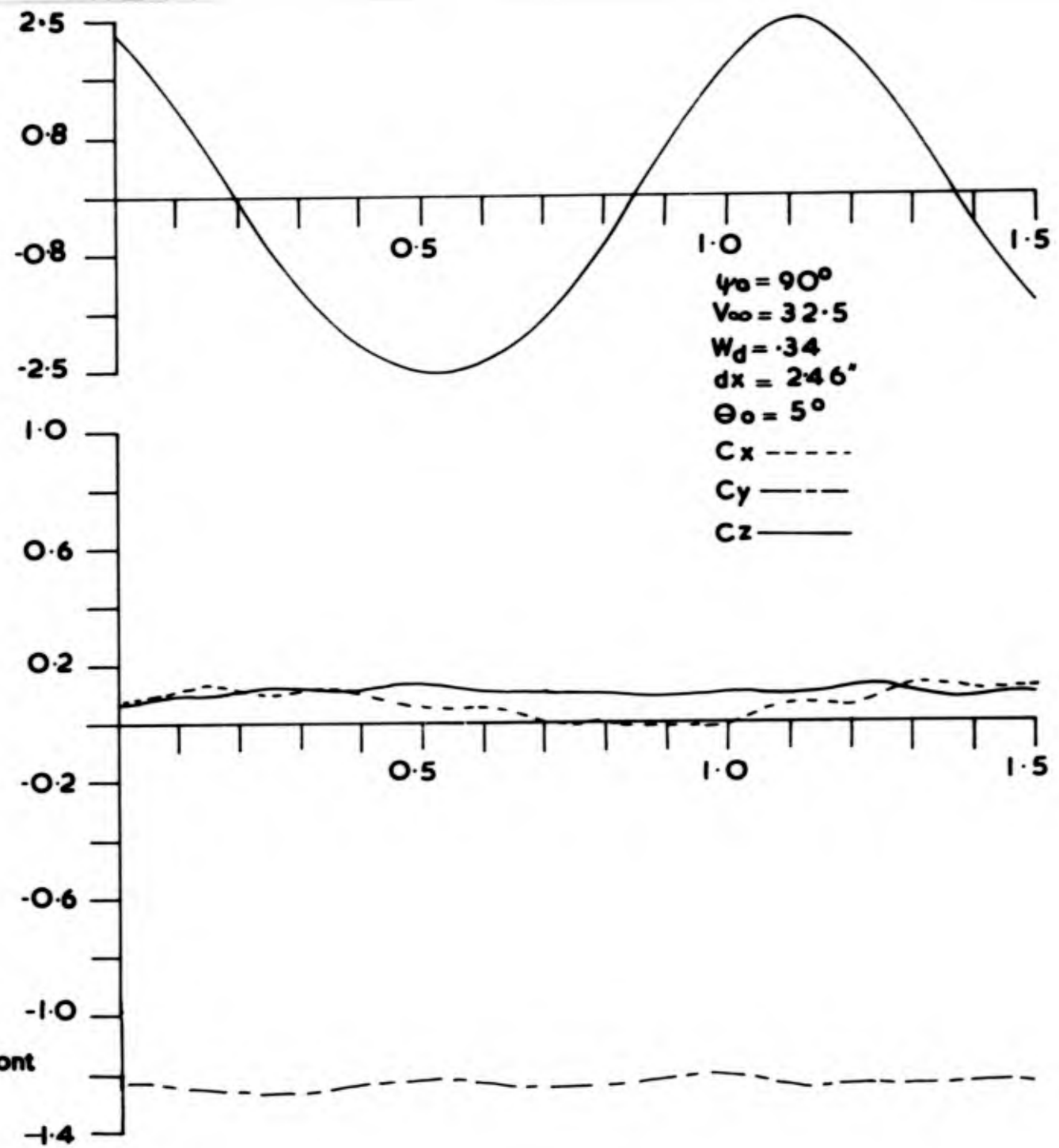

157

FIG 4.28(a)cont

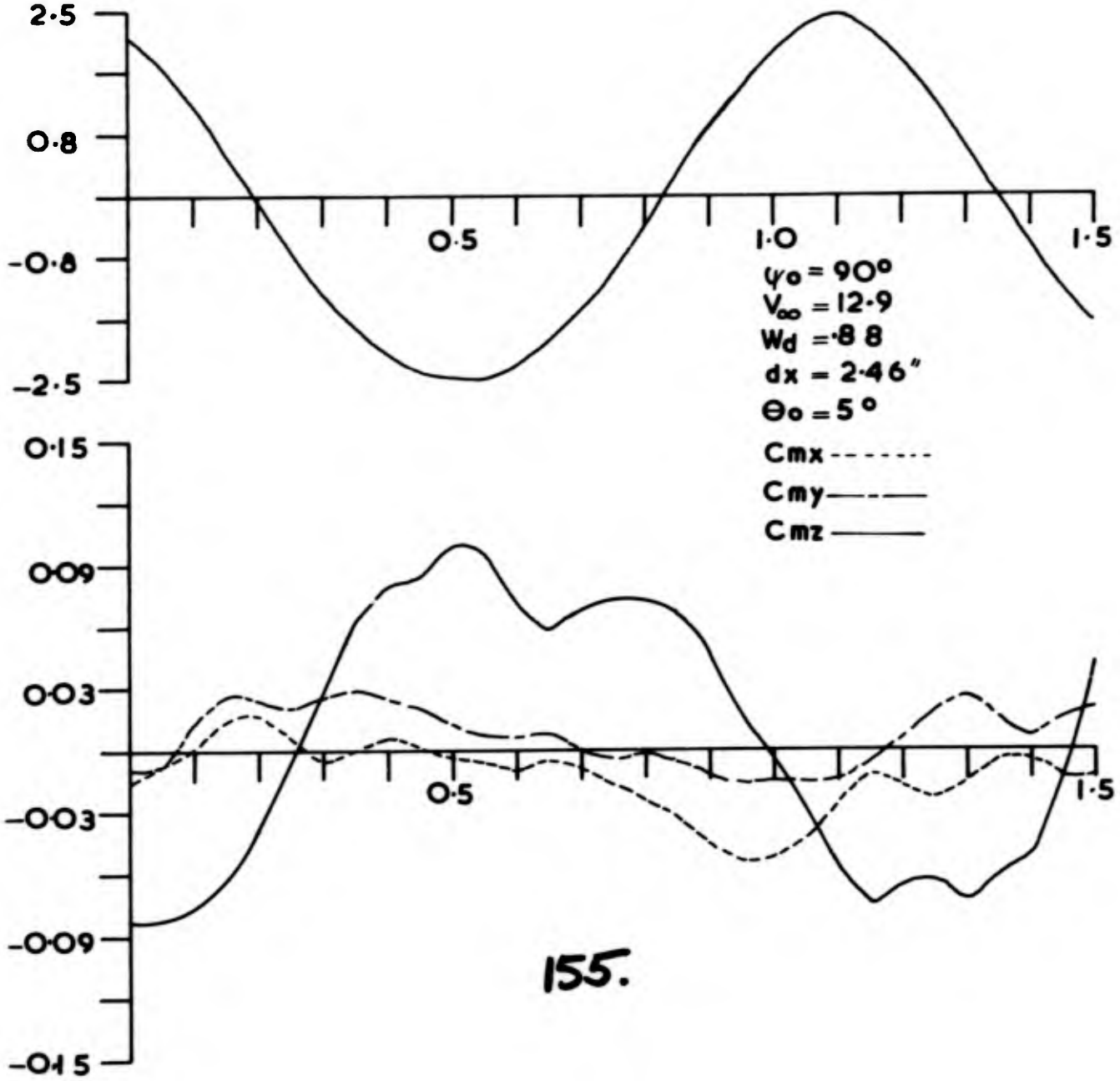
2·5
0·8
-0·8
-2·5
0·5
1·0
1·5
$\varphi_o = 90°$
$V_\infty = 12·9$
$W_d = ·88$
$dx = 2·46''$
$\Theta_o = 5°$
Cmx
Cmy
Cmz
0·15
0·09
0·03
-0·03
-0·09
-0·15
0·5
1·5

FIG 4.28(b)

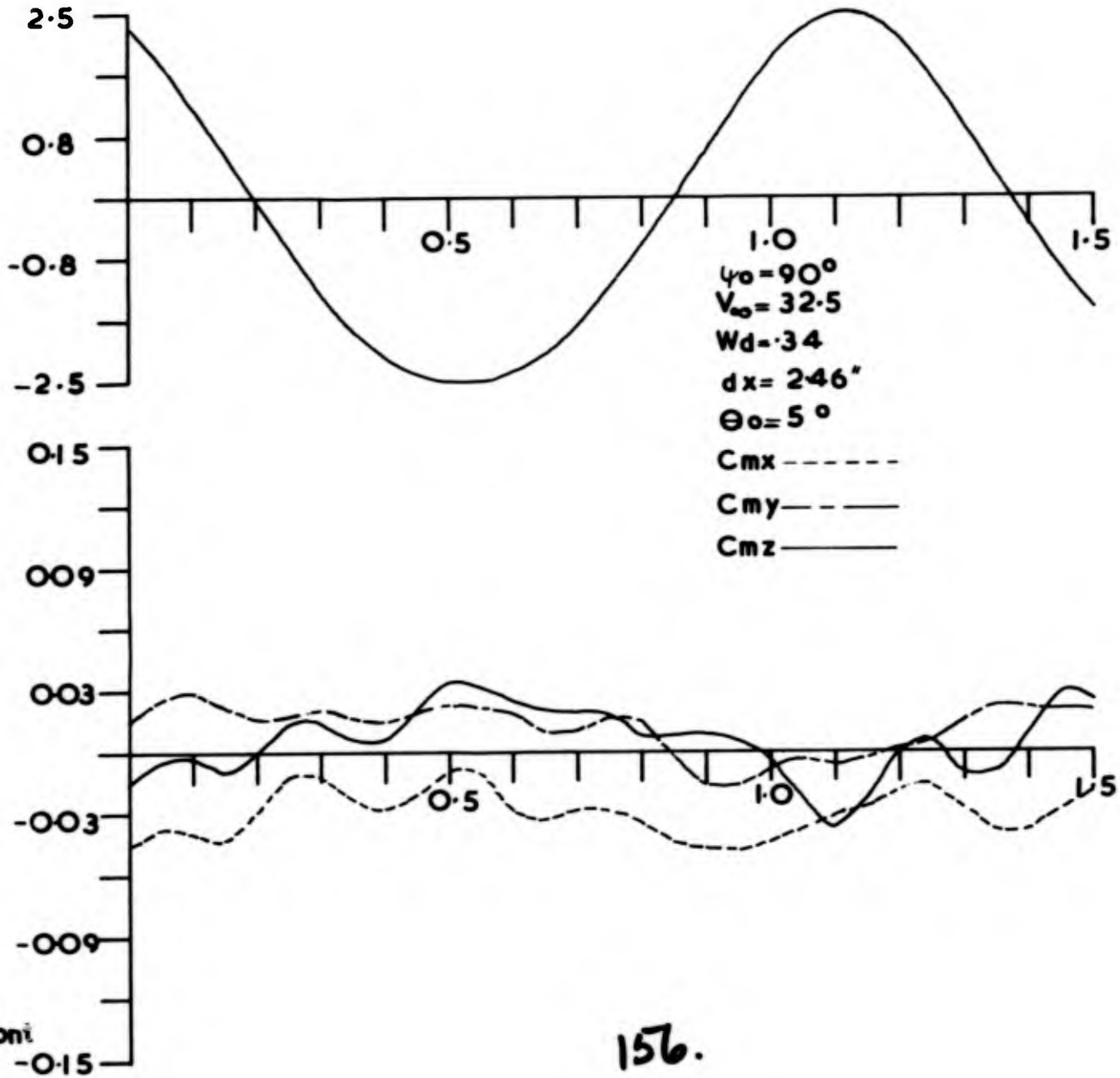

FIG 4.28(b)cont

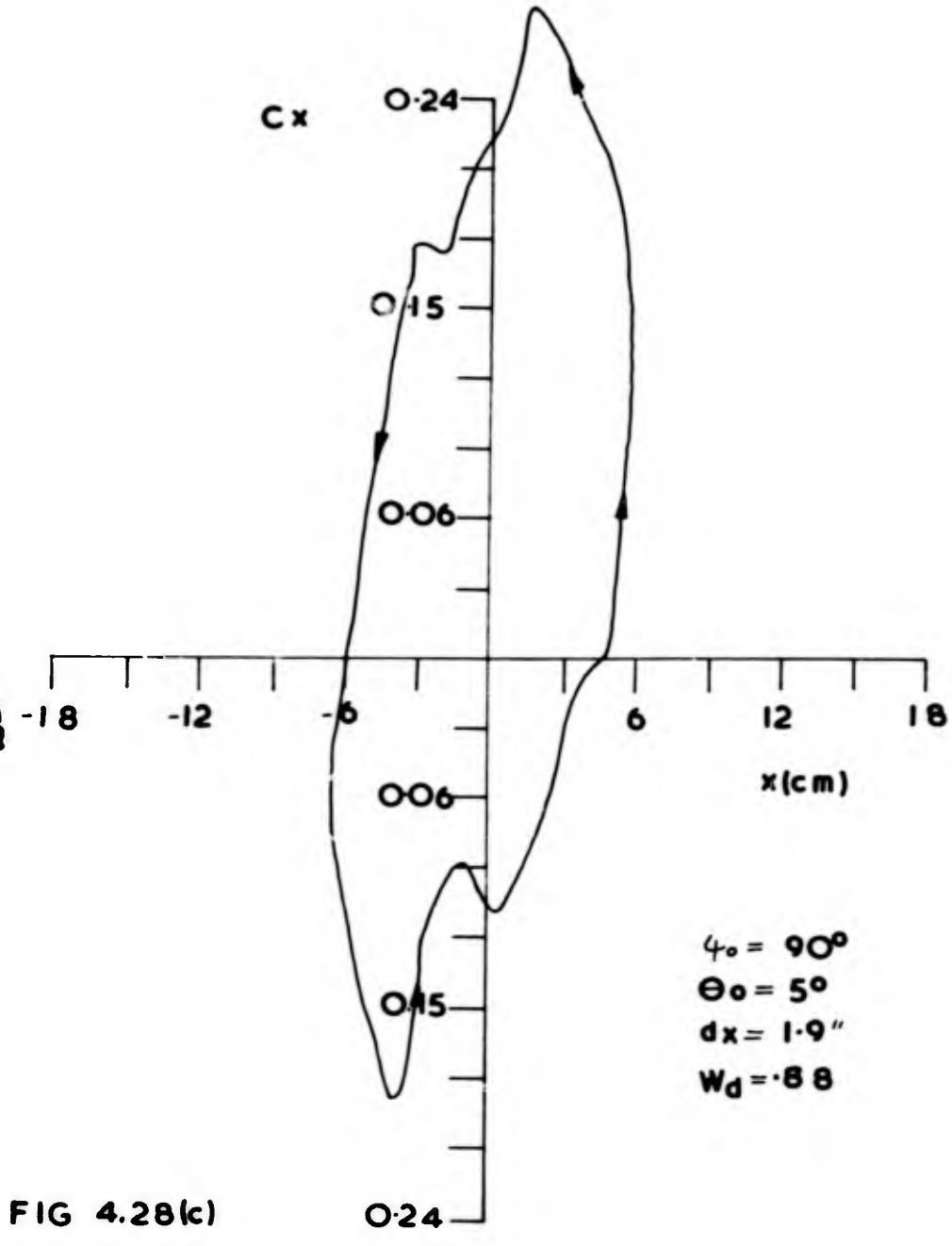

$\phi_o = 90°$
$\theta_o = 5°$
$dx = 1·9''$
$W_d = ·88$

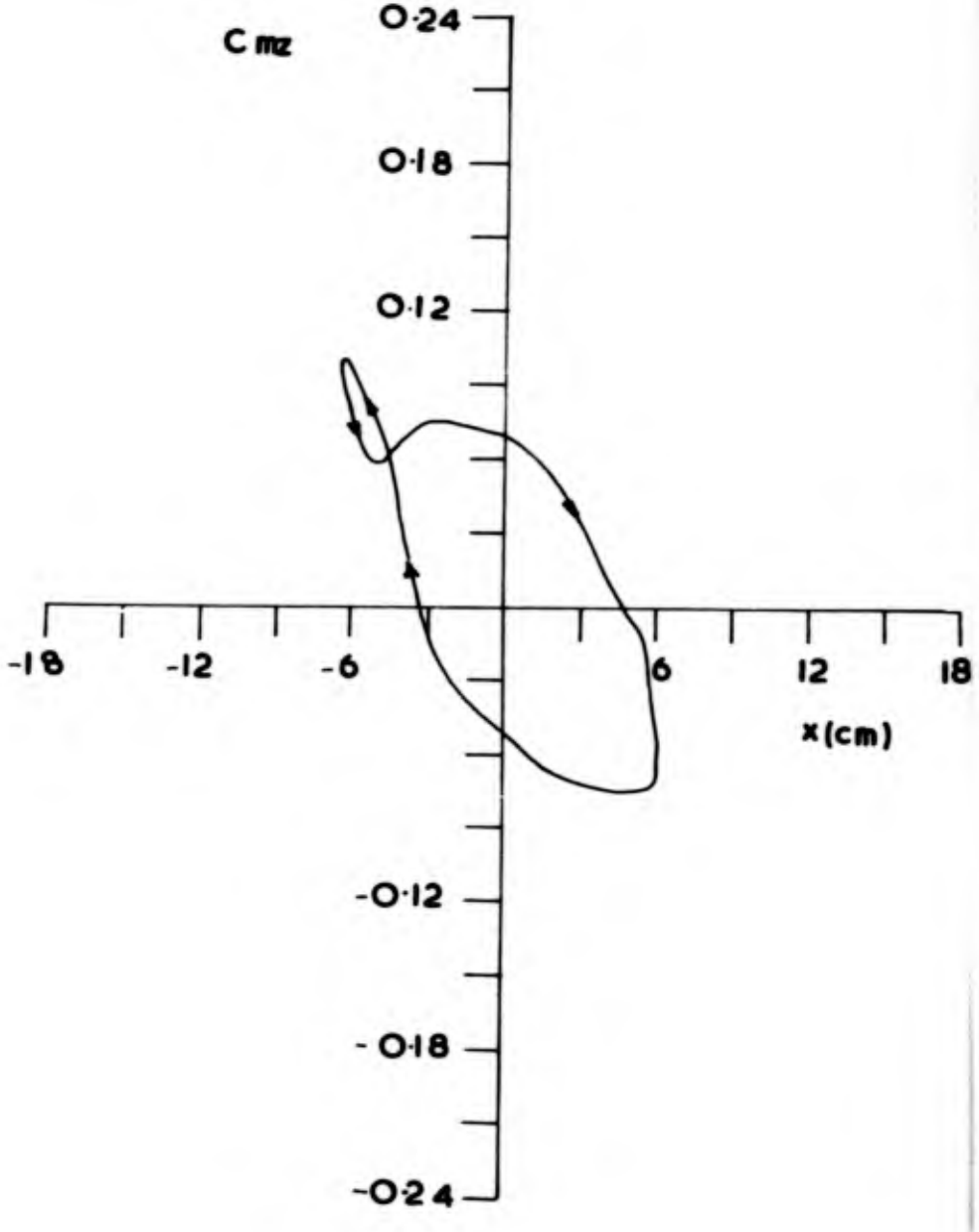

FIG 4.28(c)

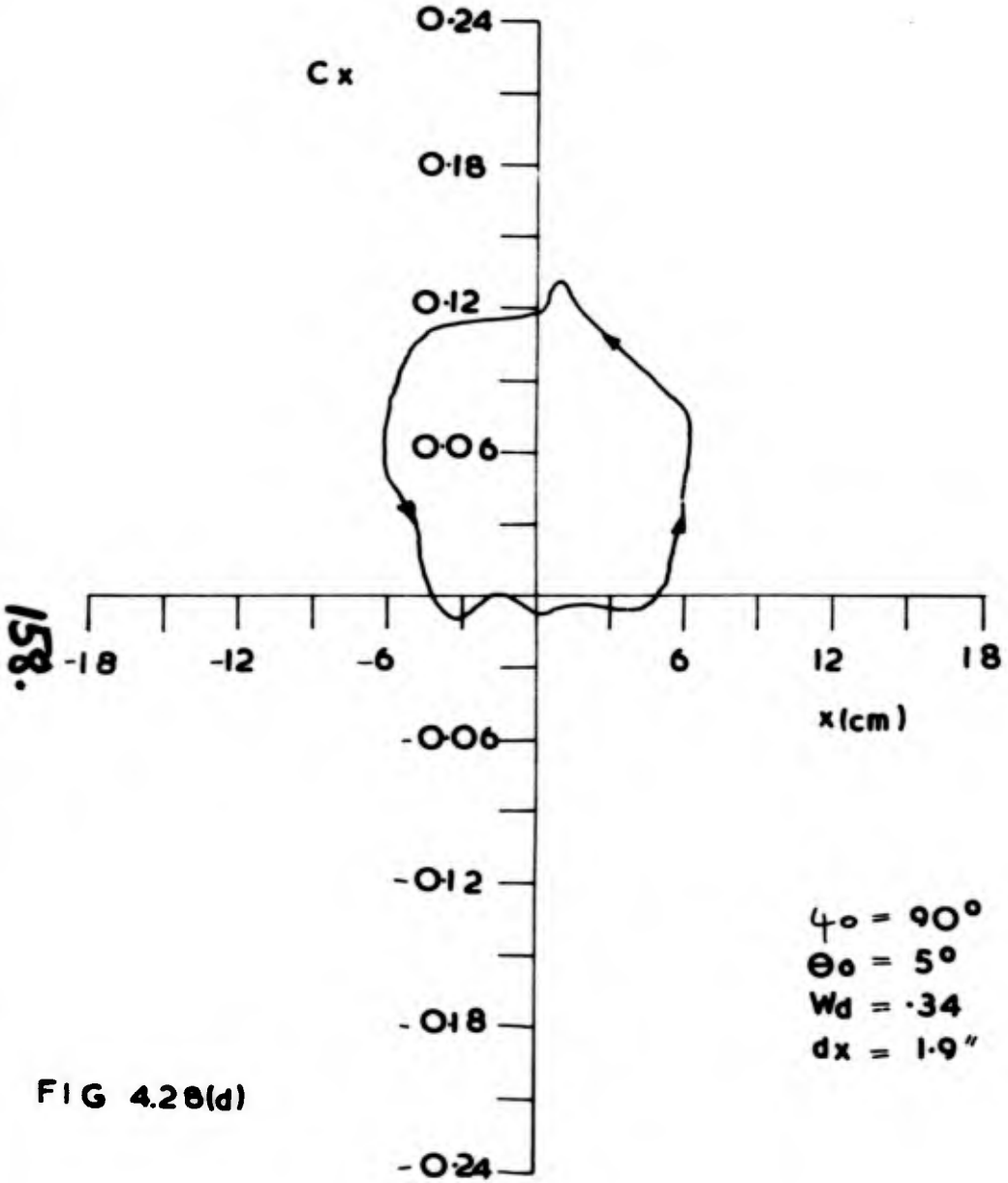

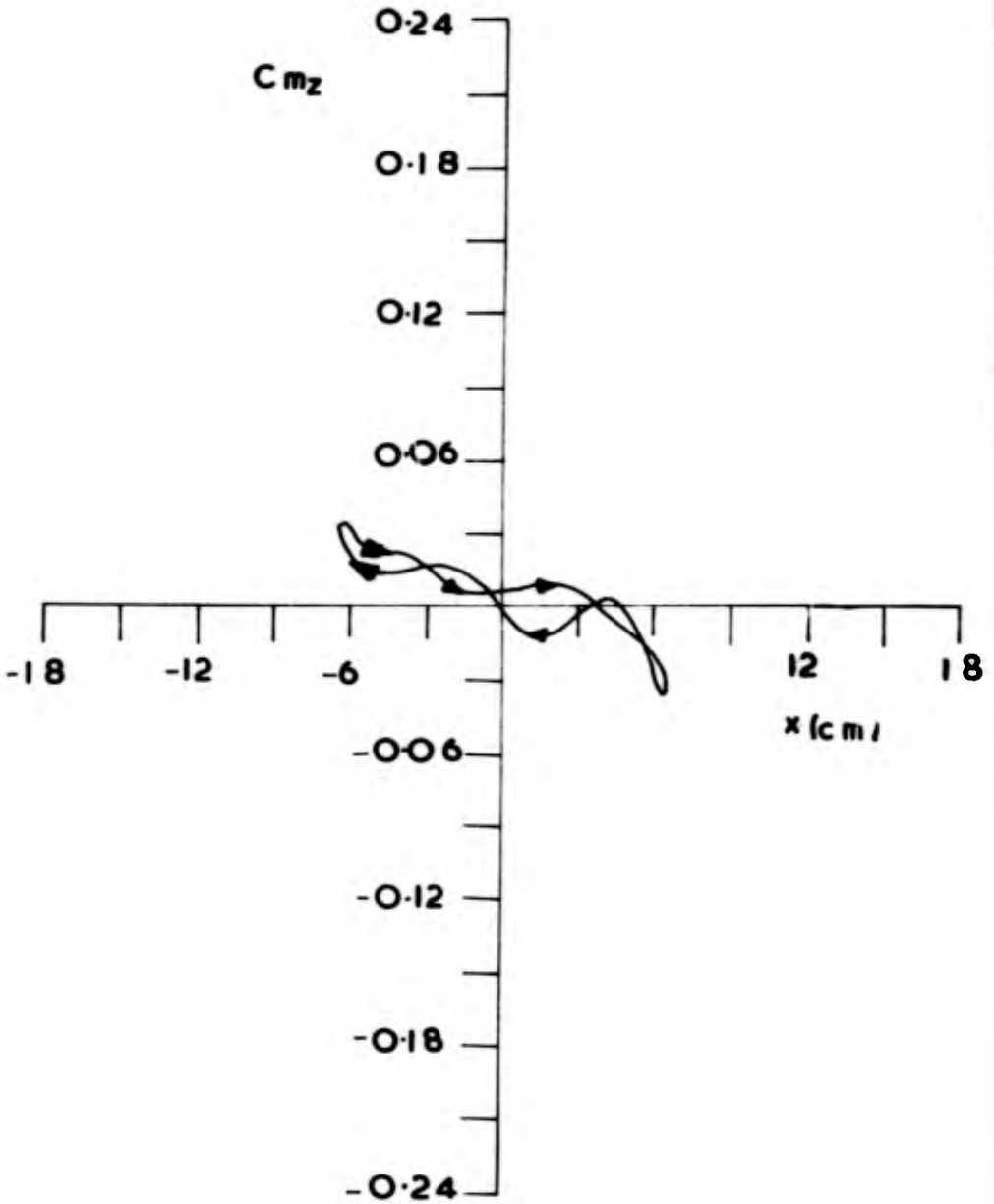

$\phi_o = 90°$
$\theta_o = 5°$
$W_d = .34$
$dx = 1.9''$

FIG 4.28(d)

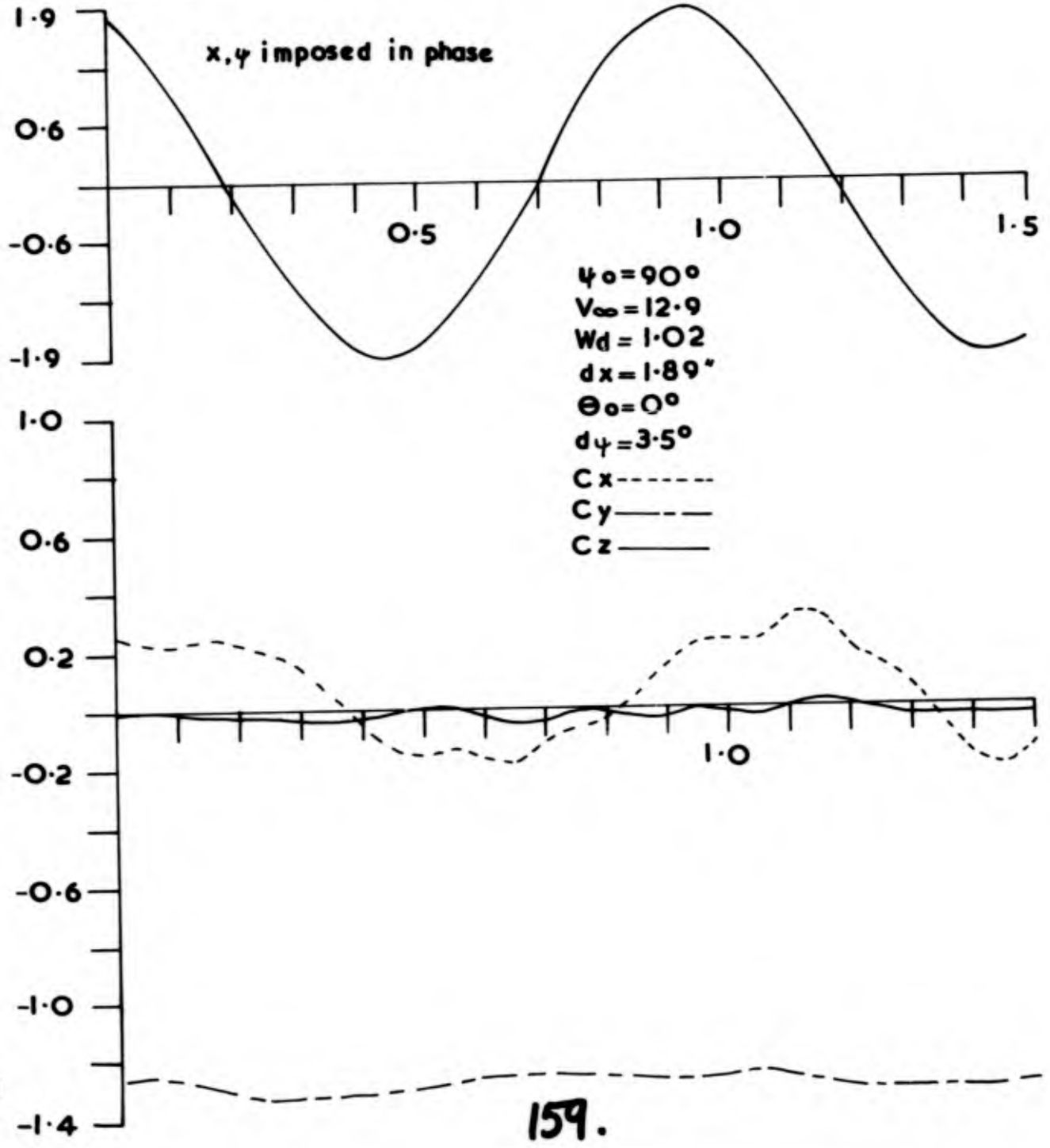
x,ψ imposed in phase
1·9
0·6
-0·6
-1·9
0·5
1·0
1·5
ψo=90°
V∞=12·9
Wd=1·02
dx=1·89"
Θo=0°
dψ=3·5°
Cx
Cy
Cz
1·0
0·6
0·2
-0·2
-0·6
-1·0
-1·4
1·0

FIG 4.29(a)

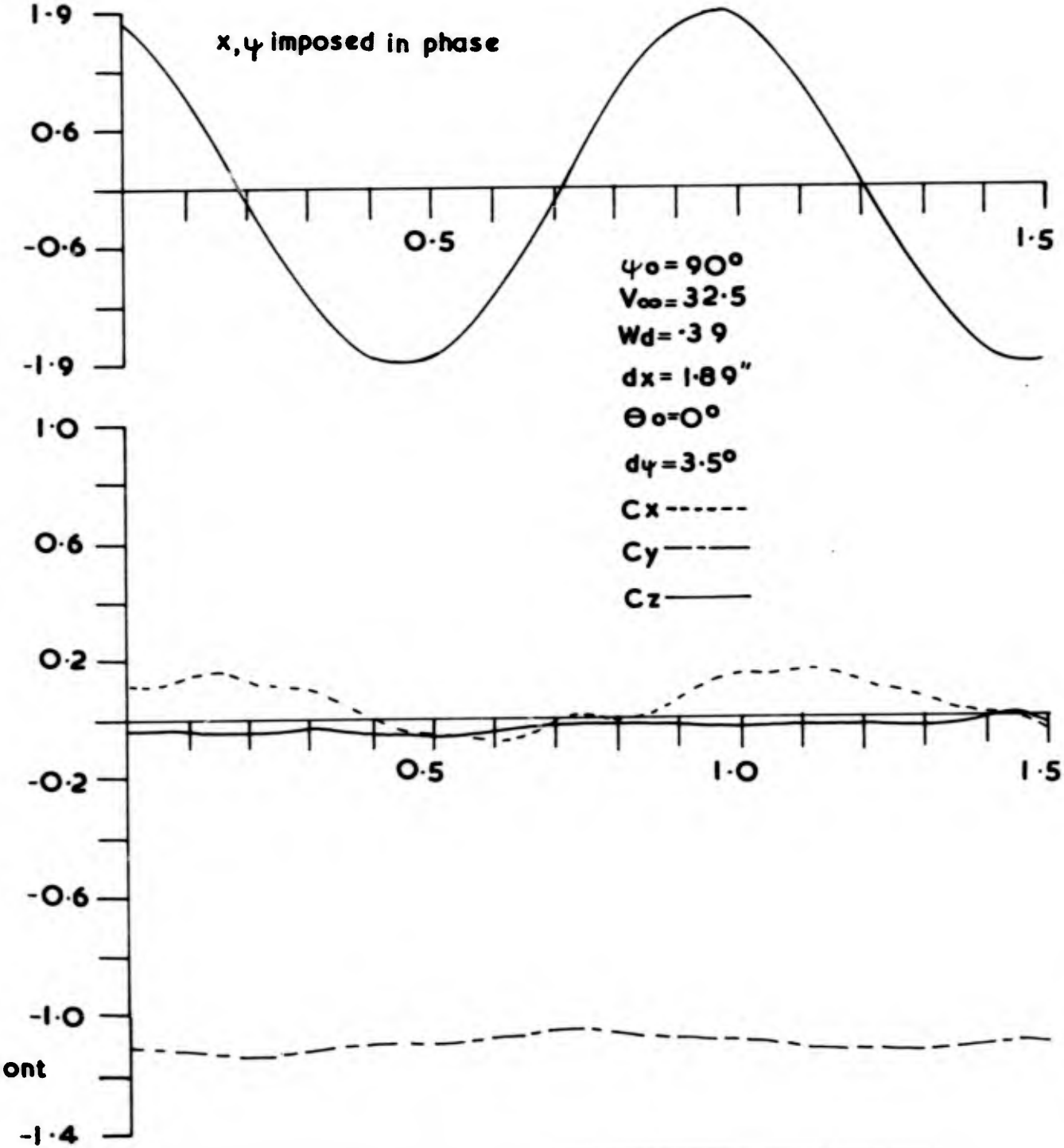

FIG 4.29(a)cont

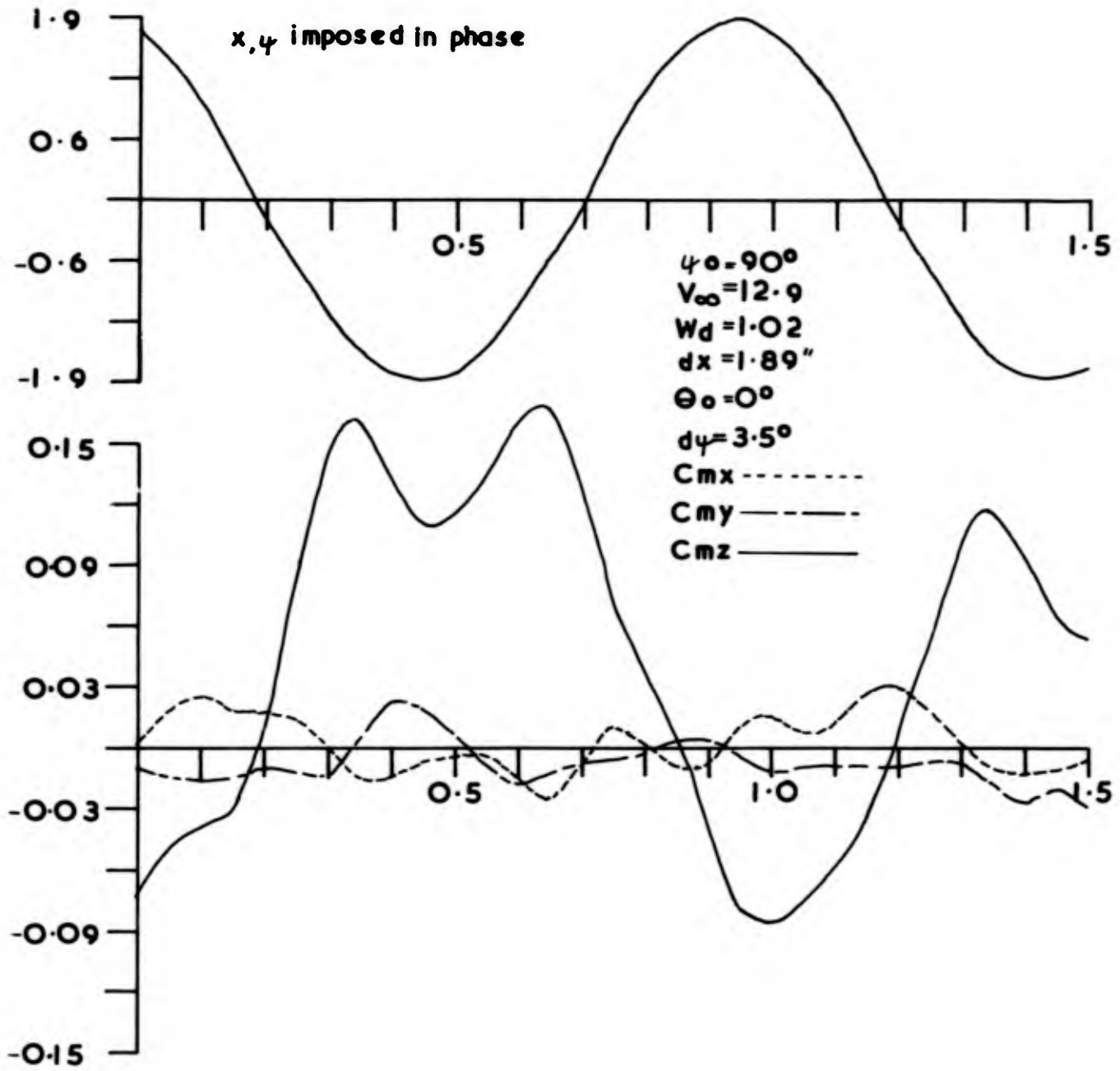
x, ψ imposed in phase
1·9
0·6
-0·6
-1·9
0·5
1·5
ψo=90°
V∞=12·9
Wd=1·02
dx=1·89"
Θo=0°
dψ=3·5°
Cmx
Cmy
Cmz
0·15
0·09
0·03
-0·03
-0·09
-0·15
0·5
1·0
1·5

FIG 4.29(b)

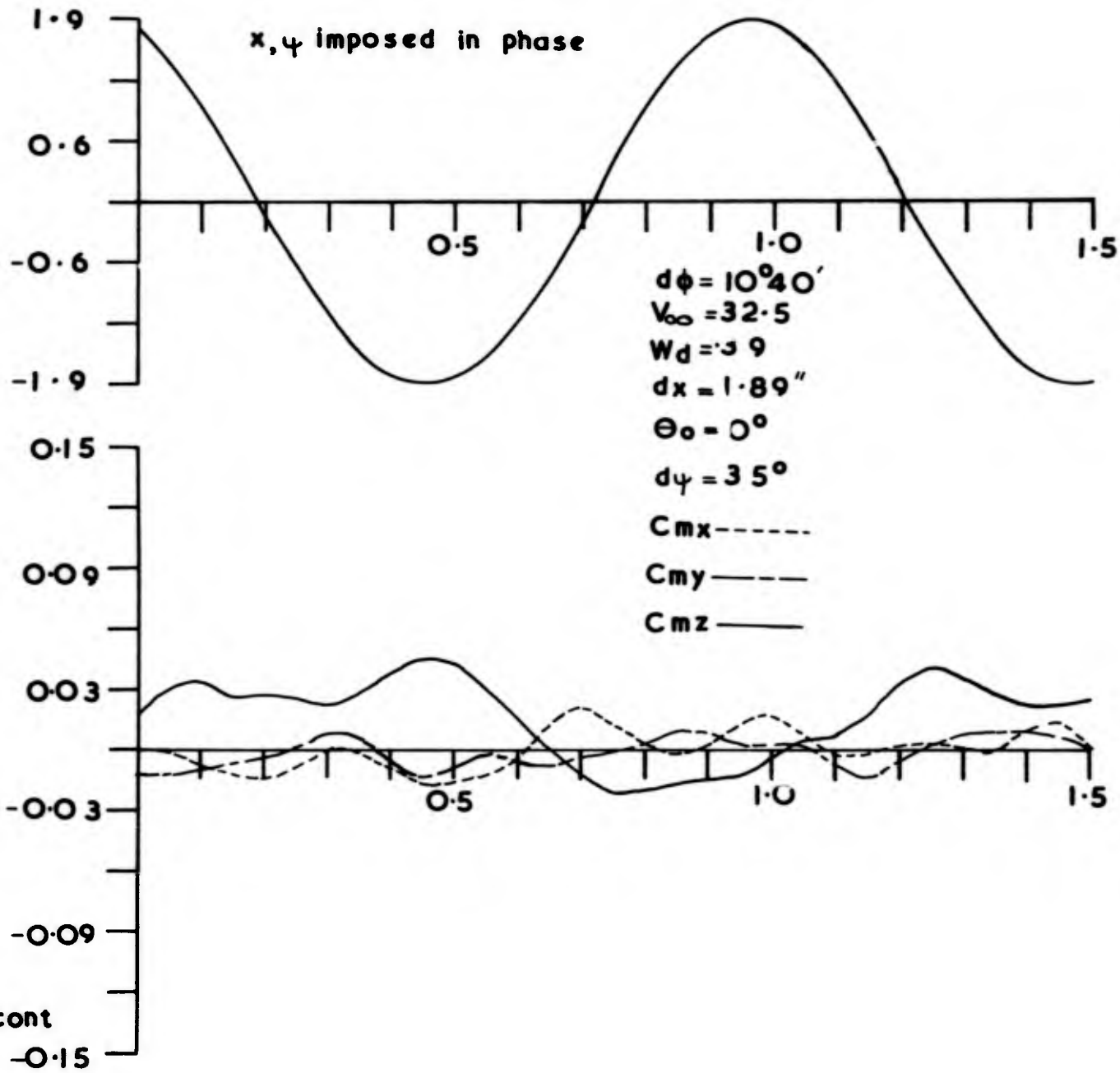

FIG 4.29(b)cont

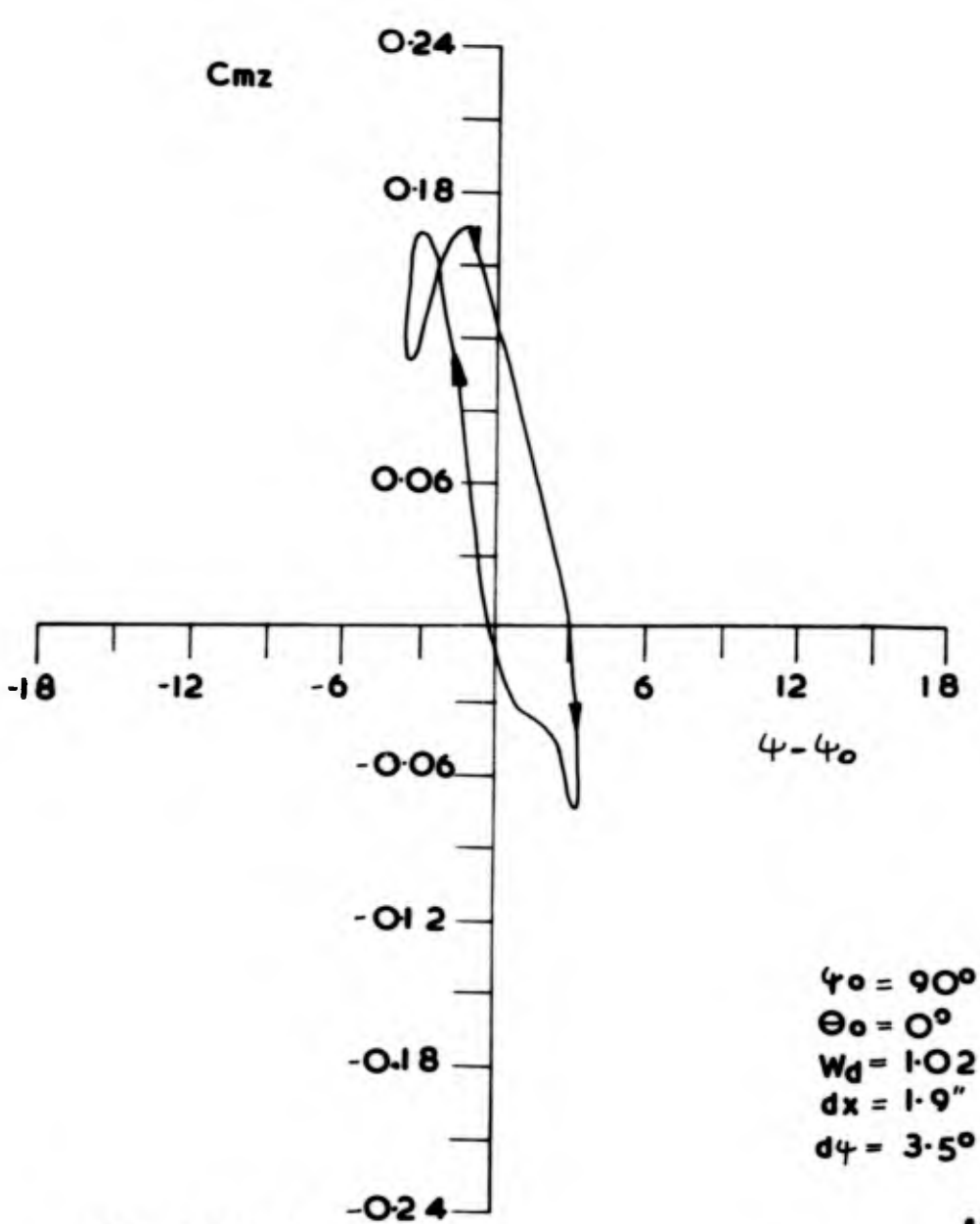

FIG 4.29(c)

ψo = 90°
θo = 0°
Wd = 1·02
dx = 1·9"
dψ = 3·5°

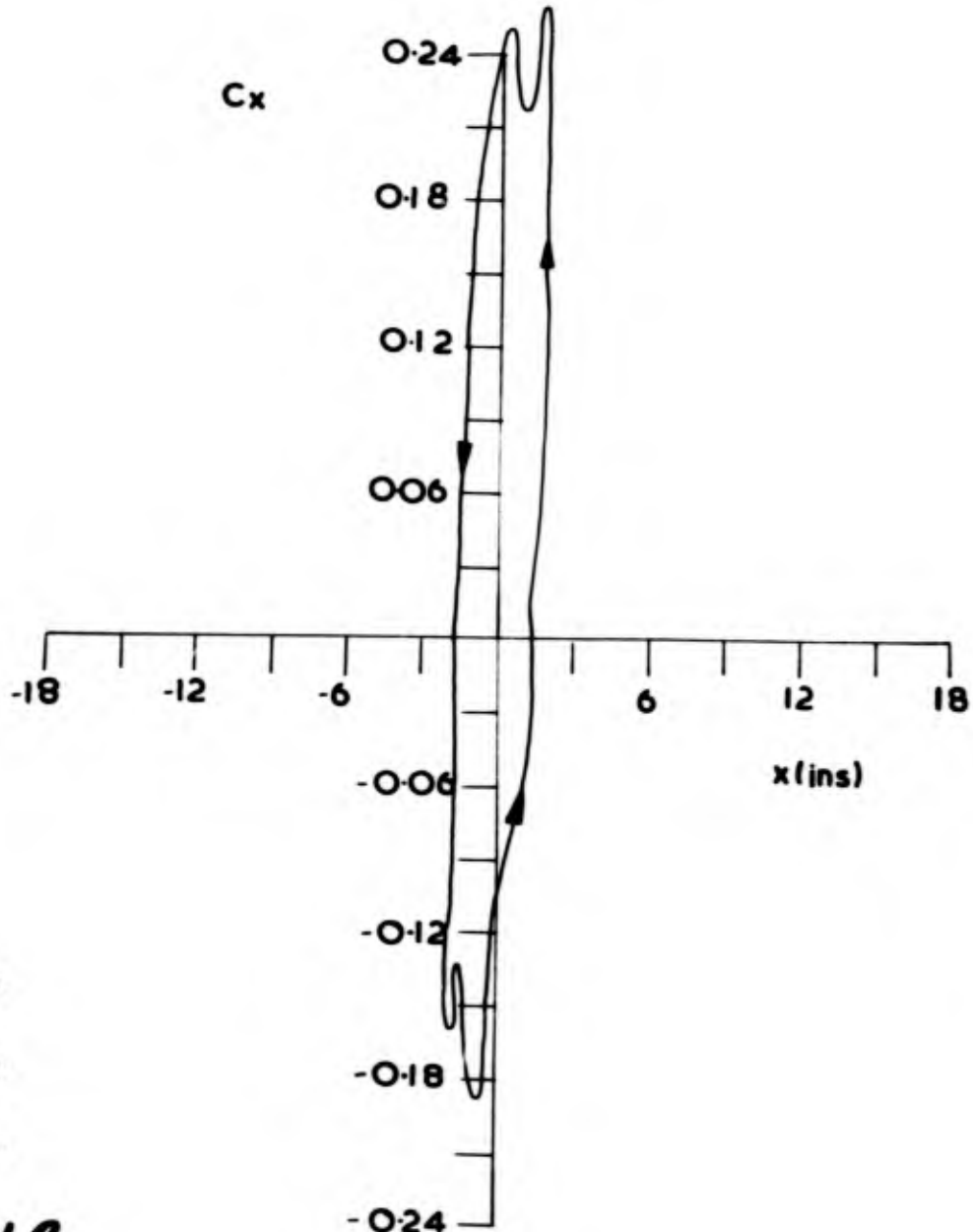

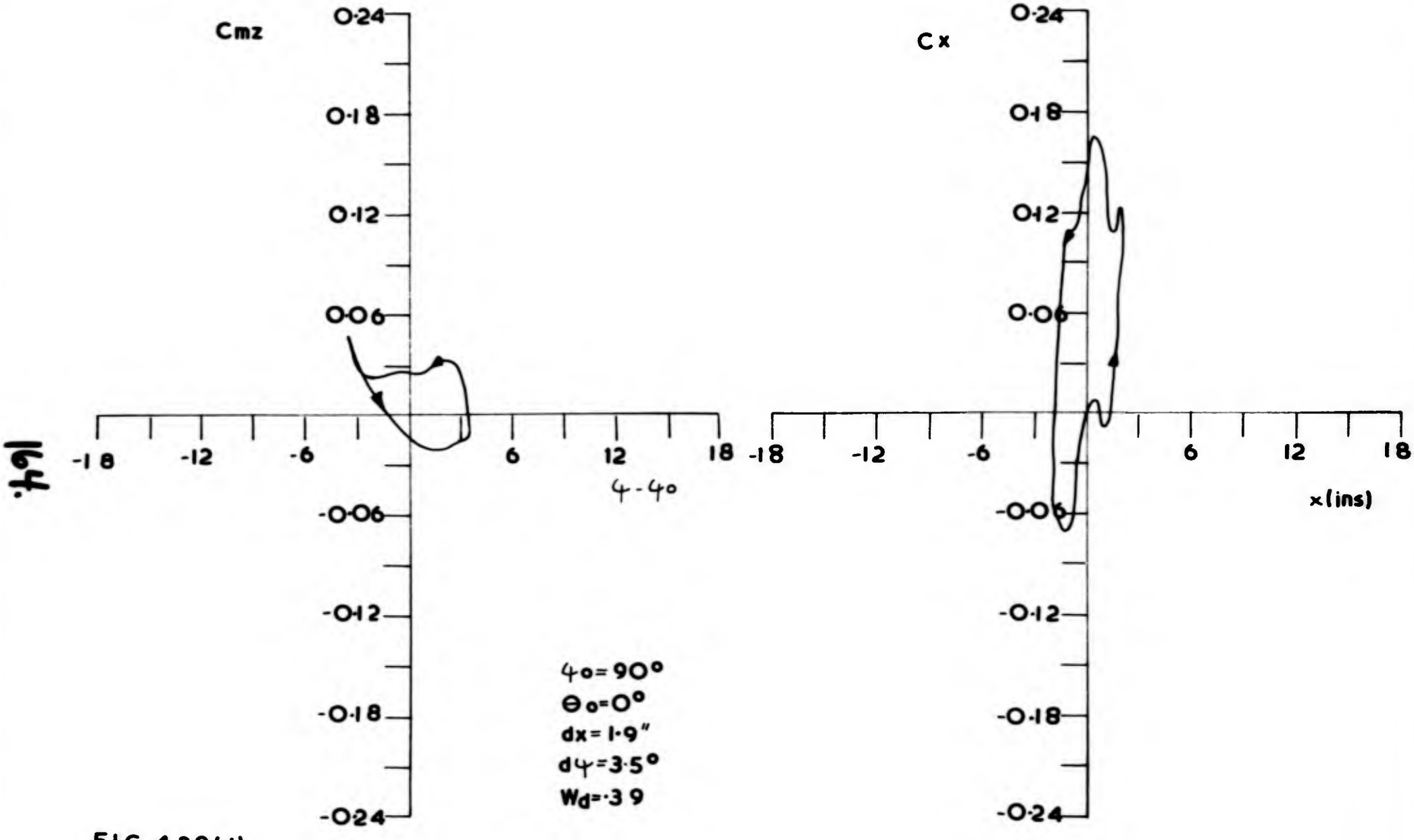
Cmz
0·24
0·18
0·12
0·06
-0·06
-0·12
-0·18
-0·24
-18
-12
-6
6
12
18
ψ - ψo
ψo = 90°
θo = 0°
dx = 1·9"
dψ = 3·5°
Wd = ·39
Cx
0·24
0·18
0·12
0·06
-0·06
-0·12
-0·18
-0·24
-18
-12
-6
6
12
18
x (ins)

FIG 4.29(d)

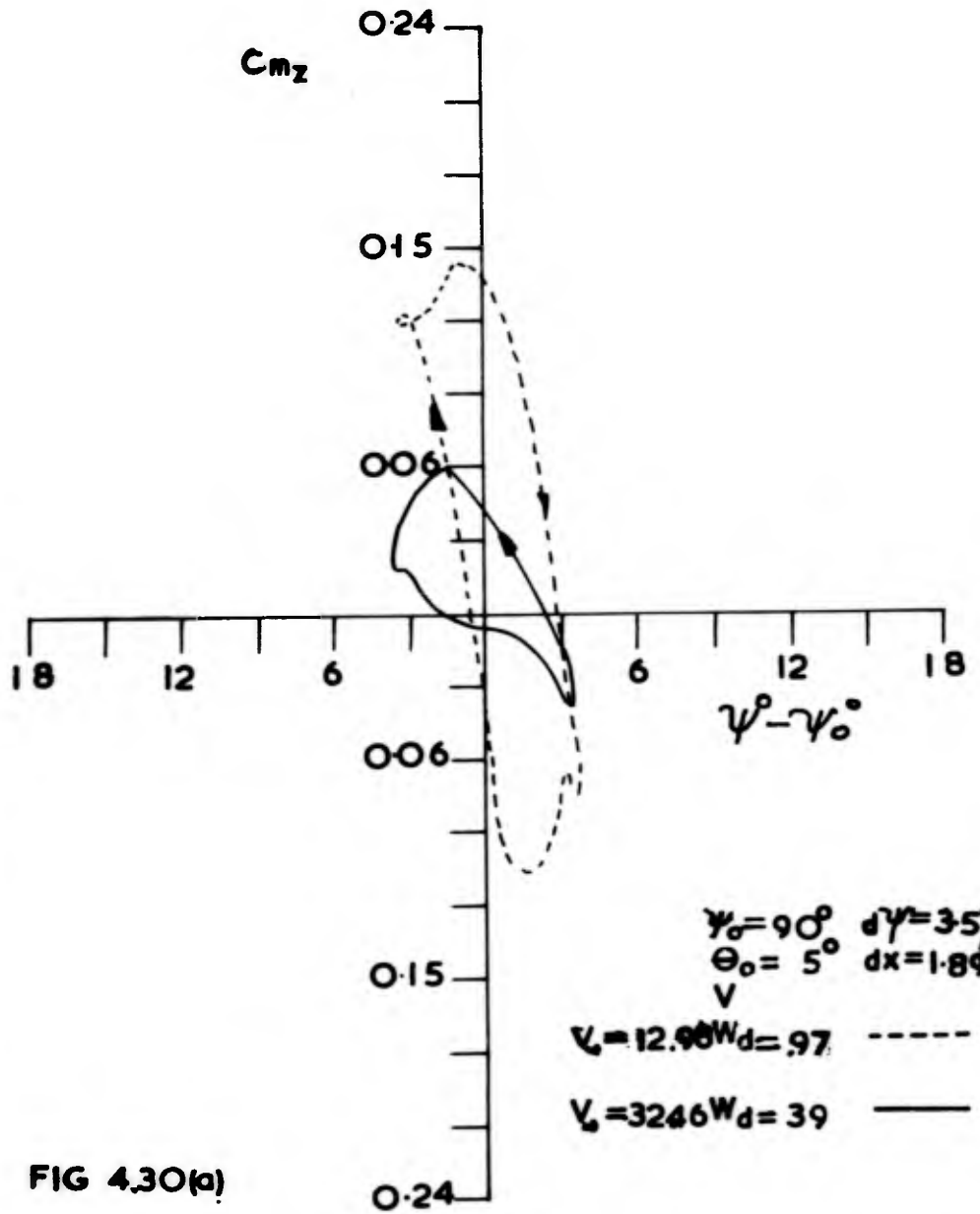

FIG 4.30(a)

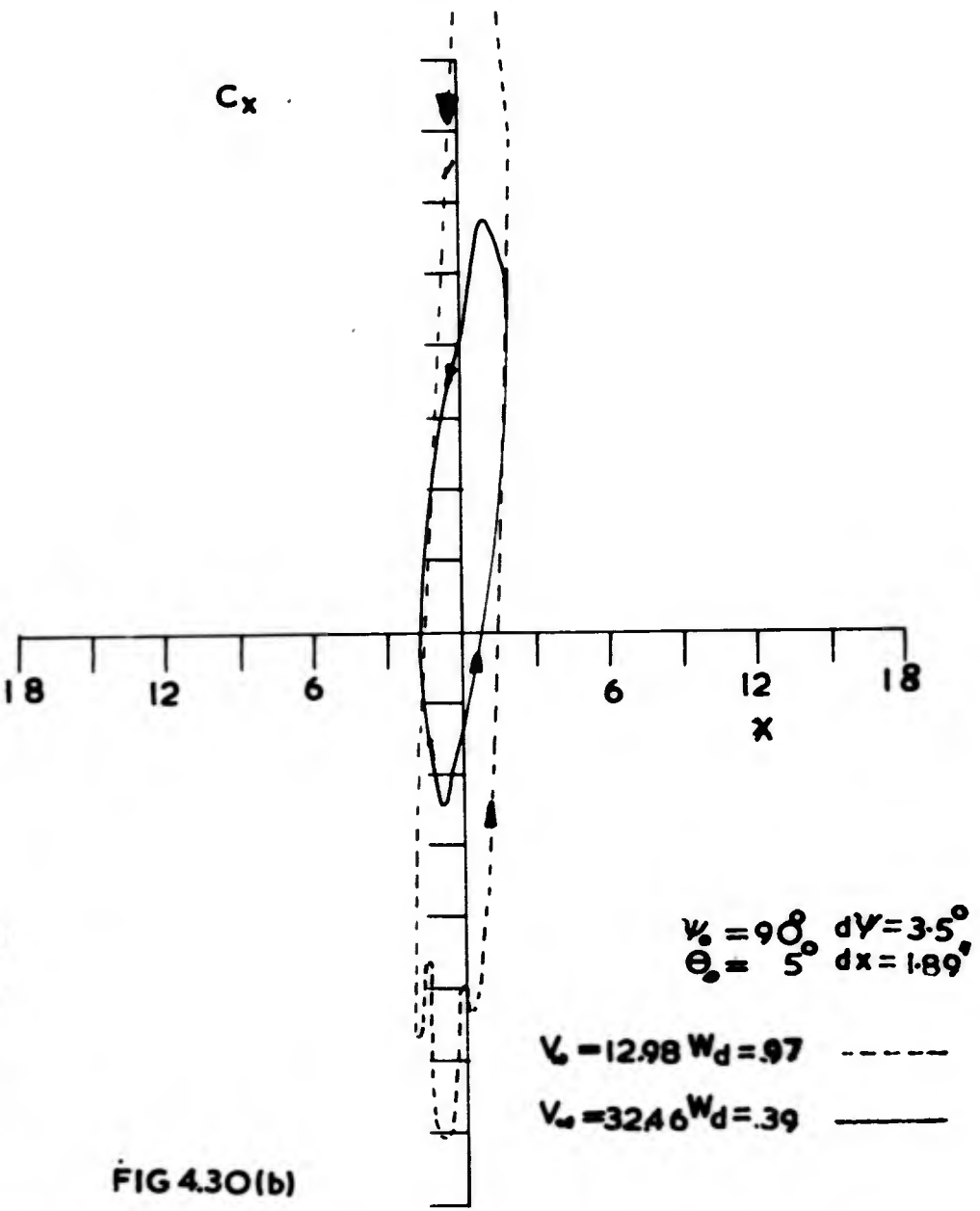

FIG 4.30(b)

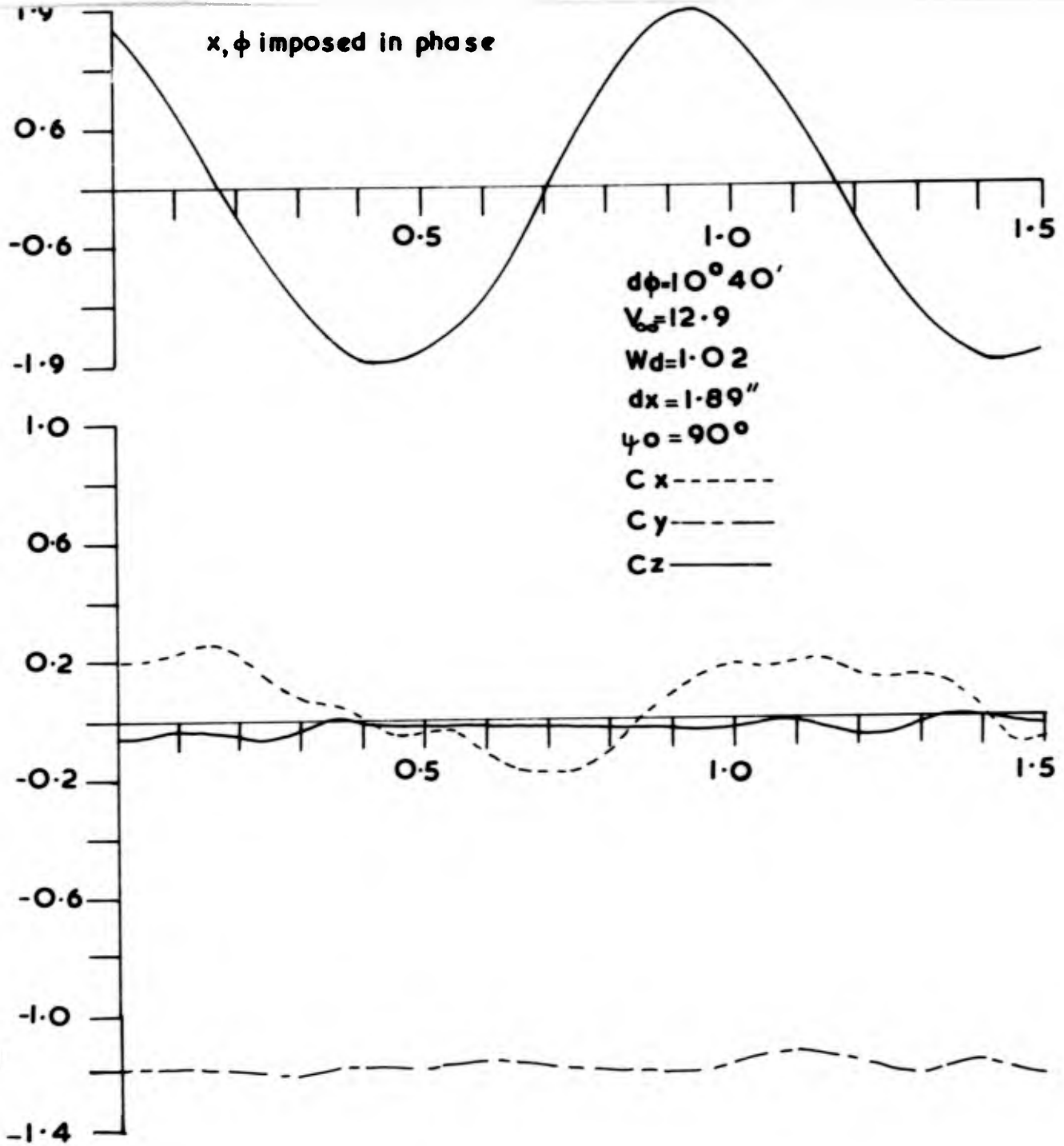
x, ϕ imposed in phase
1·9
0·6
-0·6
-1·9
0·5
1·0
1·5
dϕ-10°40'
V∞=12·9
Wd=1·02
dx=1·89"
ψo=90°
C x------
C y— - —
Cz———
1·0
0·6
0·2
-0·2
-0·6
-1·0
-1·4
0·5
1·0
1·5

FIG 4.31 (a)

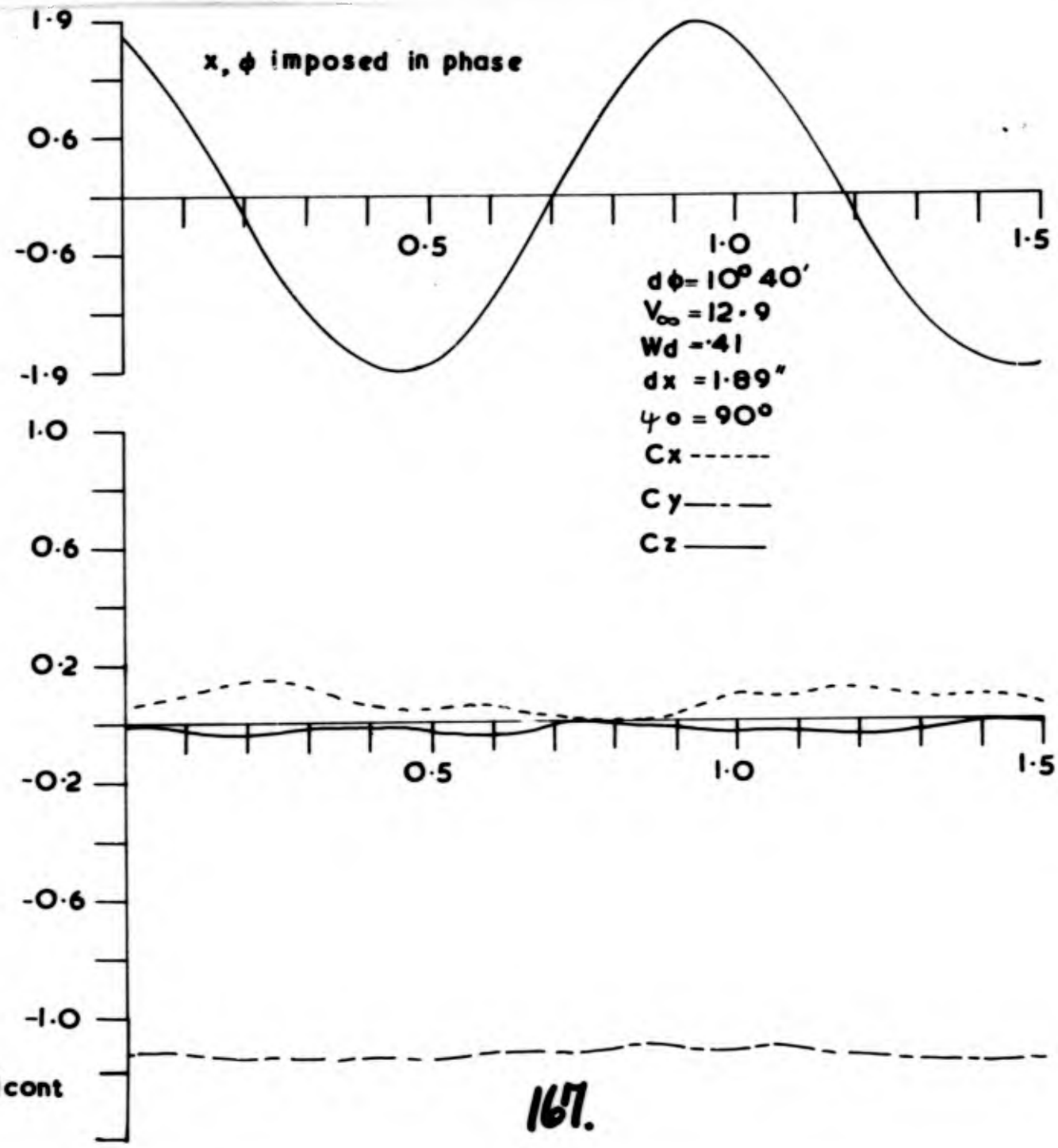

FIG 4.31 (a) cont

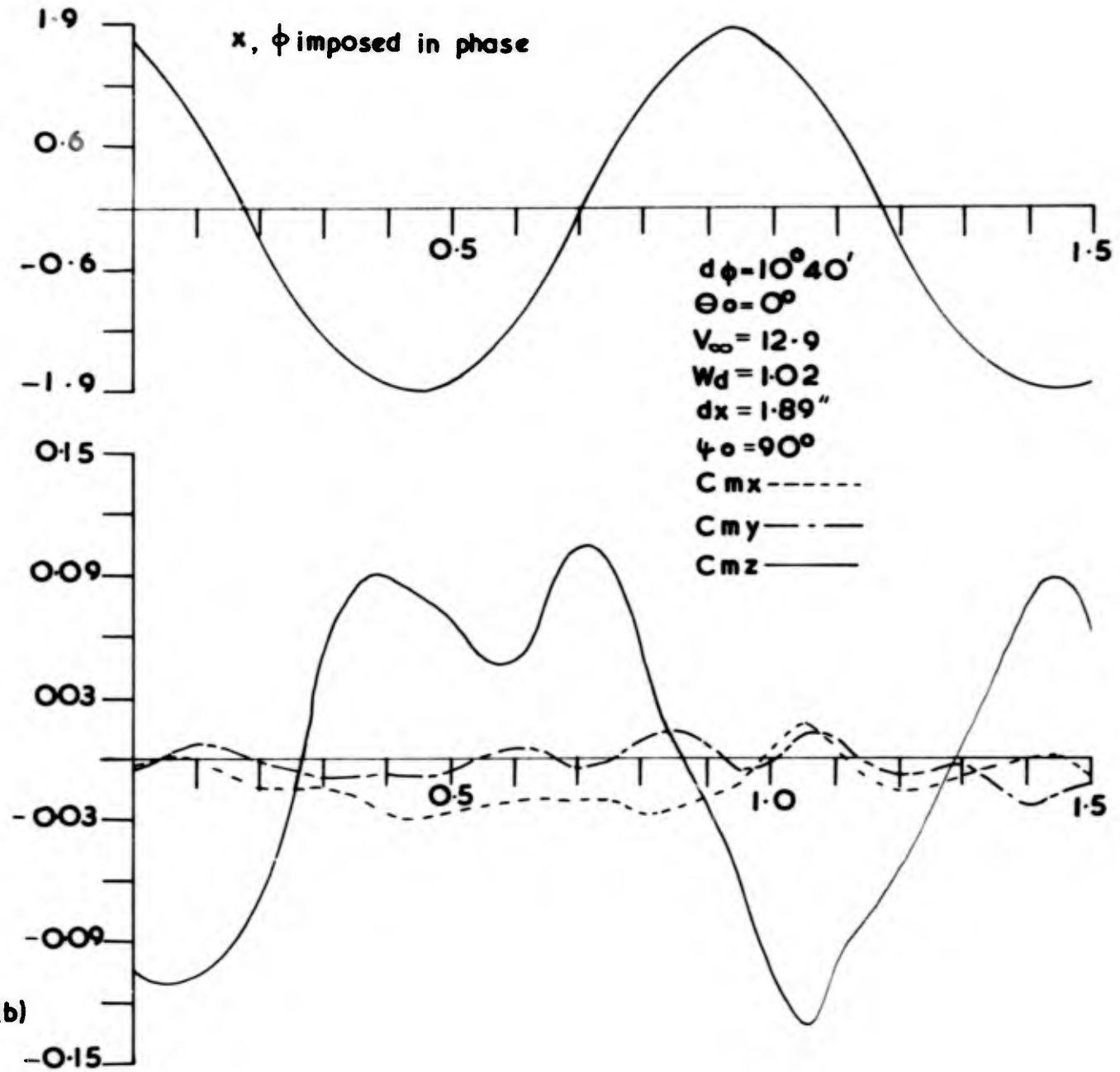
x, ϕ imposed in phase
1·9
0·6
-0·6
-1·9
0·5
1·5
dϕ=10°40'
Θo=0°
V∞=12·9
Wd=1·02
dx=1·89"
ψo=90°
Cmx
Cmy
Cmz
0·15
0·09
003
-003
-0·09
-0·15
0·5
1·0
1·5

FIG 4.31 (b)

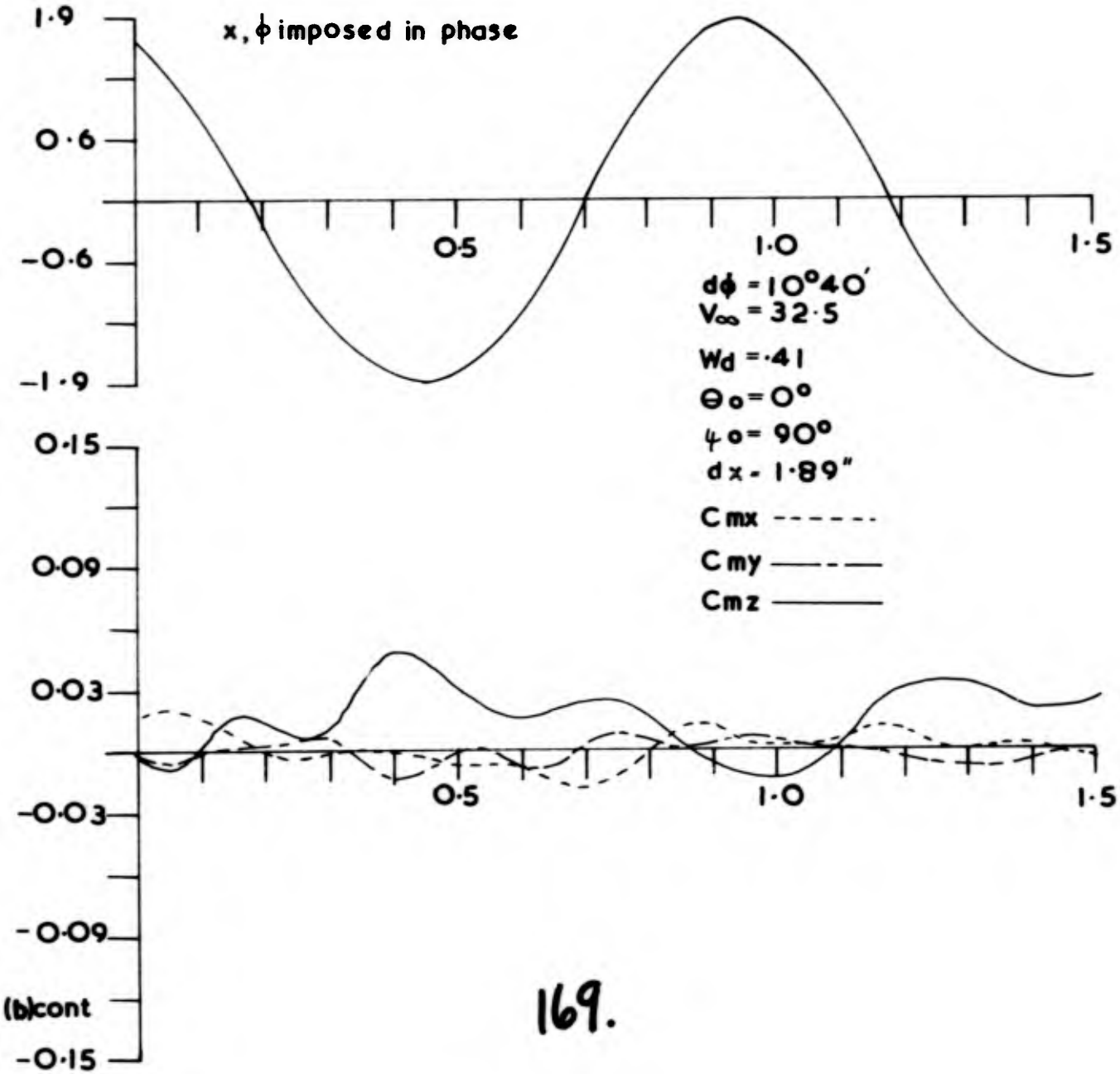

FIG 4·31 (b) cont

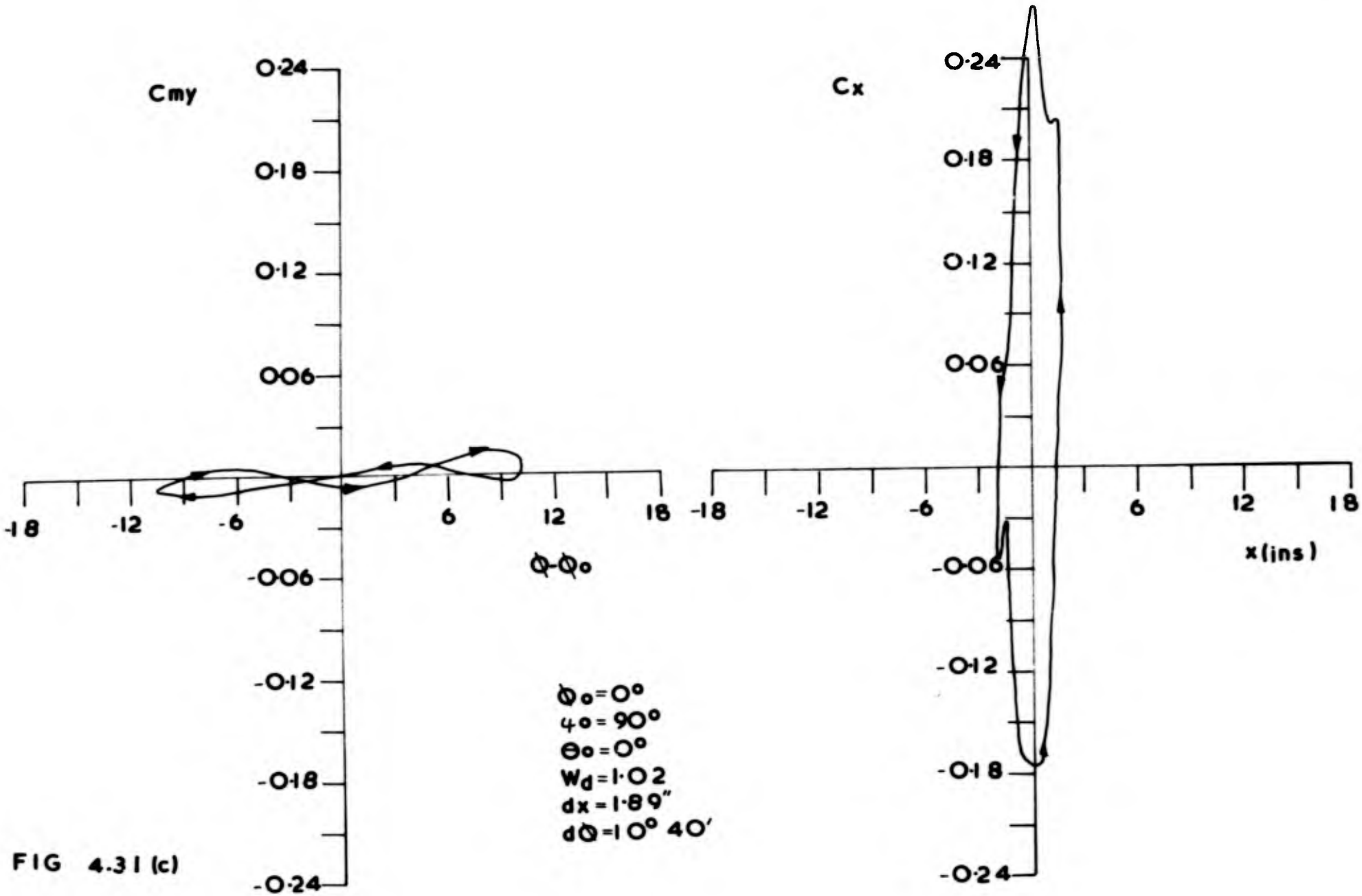
Cmy
0·24
0·18
0·12
0·06
-0·06
-0·12
-0·18
-0·24
-18
-12
-6
6
12
18
Φ-Φo
Cx
0·24
0·18
0·12
0·06
-0·06
-0·12
-0·18
-0·24
-18
-12
-6
6
12
18
x(ins)
Φo=0°
4o=90°
Θo=0°
Wd=1·02
dx=1·89"
dΦ=1° 40'

FIG 4.31 (c)

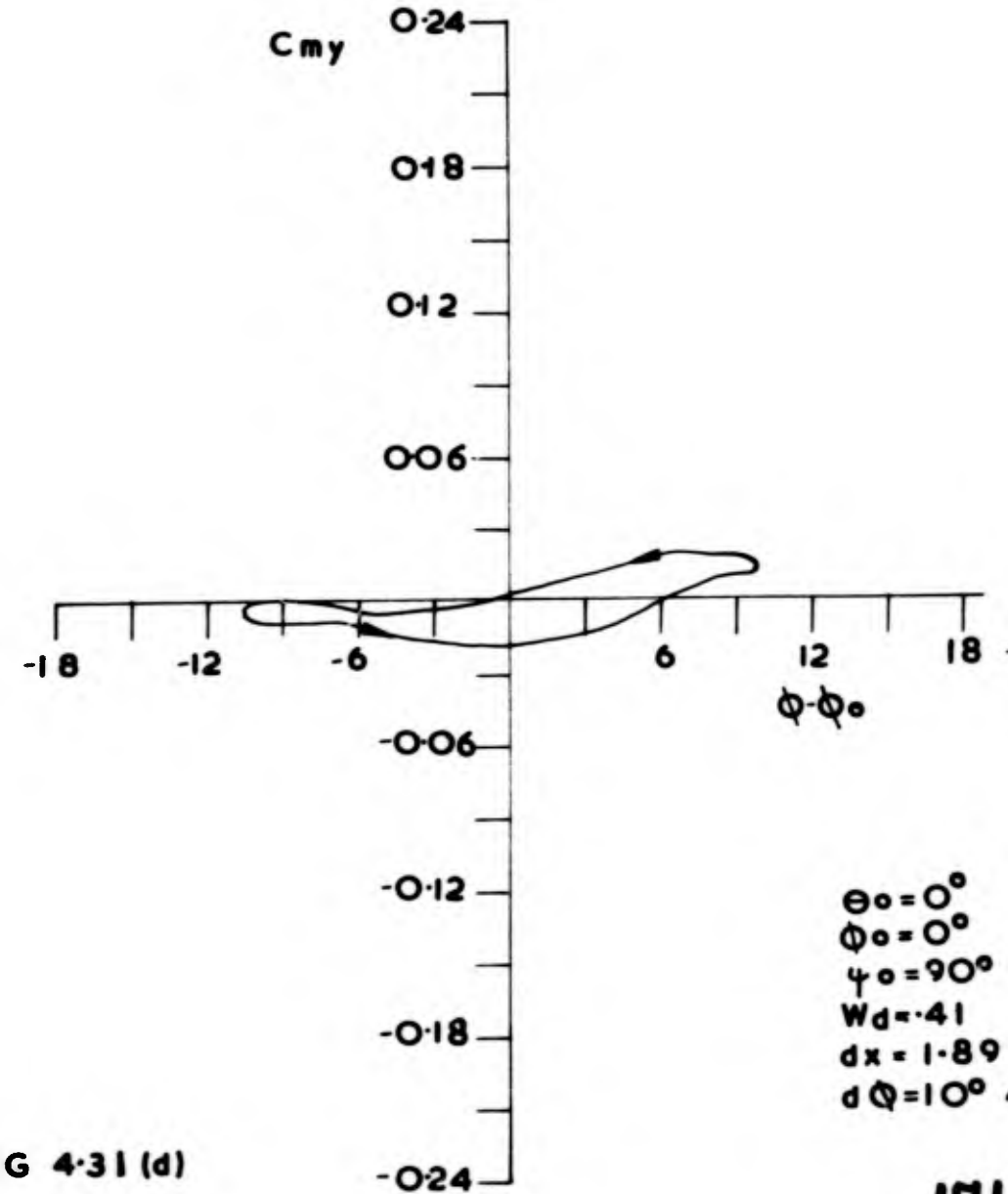

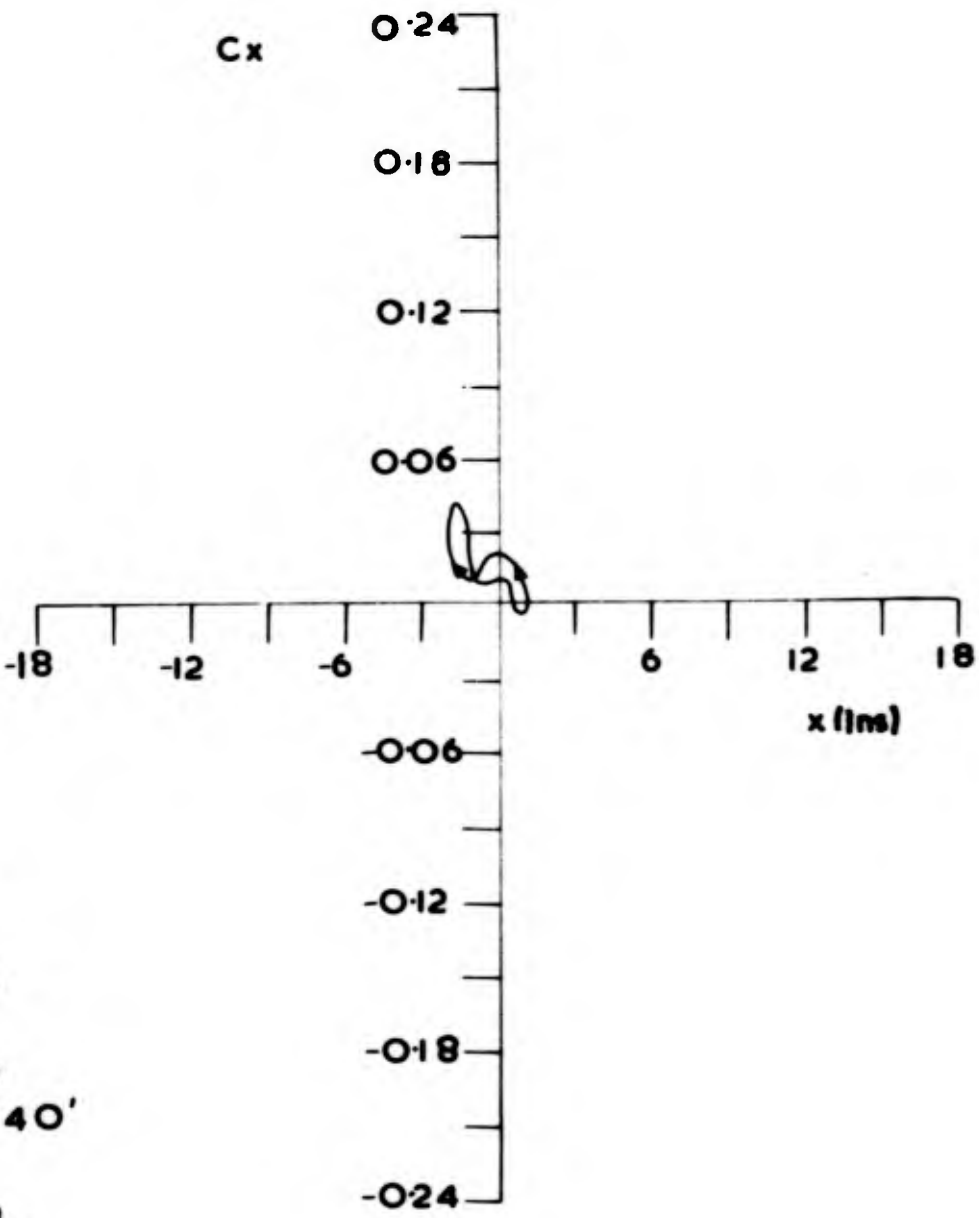

$\Theta_o = 0°$
$\Phi_o = 0°$
$\psi_o = 90°$
Wd = ·41
dx = 1·89
$d\Omega = 10°\ 40'$

FIG 4·31 (d)

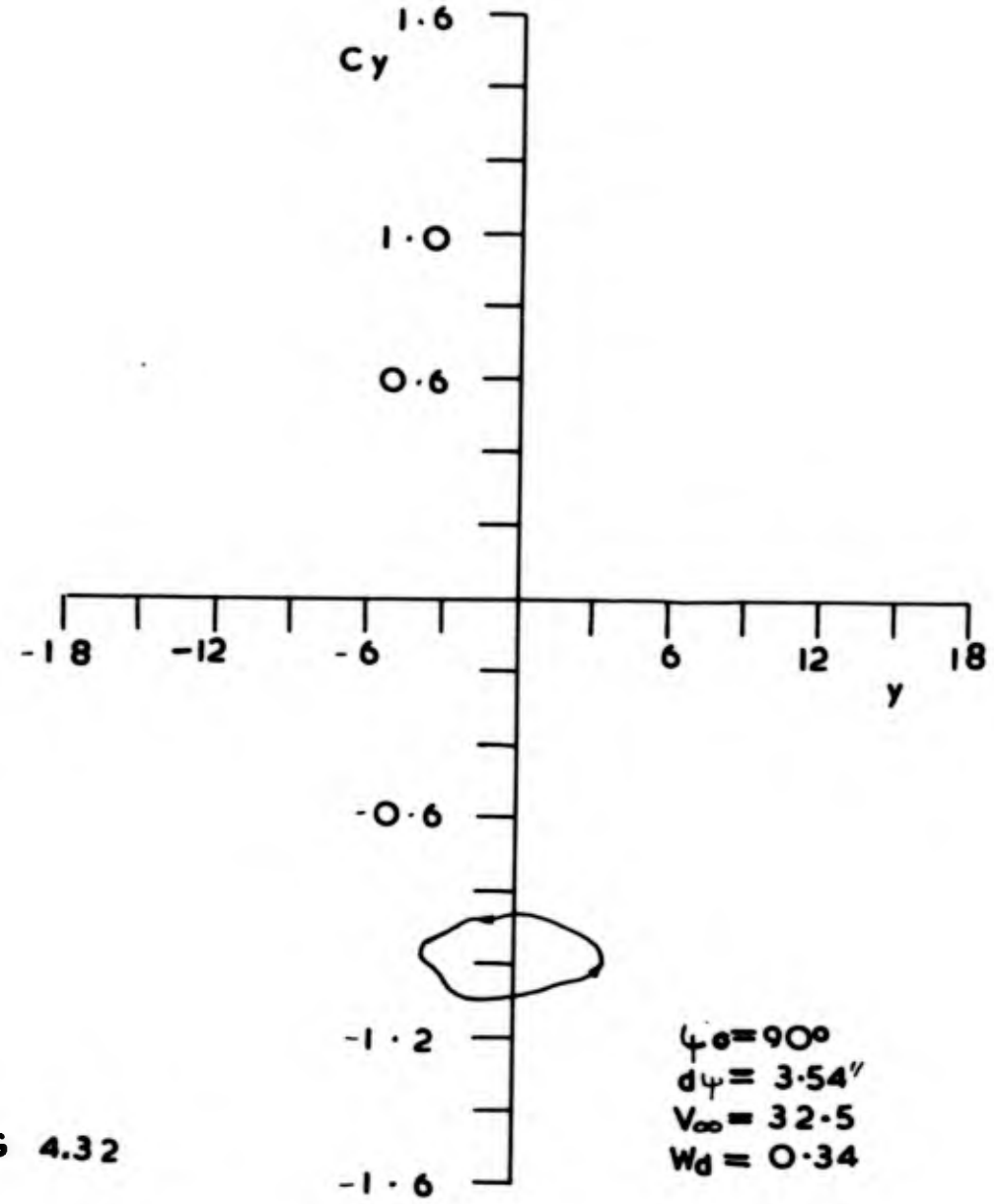

$\psi_0 = 90°$
$d\psi = 3.54''$
$V_\infty = 32.5$
$W_d = 0.34$

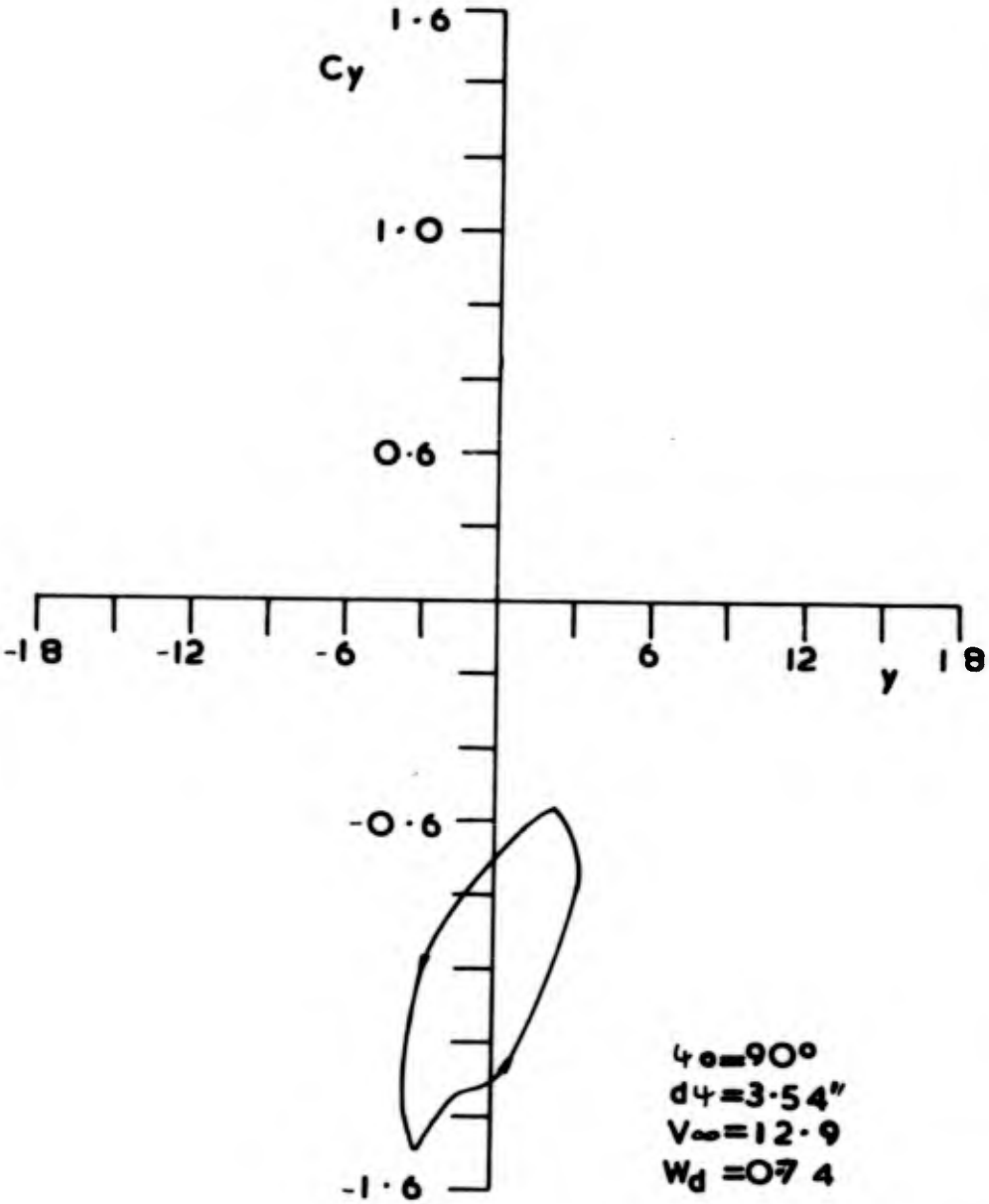

$\psi_0 = 90°$
$d\psi = 3.54''$
$V_\infty = 12.9$
$W_d = 0.74$

FIG 4.32

FIG 4.33(a)

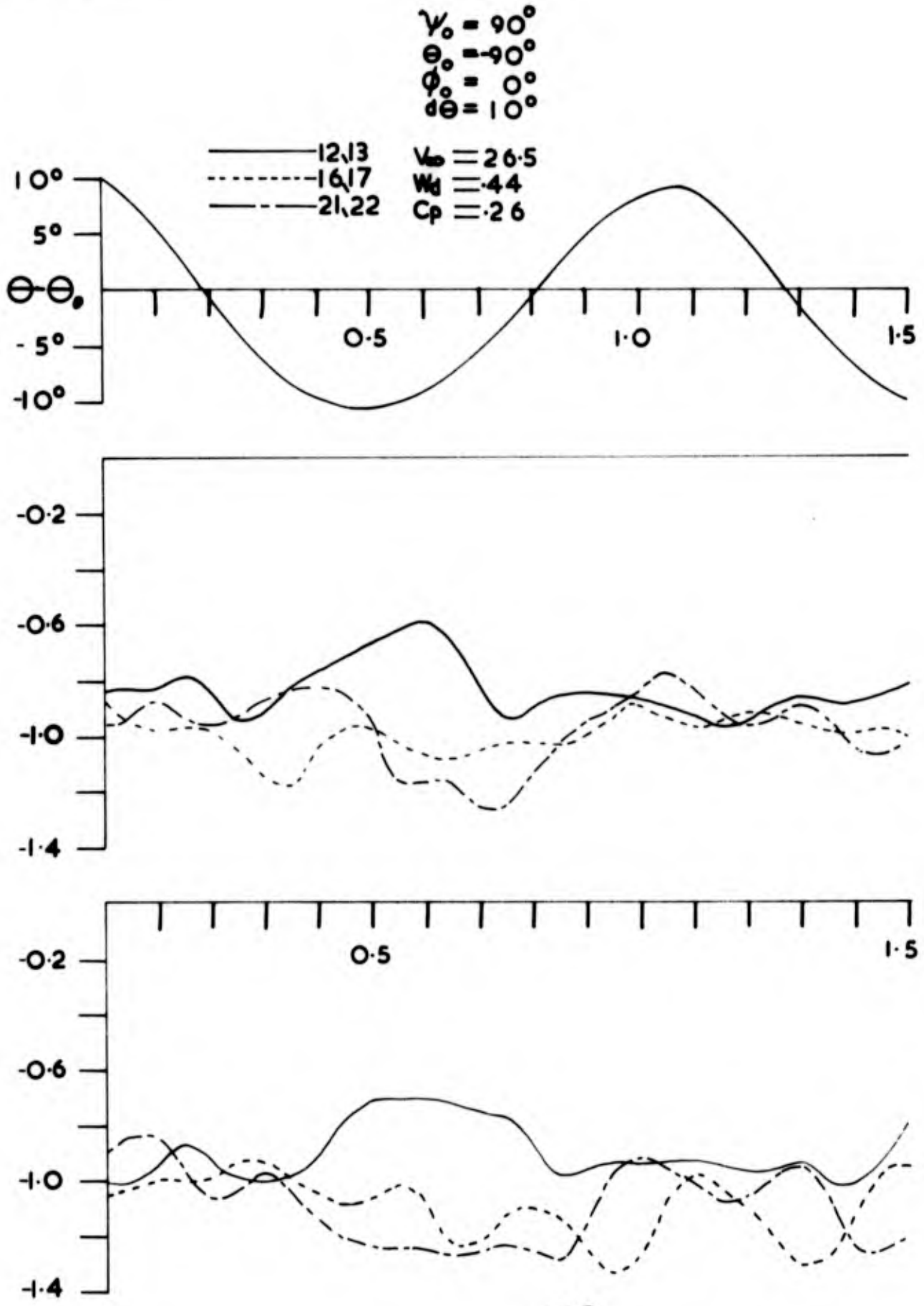
$\psi_0 = 90°$
$\theta_0 = -90°$
$\phi_0 = 0°$
$d\theta = 10°$
12,13
16,17
21,22
$V_{\infty} = 26.5$
$W_d = .44$
$C_p = .26$
10°
5°
$\theta-\theta_0$
-5°
-10°
0·5
1·0
1·5
-0·2
-0·6
-1·0
-1·4
0·5
1·5
-0·2
-0·6
-1·0
-1·4

FIG 4.33(b)

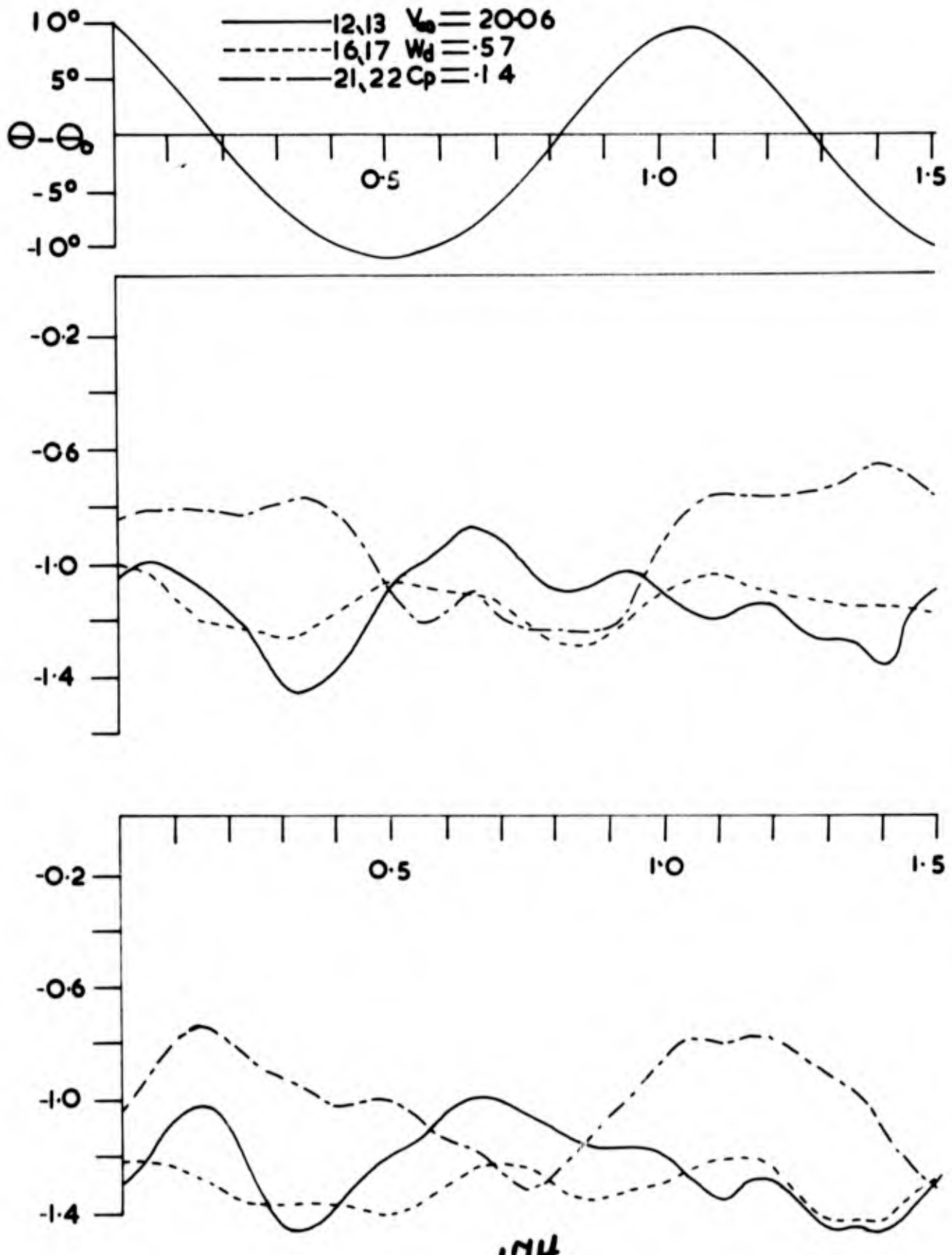
10°
5°
θ-θ₀
-5°
-10°
12,13 V∞ = 2006
16,17 Wd = ·57
21,22 Cp = ·14
0·5
1·0
1·5
-0·2
-0·6
-1·0
-1·4
0·5
1·0
1·5
-0·2
-0·6
-1·0
-1·4

FIG 4.33(c)

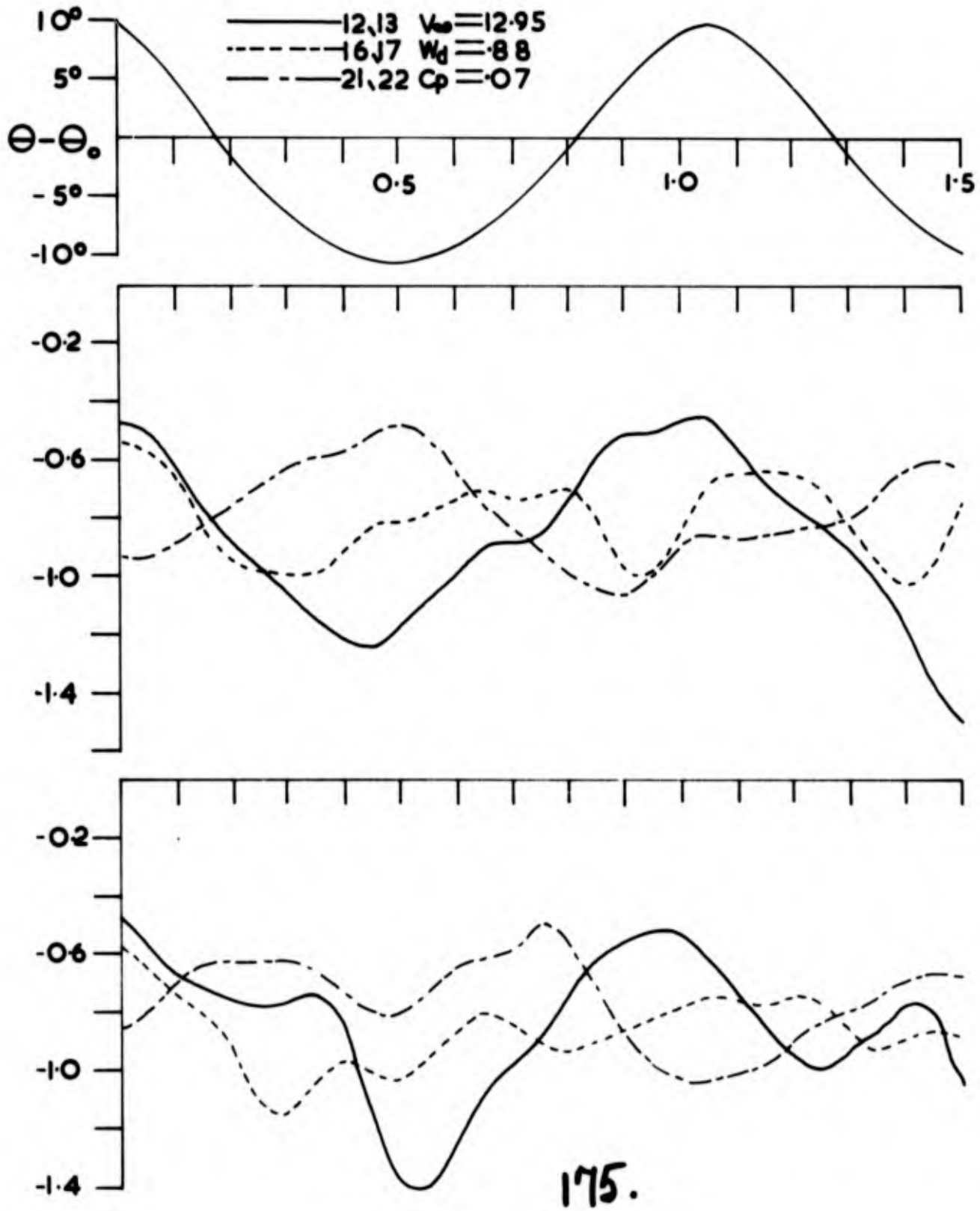
10°
5°
θ-θ₀
-5°
-10°
12,13 V∞=12·95
16,17 Wd=·88
21,22 Cp=·07
0·5
1·0
1·5
-0·2
-0·6
-1·0
-1·4
-0·2
-0·6
-1·0
-1·4

FIG 4.34(a)

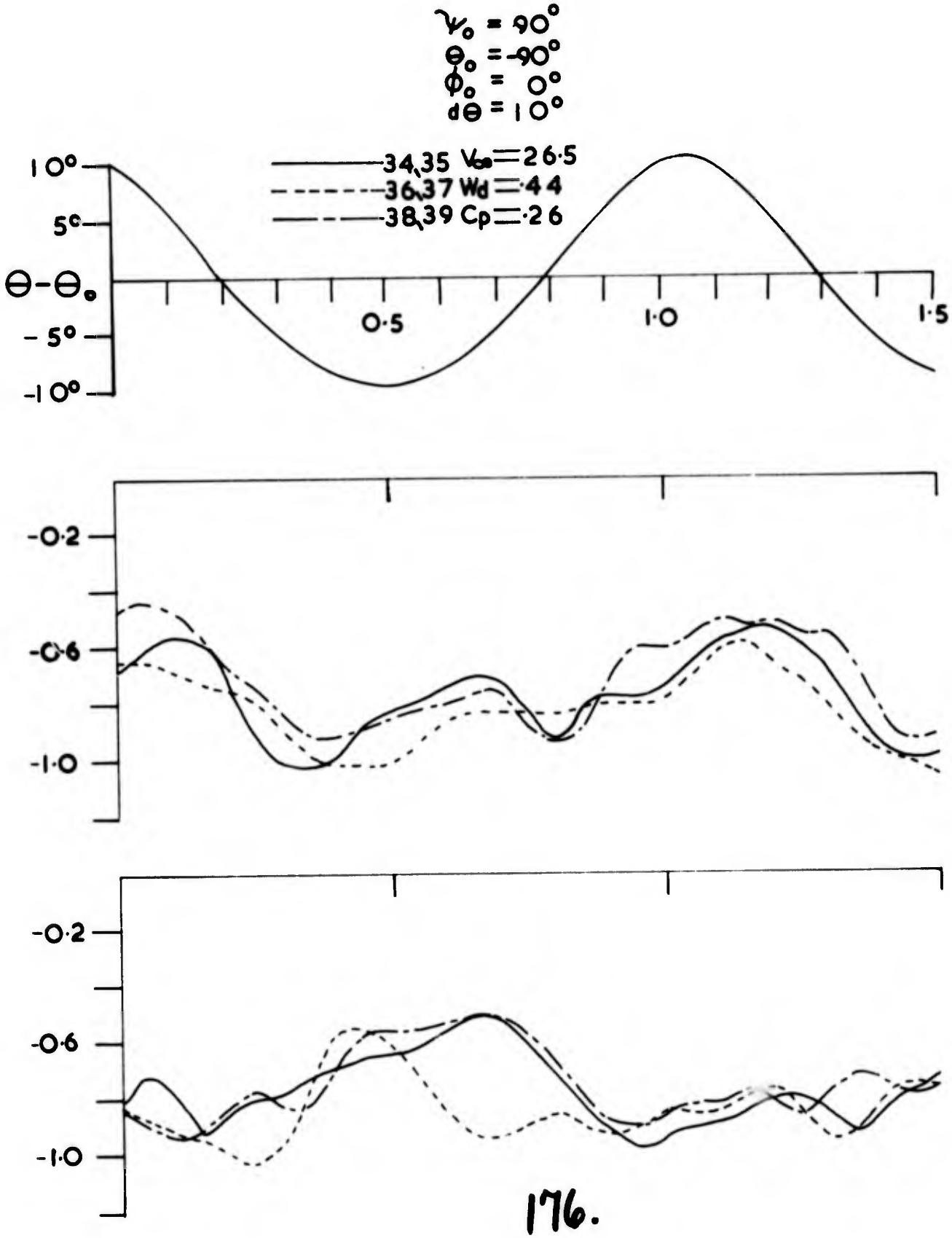
$\psi_0 = 90°$
$\theta_0 = -90°$
$\phi_0 = 0°$
$d\theta = 10°$
34,35 $V_\infty = 26.5$
36,37 Wd = ·44
38,39 Cp = ·26
10°
5°
$\theta - \theta_0$
- 5°
-10°
0·5
1·0
1·5
-0·2
-0·6
-1·0
-0·2
-0·6
-1·0

FIG 4.34(b)

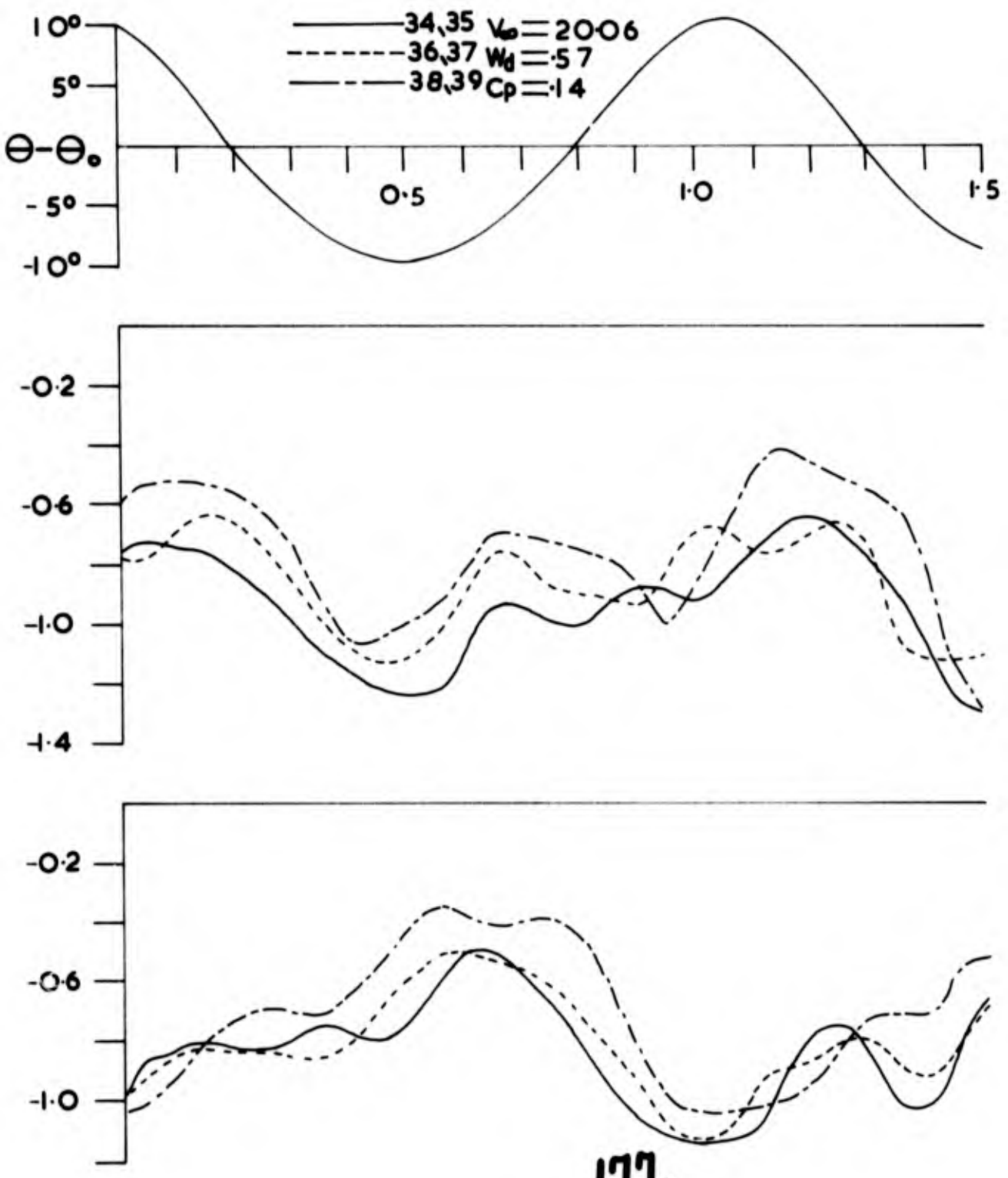
34,35 V_{∞} = 20·06
36,37 W_d = ·57
38,39 Cp = ·14
10°
5°
θ-θ₀
-5°
-10°
0·5
1·0
1·5
-0·2
-0·6
-1·0
-1·4
-0·2
-0·6
-1·0

FIG 4.34(c)

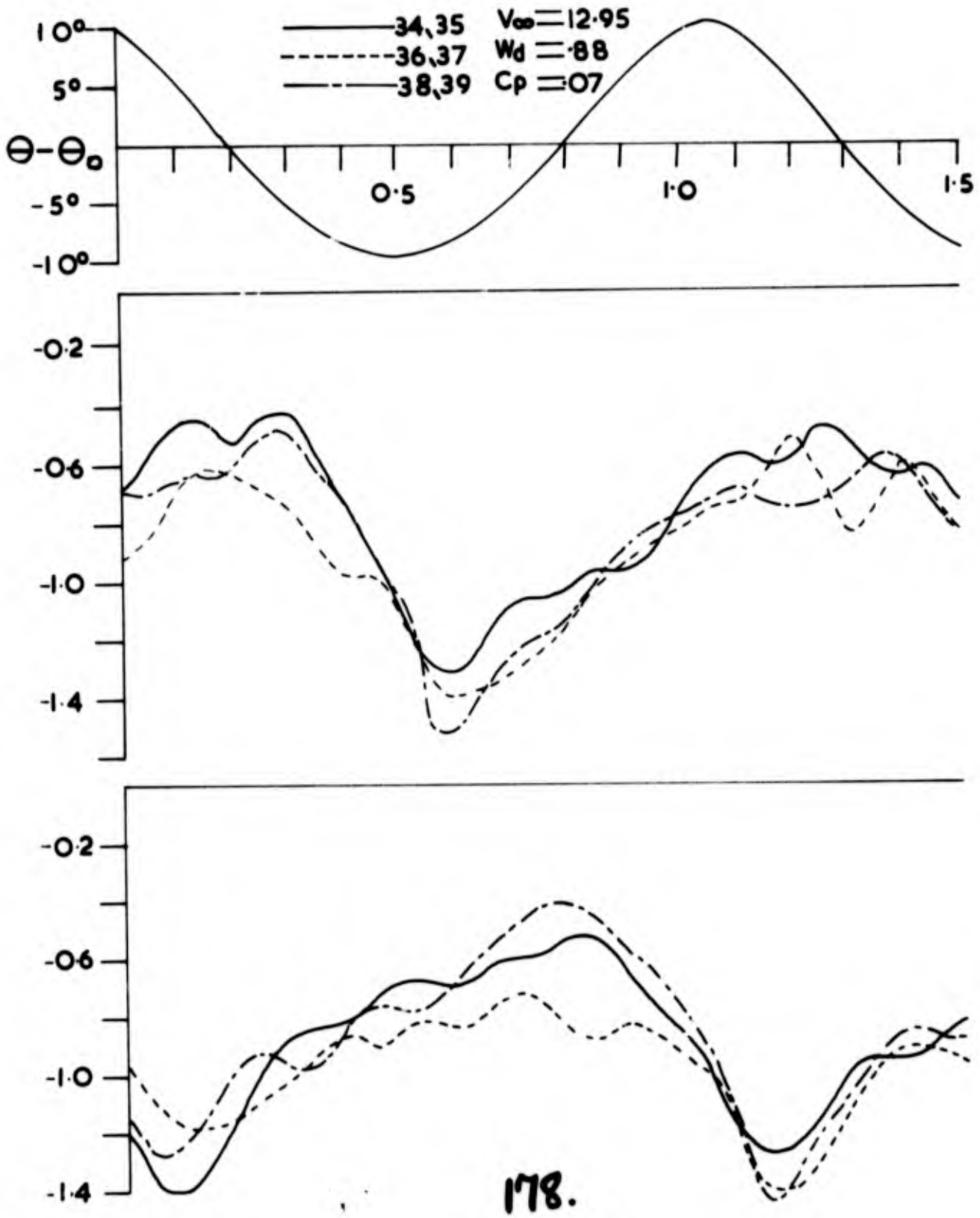
34,35 V∞ = 12·95
36,37 Wd = ·88
38,39 Cp = ·07
10°
5°
θ-θ0
-5°
-10°
0·5
1·0
1·5
-0·2
-0·6
-1·0
-1·4
-0·2
-0·6
-1·0
-1·4

FIG 4.34(d)

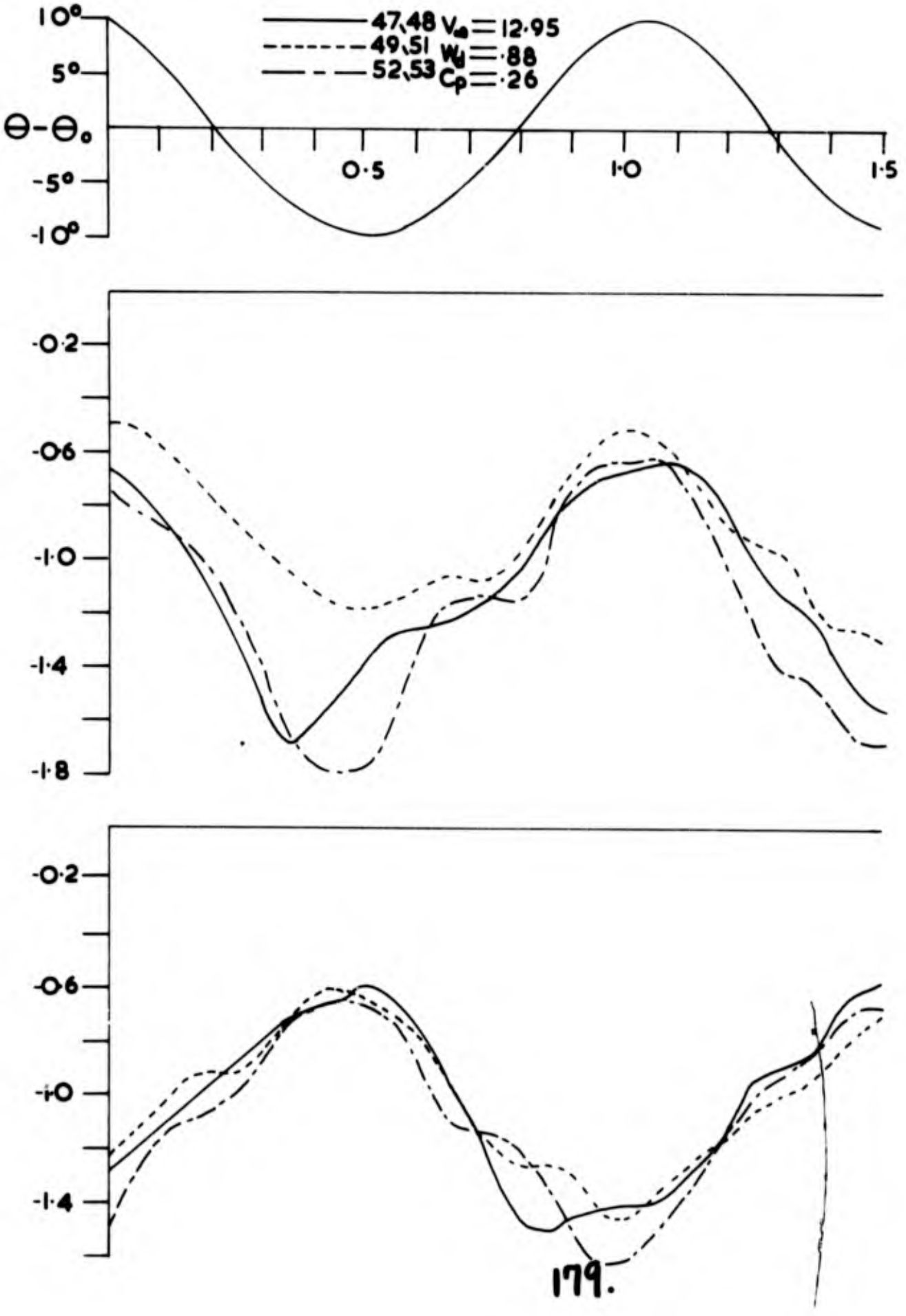
10°
5°
θ-θ₀
-5°
-10°
0·5
1·0
1·5
47,48 V∞ = 12·95
49,51 Wd = ·88
52,53 Cp = ·26
-0·2
-0·6
-1·0
-1·4
-1·8
-0·2
-0·6
-1·0
-1·4

FIG 4.34(c)

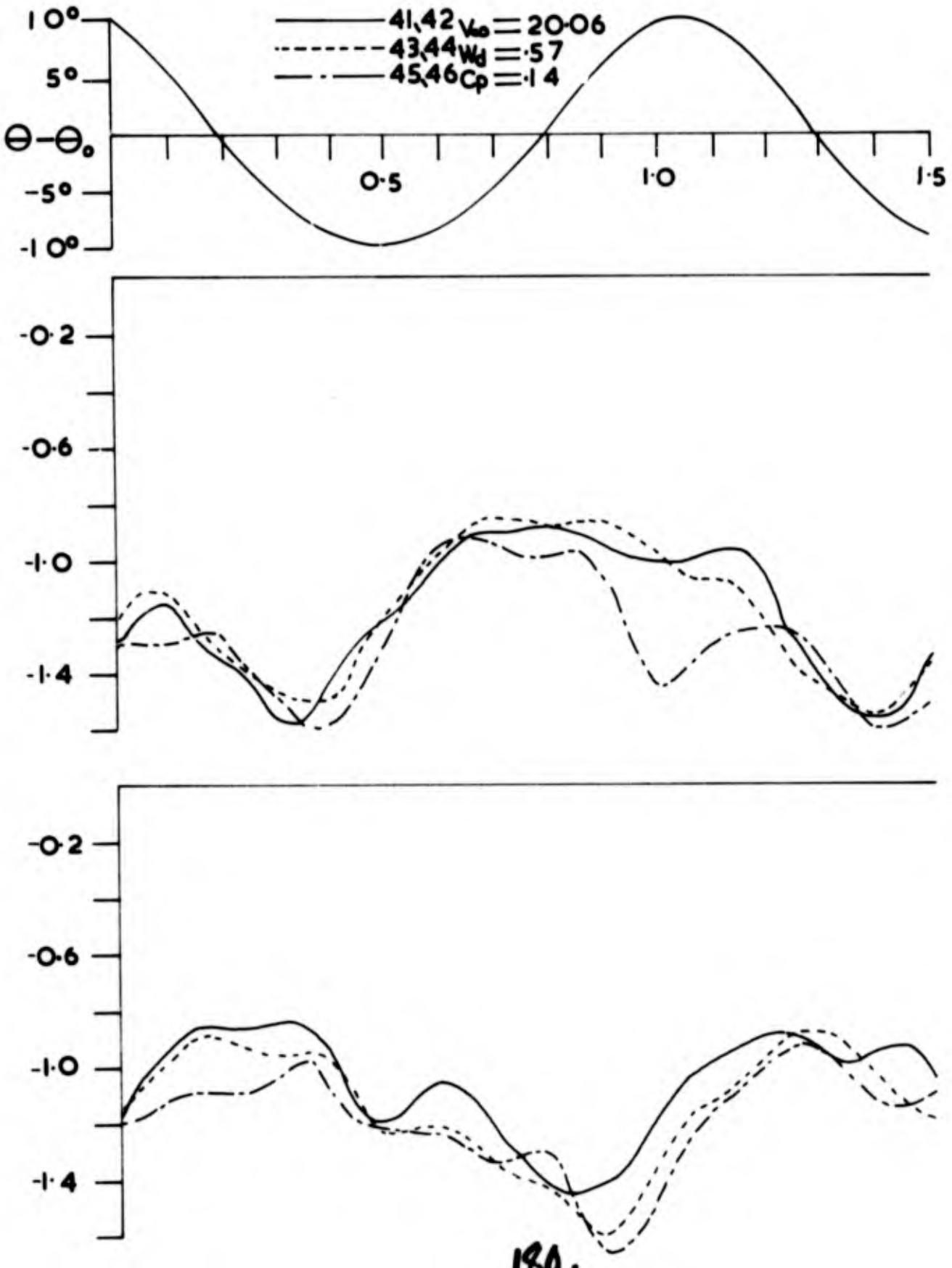
41,42 Vco = 20·06
43,44 Wd = ·57
45,46 Cp = ·14
10°
5°
θ−θ₀
−5°
−10°
0·5
1·0
1·5
-0·2
-0·6
-1·0
-1·4
-0·2
-0·6
-1·0
-1·4

FIG 4.34(1)

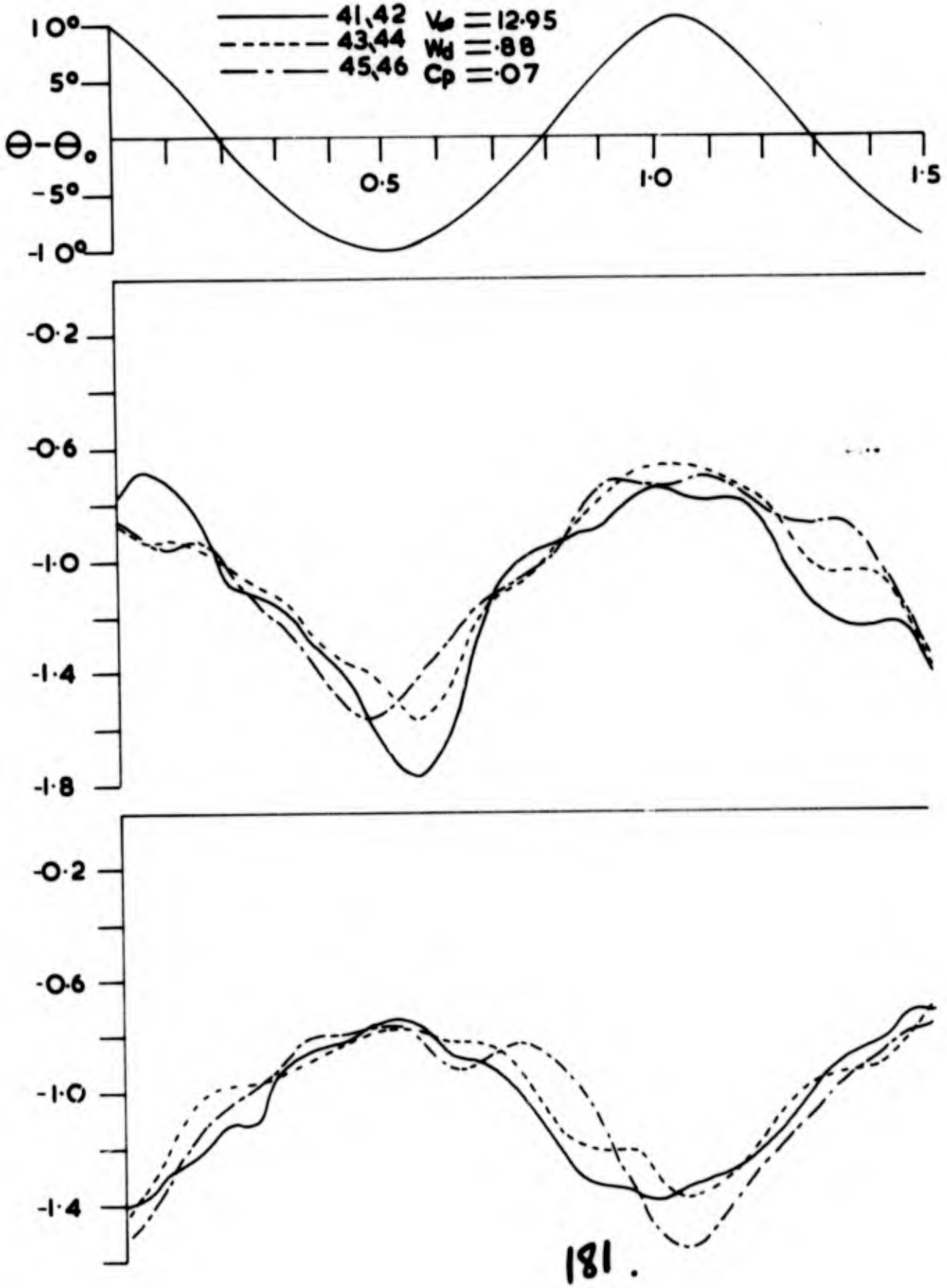
41,42
43,44
45,46
V_{∞} = 12·95
Wd = ·88
Cp = ·07
10°
5°
$\theta-\theta_0$
-5°
-10°
0·5
1·0
1·5
-0·2
-0·6
-1·0
-1·4
-1·8
-0·2
-0·6
-1·0
-1·4

FIG 4.34(g)

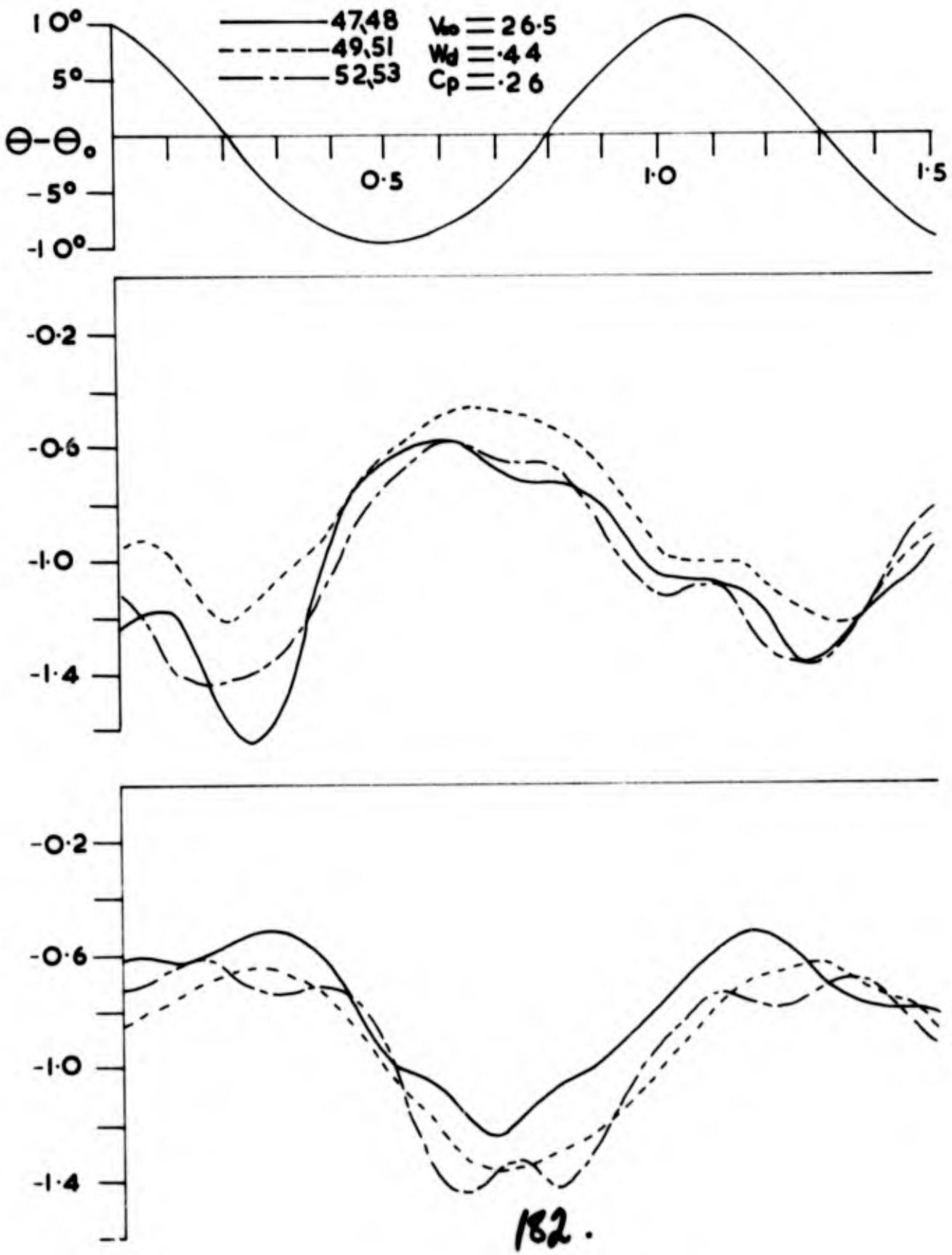
10°
5°
θ−θ₀
−5°
−10°
47,48
49,51
52,53
V∞ = 26·5
Wd = ·44
Cp = ·26
0·5
1·0
1·5
-0·2
-0·6
-1·0
-1·4
-0·2
-0·6
-1·0
-1·4

FIG 4.34(h)

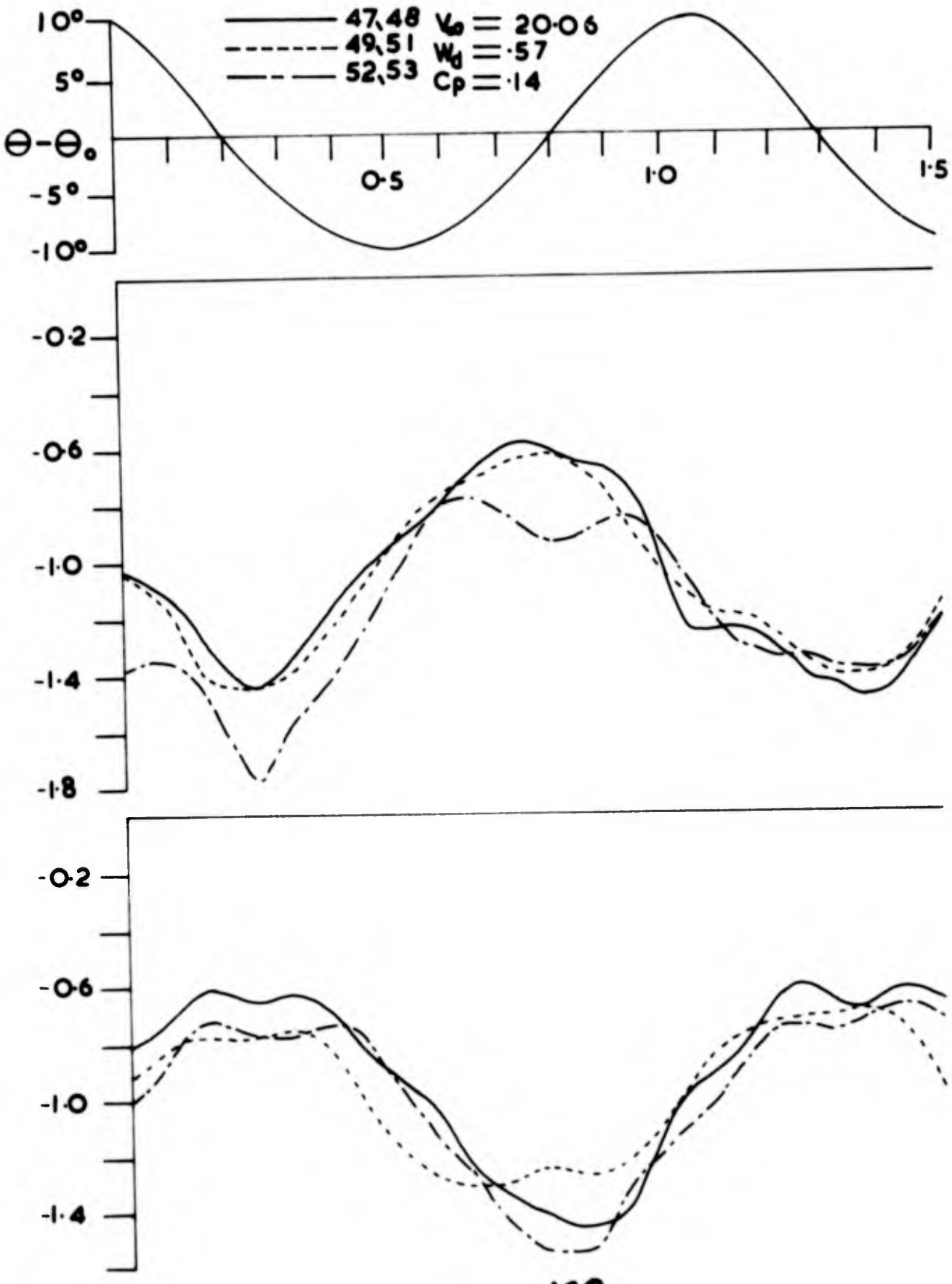
47,48
49,51
52,53
V_{∞} = 20·06
W_d = ·57
Cp = ·14
10°
5°
$\theta-\theta_0$
-5°
-10°
0·5
1·0
1·5
-0·2
-0·6
-1·0
-1·4
-1·8
-0·2
-0·6
-1·0
-1·4

FIG 4.34(i)

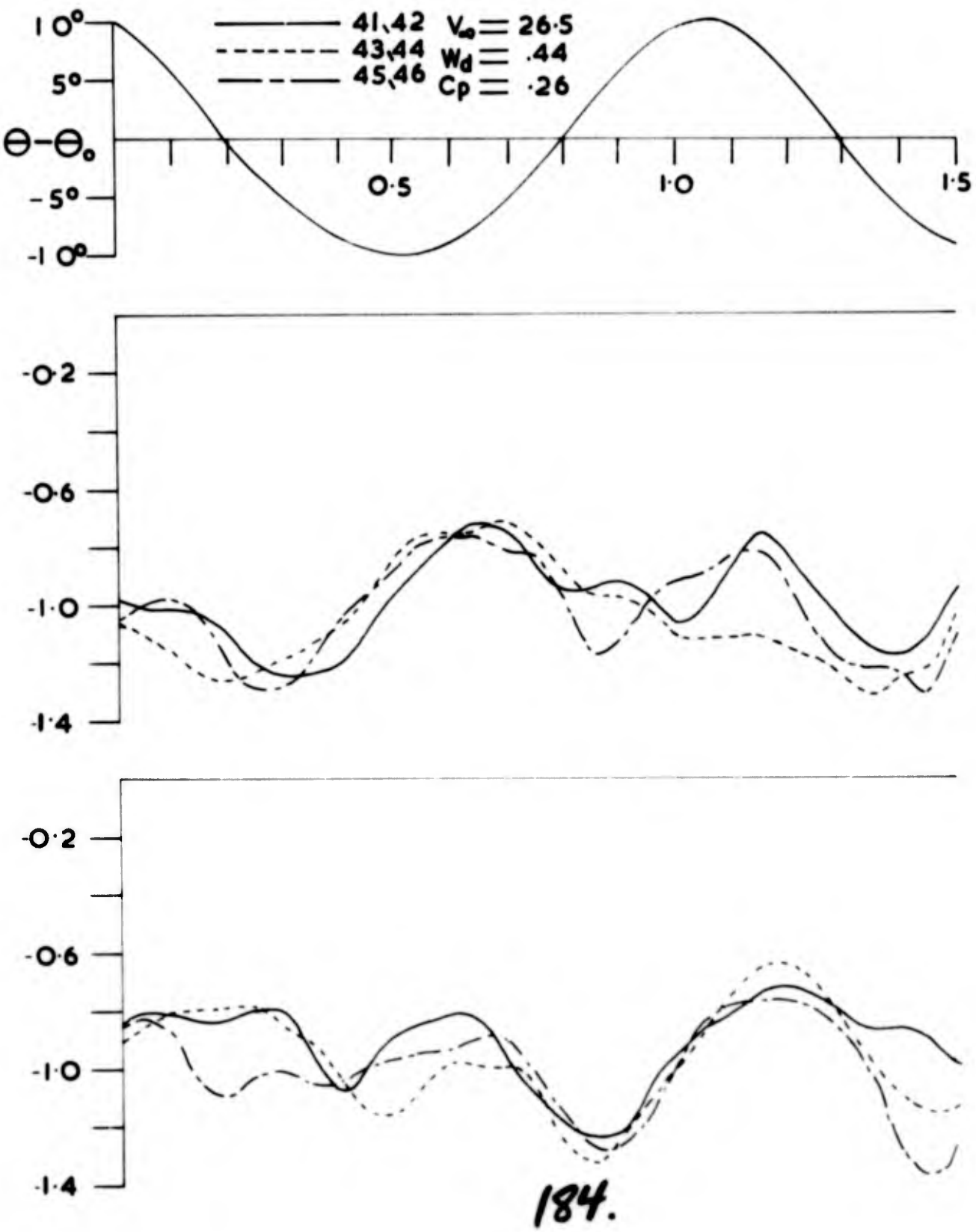
41,42
43,44
45,46
$V_\infty = 26.5$
$W_d = .44$
$C_p = .26$
$\theta - \theta_0$
10°
5°
-5°
-10°
0·5
1·0
1·5
-0·2
-0·6
-1·0
-1·4
-0·2
-0·6
-1·0
-1·4

FIG 4.35(a)

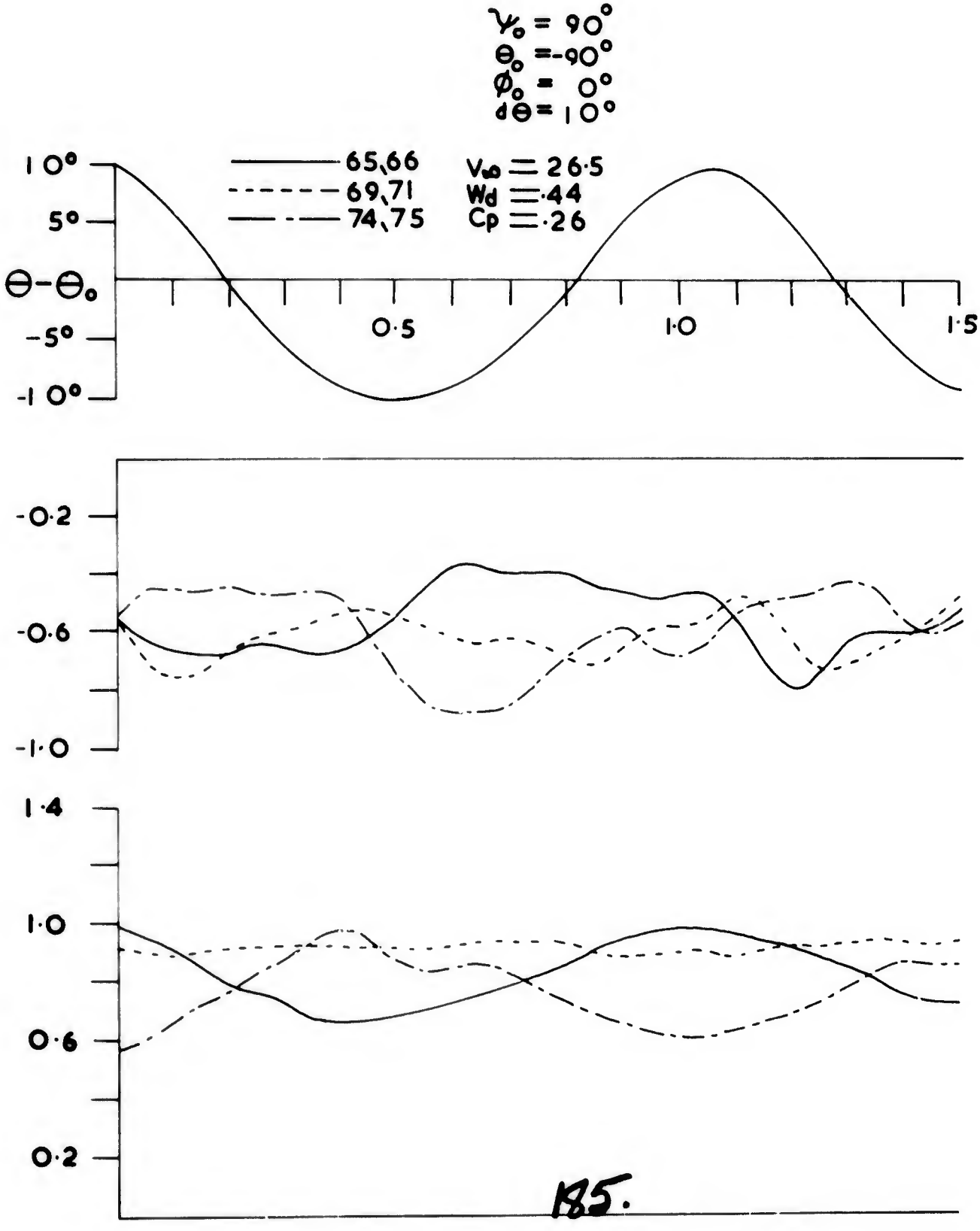
$\psi_o = 90°$
$\theta_o = -90°$
$\phi_o = 0°$
$d\theta = 10°$
65,66
69,71
74,75
$V_{\infty} = 26.5$
$W_d = .44$
$C_p = .26$
10°
5°
$\theta - \theta_o$
-5°
-10°
0·5
1·0
1·5
-0·2
-0·6
-1·0
1·4
1·0
0·6
0·2

FIG 4.35(b)

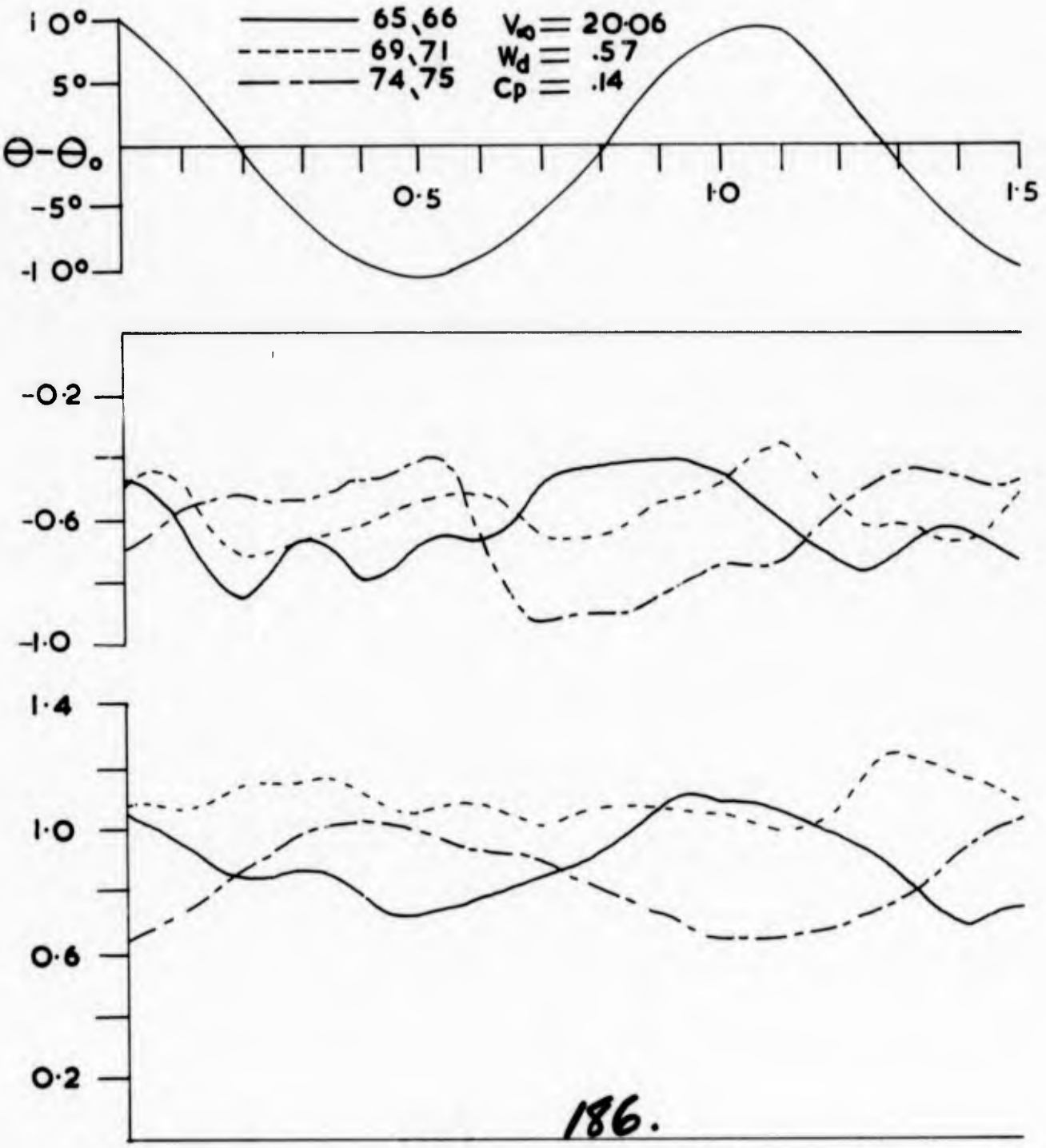
65,66
69,71
74,75
V_∞ = 20·06
W_d = .57
Cp = .14
1·0°
5°
θ-θ₀
-5°
-1·0°
0·5
1·0
1·5
-0·2
-0·6
-1·0
1·4
1·0
0·6
0·2

FIG 4.35(c)

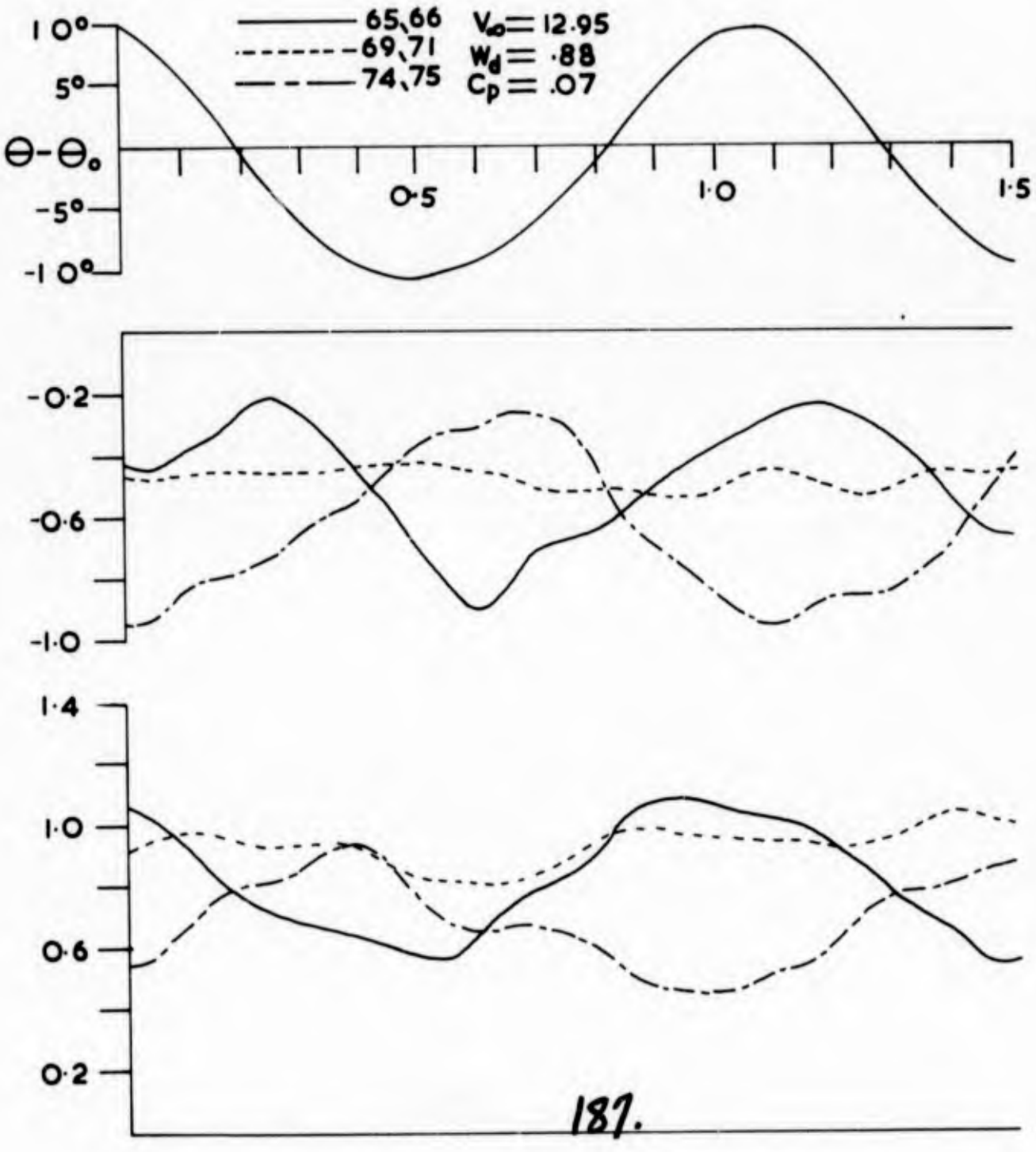
65,66
69,71
74,75
$V_\infty = 12.95$
$W_d = .88$
$C_p = .07$
$\theta - \theta_0$
10°
5°
-5°
-10°
0·5
1·0
1·5
-0·2
-0·6
-1·0
1·4
1·0
0·6
0·2

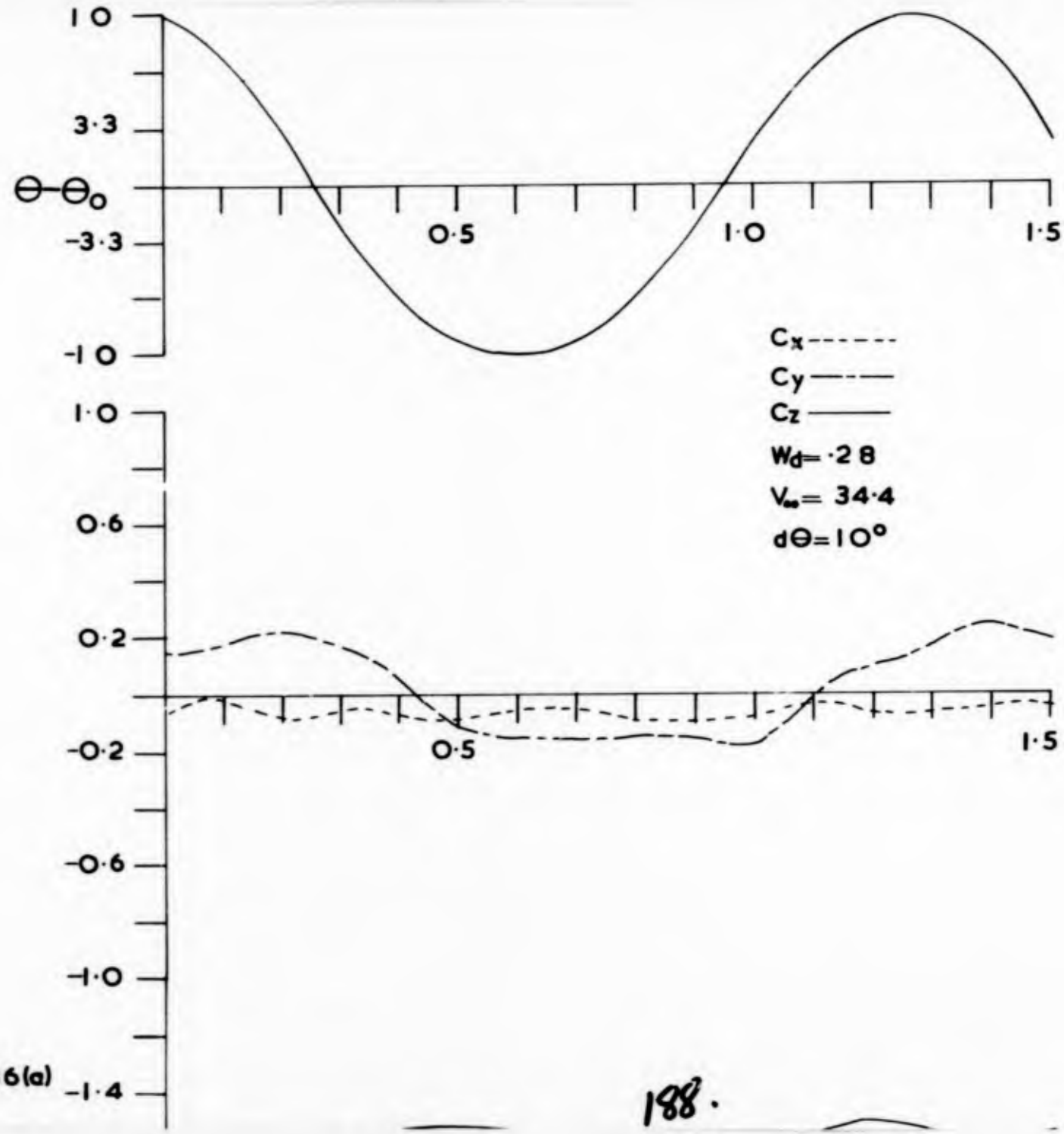
1·0
3·3
θ-θ₀
-3·3
-1·0
0·5
1·0
1·5
Cx
Cy
Cz
Wd= ·28
V∞= 34·4
dθ=10°
1·0
0·6
0·2
-0·2
-0·6
-1·0
-1·4
0·5
1·5

FIG 4.36(a)

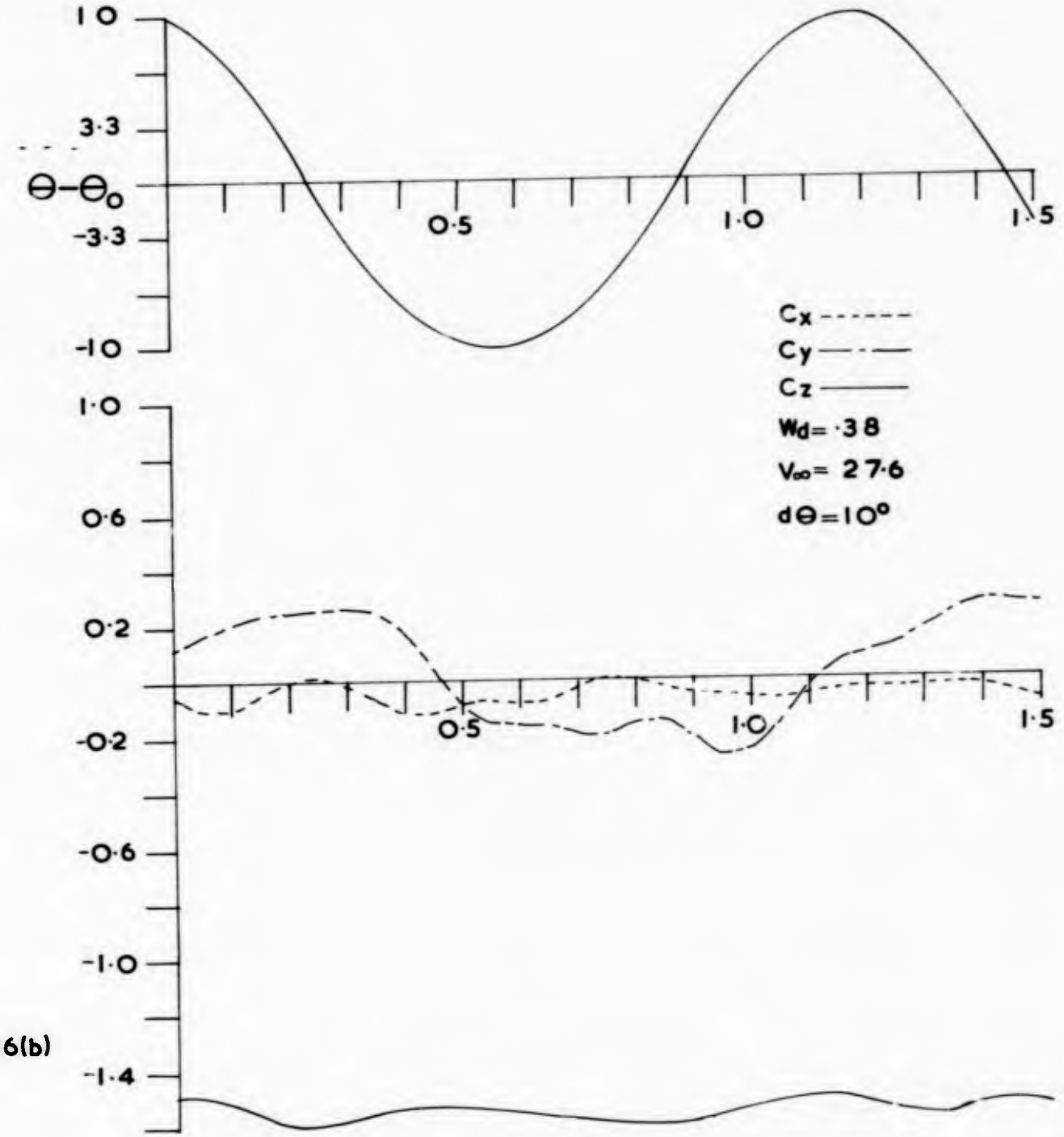
1·0
3·3
Θ−Θ0
-3·3
-10
0·5
1·0
1·5
Cx
Cy
Cz
Wd= ·38
V∞= 27·6
dΘ=10°
1·0
0·6
0·2
-0·2
-0·6
-1·0
-1·4
0·5
1·0
1·5

FIG 4.36(b)

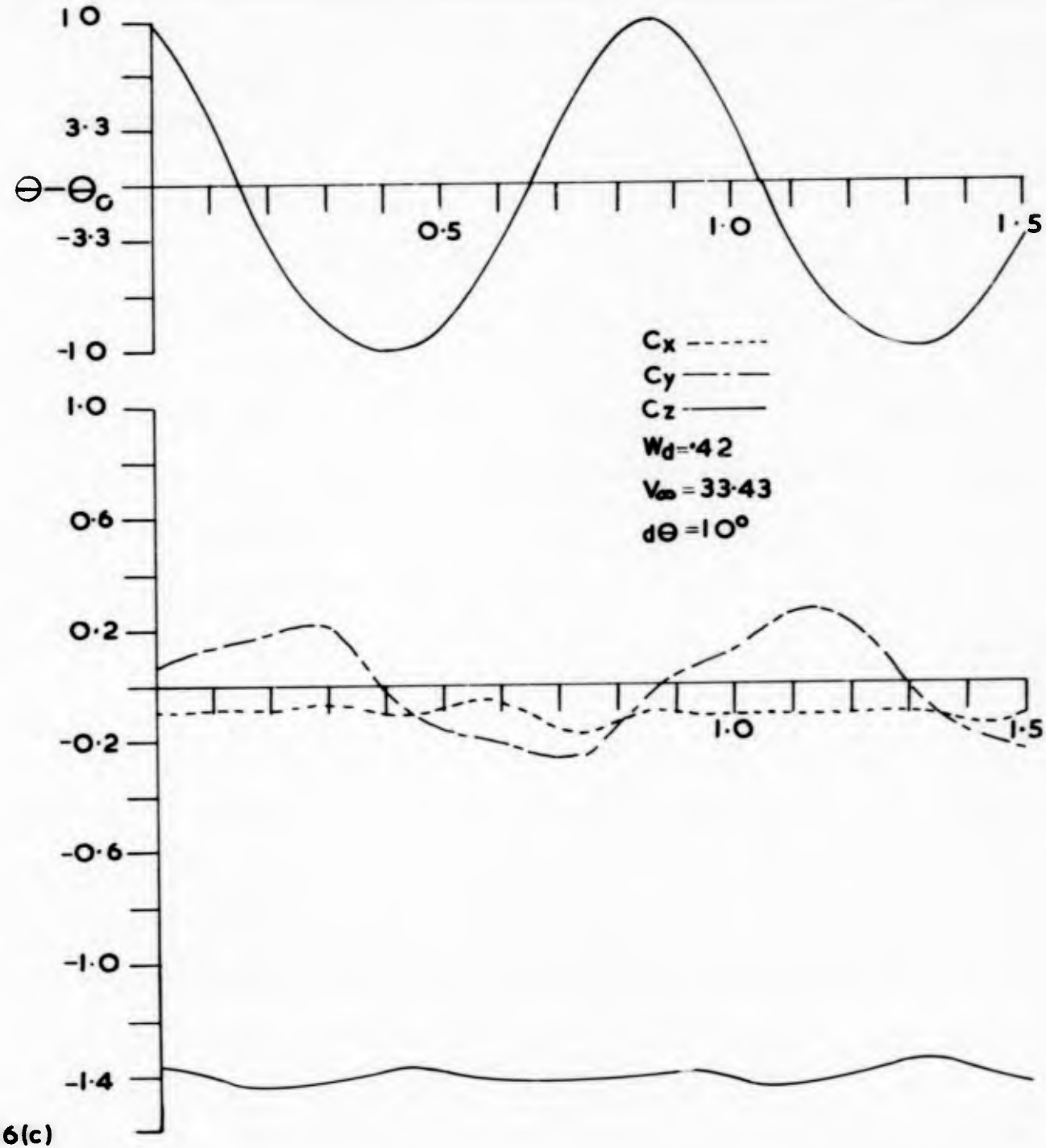
1·0
3·3
Θ−Θc
-3·3
-1·0
0·5
1·0
1·5
Cx
Cy
Cz
Wd=·42
V∞=33·43
dΘ=10°
1·0
0·6
0·2
-0·2
-0·6
-1·0
-1·4
1·0
1·5

FIG 4.36(c)

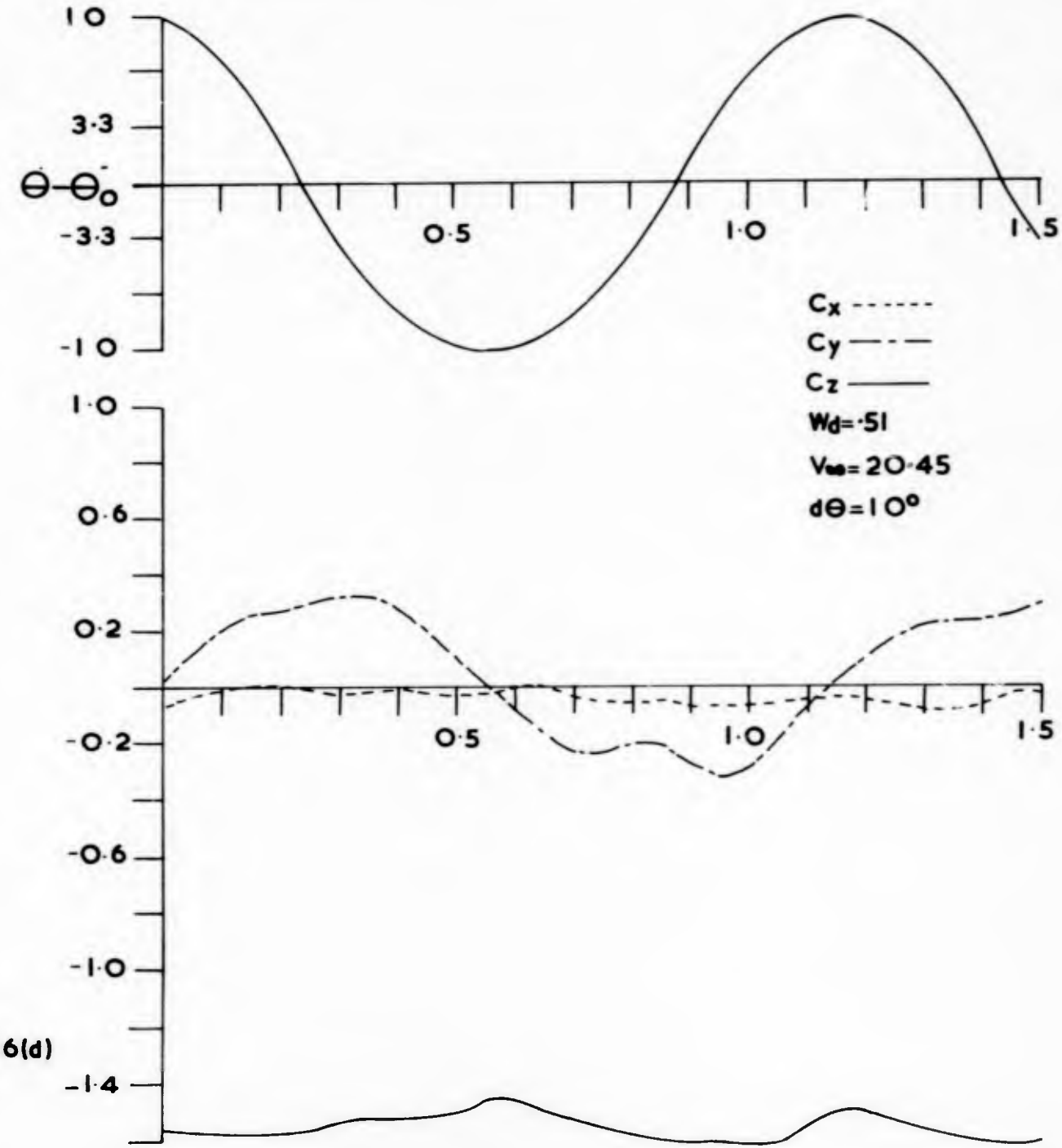
1·0
3·3
θ-θ₀
-3·3
-1·0
0·5
1·0
1·5
Cx ------
Cy —·—
Cz ——
Wd=·51
V∞=20·45
dθ=10°
1·0
0·6
0·2
-0·2
-0·6
-1·0
-1·4
0·5
1·0
1·5

FIG 4.36(d)

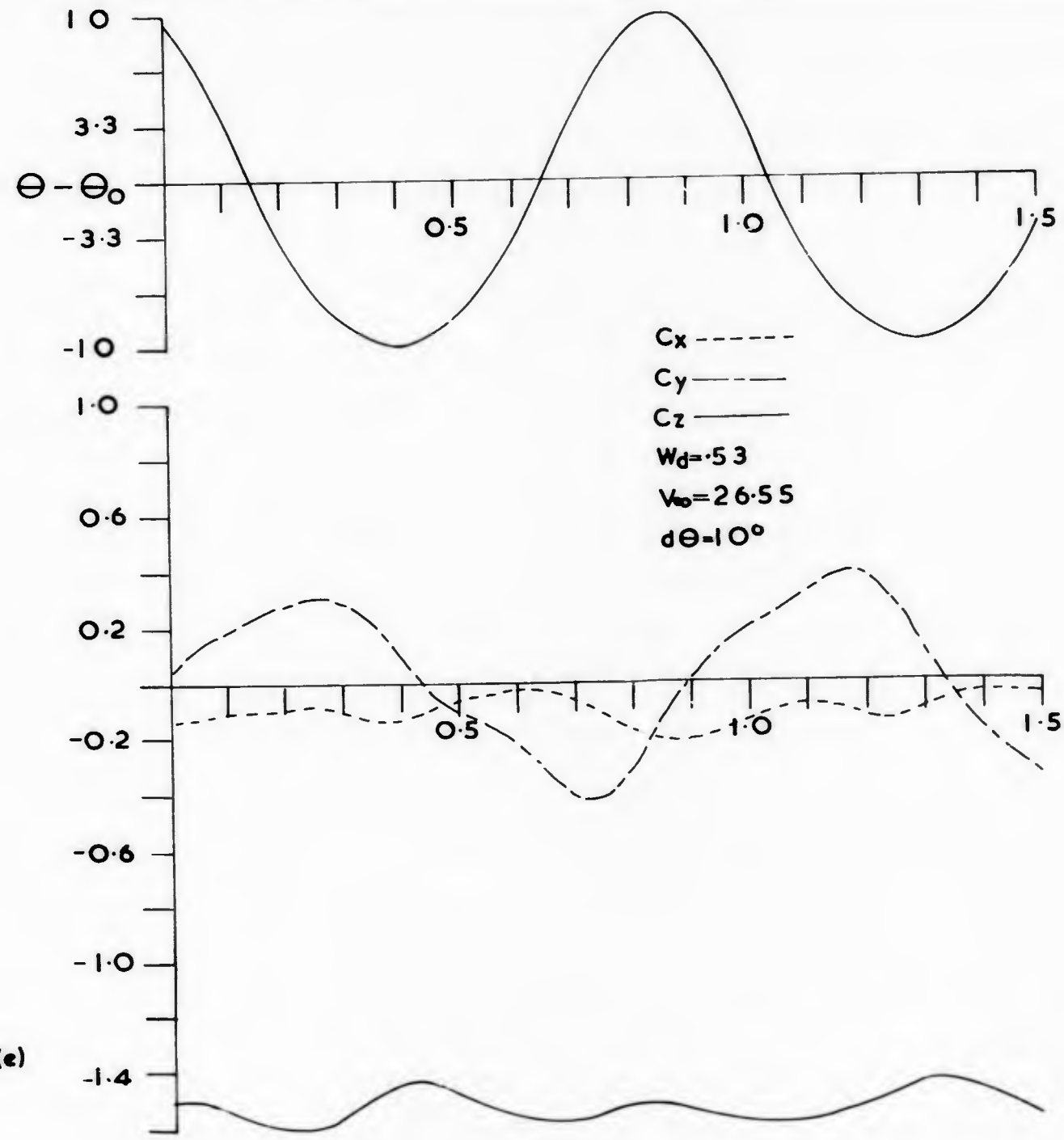
1·0
3·3
Θ − Θ₀
-3·3
-1·0
0·5
1·0
1·5
Cx
Cy
Cz
Wd=·53
V∞=26·55
dΘ=10°
1·0
0·6
0·2
-0·2
-0·6
-1·0
-1·4
0·5
1·0
1·5

FIG 4.36(e)

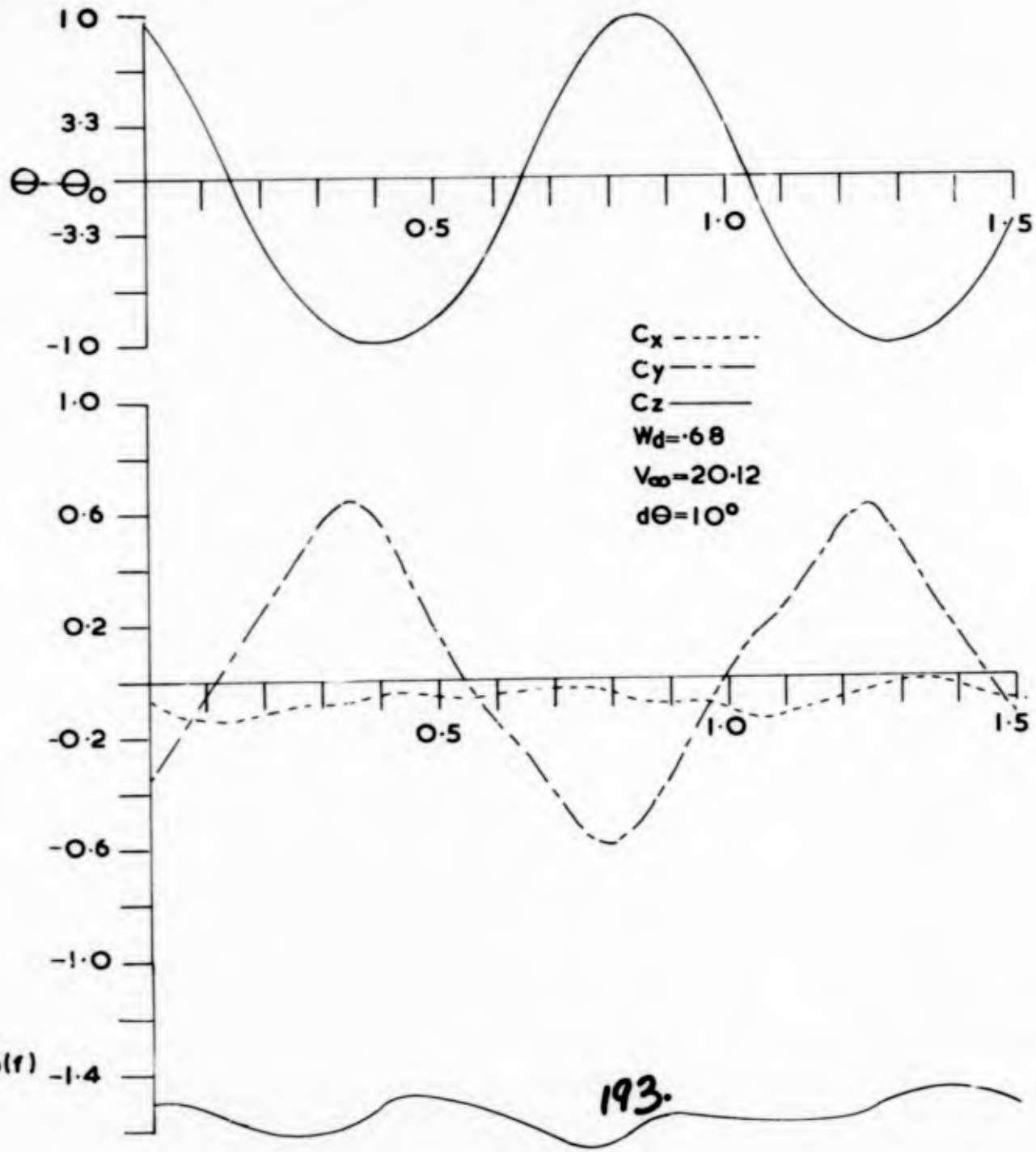
1·0
3·3
θ-θ0
-3·3
-1·0
0·5
1·0
1·5
Cx
Cy
Cz
Wd=·68
V∞=20·12
dθ=10°
1·0
0·6
0·2
-0·2
-0·6
-1·0
-1·4
0·5
1·0
1·5

FIG 4.36(f)

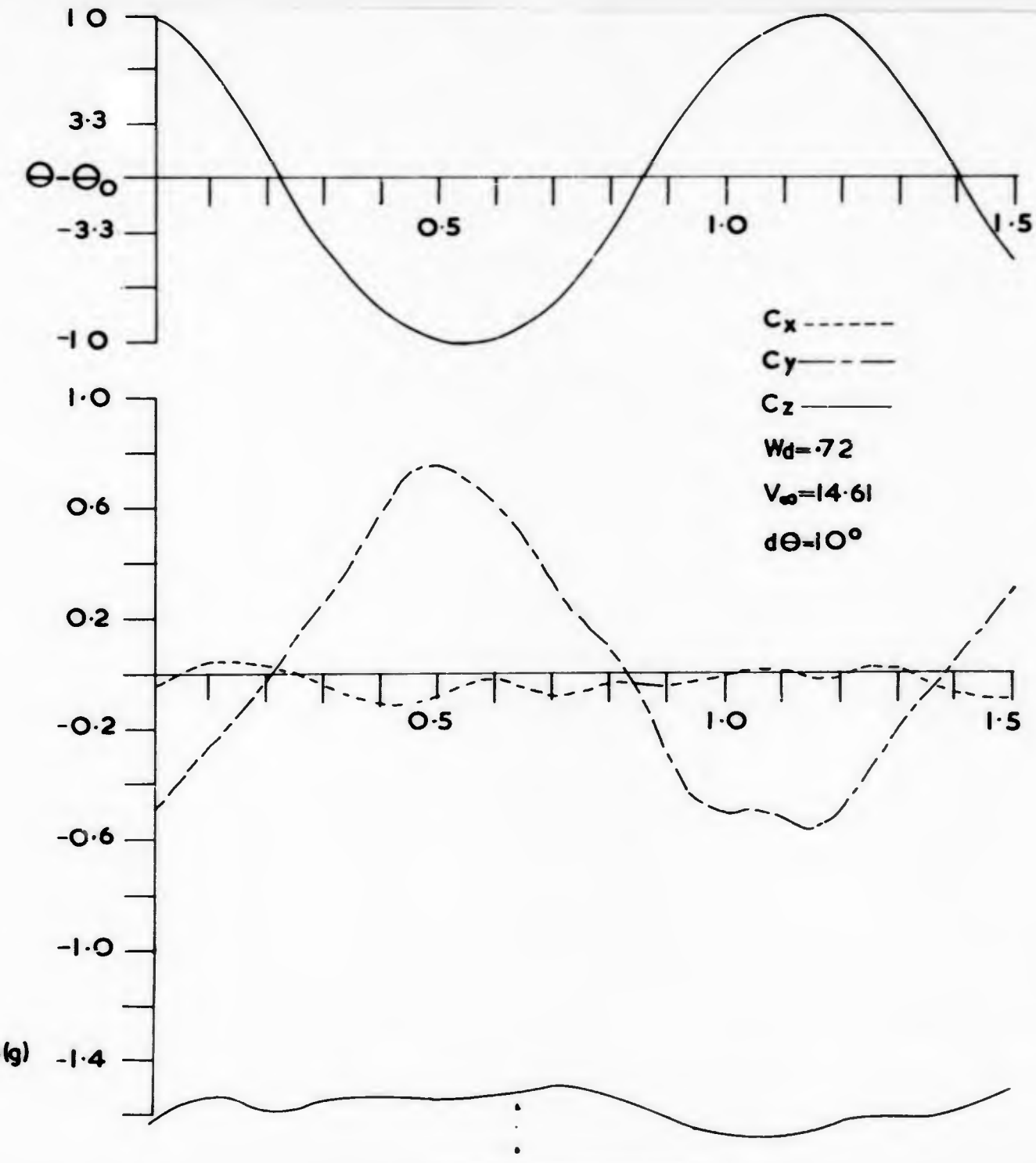
1·0
3·3
θ-θ₀
-3·3
-1·0
0·5
1·0
1·5
Cx
Cy
Cz
Wd=·72
V∞=14·61
dθ=10°
1·0
0·6
0·2
-0·2
-0·6
-1·0
-1·4
0·5
1·0
1·5

FIG 4.36(g)

FIG 4.36(h)

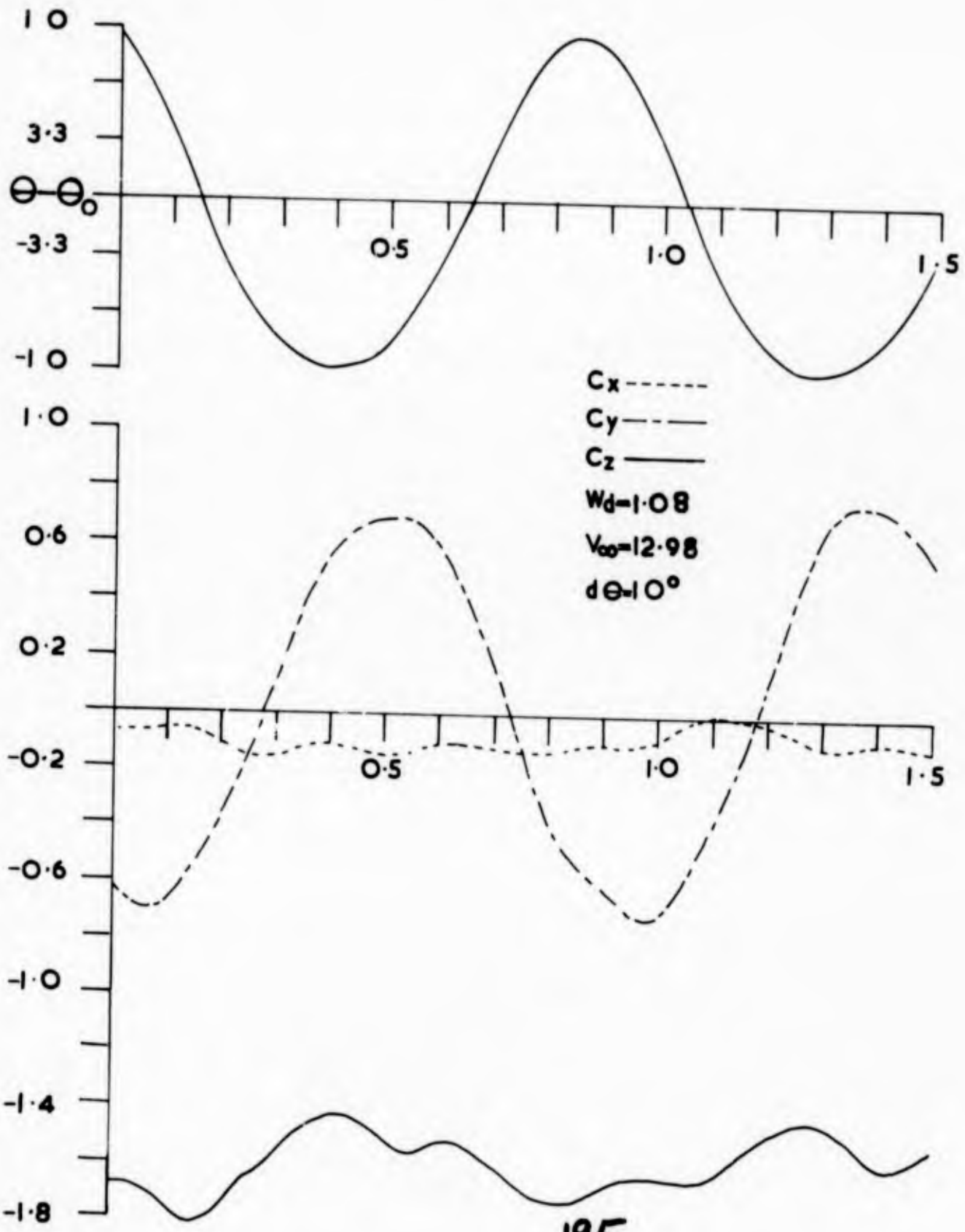
1·0
3·3
θ-θ0
-3·3
-1·0
0·5
1·0
1·5
Cx
Cy
Cz
Wd=1·08
V∞=12·98
dθ=10°
1·0
0·6
0·2
-0·2
-0·6
-1·0
-1·4
-1·8
0·5
1·0
1·5

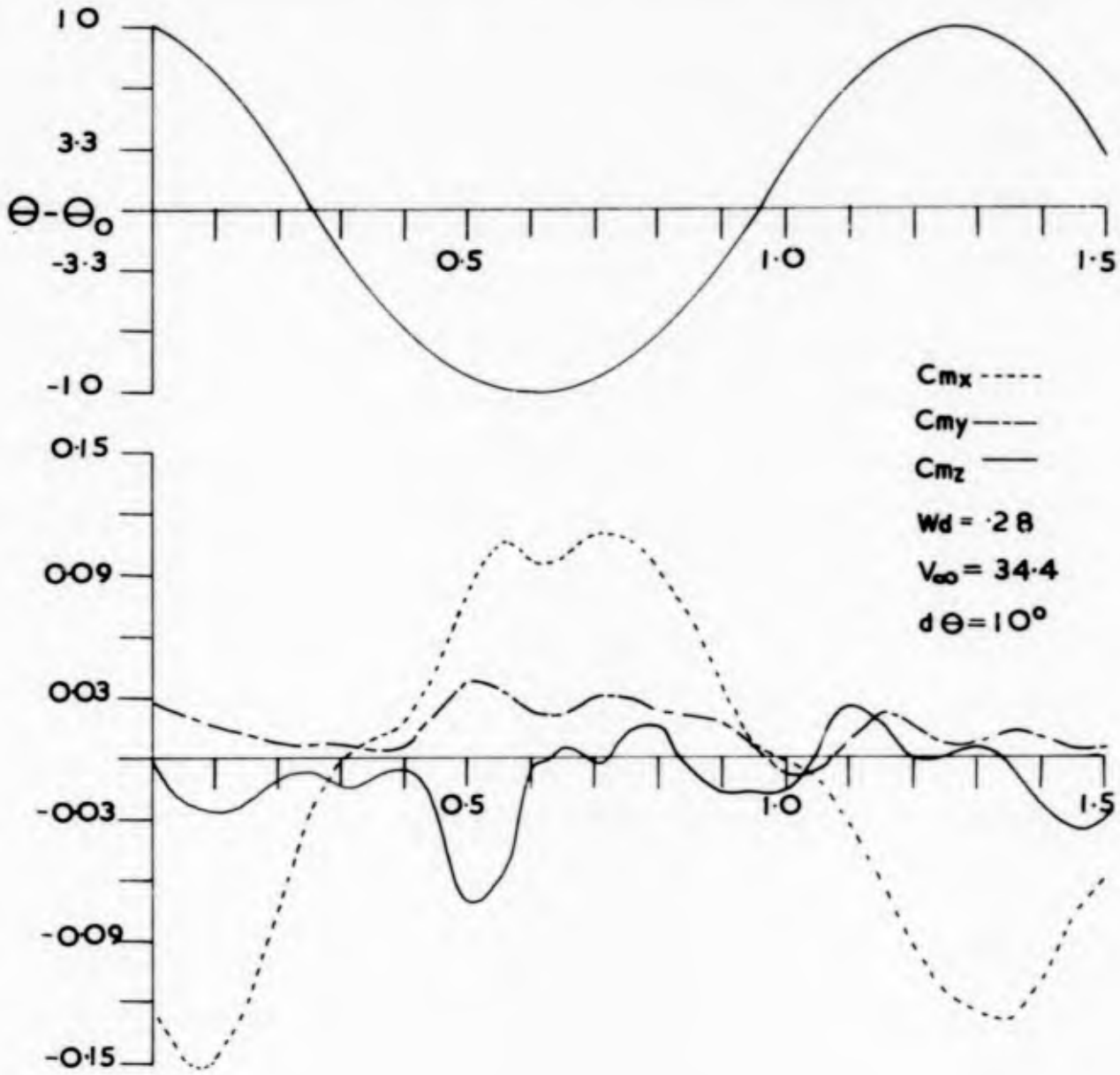
1·0
3·3
θ-θ0
-3·3
-1·0
0·5
1·0
1·5
0·15
0·09
0·03
-0·03
-0·09
-0·15
Cmx
Cmy
Cmz
Wd = ·28
V∞ = 34·4
dθ=10°

FIG 4.37(a)

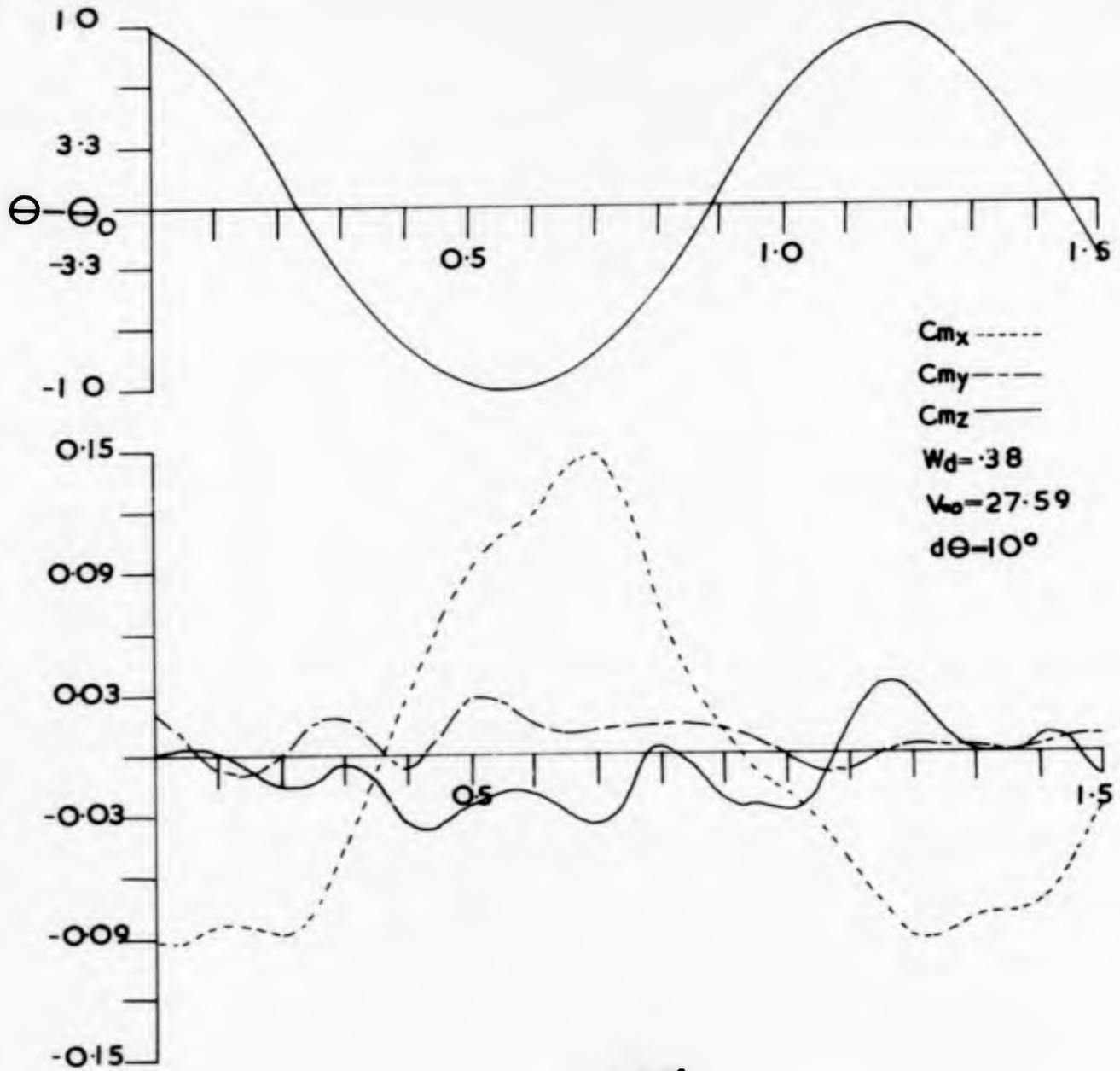
1·0
3·3
θ−θ0
-3·3
-1·0
0·5
1·0
1·5
Cmx
Cmy
Cmz
Wd=·38
V∞=27·59
dθ=10°
0·15
0·09
0·03
-0·03
-0·09
-0·15
0·5
1·5

FIG 4.37(b)

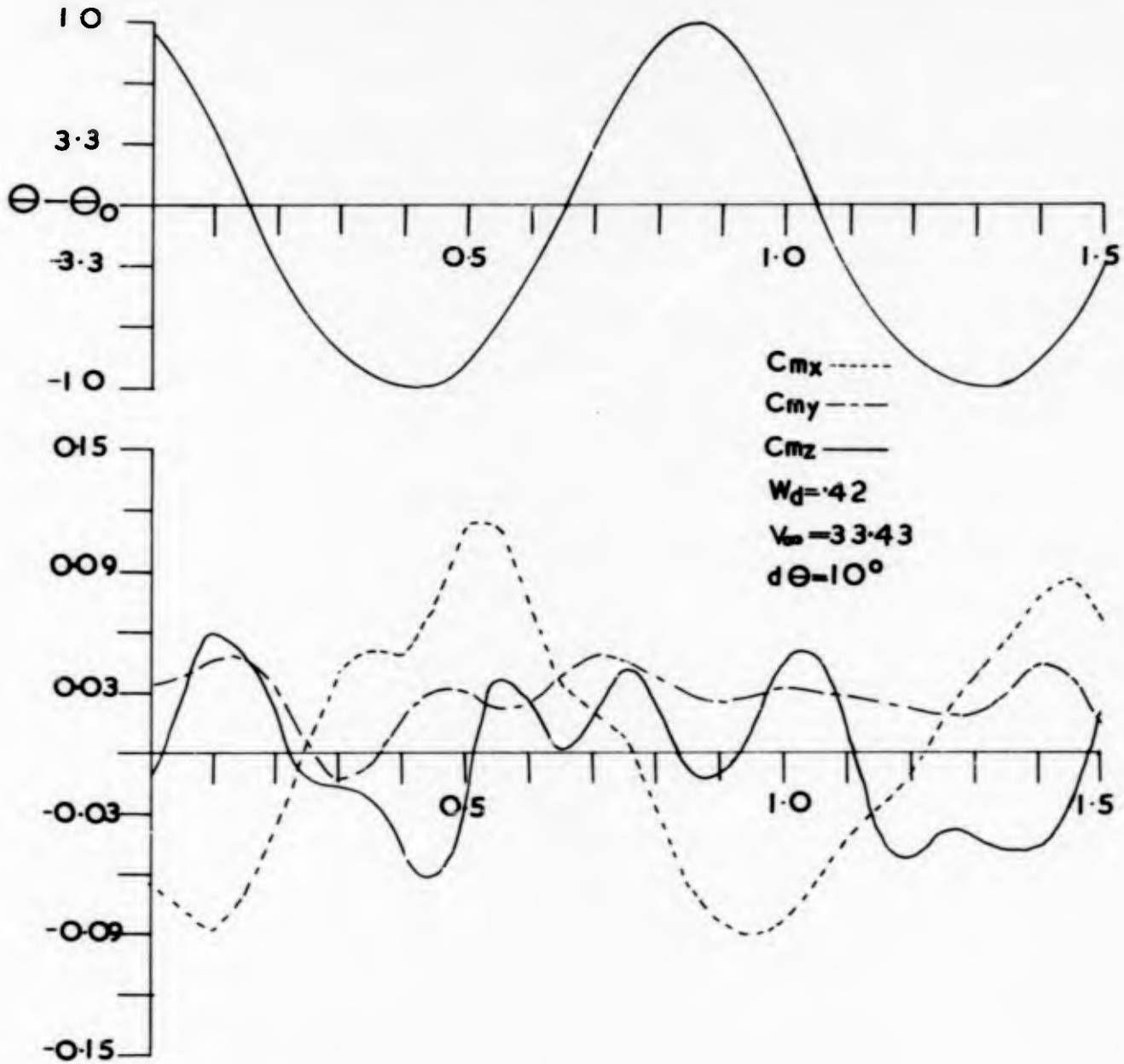
1·0
3·3
θ−θ0
-3·3
-1·0
0·5
1·0
1·5
Cmx
Cmy
Cmz
Wd=·42
V∞=33·43
dθ=10°
0·15
0·09
0·03
-0·03
-0·09
-0·15
0·5
1·0
1·5

FIG 4.37(c)

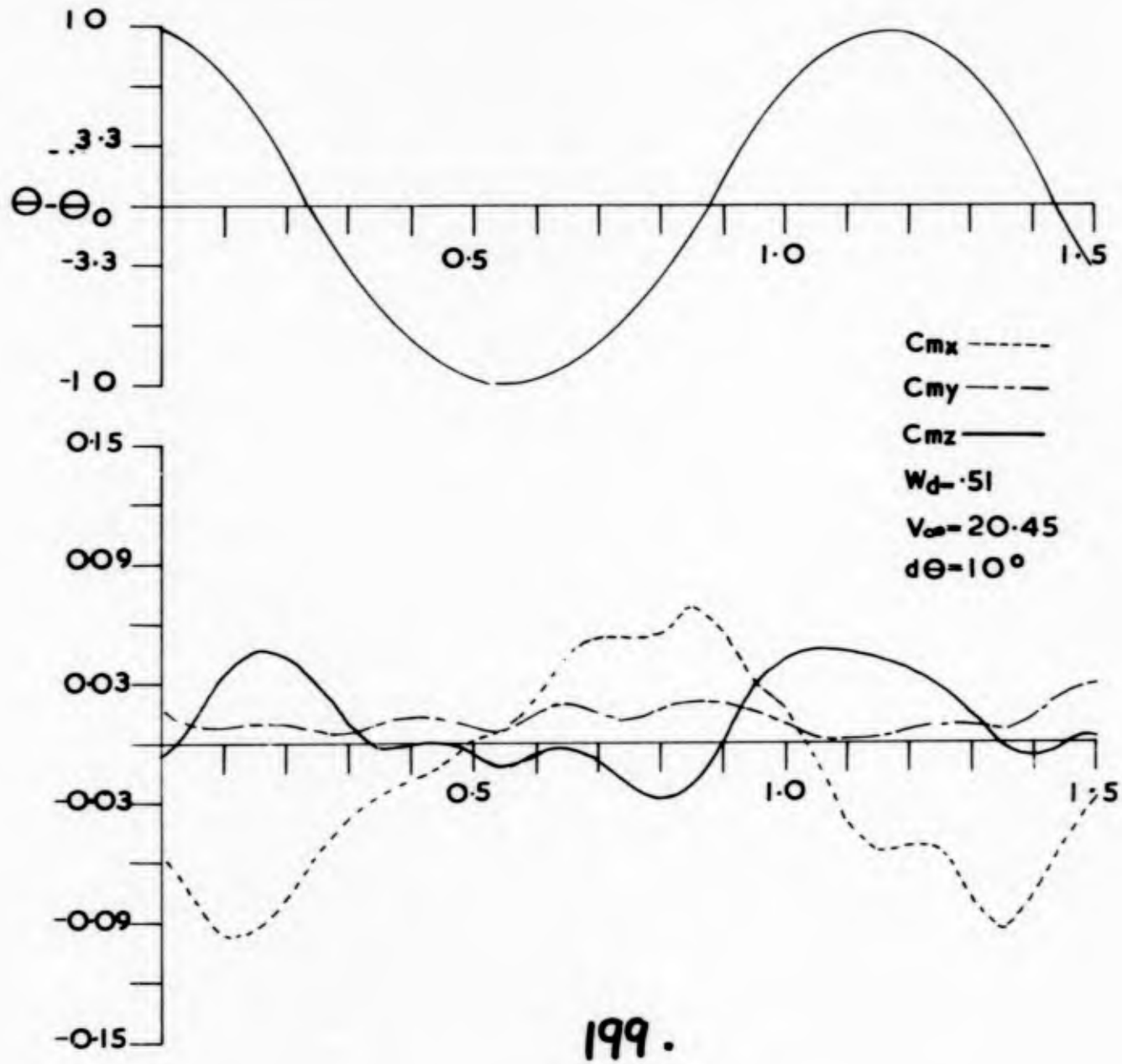
1·0
·3·3
Θ-Θ0
-3·3
-1·0
0·5
1·0
1·5
Cmx
Cmy
Cmz
Wd=·51
V∞=20·45
dΘ=10°
0·15
0·09
0·03
-0·03
-0·09
-0·15
0·5
1·0
1·5

FIG 4.37(d)

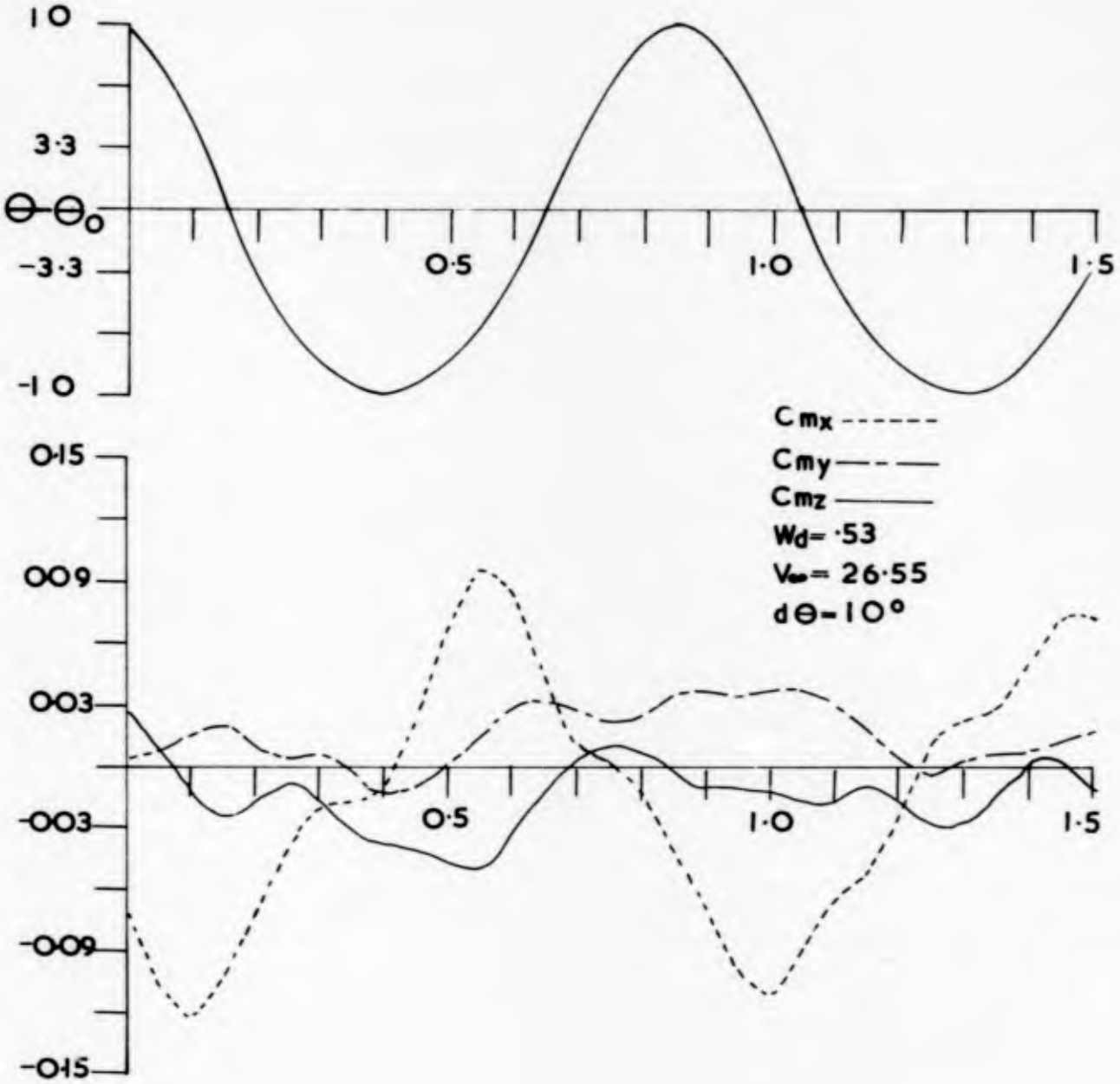
10
3·3
θ-θ0
-3·3
-10
0·5
1·0
1·5
Cmx
Cmy
Cmz
Wd= ·53
V∞= 26·55
dθ=10°
0·15
009
003
-003
-009
-015
0·5
1·0
1·5

FIG 4.37(e)

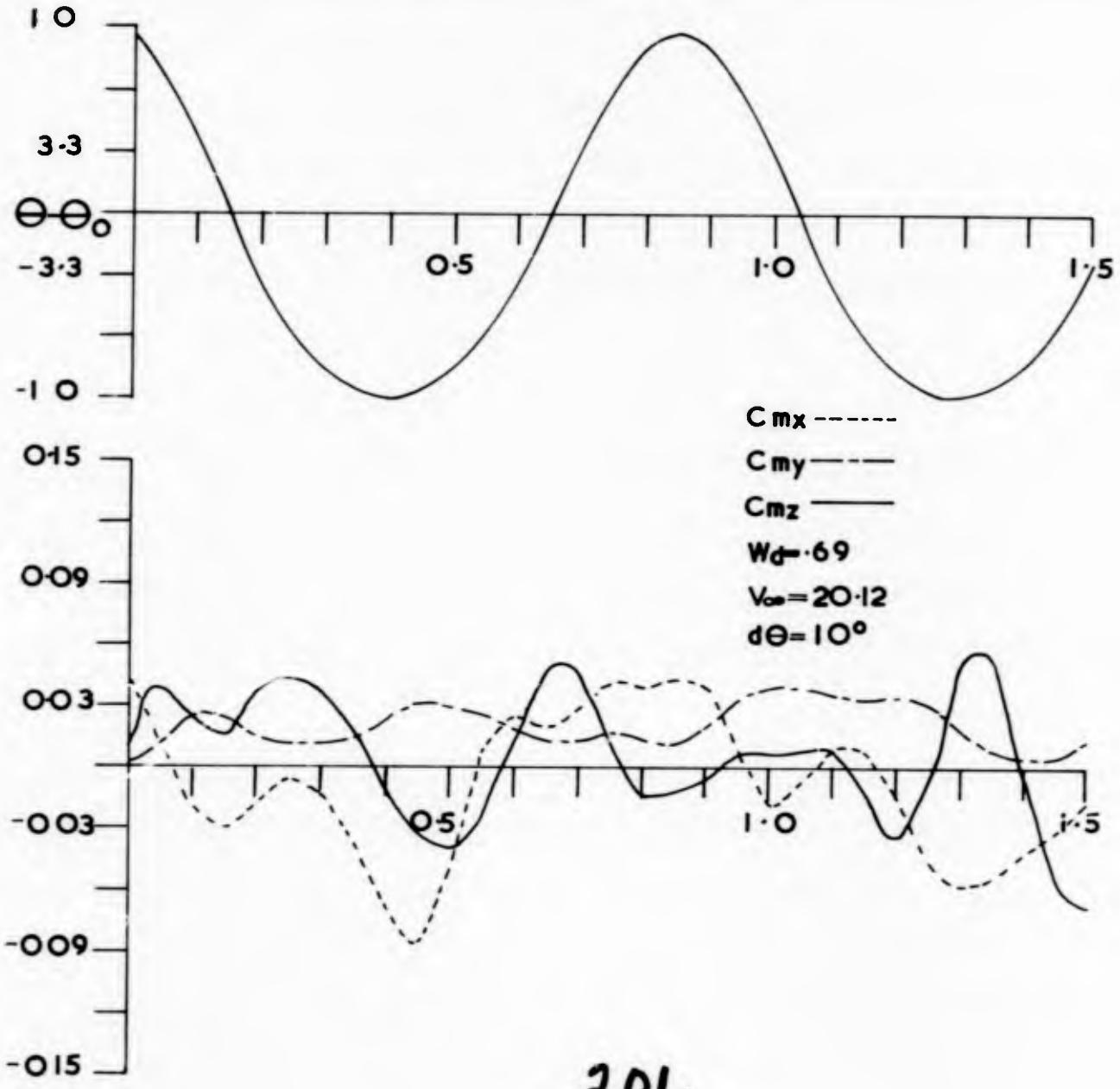
1·0
3·3
θ-θ0
-3·3
-1·0
0·5
1·0
1·5
Cmx ------
Cmy — — —
Cmz ——
Wd=·69
V∞=20·12
dθ=10°
0·15
0·09
0·03
-0·03
-0·09
-0·15
0·5
1·0
1·5

201.

FIG 4.37(f)

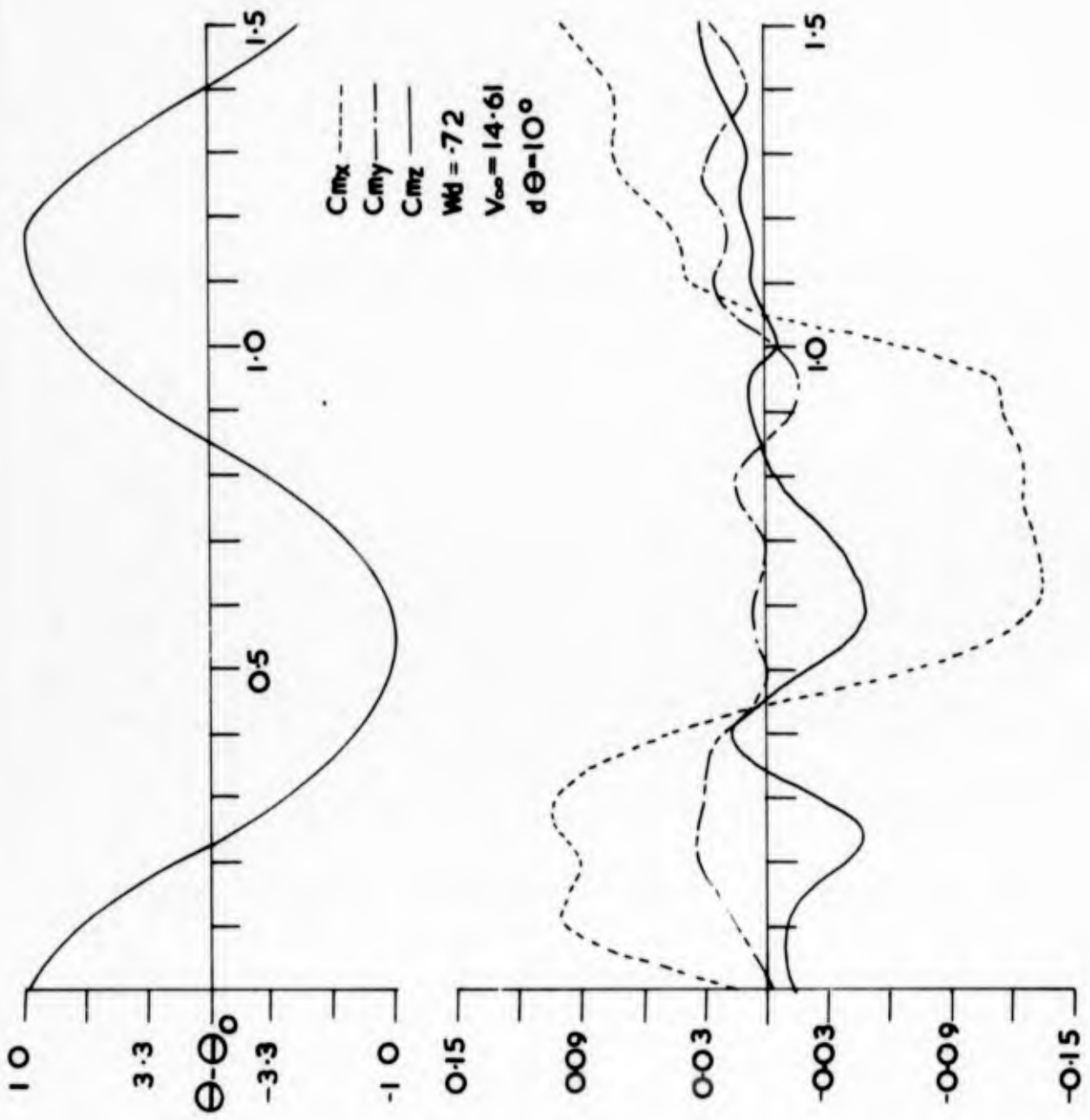
Cmx ----
Cmy —·—
Cmz ——
Wd = ·72
V∞ = 14·61
dΘ = 10°
Θ-Θ0
1·0
3·3
-3·3
-1·0
0·5
1·5
0·15
0·09
0·03
-0·03
-0·09
-0·15

FIG 4.37(g)

FIG 4.37(h)

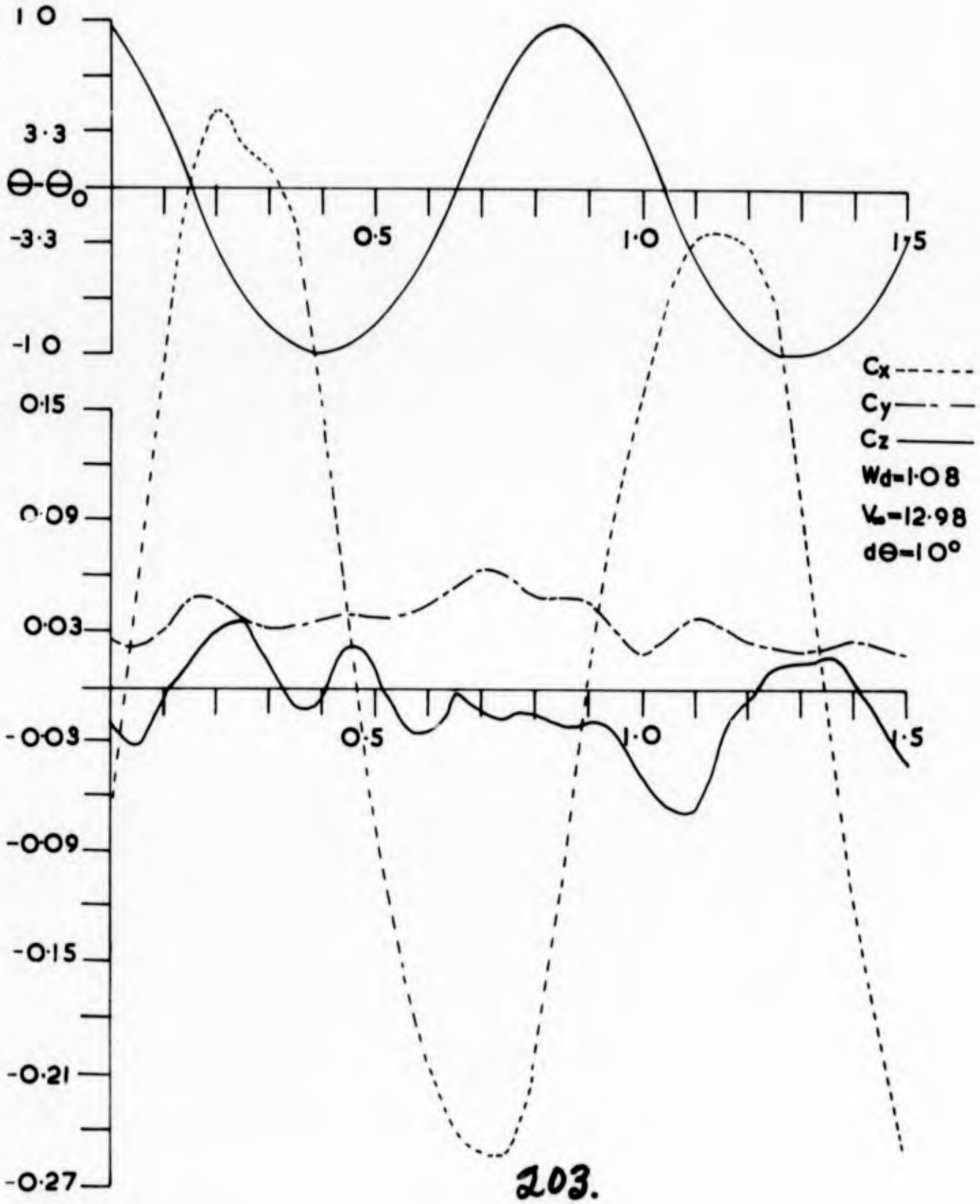
1·0
3·3
θ-θ0
-3·3
-1·0
0·5
1·0
1·5
Cx
Cy
Cz
Wd=1·08
V∞=12·98
dθ=10°
0·15
0·09
0·03
-0·03
-0·09
-0·15
-0·21
-0·27

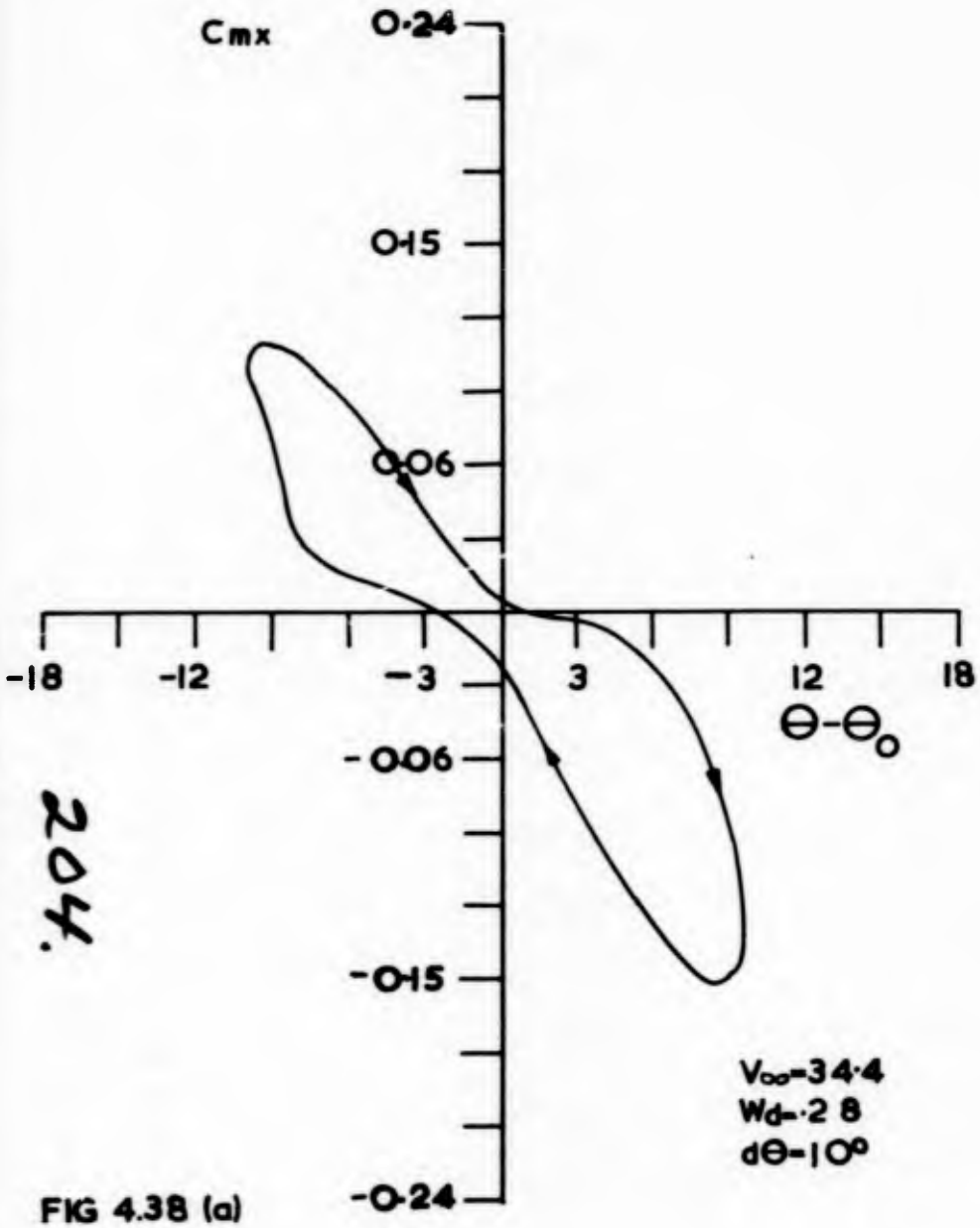

FIG 4.38 (a)

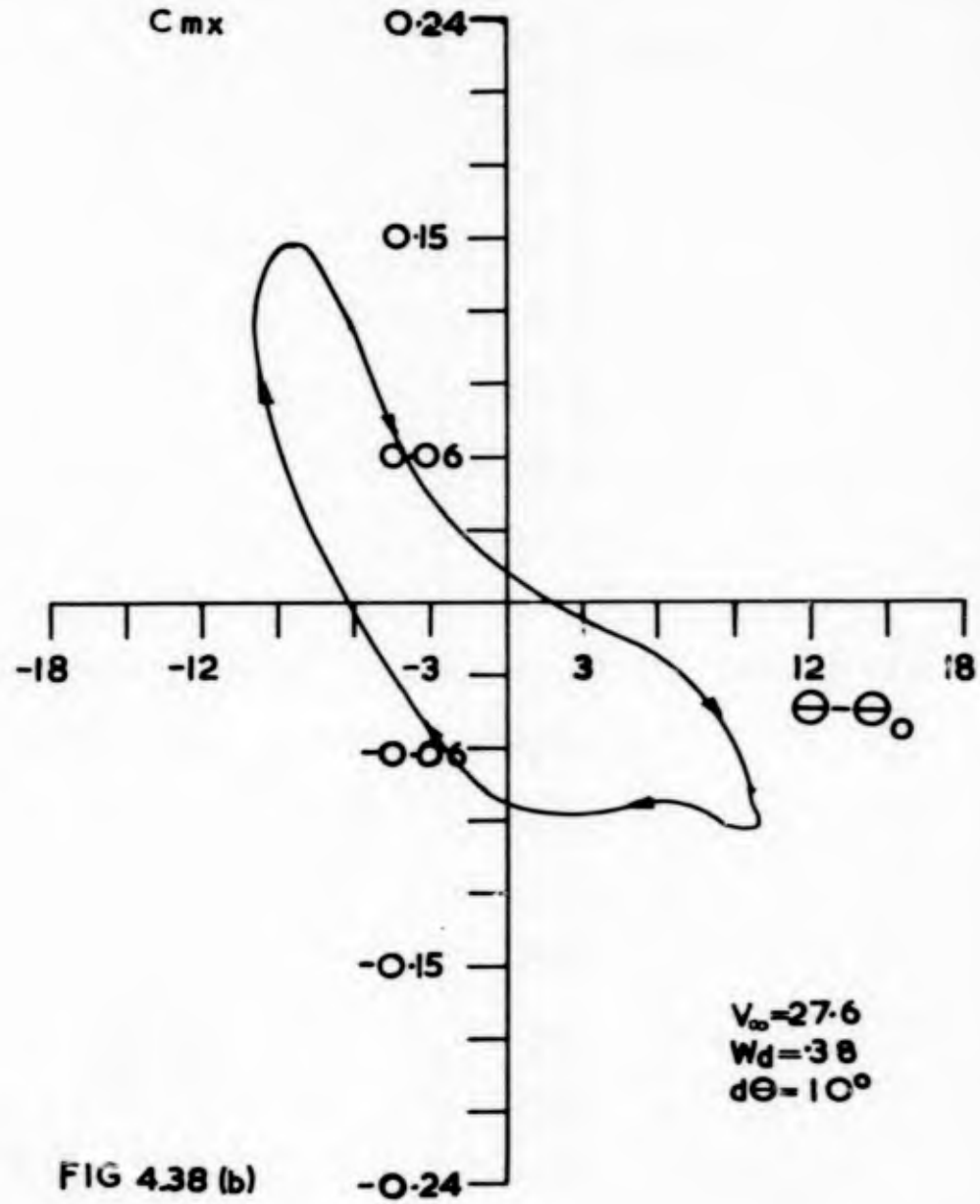

FIG 4.38 (b)

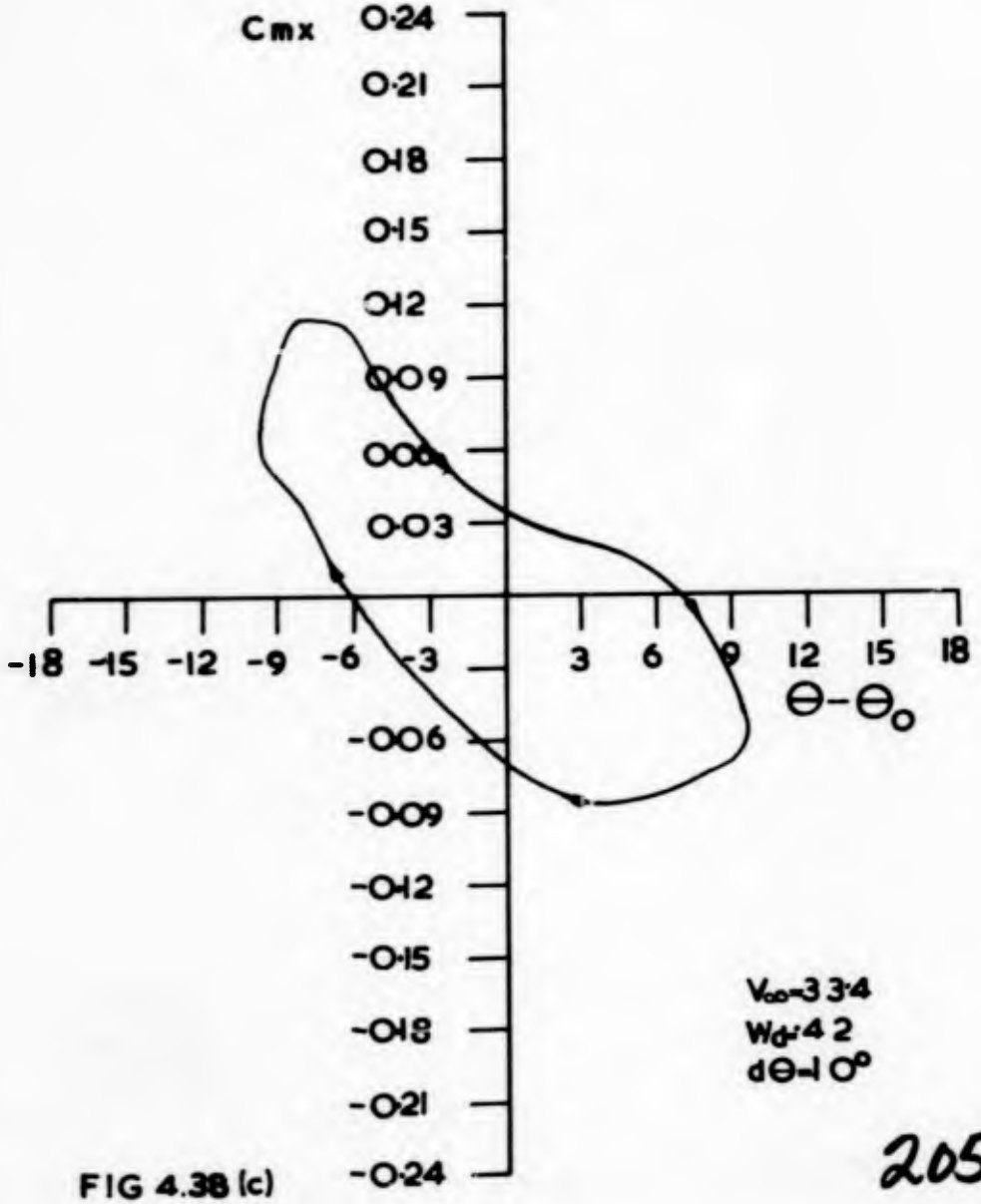

FIG 4.38 (c)

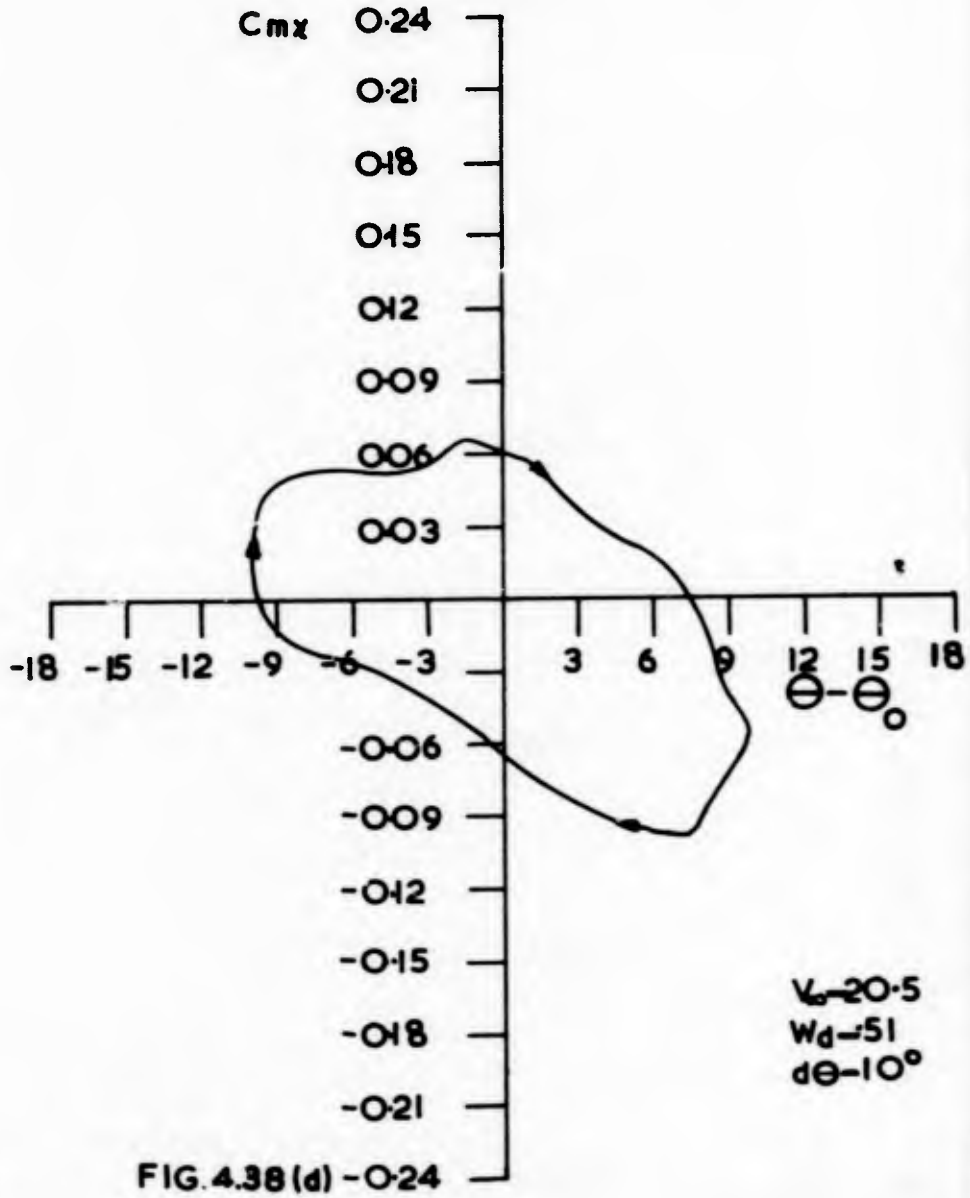

FIG. 4.38 (d)

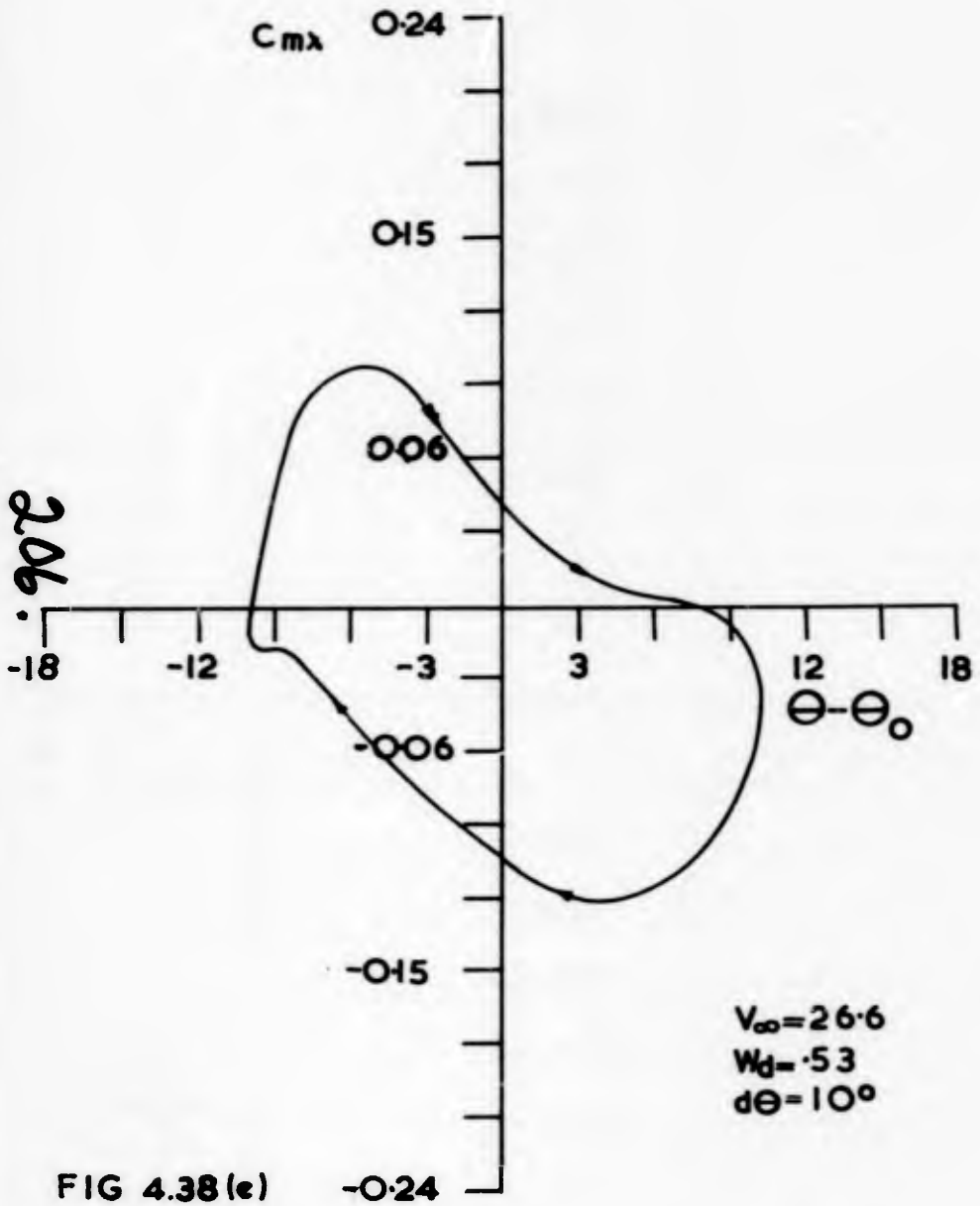

FIG 4.38 (e)

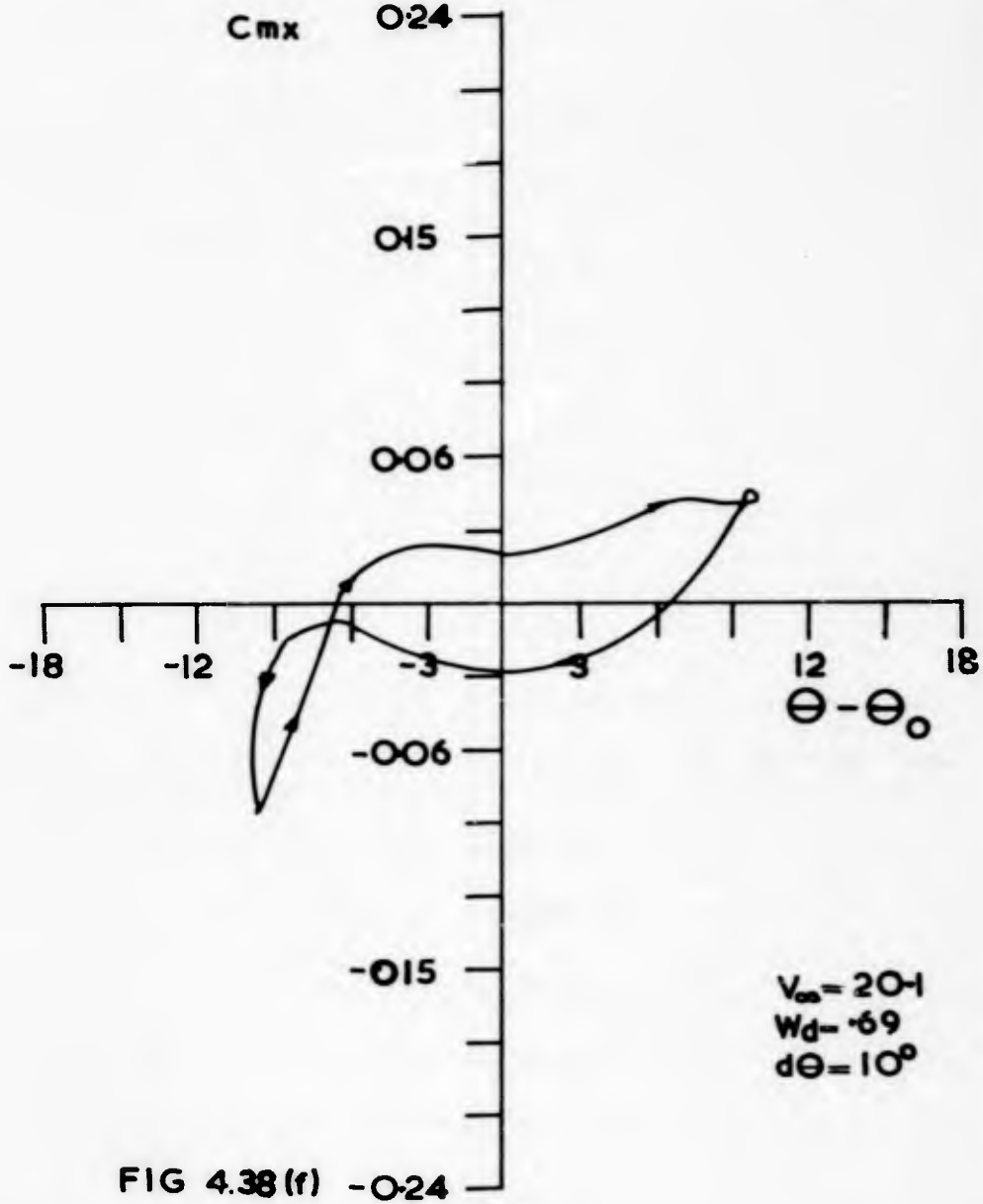

FIG 4.38 (f)

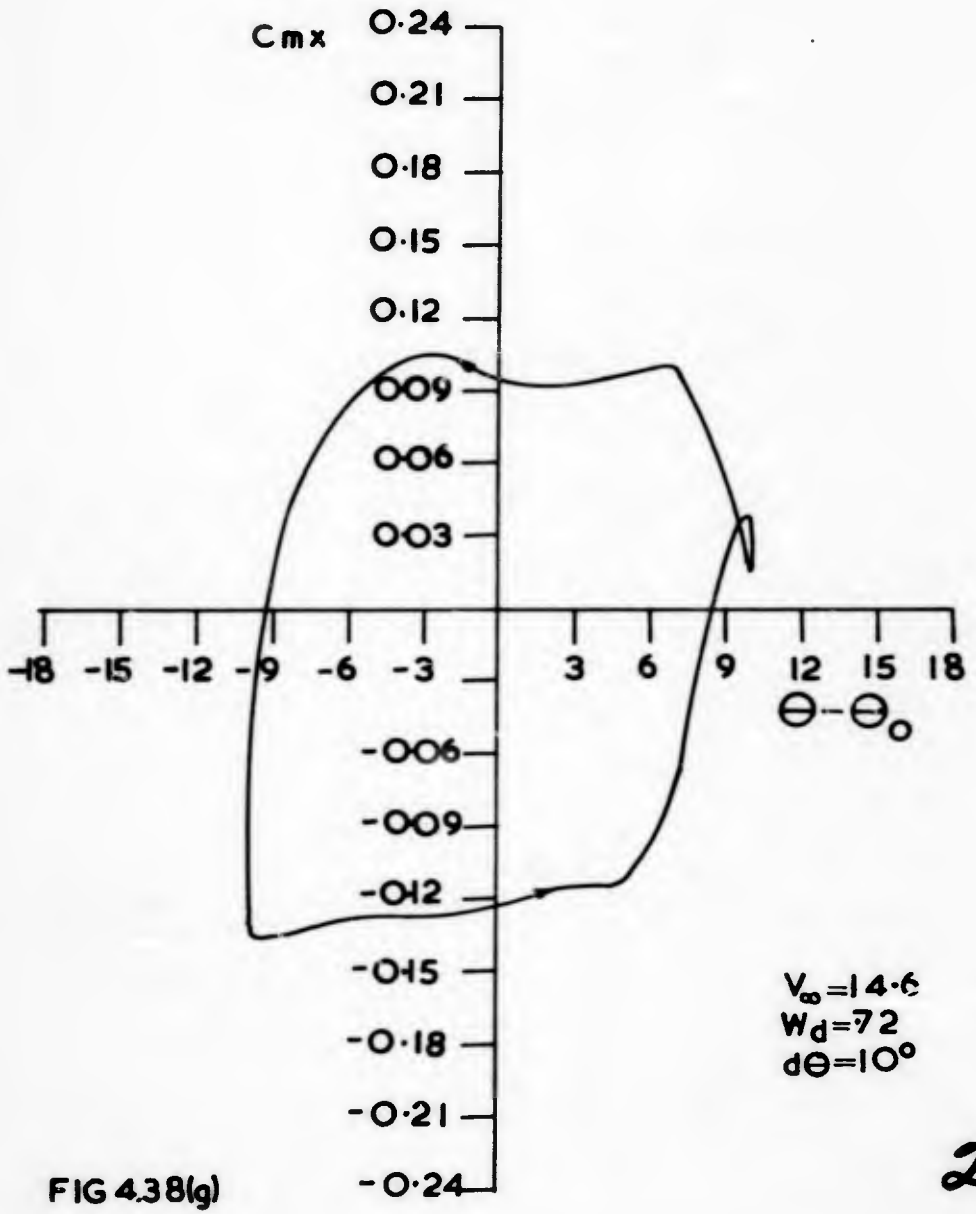

FIG 4.38(g)

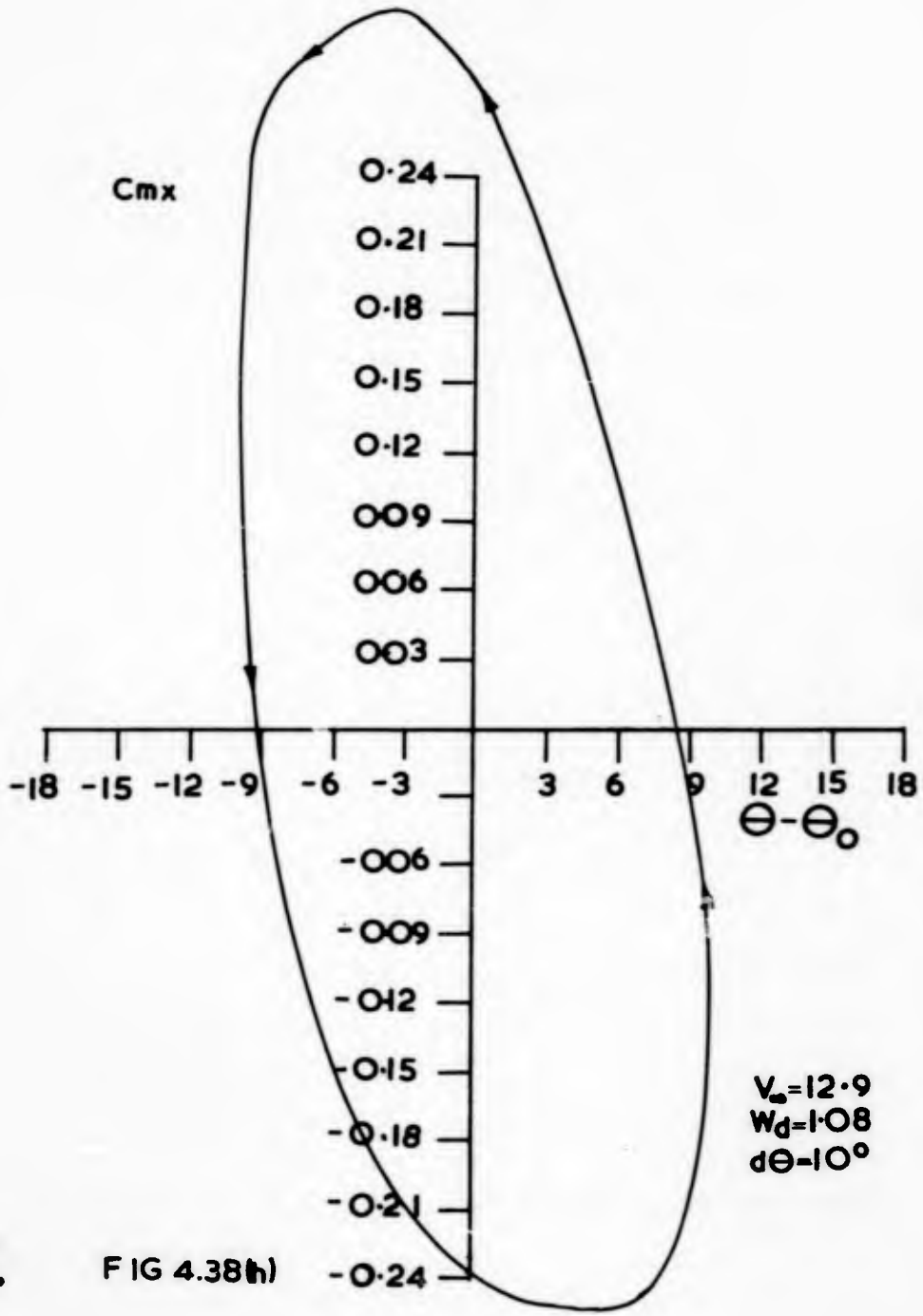

FIG 4.38(h)

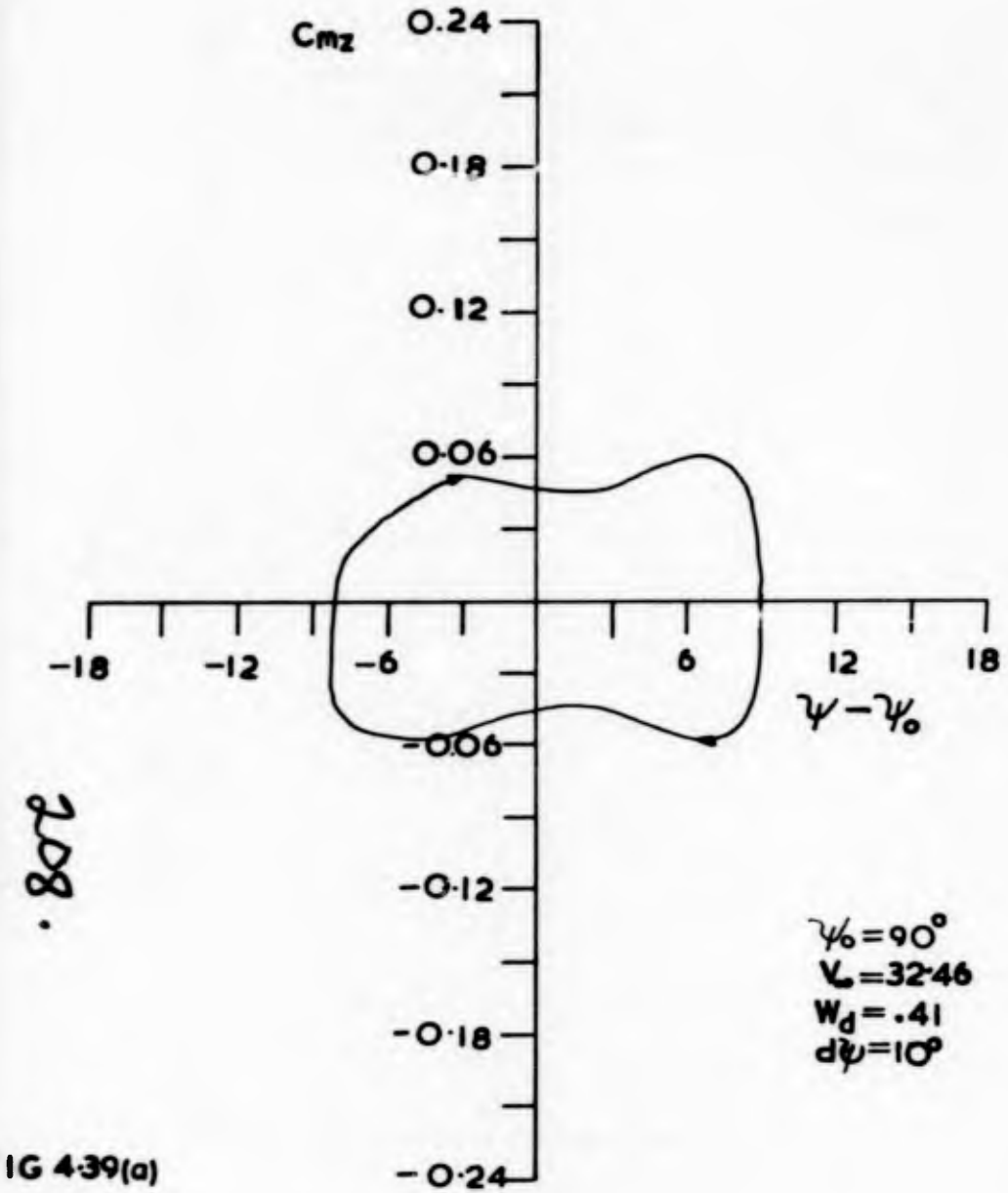

FIG 4·39(a)

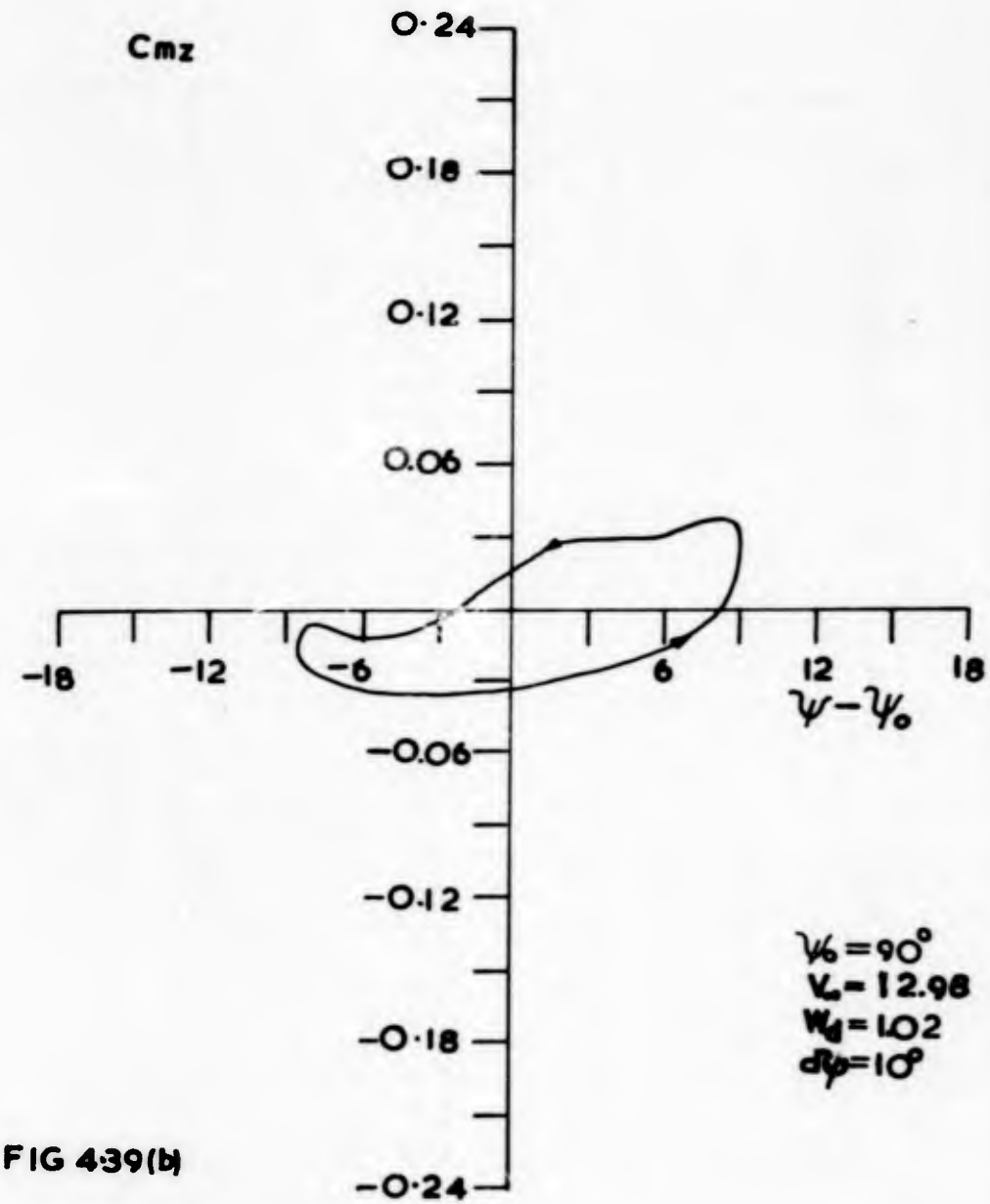

FIG 4·39(b)

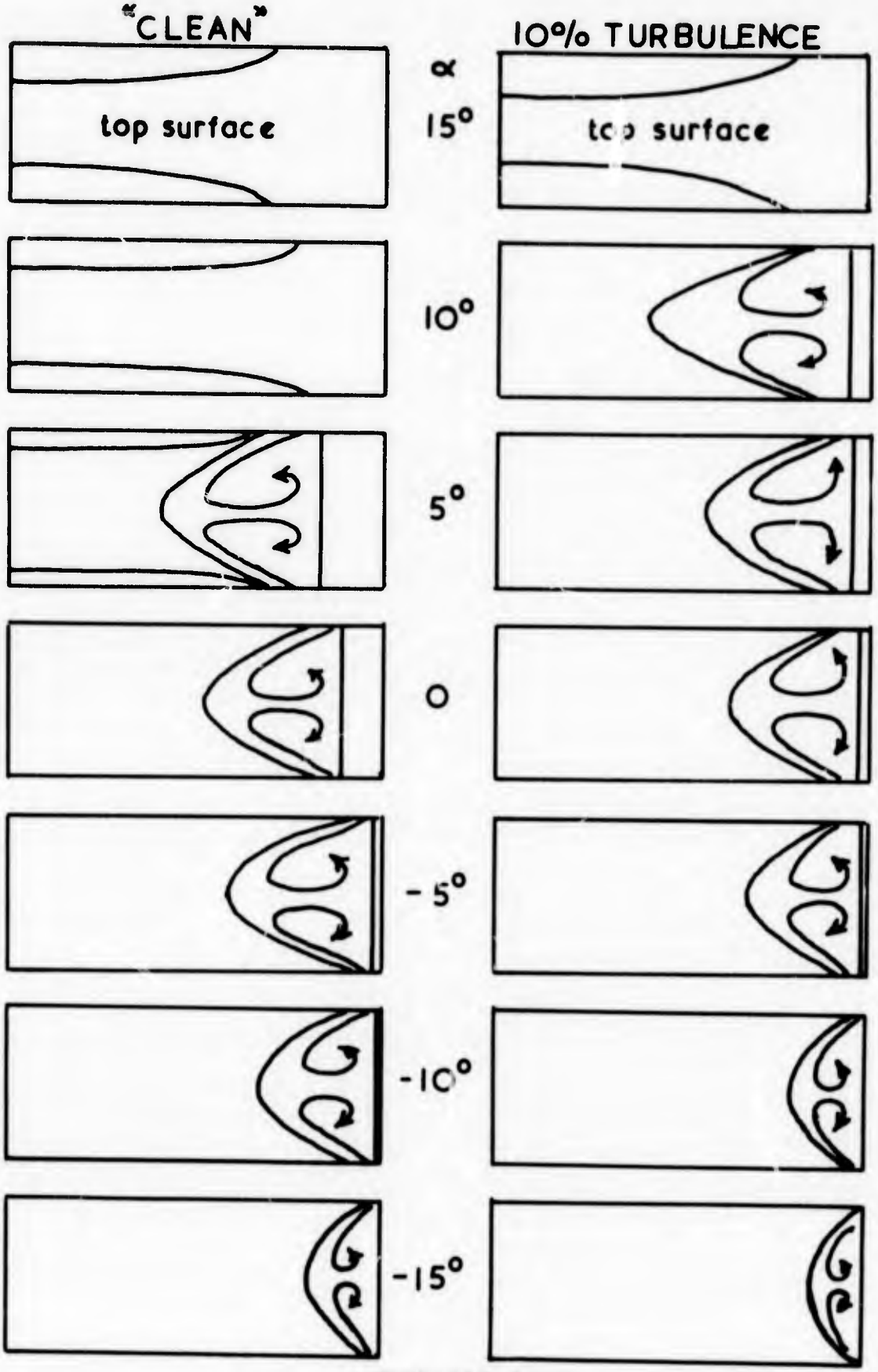

FIGURE 5·1

SEPARATION BUBBLES AND VORTEX LINES ON UPPER SURFACE OF 1:0·4:0·4 MODEL

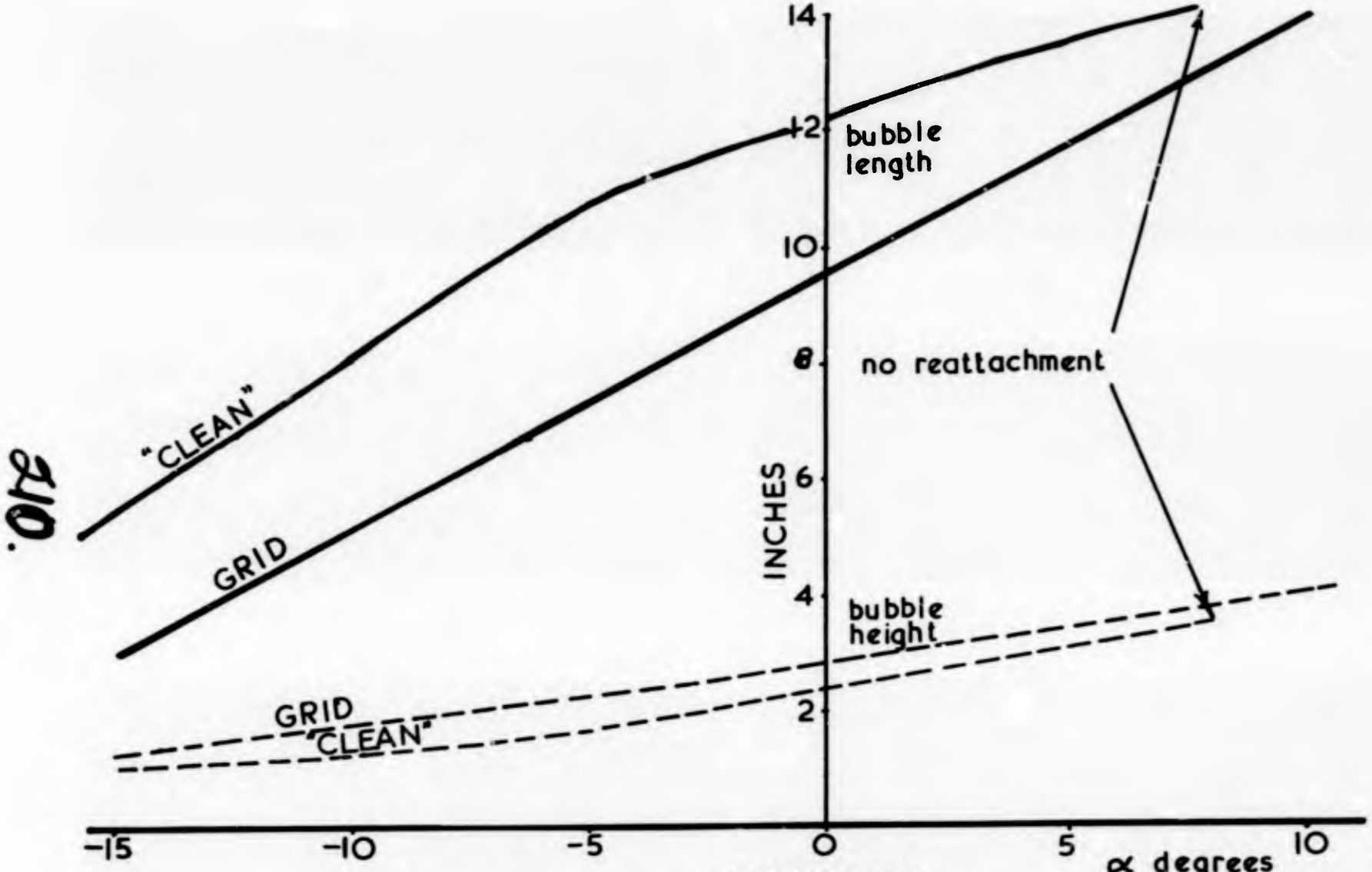

FIGURE 5·2

VARIATION OF BUBBLE LENGTH AND HEIGHT ON UPPER SURFACE OF 1:0·4:0·4 MODEL

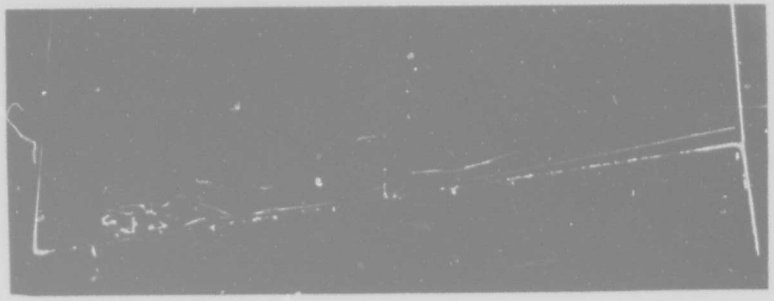

(a) 1·6" SECTION

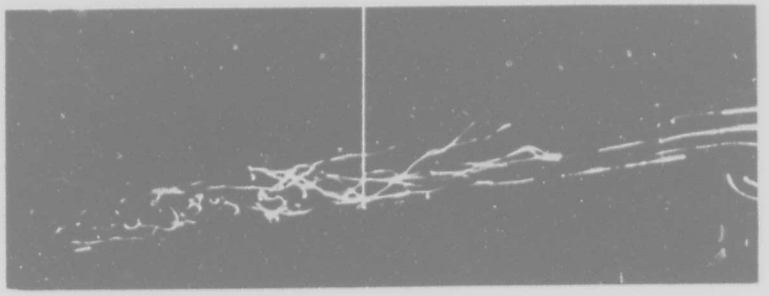

(d) 6·4" SECTION

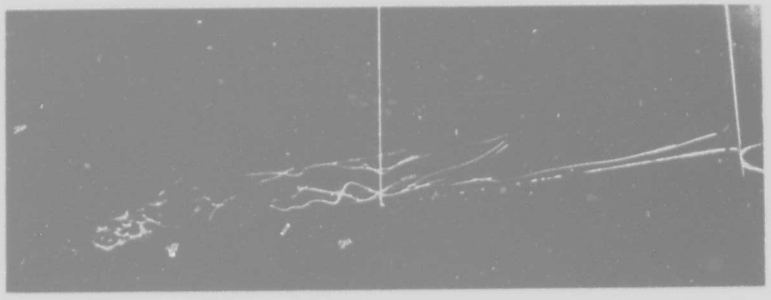

(b) 3·2" SECTION

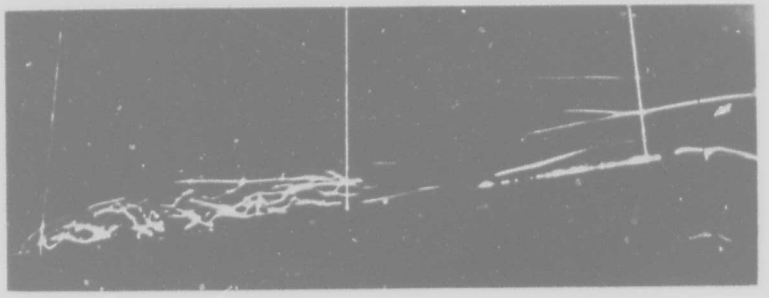

(e) 8·0" SECTION

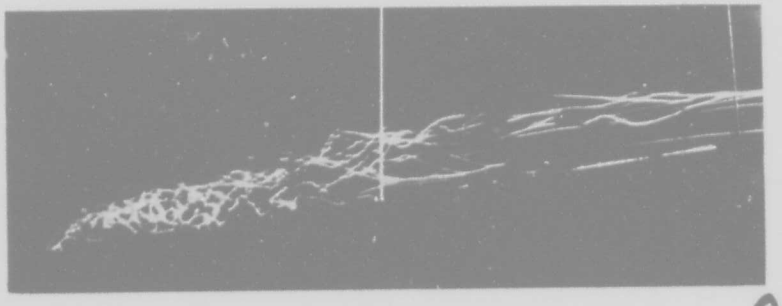

(c) 4·8" SECTION

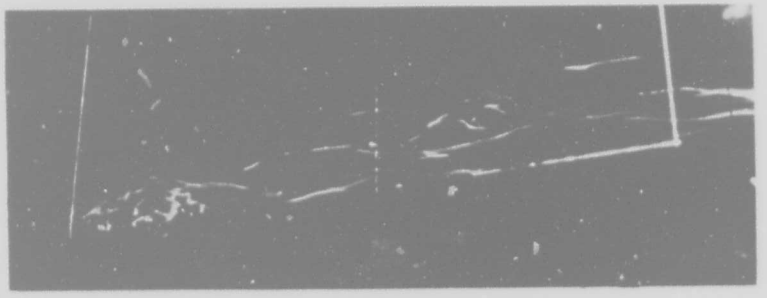

(f) 9·6" SECTION

FIG 53 SECTIONS OF HELIUM BUBBLE FLOW OVER A STATIONARY BOX $\psi_0 = +100°$

(a) 1·6" SECTION

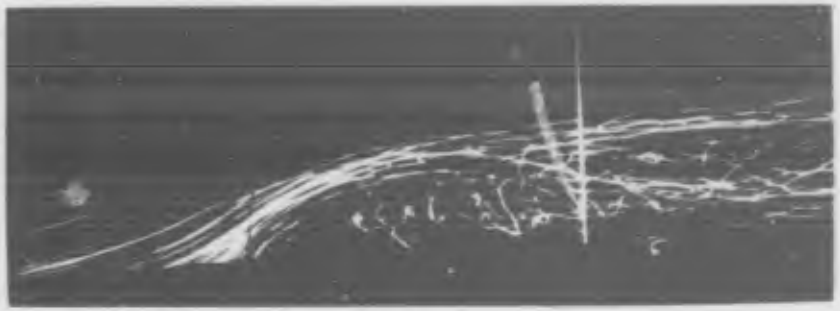

(d) 6·4" SECTION

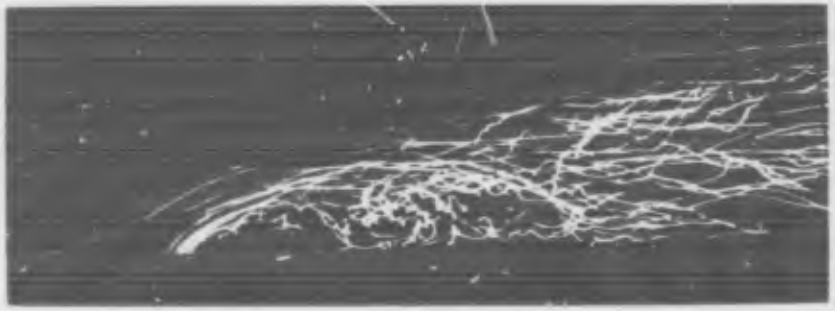

(b) 3·2" SECTION

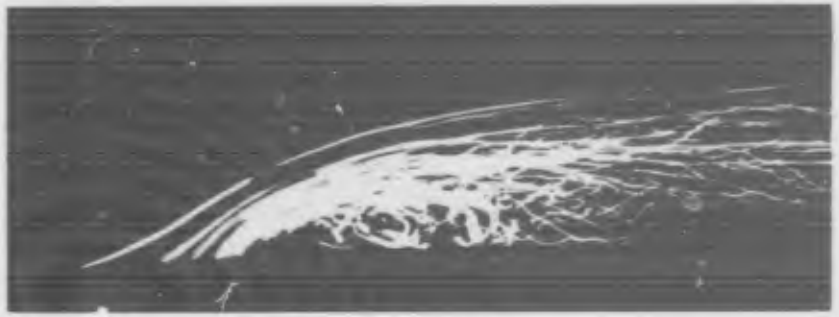

(c) 8·0" SECTION

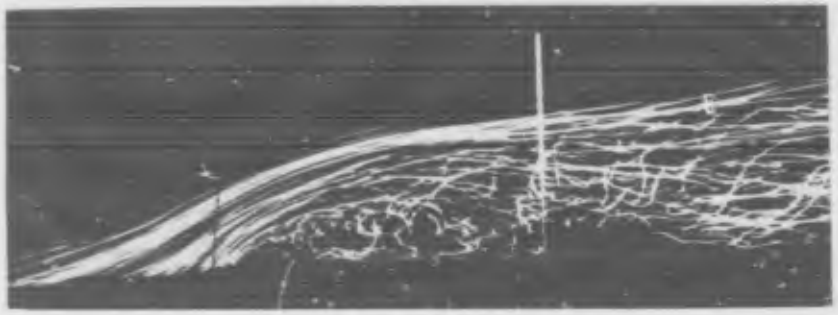

(c) 4·8" SECTION

(f) 9·6" SECTION

FIG 5·4

SECTIONS OF HELIUM BUBBLE FLOW OVER A STATIONARY BOX $\Psi_a = +90^\circ$

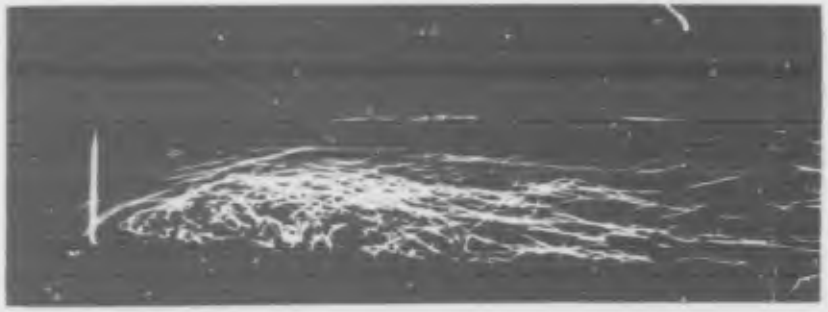

(a) 1·6" SECTION

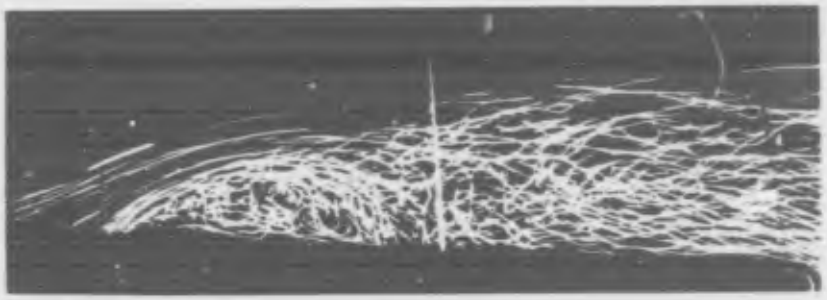

(d) 6·4" SECTION

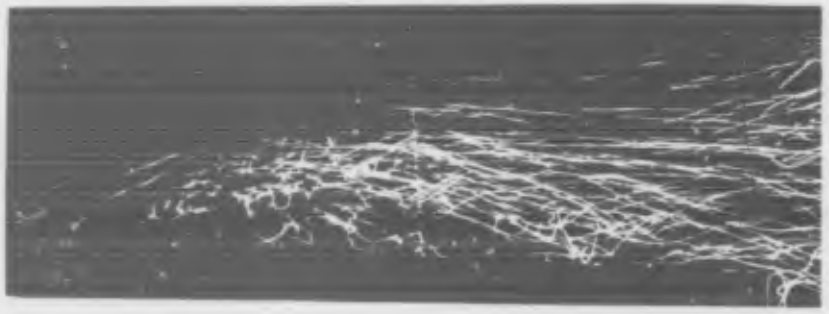

(b) 3·2" SECTION

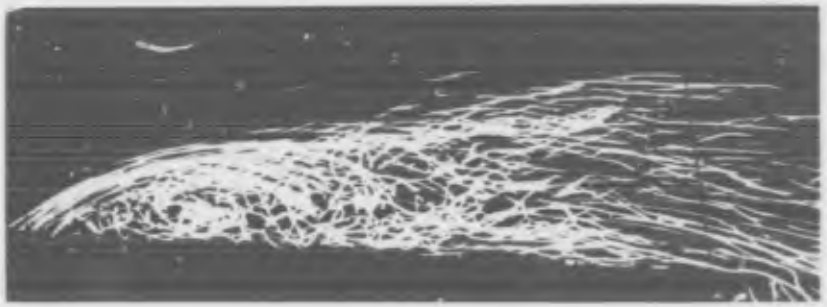

(e) 8·0" SECTION

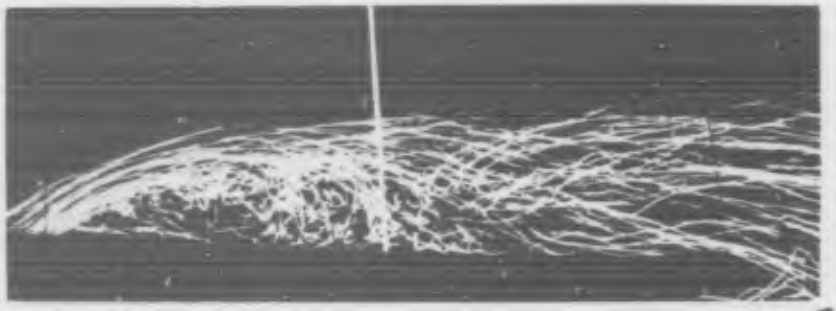

(c) 4·8" SECTION

(f) 9·6" SECTION

FIG 55 SECTIONS OF HELIUM BUBBLE FLOW OVER A STATIONARY BOX $\psi_0 = +87°$

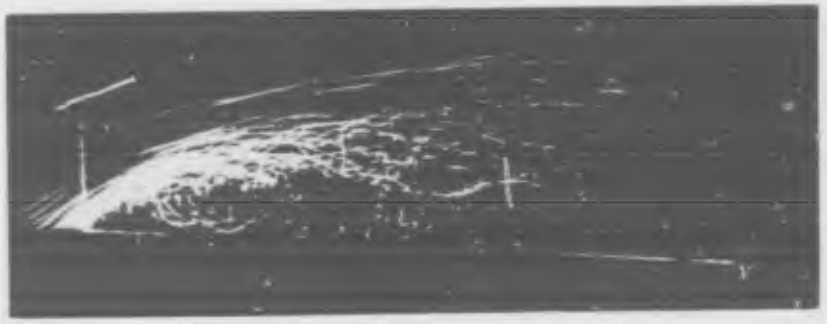

(a) 1·6" SECTION

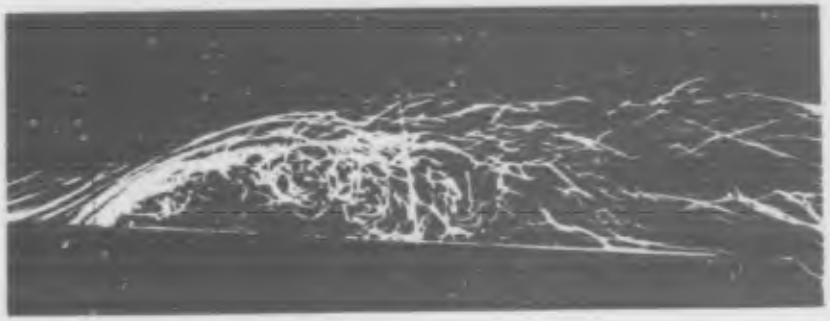

(d) 6·4" SECTION

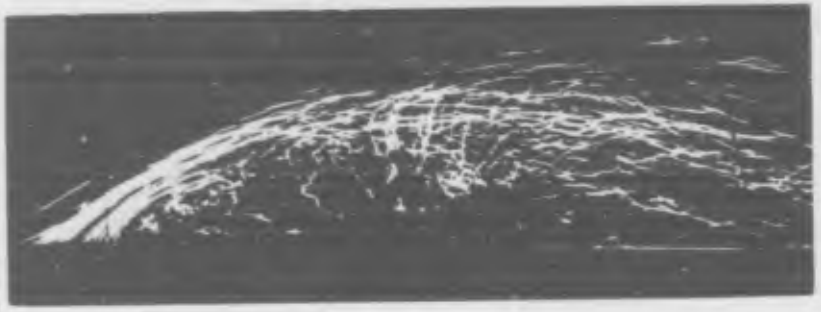

(b) 3·2" SECTION

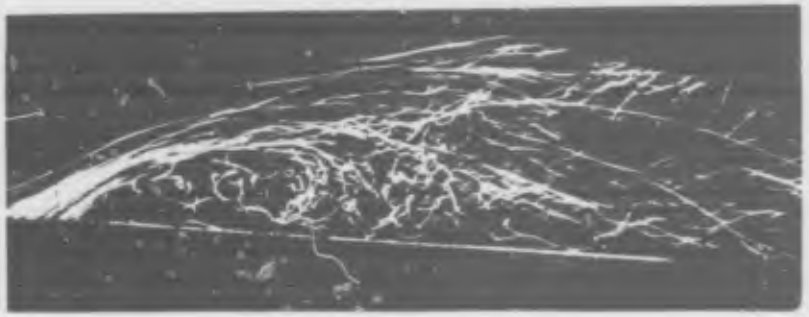

(e) 8·0" SECTION

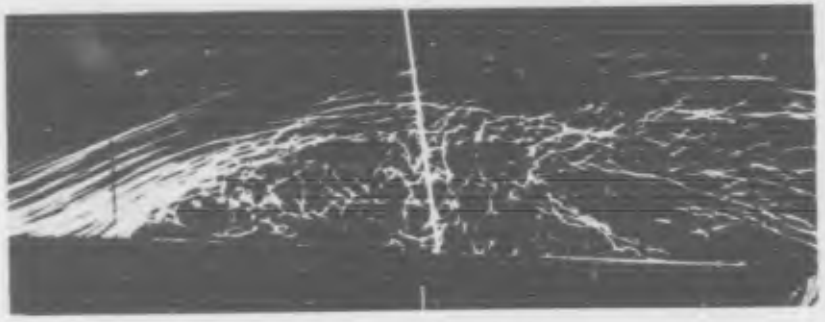

(c) 4·8" SECTION

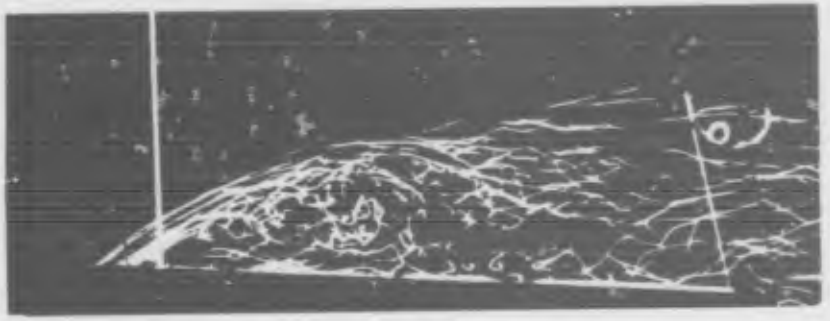

(f) 9·6" SECTION

FIG 5.6 SECTIONS OF HELIUM BUBBLE FLOW OVER A STATIONARY BOX $\Psi_0 = +85°$

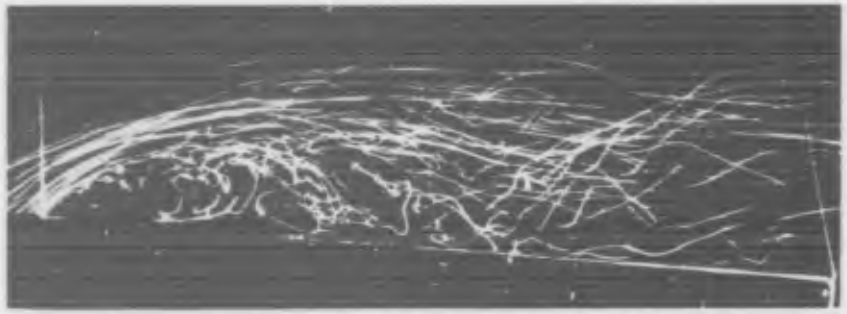

(a) 1·6" SECTION

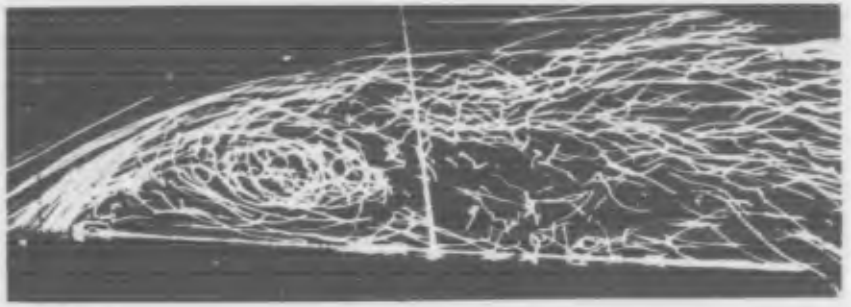

(d) 6·4" SECTION

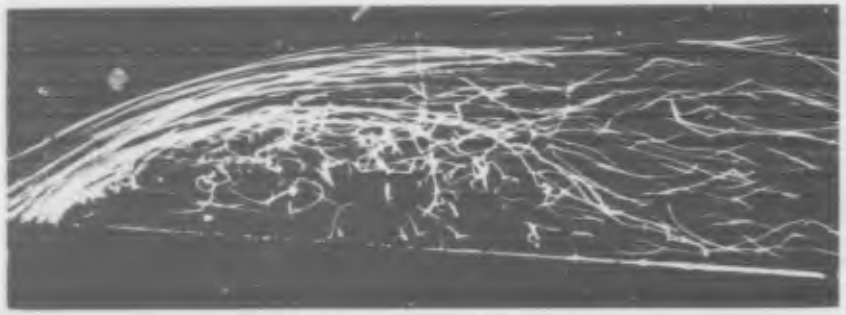

(b) 3·2" SECTION

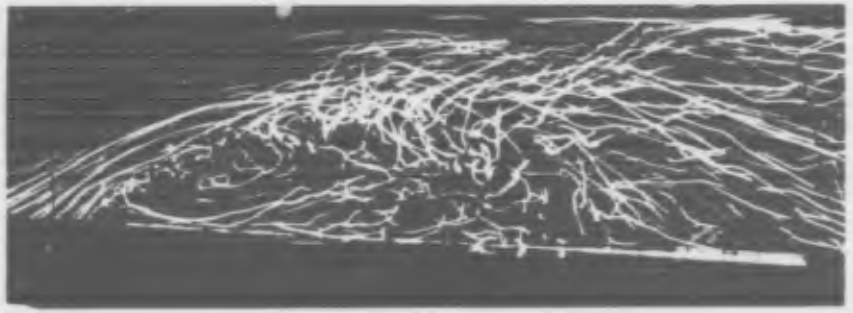

(e) 8·0" SECTION

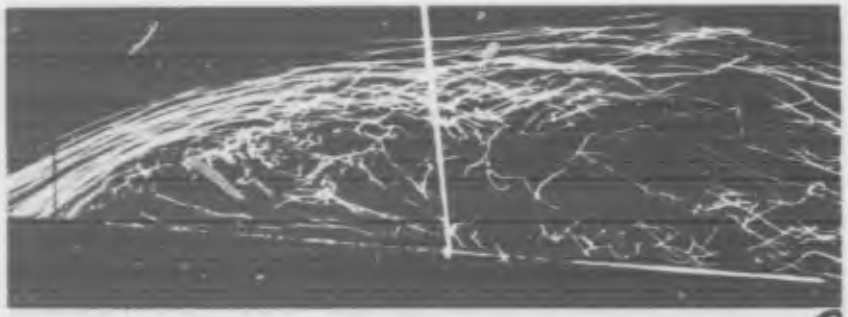

(c) 4·8" SECTION

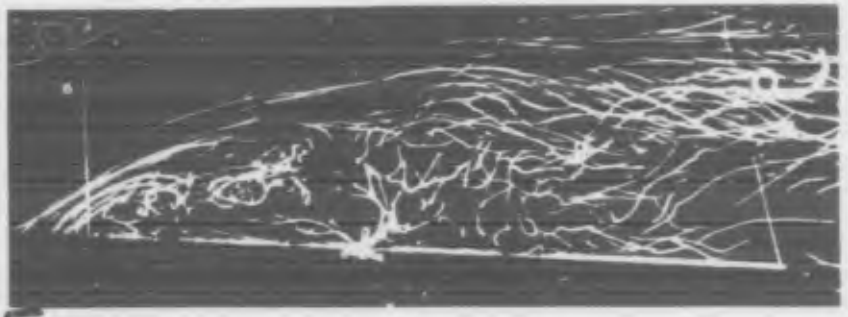

(f) 9·6" SECTION

FIG 5·7 SECTIONS OF HELIUM BUBBLE FLOW OVER A STATIONARY BOX $\gamma_0 = +83°$

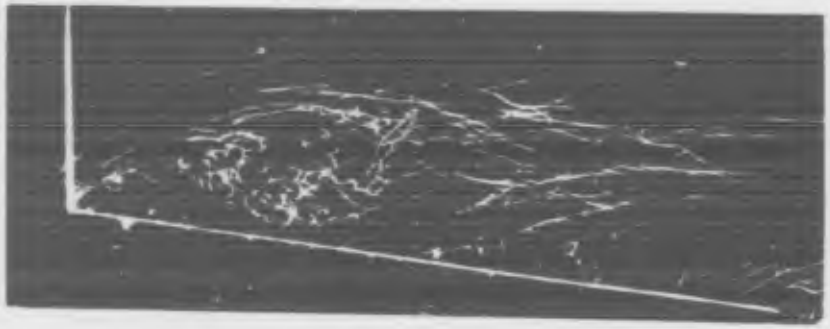

(a) 1·6" SECTION

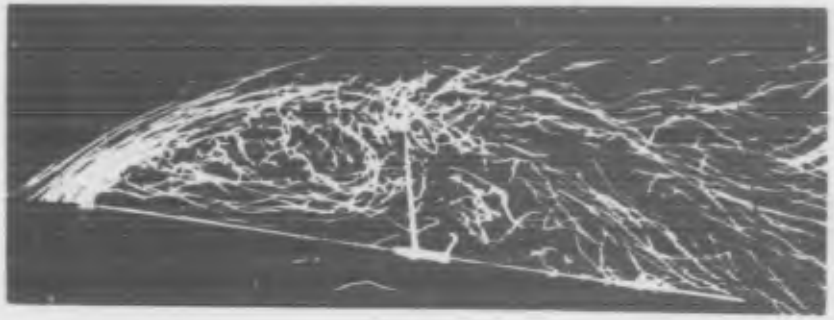

(d) 6·4" SECTION

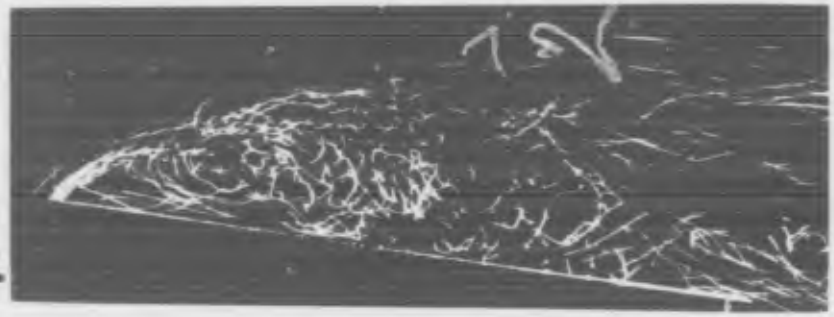

(b) 3·2" SECTION

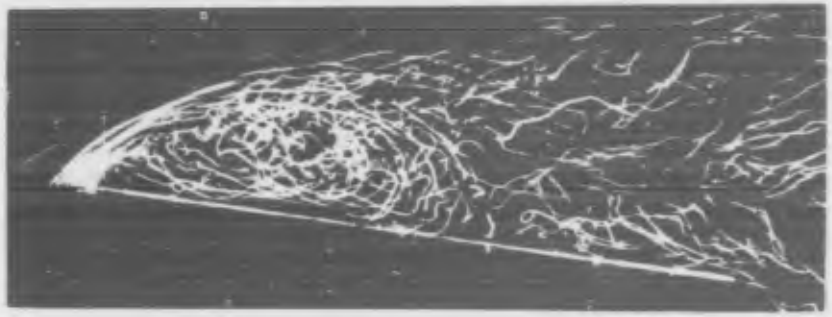

(e) 8·0" SECTION

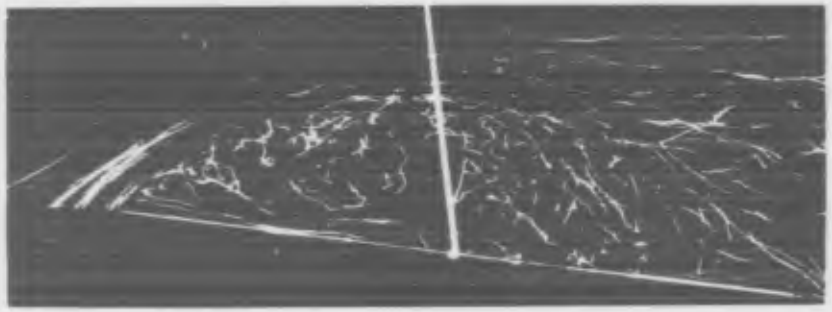

(c) 4·8" SECTION

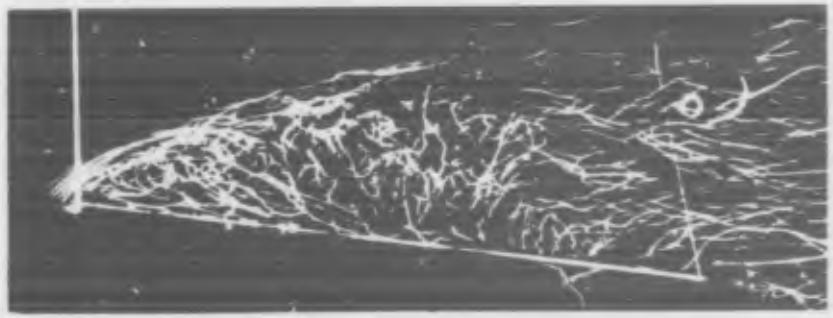

(f) 9·6" SECTION

FIG 5.8 SECTIONS OF HELIUM BUBBLE FLOW OVER A STATIONARY BOX $\Psi_0 = +80°$

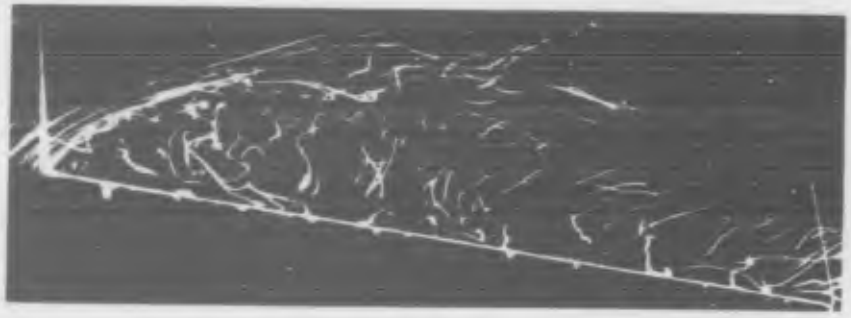

(a) 1·6 SECTION

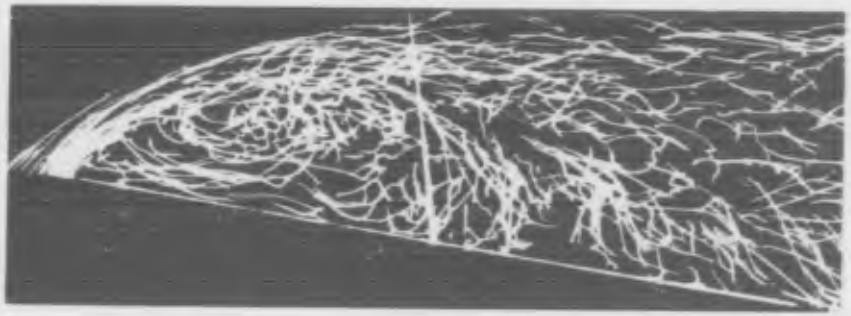

(d) 6·4 SECTION

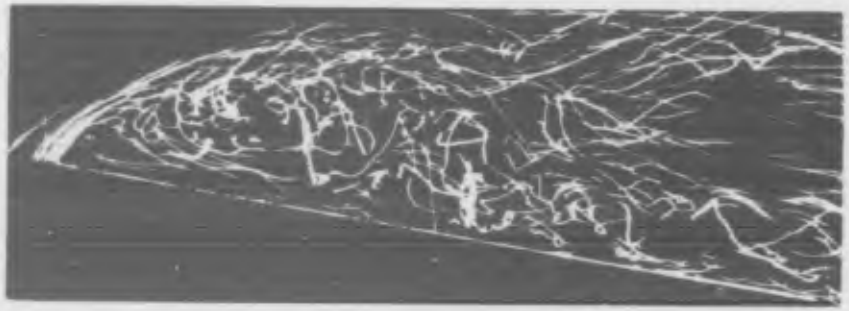

(b) 3·2 SECTION

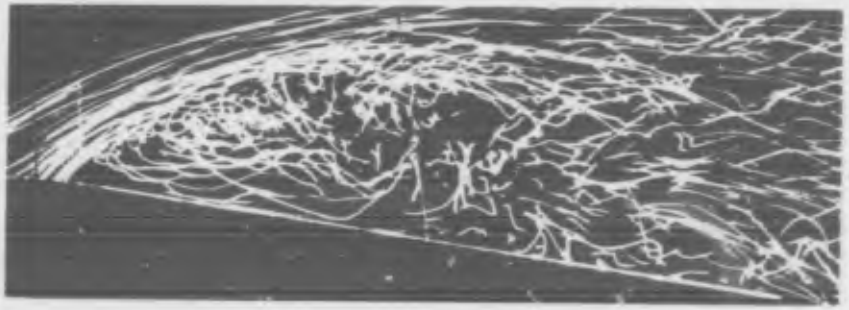

(e) 8·0 SECTION

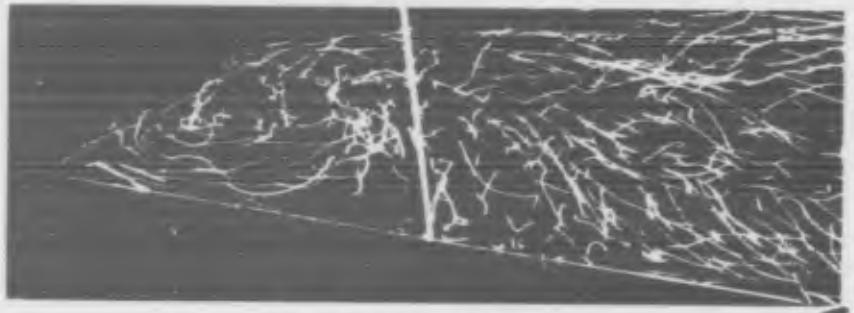

(c) 4·8 SECTION

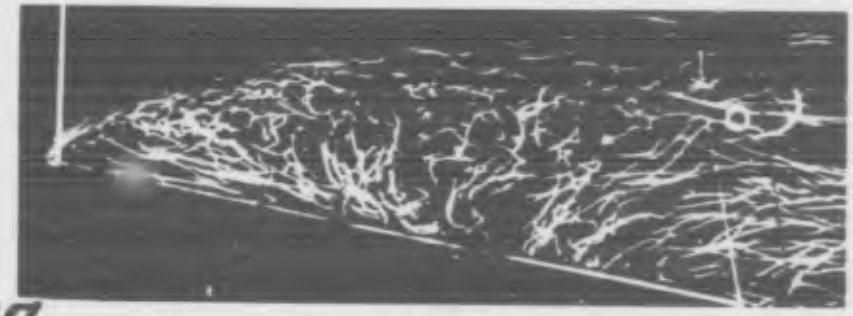

(f) 9·6 SECTION

FIG 5.9 SECTIONS OF HELIUM BUBBLE FLOW OVER A STATIONARY BOX $\Psi_0 = +78°$

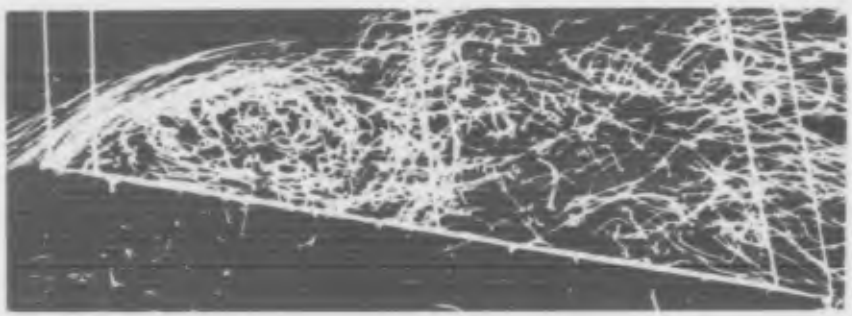

(a) $\psi_0 = 78^\circ$

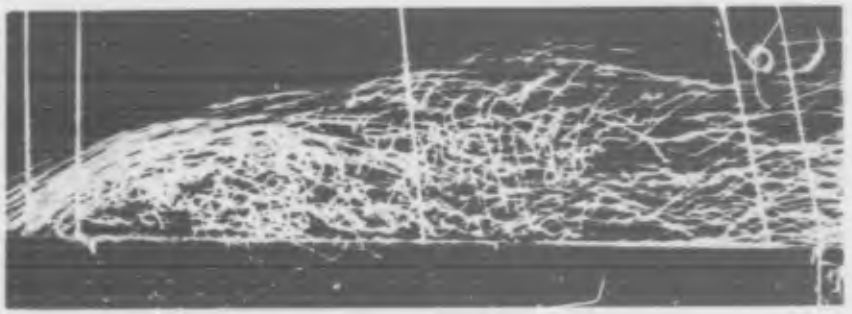

(d) $\psi_0 = 87^\circ$

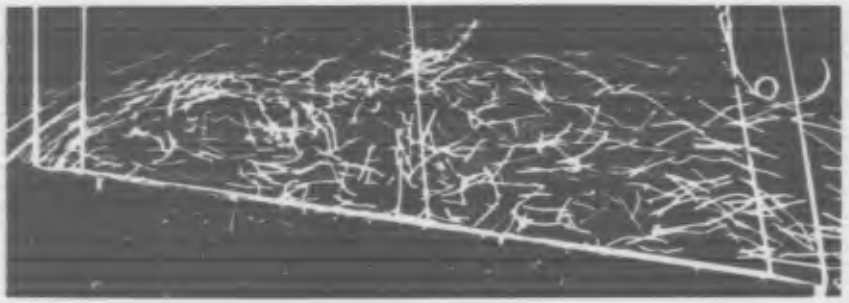

(b) $\psi_0 = 80^\circ$

(e) $\psi_0 = 90^\circ$

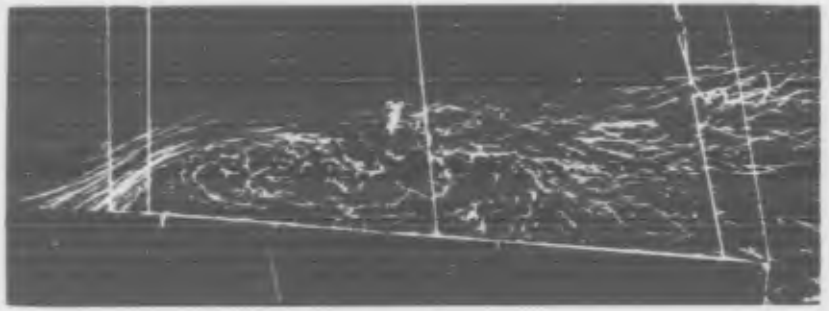

(c) $\psi_0 = 85$

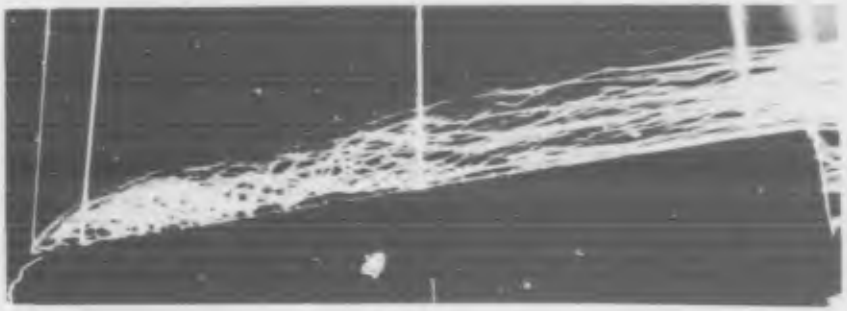

(f) $\psi_0 = 100^\circ$

FIG 5.10 HELIUM BUBBLE FLOW OVER A STATIONARY BOX AT VARIOUS INCIDENCES

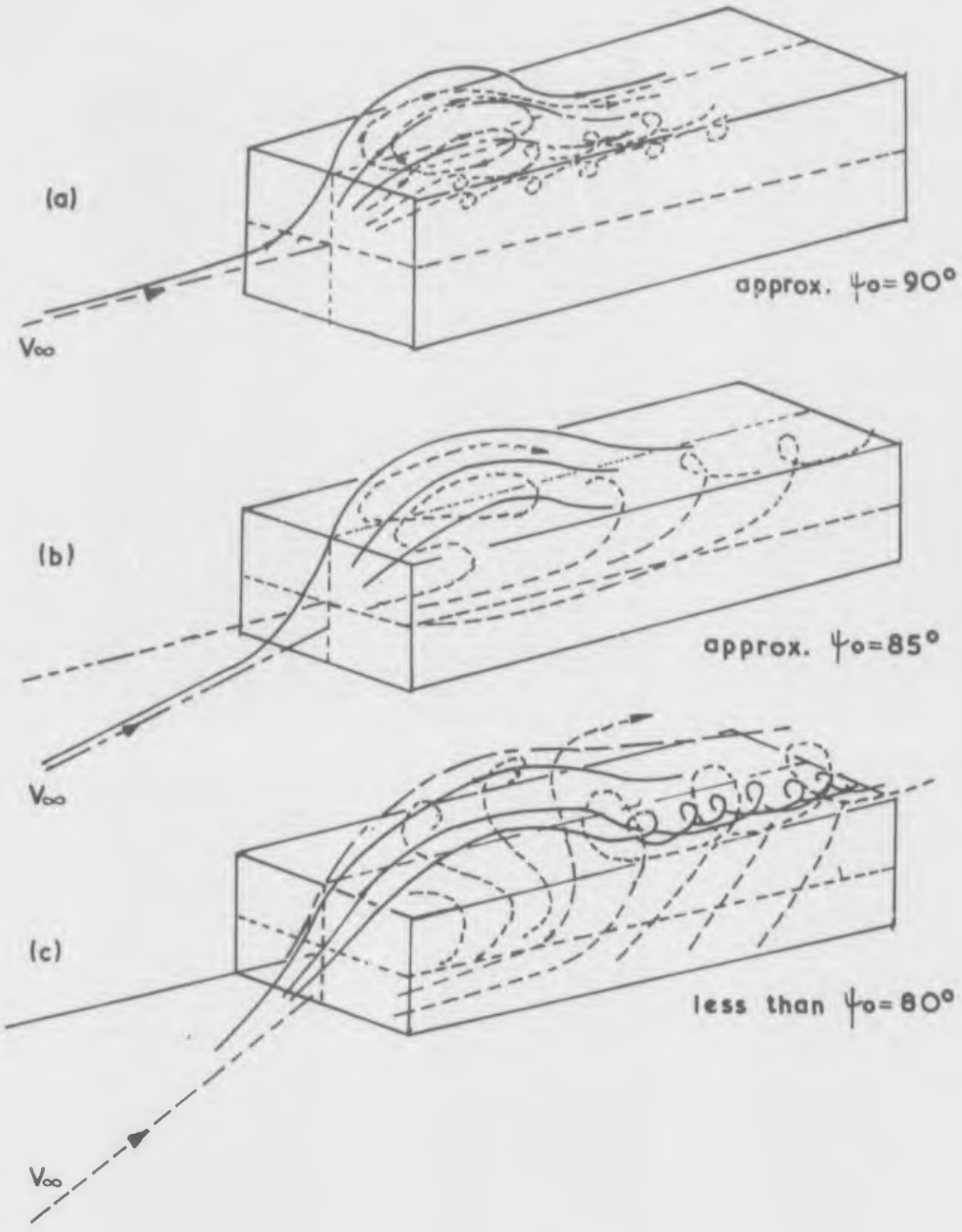

FIG 5.11

IDEALISED FLOW PATTERN OVER CONTAINER MODEL AT VARIOUS PITCH INCIDENCES

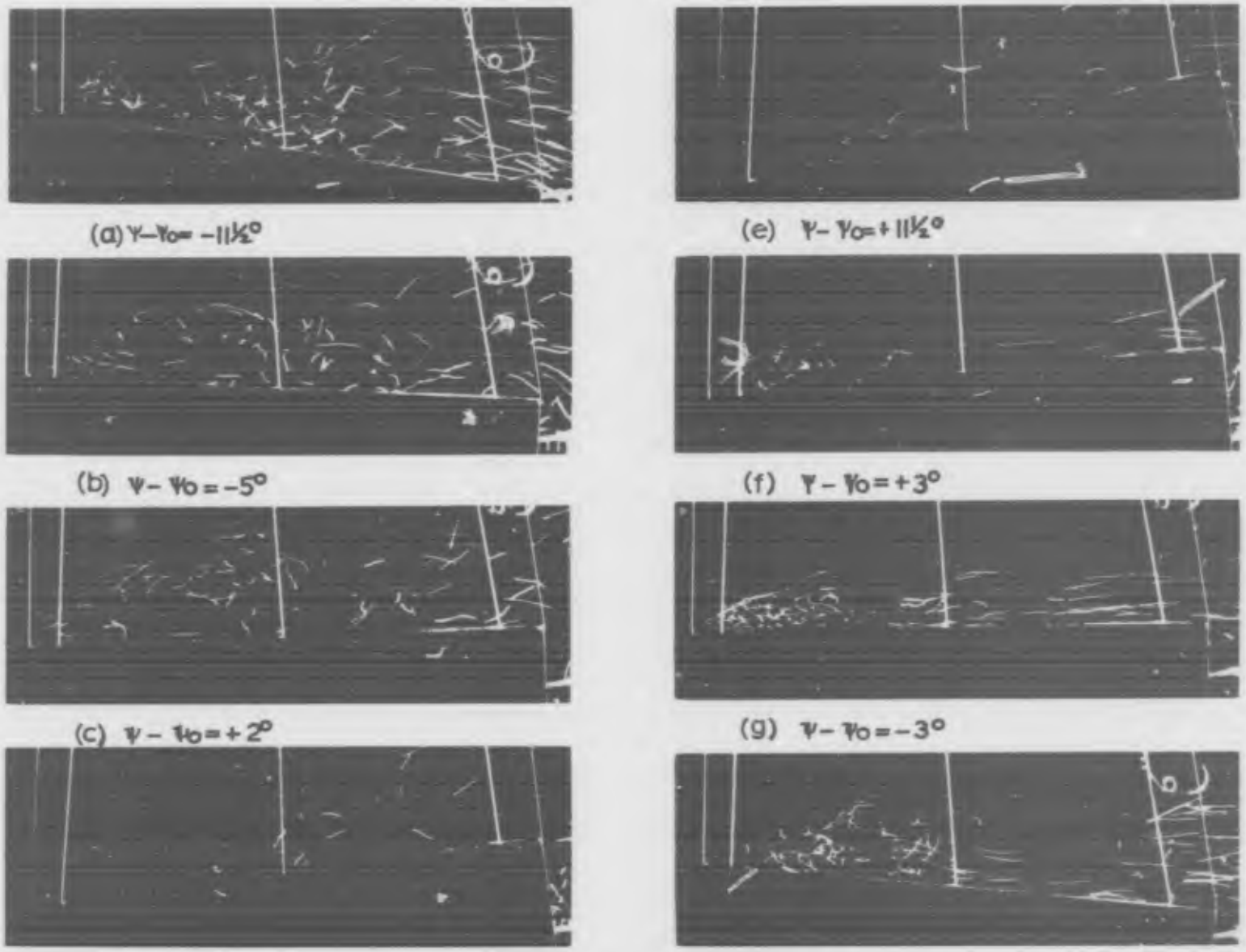

(a) $\psi - \psi_0 = -11\frac{1}{2}°$

(b) $\psi - \psi_0 = -5°$

(c) $\psi - \psi_0 = +2°$

(d) $\psi - \psi_0 = +7°$

(e) $\psi - \psi_0 = +11\frac{1}{2}°$

(f) $\psi - \psi_0 = +3°$

(g) $\psi - \psi_0 = -3°$

(h) $\psi - \psi_0 = -9°$

FIG 5.12 HELIUM BUBBLE UNSTEADY FLOW FOR A PITCH OSCILLATION $\psi_0 = +90°$ $d\psi = \pm 11.5°$ $W_d = 0.968$ $V_\infty = 6.49$

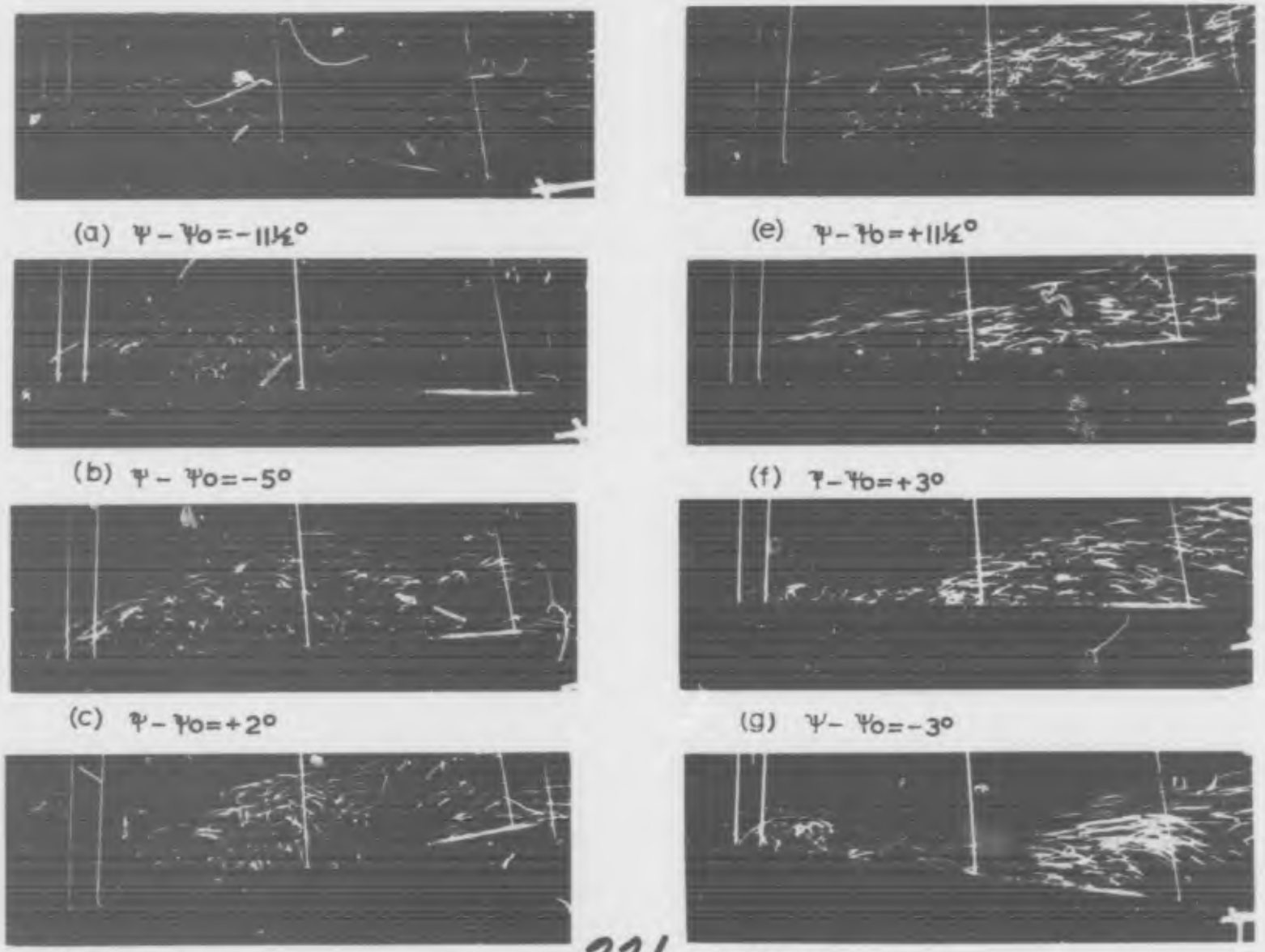

(a) $\psi - \psi_0 = -11\frac{1}{2}°$

(b) $\psi - \psi_0 = -5°$

(c) $\psi - \psi_0 = +2°$

(d) $\psi - \psi_0 = +7°$

(e) $\psi - \psi_0 = +11\frac{1}{2}°$

(f) $\psi - \psi_0 = +3°$

(g) $\psi - \psi_0 = -3°$

(h) $\psi - \psi_0 = -9°$

FIG 5.13 HELIUM BUBBLE UNSTEADY FLOW FOR A PITCH OSCILLATION $\psi_0 = +9.0°$ $d\psi = \pm 11.5°$ $W_d = 1.94$ $V_\infty = 3.24$

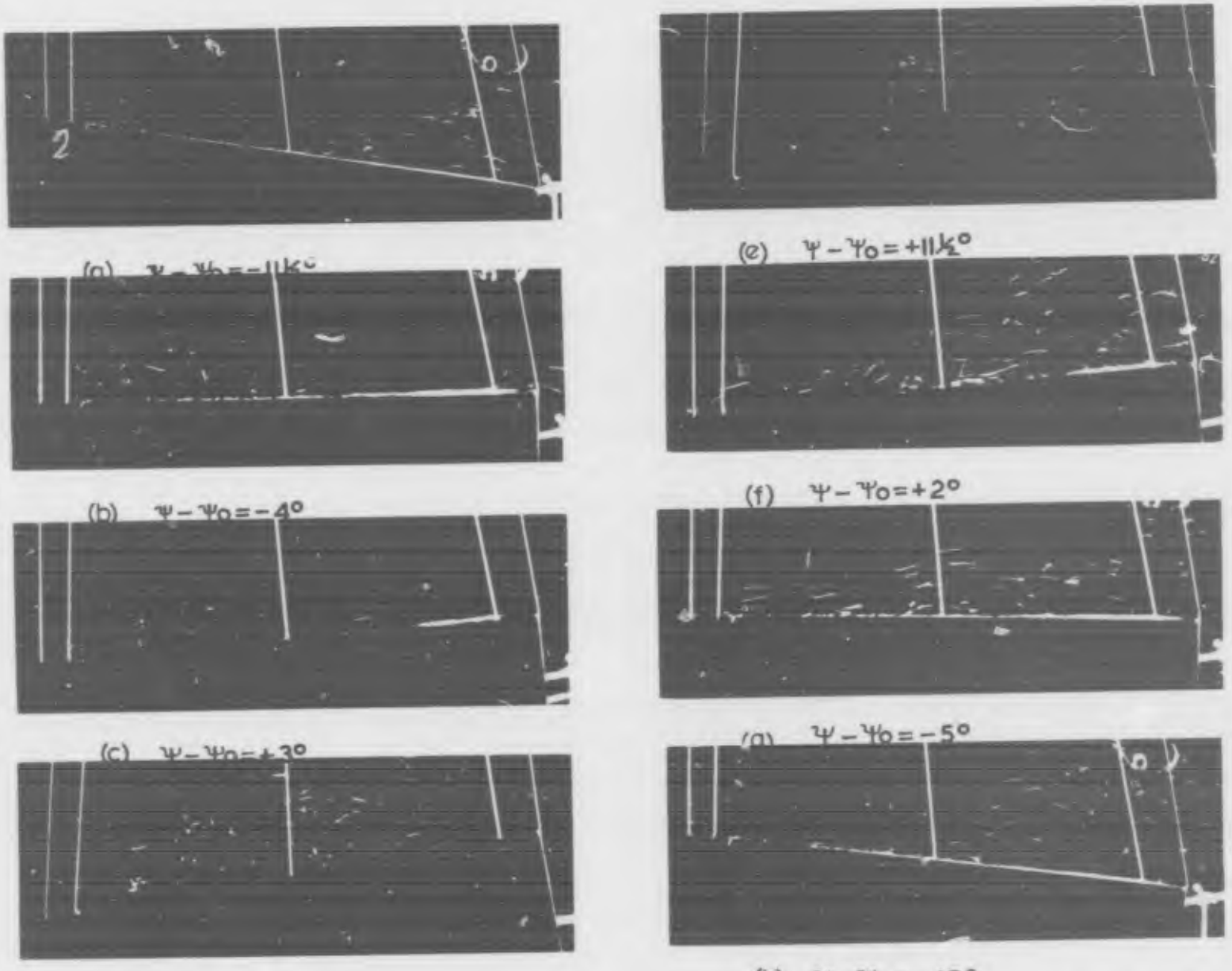

FIG 5.14 HELIUM BUBBLE UNSTEADY FLOW FOR A PITCH OSCILLATION $\psi_0 = +90°$ $d\psi = \pm 11.5°$ Wd=2.3i V_∞=3.24ft/sc

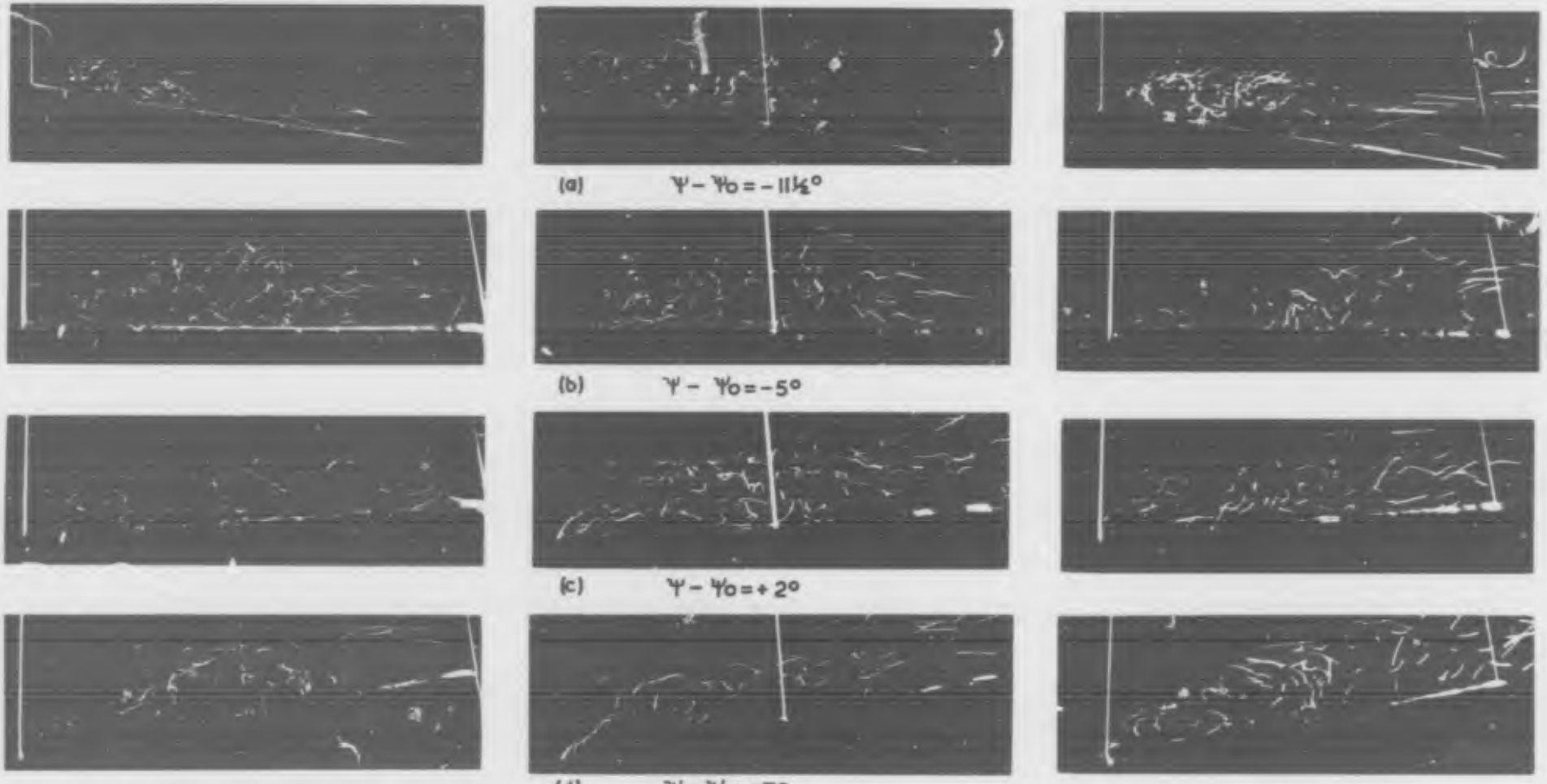

FIG 5.15 SECTIONS OF HELIUM BUBBLE UNSTEADY FLOW OVER A PITCHING CONTAINER MODEL $\Psi_0 = +90°$ $d\Psi = \pm 11.5°$ $Wd = 1.93$ $V_\infty = 3.25$ ft/sec

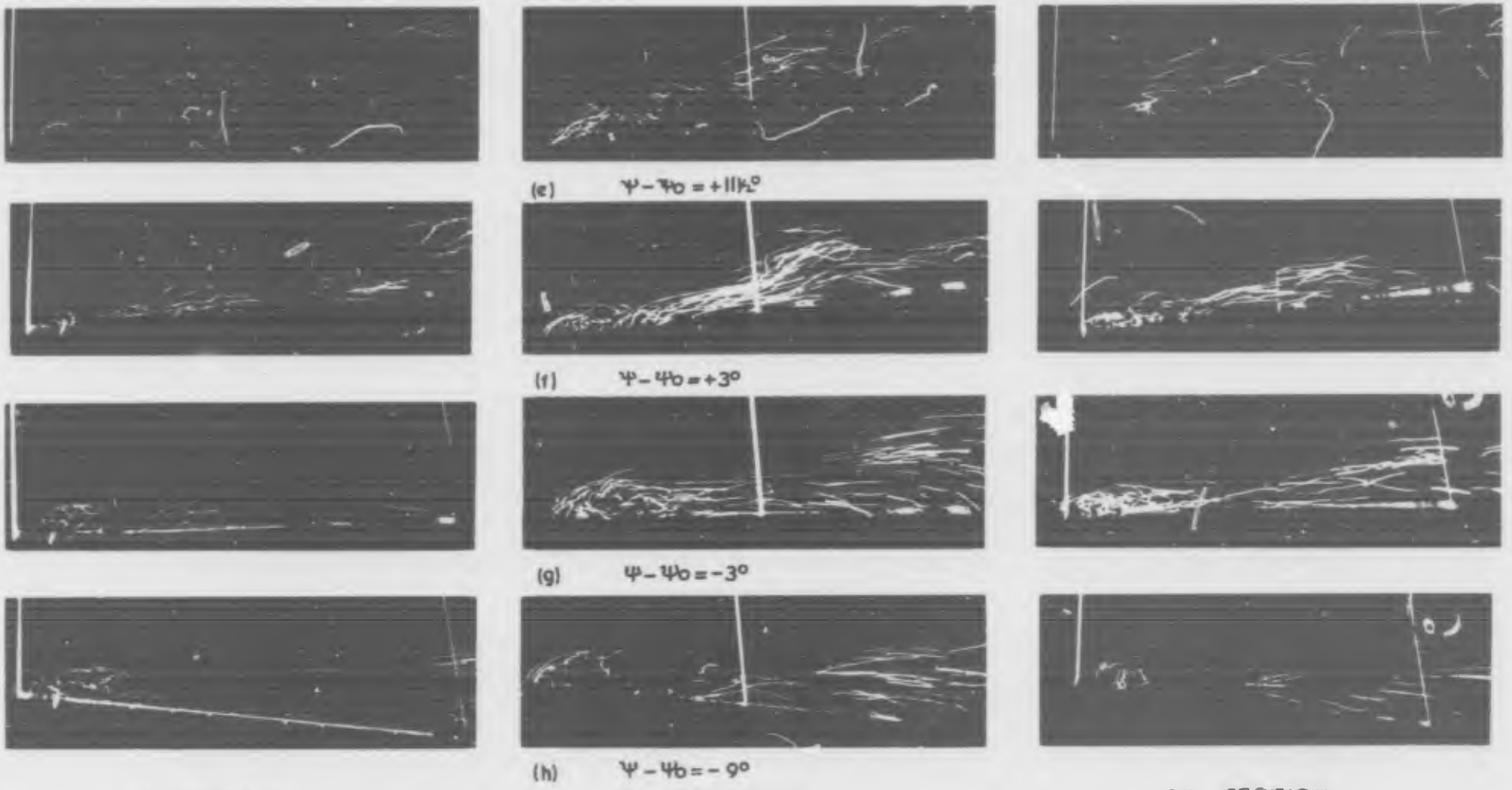

FIG 5.15 SECTIONS OF HELIUM BUBBLE UNSTEADY FLOW OVER A PITCHING CONTAINER MODEL $\Psi_o = +90°$ $d\Psi = \pm 11.5°$ $W_d = 1.93$ $V_{oc} = 3.25$ ft/sec

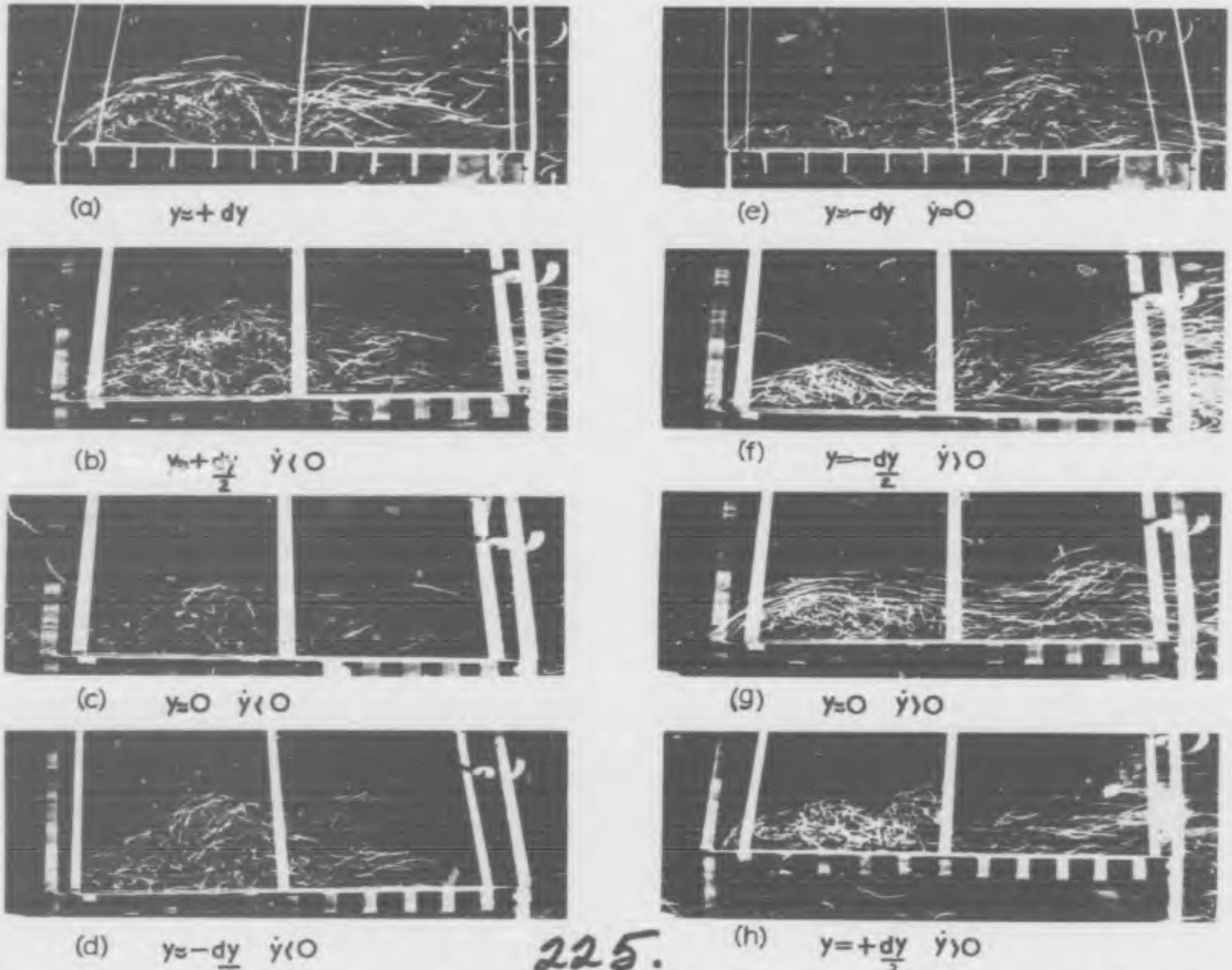

FIG 5.16 HELIUM BUBBLE UNSTEADY FLOW FORE AND AFT MOTION $\psi_b = +90^\circ$ dy = ± 3.54" Wd = 1.94 V_∞ = 3.24 ft/sec

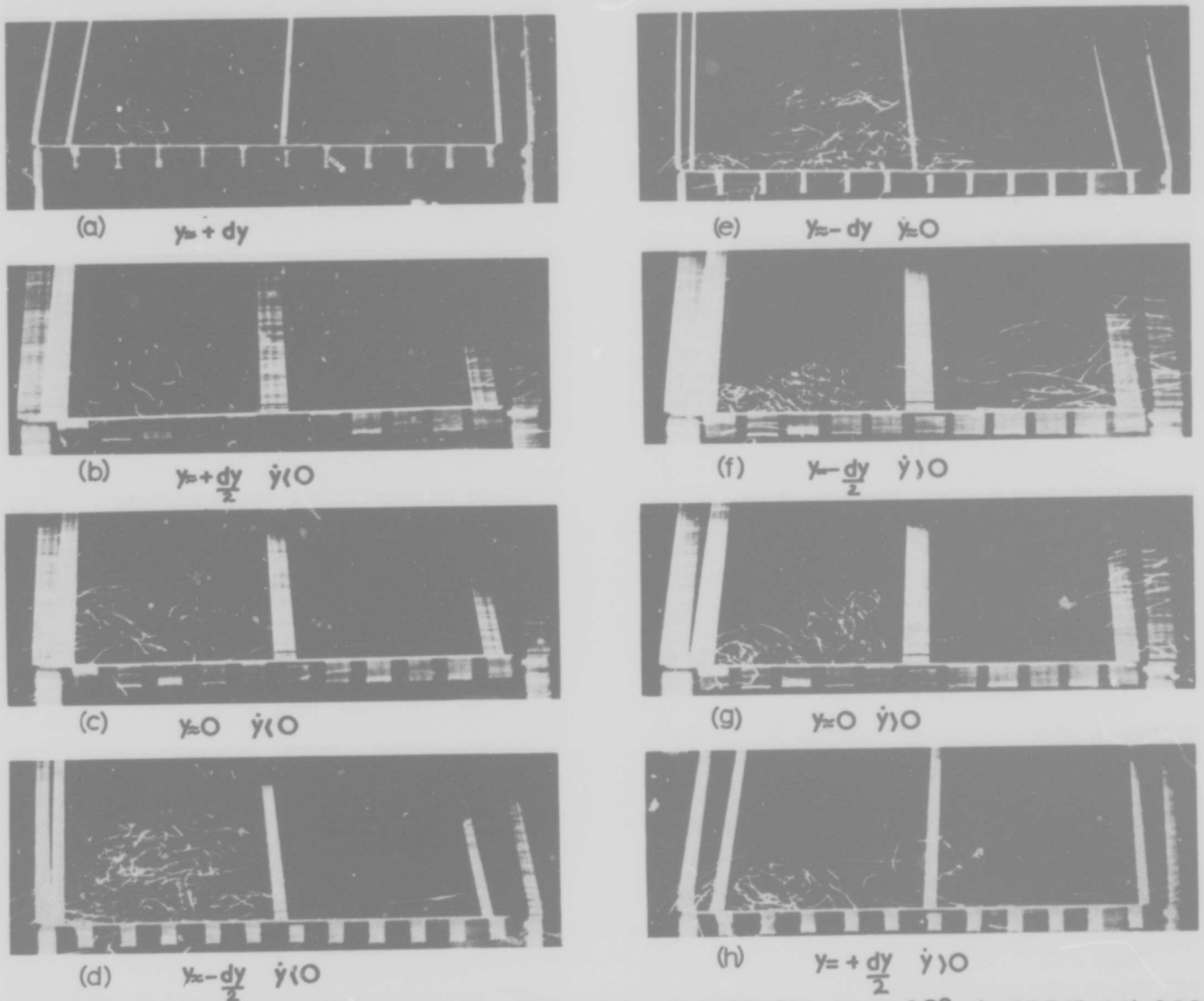

FIG 5.17 HELIUM BUBBLE UNSTEADY FLOW FORE AND AFT MOTION $\gamma_b = +90^\circ$ $dy = \pm 3.54''$ $W_d = 3.22$ $V_{bc} = 3.24$ ft/sec

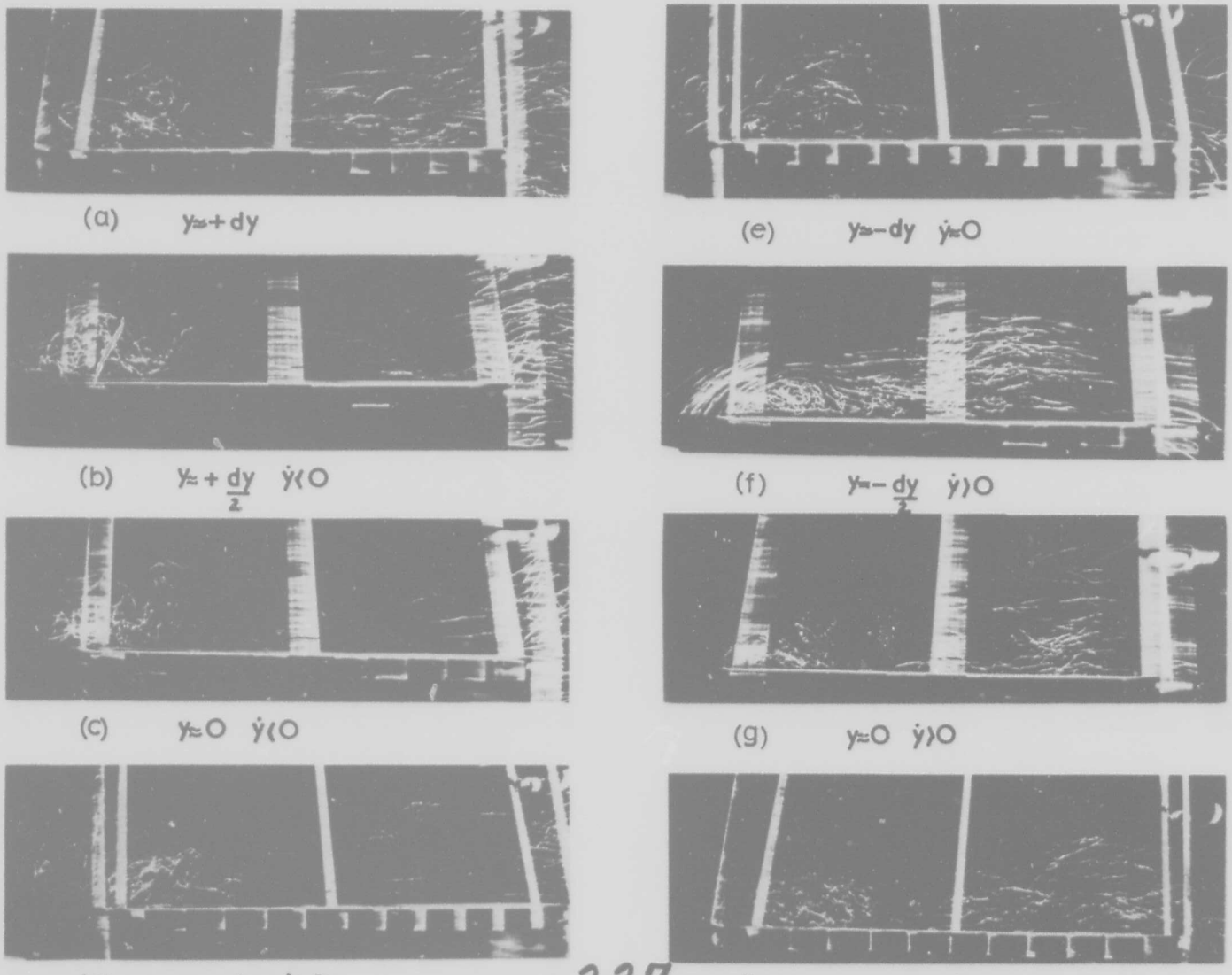

(a) $y \approx +dy$

(b) $y \approx +\frac{dy}{2}$ $\dot{y} < 0$

(c) $y \approx 0$ $\dot{y} < 0$

(d) $y \approx -\frac{dy}{2}$ $\dot{y} < 0$

(e) $y \approx -dy$ $\dot{y} \approx 0$

(f) $y \approx -\frac{dy}{2}$ $\dot{y} > 0$

(g) $y \approx 0$ $\dot{y} > 0$

(h) $y \approx +\frac{dy}{2}$ $\dot{y} > 0$

FIG 5.18 HELIUM BUBBLE UNSTEADY FLOW FORE AND AFT MOTION $\psi_o = +90^\circ$ $dy = \pm .354''$ $Wd = 5.54$ $V_\infty = 3.24$ ft/sec

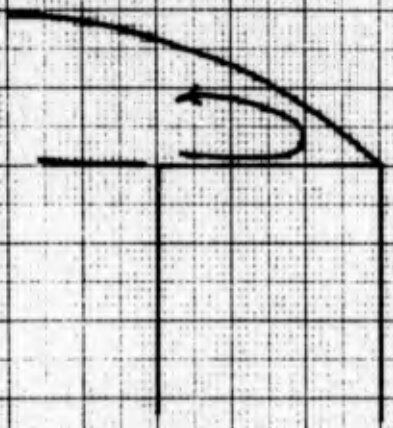

FIG 5·19 (a)

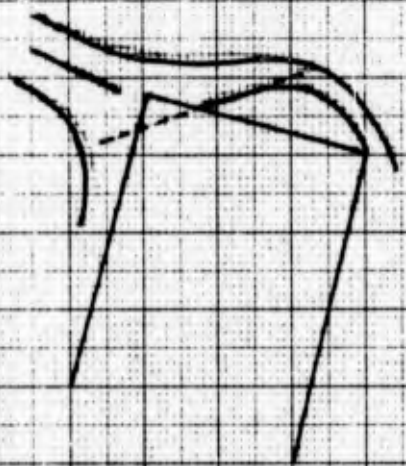

FIG 5·19 (b)

FIG 5·19 (c)

FIGURE 5·19

END FLOW FOR BROADSIDE-ON POSITION

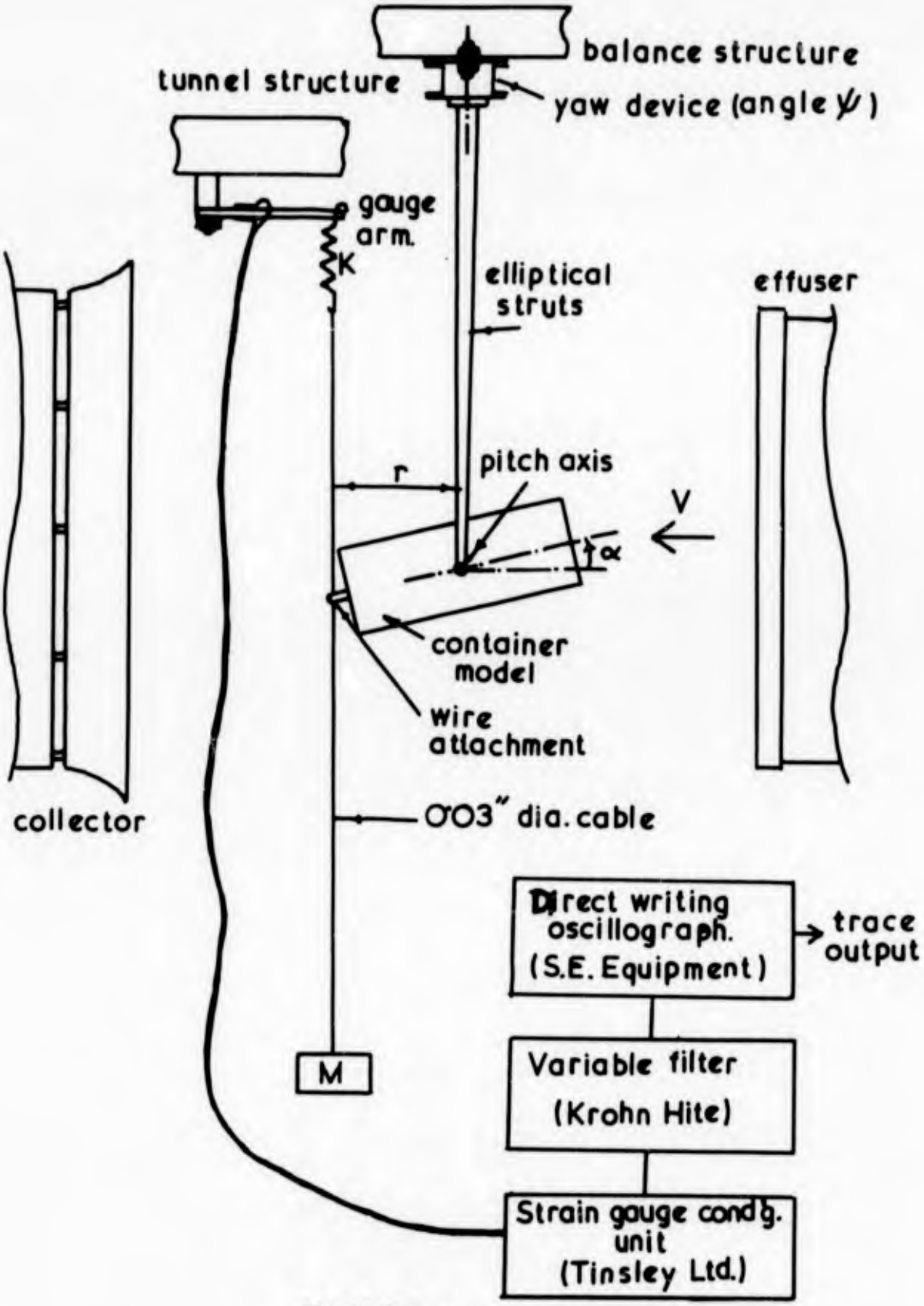

FIGURE 6·1

LAYOUT OF FREE VIBRATION TEST EQUIPMENT.

FIGURE 6·2

RESULTS FROM WIND OFF DECAYING OSCILLATION TESTS ON 1:0·4:0·4 MODEL

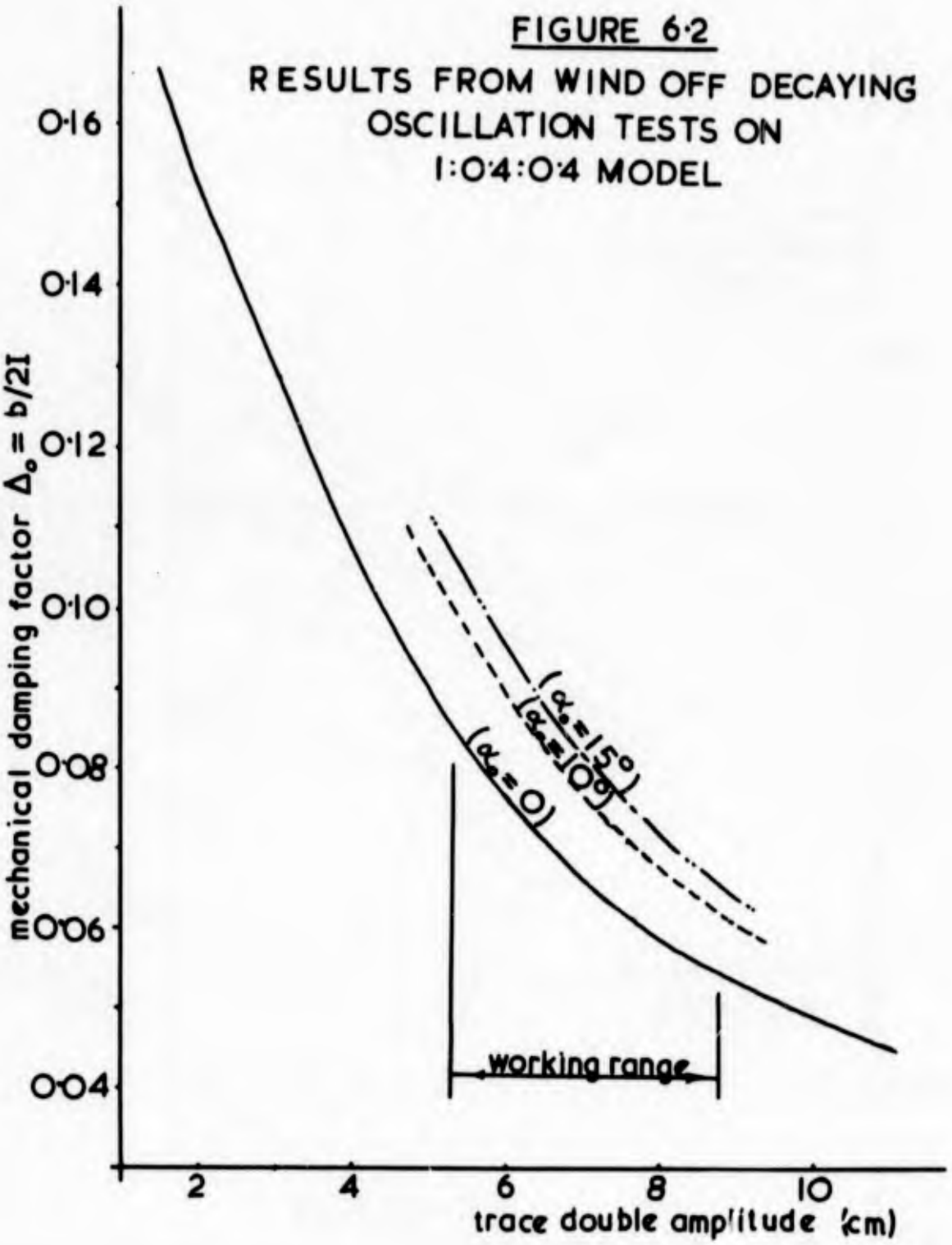

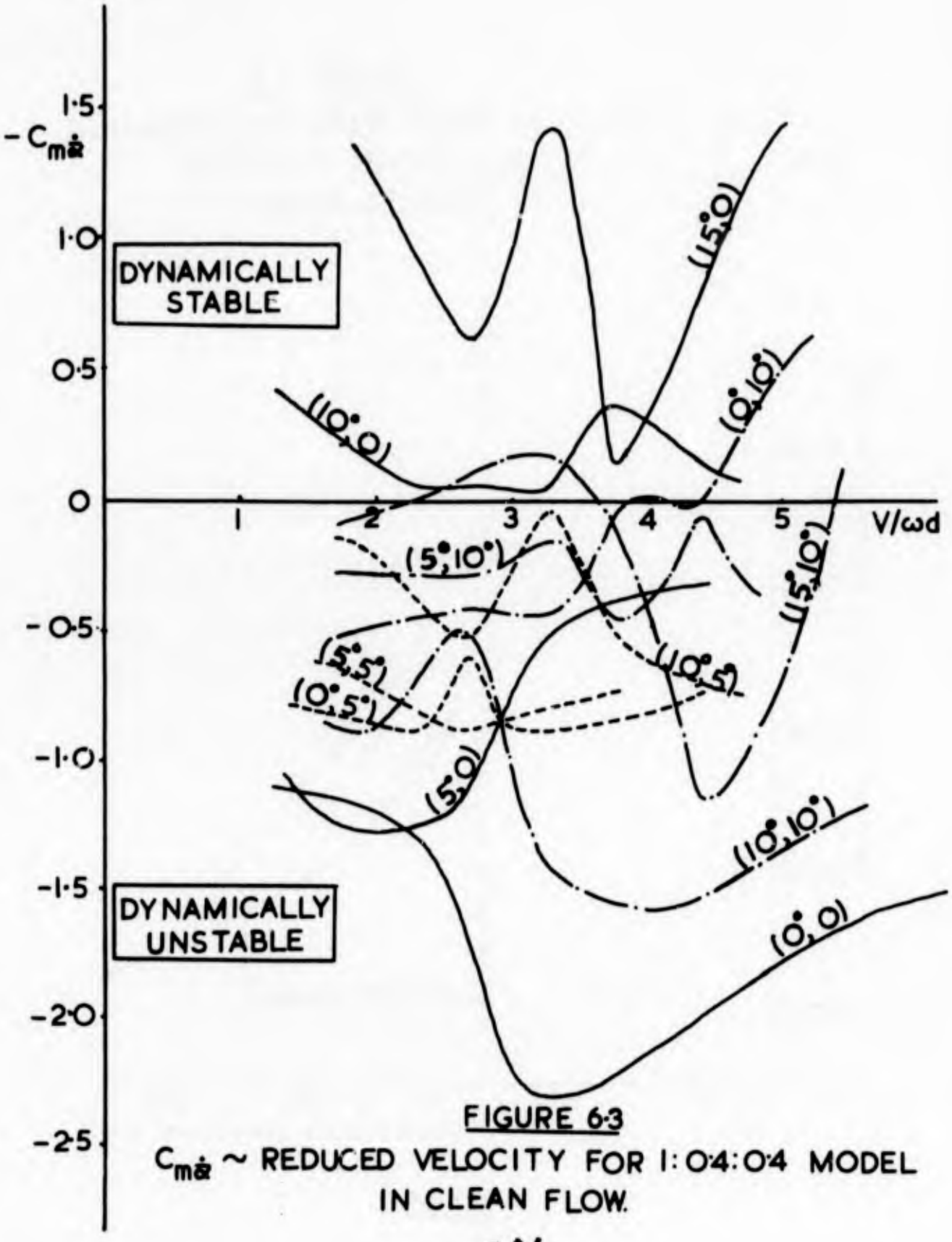

FIGURE 6·3

$C_{m\dot{\alpha}}$ ~ REDUCED VELOCITY FOR 1:0·4:0·4 MODEL IN CLEAN FLOW.

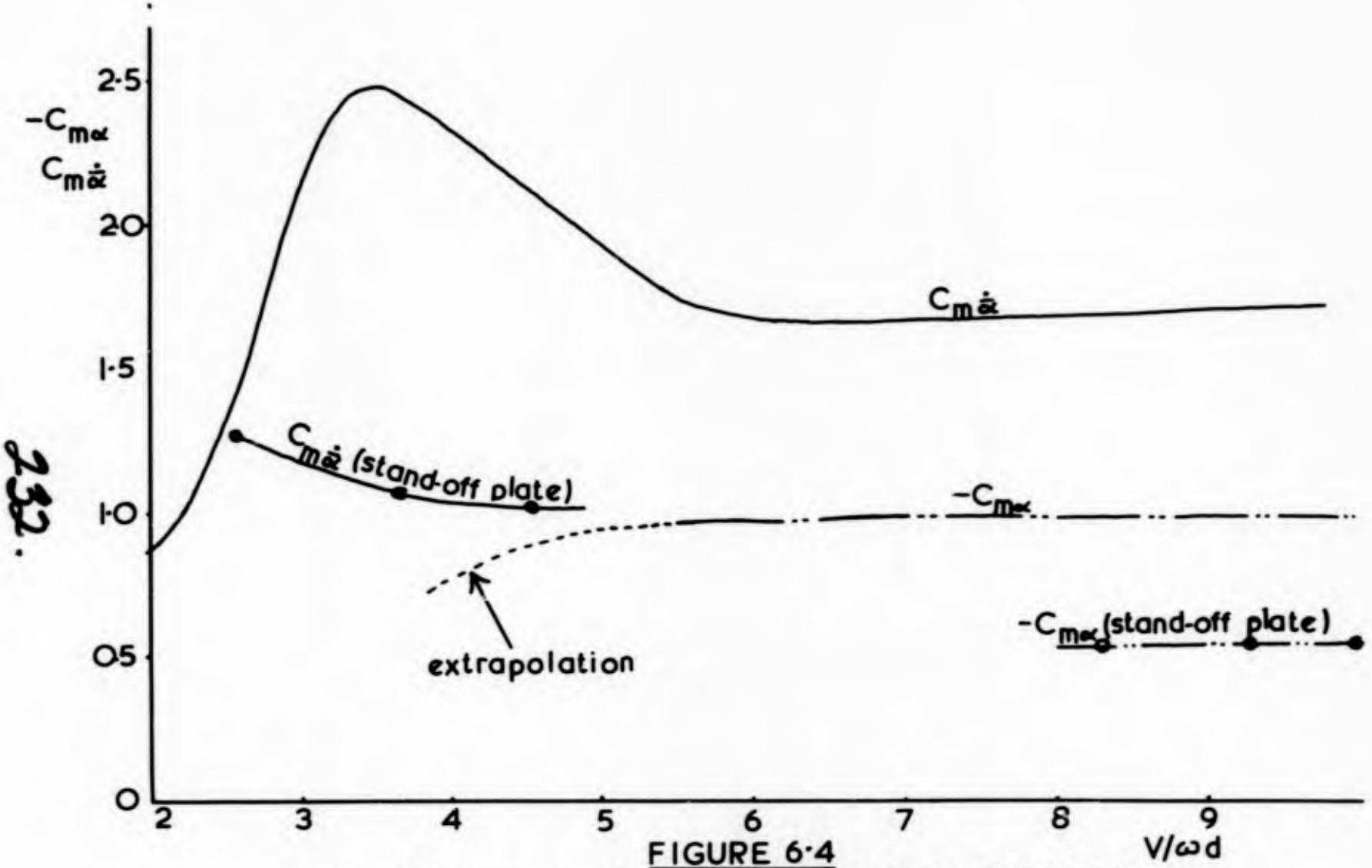

FIGURE 6·4

$C_{m\alpha}$ AND $C_{m\dot{\alpha}}$ ~ REDUCED VELOCITY FOR 1:0·4:0·4 MODEL AT $\alpha_0 = 0$, $\psi_0 = 0$ IN CLEAN FLOW.

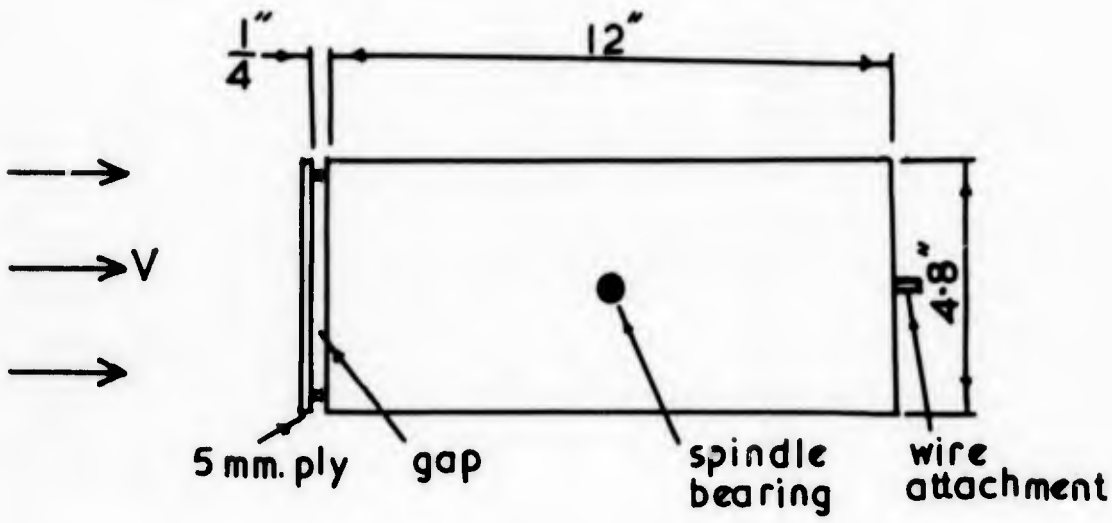

elevation and plan

FIGURE 6·5

1 : 0·4 : 0·4 MODEL WITH STAND-OFF PLATE

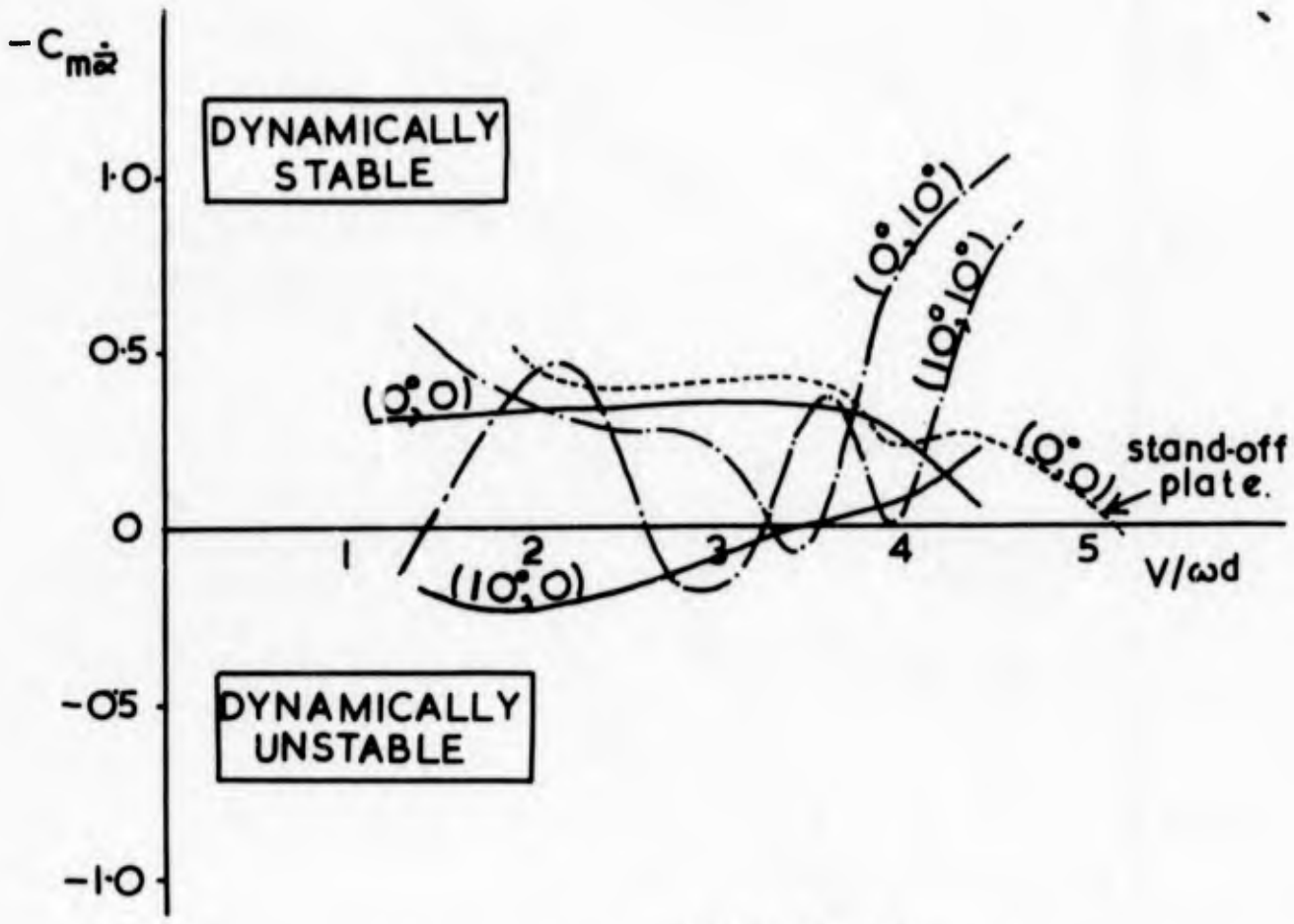

FIGURE 6·6

$C_{m\dot{\alpha}}$ ~ REDUCED VELOCITY FOR 1:0·4:0·4 MODEL IN TURBULENT FLOW

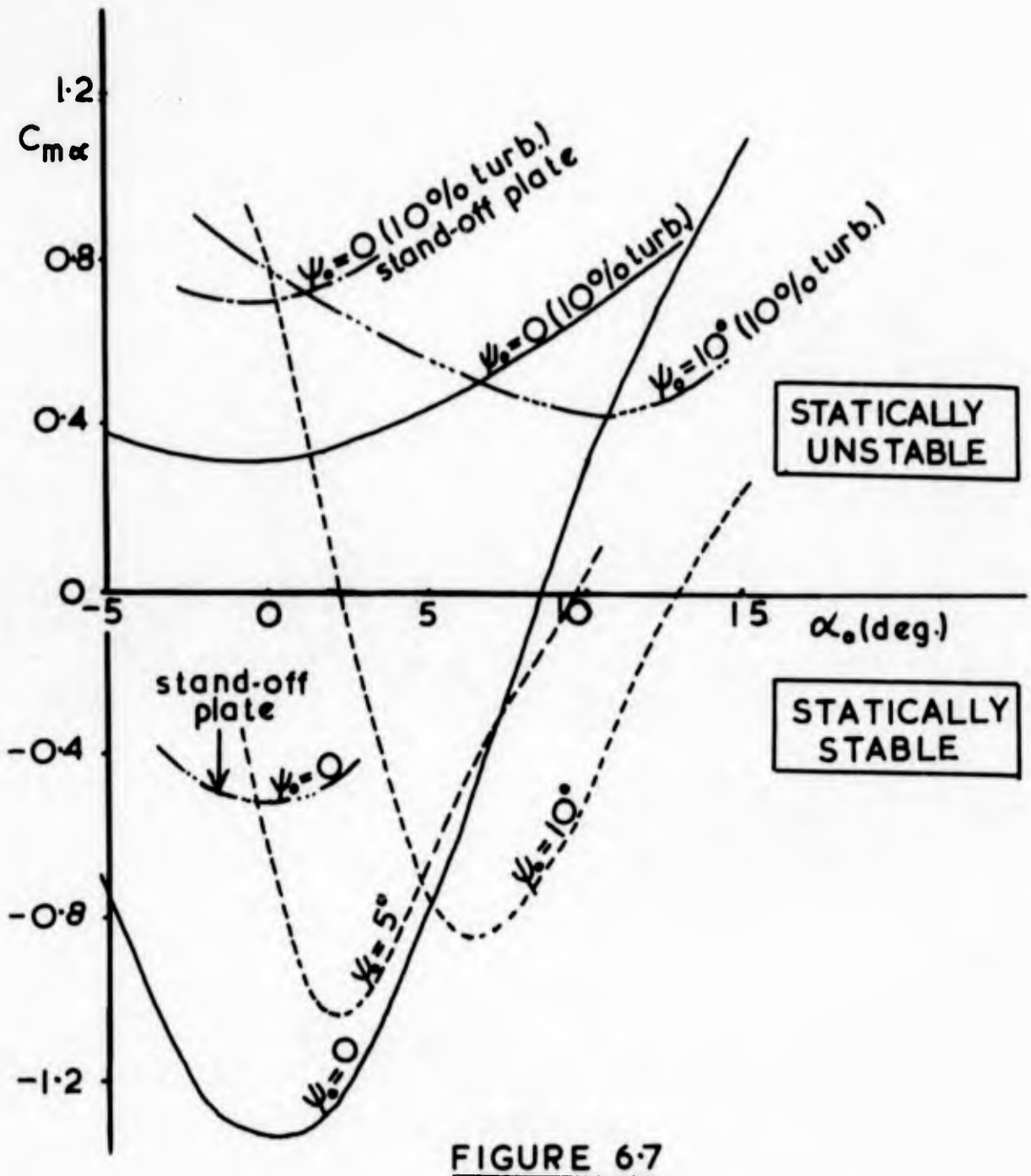

FIGURE 6·7

APPROXIMATE $C_{m\alpha}$ VALUES FOR 1:0·4:0·4 MODEL IN CLEAN AND TURBULENT FLOWS

FIGURE 6·8

$C_{m\dot{\alpha}}$ ~ REDUCED VELOCITY FOR 1:0·2:0·2 MODEL

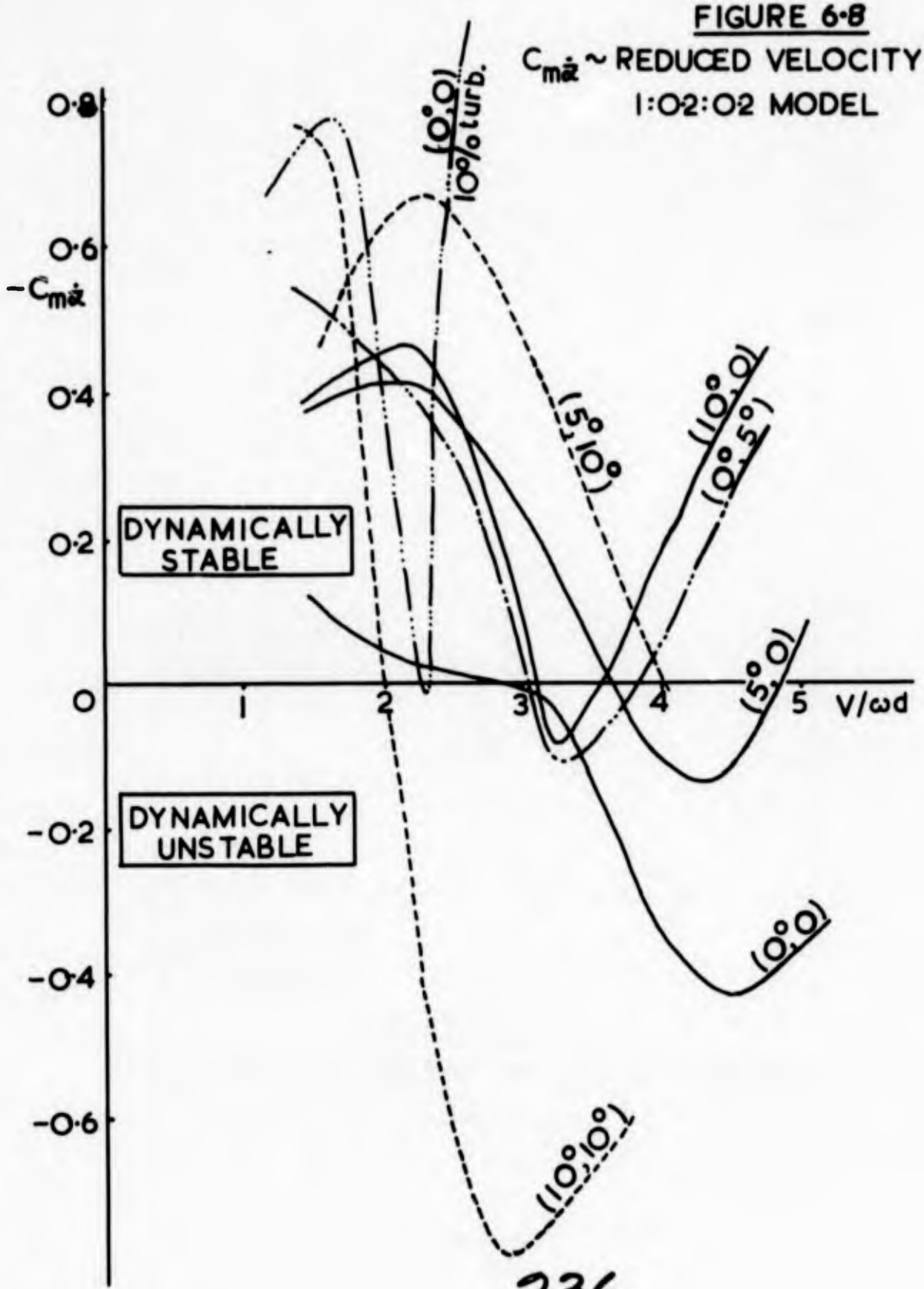

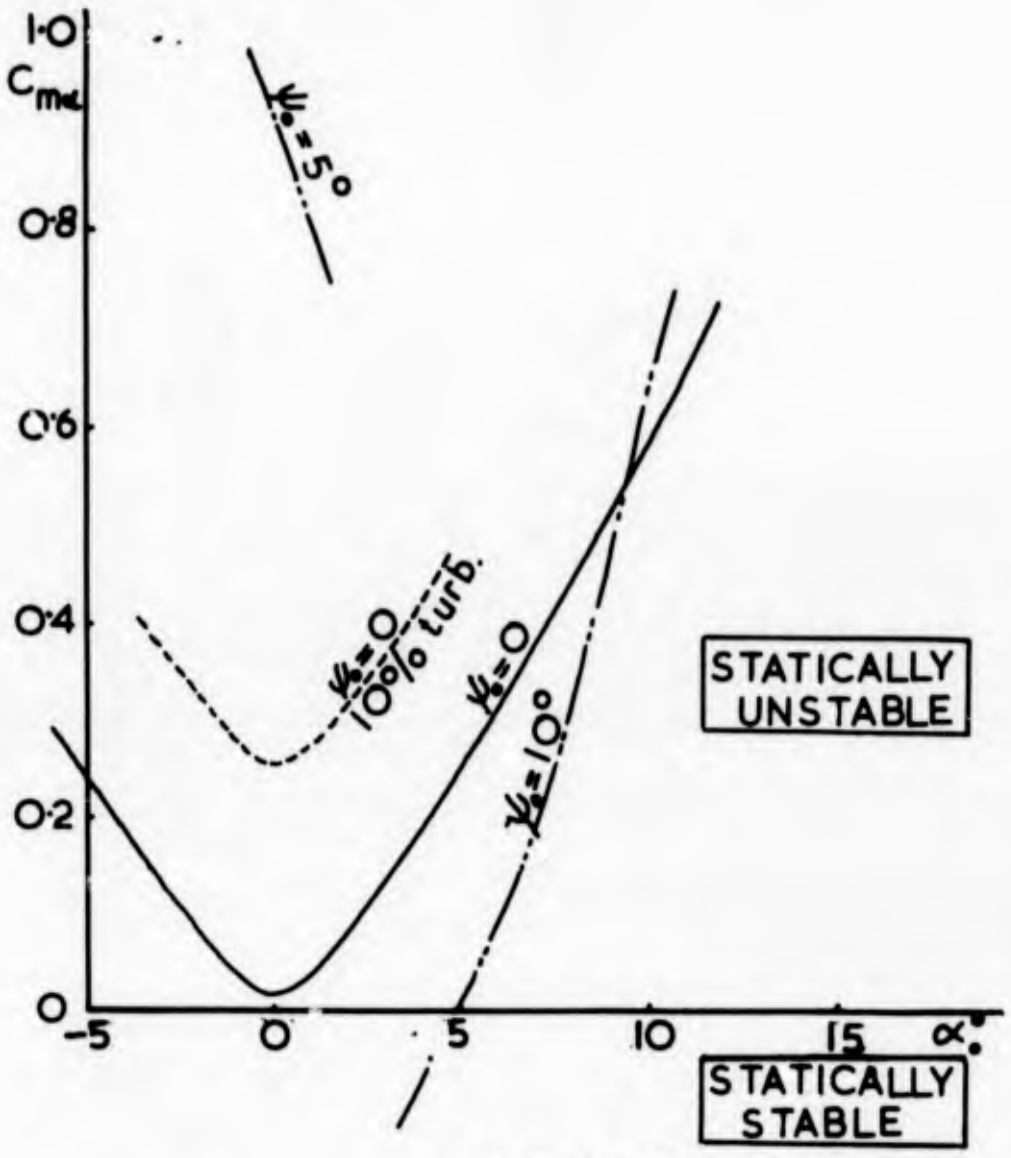

FIGURE 6·9

APROXIMATE $C_{m\alpha} \sim \alpha_0$ VARIATION FOR 1:02:02 MODEL.

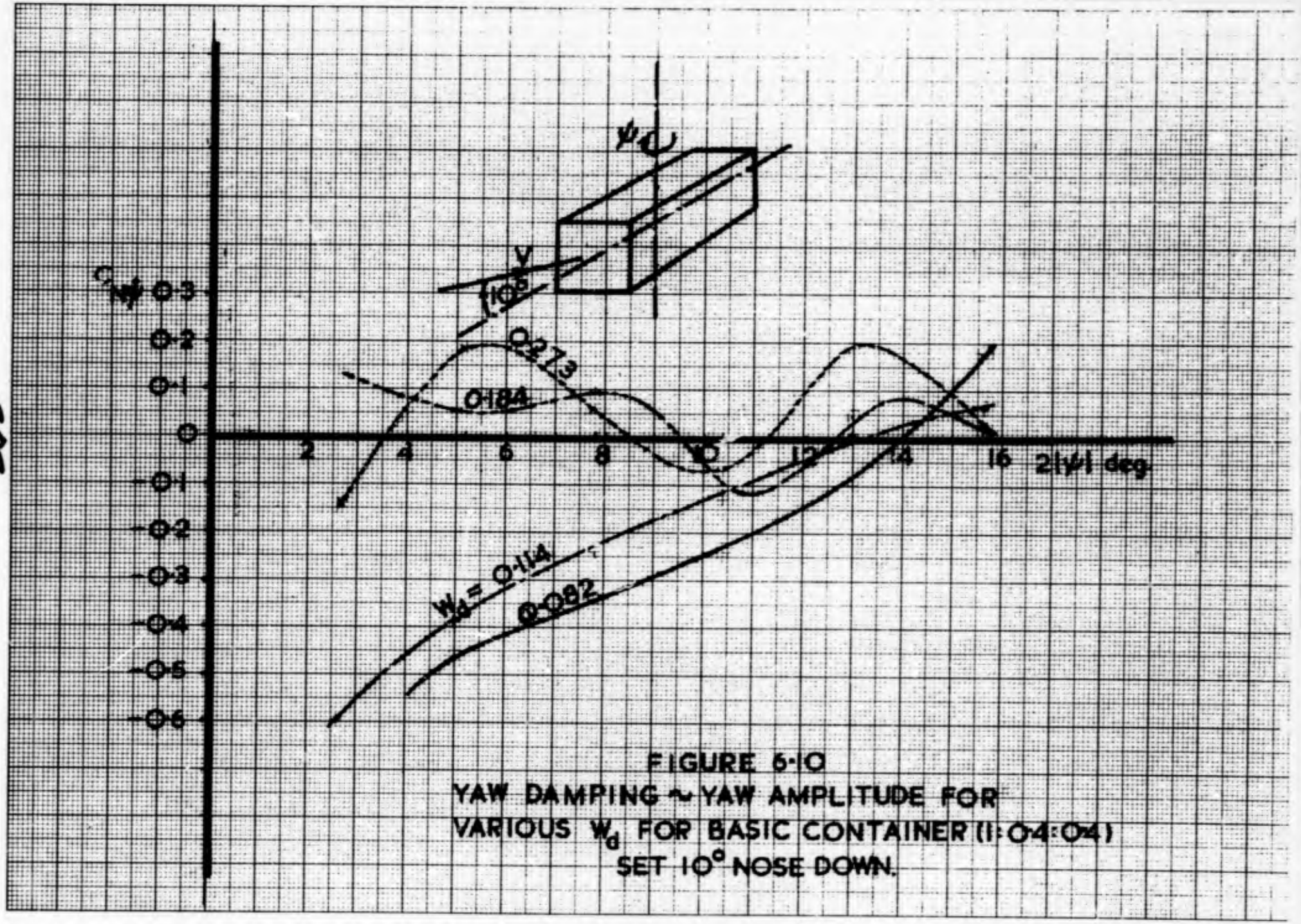

FIGURE 6·10
YAW DAMPING ~ YAW AMPLITUDE FOR
VARIOUS W_d FOR BASIC CONTAINER (1:0·4:0·4)
SET 10° NOSE DOWN.

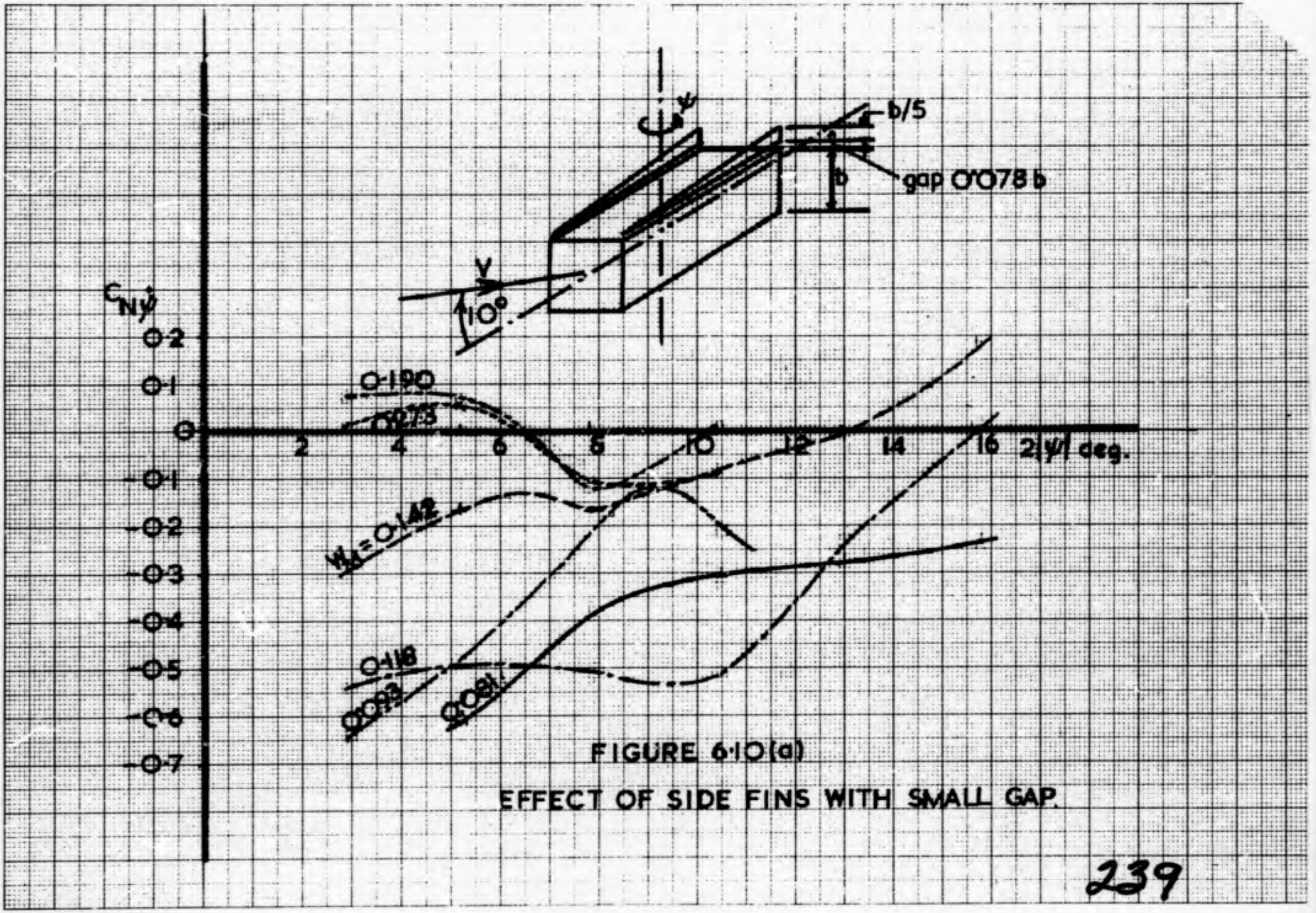

FIGURE 6·10(a)

EFFECT OF SIDE FINS WITH SMALL GAP.

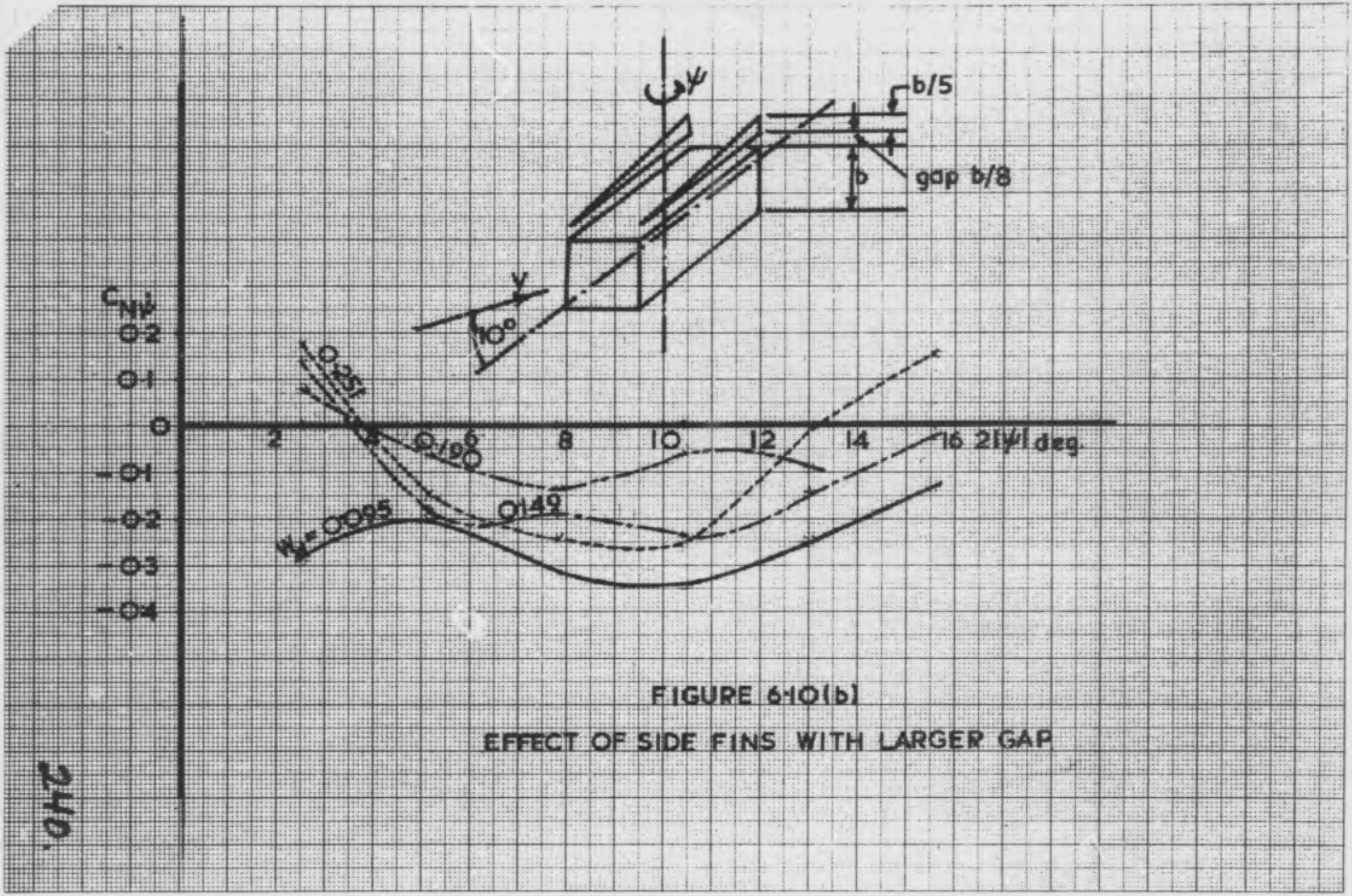

FIGURE 6·10(b)

EFFECT OF SIDE FINS WITH LARGER GAP

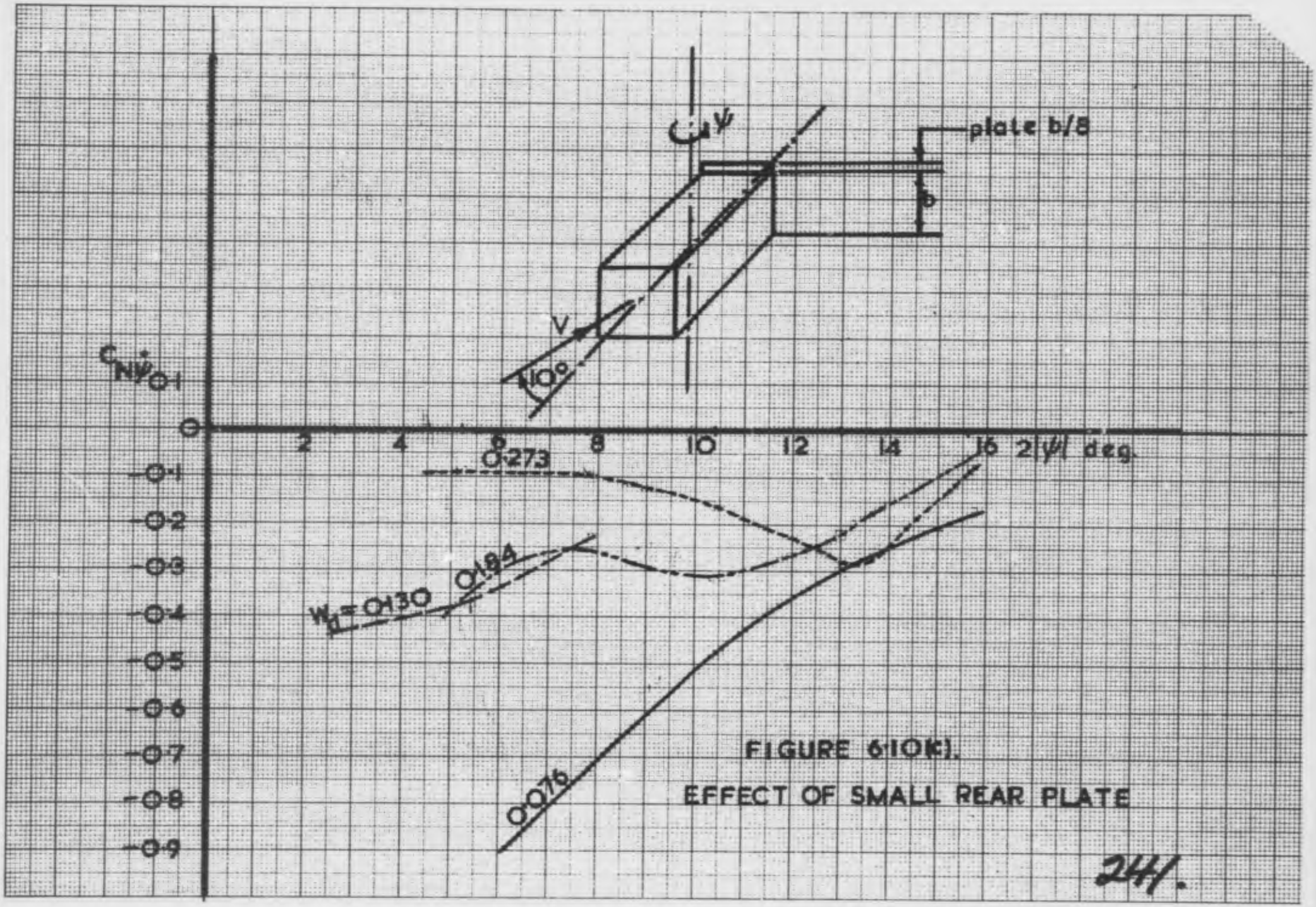

FIGURE 6·10(c).

EFFECT OF SMALL REAR PLATE

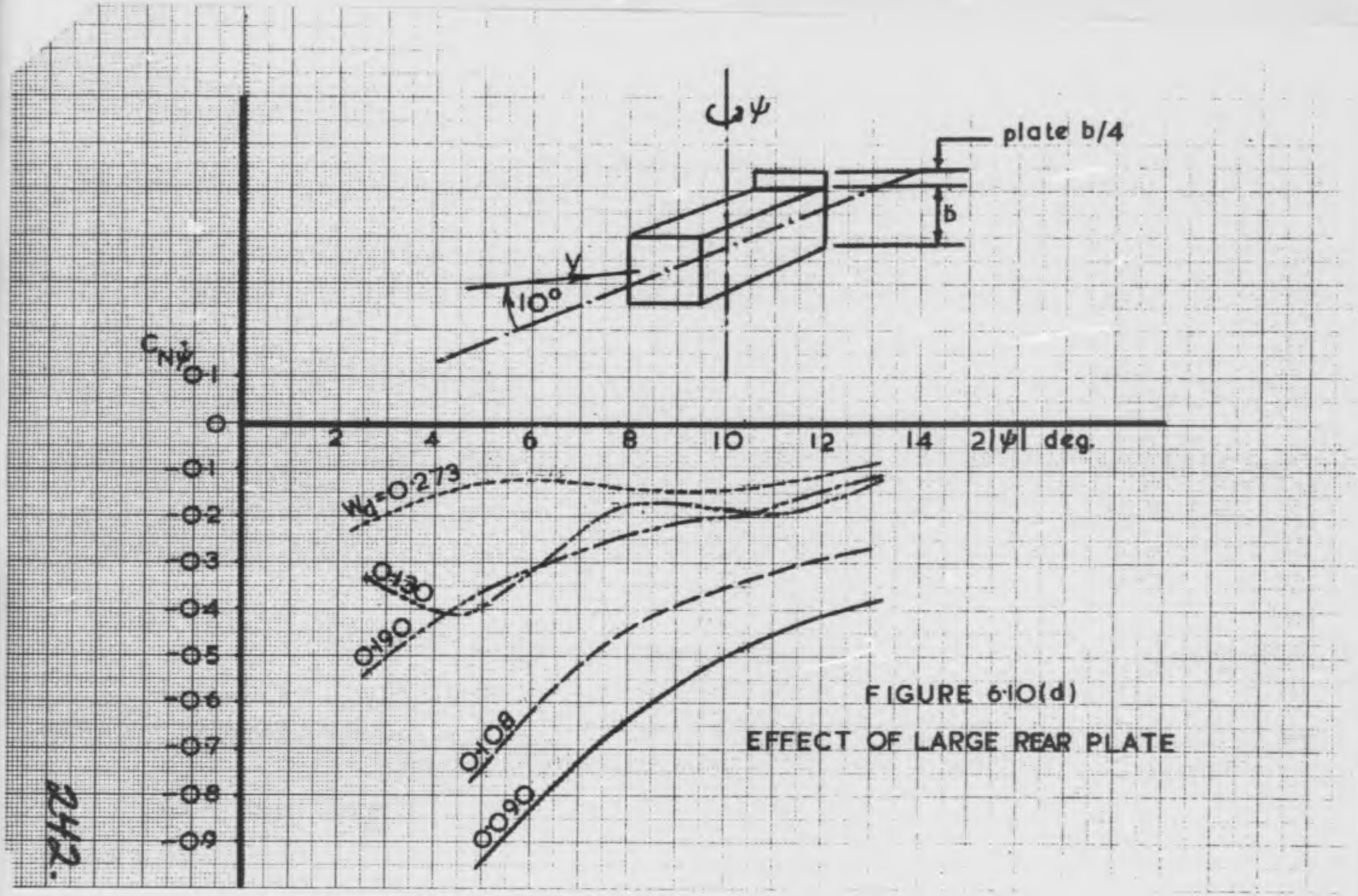

FIGURE 6·10(d)

EFFECT OF LARGE REAR PLATE

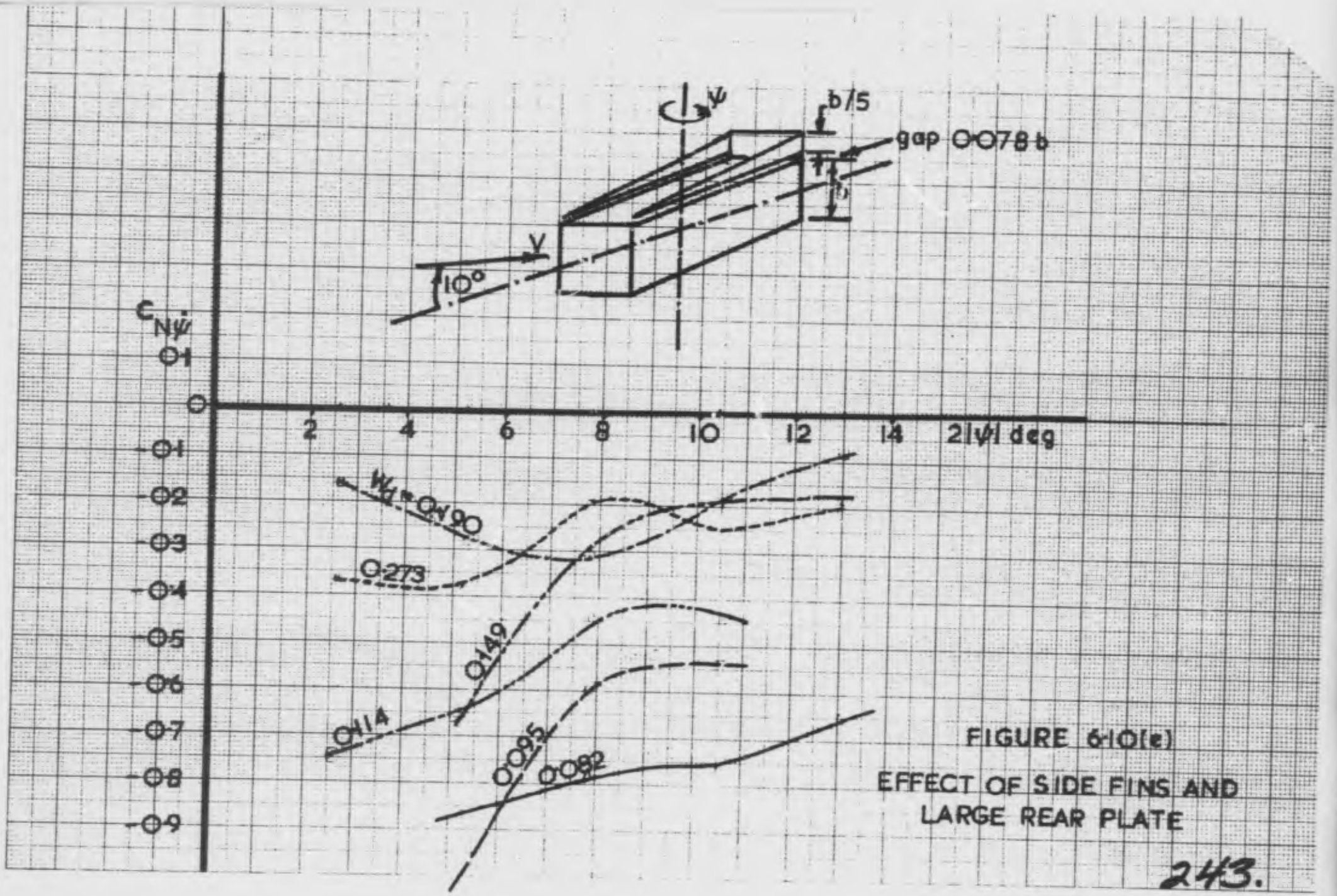

FIGURE 6·10(e)

EFFECT OF SIDE FINS AND LARGE REAR PLATE

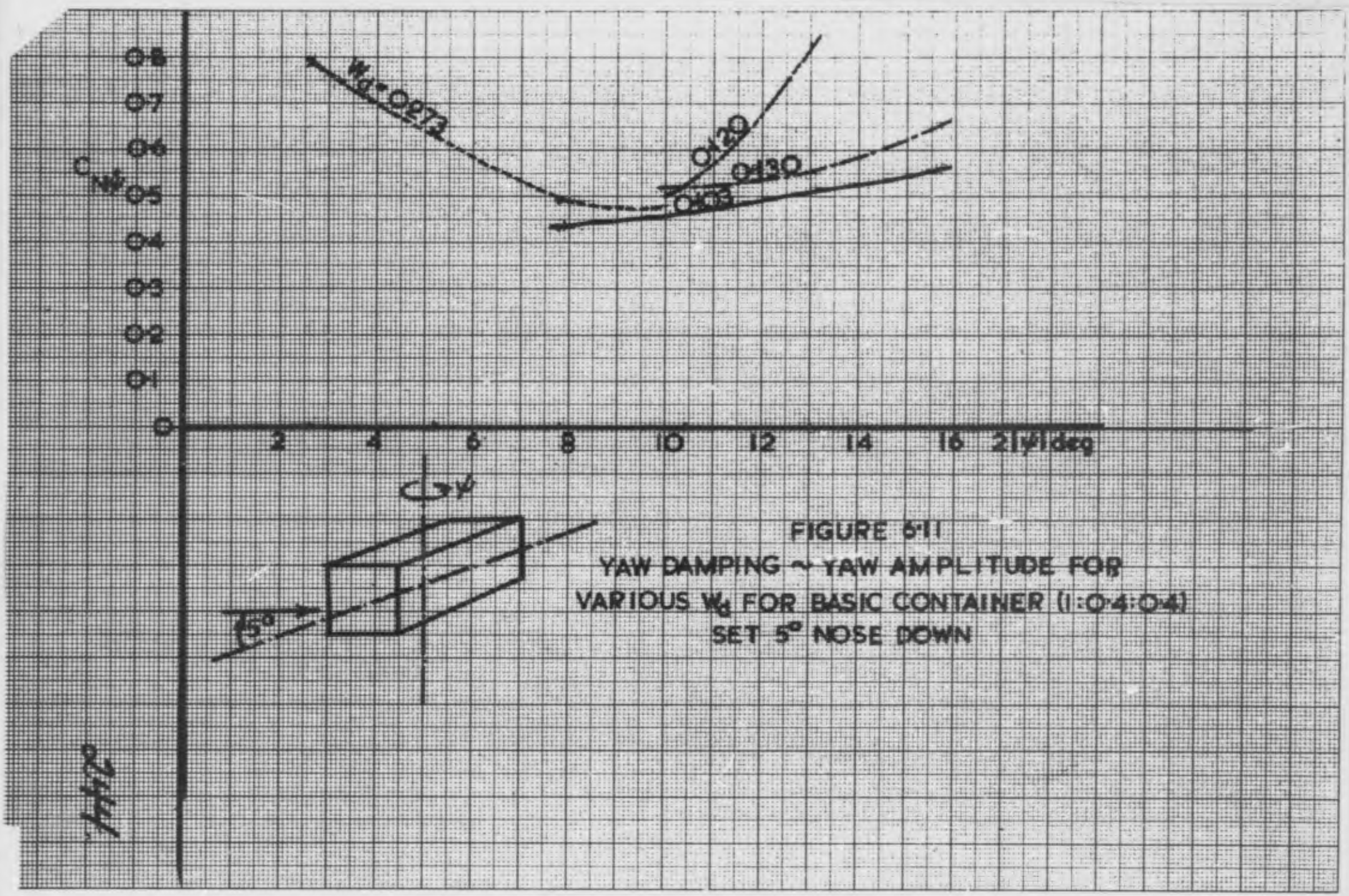

FIGURE 5·11
YAW DAMPING ~ YAW AMPLITUDE FOR
VARIOUS W_B FOR BASIC CONTAINER (1:0·4:0·4)
SET 5° NOSE DOWN

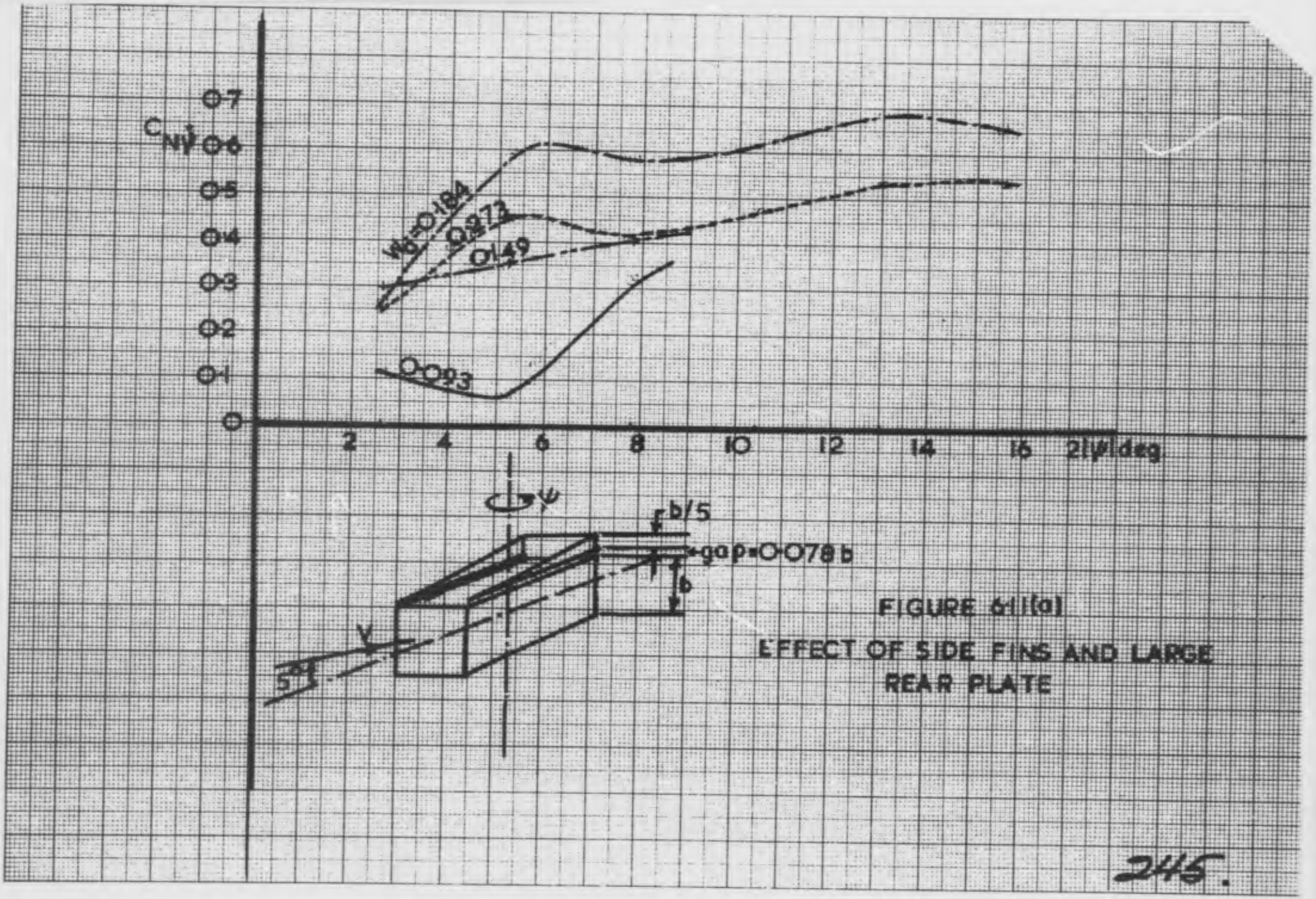

FIGURE 6·11(a)

EFFECT OF SIDE FINS AND LARGE REAR PLATE

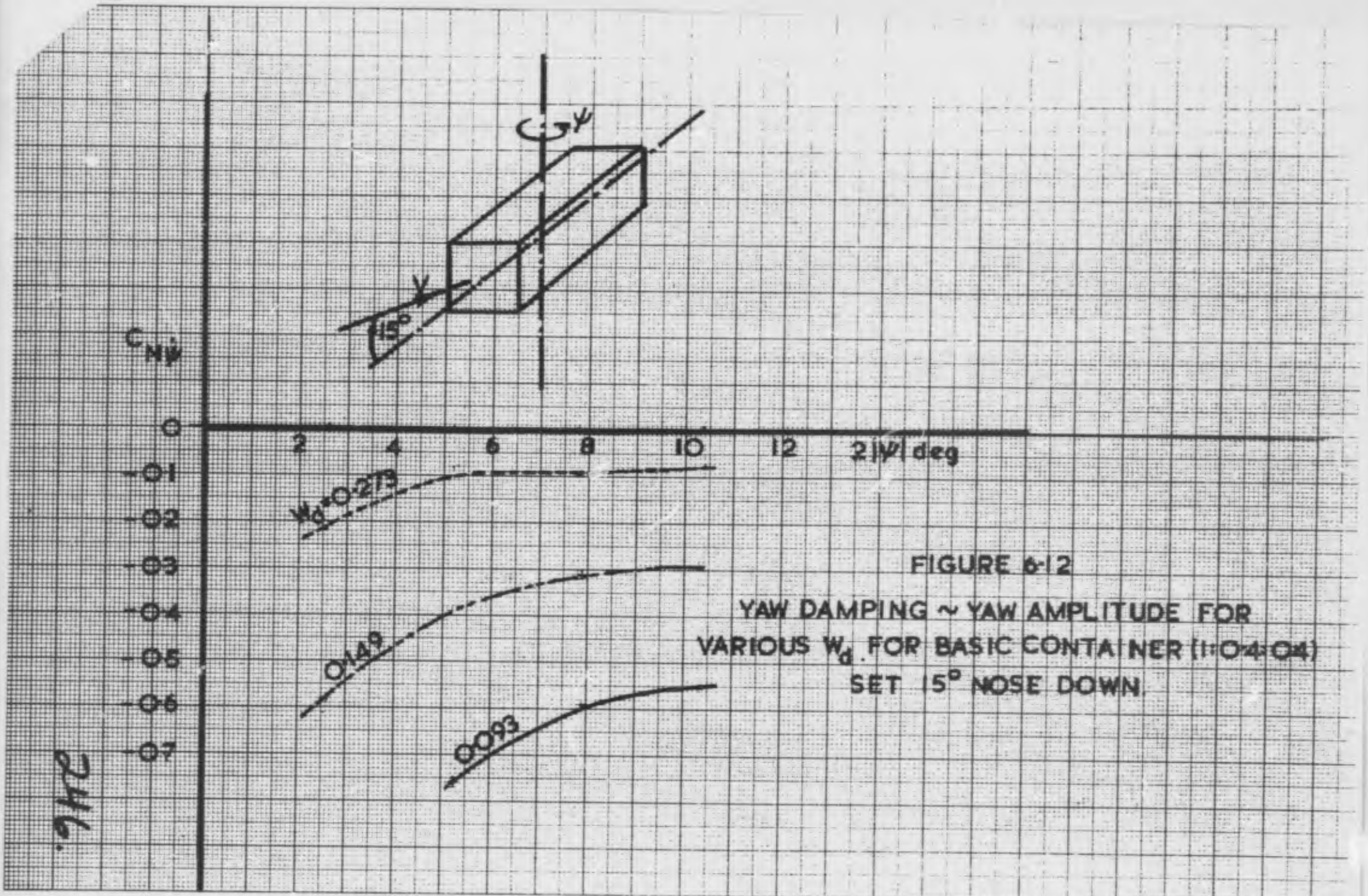

FIGURE 6-12

YAW DAMPING ~ YAW AMPLITUDE FOR VARIOUS W_d FOR BASIC CONTAINER (1·0·4·0·4) SET 15° NOSE DOWN.

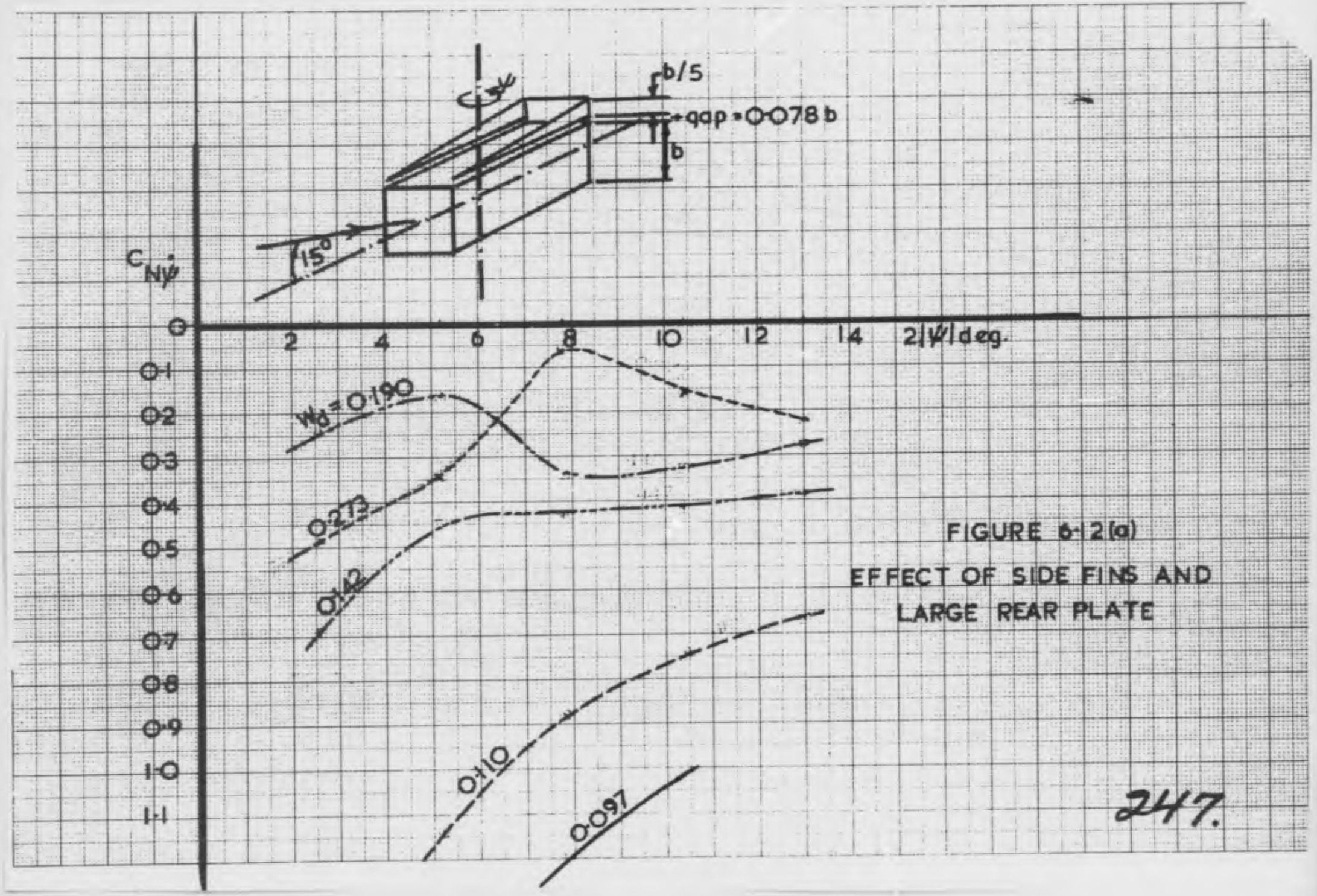

FIGURE 6·12(a)
EFFECT OF SIDE FINS AND
LARGE REAR PLATE

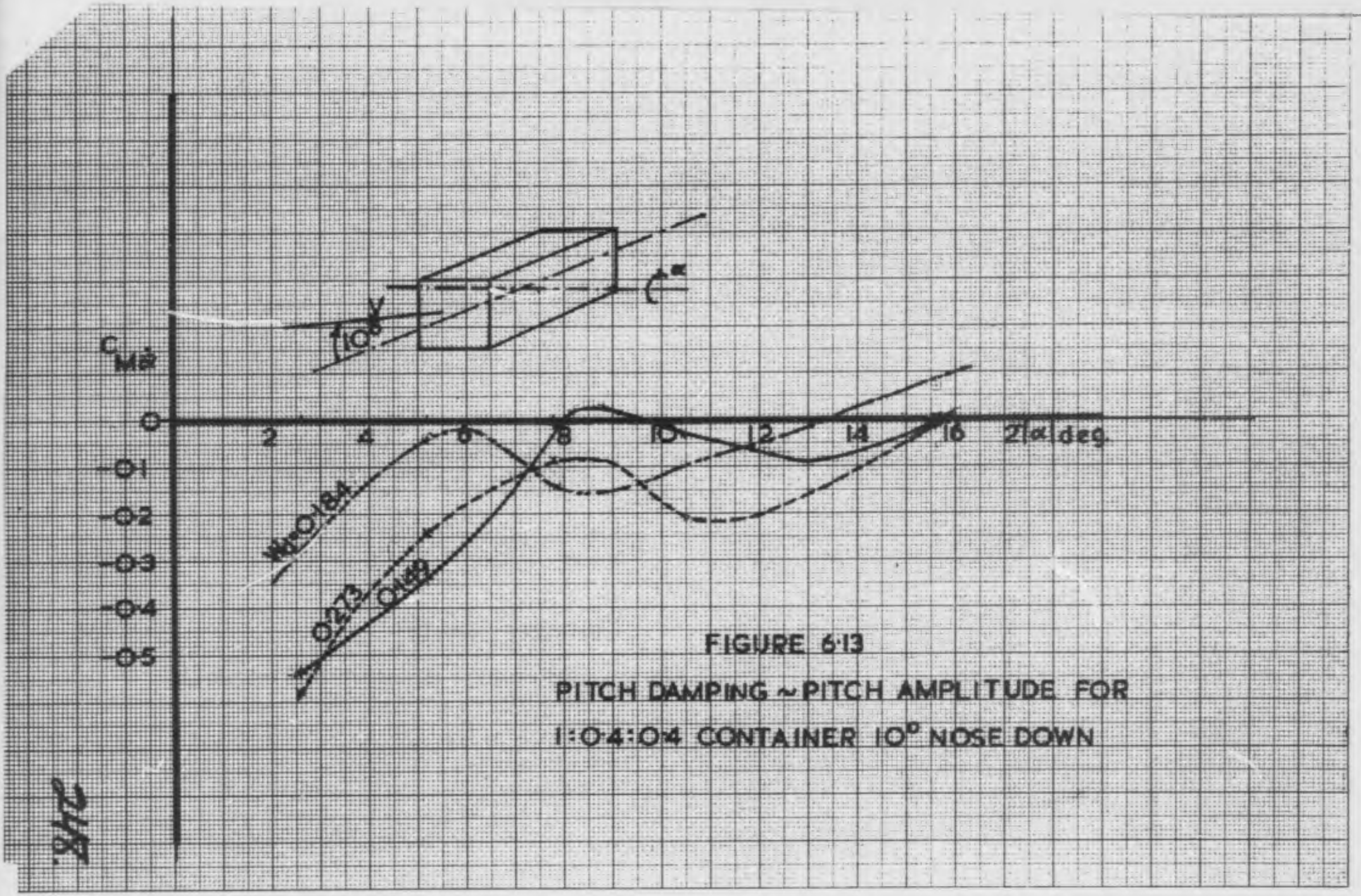

FIGURE 6·13

PITCH DAMPING ~ PITCH AMPLITUDE FOR

1:0·4:0·4 CONTAINER 10° NOSE DOWN

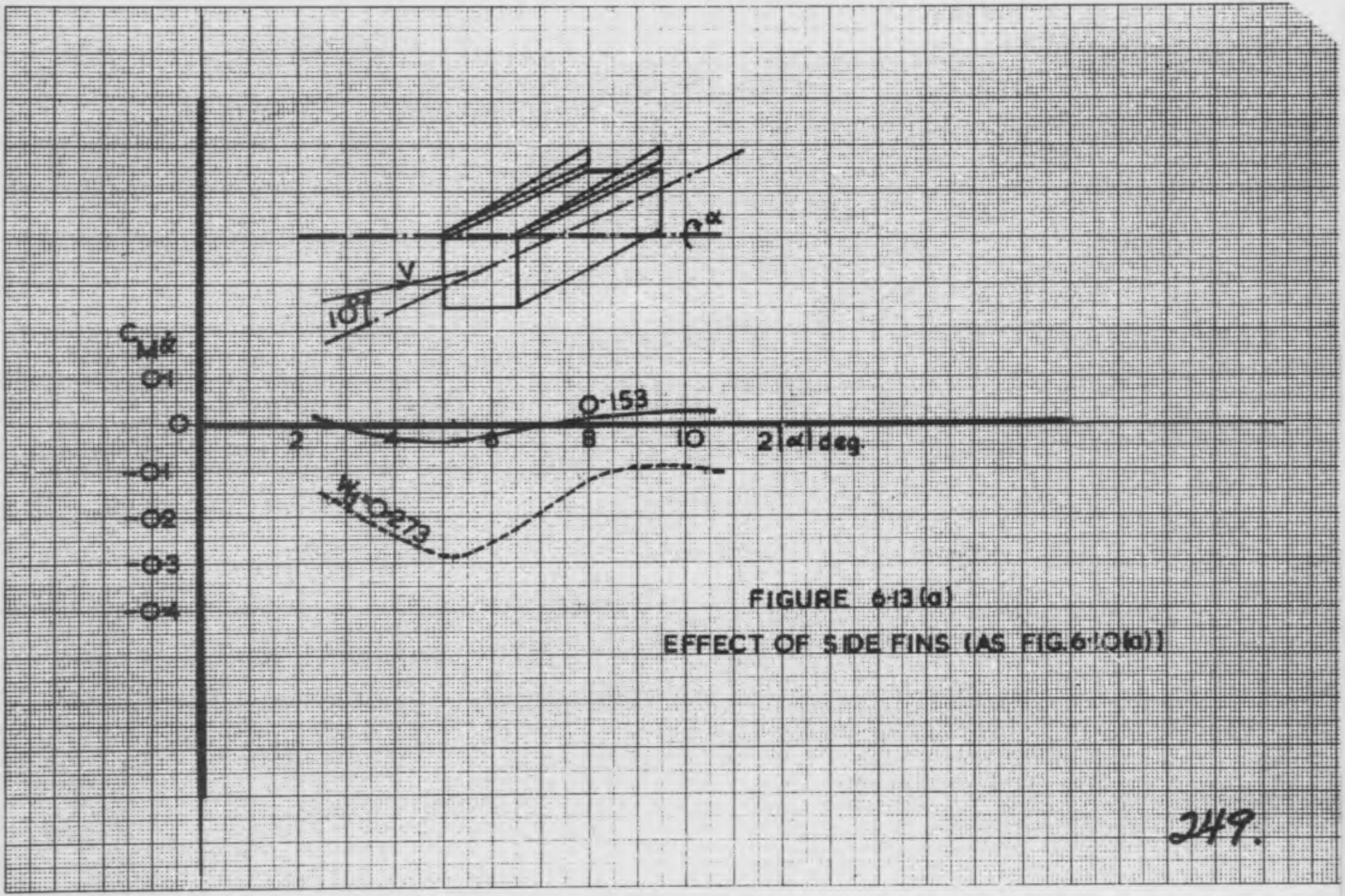

FIGURE 6·13 (a)

EFFECT OF SIDE FINS (AS FIG. 6·10 (a))

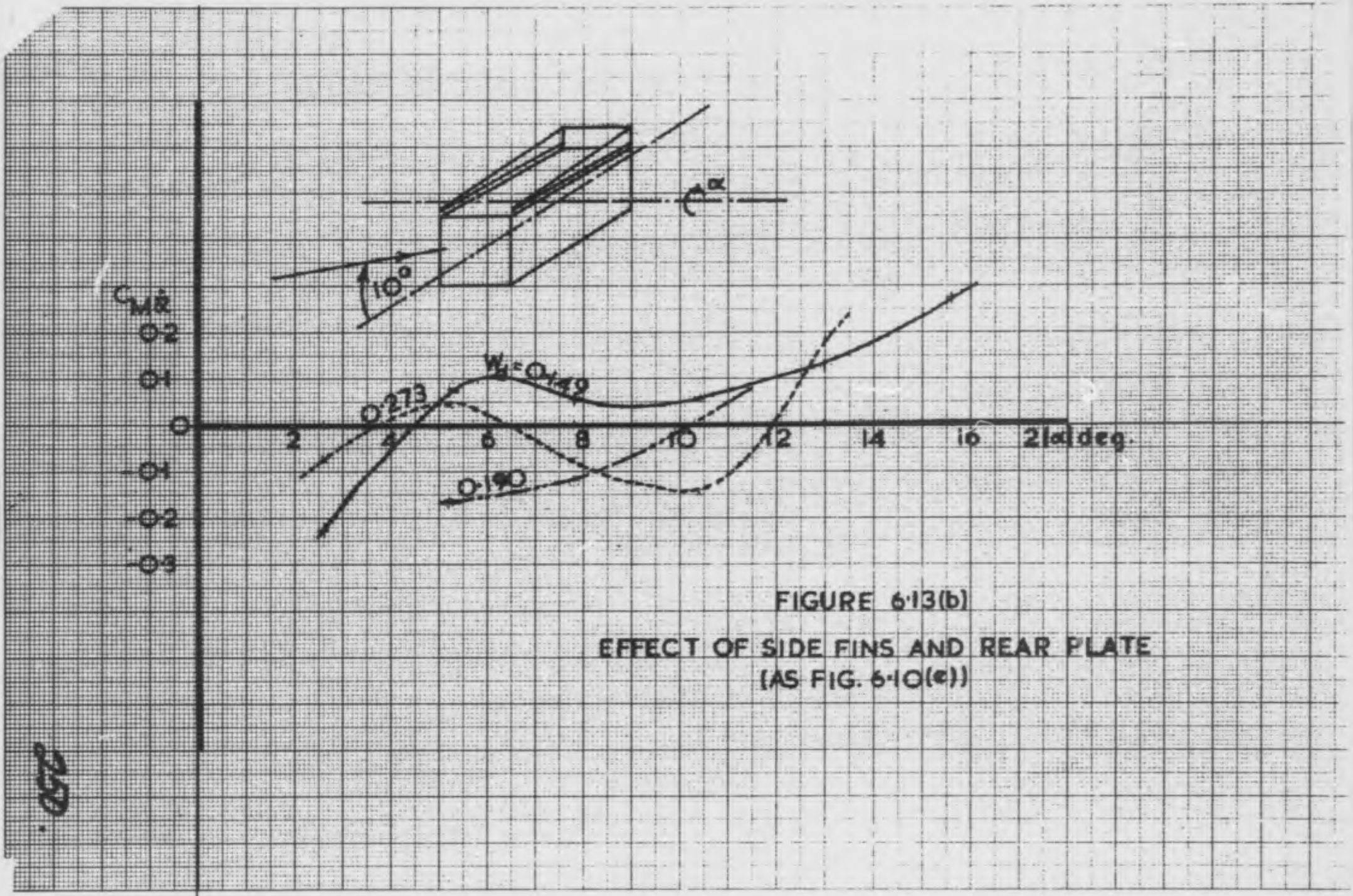

FIGURE 6·13(b)

EFFECT OF SIDE FINS AND REAR PLATE
(AS FIG. 6·10(c))

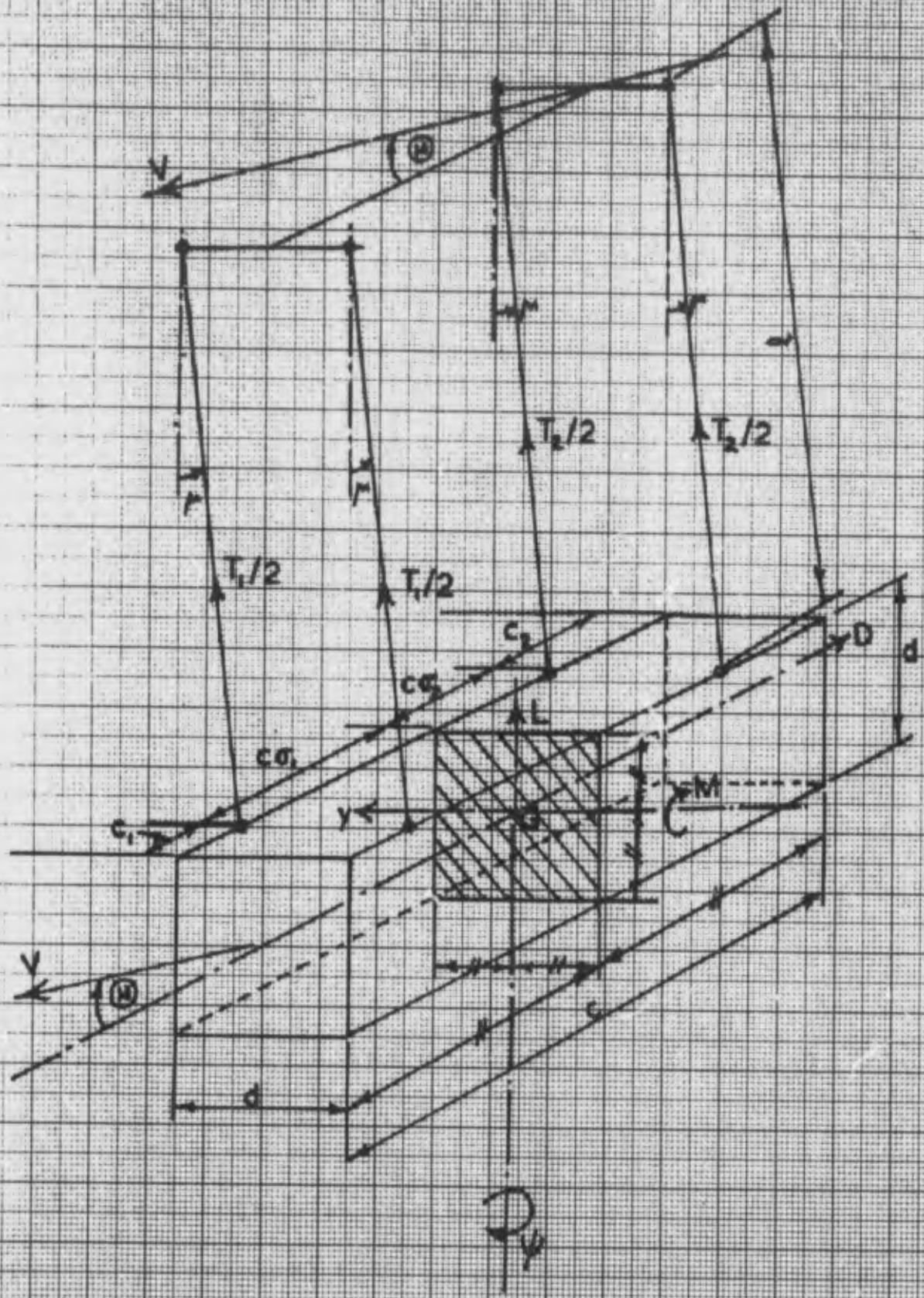

FIGURE 6.14

FOUR STROP PARALLEL CONTAINER SUPPORT

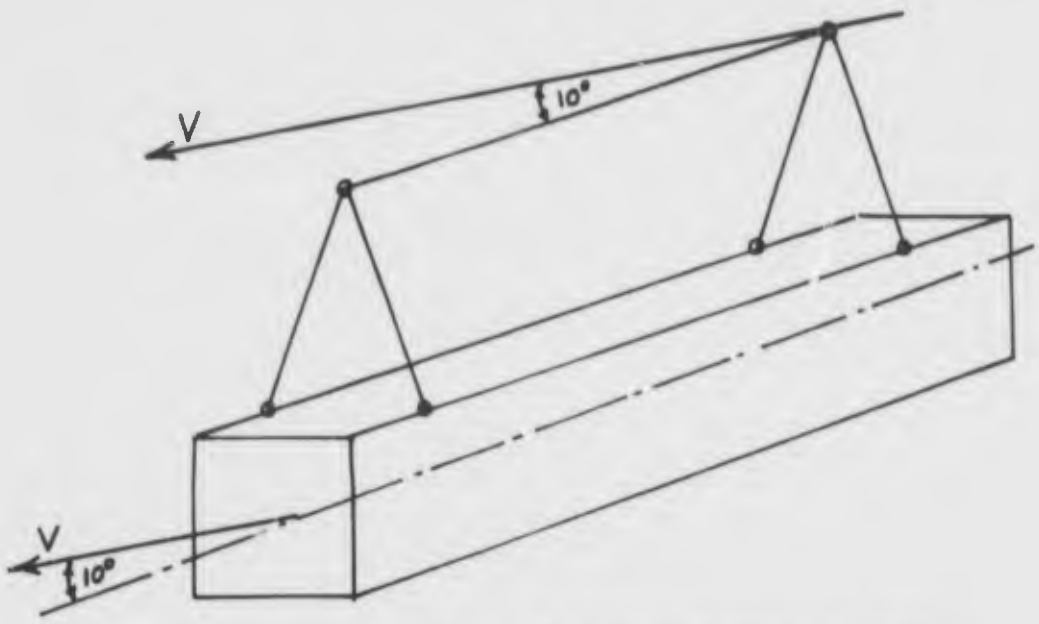

(i) 'V' STROP (AFTER SHELDON) WITH 10° NOSE-DOWN ATTITUDE.

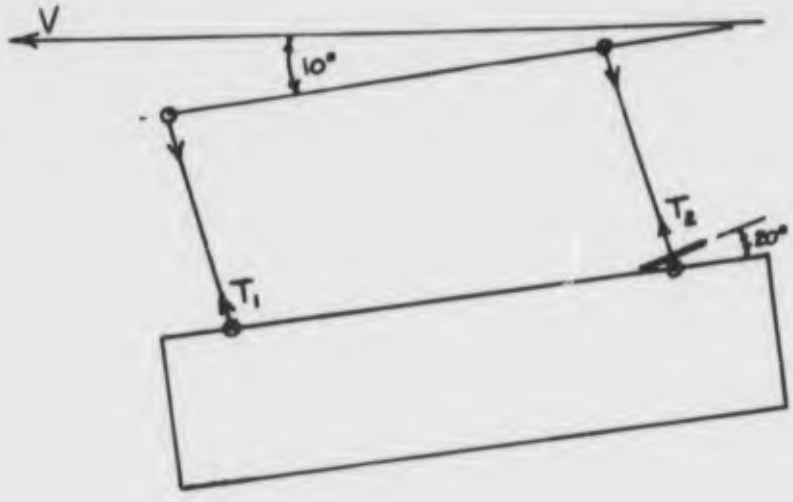

(ii) 'V' STROP IN ELEVATION VIEW WITH 20° DEFLECTOR PLATE TO MAINTAIN T_2

FIGURE 6·15

STROPPING TO ELIMINATE LATERAL FLUTTER AND DIVERGENCE

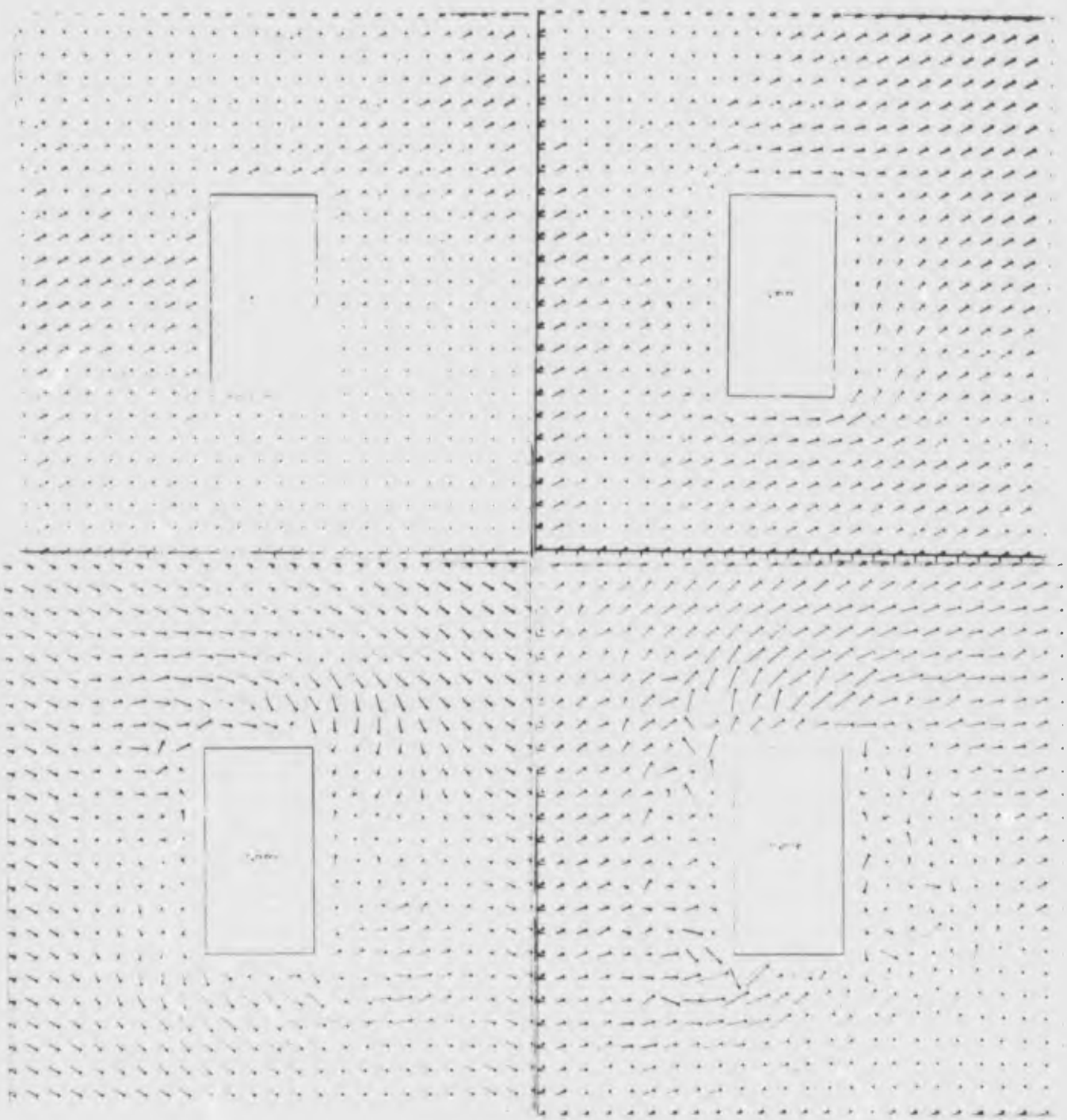

FIGURE 7·1

FLOW PATTERNS AROUND STATIONARY 2·D BOX FROM NAVIER·STOKES SOLUTION FOR 'STARTING FLOWS'.

(time from starting condition inset)

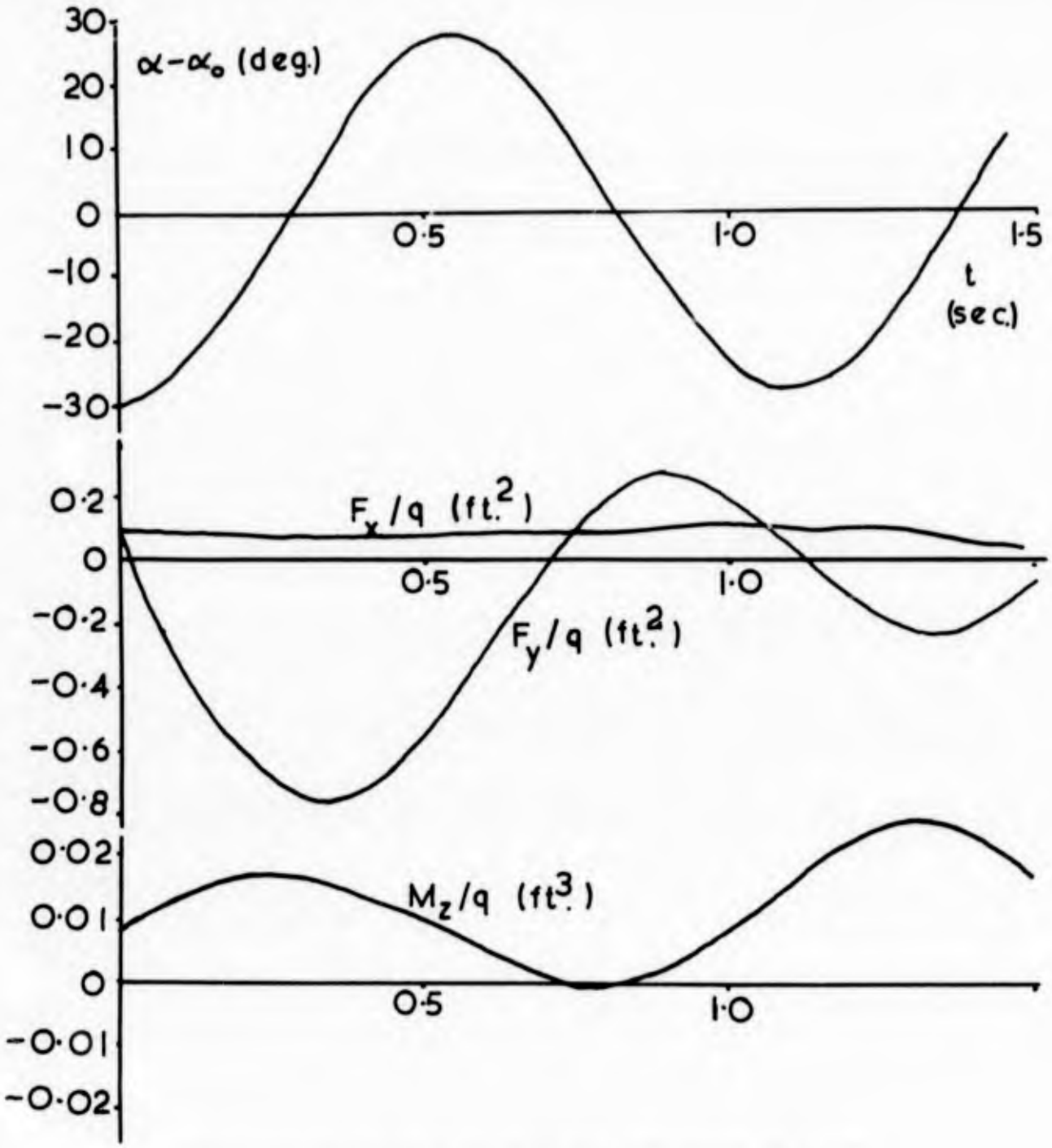

Results obtained after 3·5 seconds of flow
at $U_\infty = 1{\cdot}0$ f/s

FIGURE 7·2

FORCES AND PITCHING MOMENTS FROM THE EXPLICIT NAVIER-STOKES SOLUTION.

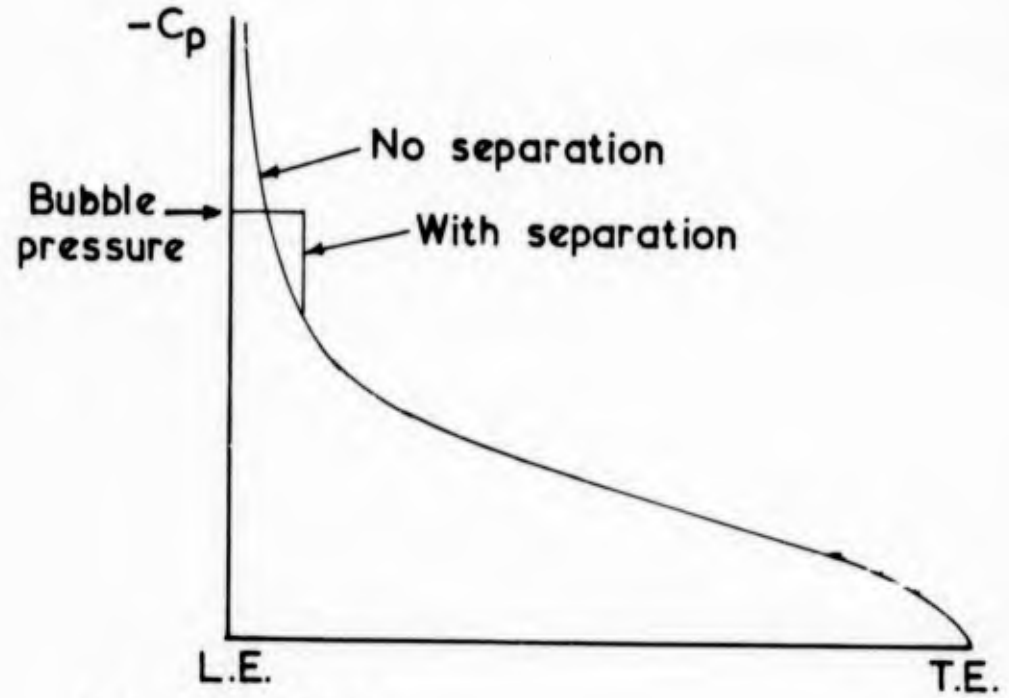

(a) AEROFOIL

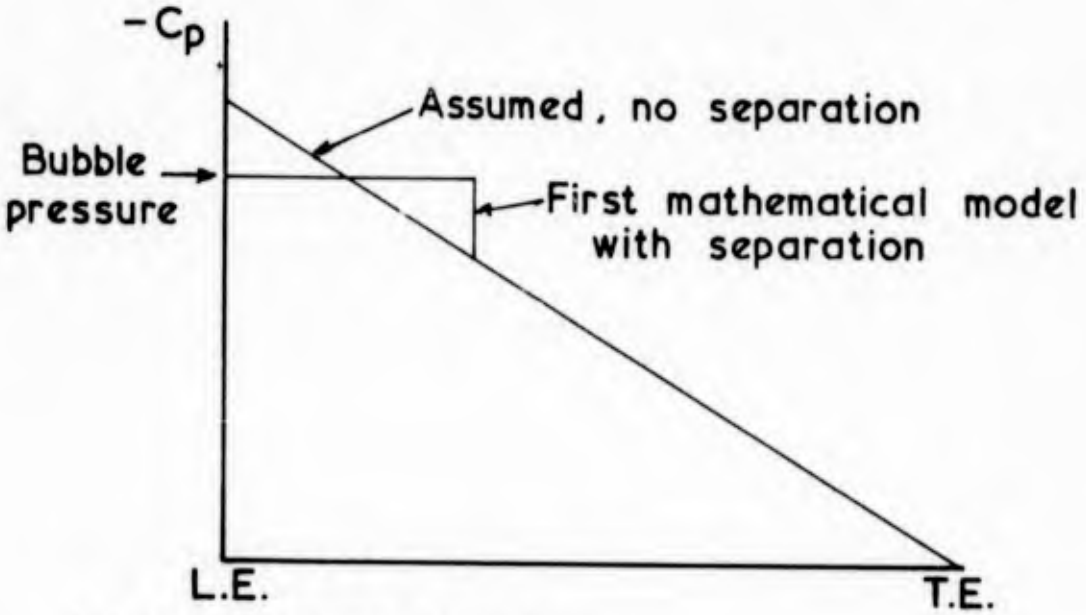

(b) CONTAINER MODEL

FIGURE 7.3 FIRST MATHEMATICAL MODEL - MODIFIED PRESSURE DISTRIBUTIONS

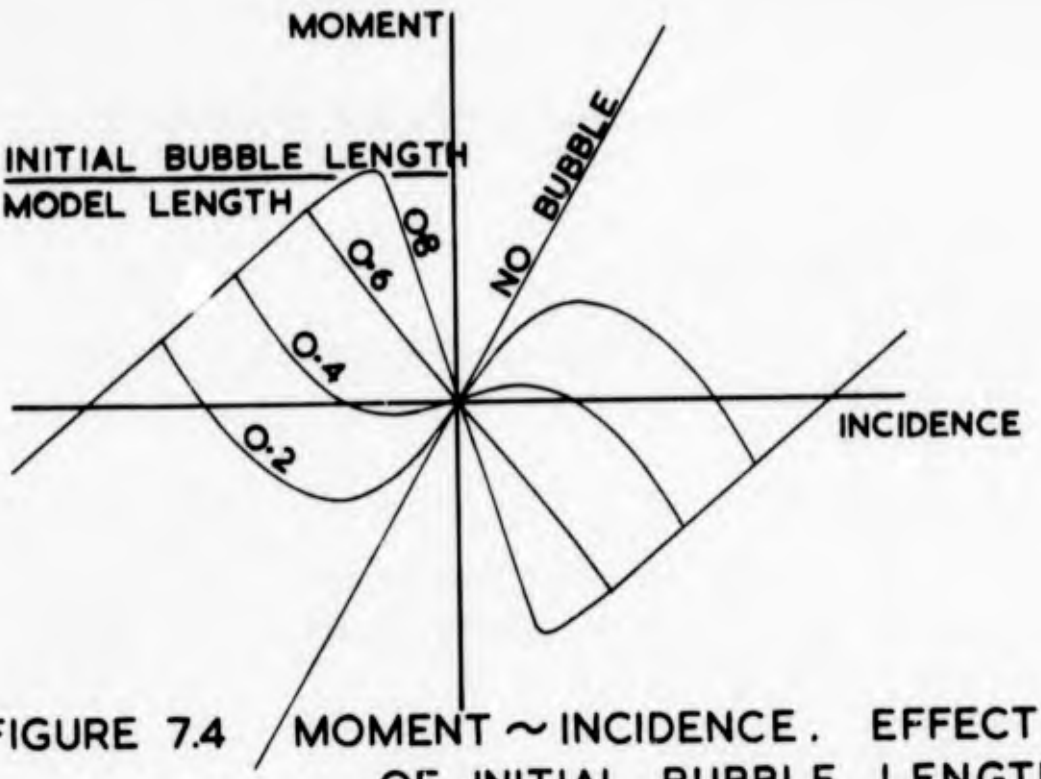

FIGURE 7.4 MOMENT ~ INCIDENCE. EFFECT OF INITIAL BUBBLE LENGTH

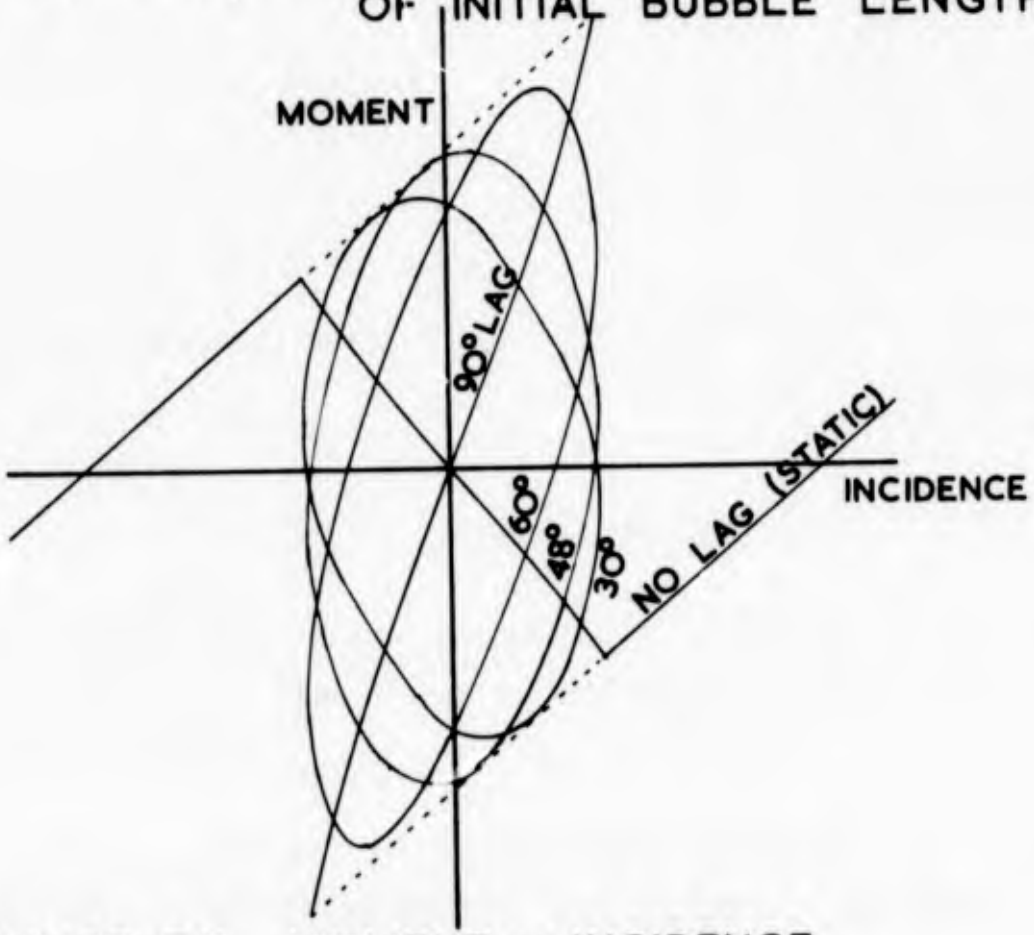

FIGURE 7.5 MOMENT ~ INCIDENCE. EFFECT OF PHASE LAG

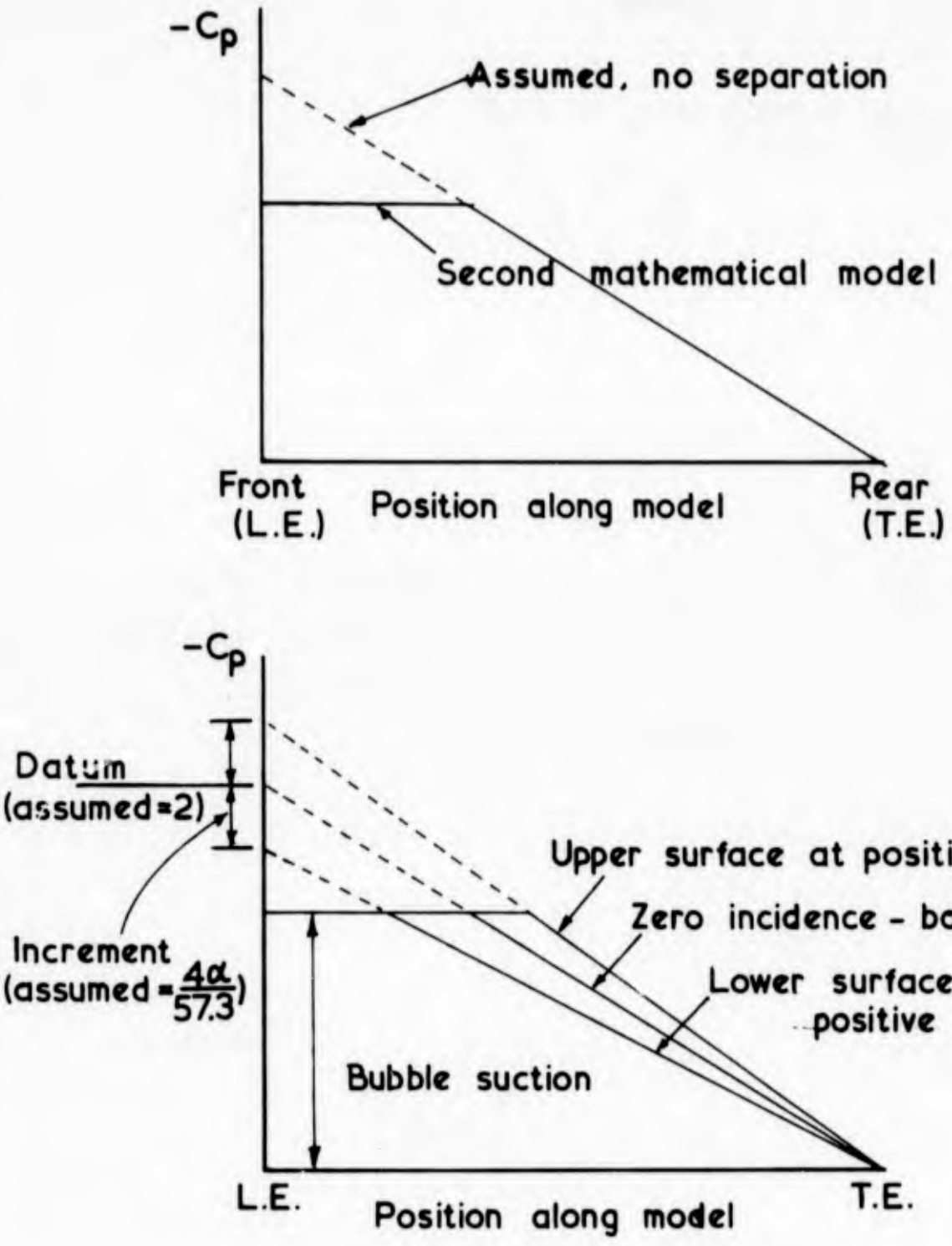

FIGURE 7.6 SECOND MATHEMATICAL MODEL - MODIFIED PRESSURE DISTRIBUTIONS - STATIC

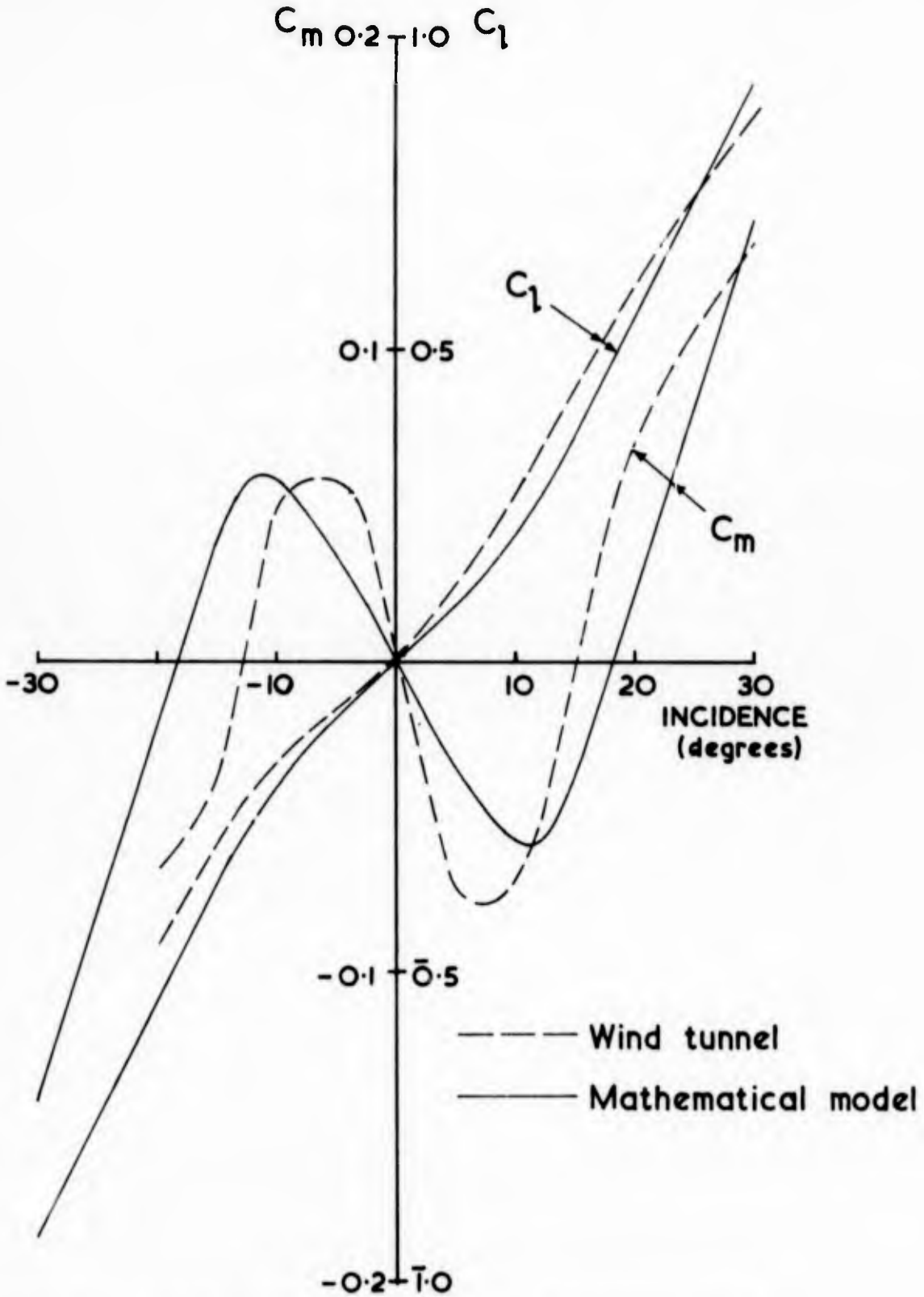

FIGURE 7.7 COMPARISON WITH EXPERIMENT

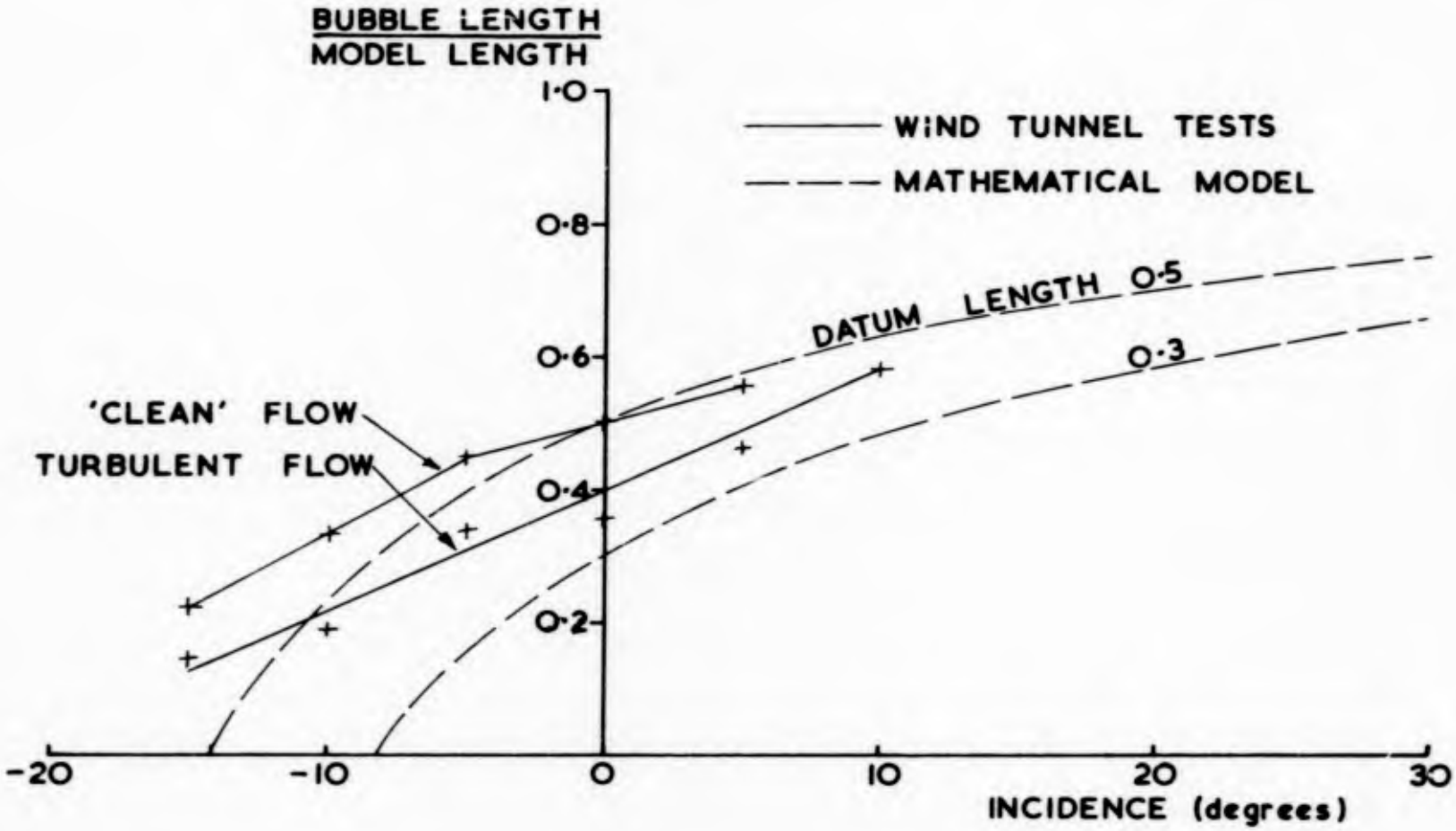

FIGURE 7.8 VARIATION OF BUBBLE LENGTH WITH INCIDENCE

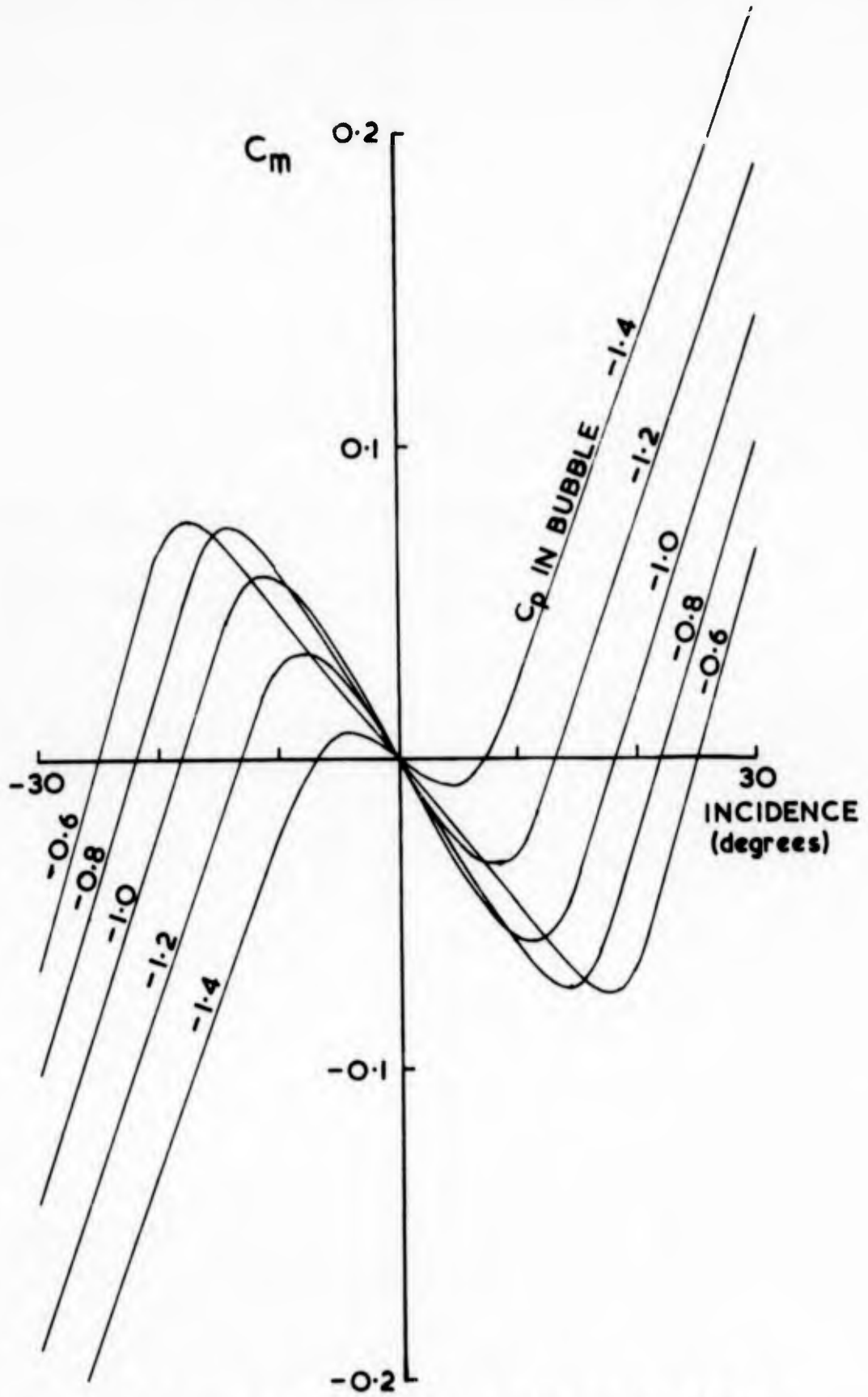

FIGURE 7.9 EFFECT OF BUBBLE SUCTION

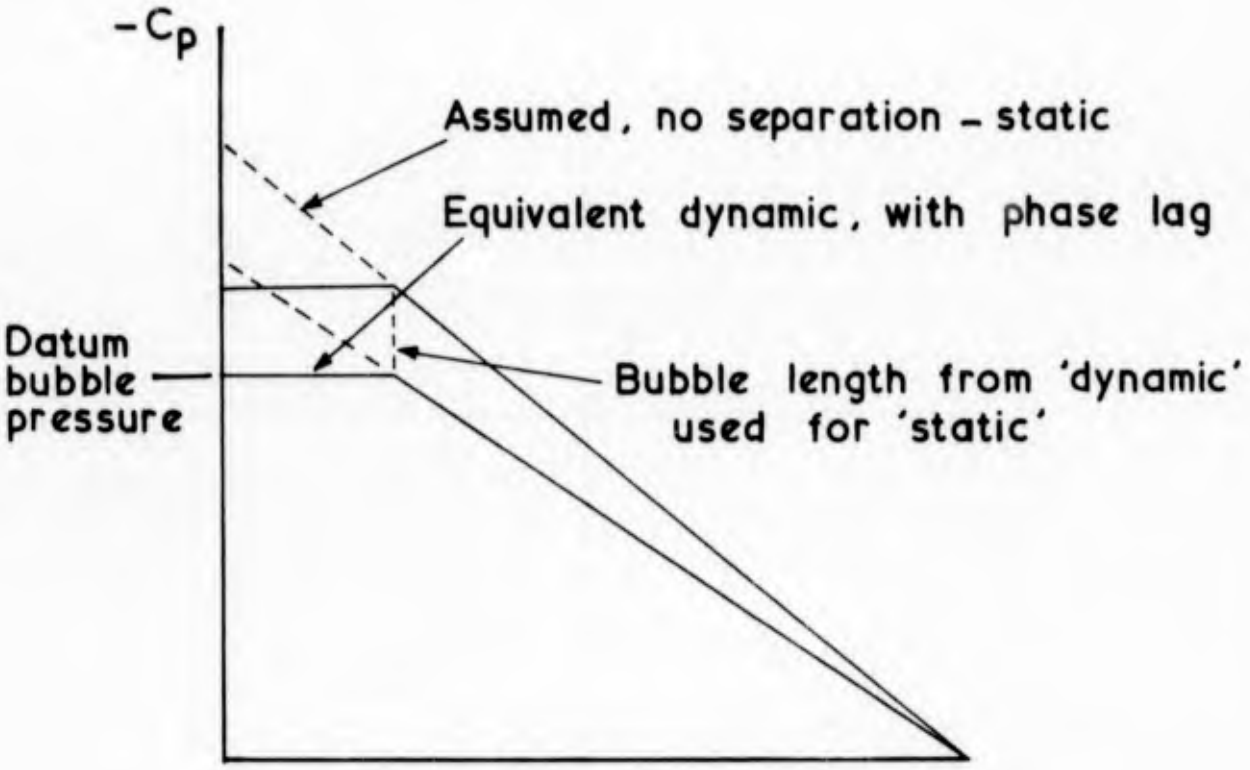

FIGURE 7.10 EFFECT OF MOTION ON BUBBLE PRESSURE

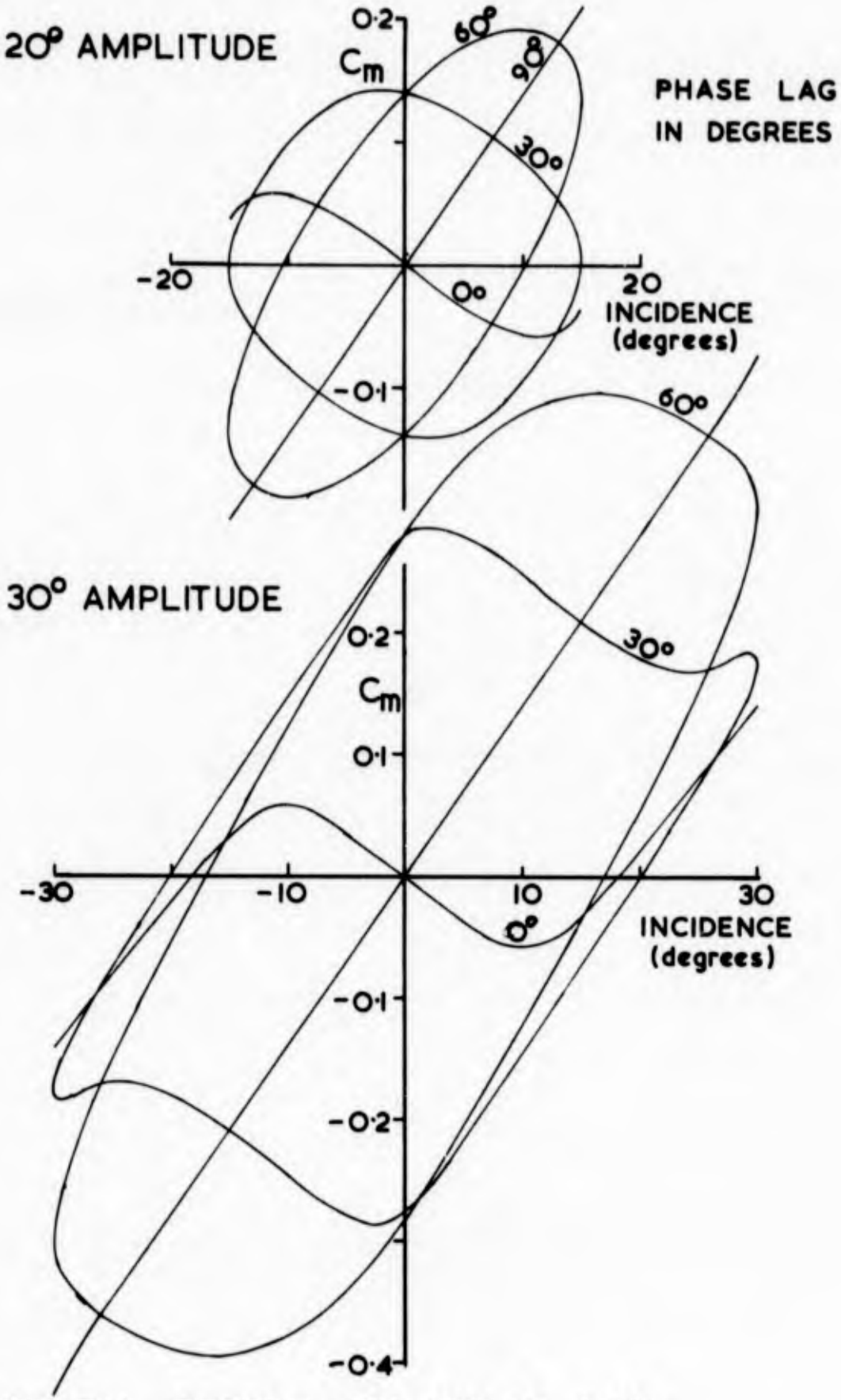

FIGURE 7.11 EFFECT OF PHASE LAG

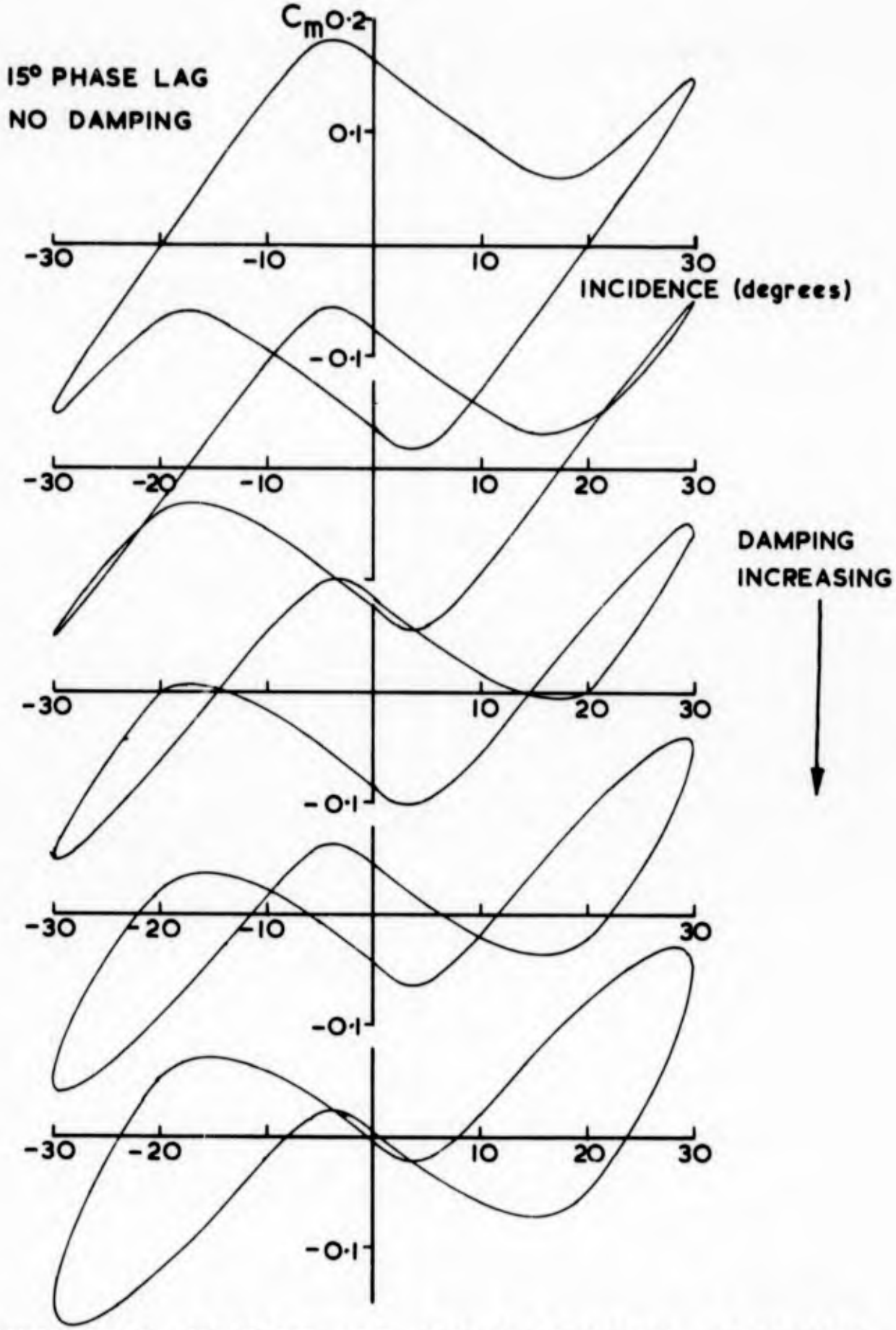

FIGURE 7.12 EFFECT OF CONVENTIONAL DAMPING

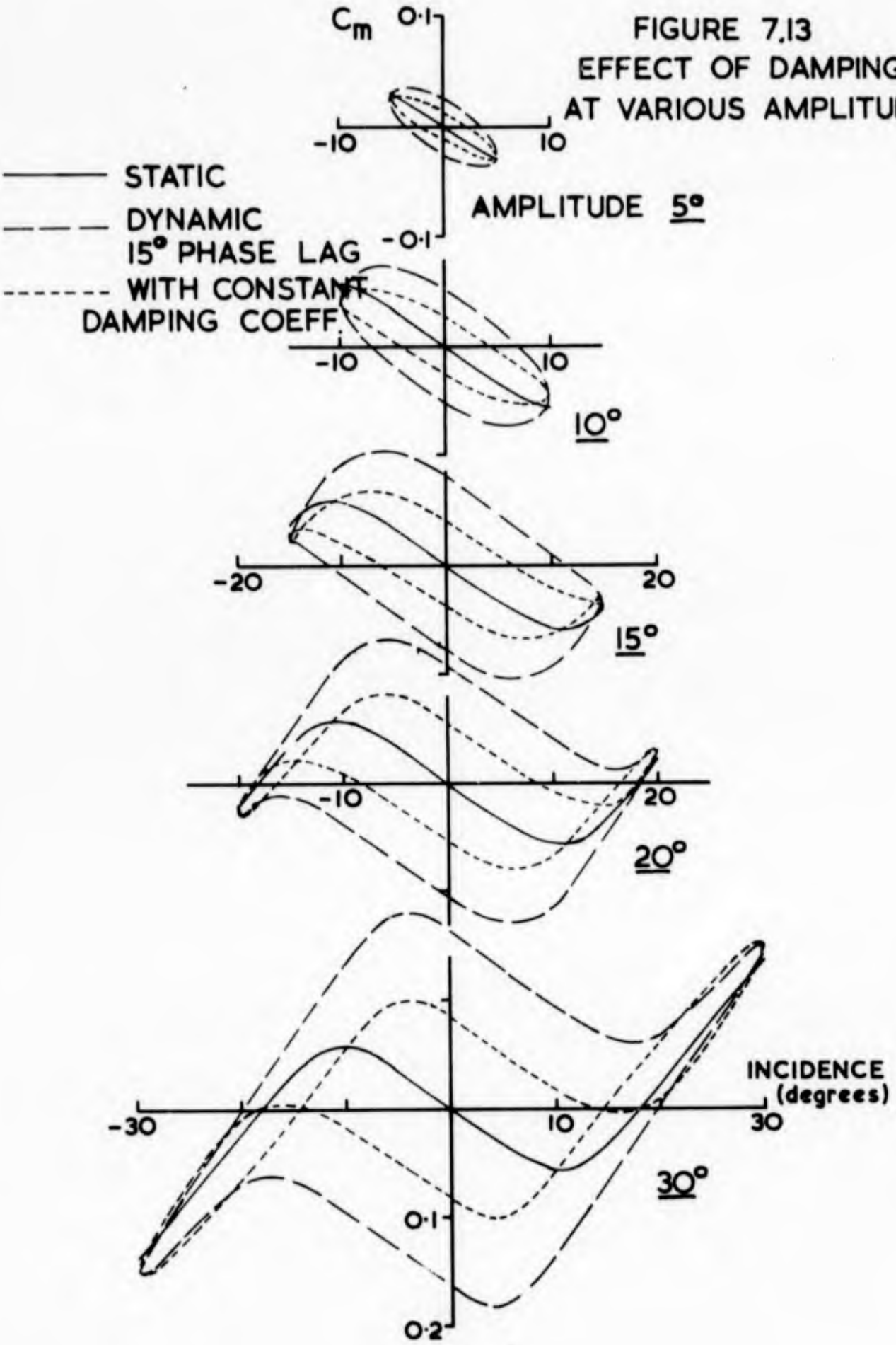

FIGURE 7.13
EFFECT OF DAMPING
AT VARIOUS AMPLITUDES

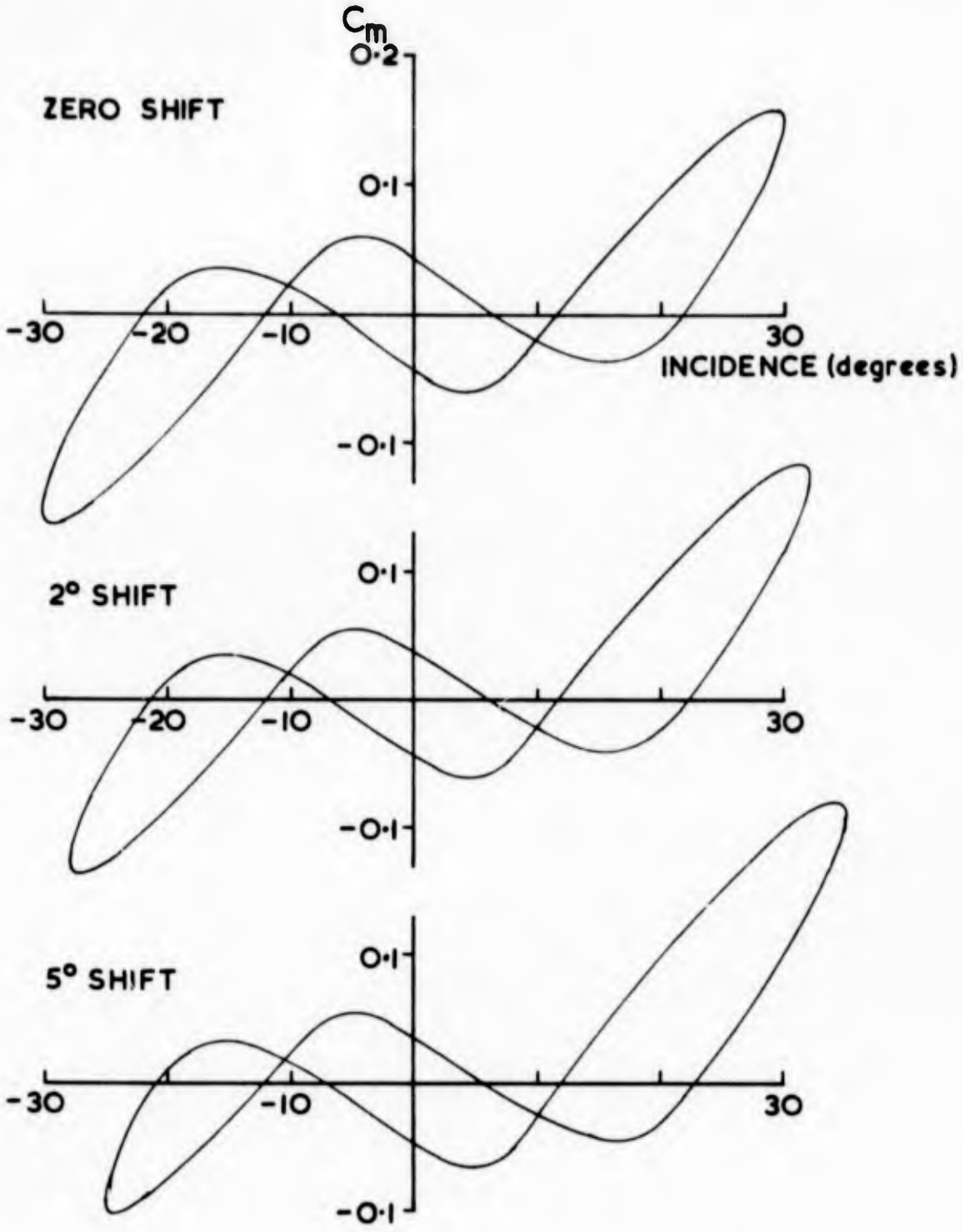

FIGURE 7.14 EFFECT OF DATUM SHIFT

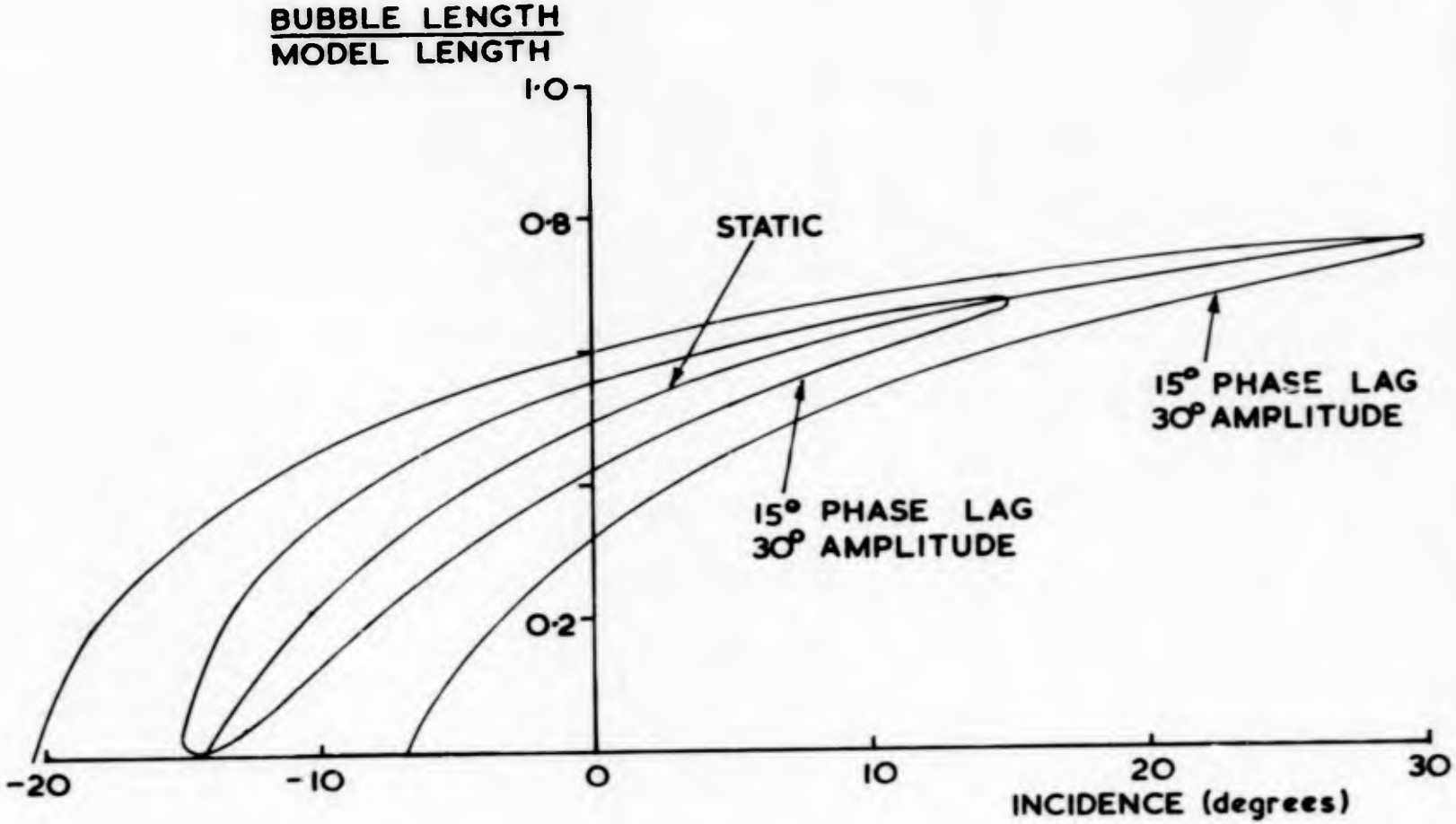

FIGURE 7.15 BUBBLE LENGTH DURING MOTION WITH PHASE LAG

Driver-Follower Crank. (See figure 8.) The follower crank angular position is given by 4.

$$\psi = \alpha_1 + \alpha_2$$

$$\alpha_1 = \tan^{-1}\frac{\sin\theta}{C + \cos\theta}$$

$$\alpha_2 = \cos^{-1}\frac{K^2 + 2C\cos\theta}{2BL}$$

$$K^2 = 1 + B^2 + C^2 - A^2$$

$$L^2 = 1 + C^2 + 2C\cos\theta$$

$$M^2 = K^2 + 2C\cos\theta$$

$$S^2 = \sqrt{4B^2L^2 - M^4}$$

$$\psi = \tan^{-1}\frac{\sin\theta}{C + \cos\theta} + \cos^{-1}\frac{K^2 + 2C\cos\theta}{2BL} \qquad (1)$$

Differentiating equation 1 with respect to time yields the following equation for the velocity of the follower crank:

$$\frac{d\psi}{dt} = \frac{d\theta}{dt}\left[\frac{1}{L^2}(C\cos\theta + 1) + \frac{C\sin\theta}{S^2}\left(2 + \frac{M^2}{L^2}\right)\right]$$

A second differentiation yields an expression for the angular acceleration of the follower crank:

$$\frac{d^2\psi}{dt^2} = \frac{d^2\theta}{dt^2}\left[\frac{1}{L^2}(C\cos\theta + 1) + \frac{C\sin\theta}{S^2}\left(2 + \frac{M^2}{L^2}\right)\right]$$
$$+\left[\left(2 + \frac{M^2}{L^2}\right)\left(\frac{2C^2\sin^2\theta\,(2B^2 - M^2)}{S^4} + \frac{C\cos\theta}{S^2}\right)\right.$$
$$\left.-\frac{2C^2\sin^2\theta}{L^2S^2}\left(1 - \frac{M^2}{L^2}\right) - \frac{C\sin\theta}{L^2}\left(1 - \frac{2(C\cos\theta + 1)}{L^2}\right)\right]\left(\frac{d\theta}{dt}\right)^2.$$

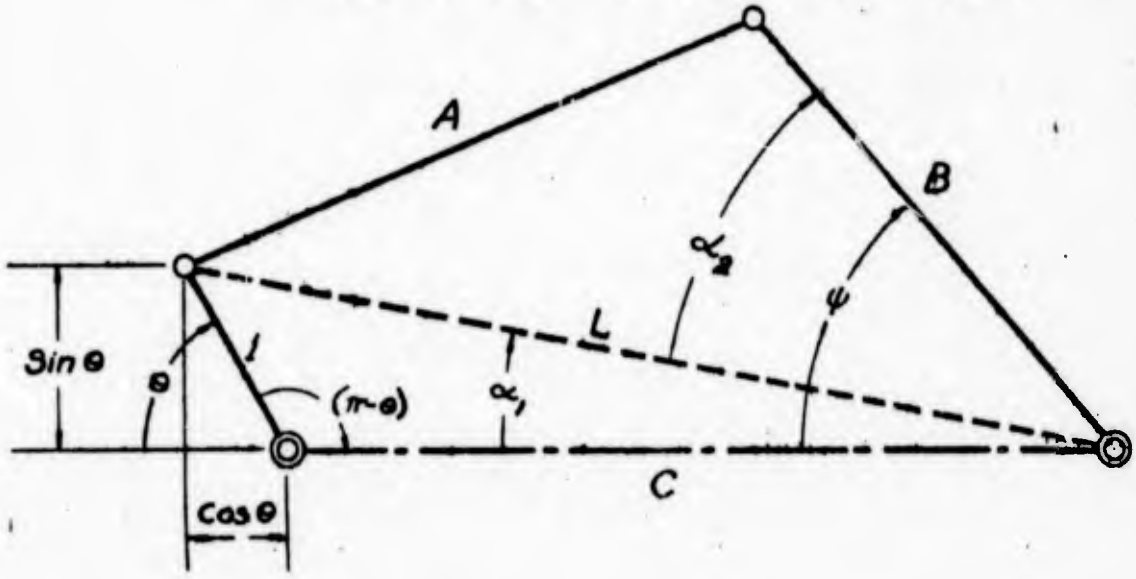

FIG A2.1

——— Experimental Trace
------ Theoretical Trace

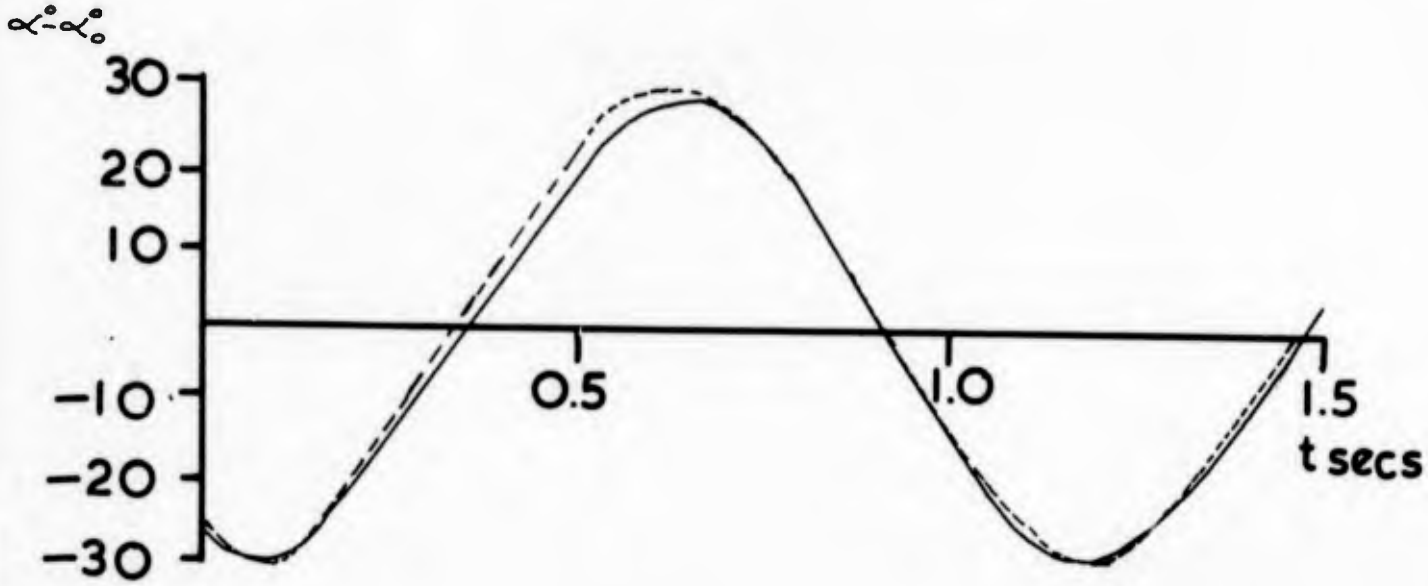

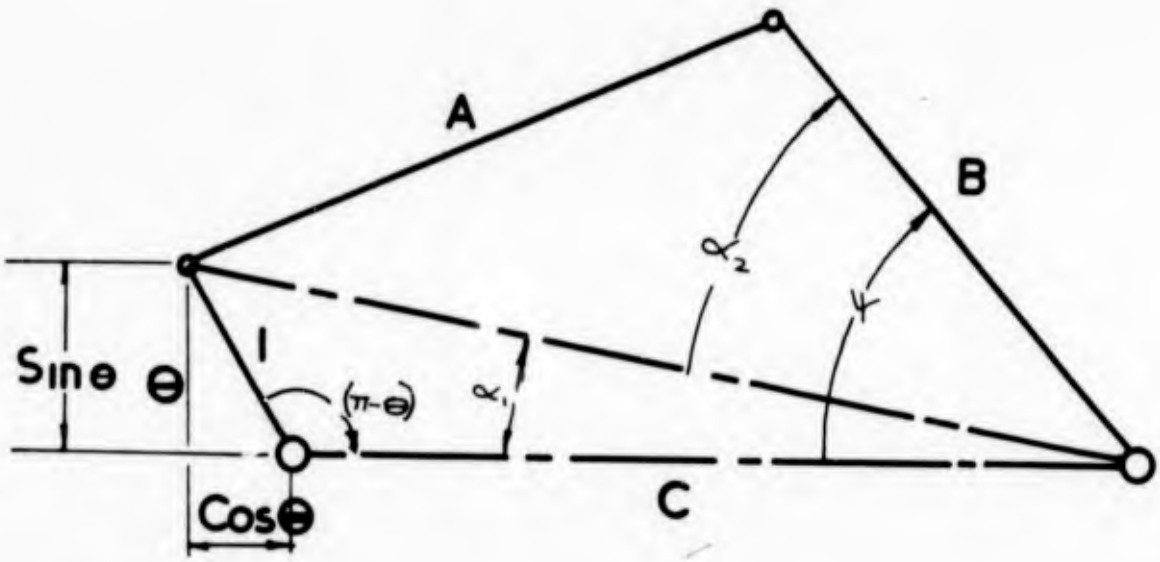

A/D=7.0
B/D=2.05
C/D=7.75
D=2.0

FIG A 2.2

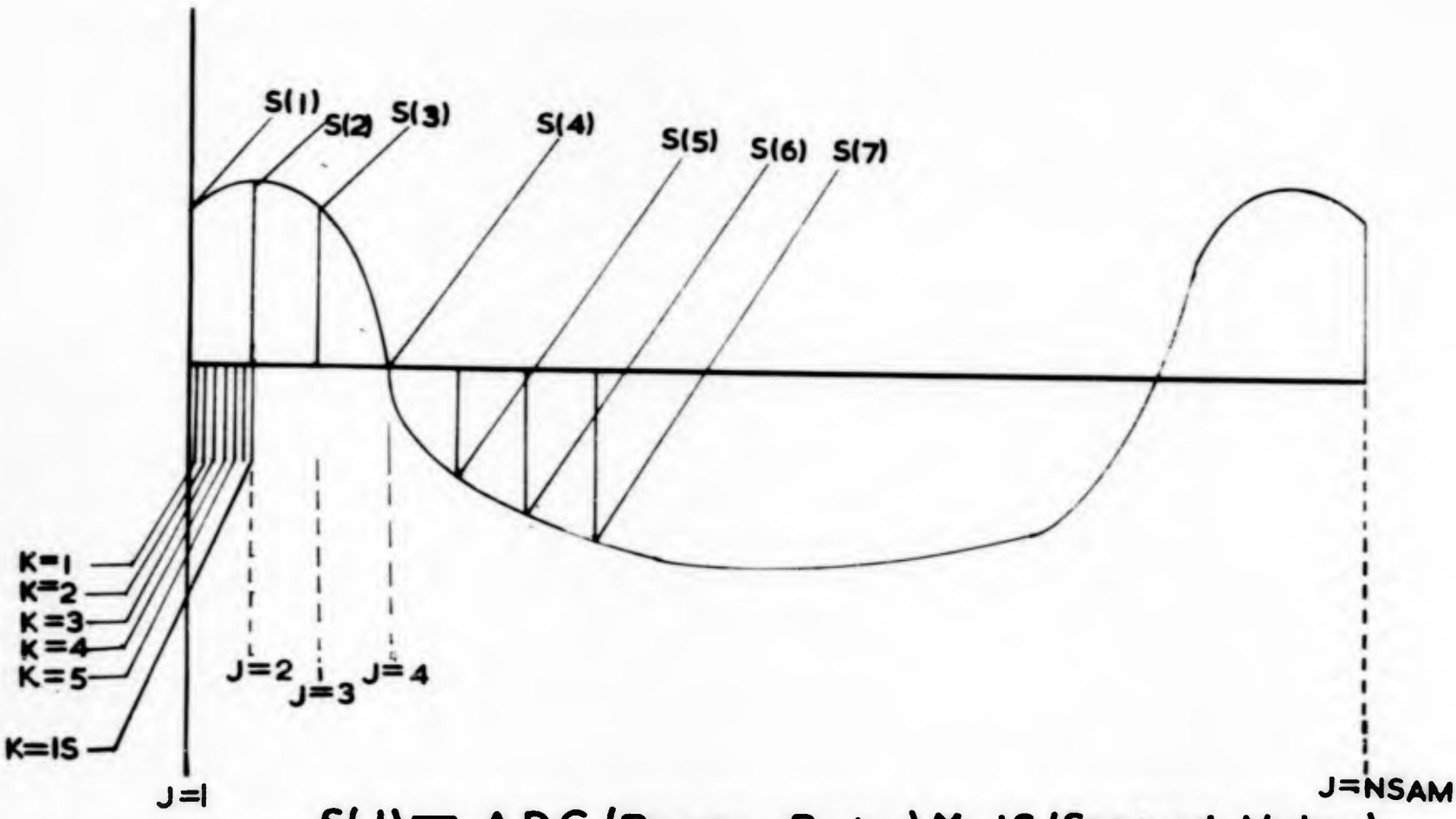

S(J) = A.D.C.(Pacer Rate) X IS (Spread Value)

TOTAL SIGNAL TIME = A.D.C.(Pacer Rate) X IS X NSAM

FIG A 3·1